

THIS WEEK

EDITORIALS

WORLD VIEW Go on, find and unleash your hidden capitalist **p.133**



TANGLED WEB The problems of invasive species control **p.135**



9/11 LEGACY The lingering health impacts of the New York attacks **p.136**

A very Turkish coup

Scientists around the world should protest efforts by the government of Turkey to erode academic autonomy. And the wider world should note the threat to democracy.

On the eve of a week-long holiday to celebrate the end of the fasting period of Ramadan, the Turkish government executed an extraordinary scientific coup. On 27 August, it issued a decree with immediate effect, giving itself tighter control of Turkey's two main scientific organizations: the funding agency TÜBİTAK and the Turkish Academy of Sciences (TÜBA), the governance of which is now so altered that it can no longer be considered an academy at all.

The move has startled and appalled Turkish scientists. It should also sound an alarm bell throughout Turkish society. The government of Prime Minister Recep Tayyip Erdoğan is also taking greater control of other sectors through a series of decrees requiring no parliamentary debate. In the past few weeks, for example, it has brought under direct government supervision ten previously independent regulatory bodies, including some financial institutions and media regulators, as well as the Natural and Cultural Assets Conservation Committee, which determines environmentally protected zones.

TÜBİTAK, the Scientific and Technological Research Council of Turkey, was already close to the government. Now that relationship has been reinforced and institutionalized. A triumvirate of president, prime minister and science minister will appoint some members of TÜBİTAK's decision-making scientific board, and nominate its president and two vice-presidents. The triumvirate lost no time, and on 30 August it replaced the incumbent president with electrical engineer Yücel Altunbaşak, rector of the TOBB University of Economics and Technology in Ankara. The government will also have much more influence over the choice of other board members.

At least TÜBİTAK is a state agency. It matters much more that the government is taking over TÜBA, which was founded in 1993 as an autonomous organization under the patronage of the prime minister. It has nearly 82 full members (from a total membership of 140) and has been doing all the things academies should do — including offering scientific advice to the government, publishing reports, and giving scholarships and awards. TÜBA has also been active in international organizations of academies such as the InterAcademy Panel, ALLEA (the organization of European academies) and the Association of Academies of Sciences in Asia (AASA).

A June decree transferred TÜBA to the Ministry of Science, Industry and Technology. The current decree raises the number of full members to 150. One-third will be appointed by the government and one-third by YÖK, the Higher Education Council, most of whose members are in turn appointed by the government or president.

The current decree also says that TÜBA will be involved in creating a series of basic-research institutes. What this means is unclear, because no budget for institutes has been announced, and the government has recently effectively closed down the only non-university basic-research institute, the Feza Gürsey Institute (see *Nature* **477**, 33; 2011). If the intention to create basic-research institutes were sincere, it would be a welcome counterbalance to this government's naïve

encouragement of only applied research. But the academy would not be the right place for them. The Soviet model of linking institutes to national academies has been discredited, and post-Soviet countries quickly moved to separate the entities.

The government has made a big mistake in interfering with TÜBA's membership. Every democratic country requires an independent academy to provide independent scientific advice. But then this government shows little respect for expert advice. It did not consult the scientific community (or even its political opposition) on the wisdom of the move — just as it didn't consult when it created a catastrophic law last year (see *Nature* **464**, 478; 2010) intended to regulate the use of genetically modified plants, but which unintentionally crippled all molecular biology research. (Scientists continue to work by ignoring the law.)

The academy is appealing to President Abdullah Gül to reverse the decree. Academies all around the world should write to Gül too. Many TÜBA members say that if this approach fails, they will resign as soon as the government's first appointments are made. They would be right to do so. At this point, international organizations of academies should formally derecognize TÜBA on the grounds that it no longer meets the membership criteria of self-governance and appointment solely on scientific merit.

Scientists around the globe need to respond to this. Although the fate of one academy may seem small on the world stage, it is symbolic of a general anti-democratic shift in a country that is pivotal in world politics. The takeover must be challenged. ■

Heavy weather

Severe storms make the public think of climate change. Scientists must work to evaluate the link.

Extreme weather makes news, as was demonstrated last month by the blanket coverage of the devastation caused to the east coast of the United States by Hurricane Irene. But was the prominence of the story a feature of modern media hype in a rolling-news world? Hardly. According to a *New York Times* analysis, when Hurricane Andrew made landfall in Florida in 1992 and killed 22 people, it received twice the traditional news coverage that Irene did.

What is new is that coverage of extreme weather is now often accompanied by a question: is this a consequence of climate change? This question was raised frequently after Hurricane Katrina smashed through New Orleans in 2005. Most climate scientists responded

equivocally, as scientists do: climate is not weather, and although all extreme weather events are now subject to human influence, global warming driven by greenhouse gases cannot be said to 'cause' any specific manifestation of weather in a simple deterministic sense.

Is that response enough? The question, after all, seems fair, given the dire warnings of worsening weather that are offered to the public as reasons to care about global warming. It may irritate some scientists, but in fact the question can be seen as a vindication of their efforts to spread the message that the climate problem is a clear and present danger. Most people associate the climate with the weather that they experience, even if they aren't supposed to. And they are right to wonder how and why that experience can, on occasion, leave their homes in pieces.

Given the growing interest, it is a good sign that scientists plan to launch a coordinated effort to quickly and routinely assess the extent to which extreme weather events should be attributed to climate change (see page 148). The ambitious idea is in the early stages, and its feasibility is yet to be demonstrated. It will require funding, access to climate data from around the world and considerable computer time. Funding agencies and climate centres must provide the necessary support.

As operational climate-attribution systems develop, it is important that they do not remain purely an academic exercise. To reach out to the public, attribution scientists could do worse than to ally themselves with meteorologists — including commercial providers of weather forecasts — to explain how climate change affects the risk of extreme weather. There is, after all, a lot of scope for the makers and presenters of daily weather reports to inform their listeners and viewers more solidly about consequences of climate change than they have chosen to do in the past.

Climate scientists, too, have an obligation to provide more coherent

answers to queries (or doubts) as to how global warming influences our weather. An attribution system with ample resources, running in near real time, could prevent scientists' answers to those questions seeming either too cautious or too alarmist and speculative. It could also prevent the public from getting the (false) impression that climate

"Most people associate the climate with the weather that they experience, even if they aren't supposed to."

research is confined to the virtual world of climate models and has little to offer when it comes to current reality, or that climate science is a quasi-experimental field that yields scary but mostly unverifiable results. The service's broad integration into people's daily lives, through the old and new mass media, would be a good way to seed greater acceptance of climate scientists' actual services to

society and the problem of climate change.

There are constraints here. Attribution is only as good as the models and statistics that power it — and the various existing climate models project different trends in future extremes in some regions. There is a lack, or poor availability, of long-term observational records, and of climate data with high spatial and temporal resolution. And however it develops, climate attribution will remain rooted in probabilities. Not even the most thorough study can work out with absolute confidence the exact fingerprint of global warming in a given weather event.

What about Irene, then? A concerted attribution effort should help to resolve, in the not-so-distant future, the ongoing controversy over the effect of climate change on hurricane formation. Whatever the result, if the exercise can prevent people from building houses along the most vulnerable coastlines, it will be worth the effort. ■

Brain burdens

Europe's shocking statistics on neurological and mental disorders demand a shift in priorities.

Research to combat diseases, one would think, would be funded in proportion to the burden inflicted on the population. The reality is very different — witness the disparity between the huge burden caused by diseases in the developing world and the scant resources for research to tackle them.

Another disparity exists, and it is universal: the significant burden of mental and neurological illnesses of the human brain compared with the small proportion of research funds available to understand and treat them. Unlike cardiovascular disease and cancer, in most cases the burdens of brain disorders tend to manifest themselves in disabilities and in effects on the lives of the people afflicted and their carers, rather than in early deaths. That makes the footprint of these conditions harder to quantify.

So it is particularly valuable that a group of brain specialists and statisticians has produced a new quantification of the burden of brain disorders across 30 European countries. Building on a previous study, they assessed more disorders, analysed the literature and consulted national experts to validate emerging perspectives. The result? A conservative estimate that, in a typical year, about 165 million people — 38% of the total population of these countries — will have a fully developed mental illness (H. U. Wittchen *et al.* *Eur. Neuropsychopharmacol.* **21**, 655–679; 2011).

The shocking statistics don't end with prevalence. A good measure of disease burden is the disability-adjusted life year (DALY) — the person-years lost in a population owing to disability and shortened life. The authors establish brain disorders — both mental and neurological — as the greatest health burden on the population, comprising 23.4% of all DALYs among men and 30.1% for women.

Many more men than women have alcohol-use disorders, especially in Eastern Europe; for both dementia and unipolar depression, the ratios of women to men are around two to one. The reasons for these latter gender differences are not understood, although depression among women seems to arise especially during their child-bearing years. The estimated number of people affected by major depression in the 30 countries studied is 30 million — the single greatest burden of all human diseases.

One piece of good news that emerges from the study is that the prevalence of individual conditions, alcoholism apart, has not grown in the past five years. The truly bad news is that only one in two people with a mental condition has ever received any professional attention, and that only 10% receive "notionally adequate" treatment — and then only after much delay following initial contact with health professionals.

What does this mean for research? The message for funding is clear: priorities need to shift. In financial terms, European research on brain diseases is much less well supported than research on cancer, information technology, agriculture and other areas (see go.nature.com/hr2jqp). The state of the science is such that it requires major investment in all aspects, from fundamental neuroscience to psychological therapies.

There are subtler messages too. Research should target not only those brain diseases in which the prevalence in ageing populations will inevitably increase, such as Alzheimer's, but also the brains of young people, both healthy and ill. Many mental disorders emerge or begin to develop in the first two decades of life. Our knowledge of the healthy adolescent brain — a stage of still-active neural development — is rudimentary. The tantalizing prospect of therapeutic or preventive psychological or pharmaceutical interventions at such ages needs to be pursued.

This will give rise to ethical quandaries — probabilistic labels of future psychiatric disorders and over-reliance on drugs are problematic. But understanding how neural circuits develop in the young, and how environmental and innate influences combine to disrupt them, is one of the most fascinating and difficult scientific challenges of our time. The new study re-emphasizes just how urgent it is. ■

➔ **NATURE.COM**

To comment online,
click on Editorials at:
go.nature.com/xhunjv



Embrace failure to start up success

An ambitious US programme aims to turn scientists into entrepreneurs. Go on, says **Steve Blank**, unleash your inner capitalist.

Facebook has a lot to answer for. Thanks largely to the massive success of the social-network company started in a university dormitory, today's image of an entrepreneur is a 20-something software developer who dropped out of college.

Yet Fairchild Semiconductor, the first silicon-chip company in what would become the entrepreneurial sprawl that is Silicon Valley, was founded in 1957 by researchers: three physicists, a metallurgist, a physical chemist and a trio of engineers — electrical, industrial and mechanical.

Unnoticed by those in mainstream commerce, scientists turned out to be great capitalists. For scientists do not fear failure. Silicon Valley took the approach that failure is an inevitable consequence of experimentation. Fairchild's founders built a company in which, when you hit a wall, you backed up and tried a different path.

Today's approach to entrepreneurialism is very different. Exceptional research teams still occasionally break into business from universities, but commercialization and venture-capital investment in the twenty-first century seems to focus on the Facebooks and Twitters of this world. Venture capitalists have brought MBAs in suits into start-up firms, who implement what they learned in business school. Scientists have largely gone back to their labs.

I am part of a National Science Foundation (NSF) project that is hoping to change this. The NSF has announced a new initiative called the Innovation Corps (I-Corps), to take the most promising research projects in US university laboratories and turn them into start-ups. The I-Corps project will train scientists for business by teaching them a process that gets them back to the roots of Silicon Valley, by embracing experimentation, learning and discovery. The NSF plans to give US\$50,000 each in seed funds to up to 100 science and engineering research projects each year, which it will select on the basis of the best science with the best potential for commercial success.

Common wisdom assumes that to become entrepreneurs, scientists and engineers must know about business. Instead, the I-Corps will teach them to approach business start-ups as research projects that they can solve through familiar scientific methods. The trial-and-error approach, which is natural to research but alien to business school, has distinct advantages. MBAs approaching a start-up typically want only to execute a pre-designed business model, based on standard principles about sales, marketing and customer reaction, which they regard as facts. By contrast, scientists recognize such variables as hypotheses. And so they tend to be happier than MBAs to test their business models with empirical data — the reactions of their prospective customers. It is a truth not always universally acknowledged that no business plan survives its first interaction

with customers. And, faced with such failure, it is scientists, not MBAs, who are most able to rethink their approach.

The NSF wants the I-Corps to solve two problems. First, support for entrepreneurs varies across the United States, from the deep experience in Silicon Valley and other high-tech clusters to much less in other areas. The I-Corps aims to spread 'best national practices' around the country. Second, the NSF wants to narrow the funding gap between the lab and venture capital. The I-Corps will move the best research forward to early-stage technology and customer development, at which point it can attract private investment.

Teams will participate in a three-month class, based on the Lean LaunchPad training our group developed in the Technology Ventures Program (<http://stvp.stanford.edu>) at Stanford University, California. I-Corps teams will build their products and get out of their labs to find potential customers and understand what they need. They'll learn how

to find a business model to turn their research into a commercial success. Ultimately, we hope that they will license their intellectual property or launch a new business, after securing funds from strategic partners, investors or NSF programmes for small businesses.

The response has been overwhelming. Open to any scientist who has received an NSF grant in the past five years, the I-Corps project has already received proposals ranging from medical sensors to terahertz field-effect transistors.

Scientists have a strong pedigree as entrepreneurs. Alongside Fairchild, the first three Silicon Valley companies to go public — Varian, Hewlett Packard and Ampex — were founded and run by scientists and engineers. They signalled that investment in technology companies could be very lucrative. In the following two

decades, venture capital invested in hardware, software and silicon, and eventually in the life sciences. Few MBAs were involved. Scientists and engineers taught themselves to become marketeers, sales people and chief executives. And venture capitalists became comfortable with funding them.

The I-Corps is an experiment in reviving this culture and exploiting what US science and Silicon Valley are great at. If it works, it will change the way we bring discoveries ripe for innovation out of the university lab and into the business world, and it will be a shining beacon for other national programmes. Success will lead to more start-ups, products we couldn't imagine, and more new jobs. And if it fails? Then we back up and try again. ■

Steve Blank is a retired Silicon Valley executive, author of *The Four Steps to the Epiphany* and blogs on entrepreneurship at www.steveblank.com.
e-mail: sblank@kandsranch.com

**FACED
WITH FAILURE,
SCIENTISTS
ARE MOST
ABLE TO
RETHINK
THEIR APPROACH.**

➔ **NATURE.COM**
Discuss this article
online at:
go.nature.com/rjpm5r

SEVEN DAYS

The news in brief

POLICY

Chimp review

A petition arguing that captive chimpanzees in the United States should be reclassified from 'threatened' to 'endangered' is gaining federal traction. On 1 September, the US Fish and Wildlife Service announced that it would review the status of captive chimps in response to the petition, submitted in March 2010 by groups led by the Humane Society of the United States. If the change goes ahead, scientists would have to petition the agency for permission to use captive chimps in research, and would have to show that the experiments served chimp conservation. See go.nature.com/v1btka for more.

Quake nuclear risk

The US Nuclear Regulatory Commission plans to ask operators of all 104 of the country's commercial reactors to launch a detailed assessment of their facilities' ability to withstand earthquakes. The draft requirements, released for comment on 1 September, came as regulators analysed damage to the North Anna reactor in Mineral, Virginia, in the wake of a magnitude-5.8 earthquake across the eastern United States on 23 August. The quake shifted fuel rods and exceeded the ground motion that the facility was designed to withstand.

Polio in China

Wild poliovirus has appeared in China for the first time since 1999. China's ministry of health said last week that, in July, an outbreak had left four young children paralysed in China's westernmost province, Xinjiang. The virus' DNA matches that of strains in Pakistan, which has already recorded 77 cases of

polio this year. Global health authorities have long worried that Pakistan's inability to wipe out polio could fuel outbreaks in neighbouring countries that have already eradicated the virus (see *Nature* 473, 427–428; 2011). China's health ministry plans to vaccinate 3.8 million children in Xinjiang this month.

Iran's nuclear plant

Iran's first commercial nuclear power plant has begun producing electricity. On 4 September, workers connected the 1,000-megawatt pressurized water reactor at Bushehr to the grid, according to the Atomic Energy Organization of Iran. The plant was begun by Siemens in

1975, but work halted in 1979 after the revolution. In 1994, Russia agreed to complete the reactor. It was scheduled to be finished in 1999, but suffered repeated delays.

Smog plans shelved

On 2 September, President Barack Obama asked the US Environmental Protection Agency to withdraw proposed stricter air-quality standards for ground-level ozone (smog). Republican politicians and business leaders had argued that the new standards would hurt the struggling economy by imposing stricter limits on industrial pollution. Environmental groups castigated Obama's decision. The draft standards, proposed

378, 888–897; 2011). The other, which looked at some 10,000 men who were firefighters in 1996, found a "modest" (but not statistically significant) excess in cancer incidence in those doing the job in September 2001 compared with those who weren't (R. Zeig-Owens *et al. Lancet* 378, 898–905; 2011), although the authors add that cancers caused by environmental exposure can take decades to develop.



P. MORGAN/REUTERS

Health legacy of 9/11 attacks

last year, aimed to limit smog concentrations to 60–70 parts per billion (p.p.b.), stricter than the 75 p.p.b. limit set in 2008 (see *Nature* 452, 266; 2008). The ozone standard will be reconsidered in 2013.

BUSINESS

US solar woes

The struggles of US solar-energy companies to compete with cheaper products sold by Chinese firms were underlined on 31 August, when high-profile start-up firm Solyndra said that it would file for bankruptcy and lay off some 1,100 employees. The company, based in Fremont, California, makes thin-film cylindrical photovoltaic modules to

be installed on commercial roof-tops; in March 2009, it had been given a US\$535-million loan guarantee by the US Department of Energy to expand manufacturing capacity. Two weeks before Solyndra's announcement, Evergreen Solar of Marlboro, Massachusetts, also filed for bankruptcy.

Arctic oil and gas

The US oil company ExxonMobil has struck a deal with Russia's state-controlled oil firm Rosneft over the exploration and extraction of oil and gas in the Arctic and the Black Sea. The deal, announced on 30 August, thwarts BP's hopes of becoming Russia's main strategic partner in exploiting the Arctic's vast hydrocarbon reserves. Instead, Exxon and Rosneft will embark on a US\$3.2-billion project to map and develop three licensed sites in the Kara Sea in the Arctic Ocean, and the Tuapse License Block in the Black Sea.

RESEARCH

Mental maladies

Every year, mental disorders afflict 38% of Europe's population, but fewer than one-third of the cases are treated, according to a 5 September report from the European College of Neuropsychopharmacology in

Utrecht, the Netherlands. The study of 30 European countries finds that the most common disorders are anxiety (14%), insomnia (7%) and depression (6.9%). Brain disorders are the biggest contributors to Europe's disease burden in terms of years of life lost and productivity declines, making up 27% of the burden. See go.nature.com/8xnbaw for more.

Chemistry revival

One of the United Kingdom's major universities, King's College London, is bringing back the chemistry department that it shut down in 2003. The shock exit eight years ago was part of a wave of closures for the country's chemistry departments, and the university's chemists were subsequently dispersed across different departments at King's. But they are now to be united in a reincarnated chemistry department that boasts 38 staff members and plans to appoint five more. The department will take its first batch of undergraduate students in 2012. See go.nature.com/giutad for more.

Outlaw found

Using DNA evidence, Australian authorities have located a legendary outlaw — 130 years after his death. Robert Clark, attorney-general for the state of Victoria,



announced on 1 September that scientists at the Victorian Institute of Forensic Medicine in Melbourne had used pathology, historical records and DNA from a living relative to identify the skeleton of Ned Kelly (pictured), a famous criminal whose body had been dumped in a prison mass grave. The whereabouts of Kelly's skull remains unknown.

PEOPLE

Polar bear inquiry

The US Department of the Interior's Office of Inspector General has defended its investigation of Charles Monnett, a wildlife biologist who studies polar bears and who returned to work last month (see *Nature* 477, 10–11; 2011) after a six-week suspension. On 1 September, global-warming sceptic Senator James Inhofe (Republican, Oklahoma) released a letter about the investigation from

COMING UP

10–13 SEPTEMBER

The European Molecular Biology Organization holds its annual meeting in Vienna. www.the-embo-meeting.org/

11–17 SEPTEMBER

Exoplanet enthusiasts gather for the second Extreme Solar Systems conference, at the Grand Teton National Park in Wyoming. go.nature.com/5hh7w3

13–16 SEPTEMBER

Researchers explore the influence of epigenetics on health at the first Epigenomics of Common Diseases meeting in Hinxton, UK. go.nature.com/t7h7yz

acting inspector-general Mary Kendall. She says that in 2010, a seasoned career official at the department made “credible” allegations of scientific misconduct against one or more employees. The investigation, says Kendall, remains ongoing.

Journal chief quits

The editor of *Remote Sensing*, Wolfgang Wagner, resigned on 2 September over the publication of a controversial paper that challenged the reliability of some of the climate models used to forecast global warming. The paper, published in July, argued that climate researchers overestimate the sensitivity of the climate to greenhouse-gas pollution. Wagner, of the Vienna University of Technology, wrote in an editorial that he now views the paper as “fundamentally flawed and therefore wrongly accepted”. See go.nature.com/13sbi1 for more.

➔ **NATURE.COM**

For daily news updates see: www.nature.com/news

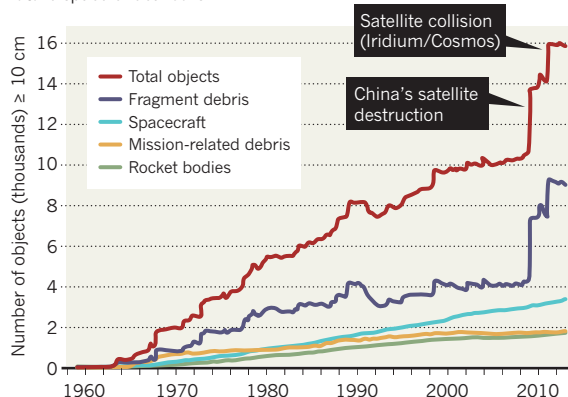
SOURCE: NAS

TREND WATCH

The threat posed by orbital debris, which can rip apart spacecraft, has reached concerning proportions, says the US National Academy of Sciences. The academy's report, released on 1 September, notes that two events — China's blowing up of a weather satellite in 2007, and an accidental collision between two satellites in 2009 — more than doubled the amount of fragment debris orbiting Earth (see chart). The United States is responsible for roughly 30% of the objects in orbit. See go.nature.com/a1q8ai for more.

SPACE TRASH

The rising amount of debris in Earth orbit is likely to jeopardize future space endeavours.



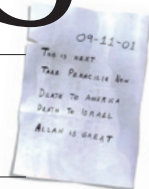
NEWS IN FOCUS

BIOMEDICINE Still no green light for the NIH's effort to speed treatments **p.141**

EXOPLANETS Flickering stars slow the hunt for other Earths **p.142**

Q&A Daniel Weinberger argues for a fresh approach to schizophrenia **p.146**

BIODEFENCE After ten years and \$60 billion, is the US safer? **p.150**



REUTERS/N. HAYASHI/GREENPEACE



Schools such as this one in Fukushima City are a high priority for clean-up efforts.

NUCLEAR POWER

Fukushima impact is still hazy

Chaos and bureaucracy hamper assessment of nuclear crisis.

BY DAVID CYRANOSKI IN TOKYO
AND GEOFF BRUMFIEL IN LONDON

Tatsuhiko Kodama began his 27 July testimony to Japan's parliament with what he knew. In a firm, clear voice, he said that the Radioisotope Center of the University of Tokyo, which he heads, had detected elevated radiation levels in the days following the meltdown of three reactors at the Fukushima Daiichi nuclear power station. But when it came to what wasn't known, he became angry. "There is no definite report from the Tokyo Electric Power Company or the government as to exactly how much radioactive material has been released from Fukushima!" he shouted.

Kodama's impassioned speech was posted

on YouTube in late July and has received nearly 600,000 views, transforming him into one of Japan's most visible critics of the government. But he is not alone. Almost six months after an earthquake and tsunami triggered the meltdowns, other researchers say that crucial data for understanding the crisis are still missing, and funding snags and bureaucracy are hampering efforts to collect more. Some researchers warn that, without better coordination, clean-up efforts will be delayed, and the opportunity to measure the effects of the worst nuclear accident in decades could be lost. Kodama and a handful of Japanese scientists have become so frustrated that they are beginning grassroots campaigns to collect information and speed the clean-up.

Since the crisis began, the Tokyo Electric Power Company and the Japanese government have churned out reams of radiation measurements, but only recently has a full picture of Fukushima's fallout begun to emerge. On 30 August, the science ministry released a map showing contamination over a 100-kilometre radius around the plant. The survey of 2,200 locations shows a roughly 35-kilometre-long strip northwest of the plant where levels of caesium-137 contamination seem to exceed 1,000 kilobecquerels per square metre. (After the 1986 Chernobyl disaster in Ukraine, areas with more than 1,480 kilobecquerels per square metre were permanently evacuated by the Soviet authorities. In Japan, the high-radiation strip extends beyond the original forced evacuation zone, but falls within a larger 'planned evacuation zone' that has not yet been completely cleared.)

EXPOSURE ESTIMATES

Japan's Nuclear and Industrial Safety Agency has also published new estimates of the total radiation released in the accident, based on models that combine measurements with what is known about the damage to the reactors. The latest figures, reported to the International Atomic Energy Agency in June, suggest that the total airborne release of caesium-137 amounts to 17% of the release from Chernobyl (see map). The government estimates that the total radiation released is 7.7×10^{17} becquerels, 5–6% of the total from Chernobyl.

Yet "there are still more questions than definite answers," says Gerald Kirchner, a physicist at Germany's Federal Office for Radiation Protection in Berlin. High radiation levels make it impossible to directly measure damage to the melted reactor cores. Perhaps the greatest uncertainty is exactly how much radiation was released in the first ten days after the accident, when power outages hampered measurements. Those data, combined with meteorological information, would allow scientists to model the plume and make better predictions about human exposure, Kirchner says.

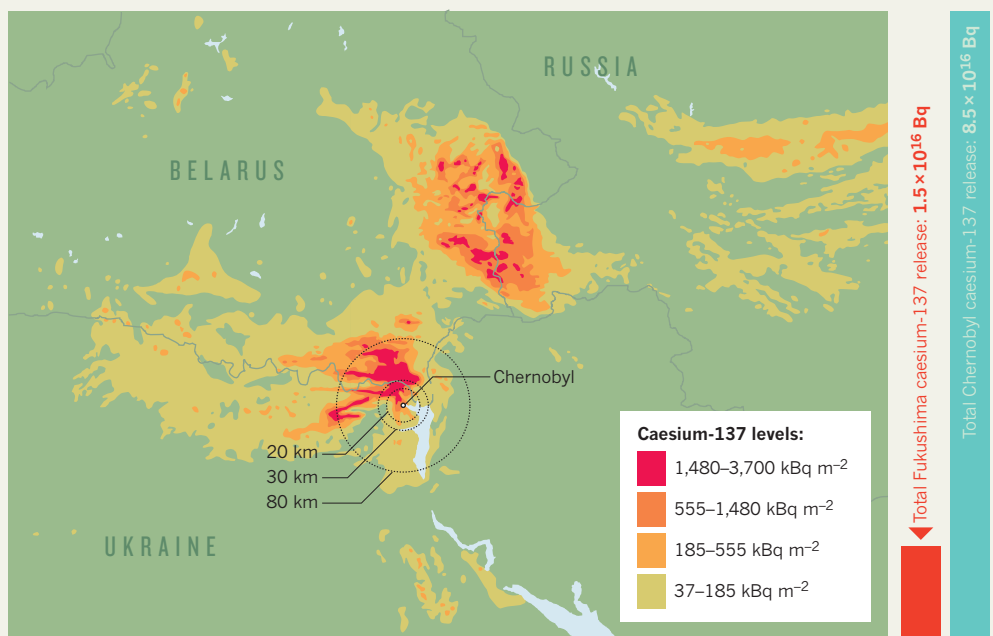
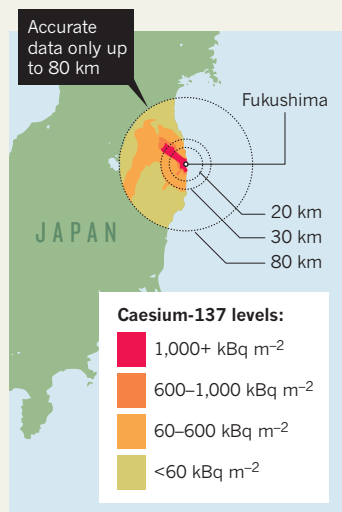
Several measurements suggest that some evacuees received an unusually high dose.

Five days after the crisis began, Shinji Tokonami, a radiation health expert at Hirosaki University, and his colleagues drove several hundred

NATURE.COM
For a video on the crisis and a briefing on the reactors, see:
go.nature.com/ulsz2n

FALLOUT COMPARISONS

New data from Fukushima show caesium-137 levels approaching those of Chernobyl — but over a much smaller area.



► kilometres from Hirosaki to Fukushima City, taking radiation measurements along the way. The results indicate that evacuees from Namie, a town some 9 kilometres north of the plant, received at least 68 millisieverts of radiation as they fled, more than three times the government's annual limit (<http://dx.doi.org/10.1038/srep00087>).

The dose is still safe, says Tokonami. Gerry Thomas, a radiation health expert at Imperial College London, adds that radiation exposures from Fukushima were far lower than those from Chernobyl. "Personally, I do not think that we will see any effects on health from the radiation, but do expect to see effects on the psychological well-being of the population," she says.

But Kodama says that residents of Namie and other towns inside the evacuation zone could have been better protected if the government had released its early models of the plume. Officials say they withheld the projections because the data on which they were based were sparse.

HOTSPOTS

Many questions also remain about the radiation now in the environment. The terrain around Fukushima is hilly, and rainwater has washed the fallout into hotspots, says Timothy Mousseau, an ecologist at the University of South Carolina in Columbia who recently travelled to the Fukushima region to conduct environmental surveys. The plant, located on the Pacific coast, continues to spew radio-nuclides into the water, adds Ken Buesseler, an oceanographer from Woods Hole Oceanographic Institution in Massachusetts. During a cruise in mid-July, his team picked up low-level radiation more than 600 kilometres away. Ocean currents can concentrate the fallout into hotspots something like those on land, making

the effect on marine life difficult to gauge.

Gathering more data is a struggle, say researchers. Tokonami says that overstretched local officials are reluctant to let his team into the region for fear that it will increase their workload. Buesseler and Mousseau add that Japan's famed bureaucracy has made it difficult for outside researchers to carry out studies. Funding has also been a problem. To complete his cruise, Buesseler turned to the Gordon and Betty Moore Foundation for a US\$3.5-million grant. Mousseau got a biotech company to sponsor his trip and has since found funding through the Samuel Freeman Charitable Trust.

Some Japanese scientists have grown so frustrated with the slow official response that they have teamed up with citizens to collect data and begin clean-up. Because radiation levels can vary widely

"There are still more questions than definite answers."

over small distances, the latest government maps are too coarse for practical use by local people, says Shin Aida, a computer scientist at Toyohashi University of Technology. Aida is proposing a more detailed map-making effort through 'participatory sensing'. Using the peer-to-peer support website 311Help (<http://311help.com>), Aida plans to have people gather samples from their homes or farms and send them to a radiation measuring centre, where the results would be plotted on a map.

Kodama, meanwhile, is advising residents in Minamisoma, a coastal city that straddles the mandatory evacuation zone. Minamisoma has set aside ¥960 million (\$12.5 million) for dealing with the nuclear fallout, and on 1 September it opened an office to coordinate the effort. "We needed to find out what's the most efficient and effective way to lower the risk," says one of the

leading officials, Yoshiaki Yokota, a member of the local school board. The first job is to collect and bury soil at schools. Residents have learned to first roll the soil in a vinyl sheet lined with zeolite that will bind caesium and prevent it from seeping into the groundwater.

Farther northwest, in the city of Date, decontamination efforts are moving from schools to nearby peach farms. On 31 August, some 15 specialists started removing the top centimetre of soil at the farms with a scoop or with suction machines, trying not to damage the peach trees' roots. They hope to lower the radiation enough to produce marketable fruit next year.

After a sluggish start, the central government is launching two pilot clean-up projects for the region. One will focus on areas like Minamisoma, where radiation is less than 20 millisieverts per year on average but includes some hotspots. The other will look at 12 sites of radiation of more than 20 millisieverts per year.

Researchers are hopeful that the chaos immediately after the crisis will soon give way to a sharper picture of the fallout and its toll. The United Nations Scientific Committee on the Effects of Atomic Radiation (UNSCEAR), which conducted many studies after the Chernobyl disaster, is working with Japanese officials to collate the stacks of data collected since the crisis began. UNSCEAR is also studying the environmental effects of the accident and the exposure of workers and evacuees, and aims to have an interim report ready by next summer.

Clean-up is the top priority, but Fukushima also offers a unique research opportunity, says Mousseau, who has worked extensively at Chernobyl. Because of Soviet secrecy, researchers missed a crucial window of opportunity in studying the Ukrainian crisis. "Japan offers us an opportunity to dig in right off the bat and really develop a profound understanding," he says. ■

HEALTH

NIH centre faces spell in limbo

Congressional paralysis threatens to stall translational medicine initiative.

BY MEREDITH WADMAN

Francis Collins, director of the US National Institutes of Health (NIH), is in danger of missing a self-imposed deadline for his hallmark priority: establishing an NIH centre dedicated to speeding new treatments from the lab to the clinic.

Collins vowed that the \$723-million National Center for Advancing Translational Sciences (NCATS) would be up and running on 1 October — in time for him to oversee its first year in operation. (Should Republicans capture the White House in November 2012, Collins could be out of a job.) But Congress must explicitly approve it in a 2012 spending bill — a document that has yet to be written and which the distracted, highly polarized body seems unlikely to pass before the new fiscal year begins on 1 October.

So the NIH and the administration are developing a plan B: drafting an ‘anomaly’ that

would allow the translational-medicine centre to launch on a reduced budget. The anomaly would be part of a stop-gap law, known as a continuing resolution, that keeps the government funded at 2011 levels while law-makers finish drawing up 2012 spending bills.

As to whether the manoeuvre will work, Kathy Hudson, the NIH deputy director for science, outreach and policy, says “we’re

“We think it’s going to happen. We just don’t know how or when.”

optimistic”. But the bar for an anomaly on a stop-gap funding bill can be high. Anomalies are usually limited to urgent matters such as emergency services that are set to expire and can’t wait for a regular spending bill. The NIH’s rush to launch the centre has also come up against vocal opposition from Denny Rehberg (Republican, Montana), who chairs the House spending subcommittee that funds the

NIH and who in June demanded more details from the agency about its plans. (He has since received them.) Rehberg’s position gives him significant, but not insuperable power; and NCATS’ ultimate goal of speeding cures to patients is a popular one in Congress.

However, the fact remains that NCATS needs affirmative attention from a preoccupied Congress. “We’re keenly aware that we need to have a line item for NCATS — that it does need to be expressly written into appropriations language,” says Margaret Anderson, the executive director of FasterCures, a think tank in Washington DC that focuses on speeding new therapies.

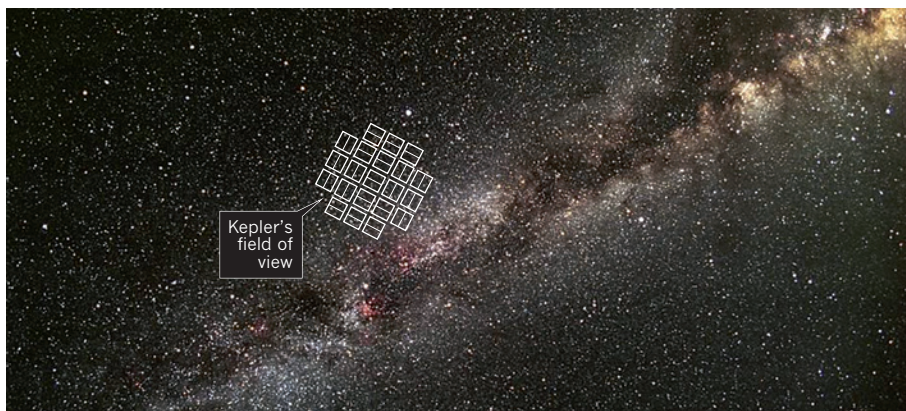
Collins, who early in his tenure declared translational medicine to be one of his top priorities, has pushed hard for the creation of the centre, which would focus on accelerating and improving the process of drug and device development. He first encountered resistance on the NIH campus, when it ►

► became clear that setting up the centre would mean dismantling and dividing up the pieces of the National Center for Research Resources, a \$1.3-billion NIH institute devoted to infrastructure and training. In Congress, Rehberg and others have questioned whether the agency is pushing the government into an area — drug development — that they say should be the preserve of industry. Collins has said that NCATS will “complement — not compete with” the private sector.

On 15 June, after Collins announced a search for a director of the new centre, Rehberg wrote to Kathleen Sebelius, who heads the Department of Health and Human Services, the NIH's parent agency, pronouncing himself “very troubled” by the search. Without an official budget amendment outlining the financing of the centre and explaining other details of the NIH's plans that would “allow us to review the proposal fully”, Rehberg wrote, “we cannot responsibly take any action on this matter”.

Under the Freedom of Information Act, *Nature* has obtained Sebelius's 6 July response to Rehberg's letter, which ran, with attachments, to 79 pages of minute detail about the structure, finances and goals of the proposed centre (see go.nature.com/4wzjil). In her covering letter, Sebelius told Rehberg that the NIH has confined itself to “preliminary planning” with the aim of an efficient launch in 2012, and adds that the agency will not hire a director “until NCATS is established”. Rehberg has not responded to multiple requests for comment over the 12 weeks since he wrote to Sebelius.

But Congress's broader budget troubles seem as likely to delay NCATS as the skirmish with Rehberg. David Moore, a veteran congressional observer and senior director for governmental relations at the Association of American Medical Colleges in Washington DC, says that the increasingly charged atmosphere around spending issues on Capitol Hill makes it impossible to predict the chances of Congress passing a bill — whether a stop gap measure or a full 2012 law — in time for NCATS to launch on 1 October. “We think it's going to happen. We just don't know how or when,” he says. ■



C. ROBERTS/NASA

The Kepler probe is searching part of the Milky Way for signs of Earth-like planets.

ASTRONOMY

Jumpy stars slow hunt for other Earths

NASA mission looks for extra time to battle stellar noise.

BY RON COWEN

The Kepler spacecraft has hit an unexpected obstacle as it patiently watches the heavens for exoplanets: too many rowdy young stars. The orbiting probe detects small dips in the brightness of a star that occur when a planet crosses its face. But an analysis of some 2,500 of the tens of thousands of Sun-like stars detected in Kepler's field of view has found that the stars themselves flicker more than predicted, with the largest number varying twice as much as the Sun. That makes it harder to detect Earth-sized bodies.

As a result, the analysis suggests that Kepler will need more than double its planned mission life of three-and-a-half years to achieve its main goal of determining how common Earth-like planets are in the Milky Way.

Kepler is currently slated to run until November 2012 and, given NASA's budget pressures, including the ever-rising cost of the James Webb Space Telescope (JWST), an extension is by no means certain. “I'm concerned that programmes like Kepler might be squeezed out in

order to have enough funding for the JWST”, says Kepler's chief data analyst, Jon Jenkins at the SETI Institute in Mountain View, California. “We need an eight-year mission to reach our goal of understanding whether there are other worlds out there like Earth.” NASA declined to comment on Kepler's chances of securing an extension; a decision is expected next spring.

In many ways, the mission has been a huge success. Earlier this year, Kepler scientists announced that the craft had discovered 1,235 candidate exoplanets, 68 of which are Earth-sized. Fifty-four of the total number of planets detected, all of them larger than Earth, orbit within the habitable zone of their parent stars, a region temperate enough for water to remain liquid on the surface of a rocky body. More exoplanet discoveries are expected to be announced next week in Moran, Wyoming, at a conference on extreme solar systems, and a new batch of Kepler data, based on 674 million observations recorded from September to December 2009, is scheduled for public release on 23 September.

In an article posted online in July and


**MORE
ONLINE**

TOP STORY



Could stem cells rescue an endangered species?
go.nature.com/v69zxu

MORE NEWS

- Electrified bacterial filaments zap uranium go.nature.com/q3odag
- Oil-spill research funds for Deepwater Horizon begin to flow go.nature.com/vnapdj
- Chinese science ministry increases funding go.nature.com/h1kslk

ON THE BLOG



Tobacco company seeks access to secret data on smoking habits go.nature.com/5cwbsx

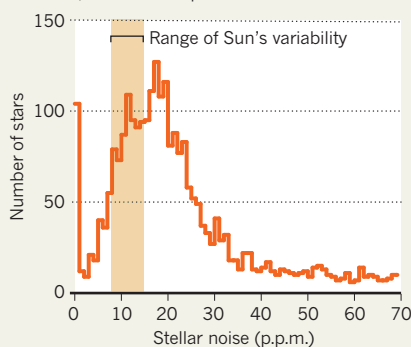
currently in press in *The Astrophysical Journal*, Kepler scientist Ron Gilliland of the Space Telescope Science Institute in Baltimore, Maryland, and his collaborators describe Kepler's noise dilemma (R. L. Gilliland *et al.* preprint at <http://arxiv.org/abs/1107.5207>; 2011). The signal of an Earth analogue is a drop in a star's luminosity of about 85 parts per million, lasting several hours, whenever such a planet passes in front of its parent star.

Before Kepler's launch in early 2009, the team had assumed that the Sun-like stars viewed by the craft would be about as quiet as the Sun, with luminosity fluctuating in a range near 10 parts per million (a 0.001% variation) over the key timescale of about 6.5 hours. But Gilliland and his colleagues found that the noise in the Kepler data is much larger (see 'Too much twinkle'), with most of it intrinsic to the stars themselves, rather than caused by instrument problems or other errors associated with recording low light levels.

Gilliland believes that the stellar equivalent of sunspots are the most likely culprits. Sunspots form when magnetic activity creates areas on the solar surface that are temporarily cooler and darker than normal, affecting the Sun's overall brightness. Gilliland suspects that such magnetic

TOO MUCH TWINKLE

In a sample of 2,500 Sun-like stars monitored by the Kepler probe, most vary in brightness more than the Sun does, which makes planets harder to see.



activity is higher among the Sun-like stars in the Kepler field than in the Sun itself, probably because they are younger. Younger stars spin faster, driving a more vigorous magnetic field.

In fact, Gilliland suggests that about half the stars in the Kepler field are younger than the Sun, even though theoretical predictions had indicated that about two-thirds would be older. If this youthful bias is true of the entire Milky Way, "that would indeed be a surprise", with far-reaching implications for how stars are born and die, Jenkins says.

But whatever the source of the stellar noise,

Gilliland says that Kepler will have to detect twice as many transits of Earth-like analogues than planned — an average of six passages per planet rather than three, at intervals of roughly a year — to be sure that a dip in starlight is a true signal of an Earth-sized body. This means that the probe will need a full eight years to attain its original goal of finding about 75% of Earth analogues among its target stars.

"We need an extended mission because the detection of Earth-sized planets hangs in the balance," says Geoff Marcy an astronomer at the University of California, Berkeley, and a member of the Kepler team.

Focusing on planet candidates that have a diameter no smaller than 1.2 times that of Earth could speed up the mission, says Gilliland, because they cast a deeper shadow and so are easier to pick out from the stellar noise. But a planet that is 20% larger than Earth may not be a rocky body like our home planet, some models suggest. It could, for instance, be a 'waterworld', with a deep ocean or a shell of ice.

If the mission is restricted to such larger planets, it may not answer the question that Kepler was built to study, says Gilliland. Finding out whether other Earths exist "is a question humans have been asking for thousands of years", says Jenkins. "It would be a real shame" if NASA ends the mission "just as Kepler is on the threshold of answering it". ■

NATURE.COM
For more on Kepler's
hunt for other
Earths, see:
go.nature.com/qoydnc

PLANETARY SCIENCE

Venus scientists fear neglect

Researchers say that infrequent visits are hindering studies of the nearest planet.

BY ERIC HAND

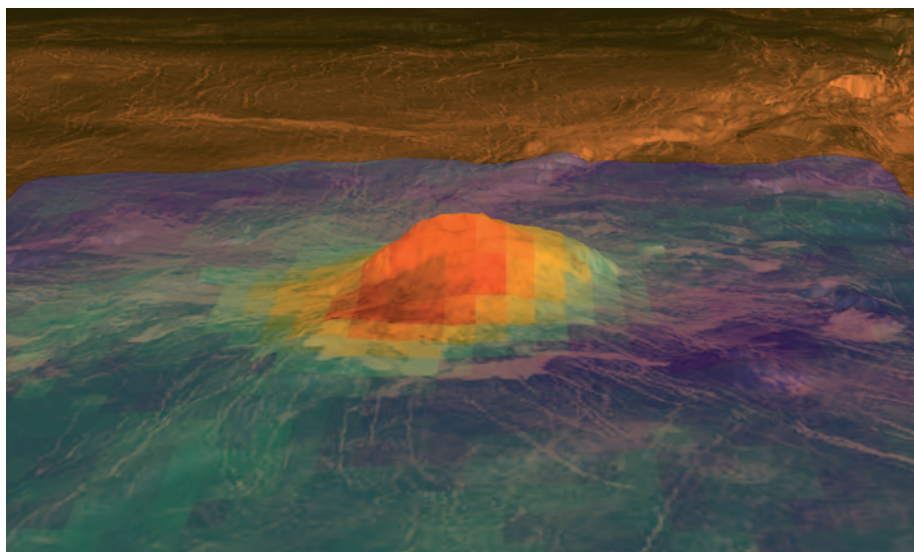
Venus would seem to be a tempting destination for planetary probes: conveniently close, and an extreme laboratory for atmospheric processes familiar on Earth. So why won't NASA send a mission there? That was the frustrated question coming from scientists at the annual meeting of NASA's Venus Exploration Analysis Group (VEXAG) near Washington DC on 30–31 August. They perceive an agency bias against Venus, a planet that hasn't seen a US mission since the Magellan probe radar-mapped its shrouded surface in the early 1990s, and which won't see one any time soon, after NASA this year rejected a bumper crop of Venus proposals.

"A lot of us are dismayed," says David Grinspoon, astrobiology curator at the Denver Museum of Nature and Science in Colorado, who is a co-investigator on several of the proposals. Some of the reasons for the planet's neglect are obvious: surface temperatures that would melt lead and thick clouds of sulphuric acid make data gathering a challenge for landers and orbiters alike. And — unlike Mars — Venus is neither a plausible haven for life nor a potential destination for astronauts.

But Grinspoon says that something more insidious is at work. Without new missions supplying data for analysis, funding for Venus research has dwindled, leading to fewer students entering the field — and a smaller constituency to lobby for missions. "Because of this feedback loop, the community has shrunk," he says. Research grants mentioning Venus have accounted for just 2% of NASA's planetary-science funding since 2005.

Internationally, things aren't much better. Europe's Venus Express, a probe cobbled together using instruments designed for missions to Mars and a comet, has only partly satisfied a craving for data since it arrived in 2006. And last December, Japan's Akatsuki spacecraft failed to enter orbit and overshot the planet.

In May, Venus researchers got a double dose of further bad news. In NASA's New Frontiers medium-class mission line, a mission to return asteroid samples prevailed over a proposed Venus lander that would have lasted a precious three hours on the surface. And there were no Venus missions among the three finalists in the Discovery low-cost planetary-mission competition, although one-quarter of the proposals had



The volcano Idunn Mons shows up as a hot spot in this thermal map taken by the Venus Express probe.

targeted the planet (see 'Forgotten planet').

Of the seven Discovery proposals for Venus missions, reviewers gave six the lowest possible ranking, guaranteeing their rejection. Only one, an atmospheric mission, received a solid 'category II' score. With so many proposals, and with mission teams averaging 20 people each, some Venus scientists wondered whether enough unbiased colleagues were left in the community to competently review the proposals. But Jim Green, director of planetary science at NASA, says that he found plenty of qualified reviewers from outside the United States. "There were just better proposals" for

other Solar System targets, he says.

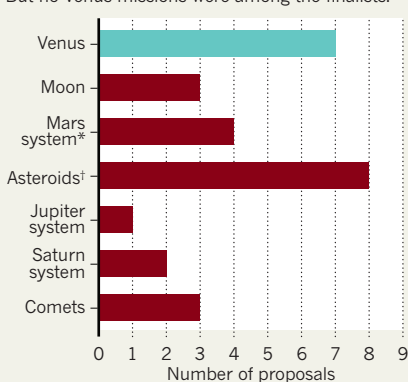
Michael New, the NASA programme scientist who ran the competition, says that Venus scientists need a clearer consensus on their goals and the measurements that they want to make. Those who want to map the surface, for instance, have not determined how much better than Magellan their radar instruments have to be. NASA may invite another round of Discovery proposals in 2012.

Grinspoon hopes that by then, the unanswered scientific questions will be impossible to ignore. He wants to know why Earth's global climate models break down on Venus, which has an atmosphere composed of 97% carbon dioxide — and what that reveals about the hidden fine-tunings of Earth models.

Similarly, Gordon Chin, a project scientist at NASA's Goddard Space Flight Center in Greenbelt, Maryland, proposed a mission that would explain why the same chemical processes that destroy ozone in Earth's atmosphere stabilize carbon dioxide in Venus's. And Suzanne Smrekar, VEXAG co-chair and a scientist at NASA's Jet Propulsion Laboratory in Pasadena, California, wants to follow up on a 2010 finding in which she and her colleagues used Venus Express data to identify hot spots on the planet's surface — evidence for volcanism within the past few million years. A clearer picture of volcanism on Venus and its history could help to explain how the planet's runaway greenhouse effect got going. "We need another laboratory to test what we think we know on Earth," says Chin. ■

FORGOTTEN PLANET

Venus was targeted by one-quarter of the 28 proposals in NASA's latest Discovery competition. But no Venus missions were among the finalists.



*Includes mission to visit the Mars moon Phobos.

†Includes mission to one of Jupiter's Trojan asteroids.

NATURE.COM
For more on Venus
science, visit:
go.nature.com/wjsaiw



Q&A Daniel Weinberger

A radical approach to mental illness

Daniel Weinberger is making a fresh start after 31 years at the National Institute of Mental Health (NIMH) in Bethesda, Maryland, where he pioneered the combined use of brain imaging and genetics in schizophrenia research. Last month, he became director of the privately funded Lieber Institute for Brain Development in Baltimore, Maryland. Founded with US\$125 million from philanthropists Stephen and Constance Lieber and Milton and Tamar Maltz, the institute's public opening is on 8 September. Weinberger talks about why it is time for new approaches to psychiatric disorders, and why he thinks his new home is the best place to pursue them.

What is the Lieber Institute for Brain Development?

It is probably the only institute in the world dedicated solely to basic and translational research on neurodevelopmental psychiatric diseases such as schizophrenia, autism spectrum disorders and bipolar disorder — all of which, we have recently understood, have their roots in abnormal brain development. Its mandate is not simply to do great basic science — although we still hope to do so — it's about changing the lives of sick people.

What limits current schizophrenia treatments?

They are all based on the hypothesis that the neurotransmitter dopamine has a key role in the disease pathology. Dopamine-based therapies transformed psychiatry when they were introduced in the 1950s, because they worked well enough to allow patients to be released from hospitals. But, even though they have been greatly refined, they remain very

inadequate. Some people will benefit a lot, but some won't benefit much at all. The treatments don't even affect some important symptoms of schizophrenia, such as cognitive defects.

Will it be easy to move beyond this?

Yes. I think we are poised to, thanks to genetic studies that have identified some risk genes, and to new technologies for studying the living brain and the post-mortem brain. Neuroimaging has shown us that the syndromes are associated with faulty brain circuitry. Why is the circuitry faulty? We don't understand the detailed pathology, but we've learned that risk genes — including, incidentally, some genes in dopamine biochemical pathways — contribute to the aetiology by affecting the development and function of the circuitry.

All this provides us with clues to guide experiments and, as a result, the science of brain function in schizophrenia has become respectable. People who wouldn't have touched

schizophrenia research with a ten-foot pole, for fear of being soiled by association with the messy biology of human behaviour — people like Ron McKay, who now leads our stem-cell programme — are now moving in.

How will the Lieber institute carry out research?

We have tried to create a Google-like working environment with computer scientists, cell biologists, clinical psychiatrists and so on working together, breaking with the traditional silo-based mentality.

We'll also have a drug-development programme directed by Sol Snyder [who identified receptors for several neurotransmitters] from the Johns Hopkins School of Medicine [in Baltimore, Maryland]. Already we have four interesting new drug targets identified from our post-mortem and genetic-imaging studies. We'll try to identify additional targets by developing cellular and animal models based on the complex genetic information. It is not a question of just knocking out a gene; we'll have to model the entire molecular pathology.

We are also starting a new collection of post-mortem brains from people who had a psychiatric disorder — as well as from controls. Our brain bank will include fetal brains so we can follow the expression of risk genes at different phases of development.

Will you have external collaborations?

Absolutely. This is one of our most important aspects. We'll have partnerships with industry and with academic institutes in the United States and other countries. For example, we'll be collecting data sets to complement the huge data set I put together at the NIMH, comprising biological and genetic information from more than 3,000 patients with schizophrenia and unaffected members of their families. The new populations will be gathered by collaborators at the University of Bari in Italy and Peking University in Beijing. We'll mine all of these data sets to try to learn how risk genes contribute to the development of psychiatric disease, and also to work out if we can predict who will respond well to existing antipsychotic drugs.

Couldn't you have done all this at the NIMH?

I wish we could have done, but it wasn't possible. Our programme had a long and successful run at the NIMH. But it may be that all research programmes have a lifespan, and institutional inertia makes it difficult to keep them fresh. Another problem is that at the National Institutes of Health [the NIMH's parent agency] — despite its best intentions — it is really difficult to build outside relationships.

What is the timeline for new therapies?

We won't be able to cure schizophrenia in the next ten years, but I'm very confident that we'll have major breakthroughs by then. ■

INTERVIEW BY ALISON ABBOTT



EXTREME MEASURES

Can violent hurricanes, floods and droughts be pinned on climate change? Scientists are beginning to say yes.

BY QUIRIN SCHIERMEIER

When the weather gets weird, as happens a lot these days, one question inevitably arises from reporters, politicians and the general public alike: is this global warming?

The question was asked after last year's catastrophic floods in Pakistan and record-breaking heat wave in Russia. It was asked again this year about the freakish tornado clusters in the southeastern United States and the devastating drought in Africa. And it was asked yet again this August as Hurricane Irene roared up the US East Coast.

For the most part, climate researchers have shied away from answering. Their mantra has been that science cannot attribute any particular drought or hurricane to climate change; the best it can do is project how the frequency of extreme weather events might change as the globe warms, through shifts in factors such as evaporation rates over the open ocean, water vapour and cloud formation, and atmospheric circulation.

Lately, however, that reluctance has started to fade. "My thinking has evolved," says Gavin Schmidt, a climate modeller at the NASA Goddard Institute for Space Studies in New York. Thanks to advances in statistical tools, climate models and computer power, "attribution of extremes is hard — but it is not impossible", he says. Two studies published last February in *Nature* showed links between extreme weather and climate change — one looking at the catastrophic flooding in the UK in 2000¹, the other at the late-twentieth-century increase in intense rainfall across the Northern Hemisphere².

Also in the past year, climate researchers in the United States and Britain have formed a loose coalition under the banner 'ACE' — Attribution of Climate-related Events — and have begun a series of coordinated studies designed to lay the foundations for a systematic weather-attribution programme. Ultimately, the group hopes to create an international system that could assess the changing climate's influence on weather events almost as soon as they happen or even before they hit, with results being announced on the nightly weather reports.

"The idea is to look every month or so into the changing odds" associated with that influence, says Peter Stott, a climate scientist with the UK Met Office's Hadley Centre in Exeter and a leader of the ACE group. Stott is writing a white paper laying out plans and requirements for a near-real-time attribution system, which he will present in October at the World Climate Research Programme conference in Denver, Colorado.

TERRIBLE TOLL

Extreme weather events are among the most destructive disasters known, whether their toll is measured in lives — some 40,000 people died as a result of Europe's record-breaking heat wave in 2003 — or in money — the US Gulf Coast suffered more than US\$80 billion in damages in September 2005 from Hurricane Katrina. Worse, that toll is escalating: figures from the US National Climatic Data Center in Asheville, North Carolina, show that the frequency of multibillion-dollar weather disasters has at least doubled since 1980.

Knowing what causes those disasters is a matter of core interest to

M. HOLLINGSHEAD/SCIENCE FRACTION/GETTY; M. METZEL/AP; M. HOLLINGSHEAD/SCIENCE FRACTION/CORBIS; J. EDDY/SPL

insurance companies who have to set rates; to civil engineers who have to decide how (or whether) to strengthen protections such as levees; and to communities, regions and nations struggling to adapt to long-term changes in climate. If the surge in frequency is a result only of natural cycles, it will probably subside someday soon. But if the increase is a result of global warming, losses and damages could continue rising indefinitely.

Reliable attribution of extreme weather events is also important for the public's understanding of climate change, and to their willingness to support measures to reduce greenhouse-gas emissions. Unlike more distant impacts of global warming such as the slowly rising sea level, the effects of local weather extremes tend to be instantly tangible and vividly remembered. Surveys suggest that people who feel they have personally experienced the effects of climate change are more likely to believe it is a real problem — and one that needs solving — than those who have not.

CHARTING A COURSE

With those imperatives in mind, the ACE group has set out to explore the climate–weather connection systematically, by feeding observational data from the UK Met Office and the US National Center for Atmospheric Research (NCAR) in Boulder, Colorado, into seasonal forecasts and long-term climate models.

Attribution, however, is no simple task: multiple factors influence a given weather event. Global climate change must have some effect: basic physics suggests that a warmer atmosphere can hold more water vapour, for example, and should therefore develop more storms, which feed on moisture and heat. But natural cycles such as El Niño have an equally obvious effect: freakish weather was a problem for humans long before anyone started pumping industrial quantities of carbon dioxide into the atmosphere.

So the goal of the ACE group is to carry out 'fractional attribution' of extreme events, estimating how much each one was influenced by anthropogenic greenhouse warming and how much by natural cycles (see 'Climate shift'). The studies that appeared in *Nature* last February^{1,2} offer pioneering examples of how to do this. In one, Pardeep Pall, an atmosphere researcher at the University of Oxford, UK, and his team generated several thousand simulations of the weather in England and Wales during the autumn of 2000. Some of the simulations included observed levels of human-generated greenhouse gases, whereas others did not. The researchers then fed the results of each simulation into a model of precipitation and river run-off to see what kind of flooding would result. In 10% of the cases, twentieth-century greenhouse gases did not affect the local flood risk. But in two-thirds of the cases, emissions increased the risk of a catastrophic flood — like the one that occurred in 2000 — by more than 90%.

Another group, led by climate scientist Seung-Ki Min of the Climate Research Division of Environment Canada in Toronto, used a similar approach. Inspired by the observation that intense rainfall in the Northern Hemisphere has worsened over the second half of the twentieth century, the group compared actual precipitation data with simulations from six different climate models, both with and without greenhouse warming. They found that the extreme precipitation patterns observed did not match anything expected from natural climate cycles, but closely matched those expected from greenhouse warming.

Such attribution studies can sometimes exonerate climate change. In one published in March³, Randall Dole and his colleagues at the National Oceanic and Atmospheric Administration in Boulder, Colorado, concluded that the intense 2010 Russian heat wave was probably a result of natural cycles.

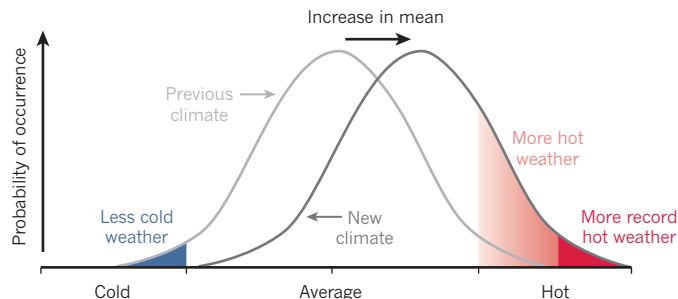
Although the basic approach seems straightforward, says Stott, fractional attribution is only as good as the climate models that drive it. "We still need to understand which types of weather events we can confidently attribute," he says, "and those for which the models are not yet good enough."

➔ NATURE.COM
Read more about extreme weather attribution:
go.nature.com/uard3z

CLIMATE SHIFT

Extreme weather events — here, very hot or cold temperatures — are rare. But a small rise in the average temperature through greenhouse warming (right-hand curve) can radically increase their frequency. Attribution research tries to quantify this effect for specific events.

SOURCE: IPCC



In general, he says, attribution is easiest with heat waves and other temperature-related events. It is much harder with precipitation-related events such as floods and droughts, as the models have to take into account not just rainfall, but soils, natural terrain and human management of rivers and wetlands. And some weather events can't yet be linked to climate change at all. The frequency of tornadoes, for example, depends on a balance between moist air convection, which encourages their formation, and wind shear, which tends to disrupt them — but scientists cannot say for sure how climate change affects that balance.

Another issue is the limited spatial resolution of climate models. At present, for example, they are far too coarse to represent small-scale 'convective' rainfall, a common phenomenon in which warm, moist air near the ground wells up to form an isolated thundercloud. Such convection is especially pronounced — and even harder to model — in mountainous regions such as the Andes or the Himalayas.

Such deficiencies in the models explain why many climate scientists remain sceptical of attribution efforts. "Scientifically unsound" is the assessment of Judith Curry, a climatologist at the Georgia Institute of Technology in Atlanta. Even converts such as Schmidt are cautious. "There is a lot of scope for doing a much better job," he says.

BEYOND THE HORIZON

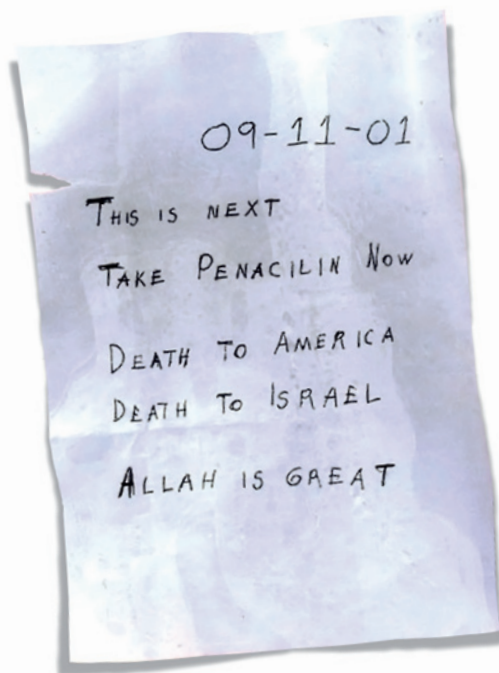
The ACE group plans to address these shortcomings in next month's white paper. As a first step, the group suggests that leading centres, such as NCAR and the Met Office, carry out fractional attribution assessments of notable weather extremes over the past 50 years, using large ensembles of coupled climate models and all available weather data. The lessons learned from these retrospective studies could then allow scientists to progress into routine attribution of recent weather, as well as climate-based forecasts of extreme weather.

It is not yet clear what such a plan would cost, or who would pay for it. Kevin Trenberth, a climate scientist with the NCAR, estimates that a few million dollars would be enough to coordinate an international service using facilities already in place at his institution, the Met Office and elsewhere. But going beyond this bare-bones effort — creating, for example, a free-standing attribution centre with monthly, seasonal and decadal forecasting capacities — would cost much more.

Given that governments on both sides of the Atlantic are slashing their budgets wherever possible, Trenberth admits that the prospects for launching such a programme anytime soon seem remote. But neither weather nor climate pays the slightest attention to what policy-makers are doing. And with events such as Hurricane Irene making themselves felt in politicians' backyards, an attribution service might someday be seen as a good investment. ■ **SEE EDITORIAL P.131**

Quirin Schiermeier is a reporter for Nature based in Munich.

1. Pall, P. et al. *Nature* **470**, 382–385 (2011).
2. Min, S.-K., Zhang, X., Zwiers, F. W. & Hegerl, G. C. *Nature* **470**, 378–381 (2011).
3. Dole, R. et al. *Geophys. Res. Lett.* **38**, L06702 (2011).



Since the anthrax attacks in 2001, some \$60 billion has been spent on biodefence in the United States. But the money has not bought quite what was hoped.

THE PRICE OF PROTECTION

BY ERIKA CHECK HAYDEN

It took one routine smallpox vaccination to expose the holes in the United States' defences against bioterrorism. In January 2009, the jab was given to 20-year-old Lance Corporal Cory Belken of the US Marine Corps, as it is to many members of the military who are about to be deployed abroad, to protect him against a potential attack with the lethal virus. But in this case, the timing was unfortunate. Two weeks after the vaccination Belken was diagnosed with leukaemia; he then underwent chemotherapy that wiped out his immune system. Suddenly, the live vaccinia virus, the milder relative of smallpox used in the vaccination, was able to multiply into a dangerous infection.

Doctors turned to their only means of counter-attack: three smallpox drugs, two of them experimental and developed as part of US efforts to build up an arsenal against potential bioterror agents. The marine received 30 times the standard dose of the first drug, an approved antibody, to no avail. The second, called STS-246, had been used in only one person

infected with vaccinia before. By the time doctors administered the third drug, CMX001, Belken had developed a bacterial infection that spread to his feet, brought him near death and required surgeons to amputate both his legs below the knees. Only after he received all three medicines did he start to recover — and it is still not known which of the drugs, if any, eventually helped.

The marine's case is just one of many events that have raised questions about the biodefence research and development enterprise that sprang from bioterror attacks in the United States ten years ago. Shortly after the terrorist attacks of 11 September 2001, anthrax spores sent to media outlets and politicians killed five people and compounded already widespread fear and horror. The incidents spurred the US government to launch a major scientific effort to develop 'countermeasures': diagnostics, vaccines and drugs against potential biological threats such as smallpox and anthrax. In a three-part strategy, the federal government poured money into basic research

at the National Institutes of Health (NIH); created the Biomedical Advanced Research and Development Authority (BARDA) to carry new concepts forward into further development and testing; and established BioShield, a US\$5.6-billion programme to purchase the finished drugs and vaccines. But none of the links in this chain has worked exactly as it was supposed to.

Between 2001 and the end of this year, the federal government will have spent \$60 billion on such biodefence efforts (see 'A decade of biodefence'), according to analyses from the Center for Biosecurity of the University of Pittsburgh Medical Center in Baltimore, Maryland. The money has helped to modernize the nation's crumbling public-health system, and BioShield has invested in a stockpile of 20 million doses of smallpox vaccine, 28.75 million doses of anthrax vaccine and 1.98 million doses of four medicines to treat complications of smallpox, anthrax and botulism. But few researchers or policy-makers seem happy with an arsenal of six drugs that

R. SACHS/CNP/SYGMA/CORBIS

address only three of the potential threats — even if they are among the most serious. “The pipeline we rely on to provide those critical countermeasures — diagnostics, vaccines, antivirals, antibiotics — is full of leaks, choke points and dead ends,” said Kathleen Sebelius, US Secretary of Health and Human Services, in a statement last year.

Critics say that the effort has been hobbled by a lack of strategic thinking, focus and coordination between the federal agencies involved, and by unrealistic expectations of what the money could buy. “There was no evidence that they looked at what our top priorities are and asked, ‘What’s needed on the basic-science side?’, ‘What’s needed on the development side?’, and ‘What’s needed in the stockpile?’,” says Andrew Pavia, an infectious-diseases doctor at the University of Utah in Salt Lake City. Until earlier this year, Pavia served on the National Biodefense Science Board, which advises the US Department of Health and Human Services (DHHS) and in March last year released a report, *Where Are The Countermeasures?*, that was critical of the federal biodefence effort.

What is more, developing therapies for diseases that are mercifully rare among humans is a unique challenge. Drug development is difficult at the best of times — and experts say that there is simply not enough money in biodefence to entice big companies into the field. “It is a bit discouraging considering we’ve spent more than \$60 billion on this in the past decade,” says Randall Larsen, a member of the Commission on the Prevention of Weapons of Mass Destruction Proliferation and Terrorism, which in a January 2010 ‘report card’ gave the nation a failing grade for its ability to prevent a bioterror attack from causing huge casualties. “The question is whether it has been spent properly,” he says.

PRIORITY PATHOGENS

That point is especially pressing now. The United States is in dire financial straits and may be forced to slash the research budgets of the NIH and other agencies if Congress does not agree on other spending cuts by 23 December. Still, some researchers think that ten years is simply too soon to expect pay-offs from a research programme that essentially started from scratch. “There have been some really important lessons received from what has admittedly been a very large investment,” says David Relman, a microbiologist at Stanford University in California who has been heavily involved in biodefence research and policy. “Perhaps with a more refined idea of the goal, [the money] might have been used in a more productive or effective way. But at the time, we didn’t really know what we needed and we didn’t know how hard it would be to make any of these things that we needed.”

A pillar of the biodefence enterprise is the US National Institute of Allergy and Infectious

Diseases (NIAID) in Bethesda, Maryland, which got a \$1.5-billion budget boost in 2003 and has so far received \$14 billion for biodefence. It is there, say critics, that some early and crucial mistakes were made.

In a series of reports issued in 2002 and 2003, the NIAID outlined its plans to fund basic research aimed at the development of treatments and vaccines for more than 50 ‘priority pathogens’ and toxins classified into three categories. Category A covers agents considered to be the most dangerous and likely to be used in an attack, such as smallpox and anthrax. Categories B and C include threats such as food- and waterborne illnesses. (The list was similar to a catalogue of ‘select agents’ kept by the US Centers for Disease Control and Prevention (CDC) in Atlanta, Georgia.) The agency also built 15 labs across the country — part of a building boom that has led, so far, to the planning, construction or renovation of nearly 20 labs for the study of dangerous pathogens at a cost of more than \$2 billion.

But some experts say that attempting to tailor vaccines and treatments to individual pathogens is misguided: some of the pathogens are difficult to turn into bioweapons or just aren’t very dangerous, and the costs of developing a large defensive arsenal are astronomical. It makes more sense, these experts say, to stockpile antibiotics and other medicines that could be used against many pathogens. “You can look at some of the vaccine investments, like for plague and [the bacterial disease] tularemia, and wonder who decided that was the highest priority, as opposed to developing new antibiotics,” says Pavia.

The NIAID reorganized its biodefence research efforts in 2007, increasing its focus on ‘broad-spectrum’ priorities that would work against multiple pathogens. And in June this year, a federal panel recommended trimming and reorganizing the CDC’s select-agent list. But the NIAID is still funding research on plague and tularemia vaccines, and defends the work, saying that research on tularemia, for example, has yielded insights about immunity that are relevant to other pathogens. Michael Kurilla, director of the Office of Biodefence Research Affairs in the NIAID’s Division of Microbiology and Infectious Diseases, points to recent work on a broad-spectrum antiviral drug that, he says, sprang from studies of the Nipah virus, a category C bioterror threat. He says that this demonstrates the value of continued work on such pathogens as well as model microbes such as the bacterium *Escherichia coli*. “If you say everyone should study *E. coli* because it’s like everything else, you won’t get those concepts that come out of some unusual bug and have other applications,” he says.

Despite the problems with basic biodefence research, critics see far more to complain about in the later stages of the process. The

A DECADE OF BIODEFENCE

► OCTOBER–NOVEMBER 2001

Anthrax-laced letters are sent to media outlets and politicians, killing five people and prompting a major FBI investigation.



J. RAEDLE/GETTY IMAGES

► JUNE 2002

US President George W. Bush signs a law creating a list of ‘select’ agents considered to be the biggest bioterror threats, including smallpox and anthrax (pictured).



EYE OF SCIENCE/SPL

► JULY 2004

Project BioShield is created: a US\$5.6-billion programme to purchase countermeasures against bioterror attacks.

► NOVEMBER 2004

VaxGen of South San Francisco, California, is awarded some \$877 million by BioShield for its anthrax vaccine. The contract is cancelled in 2006 after VaxGen fails to meet milestones.

► DECEMBER 2006

Congress creates the Biomedical Advanced Research and Development Authority (BARDA), which assumes management of BioShield.

► JULY 2008

Bruce Ivins (pictured), a scientist at the US Army Medical Research Institute of Infectious Diseases in Fort Detrick, Maryland, commits suicide as the FBI is preparing criminal charges against him for the anthrax attacks.



AP PHOTO/FREDERICK NEWS POST/S. YU

► JULY 2009

BARDA orders 45,000 doses of anthrax drug from Human Genome Sciences of Rockville, Maryland. Later, the Food and Drug Administration declines to approve the drug.

► FEBRUARY 2010

US Department of Justice concludes that Ivins alone was responsible for the anthrax attacks, and closes the investigation.

► JUNE 2011

An advisory panel recommends trimming the select-agent list to only those posing the very greatest risk, such as the Ebola virus (pictured).



AMI IMAGES/SPL

► JUNE 2011

Legislators propose reauthorizing BARDA and funding BioShield at \$2.8 billion for 2014–18.

therapies can't be rigorously tested in humans (it would be unethical to infect people with pathogens such as smallpox for testing). And government agencies had little idea how to go about developing such therapies.

The smallpox drugs CMX001 and STS-246 are cases in point. CMX001 is a version of an established antiviral drug called cidofovir that must be given as an injection. In 2000, Karl Hostetler, a chemist at the University of California, San Diego, formed Chimerix, a pharmaceutical company based in Research Triangle Park, North Carolina, to develop a cidofovir pill that could be taken by mouth.

In September 2003, the NIAID awarded Chimerix a \$36-million, five-year grant to develop CMX001 as a treatment for smallpox. The drug looked promising in tests on mice and rabbits, and Chimerix teamed up with the US Army Medical Research Institute of Infectious Diseases in Fort Detrick, Maryland, to test it in monkeys infected with the related virus monkeypox. But the drug didn't cure the disease — owing, Chimerix said, to a quirk of metabolism not relevant to humans.

Meanwhile, SIGA, a pharmaceutical company based in New York, was racing ahead with STS-246, a small molecule that blocks viral maturation. In 2006, the company reported that its drug protected monkeys from monkeypox. While Chimerix struggled for funding, the federal government continued to award money to SIGA and, in October 2010, SIGA won a BARDA contract for STS-246 worth up to \$2.8 billion. Chimerix protested — and SIGA's award was later whittled down to \$433 million.

Yet the case of the sick marine in 2009 showed that fighting biothreats can take a whole armamentarium of drugs. Belken's condition didn't improve until CMX001 was added to STS-246. "The reality is that we need two smallpox antiviral drugs," says Robert Kadlec, a former Senate staff member who helped to write the 2006 legislation that created BARDA.

The episode shows how challenging it is to develop therapies, especially when there are no good animal models or data showing whether the drug fights disease in humans. The smallpox virus infects only humans, for example, and monkeypox is an imperfect mimic. Yet authorities often need to rely on animal tests when they make expensive decisions about which drug to buy, and small biodefence companies can be dependent on the funding that results from these decisions.

"The regulatory process is still evolving, and the federal government doesn't have a clear sense of what it needs," says Jim Davis,

executive vice-president of Human Genome Sciences in Rockville, Maryland. "It's frustrating for everyone involved." In October 2009, the US Food and Drug Administration (FDA) decided not to approve an antibody against anthrax developed by Human Genome Sciences — even though BARDA had already agreed to spend \$326 million on the drug. The company had thought that it had met the FDA's criteria but, according to Davis, the agency decided that it wanted a drug that is more effective than the existing anthrax treatment, ciprofloxacin.

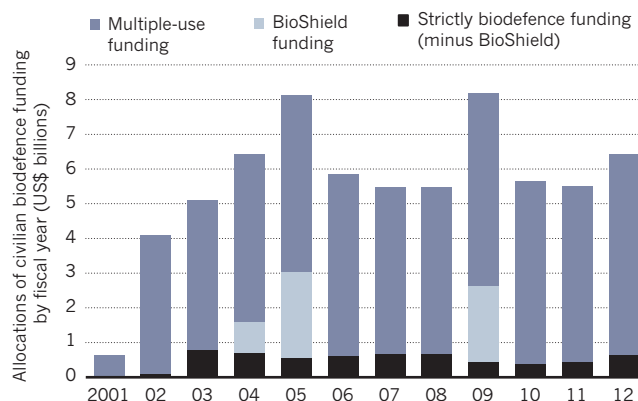
Robin Robinson, director of BARDA, says that the agency is funding the creation of better animal models. The DHHS reviewed medical countermeasures in 2010, and said that it will do more to try to help companies to bridge the gap between basic research and the clinic. The DHHS has also proposed reallocating \$170 million in existing FDA funds to help update regulatory review in biodefence.

But revamping biodefence is going to take more money — and critics say that some of the \$60 billion spent so far has simply been wasted. They point to a \$533.8-million surveillance project called BioWatch, created by the Department of Homeland Security, which has deployed detectors for airborne bioterror agents in 30 cities. The system has been criticized in part because technicians must manually collect the air filters and take them to a lab for analysis, creating a delay of 10–34 hours before results are in and hampering the system's ability to provide an early warning. In a report entitled *BioWatch and Public Health Surveillance*, released last year, a committee convened by the US National Academies said that BioWatch faces "serious technical and operational challenges". The next-generation Biowatch is designed to improve the programme.

Much of the biodefence money didn't even go into research, as a breakdown of spending shows (see 'Biodefence in billions'). The CDC has received the most so far — \$17.4 billion

BIODEFENCE IN BILLIONS

Much US biodefence funding has had additional uses, such as in public health. The government's BioShield programme buys finished drugs and vaccines.



— and put the vast majority into bolstering an underfunded public-health infrastructure. The rationale is that the nation has little chance of fighting a bioterror attack without a strong system for detecting, reporting and treating any emerging infectious disease.

Most of the biodefence spending, in fact, has spin-offs into other fields; even BARDA is involved in developing medicines against threats such as pandemic flu. In all, only \$11.99 billion of the \$60 billion has been spent on programmes solely concerned with biodefence. That's just over \$1 billion per year from 2001 to 2011.

Drug-makers often say that it takes at least \$800 million and ten years to develop a single drug, so a much greater investment is required before the biodefence effort can yield many new countermeasures. Kadlec recommends that the United States spend \$10 billion a year on biodefence in future.

FUNDING CRUNCH

Such sums seem unlikely to materialize. BioShield's funding is set to expire in 2013, and Congress has proposed refunding it at \$2.8 billion for 2014–18 — about the same as before. Cutbacks are eroding some of the gains in public-health infrastructure: local health departments have lost 29,000 jobs, some 19% of the workforce, over the past three years.

Now, say observers, the federal government must take a hard look at its biodefence programme and devise a more coordinated strategy that strikes a balance between developing pathogen-specific countermeasures and working on a more generalized resilience to infectious disease. "If the expectations were that we were going to come up with a whole armamentarium of new products by 2011, that was probably unrealistic," says Relman. "It might make sense to pick a few [threats] that are at the top of all possible lists, but then to say, a lot of the rest of the work needs to be in creating a fertile ground for innovation and product development."

"We're at a point after ten years," says Michael Osterholm, director of the University of Minnesota's Center for Infectious Disease Research and Policy in Minneapolis, "where we have got to start producing the kinds of plans and cost estimates about what it will take for a country like ours to be prepared in a moderate way." Preparing for only the worst eventualities might now be the best the nation can do. ■ [SEE COMMENT P. 153](#)

Erika Check Hayden is a senior reporter for *Nature* in San Francisco, California.

COMMENT

DEBT CRISIS US science must fight for piece of funding pie **p.155**



INSTITUTIONS Two books on why universities should get back to teaching **p.158**

EVOLUTION David Sloan Wilson's attempt to improve his home town **p.160**

ARCHITECTURE In conversation about North America's greenest building **p.161**

S. STAPLETON/REUTERS/CORBIS



Advanced Spectroscopic Portals developed by the US Science and Technology Directorate scan vehicles for radioactive material.

Homeland insecurity

In ten years of operation, the unwieldy Department of Homeland Security and its science directorate have seriously underperformed, says **Peter D. Zimmerman**.

September 11, 2001, began as a glorious day in the Washington DC area. As thousands of commuters left for work, there was no indication that, by the time they arrived, the United States would be at war, and its capital city under direct attack. Or that barely a week later, anthrax attacks would lead to the deaths of five people.

In the wake of the attacks, there was a general perception that a robust intelligence system fusing data from many sources and streams might have led to the discovery of the 9/11 plot. In October 2001, then-President George W. Bush created the Office of Homeland Security to help solve this problem; it was converted to a full cabinet

department with a bill signed in November 2002. From the start, scientific advances were seen as key to the primary Department of Homeland Security (DHS) mission. A Science and Technology (S&T) Directorate was created to contract basic and applied research to fulfil the DHS's needs.

From the beginning, the DHS has been a heterogeneous and immiscible collection of agencies with different cultures, policies, traditions, missions and responsibilities. These agencies do not function as a unified department, nor could they be expected to. The massive reorganization of the United States government to form the DHS is apparent in its seal: it has 22 stars, one for each

of the original entities smashed together to form the new organization.

The stated mission of the department was to protect US territory from terrorist attacks, accidents and natural disasters. That remit was almost instantly expanded to include the detection of counterfeit currency (formerly a task of the Secret Service), life saving at sea and on inland waterways (Coast Guard), naturalization of new American citizens (Immigration and Naturalization Service, now Citizenship and Immigration Services) and the interception of narcotics (Coast Guard, Border Patrol, Customs and Border Protection). At one point it was even suggested that the FBI and CIA, or ►

► significant parts of each, be folded into the DHS. Fortunately, this did not happen.

The S&T directorate has struggled to serve this widespread community. Plagued by cumbersome bureaucracy, budget troubles and a focus on post-terrorism response rather than terrorism prevention, it has failed to live up to reasonable expectations. Although its current undersecretary Tara O'Toole has done well with the system she inherited, the S&T budget has never been particularly stable — O'Toole calls it “lumpy and bumpy” — and the research component has been cut 81% by the most recent budget for the 2012 fiscal year. Without stable funding, you cannot embark on good research and development, nor can you hold on to good researchers.

The S&T directorate had a budget of US\$800 million in the 2004 financial year (it peaked at about \$925 million for 2006). It was criticized from the start for funneling funding almost exclusively into the Department of Energy national laboratories, rather than supporting university-based programmes or private-sector research. It is not hard to see why the first assistant secretary of homeland security for science and technology turned to the national labs. They had done excellent work, on nuclear weapons for example, and the necessary security clearances were already in place. Nevertheless, many people feel that overusing these labs may have precluded the innovations that might have come from a more broadly sourced effort.

Ten years on, it is apparent that the S&T directorate has seriously underachieved. A reorganization or slimming down of the whole DHS is needed, to help focus the S&T directorate and, hopefully, get it a larger slice of the department's budget.

UNDERWHELMING ACCOMPLISHMENTS

What has the S&T directorate actually accomplished? There have been improvements in biodetection and biological terrorism risk assessment (see page 150). And the directorate has a major role in civilian cybersecurity efforts. DHS laboratories have greatly improved the detection of home-made explosives, such as those used in the London bombings of July 2005.

When O'Toole listed 16 of the directorate's most significant results in a memo to me earlier this year, she named some decidedly low-powered accomplishments along with some significant ones in cybersecurity and power-grid security. The accomplishments included a new lightweight breathing apparatus for fire fighters; the IronKey secure USB thumb drive that can destroy its data to prevent unauthorized access; a new scanner called MagViz that will allow passengers to carry water bottles through airport security; and new hardware for making electric power

grids resilient against lightning strikes, solar storms and electromagnetic-pulse attacks. Despite some major achievements, the list is somehow underwhelming.

Public attention has focused on the department's more glamorous S&T projects, particularly those aimed at the high-priority threat of nuclear smuggling. These have been less than successful. The DHS and its partner the Domestic Nuclear Detection Office developed the Advanced Spectroscopic Portal (ASP) and the Cargo Advanced Automatic Radiographic System (CAARS), both intended to screen cargo for radioactive and nuclear material.

“Without stable funding, you cannot embark on good research and development.”

Both were doomed because they tried to respond to Congress and public fears by building silver-bullet devices that would do everything.

Tests of the ASP system were deficient in many ways. The most likely combinations of radioactive source, conveyance and shielding weren't tested, and the wrong performance metrics were chosen to compare different screening systems. The testing was subjected to withering criticism by the Government Accountability Office, Congress and a panel of the National Academies, who said that it was impossible to conclude whether the ASP would do better than current hand-held scintillators at detecting nuclear material.

“Science was outpaced by public fear,” said Francis Slakey, who follows nuclear issues for the American Physical Society. Moreover, the ASP requires helium-3 to function: a rare gas that is used in industry and some science, including ultra-cold physics. Thanks in large part to purchases for the ASP, the price of helium-3 rocketed from around \$200 a litre in 2009 to around \$2,000 a litre in 2010, putting a strain on research budgets. In the end, the ASP project flopped: on 26 July 2011, Domestic Nuclear Detection Office director Warren Stern testified that the department would only use the ASP for secondary scanning, in part because the original design specification was inadequate.

CAARS progress has not gone smoothly either. In contrast to the ASP's passive system, it fires beams from an accelerator into cargo to flag trucks and containers that need secondary, hands-on inspection. In September 2010, the Government Accountability Office accused the Domestic Nuclear Detection Office and the DHS of misleading Congress about the project's progress. Among other things, they were accused of not even consulting

with Customs and Border Protection as to whether the projected facilities would fit in the nation's seaports. On 30 September 2010, Stern said that the programme “will essentially end now”, although some of its useful technologies are likely to find employment elsewhere, in global efforts against nuclear smuggling.

COP MENTALITY

A thread in many discussions I have had about the DHS in recent weeks is that the S&T directorate suffers from ‘cop mentality’. Many of the department's personnel have backgrounds in law enforcement, leading to a heavy emphasis on post-attack response and preservation of evidence to permit prosecution of attackers. But putting offenders in prison does nothing to protect the public from incidents that might have been prevented with the proper investment in interdiction, interception and intelligence.

Instead, the S&T directorate should be working on technologies that help to anticipate acts well before they begin and the chance of success rises. The DHS is not well structured to do this.

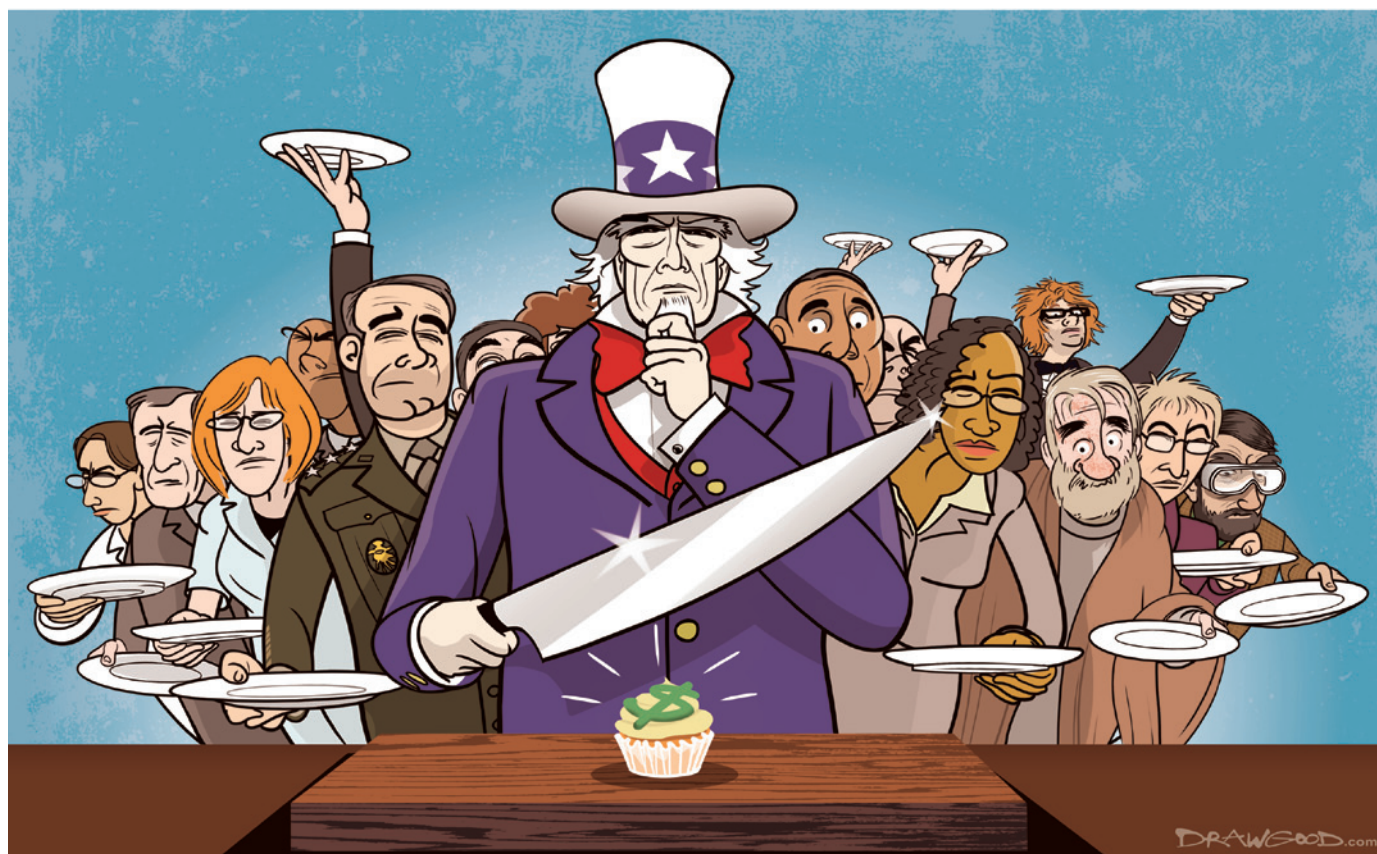
Most of the DHS officials and employees that I have met are very good. All of them want to protect the American people, and most of them work long hours for relatively low pay. Some risk their lives and health every day. They are working in a structure that is likely to be diluting their efforts and hobbling them with an inconsistent bureaucracy drawn from the 22 different organizations.

The idea of consolidating some domestic security operations wasn't a bad one. The problem was in the details. Customs and the Border Patrol, along with immigration regulation, may well be a good fit with the Transportation Security Administration and even the Animal and Plant Health Inspection Service. It's not clear to me that the Secret Service (which protects the president as well as enforcing counterfeiting laws), as one example, belongs with them.

There will be a place for science and technology in any structure designed to protect the United States, but the scope of the DHS S&T directorate — from fundamental biosciences research to very niche applied engineering — is too great for any individual entity to manage. After ten years, it is time to rethink the organization of the DHS and the role of its science directorate. Split up the department? Maybe. Recognize that it hasn't worked as is? Definitely. ■ **SEE NEWS FEATURE P.150**

Peter D. Zimmerman is in the Department of War Studies, King's College London, Strand, London WC2R 2LS, UK. He served as chief scientist of the US Senate Foreign Relations Committee from August 2001 until March 2004.
e-mail: peter.zimmerman@cox.net

► **NATURE.COM**
Airport security:
Intent to deceive?
go.nature.com/hqtbai



Crunch time for US science

Researchers must make a stronger case for funding in the face of a perfect storm of budget cuts and eroding political support, says **Jay Gullledge**.

The current US debt crisis sets the stage for a potential tipping point in federal science spending. The ideology that government-sponsored science is crucial to the well-being of society has eroded along with the cold-war security agenda, which embraced and fortified science for decades. Meanwhile, science has been pulled repeatedly into political clashes on cultural issues. Against this backdrop, the global economic crisis portends a decade-long reduction in federal budgets. To avoid a permanent retraction of government support for research, the science community must be more strategic and aggressive in conveying the value of its work to society and in gaining robust support from politicians.

US federal science spending has long been rooted in the national security agenda. The

National Science Foundation (NSF) was established shortly after the Second World War "to promote the progress of science; to advance the national health, prosperity, and welfare; to secure the national defense". NASA was established less than 10 months after the Soviets launched Sputnik 1 in 1957, in a frenzied response to the Soviets' early lead in developing ballistic missiles. Through the decades of the cold war, support for science straddled party lines.

But, after the fall of the Berlin wall, the United States stood as the sole great power and shifted its strategic emphasis from establishing scientific superiority to cultivating democratic movements in the developing world. The 11 September 2001 terrorist attacks reinforced this shift: security analysts believed that Al Qaeda and the Taliban, the main US enemies, would

be defeated by winning hearts and minds, not by building a better mouse trap.

The erosion of the cold-war security doctrine therefore removed the bipartisan backstop to science funding. The quest for economic competitiveness might reasonably have replaced it, but has not done so. For example, the America COMPETES Act, passed in 2007 and reauthorized in 2010 by Democrat-run Congresses, planned to expand the NSF's budget from US\$6.6 billion in 2008 to \$8.1 billion in 2010, but appropriators froze NSF budgets in response to the economic crisis. The current Republican-led House of Representatives is unlikely to support the increase of science budgets. Representative Ralph Hall (Republican, Texas), the recently installed chair of the House Committee on Science, Space and Technology, has said that the ►

► America COMPETES Act is “just too heavily drowned in money”.

Add to this the ‘culture wars’ that have gripped the United States for some time. They split the nation into two camps along divisive issues such as abortion, gun control and gay rights. In recent decades, some of the most contentious issues have put science in the crossfire, from evolution to tobacco health effects, stem-cell research and most recently my own area of expertise — climate change. This year, an informal survey of US Earth-science teachers found that climate change was second only to evolution in evoking protests from parents and school administrators (S. Reardon *Science* **333**, 688–689; 2011).

These divisions threaten science budgets. Hall has expressed doubts about the scientific evidence for human-induced climate change and recently sponsored an amendment to the 2011 spending bill to stop the National Oceanic and Atmospheric Administration from spending money to set up a national climate service; the bill passed with support from 227 Republicans and 6 Democrats.

ECONOMIC SHOCK

In the midst of all this, the debt-ceiling deal — formally the Budget Control Act of 2011 — has the potential to administer a massive shock to science budgets. The law requires non-defence discretionary spending (which includes science funding) to be cut by \$917 billion over the next ten years, an average of 15% per year. On top of this, an automatic trigger will reduce spending on defence and on social entitlements — the sacred cows of Republicans and Democrats, respectively, if by the end of the year Congress cannot agree on ways to reduce the deficit by \$1.2 trillion over the next decade. The two parties will therefore be strongly motivated to cut non-defence discretionary budgets as much as possible.

Whether future Congresses will soften the impact of the debt-ceiling deal depends on the pace of economic recovery, the evolution of the culture wars and the public's perception of the return on taxpayer investment in research. The scientific community can directly influence the last of these, but it needs a coherent strategy to do so. Like industry, it needs to document its net value to society and flaunt it. Unfortunately, through decades of cold-war complacency, the scientific community has developed a culture that runs counter to doing this.

An institution representing the US science community is needed to undertake a broad, ongoing, quantitative assessment of the overall contribution of science to society

“Like industry, science needs to document its net value to society and flaunt it.”



and the economy and communicate these effects to the public and politicians, through the media and other channels. As ever, the contribution to national security is a good place to start. Neutralizing today's threats — terrorism, biological and chemical weapons, nuclear proliferation, and cyberwarfare — is an intensely scientific undertaking. Social sciences are needed to tackle joblessness, food and energy insecurity, financial disruptions and climate-change-induced destabilization of developing countries. Economic development, cost savings through innovation and efficiency enhancement, environmental quality, mental health and happiness are all affected by scientific research and development.

The American Association for the Advancement of Science is the traditional home for such cross-cutting efforts, and its work is laudable. But the ongoing public misunderstanding of science shows that the established approaches are inadequate.

There are signs of new ways of thinking. In March, the American Geophysical Union hosted a gathering of the presidents and top administrators of 17 US scientific societies and research consortia, from a broad spectrum of fields, to discuss how they might cooperate to improve public understanding of climate science — a unique and remarkable effort that should be expanded.

At the same time, science institutions need to enhance their value to society by incorporating socioeconomic benefits into their missions. Although some branches of academies already embrace this role to some extent — medical, law and engineering schools, for example — basic-science and social-science schools traditionally eschew it.

► NATURE.COM
Lessons learned from MIT's search for funding:
go.nature.com/neltih

In part this is because the production of social benefits is scantily rewarded. In the words of Anthony Janetos, director of the Joint Global Change Research Institute at the University of Maryland in College Park, at a 2009 meeting of the Center for a New American Security in Washington DC: “Nobody asks me, ‘How many policy decisions did your work inform?’ Instead they ask, ‘How many papers did you publish and how much grant money did you raise for the institute?’” Both should matter.

Peer-reviewed publications, research grants and professional impact should remain the core metrics of success in academia. But the remit should be broadened so that recognized publications include assessment reports and science-based articles in public-policy, interdisciplinary and business journals. Recognized grants should include those from mission-oriented agencies, foundations and non-governmental organizations. And recognized impact must include influence on government, business and civil-society decision-makers.

The drive for international superiority during the cold war passively nourished a wide spectrum of sciences, the true value of which manifested in an array of benefits outside defence. In today's chillier strategic and political climate, the scientific community must work hard to enhance and advertise those benefits. Those in academia who worry about the erosion of curiosity-driven science should have a greater fear: the erosion of science in general. ■

Jay Gullede is the senior scientist and director for science and impacts at the Pew Center on Global Climate Change, Arlington, Virginia 22201, USA, and a non-resident senior fellow at the Center for a New American Security.
e-mail: gulledejp@pewclimate.org



The tenure system protects professors but can be a block to academic freedom for untenured staff.

HIGHER EDUCATION

Academic questions

Two provocative books skirt around why universities should get back to teaching, finds **David Helfand**.

The university of today is a fractious collection of interest groups in which customers (formerly known as students) demand high grades for their money, while researchers with large frequent-flyer accounts (formerly known as faculty) seek to minimize their teaching 'loads'. Meanwhile, property developers, who were once called academic administrators, relentlessly push for institutional expansion.

Or so a raft of books on the imminent collapse of higher education in North America would have you believe. As with most caricatures, this one contains elements of truth. I am sufficiently concerned about the state of the academy that I have taken leave from Columbia University in New York to lead a new college in Canada — Quest University — developed from scratch to place teaching and learning back at the centre. But the above portrait is oversimplified and exaggerated. Two books, Naomi Schaefer Riley's *The Faculty Lounges* and Ellen Schrecker's *The Lost Soul of Higher Education*, add to the debate — and the exaggeration.

An oft-repeated story highlights the authors' differing attitudes towards academia. When Dwight Eisenhower became president of Columbia University, two years before he became US president, he began his first faculty address with "Employees of the University..." Columbia physicist I. I. Rabi interrupted: "Excuse me, sir, but we are the University."

The Lost Soul of Higher Education: Corporatization, the Assault on Academic Freedom, and the End of the American University

ELLEN SCHRECKER

New Press: 2010. 304 pp. \$27.95

The Faculty Lounges: And Other Reasons Why You Won't Get The College Education You Paid For

NAOMI SCHAEFER RILEY

Ivan R. Dee: 2011. 216 pp. \$22.95

These authors split along similar lines: Riley decries the power that tenured professors wield across the university system, whereas Schrecker bemoans the loss of academic freedom and faculty governance brought about by the rise of corporatization. Both cannot be right; neither is.

Schrecker is a former editor of *Academe*, the magazine of the American Association of University Professors, the century-old, self-appointed guardian of the US tenure system. She presents a history of academic-freedom cases, both well known and obscure. Writing from a liberal standpoint, she argues that the "barrage" of conservative criticism now aimed at universities is not so much about curricula or concerns about taxpayer-supported radicals, but is a consequence of the progressive social mission of colleges. As the last haven for serious dissent and a vehicle for social mobility, she writes, the US university has become "a surrogate for everything that its critics dislike about American society".

Filling the critics' brief is *The Faculty Lounges*, largely an attack on the US professoriate. Riley, a former *Wall Street Journal* editor, questions whether modern political scientists should be counted on to improve US government, compared, say, to the authors of the Federalist Papers that promoted the US Constitution. One might answer yes, as politics has changed in two centuries. In her eyes, the answer is a clear no. Yet in my view she offers no serious analysis, instead packing the book with quotes from conservative organizations such as the American Council of Trustees and Alumni, whose website announces: "The barbarians are not at the gates; they are inside the walls." I have rarely been so irritated by a book with whose premise I broadly agree.

Riley's ideological purity undercuts her critique of tenure, and will put off readers who should contemplate this important issue. Schrecker fails to recognize that tenure is more about denying the academic freedom of those who don't have it than about protecting those who do. Postgraduates and tenure-track scholars fear crossing the ideas and personalities of the tenured faculty members who decide their fates. The problem with Schrecker's book is that it downplays this reality. The problem with Riley's is its conviction that faculty lounges are full of lazy, left-wing ideologues who aim to undermine democratic values.

The protection of underperforming faculty members and the suppression of freedom among the unanointed are real problems with the tenure system. But, in my view, there is a more crucial difficulty that both books ignore — the selection of professors. Most university professors are smart, but most smart people are not professors. Some social filter selects the few intellectuals who choose careers in academia. My concern is that this filter is tenure: seeking out those most attracted to lifetime security without performance reviews does not strike me as an optimal way to find people who are best suited to advancing the frontiers of knowledge and inspiring the next generation.

Schrecker goes on to criticize the proliferation of academic bureaucrats, citing a 2006 National Center for Education Statistics report that allegedly shows (although I could not check it) that there are more administrators than faculty members in US institutions of higher learning. I was struck by a different trend: faculty numbers are increasing even faster. At public four-year-degree institutions between 1989 and 2009, executive or administrative positions increased by 31%, while faculty grew by 54%. For private four-year institutions, the numbers are 93% and 214%, respectively. Meanwhile, the number of bachelor's degrees conferred rose by 52%.

Much of this faculty expansion, as both authors note, is in part-time positions: in 1989, part-timers made up just over one-third

P. TITMUS/ALAMY

of US faculty; by 2009, they were close to half the total. So, over this period, full-time faculty growth was 39% and part-time was 237%. Such positions are typically filled by scholars who are poorly paid, have little say in departmental and university affairs, and no possibility of tenure. These itinerant faculty members, once found mainly in two-year community colleges, are now prevalent throughout the academy — public and private, undergraduate colleges and research universities. Whereas women made up 28% of full professors at US degree-granting institutions in 2009, they were a majority (52%) among non-tenure-track faculty.

Both authors address this growth in expendable faculty, but differ as to its cause. Schrecker sees the problem as part of a general attack on faculty prerogatives and academic freedom. Riley sees it as a logical move to

“The growth in part-time faculty is bad for students.”

bring universities much-needed flexibility. A unique point of agreement between them, with which I agree,

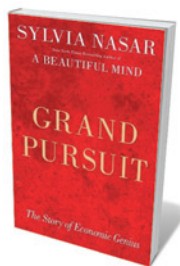
is that the growth in part-time faculty is bad for students. With limited office hours and termly contracts that exclude a role in curriculum development, part-timers are faculty in name only, without the time, resources, or support to truly educate their students.

Alternatives are possible. At Quest University Canada, a four-year-old independent institution in British Columbia that has 350 students and 25 faculty members (expected to double in five years), we have no faculty ranks, no tenure and no departments. The review and renewal of multi-year contracts for research and teaching staff are conducted by an elected committee of peers. Teaching is central to the institution's mission, and all staff share equally in this task. The mix of scholarship, curriculum development and other institutional service that, along with teaching performance, forms the basis for the review committee's judgement, is individually tailored and can vary over the course of one's career. This collegial approach fosters academic freedom, minimizes bureaucracy and places the university's focus on teaching and scholarship. Regrettably, it is unlikely to spread, owing in my view to the inherent conservatism of most academics and an unholy pact among the majority of students, faculty and administrators, all of whom benefit from the status quo.

Both books raise important questions while peddling their respective strong lines. Let's hope that the debate we sorely need in academia proceeds in a more nuanced way. ■

David Helfand is president of Quest University Canada in Squamish, British Columbia, on leave from Columbia University. e-mail: djh@astro.columbia.edu

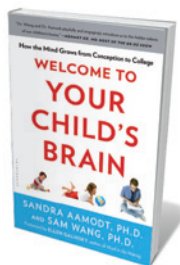
Books in brief



Grand Pursuit: The Story of Economic Genius

Sylvia Nasar SIMON & SCHUSTER 554 pp. \$35 (2011)

Sylvia Nasar, economist and author of *A Beautiful Mind* (1998), examines genius through the shaping of economics. Her tour of modern economic history takes us from Charles Dickens and journalist Henry Mayhew, who together woke the world to the scale of London poverty, through Karl Marx and the pioneering social reformers Beatrice and Sidney Webb, to great innovators such as John Maynard Keynes and Nobel prizewinner Amartya Sen. The field emerges as the 'apparatus of the mind' that Keynes saw was needed for understanding and optimizing the workings of society.



Welcome to Your Child's Brain: How the Mind Grows from Conception to College

Sandra Aamodt and Sam Wang BLOOMSBURY 336 pp. \$26 (2011)

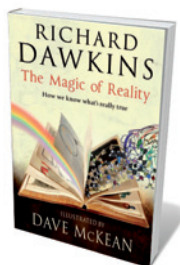
Neuroscientist Sam Wang and Sandra Aamodt, former editor-in-chief of *Nature Neuroscience*, pack into this compendium cutting-edge research on the growing brain, from birth to the age of 21. They lay out seven scientific principles behind neural development, including the interaction of genes and the environment; education; sensory experience and play; and issues such as autism, attention deficit hyperactivity disorder and growing up in poverty. With its clear graphics, this is a useful companion guide for educators and families.



American Anthrax: Fear, Crime, and the Investigation of the Nation's Deadliest Bioterror Attack

Jeanne Guillemin TIMES 336 pp. \$27 (2011)

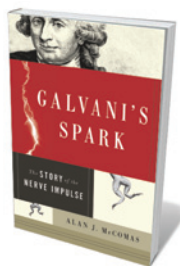
Bioterrorism is a threat that governments prepare for with huge variability. Medical anthropologist Jeanne Guillemin chronicles the deadliest such attack in the United States, when five letters carrying anthrax arrived at the Senate and at media organizations in 2001, killing five people and sparking a seven-year investigation. The event was used to justify the Iraq invasion and billions were spent on biomedical defences, yet Guillemin reminds us that the pathogen in the letters originated somewhere within the US military system.



The Magic of Reality: How We Know What's Really True

Richard Dawkins and Dave McKean BANTAM 272 pp. £20 (2011)

Faced with the strange, the sudden and the beautiful in nature, each generation of children asks the same big questions — from how the Universe began to what thunder is. Evolutionary biologist Richard Dawkins takes on the answers, with acclaimed illustrator Dave McKean, in graphic-novel style. By detailing the hard science behind natural phenomena such as species diversity, and detaching accreted myths, Dawkins strives to reveal 'magic' as an aspect of the real. Although pitched at both children and adults, this is a heavy-handed treatment that fits into neither category.



Galvani's Spark: The Story of the Nerve Impulse

Alan J. McComas OXFORD UNIVERSITY PRESS 391 pp. £40 (2011)

Serendipity met science when eighteenth-century anatomist Luigi Galvani discovered the nerve impulse — the 'spark' that drives actions, thoughts and sensations — in the twitch of a frog's leg. Neurophysiologist Alan McComas traces the shaping of neuroscience from this point by greats such as Alessandro Volta and David Hubel. From Santiago Ramón y Cajal's meticulous renderings of neural cells to Alan Hodgkin and Andrew Huxley's work on the squid giant axon, McComas chronicles the triumphs and obstacles of the field.

EVOLUTION

Small-town utopia

Kevin Laland commends a campaign to forge a better community using the principles of natural selection.

Mixing sociology, anthropology and psychology with evolution can be explosive. In 1967, Desmond Morris's book *The Naked Ape* created a furore by portraying humans as shackled by ancient animal instincts, and made contentious evolutionary arguments that, for instance, pornography is harmless. Edward O. Wilson's *Sociobiology* (1975) created another storm by proposing evolutionary explanations for xenophobia and religion. The fires were stoked a third time by evolutionary psychologists who proclaimed a revolutionary science of the mind.

Readers conscious of this backdrop might be forgiven for approaching *The Neighborhood Project*, by biologist David Sloan Wilson, with trepidation. Wilson, describing his attempts to bring evolutionary ideas to the streets of his home town, Binghamton in upstate New York, asserts that evolutionists must "walk the walk", not just talk the talk.

Ordinary people, Wilson maintains, will only take to evolutionary science when it is able to deliver practical answers to the issues that concern them, such as how to improve their children's performance at school. An expert in the study of cooperation, Wilson is acutely aware of how natural selection can favour both social and antisocial behaviour.

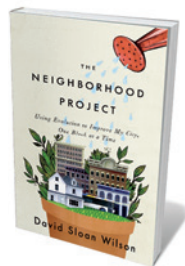
Some seven years ago he set out to see

whether the residents of Binghamton could be made more caring by improving their environment using evolutionary principles. Wilson began with a survey, asking locals to what extent they agreed with statements such as 'It is important to help other people'. He combined this information with other measures of community spirit — from the number of people who display Christmas decorations, to the rate of return of deliberately 'lost' letters. Using technology based on geographical information systems (GIS), he turned the data into maps of the city, revealing caring and less-caring areas as nice 'hills' and nasty 'valleys'.

Wilson's studies of local schoolchildren showed that those with strong social tendencies hailed disproportionately from supportive neighbourhoods; statistical analyses confirmed that this relationship was not an artefact driven by another variable, such as income. He argues that children can be made into 'good Samaritans' or 'bad eggs' by their surroundings because, like other animals, humans are predisposed to cooperate selectively with those who are likely to reciprocate.

But Wilson is not content just to study good behaviour, he wants to engender it. *The Neighborhood Project* details his efforts to "raise the valleys of my GIS maps into hills" by forging alliances with local teachers, school superintendents, politicians and business people to create an evolution-inspired task force dedicated to beautifying the city.

The indefatigable Wilson does not stop there. He goes on to conceive several other ambitious projects, including The Evolution Institute, a national think tank designed to devise public policy based on evolutionary principles, focusing initially on childhood education. Undeterred by the graveyard of past attempts to improve schooling,



The Neighborhood Project: Using Evolution to Improve My City, One Block at a Time

DAVID SLOAN WILSON
Little, Brown: 2011.
448 pp. \$25.99

Wilson assembles his dream team of evolutionists to sort out the problem.

He reaches several conclusions, including that educational practices such as learning by rote and grouping children in classes of the same age are unnatural, based on his assumption that learning in ancestral populations was much more spontaneous. He advocates other approaches that he feels more effectively exploit our evolved learning capabilities, such as the emphasis on child-directed learning in the mixed-age groups adopted by Montessori schools. His whistle-stop tour of evolutionary fixes then moves on to the global debt crisis and the nature of religion.

Will Wilson be more successful than his predecessors? One reason he might is his rich, well-informed interpretation of evolution, encompassing biological and cultural evolution, multilevel selection and a sophisticated understanding of how learning and culture build on genetic predispositions. However, it remains to be seen whether good science will translate into good policy.

Wilson writes well, and his monograph is an absorbing account of how an individual scientist can make a difference to their local community. He profiles the people he describes with great care, turning each character into a local hero. Wilson clearly has a gift for inspiring others with the potential of evolutionary science, but is sometimes in danger of getting carried away with his own zeal, even framing his ideas as 'parables' and 'commandments'.

Wilson's attempts to harness his research to improve society are admirable, but there are reasons to be cautious. Evolutionary theory is one of the most fertile, wide-ranging and stimulating of all scientific ideas, yet therein lies the danger: just about anything can be endorsed by an evolutionary hypothesis. For instance, at the first Evolution Institute workshop in 2008, one evolutionist claimed that knowledge that did not exist in ancestral environments, such as mathematics, can never be picked up spontaneously by children. Another claimed that all subjects can be learned readily in a supportive environment. Some advocated child-directed learning; others, direct instruction. Although Wilson is right to claim that evolution can deliver multiple solutions, it is also credible that some of these evolution-inspired hypotheses are wrong.

The Binghamton project is still too young to evaluate. But if Wilson succeeds, it will be a triumph for science, pluralism and common sense as much as for evolutionary biology. ■

Kevin Laland is professor of biology at the University of St Andrews, Fife KY16 9TS, UK. e-mail: knl1@st-andrews.ac.uk



Child-centred learning follows evolutionary concepts.

OCEAN/CORBIS

S. BOSCH/PNG



Q&A John Robinson Mr Sustainability

John Robinson directs the Centre for Interactive Research on Sustainability (CIRS), a hub for sustainability research that opens for business this month in an ultra-green building at the University of British Columbia (UBC) in Vancouver, Canada. Robinson explains the practical challenges involved in turning a campus into a 'living lab'.

What makes the CIRS building stand out in terms of sustainability?

The old agenda of designing buildings that do less damage is not good enough. We have to move on to the net positive agenda: can we construct buildings that actually improve the biophysical and human environment? By adding this 5,600 m² building we will actually reduce the university's total energy use.

How will it do that?

We take waste heat from the Earth and Ocean Sciences building next door, use one-third of it for our heat, and give two-thirds of it back to them. All of the water we get will be from the sky, and it will be treated so that the water leaving the building will be better quality than the rain water. And it's a wooden building, so we sequester more carbon in it (around 600 tonnes) than the amount emitted in its construction and decommissioning (525 tonnes).

What does the building look like?

When you stand in the atrium you see a big screen that displays live information about the building's performance. You can see all the main technologies, from rainwater collection to the photovoltaics. At the front, we have a 'living wall' entirely covered by vegetation: in the summer, the leaves block most

sunlight and in the winter it lets more sun through. Up a floor, you can walk out on to the green roof.

CIRS has been called North America's greenest building, but you say you don't like the label. Why not?

The term 'green' is too narrow. To most people, green means environmental. Sustainability is just as much about social justice and equity as it is about climate change and air pollution.

What are the social science aspects of this project?

The goal is to turn the occupants into inhabitants who have a sense of engagement with the building. We're going to ask everyone working there [about 150 people] to sign a sustainability charter in exchange for high air quality, individual control over air flow at the desks and access to daylight everywhere. We'll measure their health, happiness and productivity for years.

You also aim to prove that building in a green way is affordable. Is it?

Originally we thought that CIRS would cost only 8% more than the minimum standard building we're allowed to construct at UBC. Unfortunately it is more like 25%. We started

two months late, and ran into problems with rain — we had to build an extra roof during construction and bring in machinery to dry the wood. On the total cost over, say, 25 years, with all the energy savings it should be about even.

The concept for this building was born in 1999. Why has it taken so long to get built?

Anything sustainable keeps running up against the building code, or a health and safety regulation, or even 'that's not the way we do things'. We're not just talking about changing a technology, it's about changing our whole socioeconomic trajectory.

What obstacles did you hit?

We had to demonstrate that we could build this out of wood and it wouldn't be a fire hazard. One way they test this is to simulate how fast the building can be evacuated and how fast fire trucks can get there. Someone said, 'Wait a minute — weren't we talking about having water storage for the rainwater? Why can't we use that?' It eliminated our problem. We also used a lot of pine-beetle-killed wood. That's a huge issue in British Columbia: last year the dead wood released more carbon than the province's anthropogenic emissions. However, that may end up costing us a sustainability point. The wood isn't Forest Stewardship Council certified; it's clear-cut. We've been arguing for an exemption. But so far that hasn't been granted.

The UBC sustainability initiative, which you direct, aims to cut net carbon emissions by 67% by 2020, and by 100% by 2050. How?

We arrange for companies to use the campus as a test bed for innovative technologies. But ultimately it's about integrated systems. We need to treat our campus as a living lab, and build more than a smart grid. We need a smart energy system that includes all sources and uses of energy — from waste to food.

How important is it for universities to act?

Every university on the planet has a moral imperative and a strategic opportunity to use their facility as a test bed. UBC is a large area with a single owner, we have our own utility systems, we teach and do research, and we're public, so we can take risks and be forgiving about whether we get payback. Also, it's exciting to see what can be done on the community or neighbourhood scale.

What is the biggest lesson you have learned?

Three years ago I wouldn't have believed I could have the job I have now. It happened lightning fast; it's the old story of the overnight success that took 20 years. Ideas that seem crazy and impossible can become 'of course'. That gives me hope. ■

INTERVIEW BY NICOLA JONES

Correspondence

US private funder on indirect costs

As vice-president of the James S. McDonnell Foundation (JSMF), I wish to clarify our position on the recovery of indirect research costs, which include overheads such as administration and building-maintenance costs (*Nature* **476**, 385; 2011). You are correct in that the JSMF does not allow applicant institutions to include indirect costs as a component of budget requests; however, this should not be branded as a 'refusal' to fund indirect costs.

The JSMF, like many private foundations, considers it inappropriate for institutions to request indirect costs from private funders. In the United States, recovery of indirect costs by universities is negotiated with federal funding agencies because most US-funded research is done on university campuses.

It is unfortunate that a misunderstanding over the history and reasons for recovering indirect costs continues to strain relations between universities and private funders. A core mission of universities and education is the creation of new knowledge through research and scholarship. Grants from private funders such as the JSMF are helping universities to realize these goals; contrary to common belief, foundation grants are budget-relieving, not budget-additive. Providing for indirect costs would be incompatible with this traditional relationship.

Susan M. Fitzpatrick *James S. McDonnell Foundation, St. Louis, Missouri, USA.*
susan@jsmf.org

Improve China's sustainability targets

China's national and local governments have defined various eco-indicators to promote sustainable development. Some revisions are needed to improve economic

performance, environmental quality and social development.

The State Council, for example, has proposed national emission-reduction targets in its latest five-year plan (2011–15), for which the eco-indicator is a reduction in carbon dioxide emissions per unit of gross domestic product by 40–45% in 2020 relative to 2005 levels (see go.nature.com/4k3mqo). Others include circular-economy indicators released by the National Development and Reform Commission in 2007 to address the environmental degradation and resource scarcity associated with rapid economic development (H. Li *et al.* *Energy* **35**, 4273–4281; 2010); national eco-industrial park indicators set up by the environment ministry in 2006 (Y. Geng *et al.* *J. Ind. Ecol.* **13**, 15–26; 2009); regional sustainable-development indicators brought in by the science ministry in 2009; and national environmental-living indicators put forward this year by the housing ministry.

Most of these indicators are relative. Given China's rapid economic development, a reduction in terms of ratio-based indicators may not mean a net reduction in emissions and consumption of materials or energy.

There is no provision in sustainable-development plans generally for prevention-oriented indicators that reduce — rather than support — recycling and reuse. However, curtailing the production of reusable waste materials by promoting such an indicator would disadvantage producers and consumers who would benefit more from reuse-and-recycling indicators.

Autonomy and lack of standardization allow local government officials to cherry-pick their achievements to collect political credits and encourage them to select indicators that cast them in a positive light.

Data collection on eco-indicators is complicated when it involves different

agencies. Officials need to secure cooperation from other relevant government agencies to guarantee the validity and accuracy of such data.

Most eco-indicators are voluntary and can be pursued with different intentions. The relatively rich regions of eastern China have a genuine interest in improving resource efficiency and environmental performance. The poorer western regions are more likely simply to want to gain access to national financial subsidies.

Geng Yong *Institute of Applied Ecology, Chinese Academy of Sciences, Shenyang, China.*
gengyong@iae.ac.cn

Flagging flora: help from bacteriocins?

With regard to Martin Blaser's concerns about the collateral damage to commensal bacteria caused by overuse of broad-spectrum antibiotics (*Nature* **476**, 393–394; 2011), there are some potent alternatives in the pipeline.

Bacteriocins are peptide antimicrobials that could be harnessed to control a variety of problematic pathogens. Many bacteriocins act only on a narrow range of targets and are active at very low (nanomolar) concentrations. For example, we found that thuricin CD specifically eliminates *Clostridium difficile* bacteria from among the trillions of bacteria in a model gut system (M. C. Rea *et al.* *Proc. Natl Acad. Sci. USA* **108**, S4639–S4644; 2011). Diarrhoea associated with *C. difficile* infection is an often-fatal disease resulting from the growth of antibiotic-resistant spores after disruption of the gut microbiota by antibiotics.

Researchers are beginning to identify microbes and human microbial populations that are associated with conditions as wide-ranging as liver, coeliac and inflammatory bowel diseases, obesity, diabetes,

irritable bowel syndrome, colon cancer, pouchitis and even mental health. We believe that bacteriocins could be used in the future to design and shape 'healthy' bacterial communities.

Paul D. Cotter, R. Paul Ross *Teagasc Food Research Centre and Alimentary Pharmabiotic Centre, Cork, Ireland.*
paul.cotter@teagasc.ie
Colin Hill *Alimentary Pharmabiotic Centre, Cork, and University College Cork, Ireland.*
Competing financial interests declared. See go.nature.com/lb1n8e.

Flagging flora: heart disease link

Martin Blaser highlights the connection between the human intestinal microbiota and diabetes, obesity and inflammatory diseases (*Nature* **476**, 393–394; 2011). Another link is the metabolism by the gut flora of the dietary lipid phosphatidylcholine to produce molecules such as trimethylamine N-oxide, which can predict cardiovascular disease (Z. Wang *et al.* *Nature* **472**, 57–63; 2011).

The surge in heart disease and diabetes started to emerge around the time of the Second World War, when the use of antibiotics first became widespread. Although the causes of this surge are likely to be multifactorial, it is important that we study and preserve our own internal biodiversity.

Sean Davidson Hatter *Cardiovascular Institute, University College London, UK.*
s.davidson@ucl.ac.uk

CONTRIBUTIONS

Correspondence may be sent to correspondence@nature.com after consulting the author guidelines at go.nature.com/cmchno. Readers are also welcome to comment online: www.nature.com/nature.

ASTROPHYSICS

Broad escape from the abyss

New ultra-high-resolution images of the radio galaxy M87 show the origin of a jet very close to the galaxy's black hole, revealing that jets start as broad flows before straightening into nearly cylindrical beams. [SEE LETTER P.185](#)

ALAN P. MARSCHER

Black holes are extraordinarily compact and lie at great distances from us, so telescopes generally cannot resolve phenomena that occur close to their borders. Fortunately, the giant elliptical galaxy M87, whose nucleus contains a supermassive black hole (a black hole with a mass of 6×10^9 Suns), is near enough to offer a close-up view of the high-speed jet that is launched from near the black hole. On page 185 of this issue, Hada *et al.*¹ demonstrate that radio images made with the technique of very-long-baseline interferometry directly probe the black hole–jet connection in M87. The images reveal that high-energy plasma fans out from near the black hole to form a broad jet that becomes more cylindrical farther downstream.

Black holes have a deserved reputation as the ultimate vacuum cleaners of the Universe, sucking into gravitational oblivion the cosmic litter of gas and dust that happens to enter their realm. But not all matter that falls towards these monsters becomes trapped

inside the black hole's event horizon, from which nothing — not even light — can escape. In fact, many black holes are sloppy eaters: the energy contained in the 'crumbs' of matter that are left rivals that of the 'food' consumed. This phenomenon has posed a difficult challenge for astrophysicists, who have been struggling for several decades to explain how the crumbs form the jets of high-energy particles that stream out from the centres of galaxies containing supermassive black holes.

Hada *et al.*¹ observed the M87 jet with the Very Long Baseline Array (VLBA) operated by the US National Radio Astronomy Observatory. The VLBA is an interferometer consisting of ten 25-metre-diameter radio antennas, located at various sites from the Virgin Islands to Hawaii, that all point at the same object simultaneously and measure the radio signals from it as Earth rotates. This produces the data needed to create an image with angular resolution similar to that of a huge radio dish with a diameter almost equal to that of Earth. Details can be seen on scales of 0.0001 arc-seconds, 400 times finer than the resolving

power of the Hubble Space Telescope at visible wavelengths.

One of the main questions surrounding the launching of jets from near a black hole is the distance required for the flow to focus into a very narrow opening angle of at most a few degrees. Previous studies^{2,3} found that this focusing occurs a short distance downstream of the flow's brightest feature (the core), which is seen in VLBA images obtained at a frequency of 43 gigahertz. But the data were insufficient to determine the location of the black hole in the images. Hada *et al.*¹ have now overcome this problem by obtaining data at six frequencies, ranging from 2.3 to 43 GHz, by which they could measure the change in location of the core as a function of frequency. The opacity of the jet increases towards lower frequencies, and so radio waves at these frequencies can escape only from the less dense sections of the jet farther downstream from the black hole. By measuring the shift of core location versus frequency, the authors have determined the convergence point of the jet. In doing so, they have found that the core at

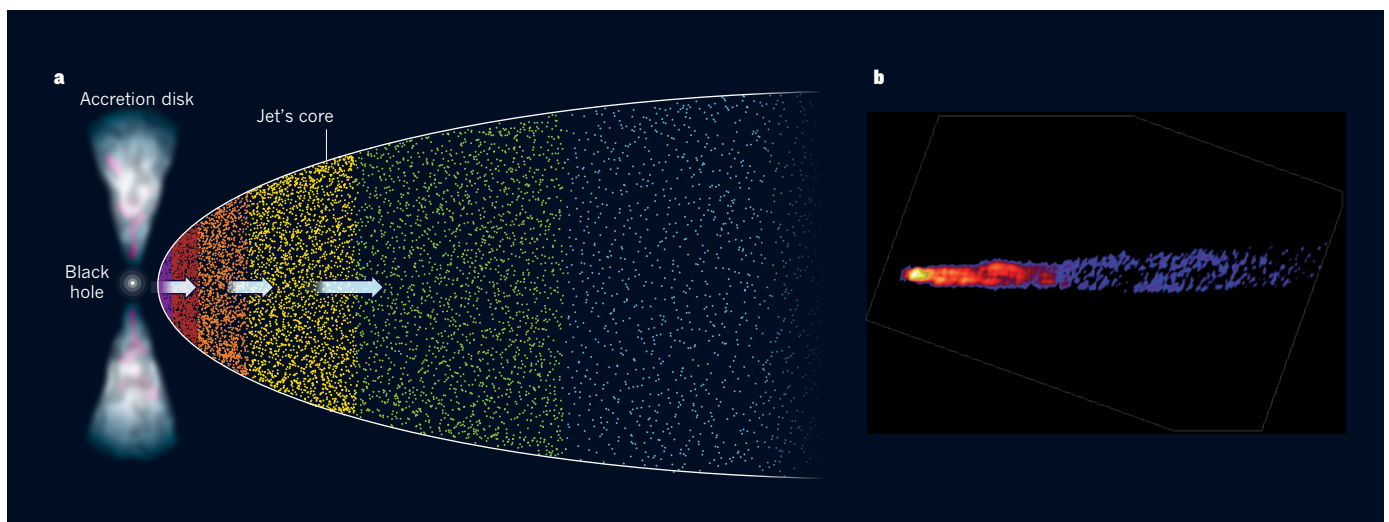


Figure 1 | Jet width and distance from the black hole in M87. **a**, The radio images of Hada *et al.*¹ indicate that, in the giant elliptical galaxy M87, a jet of high-energy particles (coloured dots) starts as a broad flow close to the galaxy's central black hole and accretion disk (the cross-section of which is shown as two wedges), becoming more cylindrical and faster (as indicated by arrows) with distance from the black hole. Within the jet's brightest region (core), colours correspond to jet sections that have

different particle densities and that are observed at different frequencies, from about 200 GHz (purple, more dense) to 5 GHz (blue, less dense). **b**, The actual jet is seen here in an image obtained with the Very Long Baseline Array at a frequency of 15 GHz (yellow is brightest, blue is faint, black is undetected). The sketch in **a** fits into the core (yellow area) of the jet in **b**. (Image courtesy of NRAO/AUI and Y. Y. Kovalev, MPIfR and ASC Lebedev.)

43 GHz is located only 14 to 23 Schwarzschild radii from the black hole. (The Schwarzschild radius is the distance between the black hole's centre and its event horizon if the black hole does not spin, and up to twice this distance if it spins rapidly.) This value is surprisingly small, because estimates^{4,5} of the black-hole-to-core distance in quasars, which are more-luminous cousins of M87, are more than 100,000 times the Schwarzschild radius.

Hada and colleagues' results¹ show that the jet flows into a broad angle between the black hole and core before becoming tightly focused farther out (Fig. 1). This agrees with predictions of some theoretical models^{6,7} that explain jets as the products of magnetic fields twisted by the differential rotation of the ionized gas swirling around the black hole. In such models, the flow accelerates and narrows over hundreds to about 100,000 Schwarzschild radii, with faster jets requiring greater distances.

How are we to reconcile the short black-hole-to-core distance of M87 with the much longer

distance inferred in some quasars? Perhaps jets spread out more rapidly in lower-luminosity objects because there is less hot ionized gas in the nucleus to confine the flow. Another possibility is that the jet consists of an ultra-fast (99% of the speed of light) spine surrounded by a slower (perhaps 90% of the speed of light) sheath. In quasars with bright jets, the spine points almost right at us, so we see the radiation beamed in our direction, whereas emission from the sheath is too weak to be noticed. The jet of M87 is more inclined to our line of sight, by 15–25°, so the spine is relatively dim, allowing us to see the slower sheath. The images of M87 thereby reveal slower regions of the jet that are close to the black hole, whereas in quasars the jets become bright only where the spines reach their terminal velocity at much greater distances from the black holes.

The ability to image jets on such small scales in M87 implies that very-long-baseline interferometry can explore phenomena even closer to black holes by observing at higher frequencies

of 86, 230 or even 350 GHz, at which the resolution is two to eight times finer than at 43 GHz. In combination with monitoring of time variations in the radiation at infrared, visible, X-ray and γ -ray frequencies, such observations would act as an 'event-horizon telescope'⁸. ■

Alan P. Marscher is in the Department of Astronomy and the Institute for Astrophysical Research, Boston University, Boston, Massachusetts 02215, USA.
e-mail: marscher@bu.edu

1. Hada, K. *et al.* *Nature* **477**, 185–187 (2011).
2. Junor, W., Biretta, J. A. & Livio, M. *Nature* **401**, 891–892 (1999).
3. Kovalev, Y. Y., Lister, M. L., Homan, D. C. & Kellermann, K. I. *Astrophys. J.* **668**, L27–L30 (2007).
4. Marscher, A. P. *et al.* *Nature* **452**, 966–969 (2008).
5. Marscher, A. P. *et al.* *Astrophys. J.* **710**, L126–L131 (2010).
6. Vlahakis, N. & Königl, A. *Astrophys. J.* **605**, 656–661 (2004).
7. Komissarov, S. S. *Mem. Soc. Astron. Ital.* **82**, 95–103 (2011).
8. Doeleman, S. S. *et al.* *Nature* **455**, 78–80 (2008).

NEUROSCIENCE

When lights take the circuits out

Circuit-level perturbations in the brain's electrical activity may underlie social-interaction deficits seen in people with schizophrenia and autism. A new optogenetic tool was instrumental in making this discovery. [SEE ARTICLE P.171](#)

JOÃO PEÇA & GUOPING FENG

On page 171 of this issue, Yizhar *et al.*¹ add to our understanding of the neuronal circuits that control mammalian behaviour. By tuning neuronal activity with light, they show that 'hijacking' specific brain circuits in the mouse prefrontal cortex (but not the visual cortex, for example) can selectively disrupt the normal responses to social stimuli and social interaction.

Information processing across neuronal circuits in the brain determines thoughts, shapes emotions and regulates behaviours. It will therefore come as no surprise if dysfunctions affecting synaptic communication between neurons and neuronal circuits reside at the core of several neuropsychiatric disorders. This assumption has led to considerable efforts to explore how circuit activity and information processing might differ between the healthy and the diseased brain. In recent years, one particular theory has gained substantial traction — that disorders such as autism and schizophrenia arise from imbalances in the ratio of excitatory to inhibitory synaptic inputs (E/I balance)

in discrete neuronal populations^{2,3}.

Symptoms of various psychiatric disorders may arise from common features at cellular and circuit levels. These common features could therefore account, at least in part, for the convergence seen in the traits of broad-spectrum disorders such as autism that have a varied range of causes. Yizhar *et al.*¹ set out to directly test the hypothesis that an increase in E/I balance may underlie some of the common symptoms of neuropsychiatric diseases.

For this investigation, the authors made use of a novel optogenetic tool. Optogenetics is based on the expression of a light-sensitive ion channel in the membrane of discrete populations of neurons. Light is usually delivered through the skull to those neurons by an optical fibre, causing the channels to open. Optogenetics has allowed researchers to directly and rapidly manipulate neuronal firing, probe neuronal-circuit function and control behaviour on very fast timescales — within milliseconds. For example, in disorders in which the underlying neural-circuit dysfunction is well understood, optogenetics has been used successfully not only to mimic the expected behavioural deficiencies, but also to positively

modulate symptoms in animal models of the relevant disorder⁴ (Fig. 1).

Recently, Yizhar and colleagues⁵ introduced step-function optogenetic channels. Tools of this new generation have been modified to remain open for longer periods of time (seconds to minutes) after light activation. This allows the induction of successive, sub-threshold neuronal activation to bring cells close — although not all the way — to firing. The functional consequence of this is modulation of the properties of endogenous neuronal circuits as a whole, without 'overloading' or overriding normal neuronal firing.

For their latest study¹, the authors developed step-function optogenetic channels with improved temporal stability to prime distinct populations of neurons in the prefrontal cortex of the mouse brain so that these could more readily become active in response to native neural-network activity over long periods of time. They were thus able to manipulate neuronal E/I ratios in this brain region: when the targeted populations were excitatory neurons, the functional network output corresponded to an increase in E/I ratio; when they were inhibitory neurons, the E/I ratio decreased. On the basis of these manipulations, Yizhar *et al.* report that increased — but not reduced — E/I balance in the prefrontal cortex leads to well-defined behavioural impairments and a striking perturbation in sociability in mice.

Although these data provide strong evidence that alterations in the cortical E/I balance directly affect social behaviour in mice, we should avoid adopting a simplistic view of the implications of changes in this ratio. Recent genetic and genomic studies have identified a large number of candidate genes for autism, many of which encode proteins crucial to

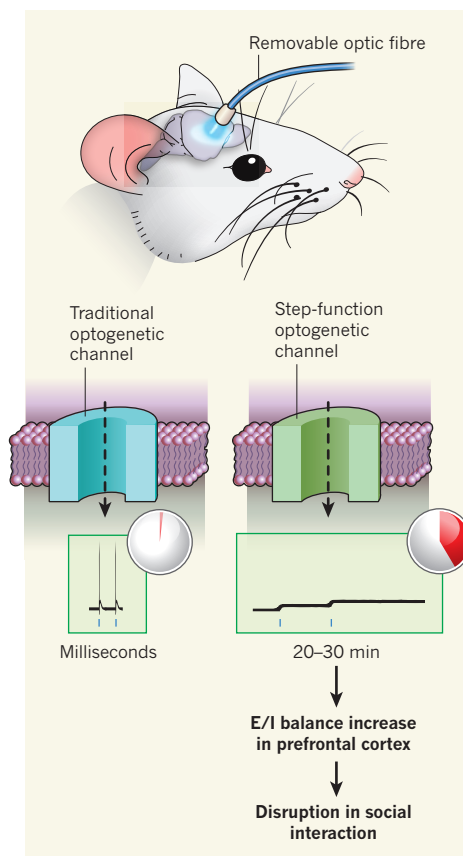


Figure 1 | Optogenetics and analysis of social dysfunction. Yizhar *et al.*¹ used step-function optogenetic channels to analyse the excitation–inhibition (E/I) balance in specific neural circuits within the prefrontal cortex of the mouse brain. Like traditional optogenetic channels, this latest tool is activated in response to light delivered by optic fibres through the animal's skull; this in turn allows ions to enter the neuron (dashed arrows). Step-function optogenetic channels, however, do not necessarily induce immediate firing by their host neuron. Instead, they cause a gradual increase in neuronal depolarization, increasing the probability of the neuron firing in response to endogenous stimuli over 20–30 minutes. This gave the authors sufficient time to perform behavioural analysis on the animals without the optic fibre being attached. They found that increasing the E/I balance in the prefrontal cortex disrupts social interaction between mice.

synaptic development and function⁶. Moreover, introduction of a mutation seen in patients with autism (the R451C mutation in the protein neuroligin-3) into the equivalent mouse protein increases inhibitory synaptic transmission⁷. So to clarify the significance of E/I ratios in disease states, future studies should traverse the added level of complexity arising from relevant human mutations in relation to regional and cell-type-specific gene expression. Such studies should also consider whether the broader circuits affected have an inhibitory or an excitatory effect on their downstream neuronal targets.

Yizhar and colleagues' paper¹ highlights a

notable point — to unravel the complexity of the mammalian brain, it is essential to understand the functioning of circuits in both healthy and diseased brains. Combining information arising from observation, and control, of neuronal circuits will also be crucial in such efforts⁸. Together, these approaches should not only magnify our ability to predict how changes in circuit function may lead to abnormal behaviours, but also give a glimpse of how circuit-level manipulations might ultimately be used for the treatment of neuropsychiatric disorders. ■

João Peça and Guoping Feng are at the McGovern Institute for Brain Research,

Department of Brain and Cognitive Sciences, Massachusetts Institute of Technology, Cambridge, Massachusetts 02139, USA. e-mail: fenggp@mit.edu

1. Yizhar, O. *et al.* *Nature* **477**, 171–178 (2011).
2. Rubenstein, J. L. R. & Merzenich, M. M. *Genes Brain Behav.* **2**, 255–267 (2003).
3. Kehrer, C., Maziashvili, N., Dugladze, T. & Gloveli, T. *Front. Mol. Neurosci.* **1**, 6 (2008).
4. Kravitz, A. V. *et al.* *Nature* **466**, 622–626 (2010).
5. Berndt, A. *et al.* *Nature Neurosci.* **12**, 229–234 (2008).
6. van de Lagemaat, L. N. & Grant, S. G. N. *Neuron* **67**, 8–10 (2010).
7. Tabuchi, K. *et al.* *Science* **318**, 71–76 (2007).
8. Miesenböck, G. & Kevrekidis, I. G. *Annu. Rev. Neurosci.* **28**, 533–563 (2005).

METABOLISM

Let them eat fat

A specialist neuron uses an intriguing process to help control the body's response to hunger. A lipid pathway involving the breakdown of cellular components regulates the expression of a neuropeptide that affects feeding and body weight.

SCOTT M. STERNSON

When resources become scarce, we tighten our belts and make do with what we have. This is also true for our bodies, which in the absence of food intake start to consume themselves. In a paper published in *Cell Metabolism*, Kaushik *et al.*¹ describe how, when mice are deprived of food, a specialized starvation-sensitive neuron dines on fat released from body stores. Strikingly, the authors find that disrupting this process in these neurons results in leaner, lighter mice, even when food is freely available.

Hunger results from food deprivation and leads to food seeking and consumption. An internal sensory system detects signals of energy deficit circulating in the blood and modulates neural circuits that regulate these behaviours. A neuron that is crucially involved in this system is defined by its expression of the gene *Agouti-related protein (Agrp)*, which encodes the AgRP neuropeptide.

The AgRP neuropeptide increases feeding and body weight when injected into the brain. Furthermore, AgRP-expressing neurons have properties expected of a starvation-sensing system: they alter their firing rate and gene expression in response to signals from hormones and metabolites such as ghrelin, leptin, glucose and fatty acids. Without these neurons, mice stop eating². Conversely, voracious eating can be induced in well-fed mice by increasing the electrical activity of these neurons^{3,4}. It is therefore clear that the regulation of AgRP-neuron function is important for controlling hunger-related behaviour.

During food deprivation, changes occur

in the body to conserve energy and to signal the need to replenish energy levels by eating. The body switches to using stored fat as a fuel, releasing free fatty acids into the blood that can be sensed by the brain. Kaushik *et al.*¹ examine the influence of this process on AgRP neurons in cell culture and in mice.

The authors explore an unusual mechanism for modulating *Agrp* gene expression by investigating the role of macroautophagy (here termed autophagy) in fatty-acid utilization. Autophagy is a regulated, cannibalistic process in which cells consume and recycle their components (such as damaged organelles) and use their internal structures as a fuel source during starvation. In autophagy, cellular components are enveloped in a membrane-bounded vesicle called an autophagosome for transport to an organelle known as the lysosome for degradation. Some of the authors of the current study previously discovered an intriguing mechanism in liver cells whereby the autophagy pathway can mobilize stored fat as a fuel source⁵.

Kaushik *et al.*¹ report that a similar pathway operates in AgRP neurons, with consequences that seem to extend beyond fuel utilization. They propose that AgRP neurons accumulate free fatty acids from the blood during food deprivation and that these fatty acids are then quickly converted into triglyceride fats and stored in lipid droplets (Fig. 1). These lipids are rapidly remobilized through autophagy of the lipid droplet, and free fatty acids are reformed for use as fuel. The authors suggest that this circuitous pathway provides a mechanism for regulatory control over the accumulation of free fatty acids in the cell, so that they can be used in an orderly fashion. It remains to be seen

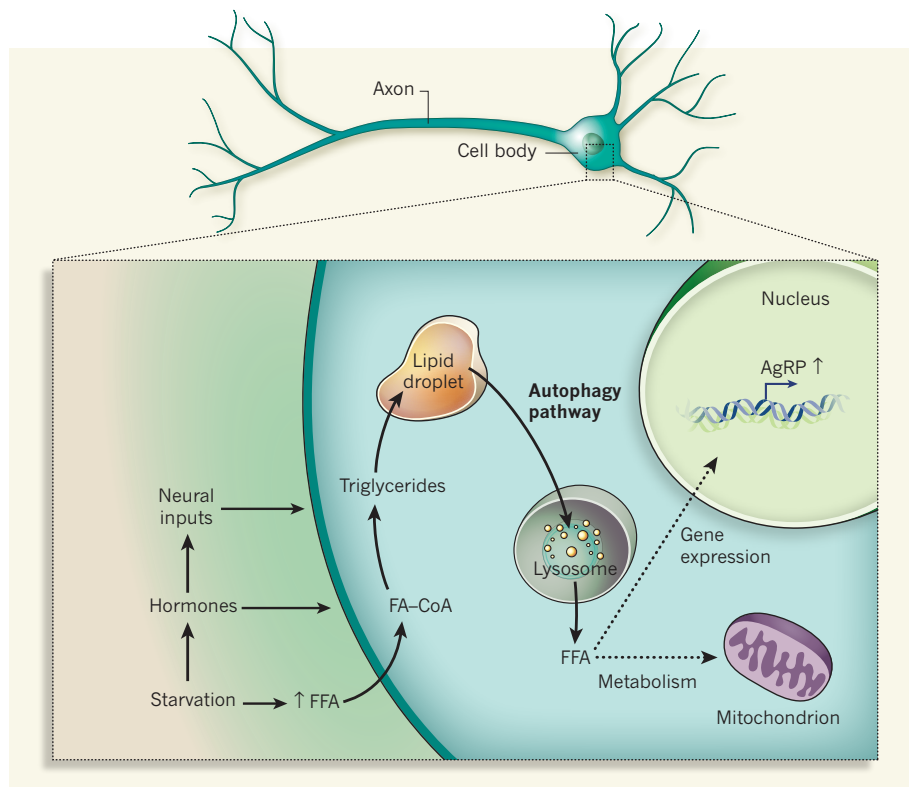


Figure 1 | Fatty-acid regulation of starvation-sensitive neurons. Neurons expressing the neuropeptide AgRP respond to raised concentrations of circulating free fatty acids (FFA) released from fat stores, as well as to other hunger signals such as hormones and neural inputs. Kaushik *et al.*¹ show how these fatty acids are taken up and processed into triglycerides via fatty acid-coenzyme A thioesters (FA-CoA) for storage in lipid droplets. The fatty acids can be released again through the autophagy pathway, in which lysosomes degrade the lipid droplets. These fatty acids increase *AgRP* gene expression in the nucleus and are also available for metabolism in the mitochondria.

whether this process operates in other neurons.

A key finding from these experiments is that *AgRP* expression, which promotes eating, is increased by free fatty acids. In addition, this effect on gene expression requires lysosomal processing, as would be expected of the autophagy pathway.

There is a clear consequence of disrupting this lipid-utilization scheme in mice. Using genetic elimination of a crucial component of the autophagy pathway in AgRP neurons, the authors find that, relative to controls, mice eat less when re-fed after food deprivation and their body weight decreases. They go on to show that expression of the AgRP neuropeptide is reduced in these mice, which they suggest is why the mice eat less and weigh less.

These results¹ should be considered in the light of other studies demonstrating a role for fatty-acid metabolism in the regulation of *AgRP* expression. For example, *AgRP* expression is reduced when fatty-acid utilization is inhibited by eliminating an uncoupling protein involved in the activity of the mitochondrion, the cell's energy-producing organelle⁶. One implication is that the autophagy pathway could be linked to the transport of fatty acids for mitochondrial metabolism. Then there is the question of how cellular fatty acids regulate *AgRP*. One possibility for future investigation is the involvement of the transcription factor FoxO1, which regulates

AgRP expression according to hunger status⁷.

It is not yet clear whether disruption of the autophagy pathway in AgRP neurons regulates feeding and body weight solely through the lipid-processing mechanisms described here. It will therefore be essential to explore the effect of this pathway on the electrical activity of AgRP neurons, on their development, and on their interaction with other mediators of AgRP-neuron function, such as synaptic input and hormonal regulation.

Could blocking this cannibalistic process be used to reduce body weight? Possibly, but the autophagy pathway is ubiquitous in cells throughout the body, so extensive investigation will be needed to find selective points of entry for therapeutic interference in obesity and eating disorders. ■

Scott M. Sternson is at the Janelia Farm Research Campus, Howard Hughes Medical Institute, Ashburn, Virginia 20147, USA.
e-mail: sternsons@janelia.hhmi.org

1. Kaushik, S. *et al.* *Cell Metab.* **14**, 173–183 (2011).
2. Luquet, S., Perez, F. A., Hnasko, T. S. & Palmiter, R. D. *Science* **310**, 683–685 (2005).
3. Aponte, Y., Atasoy, D. & Sternson, S. M. *Nature Neurosci.* **14**, 351–355 (2011).
4. Krashes, M. J. *et al.* *J. Clin. Invest.* **121**, 1424–1428 (2011).
5. Singh, R. *et al.* *Nature* **458**, 1131–1135 (2009).
6. Andrews, Z. B. *et al.* *Nature* **454**, 846–851 (2008).
7. Kitamura, T. *et al.* *Nature Med.* **12**, 534–540 (2006).



50 Years Ago

The normal method of concentrating a substance in solution is by distillation. In the course of certain experiments it was found that it is possible to do so to a certain extent by refrigeration. A column of skim milk in a 250-ml. cylinder was frozen between -5° and -10° C. The frozen column was taken out and allowed to thaw at room temperature ... The melted column showed a graded separation, ranging from solid concentration at the bottom to a thin, watery layer at the top ... Solutions of copper sulphate, potassium permanganate and potassium ferrocyanide, similarly frozen and thawed, yield a higher concentration of the salts at the bottom of the column, at once evident by the greater intensity of colour ... It is perhaps typical of cryoscopic concentration of solutes.

From *Nature* 9 September 1961

100 Years Ago

Just about three o'clock this afternoon (I had a few minutes previously asked the time at the village post office) I witnessed a remarkable and very beautiful phenomenon. Coming through a woodland walk, I was caught by a heavy downpour of rain. As it was passing away, the sun shone down from a suddenly clear sky over the tops of the trees behind and to the right. Instantly ... not more than three yards from where I stood, a perfect miniature rainbow was formed, its highest part being just about level with my eyes. It appeared broader than an ordinary rainbow, and much the greater portion was of one deep violet colour, the remaining colours forming merely a narrow border above. Very vivid at first, it quickly faded away, as the shower came to an end.

From *Nature* 7 September 1911

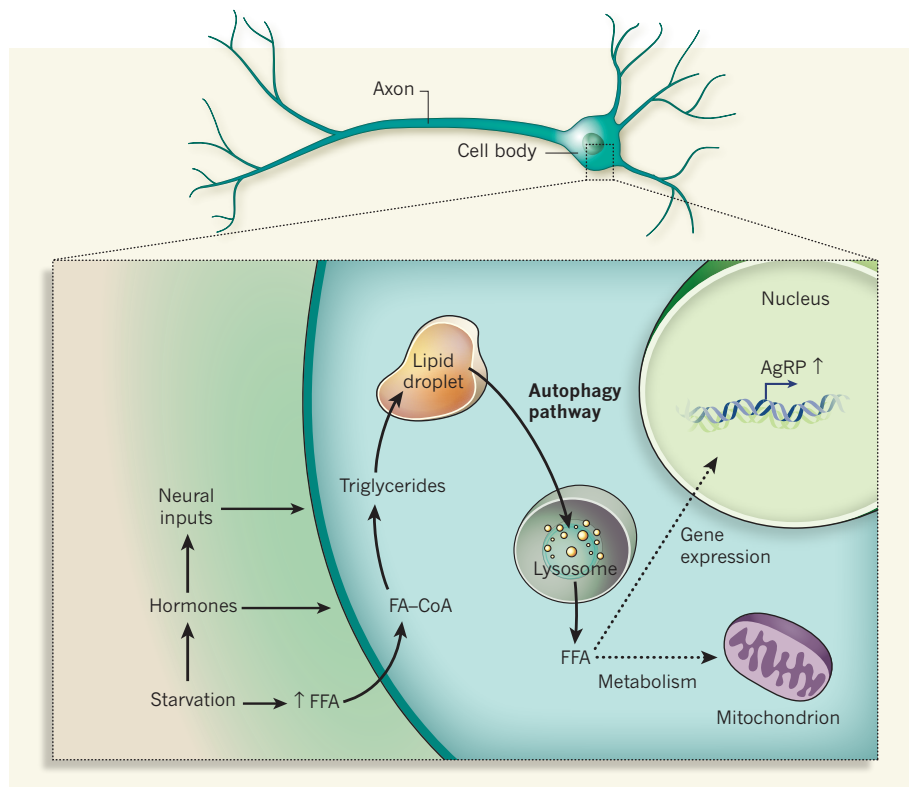


Figure 1 | Fatty-acid regulation of starvation-sensitive neurons. Neurons expressing the neuropeptide AgRP respond to raised concentrations of circulating free fatty acids (FFA) released from fat stores, as well as to other hunger signals such as hormones and neural inputs. Kaushik *et al.*¹ show how these fatty acids are taken up and processed into triglycerides via fatty acid-coenzyme A thioesters (FA-CoA) for storage in lipid droplets. The fatty acids can be released again through the autophagy pathway, in which lysosomes degrade the lipid droplets. These fatty acids increase *AgRP* gene expression in the nucleus and are also available for metabolism in the mitochondria.

whether this process operates in other neurons.

A key finding from these experiments is that *AgRP* expression, which promotes eating, is increased by free fatty acids. In addition, this effect on gene expression requires lysosomal processing, as would be expected of the autophagy pathway.

There is a clear consequence of disrupting this lipid-utilization scheme in mice. Using genetic elimination of a crucial component of the autophagy pathway in AgRP neurons, the authors find that, relative to controls, mice eat less when re-fed after food deprivation and their body weight decreases. They go on to show that expression of the AgRP neuropeptide is reduced in these mice, which they suggest is why the mice eat less and weigh less.

These results¹ should be considered in the light of other studies demonstrating a role for fatty-acid metabolism in the regulation of *AgRP* expression. For example, *AgRP* expression is reduced when fatty-acid utilization is inhibited by eliminating an uncoupling protein involved in the activity of the mitochondrion, the cell's energy-producing organelle⁶. One implication is that the autophagy pathway could be linked to the transport of fatty acids for mitochondrial metabolism. Then there is the question of how cellular fatty acids regulate *AgRP*. One possibility for future investigation is the involvement of the transcription factor FoxO1, which regulates

AgRP expression according to hunger status⁷.

It is not yet clear whether disruption of the autophagy pathway in AgRP neurons regulates feeding and body weight solely through the lipid-processing mechanisms described here. It will therefore be essential to explore the effect of this pathway on the electrical activity of AgRP neurons, on their development, and on their interaction with other mediators of AgRP-neuron function, such as synaptic input and hormonal regulation.

Could blocking this cannibalistic process be used to reduce body weight? Possibly, but the autophagy pathway is ubiquitous in cells throughout the body, so extensive investigation will be needed to find selective points of entry for therapeutic interference in obesity and eating disorders. ■

Scott M. Sternson is at the Janelia Farm Research Campus, Howard Hughes Medical Institute, Ashburn, Virginia 20147, USA.
e-mail: sternsons@janelia.hhmi.org

1. Kaushik, S. *et al.* *Cell Metab.* **14**, 173–183 (2011).
2. Luquet, S., Perez, F. A., Hnasko, T. S. & Palmiter, R. D. *Science* **310**, 683–685 (2005).
3. Aponte, Y., Atasoy, D. & Sternson, S. M. *Nature Neurosci.* **14**, 351–355 (2011).
4. Krashes, M. J. *et al.* *J. Clin. Invest.* **121**, 1424–1428 (2011).
5. Singh, R. *et al.* *Nature* **458**, 1131–1135 (2009).
6. Andrews, Z. B. *et al.* *Nature* **454**, 846–851 (2008).
7. Kitamura, T. *et al.* *Nature Med.* **12**, 534–540 (2006).



50 Years Ago

The normal method of concentrating a substance in solution is by distillation. In the course of certain experiments it was found that it is possible to do so to a certain extent by refrigeration. A column of skim milk in a 250-ml. cylinder was frozen between -5° and -10° C. The frozen column was taken out and allowed to thaw at room temperature ... The melted column showed a graded separation, ranging from solid concentration at the bottom to a thin, watery layer at the top ... Solutions of copper sulphate, potassium permanganate and potassium ferrocyanide, similarly frozen and thawed, yield a higher concentration of the salts at the bottom of the column, at once evident by the greater intensity of colour ... It is perhaps typical of cryoscopic concentration of solutes.

From *Nature* 9 September 1961

100 Years Ago

Just about three o'clock this afternoon (I had a few minutes previously asked the time at the village post office) I witnessed a remarkable and very beautiful phenomenon. Coming through a woodland walk, I was caught by a heavy downpour of rain. As it was passing away, the sun shone down from a suddenly clear sky over the tops of the trees behind and to the right. Instantly ... not more than three yards from where I stood, a perfect miniature rainbow was formed, its highest part being just about level with my eyes. It appeared broader than an ordinary rainbow, and much the greater portion was of one deep violet colour, the remaining colours forming merely a narrow border above. Very vivid at first, it quickly faded away, as the shower came to an end.

From *Nature* 7 September 1911

GEOSCIENCE

Earth's patchy late veneer

A 'late veneer' of meteoritic material, added after Earth's core had formed, may be the source of our noble metals. Its absence from some parts of Earth's mantle will now force a rethink about this late accretion. [SEE LETTER P.195](#)

THORSTEN KLEINE

Earth's metallic core is the major repository of the highly siderophile ('iron-loving') elements, which include gold, rhenium and the platinum-group elements. Their strong affinity for iron means that their abundance in Earth's mantle is very low — but not as low as might be expected. One popular explanation for this discrepancy is that a late veneer of primitive meteoritic material was added to Earth's mantle after core formation had ceased¹. On page 195 of this issue, Willbold and colleagues² add weight

to this theory by using an isotope of tungsten to show that the late veneer is missing from some areas of the mantle. Our understanding of Earth's late accretion may need to change as a result.

Energetic collisions between Moon- to Mars-sized planetary embryos during Earth's growth caused widespread melting, facilitating the separation of molten metal from surrounding liquid silicate in a magma ocean. The molten iron sank towards Earth's centre, removing the siderophile elements to the core. However, highly siderophile elements are present in Earth's mantle in much higher

amounts than are predicted from metal–silicate partition experiments at atmospheric pressure³. One explanation is that the affinity of these siderophile elements for iron may have decreased under the very high pressures and temperatures found at the bottom of a deep magma ocean⁴. This model seems to work for some highly siderophile elements⁵, but not for all of them⁶.

An alternative explanation calls for the addition of 0.5–1% of primitive meteoritic material after the core had formed¹. This 'late veneer' might also have included ingredients essential for life, such as water, carbon and other volatile compounds. As is evident from large impact basins on the Moon, Earth continued to accrete material after the giant impact that resulted in the formation of the Moon and the final segregation of Earth's core, some 4.5 billion years ago (Fig. 1). This period of late accretion lasted for about 500 million years and ended catastrophically with a terminal bombardment 4.0 billion to 3.8 billion years ago. Although there is strong visual evidence for late accretion, it is not clear whether the mass added was sufficient to account for the abundance of highly siderophile elements in Earth's mantle.

Willbold and colleagues² approach the problem in a new way by looking for small variations in the abundance of the tungsten isotope ^{182}W , generated by the decay of the now-extinct hafnium isotope ^{182}Hf . The tungsten isotopic composition of Earth's mantle is different from that of the putative late veneer, which presumably consisted of chondritic meteorites — bits and pieces left over from the earliest stages of planet formation and considered to be the main building blocks of Earth. These differences in ^{182}W abundance are the result of core formation, during which hafnium remained in the mantle while tungsten preferentially partitioned into the core⁷. Radioactive decay of ^{182}Hf to ^{182}W then resulted in an enrichment of ^{182}W in the mantle relative to chondrites by about two parts in 10,000 (or 2ϵ ; Fig. 1).

Given the different ^{182}W composition in Earth's mantle and in chondrites, the addition of a late veneer should be recorded in the tungsten isotopes. However, the expected effects are vanishingly small. Willbold and colleagues² have made tungsten-isotope measurements of unprecedented precision and show that the abundance of ^{182}W in most of the accessible silicate Earth is invariant. However, they find that samples from the Isua greenstone belt in western Greenland are slightly enriched in ^{182}W compared with the average for Earth's mantle. The magnitude of this small enrichment is exactly that predicted for the added mass of chondritic material required to account for the concentrations of highly siderophile elements in the mantle. These results therefore provide strong support for the late-veneer model.

The importance of Willbold and colleagues'

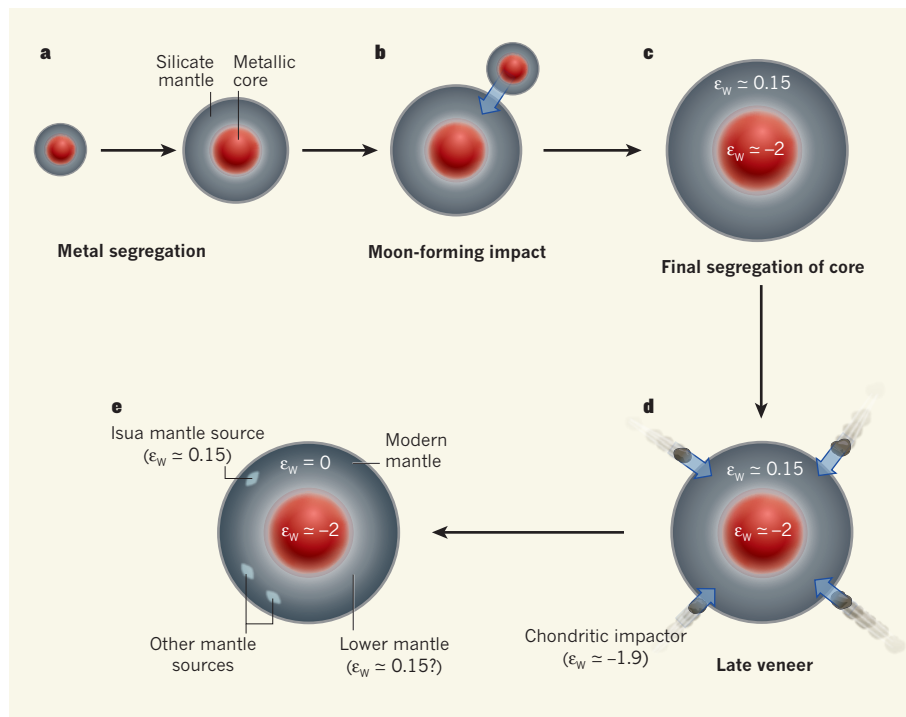


Figure 1 | Earth's accretion and effects of the late veneer. a–c, Accretion and core formation (4.567 billion to about 4.5 billion years ago). a, Siderophiles are removed from the silicate mantle to the metallic core. b, Moon-forming impact and end of Earth's main accretion. c, Final segregation of the core: mantle is depleted of highly siderophile elements, now concentrated in the core; ϵ_W ($\epsilon^{182}\text{W}$) denotes tungsten-isotope enrichment as parts per 10,000 relative to the modern terrestrial mantle. d, e, Late accretion (about 4.5 billion to 3.8 billion years ago) following core formation. d, Highly siderophile elements are replenished in the mantle by a late veneer of chondritic meteorites. e, Addition of the late veneer reduces mantle ^{182}W enrichment to an ϵ_W of zero. Willbold *et al.*² propose that rocks from Isua in Greenland have the same ^{182}W enrichment ($\epsilon_W \approx 0.15$) as the mantle had before the late veneer formed, indicating that some domains within Earth's mantle may have escaped addition of the late veneer.

study goes far beyond this, however. All of the Isua samples analysed derive from a mantle source that was established very shortly after the final stage of Earth's accretion⁸, so it may not be surprising that they preserve a signature of Earth's mantle before the arrival of the late veneer. Given that the Isua samples seem to lack the late-veneer component, they would be expected to be very poor in the highly siderophile elements. Surprisingly, they are not, for reasons that are not understood. Nevertheless, their osmium (¹⁸⁷Os) isotopic composition is different from that of chondrites⁹, consistent with the absence of the late veneer in their source.

Tungsten-182 enrichments have also been identified in 2.8-billion-year-old rocks called komatiites¹⁰, which derive from deep-rooted mantle sources. Osmium-187 is the decay product of rhenium-187, and the ¹⁸⁷Os enrichment in these and many other komatiitic lavas¹¹ may reflect rhenium–osmium fractionation during core formation in a deep magma ocean, a signature that has otherwise been overprinted by the late veneer.

Ultimately, it may transpire that the late veneer was deposited in large patches, perhaps by a few big impactors. In that case, some areas of Earth's mantle would not have received such late accreted material and would

have remained isolated from the rest of the mantle throughout the planet's history (Fig. 1). Future studies should use both tungsten and osmium isotopic data to identify such mantle domains: this could potentially distinguish signatures left behind during the final stages of core segregation from those of the late veneer. ■

Thorsten Kleine is at the Institute for Planetology, University of Münster, Wilhelm-Klemm-Strasse 10, 48149 Münster, Germany.
e-mail: thorsten.kleine@uni-muenster.de

1. Kimura, K., Lewis, R. S. & Anders, E. *Geochim. Cosmochim. Acta* **38**, 683–701 (1974).
2. Willbold, M., Elliott, T. & Moorbath, S. *Nature* **477**, 195–198 (2011).
3. Walker, R. J. *Chem. Erde* **69**, 101–125 (2009).
4. Murthy, R. *Science* **253**, 303–306 (1991).
5. Righter, K., Humayun, M. & Danielson, L. *Nature Geosci.* **1**, 321–323 (2008).
6. Brenan, J. M. & McDonough, W. F. *Nature Geosci.* **2**, 798–801 (2009).
7. Kleine, T. *et al.* *Geochim. Cosmochim. Acta* **73**, 5150–5188 (2009).
8. Caro, G., Bourdon, B., Birck, J.-L. & Moorbath, S. *Nature* **423**, 428–432 (2003).
9. Frei, R., Polat, A. & Meibom, A. *Geochim. Cosmochim. Acta* **68**, 1645–1660 (2004).
10. Touboul, M., Puchtel, I. S. & Walker, R. J. *Miner. Mag.* **75**, 2026 (2011).
11. Walker, R. J., Morgan, J. W. & Horan, M. F. *Science* **269**, 819–822 (1995).

CANCER

Let sleeping DNA lie

In hereditary breast and ovarian cancers caused by absence of the BRCA1 protein, genomic instability may ensue from the 'awakening' of repetitive DNA sequences in structurally condensed chromosomal regions. [SEE ARTICLE P.179](#)

ASHOK R. VENKITARAMAN

The discovery in the mid-1990s that inactivation of the gene *BRCA1* predisposes women to breast and ovarian cancer sparked an intensive search for the tumour-suppressive role of this gene. But rather than coming up with a single unifying model, more than 15 years of effort have spawned myriad apparently relevant biological functions. On page 179 of this issue, Verma and colleagues (Zhu *et al.*¹) report a finding that might herald a breakthrough — an enzymatic activity of the BRCA1 protein that helps to maintain distinct chromosomal regions and their associated proteins in a structurally condensed state, known as constitutive heterochromatin, may underlie its tumour-suppressive effect.

The centromeric sites of chromosomes are flanked by repetitive sequences called satellite DNA (Fig. 1a). Together with their associated proteins, these sequences form a type of constitutive heterochromatin known as

pericentric heterochromatin. Zhu *et al.* find that BRCA1 loss changes the structure of this heterochromatin, activating transcription in these usually silent genomic regions. In particular, there is a marked increase in transcripts emanating from satellite DNA.

The authors¹ further show that, surprisingly, transcription of the normally silent satellite DNA evokes several of the cellular characteristics known to follow BRCA1 loss — such as the occurrence of spontaneous DNA breaks and defects in DNA repair by the process of homologous recombination (reviewed in ref. 2). Moreover, they find that chromosomes segregate abnormally during mitotic cell division, as was shown previously to occur after disruption of the pericentric heterochromatin (reviewed in ref. 3). These results suggest that derepression of satellite-DNA transcription may be the root cause of several of the cellular defects that lead to genomic instability after BRCA1 loss (Fig. 1b).

The BRCA1 protein contains a RING

domain, which forms a heterodimer with the RING partner protein BARD1 to generate an E3 ubiquitin-ligase enzyme; such enzymes attach the small peptide ubiquitin to lysine amino-acid residues on their protein substrates. Depending on its precise nature (for example, where it occurs), ubiquitination generally alters the substrate's activity or its propensity to be degraded. Although neither the characteristics nor the functions of BRCA1-dependent ubiquitination are yet understood, Zhu *et al.*¹ show that normal BRCA1, but not its catalytically inactive forms, can reverse expression of satellite-DNA transcripts in BRCA1-deficient cells. So the E3-ligase activity of BRCA1 is at least necessary to maintain heterochromatin.

A clue to why this is so comes from the authors' observation that the pericentric heterochromatin is enriched both in BRCA1 and in a ubiquitinated form of the histone protein H2A that has been implicated⁴ in regulating transcription. They find that loss of BRCA1 is accompanied by decreased levels of ubiquitinated H2A in the pericentric heterochromatin, and that this defect can be corrected by normal BRCA1 but not by its catalytically inactive forms. So it seems that BRCA1 is necessary for the enrichment of ubiquitinated H2A in heterochromatin, but whether BRCA1 is directly responsible for H2A ubiquitination, or recruitment, *in vivo* remains unknown (Fig. 1).

Zhu *et al.*¹ find that H2A fused to a single ubiquitin moiety could partially reverse satellite-DNA transcription that follows BRCA1 loss, but it is not clear whether this fusion protein must preferentially localize to heterochromatin to effect the reversal. H2A-ubiquitin could also — at least partially — ameliorate several of the cellular defects associated with BRCA1 loss (such as growth arrest or impaired homologous recombination), strengthening the tie between satellite-DNA derepression and these abnormalities. These findings collectively indicate that BRCA1 maintains pericentric heterochromatin through ubiquitinated H2A by a mechanism that is still unclear.

Several findings of the present study are provocative in relation to published work in related fields. For instance, H2A ubiquitination also occurs at sites of DNA breakage — where it is mediated by the RNF8 and RNF168 proteins — and is responsible for the recruitment of BRCA1 to these sites⁵. In this setting, therefore, H2A ubiquitination seems to be independent of BRCA1, although the exact nature of this modification following DNA breakage is probably distinct from that occurring in constitutive heterochromatin. A related issue concerns other ubiquitin ligases known to target H2A. Depletion of the RING

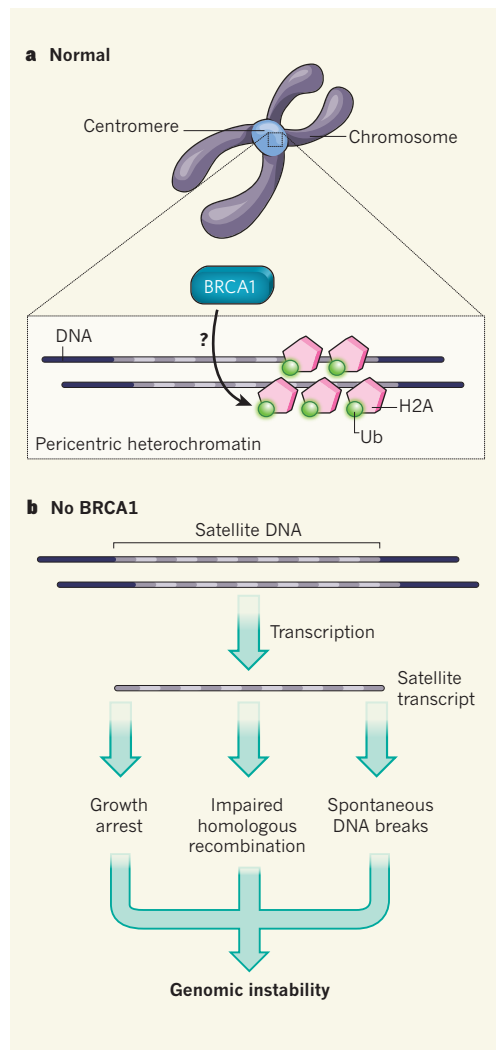


Figure 1 | BRCA1 loss, satellite-DNA transcription and genomic instability. **a**, Zhu *et al.*¹ show that BRCA1 promotes enrichment of ubiquitinated (Ub) histone protein H2A in pericentric heterochromatin, although how it does so remains unclear. **b**, Loss of BRCA1 triggers enhanced transcription of the normally silent repetitive satellite DNA sequences surrounding chromosome centromeres, and is accompanied by a decrease in Ub-H2A levels in pericentric heterochromatin. This suffices to induce genome instability following complete loss of BRCA1. Whether derepression of satellite-DNA transcription also occurs in heterozygous carriers of a BRCA1 mutation, who are prone to breast and ovarian cancers, is not known.

ubiquitin ligases involved in the silencing of gene expression by the Polycomb-group proteins markedly decreases the total cellular abundance of ubiquitinated forms of H2A⁶; yet surprisingly, Zhu *et al.* find that enrichment of ubiquitinated H2A in heterochromatin is unaffected by such depletion. These considerations suggest that only a small pool of H2A, which may carry a distinct ubiquitin mark, mediates the role of BRCA1 in satellite-DNA repression.

Much evidence implicates BRCA1 in the error-free repair of DNA breaks by homologous recombination: defects in this process

are thought to be responsible for the structural abnormalities in chromosomes and increased rate of mutations seen in BRCA1-deficient cells².

Zhu and colleagues' findings challenge our understanding of the role of BRCA1 in homologous recombination, which has been thought mainly to involve participation of BRCA1 in the formation and function of multiprotein complexes that accumulate at sites of DNA breakage (see refs 7 and 8, for example). Instead, the authors¹ suggest that satellite-DNA derepression following BRCA1 loss suffices to explain defective homologous recombination in BRCA1-deficient cells. Similarly, whereas an earlier study⁹ suggested that the E3 ubiquitin-ligase activity of BRCA1 is dispensable for the repair of DNA breaks, Zhu *et al.* propose that satellite-DNA repression by this enzymatic activity of BRCA1 is necessary for the repair of such lesions. It is not yet clear how these findings can be reconciled; clues might come from a detailed study of the effects of overexpression of satellite transcripts on the course of DNA-break repair.

Notably, Zhu *et al.*¹ report that satellite-DNA derepression occurs in mouse and human tumours lacking BRCA1. Whether, and how, this event promotes cancer development in carriers of germline BRCA1 mutations is not yet evident. Inheritance of a single mutant copy of BRCA1 is enough for cancer predisposition², but whether such BRCA1 heterozygosity also suffices to derepress transcription of satellite DNA is not known. As derepression of satellite DNA has been detected¹⁰ in many human epithelial tumours, it might be more generally associated with late stages of cancer development. Regardless of the remaining ambiguities, in describing an association between satellite-DNA transcription, BRCA1 loss and genomic instability, Zhu and colleagues' work reveals an intriguing new pathway for tumour suppression. ■

Ashok R. Venkitaraman is at the MRC Cancer Cell Unit, Hutchison-MRC Research Centre, Hills Road, Cambridge CB2 0XZ, UK.

e-mail: arv22@hutchison-mrc.cam.ac.uk

1. Zhu, Q. *et al.* *Nature* **477**, 179–184 (2011).
2. Venkitaraman, A. R. *Annu. Rev. Pathol.* **4**, 461–487 (2009).
3. Maisson, C. & Almouzni, G. *Nature Rev. Mol. Cell Biol.* **5**, 296–304 (2004).
4. Higashi, M., Inoue, S. & Ito, T. *Exp. Cell Res.* **316**, 2707–2712 (2010).
5. Van Attikum, H. & Gasser, S. *Trends Cell Biol.* **19**, 207–217 (2009).
6. Wang, H. *et al.* *Nature* **431**, 873–878 (2004).
7. Zhang, F. *et al.* *Curr. Biol.* **19**, 524–529 (2009).
8. Sy, S. M., Huen, M. S. & Chen, J. *Proc. Natl Acad. Sci. USA* **106**, 7155–7160 (2009).
9. Reid, L. J. *et al.* *Proc. Natl Acad. Sci. USA* **105**, 20876–20881 (2008).
10. Ting, D. T. *et al.* *Science* **331**, 593–596 (2011).

Neocortical excitation/inhibition balance in information processing and social dysfunction

Ofer Yizhar^{1,2*}, Lief E. Fenno^{1,3*}, Matthias Prigge⁴, Franziska Schneider⁴, Thomas J. Davidson¹, Daniel J. O'Shea^{1,3}, Vikaas S. Sohal^{1,5}, Inbal Goshen¹, Joel Finkelstein¹, Jeanne T. Paz⁶, Katja Stehfest⁴, Roman Fudim⁴, Charu Ramakrishnan¹, John R. Huguenard⁶, Peter Hegemann⁴ & Karl Deisseroth^{1,7,8,9}

Severe behavioural deficits in psychiatric diseases such as autism and schizophrenia have been hypothesized to arise from elevations in the cellular balance of excitation and inhibition (E/I balance) within neural microcircuitry. This hypothesis could unify diverse streams of pathophysiological and genetic evidence, but has not been susceptible to direct testing. Here we design and use several novel optogenetic tools to causally investigate the cellular E/I balance hypothesis in freely moving mammals, and explore the associated circuit physiology. Elevation, but not reduction, of cellular E/I balance within the mouse medial prefrontal cortex was found to elicit a profound impairment in cellular information processing, associated with specific behavioural impairments and increased high-frequency power in the 30–80 Hz range, which have both been observed in clinical conditions in humans. Consistent with the E/I balance hypothesis, compensatory elevation of inhibitory cell excitability partially rescued social deficits caused by E/I balance elevation. These results provide support for the elevated cellular E/I balance hypothesis of severe neuropsychiatric disease-related symptoms.

The neurophysiological substrates of most psychiatric disorders are poorly understood, despite accumulating information on genetic factors associated with complex behavioural phenotypes such as those observed in autism and schizophrenia^{1–4}. One emerging principle is that a range of seemingly unrelated genetic abnormalities can give rise to the same class of psychiatric phenotype (such as social behaviour dysfunction)⁵, highlighting the need to identify simplifying circuit-level concepts^{6–8} that could unify diverse genetic factors under a common pathophysiological principle. One such hypothesis is that elevation in the ratio of cortical cellular excitation to inhibition (cellular E/I balance), for example through increased activity in excitatory neurons or reduction in inhibitory neuron function, could give rise to the social and cognitive deficits observed in diseases such as autism^{6,7,9,10}. This hypothesis would unify diverse streams of pathophysiological evidence^{11–15}, including the suggestion that many autism-related genes are linked to gain-of-function phenotypes in ion channels and synaptic proteins¹⁶, that the autistic state is associated with hyperactivity in frontal brain regions^{17–19} with elevated high-frequency cortical oscillations^{20,21} and that ~30% of autistic patients show clinically apparent seizures^{22,23}. However, it is not clear if such an imbalance would impart its disease-relevant effects by influencing development^{9,10,24} or real-time function; moreover, the hypothesis has been neither directly testable nor universally accepted^{25–27}, although much pioneering work^{8–30} may have a bearing on this question.

Although the motivations for social interaction may vary among species, a common theme (independent of motivation) is that social interactions are challenging owing to high levels of uncertainty, and can require rapid interpretation of complex social stimuli to inform

the moment-to-moment generation, refinement and selection of models for the actions of other individuals. Social behaviour assays for experimental mammals such as mice are available, as well as optogenetic methods for direct causal testing of hypotheses regarding the role of activity in specified neuronal populations^{31,32}. Using optogenetics, selectively favouring excitation of one population over another (for example with a bistable step-function opsin (SFO), which can depolarize neurons for prolonged periods^{33,34}) could address the E/I balance hypothesis, but membrane depolarizations induced by known SFOs^{33,35} are not sufficiently stable after a single light flash over the period required for complex behavioural testing. Nor has it been possible thus far to independently excite multiple cell groups within the same volume of tissue, important for testing aspects of the balance hypothesis. Potential strategies exist to manipulate independent neuronal populations in the context of known potent blue-light-activated (~460 nm peak) excitatory tools³⁶, but currently available redshifted channelrhodopsins are not suitable for combinatorial control because redshifts of less than 50 nm^{37,38} do not translate into separable channels of control *in vivo*, and the most redshifted channelrhodopsin (>70 nm; VChR1) suffers from low expression levels and weak photocurrents³⁹.

To enable combinatorial interrogation of E/I balance in experimental animals, we therefore first created several novel optogenetic tools: a series of chimaeric redshifted opsins comprised of sequences from ChR1⁴⁰ and VChR1³⁹, and a stable SFO operative over the 30 min timescale. We then directly tested the E/I balance hypothesis by optogenetically elevating cellular E/I balance in medial prefrontal

¹Department of Bioengineering, W083 Clark Center, 318 Campus Drive West, Stanford University, Stanford, California USA. ²Department of Neurobiology, Weizmann Institute of Science, Rehovot 76100, Israel. ³Neuroscience Program, W083 Clark Center, 318 Campus Drive West, Stanford University, Stanford, California 94305, USA. ⁴Institute of Biology, Experimental Biophysics, Humboldt-Universität, Invalidenstraße 42, D-10115 Berlin, Germany. ⁵Department of Psychiatry, University of California, San Francisco, San Francisco, California 94143, USA. ⁶Department of Neurology and Neurological Science, W083 Clark Center, 318 Campus Drive West, Stanford University, Stanford, California 94305, USA. ⁷Howard Hughes Medical Institute, W083 Clark Center, 318 Campus Drive West, Stanford University, Stanford, California 94305, USA. ⁸Department of Psychiatry and Behavioral Sciences, W083 Clark Center, 318 Campus Drive West, Stanford University, Stanford, California 94305, USA. ⁹CNC Program, W083 Clark Center, 318 Campus Drive West, Stanford University, Stanford, California 94305, USA.

*These authors contributed equally to this work.

cortex (mPFC) during behaviours relevant for social function and learning in freely moving mice.

Development of a stabilized SFO

We first sought to generate an SFO suitably stable for mammalian behaviour. We hypothesized that combining previously characterized SFO mutations (C128S³³ and D156A³⁵), both shown to confer minute-scale deactivation kinetics, would synergistically stabilize the open channel state. We generated and purified from *Pichia pastoris* the ChR2 mutants C128S, D156A and C128S/D156A (Supplementary Fig. 1a) to measure intrinsic open-state stability in the absence of potentially confounding cellular properties. Time-resolved spectroscopy to measure photocycle progression showed expected rapid absorbance changes with light delivery that largely recovered within several minutes for single mutants C128S (Fig. 1a) and D156A (Fig. 1b). In contrast, the double mutant C128S/D156A showed remarkable stability of the activated state, with little detectable return to the dark state even after 30 min (Fig. 1c and Supplementary Fig. 1b). We next performed whole-cell recordings from neurons expressing this construct (Supplementary Fig. 1c). Consistent with spectroscopic observations, neurons expressing ChR2(C128S/D156A) gave rise to far more stable photocurrents than those induced by either single mutant^{33,35} (Fig. 1d). A spontaneous deactivation time constant of 29 min was observed for ChR2(C128S/D156A) ($r^2 = 0.91$), 4.2-fold longer than D156A (6.9 min, $r^2 = 0.83$) (Fig. 1e). Peak photocurrents in neurons expressing ChR2(C128S/D156A) or ChR2(D156A) were comparable (231.08 ± 31.19 pA; $n = 9$ cells and 320.96 ± 78.26 pA; $n = 7$ cells, respectively; $P = 0.26$). The double mutant could be deactivated with either 590 or 405 nm light (Fig. 1f, g and Supplementary

Fig. 1d, e). We refer to the double-mutant gene and protein as the stable SFO (SSFO).

As slow channelrhodopsins enable transduced cells to act as photon integrators across time³³, we hypothesized that the SSFO would enable photoactivation with extremely low light power. Indeed, intensities as low as $8 \mu\text{W mm}^{-2}$ generated hundreds of picoamperes of whole-cell photocurrent in neurons expressing SSFO (Fig. 1h). Photocurrent amplitude increased with monoexponential kinetics during illumination (Fig. 1h, left) whereas activation time constants were linearly dependent on activation power on a log-log scale until the channel-intrinsic millisecond-scale activation time constant (τ_{on}) was approached (Fig. 1h, middle; $n = 27$ recordings from 5 cells). The total number of photons required for photocurrents to reach a fixed fraction of I_{max} was constant over many orders of magnitude of light power (Fig. 1h, right; $9.1 \times 10^8 \pm 1.6 \times 10^8$ photons; $n = 27$ recordings from 5 cells). Taken together, these data indicate that SSFO acts as an integrator with photocurrent determined by total photon exposure.

Consequences of altered E/I balance

To validate the SSFO *in vivo*, we performed optrode recordings⁴¹ in anaesthetized mice expressing SSFO in prelimbic and infralimbic subregions of the mPFC. To modulate excitation, we used adeno-associated virus (AAV) expressing SSFO-EYFP (EYFP, enhanced yellow fluorescent protein) under control of the CaMKII α promoter (CaMKII α :SSFO; Supplementary Methods). To modulate inhibition we expressed a double-floxed inverted open-reading-frame (DIO) AAV³² encoding SSFO-EYFP in PV::Cre (PV, parvalbumin) transgenic mice (PV::SSFO), where expression of SSFO-EYFP is restricted to GABAergic PV neurons³² (Supplementary Fig. 2). Using extracellular

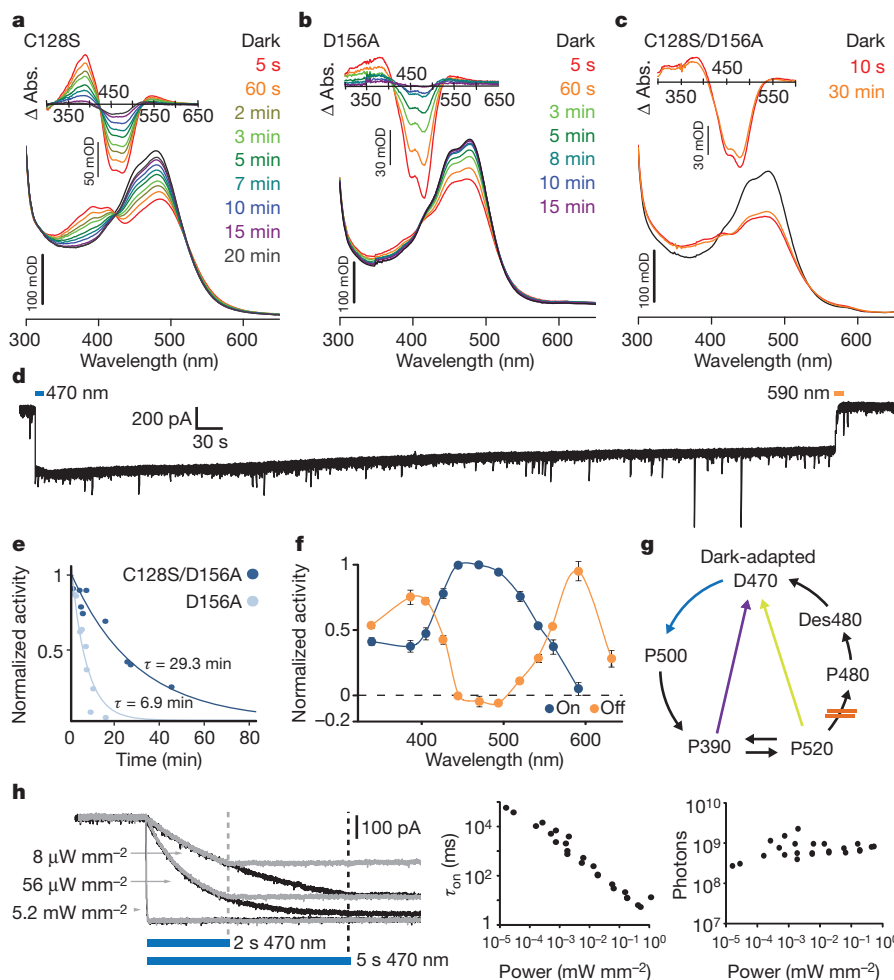


Figure 1 | Kinetic and absorbance properties of a stabilized SFO. **a–c**, Absorption spectra recorded after illumination with 450 nm light for 30 s.

Absorption difference spectra ($\Delta \text{Abs.}$) taken from the corresponding absorption spectra are shown in the insets. Spectra were collected at the indicated times after the end of illumination; note prominent recovery after 3 min in the single mutants, in contrast to the double mutant. **d**, Representative whole-cell patch-clamp recording of photocurrent in a cultured hippocampal neuron expressing ChR2(C128S/D156A) SSFO. Blue and orange bars indicate activation and deactivation light pulses. **e**, Monoexponential fits of photocurrent decay in cells expressing ChR2(C128S/D156A) (dark blue; $\tau = 29$ min) or ChR2(D156A) (light blue; $\tau = 6.9$ min). **f**, Activation (blue) and deactivation (orange) spectra recorded from cultured neurons expressing ChR2(C128S/D156A). **g**, Simplified photocycle scheme; in C128S/D156 mutants the transition P520 to P480 is probably slowed down or blocked, avoiding the desensitized state Des480 which cannot be reactivated with 470 nm light. Both yellow and violet light (yellow and violet arrows) shuttle the channels to an inactive state (see Supplementary Fig. 1). **h**, Whole-cell photocurrent responses of a cultured neuron expressing SSFO to 470 nm light pulses of indicated power (left). Pulse lengths were 2 s (grey traces) or 5 s (black traces). Dashed lines mark light pulse termination. Apparent time constants for activation (τ_{on}) are shown on a log-log plot versus light power ($n = 27$ recordings from 5 cells; middle). Within this broad range of light power, the calculated number of incident photons arriving at each cell for photocurrents to reach the exponential curve constant (63% of I_{max}) for that cell was constant (right). Each point represents a photon number from a single recording at a given light power.

recordings in anaesthetized mice to access this medial structure, we observed significant light-induced changes in multiunit activity restricted to transduced regions of the mPFC (Supplementary Fig. 3). In mice expressing CaMKII α ::SSFO, multiunit spike rates increased within the transduced area as expected (Supplementary Fig. 3b, c, e, f). Conversely, in PV::SSFO mice (despite the sparseness of PV cells and incomplete transduction; Supplementary Fig. 2), multiunit activity profoundly decreased after an identical 1 s pulse of 473 nm light and returned to near-baseline levels after a 2 s 561 nm pulse (Supplementary Fig. 3b, d, e; subsequent behavioural work described later used identical opsin-expression experimental conditions). We next examined the effects of altered E/I balance on prefrontal information transmission using whole-cell patch-clamp recordings. In the presence of ongoing synaptic activity, CaMKII α ::SSFO activation increased synaptic input onto both expressing and non-expressing pyramidal cells (Supplementary Fig. 4a, b). To test the input–output relationship, we stimulated CaMKII α ::SSFO neurons with trains of simulated excitatory post-synaptic currents (sEPSCs) designed to span a wide range of sEPSC rates over time³² (Supplementary Fig. 4c and Supplementary Methods). Elevation of the cellular E/I balance in these slices by activation of CaMKII α ::SSFO led to saturation of the input–output (*I–O*) curve and a reduction in *I–O* mutual information (Supplementary Fig. 4d–i). In contrast, activation of SSFO in PV cells potentially reduced ongoing synaptic activity (Supplementary Fig. 5a) and decreased *I–O* curve gain in recorded pyramidal cells, as expected via synaptic inhibition.

However, the shape of the *I–O* curve was preserved with only a small reduction in dynamic range but no change in saturation and no significant effect on *I–O* mutual information (Supplementary Fig. 5b–g). Overall, the reduction in principal neuron information throughput after light activation in CaMKII α ::SSFO slices was 4.8-fold larger than in PV::SSFO slices ($P = 0.0144$; across a wide range of analysis parameters, Supplementary Fig. 5h). These results indicate that at the principal neuron level, information processing may be more impaired by increased E/I balance.

We next examined the effects of this elevated cellular E/I balance on behaviour. We expressed SSFO in either mPFC excitatory or inhibitory PV-expressing neurons as described earlier, and implanted a chronic fibre-optic connector terminating dorsal to the mPFC (Fig. 2a, b). We confirmed, using c-Fos staining as a marker of activity, that in the awake state neural activity could be increased or decreased by activation of SSFO in pyramidal and PV neurons respectively (Fig. 2c and Supplementary Fig. 6a). In behavioural tests, all mice received a single 2 s pulse of 473 nm light through the implanted fibre-optic connector, followed by removal of the fibre optic 1 min before introduction into the behavioural chamber, capitalizing on the stability of the SSFO. Exploration of a new same-sex juvenile introduced to the experimental animal home cage was virtually abolished in the elevated E/I (CaMKII α ::SSFO) group following SSFO activation (Fig. 2d and Supplementary Videos 1 and 2; $n = 8$ CaMKII α ::SSFO mice and $n = 6$ controls; $P < 0.0005$); PV::SSFO mice showed no effect of

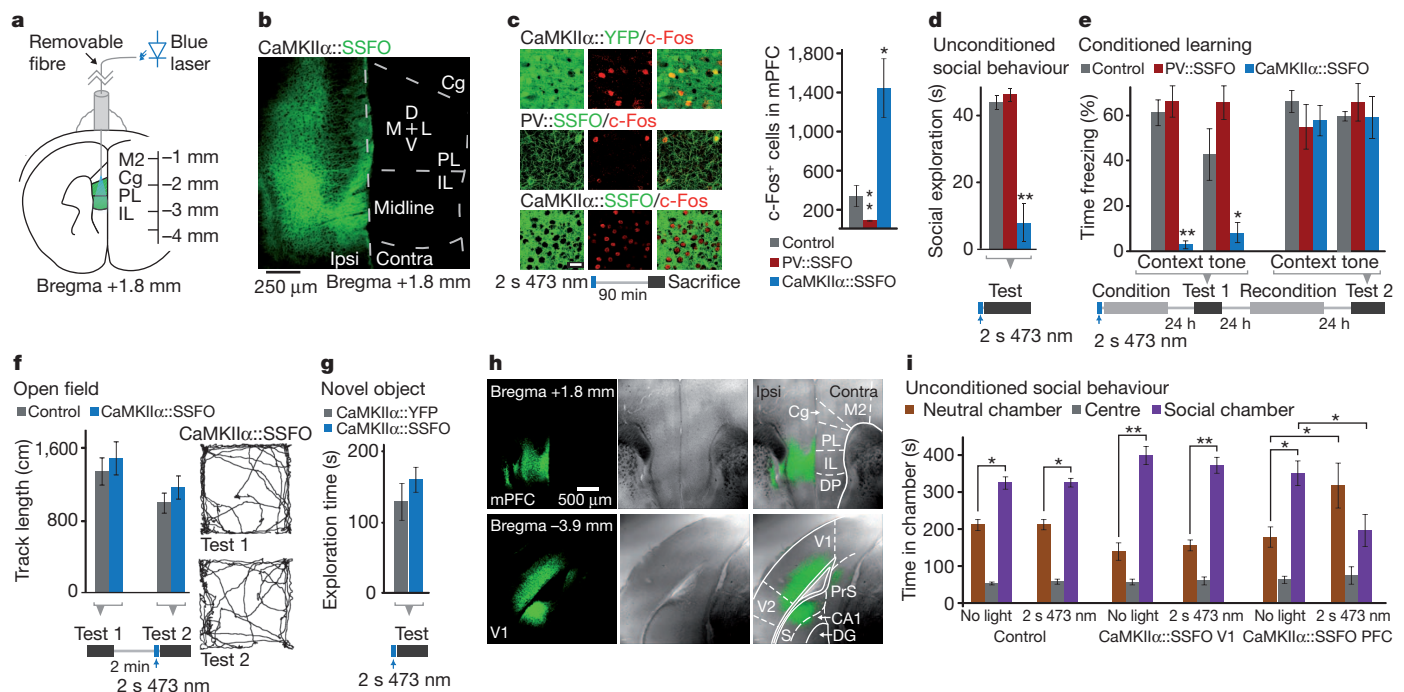


Figure 2 | Elevated, but not reduced, prefrontal E/I balance leads to behavioural impairment. **a**, Experimental setup for behavioural experiments. Green region marks viral injection area; fibre-optic connector was attached to the light guide only transiently before testing. Cg, cingulate cortex; IL, infralimbic cortex; M2, secondary motor cortex; PL, prelimbic cortex. **b**, Confocal image from a mouse injected with CaMKII α ::SSFO–EYFP virus shows expression in prelimbic and infralimbic cortex. D, dorsal; L, lateral; M, medial; V, ventral. Contra, contralateral; Ipsi, ipsilateral. **c**, Representative images of prefrontal slices from PV::SSFO and CaMKII α ::SSFO mice stained for c-Fos 90 min after a 2 s 473 nm light pulse. Scale bar, 25 μ m. Graph shows average c-Fos-positive cell counts in the mPFC of control, CaMKII α ::SSFO and PV::SSFO mice. **d**, Social exploration in control, CaMKII α ::SSFO and PV::SSFO mice of a juvenile intruder in the home cage. CaMKII α ::SSFO mice showed a significant reduction in social exploration. **e**, Mice administered one 2 s 473 nm pulse of light before fear conditioning were tested the next day for freezing in response to the conditioned context or auditory cue;

CaMKII α ::SSFO mice were significantly impaired in freezing responses to both conditioned stimuli. On the following day, mice were reconditioned without optical stimulation and freezing was evaluated 24 h later. All mice showed similar freezing behaviour in the absence of light. **f**, Open-field exploration in CaMKII α ::SSFO (blue) and CaMKII α ::EYFP (grey) mice, before (Test 1) and after (Test 2) light activation. Example tracks from a CaMKII α ::SSFO mouse are shown. **g**, Novel object exploration over a 10 min period is similar in mice expressing CaMKII α ::SSFO (blue) and CaMKII α ::EYFP (grey). **h**, Phase contrast and fluorescence images of coronal sections from wild-type mice injected with CaMKII α ::SSFO in PFC (top) or V1 (bottom). **i**, Social behaviour in the three-chamber test is impaired following a 2 s 473 nm light pulse in mice expressing CaMKII α ::SSFO in the PFC ($n = 5$), but not in control mice ($n = 6$) or in mice expressing CaMKII α ::SSFO in V1 ($n = 8$). Time spent in a given chamber after stimulation is only significantly altered in mice expressing CaMKII α ::SSFO. All bar graphs depict mean \pm s.e.m. (* $P < 0.05$, ** $P < 0.005$).

SSFO activation (Fig. 2d; $n = 6$ PV::SSFO mice; $P > 0.1$). To test episodic learning (also impaired in autism and schizophrenia^{42,43}), we next subjected the same mice to a fear conditioning protocol immediately following SSFO activation. The elevated E/I (CaMKII α ::SSFO) mice showed no conditioned responses 24 h after conditioning (Fig. 3e; to either context, $P < 0.0005$; or tone, $P < 0.05$, compared with controls). We then reconditioned the same mice in the absence of light activation of SSFO. Twenty-four hours later, responses of these mice were indistinguishable from controls (Fig. 2e; $P > 0.1$ cue and context). The reduced E/I balance (PV::SSFO) group showed no significant impairment compared with controls to either tone or context (Fig. 2e; $P = 0.09$ and $P = 0.56$, respectively). Elevated E/I balance-induced deficits were not a result of motor impairment as, in the same mice, open-field behaviour was normal (Fig. 2f and Supplementary Fig. 6b; $n = 8$ CaMKII α ::SSFO mice and $n = 6$ CaMKII α ::EYFP mice; Supplementary Fig. 8d shows unchanged immediate foot-shock response in CaMKII α ::SSFO mice). Additionally, CaMKII α ::SSFO mice showed no abnormalities in exploration of a novel object (Fig. 2g; $n = 8$ CaMKII α ::SSFO and $n = 10$ CaMKII α ::EYFP mice; $P = 0.47$).

We next examined whether the social impairment induced by altered E/I balance could arise in any cortical region. We tested three groups of mice: CaMKII α ::SSFO virus in the mPFC, as earlier ($n = 5$; Fig. 2h, top); control virus in the mPFC ($n = 6$); and CaMKII α ::SSFO virus in the primary visual cortex (Fig. 2h, bottom; V1 area 17; $n = 8$), an area in which microstimulation generates potent internal visual stimuli⁴⁴. These mice were tested in the three-chamber social exploration paradigm⁴⁵, an independent measure of social interaction. We found that control mice and CaMKII α ::SSFO V1 mice preferred the chamber with a novel conspecific mouse, in both no-light and light conditions (Fig. 2i). In contrast, CaMKII α ::SSFO mPFC mice exhibited normal social exploration at baseline, but significantly reduced social exploration after SSFO activation (Fig. 2i). This impairment in social behaviour was not correlated with an increased-anxiety phenotype in the elevated plus maze (Supplementary Fig. 6d). Viral targeting was evaluated post-hoc and revealed CaMKII α ::SSFO expression in targeted regions in all mice tested (Fig. 2h and Supplementary Fig. 7). Taken together, these experiments indicate that elevated, but not reduced, cellular E/I balance in the mPFC significantly impairs social behaviour

and conditioning, and that this deficit does not result from changes in anxiety or locomotion.

E/I balance elevation elicits rhythmic activity

Behavioural impairment in both autism and schizophrenia has been associated with elevated baseline (non-evoked) high-frequency activity in the 30–80 Hz range^{20,21,46}. To examine the activity patterns in awake behaving mice during E/I balance modulation, we designed a chronic multi-site optrode (CMO; Fig. 3a and Methods) to sample activity both in modulated mPFC and in unmodulated regions above and below the mPFC. We hypothesized that temporal stability and photon integration of SSFO would allow light delivery with superficial (non-brain penetrating) fibre-optic placement (Supplementary Fig. 8a, b), and verified that superficial light delivery could modulate SSFO-expressing mPFC cells using c-Fos quantification and behavioural testing (Supplementary Fig. 8c–e). We used CMOs to record neural activity in CaMKII α ::SSFO mice; fibre placement was superficial and electrode positions were confirmed post-hoc by electrolytic lesioning (Fig. 3b). We found that CaMKII α ::SSFO mice with CMO implants had normal baseline social behaviour that was impaired after a 1 s 473 nm pulse (Fig. 3c; $n = 3$, $P = 0.044$). Novel object exploration was unaffected by stimulation, consistent with previous findings (Fig. 3c; $P = 0.82$). The activation pulse did not significantly alter locomotor behaviour in either the home cage (not shown) or a novel open field, although the latter trended towards reduced anxiety (Supplementary Fig. 8f and Supplementary Video 3).

We recorded multiunit activity and local field potentials simultaneously on all channels during these behaviour trials. In the home cage, we observed significant increases in multiunit activity after a 1 s 473 nm light pulse in channels within the SSFO-expressing regions (Supplementary Fig. 8g, h; $77 \pm 18\%$ on modulated channels, compared with $-3.4 \pm 4.4\%$ on unmodulated channels; $n = 4$ modulated and 4 unmodulated channels in 3 mice averaged over 4 sweeps per mouse; $P = 0.02$). Modulated channels showed a marked increase in high-frequency activity with a peak at 80 Hz after SSFO activation (Fig. 3e) delimited to the activation period (Fig. 3d, e, left). Channels with increased high-frequency activity had concomitant reduction of lower frequencies (Fig. 3e, right, inset). High-frequency activity was

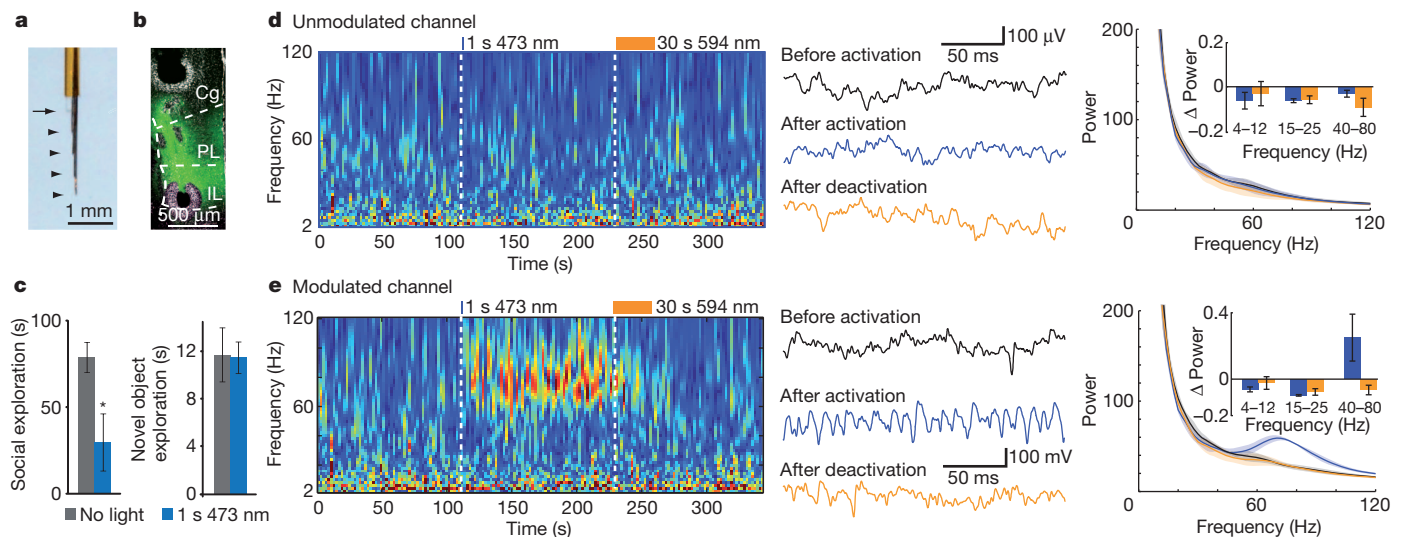


Figure 3 | Elevated cellular E/I balance in the mPFC drives baseline high frequency rhythmicity in freely moving, socially impaired mice.

a, Implantable CMO for awake, behaving recordings in mouse M2 and PFC. Arrowheads indicate wire termination sites; arrow shows cleaved end of fibre-optic connector. **b**, Electrolytic lesions mark the sites from which recordings were taken in a mouse expressing CaMKII α ::SSFO. **c**, Social (left) and novel object exploration (right) before (grey) and after (blue) activation with 473 nm light in mice used for CMO recordings ($n = 3$ mice). **d, e**, Local-field-potential

wavelet spectrogram from a representative unmodulated channel (**d**) and a representative modulated channel (**e**). Example traces are shown for the baseline, activation and deactivation periods. Average wavelet spectra for the three indicated periods ($n = 5$ trials in 1 mouse) and population data (insets; $n = 3$ mice) are shown, demonstrating a specific increase in gamma rhythmicity on the modulated channel after SSFO activation in PFC pyramidal neurons. All bar graphs depict mean \pm s.e.m. (* $P < 0.05$).

consistently increased in experiments where a 1 s 473 nm pulse was delivered during testing in the open field (Supplementary Fig. 8i and Supplementary Movie 3), during social exploration (Supplementary Fig. 8j and Supplementary Movie 5) and during novel object exploration (Supplementary Fig. 8k). Together, these data reveal that elevated rhythmic high-frequency activity, a disease correlate in clinical conditions, is elicited (along with social deficits) as a result of elevating cellular E/I balance in freely behaving mammals.

Development of potent redshifted control

We next sought to complement SSFO with a redshifted, fast-kinetic-response excitatory ChR for combinatorial control in the mPFC. Neurons expressing VChR1 showed weak expression (Fig. 4a) and small photocurrents (Supplementary Fig. 9a), consistent with previous findings³⁹. Adding a Kir2.1 trafficking signal⁴⁷ (ts) to generate VChR1-ts-EYFP only modestly enhanced photocurrents (Supplementary Fig. 9a). We next systematically produced ChR1/VChR1 chimaeras and screened for enhanced membrane expression and photocurrent in HEK cells. We observed markedly improved membrane expression when VChR1 helices 1 and 2 were replaced with ChR1 homologues (Supplementary Fig. 9b) and selected two of these (fused at ChR1 Ala 145 or Trp 163) for further characterization (Supplementary Fig. 9a, c, d). In cultured neurons, the latter variant expressed more robustly and trafficked well to the membrane (Fig. 4a and Supplementary Fig. 9e, f) with enhanced peak photocurrents (888 ± 128 pA, $n = 11$ cells;

$P < 0.0005$) compared with VChR1 (Supplementary Fig. 9a). The action spectrum remained redshifted (Supplementary Table 1 and Fig. 4d), while ion selectivity was similar to ChR2 and VChR1 (Supplementary Fig. 9g). The Kir2.1 trafficking sequence⁴⁷ further increased photocurrents (1104 ± 123 pA, $n = 12$ cells; Fig. 4e, Supplementary Fig. 9a and Supplementary Tables 1, 2). This ChR1/VChR1 chimaera contains no ChR2 sequence at all and is referred to here as C1V1.

Fast deactivation³⁷ of a redshifted opsin would be optimal for temporal and spectral separation from SSFO. However, C1V1-ts-EYFP photocurrents decayed >10-fold more slowly than those of ChR2, and indeed more slowly than those of VChR1 (Fig. 4c; τ_{off} 156 ± 12 ms and 132 ± 12 ms for C1V1-ts-EYFP ($n = 4$) and VChR1-EYFP ($n = 5$), respectively; Supplementary Table 1). To enhance photocurrent kinetics of C1V1, we used structural models to search the chromophore region^{33,37} (Fig. 4b) for residues that might modulate photocycle kinetics, inactivation and blue absorption. We found that the E162T mutation (homologous to a ChETA mutation in ChR2) and the E122T mutation both significantly reduced τ_{off} (Fig. 4c). The combined E122T/E162T mutation synergistically enhanced photocurrent temporal precision while maintaining robust photocurrent sizes and reducing the residual shorter-wavelength response observed in VChR1 and C1V1(E162T) (Fig. 4c–e). Photocurrent sizes generally correlated with fluorescence intensity across constructs (Supplementary Fig. 9h), but C1V1(E122T/E162T) cells showed stronger photocurrents than ChR2(H134R) cells at equivalent fluorescence levels (Fig. 4f).

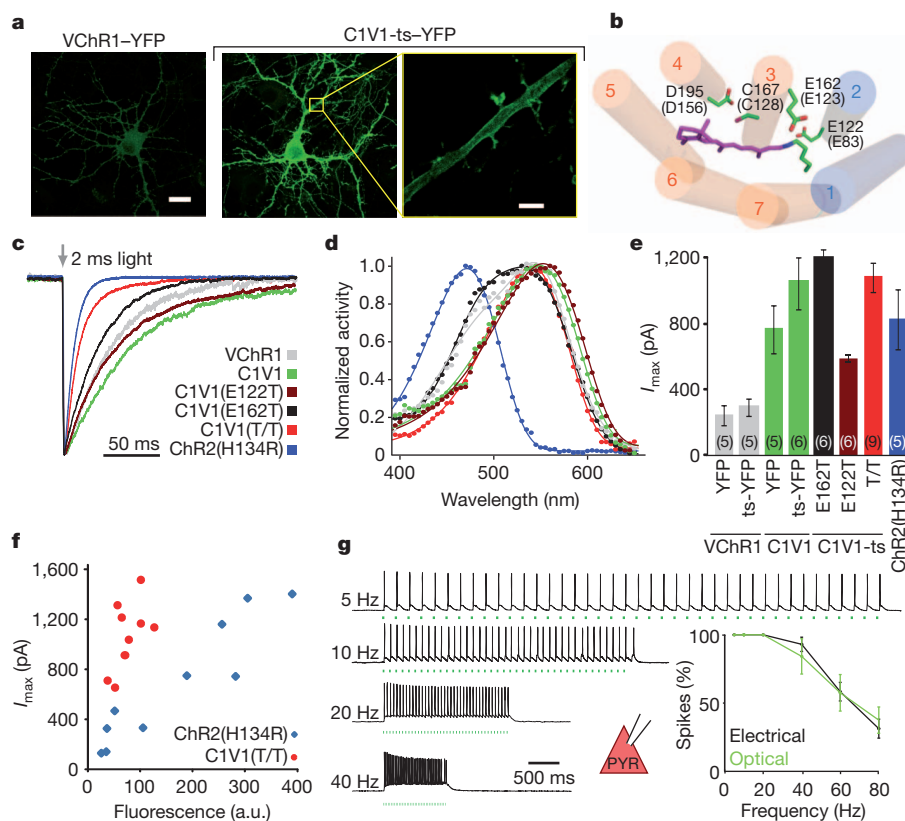


Figure 4 | Multistep engineering of a potent redshifted ChR. **a**, Confocal images of cultured hippocampal neurons transfected with VChR1-EYFP or C1V1-ts-EYFP under the control of the CaMKII α promoter. Yellow box denotes region expanded in the last panel, showing dendritic membrane localization of C1V1-ts-EYFP. Scale bars: 20 μ m (left, middle), 4 μ m (right). **b**, Model of the C1V1 chromophore binding pocket, showing ChR1 helices in blue, VChR1 helices in orange, the retinal Schiff base (RSB) in purple, and key amino acid residues (with corresponding ChR2 numbering in parentheses and the modelled location of the SSFO mutations C128 and D156 shown for context). **c**, Representative traces and summary plot of channel closure time constant (τ_{off}) in cultured neurons expressing the indicated channelrhodopsins; traces are normalized to peak current. **d**, Action spectra collected for the

indicated channelrhodopsins (colour code as in c). Photocurrents were collected with 2 ms light pulses in HEK293 cells. **e**, Mean peak photocurrents recorded in cultured neurons expressing the indicated channelrhodopsins in response to a 2 ms 542 nm light pulse. Colours are as indicated in c; numbers in brackets indicate n . **f**, Fluorescence-photocurrent relationship in ChR2(H134R) (blue) and C1V1(E122T/E162T) (red). a.u., arbitrary units. **g**, Acute slice recordings in prefrontal pyramidal neurons (PYR) expressing C1V1(E122T/E162T) and stimulated with 560 nm light pulse trains or current injections at the indicated frequencies. Summary graphs show light and current-evoked spike probability versus stimulation frequency ($n = 6$; $P > 0.4$ at all frequencies). All error bars indicate s.e.m.

Next we injected mice with AAV5-CaMKII α ::C1V1(E122T/E162T)-ts-EYFP virus in the mPFC and recorded from expressing neurons in acute slices. The frequency responses to trains of 2 ms light pulses or current injection pulses were indistinguishable (Fig. 4g; $n = 6$ cells in 2 slices), suggesting that in this case properties and not opsin kinetics limit performance (Supplementary Fig. 10). We next found that with C1V1(E122T) (the most redshifted of all variants although somewhat slower than C1V1(E122T/E162T); Fig. 4d) reliable spiking with 630 nm light could be obtained (Supplementary Fig. 11). Lastly, using AAV5-CaMKII α ::C1V1(E122T/E162T) together with AAV5-EF1 α ::ChR2(H134R), we were able to differentially drive spiking in cortical pyramidal and PV neurons with 560 nm and 405 nm light, respectively (Supplementary Fig. 12). Combinatorial excitation was also possible with SSFO and C1V1, as peak frequencies of evoked rhythmic circuit activity generated in prefrontal cortical slices by C1V1 activation seemed to be shifted to higher frequencies by co-activation of SSFO in PV neurons (Supplementary Fig. 13). Furthermore, using C1V1 and ChR2 we were able to independently activate axons of two converging excitatory pathways (cortico-thalamic and thalamo-cortical) onto thalamic reticular nucleus neurons, observing that under these conditions the temporal coincidence of subthreshold synaptic inputs from each pathway can evoke spiking in target

neurons (Supplementary Fig. 14). Together these results indicated that combinatorial control within intact tissue is enabled with these C1V1 variants.

Increased inhibition modulates behavioural deficits

In principle, an elevated E/I ratio could be achieved not only by increasing excitation but also by reducing inhibition, although this loss-of-function approach might be operative only under high baseline activity of the inhibitory cells (Supplementary Figs 6c, 15). However, a question salient to the elevated cellular E/I ratio hypothesis is whether adding an additional disruption in the form of increased inhibition could ameliorate behavioural deficits associated with elevated E/I balance. For this experiment, we first had to verify that combinatorial excitation could be feasible *in vivo*. We therefore explored combinatorial excitation of mPFC pyramidal and PV neurons *in vivo* with optrode recordings (Fig. 5a, left). To examine inhibitory effects of PV cell activity on pyramidal neuron spiking *in vivo*, we expressed CaMKII α ::C1V1(E122T/E162T) and DIO::ChR2(H134R) in the mPFC of PV::Cre mice. Using an optrode, we applied 5 Hz 405 nm pulses (to activate ChR2 in PV cells) followed by 5 Hz 561 nm pulses (to activate C1V1 in pyramidal neurons) while varying inter-pulse interval (Fig. 5a, right). The fidelity of green-light-evoked

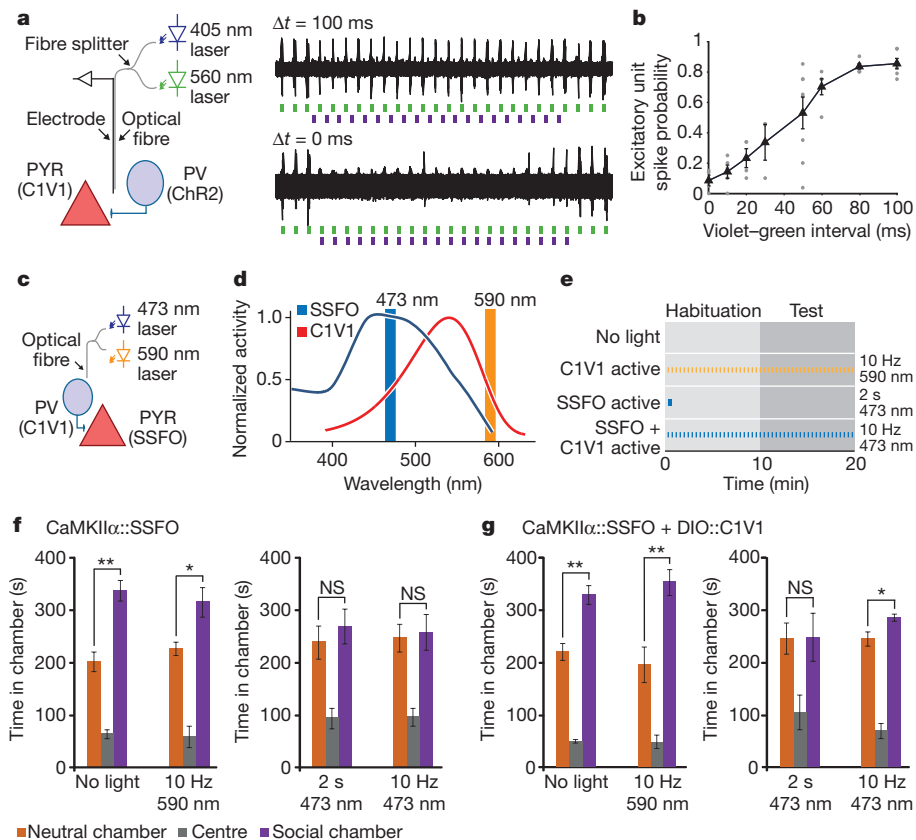


Figure 5 | Combinatorial optogenetics enables partial reversal of elevated E/I-balance social behaviour disruption. **a**, mPFC optrode recording in an anaesthetized PV::Cre mouse injected with CaMKII α ::C1V1(E162T)-ts-EYFP and Ef1a-DIO::ChR2-EYFP (diagram illustrates experimental setup). Violet (405 nm) light pulses are presented with variable delay (Δt) relative to green light pulses (example traces). **b**, Summary graph shows probability of green-light-evoked spikes with violet pulses preceding the green light pulses by the indicated delays. Individual points are from single recordings. Black line shows average for all recordings (>3 recording sites per bin). **c**, Experimental paradigm for SSFO activation in pyramidal neurons and C1V1 activation in PV neurons. **d**, Action spectra of SSFO (blue) and C1V1(E122T/E162T) (C1V1, red). Orange and blue vertical lines indicate stimulation wavelengths used in the experiments. **e**, Experiment design and pulse patterns; no-light control was

used for baseline behaviour; 2 s 473 nm light for prolonged SSFO activation; 10 Hz 473 nm for co-activation of SSFO and C1V1; 10 Hz 590 nm for C1V1 activation. **f**, Mice expressing CaMKII α ::SSFO ($n = 7$) showed significant social preference at baseline, but exhibited social dysfunction after either 2 s 473 nm activation or during 10 Hz 473 nm activation. **g**, Mice expressing both CaMKII α ::SSFO and DIO-PV::C1V1 ($n = 7$) showed impaired social behaviour after a 2 s 473 nm pulse, but showed partially restored social behaviour during the 10 Hz 473 nm light stimulation. Activation of C1V1 alone with 10 Hz 590 nm pulses did not impair social behaviour. NS, not significant. Supplementary Fig. 16 shows normal social behaviour under all illumination conditions in YFP-expressing control cohorts. All error bars indicate s.e.m. ($*P < 0.05$; $**P < 0.005$).

events dropped as the inter-pulse interval decreased, with maximal excitatory responses observed with an interval of 100 ms (Fig. 5a, top trace) and responses were nearly abolished when light pulses were presented with sufficient synchrony (Fig. 5a, bottom trace; summary data in Fig. 5b). These data demonstrate combinatorial optogenetic control within an intact mammal.

We next leveraged combinatorial optogenetics *in vivo* to excite mPFC pyramidal cells with SSFO and PV neurons with C1V1 (E122T/E162T) in freely moving mice (Fig. 5c; referred to here as SSFO/C1V1 mice; $n = 7$). Control cohorts were injected with CaMKII α ::SSFO virus alone ($n = 7$) or with CaMKII α ::EYFP ($n = 8$). Mice were tested in the three-chamber social test under four different illumination paradigms, designed to examine behaviour with baseline properties, elevated excitatory tone, elevated inhibitory tone and co-elevated excitatory and inhibitory tone (Fig. 5d, e). All mice showed significant preference for the social chamber during baseline testing (Fig. 5f, g and Supplementary Fig. 16; CaMKII α ::SSFO mice, $P = 0.0002$; SSFO/C1V1 mice, $P = 0.0014$; CaMKII α ::EYFP mice, $P = 0.0029$). Under pulsed laser light at 590 nm, all mice showed significant preference for the social chamber (Fig. 5f, g and Supplementary Fig. 16; CaMKII α ::SSFO mice, $P = 0.02$; SSFO/C1V1 mice, $P = 0.0048$; CaMKII α ::EYFP mice, $P = 0.039$). After a 2 s 473 nm pulse given at the beginning of the test, neither the CaMKII α ::SSFO nor the SSFO/C1V1 mice preferred the social chamber (Fig. 5f, g and Supplementary Fig. 16; $P = 0.52$ and $P = 0.96$, respectively). Lastly, we sought to ameliorate the behaviour deficit by compensating cellular E/I balance, co-activating SSFO in excitatory cells and C1V1 (E122T/E162T) in inhibitory cells by pulsing 10 Hz 473 nm light throughout the test period (Fig. 5f, g). CaMKII α ::SSFO mice (with no C1V1 (E122T/E162T)) and thus experiencing purely cellular E/I balance elevation) showed no significant preference for the social chamber (Fig. 5f; $P = 0.81$); in contrast, despite the sparseness of the PV population and incomplete transduction under these conditions (Supplementary Fig. 2) SSFO/C1V1 showed modest but significant preference for the social chamber (Fig. 5g; $P = 0.026$). Control CaMKII α ::EYFP mice significantly preferred the social chamber under both the 2 s 473 nm and the 10 Hz 473 nm paradigms (Supplementary Fig. 16). Together, this series of experiments indicate that social deficits seen with elevated mPFC cellular E/I balance may be partially reduced by restoring balance with increased inhibitory tone.

Discussion

Several lines of evidence have indicated the involvement of elevated cellular E/I balance in the aetiology of medication-unresponsive social and information-processing impairments in autism and schizophrenia, although it has been unclear if such an effect would operate on the acute or chronic timescale^{3,9,10,23,28,48}. Moreover, the tight interplay and complexity of excitation and inhibition within cortical microcircuitry have precluded the direct investigation of cell- and circuit-level effects of changes in cellular E/I balance; for example, cell-specific pharmacological agents are lacking, and homeostatic processes can occur downstream of synaptic and intrinsic excitability alterations. We therefore sought to investigate the effects of this altered cellular E/I balance on the acute timescale and quantify the effects on information transmission, network activity and animal behaviour. To stably modulate neural activity in awake animals, we produced an SSFO that enabled combined spectral/temporal separation when used together with red-shifted opsins (C1V1 variants), developed as chimaeras along with combinatorial mutagenesis of the chromophore region to enhance potency, kinetics and spectral properties.

With these new tools, we obtained causal support for the elevated cellular E/I balance hypothesis, and identified circuit-physiology manifestations of the resulting social dysfunction. SSFO activation in prefrontal cortical excitatory (but not inhibitory) neurons led to profound, yet reversible, impairments in social function and cognition without motor abnormalities or increased anxiety. To understand more fully the elevated E/I state, we probed both *in vitro* and *in vivo* the

underlying circuit-physiology manifestations. Despite the complexity resulting from the broad range of circuit phenomena that a cellular E/I balance modulation could initiate, we found that cellular E/I balance elevation, but not reduction under these conditions, altered the transfer functions of principal neurons in a way that quantitatively impaired information transmission within cortical circuitry. The effects of elevated E/I balance on social behaviour showed evidence of specificity for the PFC, as increasing the E/I ratio in primary visual cortex did not impair social behaviour. The PFC network, with its extensive sub-cortical connectivity, might therefore be particularly susceptible to eliciting psychiatric symptom-related effects in the setting of subtle changes in E/I balance, a notion that is supported by observed alterations in PFC inhibitory markers associated with psychiatric disease^{12,13,48–50} and the altered PFC rhythmicity observed in autistic individuals²⁰. And using spectrottemporal separation of the activity of SSFO and C1V1, we found that increased cellular inhibition moderately ameliorated the social behaviour deficits in mice that had been subjected to elevation of cellular E/I balance.

We also identified correspondence between a clinical marker of disease states linked to social dysfunction (elevated baseline gamma power) and electrophysiological findings during free behaviour in the elevated cellular E/I state. We found that the elevated E/I state was associated with robust, stable high-frequency power in the 30–80 Hz range generated by and manifested within the regions directly experiencing elevated cellular E/I balance. Stimulus-evoked gamma oscillations had previously been shown to be important for refining information flow through cortical circuitry³², but high baseline (unevoked) gamma oscillations may interfere with cortical function and contribute to disease states^{20,21}. Together, these temporally delimited, cell-type-specific optogenetic manipulations (although fully capable of causing either acute or chronic changes in complex local circuit processing and input–output relationships) distinguish direct real-time effects of cellular E/I balance changes *in vivo* from the many possible developmental and structural alterations that could occur with more chronic interventions^{25–29}. Despite the complexity of homeostatic processes that contribute to behavioural phenotypes in genetic models, our data are consistent with the E/I balance hypothesis and with recent reports of impaired social function and learning in mouse models of Rett syndrome^{28,29}. In sum, these findings may represent a step towards understanding the pathophysiology of social and information-processing dysfunction, and despite the complexity of cortical processing, together provide causal support for the cellular E/I balance elevation hypothesis of severe psychiatric disease symptomatology on the cellular, circuit and behavioural levels.

METHODS SUMMARY

C1V1 was cloned by overlap extension PCR, fusing the N-terminal sequence of the *Chlamydomonas reinhardtii* ChR1 coding sequence⁴⁰ with the C-terminal sequence of *Volvox carterii* ChR1³⁹. SSFO mutants were generated by site-directed mutagenesis of the humanized ChR2 sequence. Constructs were cloned into the pLenti or pAAV-MCS backbone under control of the CaMKII α promoter or using a double-floxed inverted open-reading frame (ORF) Cre-dependent backbone³². Maps and clones are available at <http://www.optogenetics.org>.

Virus was stereotactically injected 2–3 weeks before physiological experiments or behavioural testing. Optrode recordings in anaesthetized mice were conducted as described⁴¹ using a dual-laser system with either 473 nm and 561 nm lasers for SSFO experiments or 405 nm and 561 nm lasers for combinatorial excitation experiments with ChR2 and C1V1.

Recordings in behaving mice were performed using custom-built 4-microwire arrays attached to an optical fibre. Arrays were designed to sample from a large anatomical volume including transduced and untransduced tissue. Data were analysed in Matlab, using custom software; spectral analysis was performed using the wavelet method³².

Received 17 September 2010; accepted 10 July 2011.

Published online 27 July 2011.

1. Pardo, C. A. & Eberhart, C. G. The neurobiology of autism. *Brain Pathol.* **17**, 434–447 (2007).

2. O'Donovan, M. C., Craddock, N. J. & Owen, M. J. Genetics of psychosis; insights from views across the genome. *Hum. Genet.* **126**, 3–12 (2009).
3. Südhof, T. C. Neuroligins and neuroligins link synaptic function to cognitive disease. *Nature* **455**, 903–911 (2008).
4. Patterson, P. H. Modeling autistic features in animals. *Pediatr. Res.* **69**, 34R–40R (2011).
5. Walsh, T. *et al.* Rare structural variants disrupt multiple genes in neurodevelopmental pathways in schizophrenia. *Science* **320**, 539–543 (2008).
6. Markram, K. & Markram, H. The intense world theory—a unifying theory of the neurobiology of autism. *Front. Hum. Neurosci.* **4**, 224 (2010).
7. Vattikuti, S. & Chow, C. C. A computational model for cerebral cortical dysfunction in autism spectrum disorders. *Biol. Psychiatry* **67**, 672–678 (2010).
8. Kehr, C., Maziashvili, N., Dugladze, T. & Gloveli, T. Altered excitatory-inhibitory balance in the NMDA-hypofunction model of schizophrenia. *Front. Mol. Neurosci.* **1**, 6 (2008).
9. Rubenstein, J. L. Three hypotheses for developmental defects that may underlie some forms of autism spectrum disorder. *Curr. Opin. Neurol.* **23**, 118–123 (2010).
10. Rubenstein, J. L. & Merzenich, M. M. Model of autism: increased ratio of excitation/inhibition in key neural systems. *Genes Brain Behav.* **2**, 255–267 (2003).
11. Gogolla, N. *et al.* Common circuit defect of excitatory-inhibitory balance in mouse models of autism. *J. Neurodevel. Disord.* **1**, 172–181 (2009).
12. Hashimoto, T. *et al.* Conserved regional patterns of GABA-related transcript expression in the neocortex of subjects with schizophrenia. *Am. J. Psychiatry* **165**, 479–489 (2008).
13. Hashimoto, T. *et al.* Gene expression deficits in a subclass of GABA neurons in the prefrontal cortex of subjects with schizophrenia. *J. Neurosci.* **23**, 6315–6326 (2003).
14. Belforte, J. E. *et al.* Postnatal NMDA receptor ablation in corticolimbic interneurons confers schizophrenia-like phenotypes. *Nature Neurosci.* **13**, 76–83 (2010).
15. Blatt, G. J. *et al.* Density and distribution of hippocampal neurotransmitter receptors in autism: an autoradiographic study. *J. Autism Dev. Disord.* **31**, 537–543 (2001).
16. Bourgeron, T. A synaptic trek to autism. *Curr. Opin. Neurobiol.* **19**, 231–234 (2009).
17. Belmonte, M. K., Gomot, M. & Baron-Cohen, S. Visual attention in autism families: 'unaffected' sibs share atypical frontal activation. *J. Child Psychol. Psychiatry* **51**, 259–276 (2010).
18. Gomot, M., Belmonte, M. K., Bullmore, E. T., Bernard, F. A. & Baron-Cohen, S. Brain hyper-reactivity to auditory novel targets in children with high-functioning autism. *Brain* **131**, 2479–2488 (2008).
19. Dichter, G. S., Felder, J. N. & Bodfish, J. W. Autism is characterized by dorsal anterior cingulate hyperactivation during social target detection. *Soc. Cogn. Affect. Neurosci.* **4**, 215–226 (2009).
20. Orekhova, E. V. *et al.* Excess of high frequency electroencephalogram oscillations in boys with autism. *Biol. Psychiatry* **62**, 1022–1029 (2007).
21. Rojas, D. C., Maharajh, K., Teale, P. & Rogers, S. J. Reduced neural synchronization of gamma-band MEG oscillations in first-degree relatives of children with autism. *BMC Psychiatry* **8**, 66 (2008).
22. Gillberg, C. & Billstedt, E. Autism and Asperger syndrome: coexistence with other clinical disorders. *Acta Psychiatr. Scand.* **102**, 321–330 (2000).
23. Canitano, R. Epilepsy in autism spectrum disorders. *Eur. Child Adolesc. Psychiatry* **16**, 61–66 (2007).
24. Rippon, G., Brock, J., Brown, C. & Boucher, J. Disordered connectivity in the autistic brain: challenges for the “new psychophysiology”. *Int. J. Psychophysiol.* **63**, 164–172 (2007).
25. Dani, V. S. *et al.* Reduced cortical activity due to a shift in the balance between excitation and inhibition in a mouse model of Rett syndrome. *Proc. Natl Acad. Sci. USA* **102**, 12560–12565 (2005).
26. Etherton, M. R., Blaiss, C. A., Powell, C. M. & Südhof, T. C. Mouse neuroligin-1 α deletion causes correlated electrophysiological and behavioral changes consistent with cognitive impairments. *Proc. Natl Acad. Sci. USA* **106**, 17998–18003 (2009).
27. Tabuchi, K. *et al.* A neuroligin-3 mutation implicated in autism increases inhibitory synaptic transmission in mice. *Science* **318**, 71–76 (2007).
28. Chao, H. T. *et al.* Dysfunction in GABA signalling mediates autism-like stereotypies and Rett syndrome phenotypes. *Nature* **468**, 263–269 (2010).
29. Moretti, P. *et al.* Learning and memory and synaptic plasticity are impaired in a mouse model of Rett syndrome. *J. Neurosci.* **26**, 319–327 (2006).
30. Rinaldi, T., Perrodin, C. & Markram, H. Hyper-connectivity and hyper-plasticity in the medial prefrontal cortex in the valproic acid animal model of autism. *Front. Neural Circuits* **2**, 4 (2008).
31. Adamantidis, A. R., Zhang, F., Aravanis, A. M., Deisseroth, K. & de Lecea, L. Neural substrates of awakening probed with optogenetic control of hypocretin neurons. *Nature* **450**, 420–424 (2007).
32. Sohal, V. S., Zhang, F., Yizhar, O. & Deisseroth, K. Parvalbumin neurons and gamma rhythms enhance cortical circuit performance. *Nature* **459**, 698–702 (2009).
33. Berndt, A., Yizhar, O., Gunaydin, L. A., Hegemann, P. & Deisseroth, K. Bi-stable neural state switches. *Nature Neurosci.* **12**, 229–234 (2009).
34. Diester, I. *et al.* An optogenetic toolbox designed for primates. *Nature Neurosci.* **14**, 387–397 (2011).
35. Bamann, C., Gueta, R., Kleinlogel, S., Nagel, G. & Bamberg, E. Structural guidance of the photocycle of channelrhodopsin-2 by an interhelical hydrogen bond. *Biochemistry* **49**, 267–278 (2010).
36. Yizhar, O., Fenno, L., Davidson, T. J., Mogri, M. & Deisseroth, K. Optogenetics in neural systems. *Neuron* **71**, 9–34 (2011).
37. Gunaydin, L. A. *et al.* Ultrafast optogenetic control. *Nature Neurosci.* **13**, 387–392 (2010).
38. Wen, L. *et al.* Opto-current-clamp actuation of cortical neurons using a strategically designed channelrhodopsin. *PLoS ONE* **5**, e12893 (2010).
39. Zhang, F. *et al.* Red-shifted optogenetic excitation: a tool for fast neural control derived from *Volvox carter*. *Nature Neurosci.* **11**, 631–633 (2008).
40. Nagel, G. *et al.* Channelrhodopsin-1: a light-gated proton channel in green algae. *Science* **296**, 2395–2398 (2002).
41. Gradinaru, V. *et al.* Targeting and readout strategies for fast optical neural control *in vitro* and *in vivo*. *J. Neurosci.* **27**, 14231–14238 (2007).
42. Lind, S. E. & Bowler, D. M. Episodic memory and episodic future thinking in adults with autism. *J. Abnorm. Psychol.* **119**, 896–905 (2010).
43. D'Argembeau, A., Raffard, S. & Van der Linden, M. Remembering the past and imagining the future in schizophrenia. *J. Abnorm. Psychol.* **117**, 247–251 (2008).
44. Ni, A. M. & Maunsell, J. H. Microstimulation reveals limits in detecting different signals from a local cortical region. *Curr. Biol.* **20**, 824–828 (2010).
45. Moy, S. S. *et al.* Sociability and preference for social novelty in five inbred strains: an approach to assess autistic-like behavior in mice. *Genes Brain Behav.* **3**, 287–302 (2004).
46. Wilson, T. W., Rojas, D. C., Reite, M. L., Teale, P. D. & Rogers, S. J. Children and adolescents with autism exhibit reduced MEG steady-state gamma responses. *Biol. Psychiatry* **62**, 192–197 (2007).
47. Gradinaru, V. *et al.* Molecular and cellular approaches for diversifying and extending optogenetics. *Cell* **141**, 154–165 (2010).
48. Lewis, D. A., Hashimoto, T. & Volk, D. W. Cortical inhibitory neurons and schizophrenia. *Nature Rev. Neurosci.* **6**, 312–324 (2005).
49. Lewis, D. A., Volk, D. W. & Hashimoto, T. Selective alterations in prefrontal cortical GABA neurotransmission in schizophrenia: a novel target for the treatment of working memory dysfunction. *Psychopharmacology (Berl.)* **174**, 143–150 (2004).
50. Lisman, J. E. *et al.* Circuit-based framework for understanding neurotransmitter and risk gene interactions in schizophrenia. *Trends Neurosci.* **31**, 234–242 (2008).

Supplementary Information is linked to the online version of the paper at www.nature.com/nature.

Acknowledgements We thank the K.D., P.H. and J.R.H. laboratories for discussions on the manuscript. We are grateful to S. Pak, Z. Chen and C. Perry for technical assistance. O.Y. is supported by the Human Frontier Science Program. L.E.F. is supported by the Stanford MSTP program. P.H. is supported by the DFG (HE3824/9-1 and 17-1, Cluster of Excellence: Unifying Concepts in Catalysis), and K.D. by NIMH, NIDA, NINDS, the DARPA REPAIR program, CIRM and the Yu, Woo, Snyder and Keck Foundations.

Author Contributions O.Y., M.P., F.S. and C.R. designed and cloned all DNA constructs; O.Y. and L.E.F. contributed to all neuronal electrophysiology and behavioural experiments; T.J.D. designed the CMO implant; I.G. and J.F. contributed to behaviour and histology experiments; D.J.O. and V.S.S. contributed to slice electrophysiology and mutual information analysis; K.S. and R.F. performed spectroscopy experiments; M.P. and F.S. performed HEK cell experiments; P.H. analysed and supervised spectroscopy and HEK cell work; J.T.P. and J.R.H. conducted and analysed, and J.R.H. supervised, thalamic slice experiments. K.D. supervised all aspects of the project and O.Y., L.E.F. and K.D. wrote the manuscript.

Author Information Reprints and permissions information is available at www.nature.com/reprints. The authors declare no competing financial interests. Readers are welcome to comment on the online version of this article at www.nature.com/nature. Correspondence and requests for materials should be addressed to O.Y. (ofer.yizhar@weizmann.ac.il), P.H. (hegemape@rz.hu-berlin.de) or K.D. (deissero@stanford.edu).

BRCA1 tumour suppression occurs via heterochromatin-mediated silencing

Quan Zhu^{1*}, Gerald M. Pao^{1*}, Alexis M. Huynh^{1†}, Hoonkyo Suh^{1†}, Nina Tonnu¹, Petra M. Nederlof², Fred H. Gage¹ & Inder M. Verma¹

Mutations in the tumour suppressor gene *BRCA1* lead to breast and/or ovarian cancer. Here we show that loss of *Brcal* in mice results in transcriptional de-repression of the tandemly repeated satellite DNA. *Brcal* deficiency is accompanied by a reduction of condensed DNA regions in the genome and loss of ubiquitylation of histone H2A at satellite repeats. BRCA1 binds to satellite DNA regions and ubiquitylates H2A *in vivo*. Ectopic expression of H2A fused to ubiquitin reverses the effects of BRCA1 loss, indicating that BRCA1 maintains heterochromatin structure via ubiquitylation of histone H2A. Satellite DNA de-repression was also observed in mouse and human *BRCA1*-deficient breast cancers. Ectopic expression of satellite DNA can phenocopy BRCA1 loss in centrosome amplification, cell-cycle checkpoint defects, DNA damage and genomic instability. We propose that the role of BRCA1 in maintaining global heterochromatin integrity accounts for many of its tumour suppressor functions.

Breast cancer susceptibility gene 1 (*BRCA1*) was identified as a hereditary cancer susceptibility gene that increased¹ the risk for the development of breast and ovarian cancer in *BRCA1* mutation carriers to as high as 95% by age 70 (ref. 2). The *BRCA1* protein contains a RING finger domain in the amino terminus with ubiquitin E3 ligase activity and two BRCT repeats in the carboxy terminus³. *BRCA1* is highly expressed in proliferative cells and its loss leads most prominently to genetic instability and growth arrest. These observations have implicated *BRCA1* in a multitude of disparate cellular functions, including DNA damage repair, cell-cycle checkpoint activation, transcriptional regulation, DNA replication, centrosome function and X-chromosome inactivation, among others⁴. Presently no unifying mechanistic framework exists to tie the reported biochemical activities of *BRCA1* to its tumour suppressor function³.

Heterochromatic centres in *Brcal* knockout cells

High levels of *BRCA1* expression have been found in the embryonic neuroectoderm⁵, the postnatal cerebellum⁶ and the subgranular zone of the dentate gyrus in the adult brain, which are the sites of embryonal and adult neurogenesis, respectively. We initially set out to study the contribution of *Brcal* to neural stem cell (NSC) proliferation through the targeted deletion of *Brcal* in nestin-expressing NSCs (Supplementary Fig. 1a). As expected, the levels of *Brcal* protein and RNA are significantly reduced in the brains of *Brcal* knockout mice (Fig. 1a and Supplementary Fig. 1b). To characterize the mutant brains, we performed microarray analyses and found evidence of altered epigenetic regulation in the absence of *Brcal* as some imprinted genes are deregulated (Supplementary Table 1). Most notably, upregulation of both *Igf2* and *H19* expression has been verified by quantitative reverse transcription polymerase chain reaction (qRT-PCR) experiments using cortical RNA samples (Fig. 2a).

Heterochromatic centres are highly condensed regions of heterochromatin with repetitive tandem DNA that can be visualized by 4',6-diamidino-2-phenylindole (DAPI) staining. In neurons these centres are particularly prominent. We analysed the nuclei of the mutant

brains by DAPI staining and found a marked reduction in the number of heterochromatic foci in cells, especially in the perinuclear region, when compared to control cortices (4.88 foci per cell to 1.99 foci per cell) (Student's *t*-test, $P < 0.0005$) (Fig. 1b). Moreover, the size of the heterochromatic foci appeared to be larger and more diffuse in mutant brains. These observations indicate a defective heterochromatic structure in *Brcal*-deficient cells. To study the nature of this defect, we stained the nuclei of cortical cells for heterochromatin protein 1 (HP1)⁷, a bona fide pericentric heterochromatin-associated protein, and found that HP1 localized to heterochromatic centres. The number of HP1-positive foci in mutant cortices was decreased from 2.86 foci per cell to 2.13 foci per cell (Student's *t*-test, $P < 0.0005$) (Fig. 1c, top row and Supplementary Fig. 1c, left panel). Moreover, immunoblotting of cerebellar samples showed that the protein levels of all three HP1 protein isoforms (HP1 α , HP1 β and HP1 γ) were severely reduced in knockout mice compared to controls (Supplementary Fig. 1d). The repressive histone H1 also displayed aberrant staining and was more diffuse in *Brcal* mutant cortices (Supplementary Fig. 2a). Other previously characterized repressive histones, such as macro H2A1, and heterochromatin markers, such as histone H3 dimethyl Lys9, did not appear to be affected by *Brcal* knockout (Supplementary Fig. 2b). Because we have previously shown that the *BRCA1* protein preferentially monoubiquitylates histone H2A *in vitro* through its N-terminal RING finger⁸, we investigated whether *BRCA1* is involved in heterochromatin formation through histone H2A ubiquitylation. We found that the staining of monoubiquitylated histone H2A, which has recently been implicated in polycomb-mediated silencing⁹, corresponded to the heterochromatic centres described in Fig. 1b and that the staining signal was reduced in *Brcal* mutant brains (Fig. 1c, bottom row and Supplementary Fig. 1c, right panel). We verified the cell-autonomous nature of our observations using cultured embryonic neural progenitor cells (NPCs) *in vitro*. Ten days after neuronal differentiation, the *Brcal*-deficient cells displayed a significant reduction in the number of heterochromatic centres (7.85 foci per cell versus 5.00 foci per cell, Student's *t*-test,

¹Laboratory of Genetics, The Salk Institute for Biological Studies, La Jolla, California 92037, USA. ²Department of Pathology, the Netherlands Cancer Institute, 1066 CX, Amsterdam, The Netherlands. [†]Present addresses: Department of Medicine, Beth Israel Medical Center, Albert Einstein College of Medicine, New York, New York 10461, USA (A.M.H.); Stem Cells and Regenerative Medicine, Lerner Research Institute/Cleveland Clinic, 9500 Euclid Avenue, Cleveland, Ohio 44195, USA (H.S.).

*These authors contributed equally to this work.

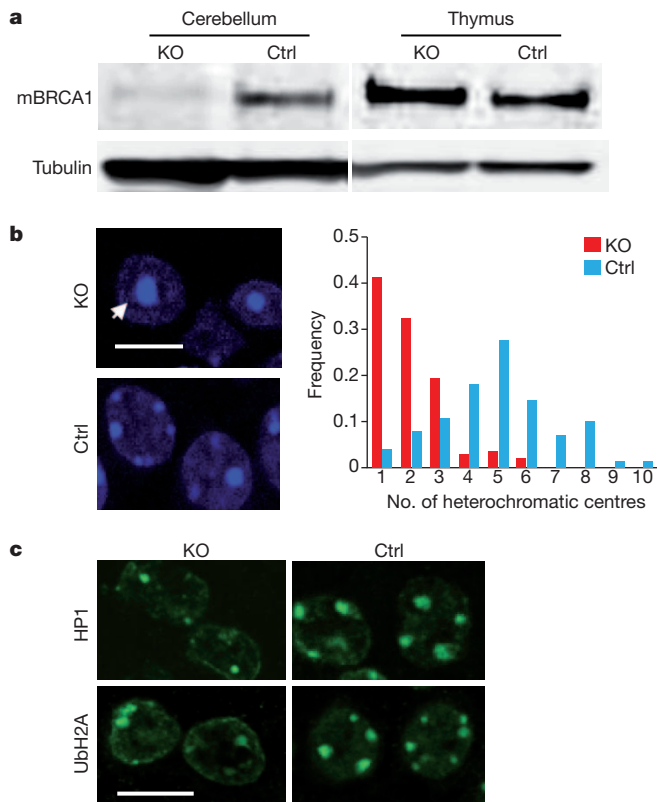


Figure 1 | *Brca1* deficiency impairs heterochromatin structure.

a, Expression of BRCA1 is diminished in the *nestin-Cre Brca1* knockout brains as shown by immunoblotting. KO, samples from a P7 *Brca1* knockout (*Brca1*^{+/−}; *Brca5-13cK*^{+/−}; *nestin-cre*⁺) mouse; Ctrl, samples from a control P7 (*Brca1*^{+/−}; *Brca5-13cK*^{+/−}; *nestin-cre*[−]) mouse. Top panel, BRCA1 immunoblot; lower panel, tubulin loading control. **b**, Lack of BRCA1 induces changes in the nuclear morphology of P7 knockout cortical cells. The numbers of strong DAPI staining nuclear foci per cell were counted and their frequencies plotted (right panel). **c**, Confocal microscopic images of brain sections from *Brca1* conditional knockout and control mice (P7) stained with antibodies against HP1 and ubiquitin–H2A (UbH2A).

$P < 0.0005$) (Supplementary Fig. 2c). Taken together, these data strongly suggest that cells lacking BRCA1 are impaired in the organization of heterochromatin structure.

Heterochromatic silencing disruption

To ascertain that the observed heterochromatic structural deficiencies are of functional importance, we investigated the transcriptional status of known silenced genes. Defects are expected to result in de-repression of normally silenced genes in heterochromatic regions¹⁰. The murine pericentric heterochromatin consists of stretches of highly repetitive DNA elements, including the major and minor satellite repeats, which make up ~3% and ~0.45% of the mouse genome, respectively¹¹. Quantitative RT–PCR experiments showed that the levels of major and minor satellite transcripts were elevated 10.2-fold and 27.3-fold, respectively, in the *Brca1* mutant cortices, indicating a loss of repression in constitutive heterochromatin (Fig. 2a). Other interspersed repetitive elements such as IAP1, SINE1 and the L1 LINE element were largely unaffected. This effect was cell autonomous as it was observed *in vitro* in cultured embryonic NPCs (Supplementary Fig. 3a). The defects in heterochromatic repression in *Brca1*-deficient mouse cells could be reversed by re-expression of human *BRCA1* using a lentiviral vector (Fig. 2b). Heterochromatin repression by BRCA1 is not unique to neural cells because deletion of *Brca1* in fibroblasts from postnatal day 7 (P7) mouse ribcages also showed upregulation of both satellite transcripts (Supplementary Fig. 3b). Because *Brca1* is a tumour suppressor in breast cancer we next generated mice harbouring a

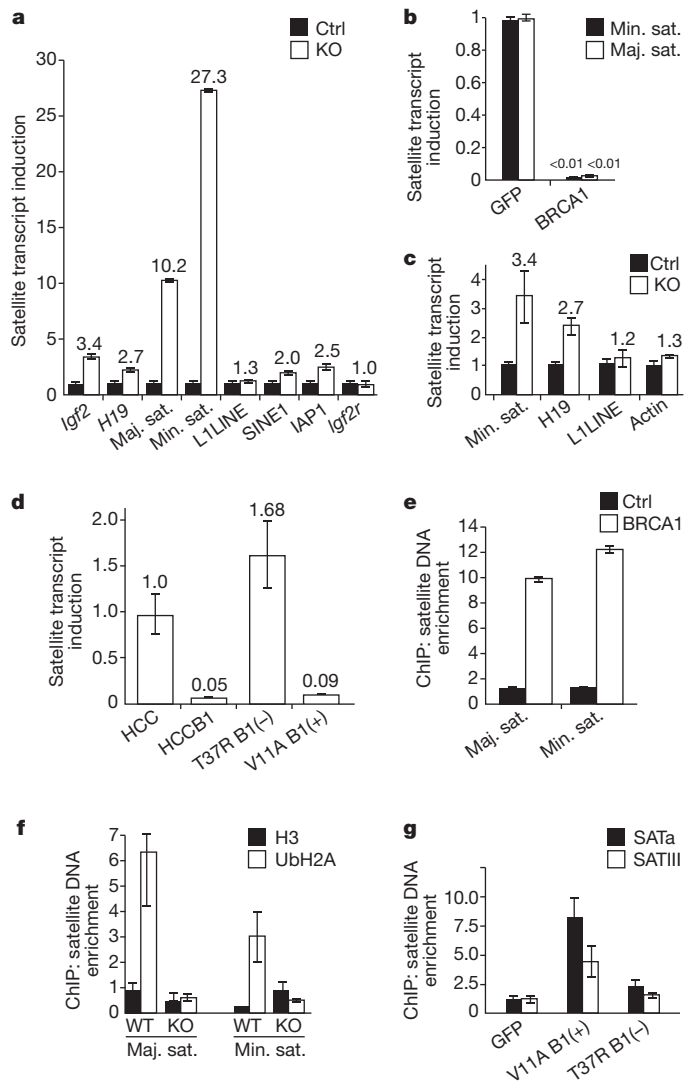


Figure 2 | BRCA1 and its ubiquitin E3 ligase activity are required for gene silencing in constitutive heterochromatin. **a**, Quantitative RT–PCR showing that heterochromatic regions or certain imprinted genes (*Igf2* and *H19* but not *Igf2r*) are upregulated in *Brca1* knockout brains. Internal controls: cyclophilin or 18S RNA. Fold induction (y axis) denotes transcript enrichment over control which is defined as 1. **b**, Rescue of the BRCA1-mediated repression in NPCs by exogenous human BRCA1 but not GFP after infection with retroviral *cre-GFP*. y-axis values are defined where the levels of satellite transcripts in the absence of BRCA1 are defined as 1.0. **c**, Quantitative RT–PCR experiments showing that heterochromatic regions or imprinted genes are upregulated in *Brca1* knockout mammary glands (6-week-old virgin). y axis indicates fold over control levels. **d**, The ubiquitin E3 ligase activity of BRCA1 is required for heterochromatin silencing. HCC1937 cells were reconstituted with either wild-type BRCA1 (HCCB1) or BRCA1 with a mutation in the RING domain (T37R)²³. y axis indicates the fold over endogenous unmodified HCC1937 levels defined as 1.0. **e**, P7 cerebellar ChIP experiments with antibodies against mouse BRCA1 or VSVG protein as a control (e) and ubiquitin–histone H2A or histone H3 protein as a control (f). Enrichment of major (Maj. sat.) and minor (Min. sat.) satellite DNA was measured by quantitative PCR relative to 18S control. y axis denotes fold amplification over wild-type controls. **g**, ChIP experiments were performed using mono-ubiquitylated histone H2A antibody (y axis is expressed in arbitrary units) as in f and HCC1937 cells reconstituted with GFP, BRCA1 (V11A) or a mutant (T37R) (y axis units are expressed in fold enrichment over the control GFP antibody). Error bars are shown as s.d. Each result shown is representative of three independent experiments.

mammary-gland-specific deletion of *Brca1* and analysed the integrity of heterochromatin by qRT–PCR experiments (Fig. 2c). The result demonstrated that lack of *Brca1* in mammary glands from 6-week-old virgin female mice disrupted heterochromatic satellite DNA

silencing as well as imprinted *H19* epigenetic regulation, consistent with our findings in *Brca1* null brains (Fig. 2a).

The silencing of constitutive heterochromatin by BRCA1 is also not limited to mouse cells, as satellite transcripts from human HeLa cells were upregulated upon expression of a short hairpin (sh)RNA targeting *BRCA1* (Supplementary Fig. 4a). Similarly, reconstitution of the human *BRCA1*-deficient cell line HCC1937 with a retrovirus expressing wild-type *BRCA1* repressed the expression of satellite DNA transcripts about 20-fold (Fig. 2d). To determine whether the N-terminal RING domain of BRCA1 is important for the heterochromatic silencing function, we reconstituted HCC1937 cells with either a pathogenic BRCA1 mutant devoid of ubiquitin ligase activity (T37R, known to confer increased cancer risk) or a polymorphic variant (V11A, indistinguishable from wild type). The BRCA1(T37R) mutant failed to repress satellite transcripts whereas the BRCA1(V11A) mutant repressed the satellite transcripts to an extent similar to wild-type BRCA1 (Fig. 2d). The lack of repressive activity was not due to reduced binding of BARD1, the natural heterodimeric partner of BRCA1, as both BRCA1(T37R) and BRCA1(V11A) immunoprecipitated BARD1 similarly (Supplementary Fig. 4b). To verify further the involvement of the E3-ligase activity of BRCA1, we assessed the effects of BARD1 knockdown on satellite DNA transcription, as the heterodimerization between BRCA1 and BARD1 is required for optimal E3 ligase activity^{8,12}. Expression of a shRNA against *BARD1* elevated the satellite DNA transcription in the BRCA1-reconstituted HCC1937 cells but not in the HCC1937 cells where BRCA1 is absent and the satellite repeat transcription is already de-repressed (Supplementary Fig. 4c). These results from cultured human cells are consistent with data obtained from the *Brca1*-deficient mouse brains, fibroblasts and mammary glands in which satellite DNA transcript induction was observed. Moreover, it seems that the ubiquitin E3 ligase activity of BRCA1 is essential for its role in gene silencing in constitutive heterochromatin.

Relationship between BRCA1 and heterochromatin

To gain a mechanistic insight into the role of BRCA1 in maintaining heterochromatin structure, we first investigated whether BRCA1 directly associates with the constitutive heterochromatic region *in vivo*. Chromatin immunoprecipitation (ChIP) experiments showed that BRCA1 was enriched on major and minor satellite DNA (Fig. 2e) in mouse cells and on various alpha satellite sequences in HeLa cells (Supplementary Fig. 4d).

We next tested whether BRCA1 influenced histone ubiquitylation *in vivo*. The results of ChIP experiments showed that ubiquitylated histone H2A was enriched in both major and minor satellite regions when compared with a histone H3 antibody (Fig. 2f). However, this satellite region enrichment was abrogated in the absence of BRCA1, indicating that BRCA1 integrity is essential for the accumulation of ubiquityl-histone H2A at satellite repeats *in vivo*. Our data also show that ubiquityl-histone H2A is enriched at the satellite regions of the mouse genome to a greater extent than at other interspersed repeats such as LINE1 (data not shown), indicative of a distinct heterochromatin. If BRCA1 is indeed the ubiquitin ligase for pericentric heterochromatic histone H2A, it would imply that the integrity of the RING finger is required for the accumulation of ubiquitylated histone H2A at satellite repeats, as we have shown that the same region is critical for transcriptional silencing in heterochromatin (Fig. 2d). To test this hypothesis, ChIP experiments were performed using HCC1937 cells reconstituted with BRCA1(T37R), BRCA1(V11A), or GFP (Fig. 2g). BRCA1(T37R) failed to significantly enrich ubiquitylated histone H2A at satellite regions, in a manner similar to GFP control, whereas the polymorphic BRCA1(V11A) showed enrichment of ubiquitylated histone H2A within the same regions. A distinct mutant, BRCA1(I26A), that has been reported to not destabilize the interaction with BARD1 but has no ubiquitin ligase activity¹³ fails to complement the loss of BRCA1 (Supplementary Fig. 5). The ubiquitin ligase function of BRCA1 seems to be specific, as deletion of *Ring1B* (also called *Rnf2*)

or knockdown of *RNF8* fails to appreciably de-repress satellite transcription (Supplementary Fig. 6). These findings provide further evidence that the ubiquitin ligase activity of BRCA1 is essential for the maintenance of the ubiquityl-histone H2A mark within constitutive heterochromatic regions not only in mouse tissue but also human cells derived from breast cancers.

Ubiquitylated histone H2A rescues BRCA1

To assess the contribution of (mono)ubiquityl-histone H2A to the function of BRCA1 in heterochromatic silencing we generated a lentiviral vector construct expressing an H2A-Ub fusion protein that mimics the natural ubiquityl-histone H2A (Fig. 3a). This was accomplished by fusing a single ubiquitin moiety to the C terminus of histone H2A in lieu of the modification of lysine 119. Subnuclear fractionation of cells expressing this fusion protein shows that the H2A-Ub protein and mutants can be incorporated into cellular chromatin (Supplementary Fig. 7). *BRCA1*-deficient HCC1937 cells were transduced with lentivirus expressing the H2A-Ub fusion protein. Quantification of the levels of satellite DNA transcription showed that H2A-Ub expression can re-establish silencing of the satellite repeats (mcBox, SATa and SATIII) within heterochromatin in *BRCA1*-deficient human cells, indicating that monoubiquityl-H2A is likely to be the main target of BRCA1 ubiquitin E3 ligase that mediates silencing at constitutive heterochromatin (Fig. 3b). Ectopic expression of H2A-Ub (Supplementary Fig. 8) in murine NPCs restored the levels of satellite DNA silencing to more than 90% of endogenous wild-type silencing (Fig. 3c). Mutations within the ubiquitin domain of the fusion protein reduced the ability to restore silencing of the H2A-Ub fusion protein (Supplementary Fig. 9a). H2A-Ub expression in wild-type cells had no significant effect on the transcription of satellite DNA. To investigate whether the ubiquitylation of histone H2A affected previously well-documented BRCA1 functions, we tested if the restored satellite DNA silencing in *Brca1* null cells had any of the expected consequences. It has been reported that primary *Brca1* null cells display a severe growth defect and *p53*-activated apoptosis and that *p53* inactivation largely rescues the growth defect¹⁴. By performing 5-bromodeoxyuridine (BrdU) incorporation assays, we found that ectopic expression of H2A-Ub led to a restoration of over 75% of proliferation in *Brca1*-deficient cells, only slightly lower than a *p53* knockdown (Fig. 3d). Again, in this case expression of H2A-Ub bypassed the requirement for BRCA1. Notably, although *p53* is able to rescue the proliferative defect of *Brca1*-deficient cells, it does not rescue the formation of heterochromatic centres, or the de-repression of satellite transcripts (Supplementary Fig. 10). We also evaluated the ability of H2A-Ub to suppress apoptosis. Staining for an apoptotic marker, active caspase 3, showed a similar result (Fig. 3e) to what was seen for BrdU incorporation or transcriptional silencing. Thus, H2A-Ub can suppress the apoptosis induced by loss of *Brca1*. Taken together, ectopic expression of H2A-Ub not only restored silencing but also rescued the proliferative defect and apoptosis of *Brca1*-deficient cells. This rescue of the proliferative capacity of H2A-Ub is specific for the ubiquitylation modification, as mutations within the ubiquitin domain can abrogate the effect (Supplementary Fig. 9b, c). Homologous recombination, another reported cellular process in which BRCA1 has been implicated, can also be rescued by ectopic H2A-Ub expression in the absence of BRCA1, whereas the same protein with a triple point mutation within the ubiquitin domain is unable to complement (Supplementary Fig. 11). Thus, monoubiquityl-H2A is probably the principal target of BRCA1 for maintaining heterochromatin integrity *in vivo*.

Heterochromatin and BRCA1 tumour suppression

We next investigated the significance of heterochromatin function in BRCA1-mediated tumour suppression. Mouse breast tumours (Fig. 4a) were harvested from animals where BRCA1 was deleted in the mammary gland (also shown in Fig. 2c). Analyses by qRT-PCR

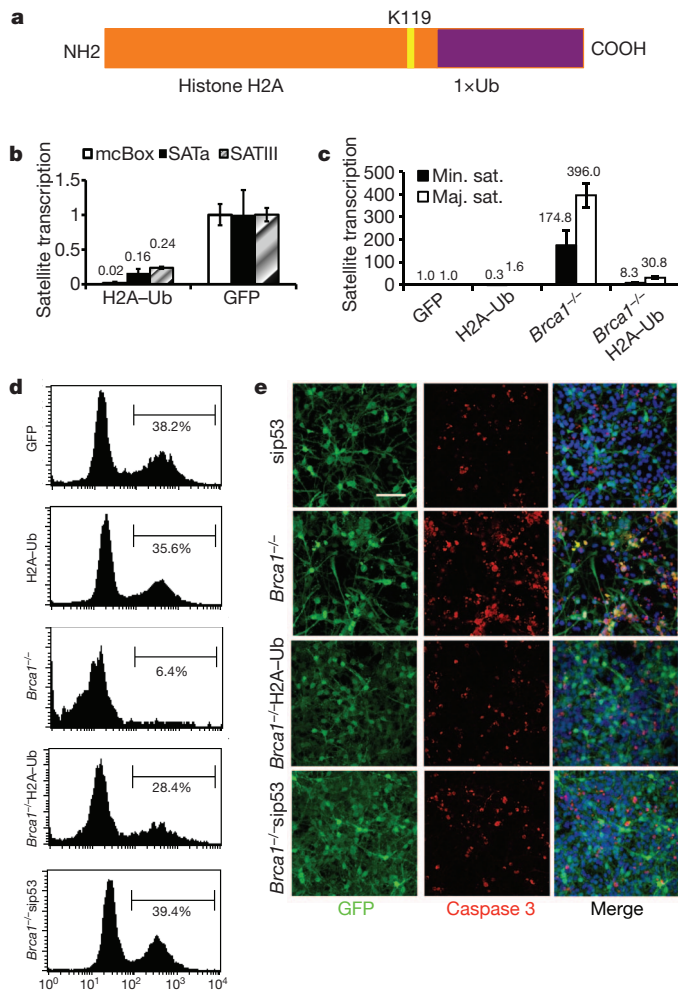


Figure 3 | Ubiquitylated histone H2A is directly involved in BRCA1-mediated heterochromatic silencing. **a**, A diagram showing the artificial ubiquitin–H2A (H2A–Ub) expression vector. **b**, HCC1937 cells were infected with a lentiviral vector expressing ubiquitylated histone H2A mimic fusion protein or GFP as a control and the transcription levels of alpha satellite variants (mcBox, SATa and SATIII) were measured by qRT–PCR. *y* axis denotes satellite RNA levels where 1.0 is the endogenous level of the *BRCA1*-deficient HCC1937 cell line. **c**, Ectopic expression of H2A–Ub re-established heterochromatin silencing in *Brca1* null NPCs. NPCs were infected with GFP alone, H2A–Ub, *cre*-GFP alone and *cre*-GFP co-infected with H2A–Ub. The levels of satellite DNA transcription were measured by qRT–PCR expressed in fold over endogenous background levels, which are defined as 1.0. **d**, NPCs showed increased proliferation upon expression of H2A–Ub in *Brca1* null NPCs. Two days after infection, cells were labelled with BrdU before fixation, immunostaining and FACS analysis. The result shown is representative of three independent experiments. *y* axis denotes cell numbers. sip53, a lentivirus expressing shRNA targeting tumour suppressor *p53*. **e**, NPCs show reduced apoptosis upon expression of H2A–Ub in *Brca1* null NPCs. NPCs were cultured and infected as in **d**. Cells were fixed, immunostained with anti-activated caspase 3 antibody and subjected to confocal imaging. Error bars are shown as s.d. Scale bar: 100 μ m.

showed disrupted satellite DNA silencing in *Brca1*-deficient mouse mammary tumours, but not in tissues where *Brca1* is intact (Fig. 4b). Furthermore, we analysed satellite transcripts in human breast tumours derived from eight individual BRCA1 mutation carriers and found significant de-repression of the expression of alpha satellite repeats: CFXr and SATa (two of human alpha satellite DNA sequences; Fig. 4c). The differences are apparent, even without normalizing for any other factors (for example, the percentage of non-tumour cell contamination), in comparison with a cohort of normal breast biopsies.

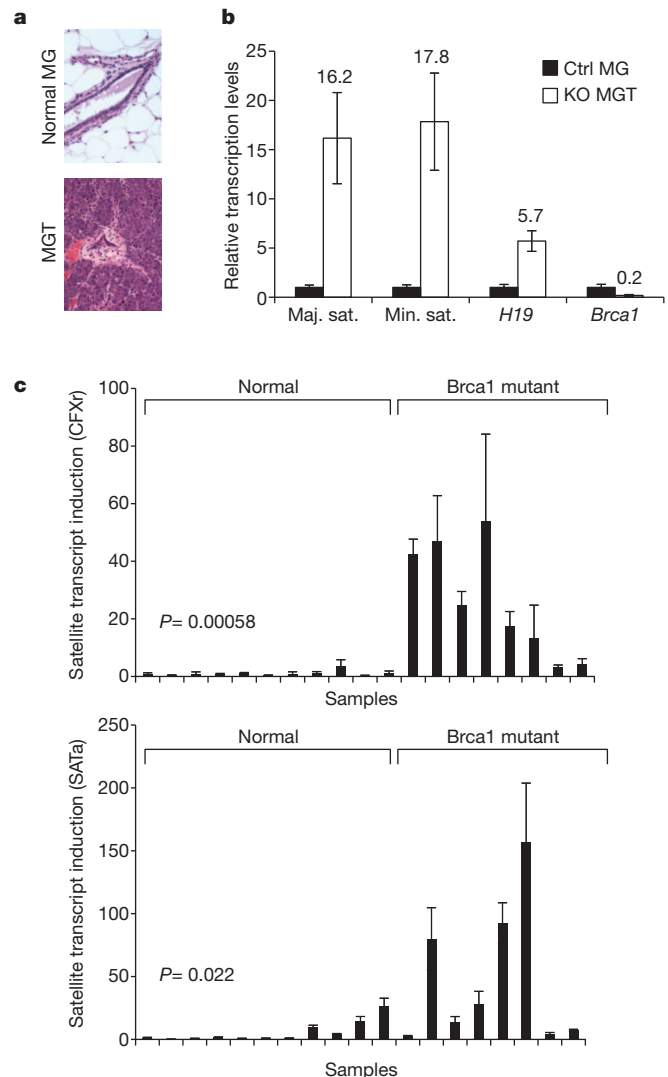


Figure 4 | De-repression of satellite DNA transcription occurs in *Brca1*-deficient breast cancers. **a**, Haematoxylin/eosin staining of *Brca1* knockout mouse breast cancer. Because *Brca1* knockout female mice develop mammary tumours very rarely, these mice were crossed into a *p53* heterozygous background for accelerated tumorigenesis. MG, mammary gland from normal mouse littermates; MGT, mammary tumours from *Brca1* knockout mouse (*Brca1*^{-/-}; *Brca5-13cK*^{+/+}; *MMTV-cre*⁺; *p53*^{+/+}) developed at 6 months. **b**, Quantitative RT–PCR experiments showing that heterochromatic regions and imprinted genes are upregulated in mouse *Brca1* knockout breast cancer in comparison to that of wild-type mammary glands from littermates (internal control 18S RNA). The result shown is an aggregate of five mouse independent sample pairs. **c**, Quantitative RT–PCR experiments showing that the satellite DNA transcripts CFXr and SATa are significantly de-repressed (Student's 2-tailed *t*-test) in human BRCA1 mutant breast tumours (*n* = 8) in comparison with that of normal breast tissues (*n* = 11). *C_t* values of each sample were normalized with *GAPDH*. Error bars indicate s.d.

Satellite-transcript-induced genomic instability

To investigate whether the observed satellite DNA de-repression in mouse and human breast cancers is either an epiphenomenon or of aetiological significance for the genesis of cancer, we ectopically expressed satellite RNA from a transduced lentiviral vector (Fig. 5a) in cultured primary human mammary epithelial cells (HMECs). These cells increased abnormal mitotic figures, including bridged and lagging chromosomes and disorganized metaphases shown by DAPI staining (Fig. 5b and Supplementary Fig. 12). Immunofluorescence staining of pericentrin and tubulin revealed amplified centrosomes, as previously described in *BRCA1* (ref. 15) null cells (Fig. 5c). Cells overexpressing satellite RNA also displayed numerous foci of γ H2AX (Fig. 5d), a

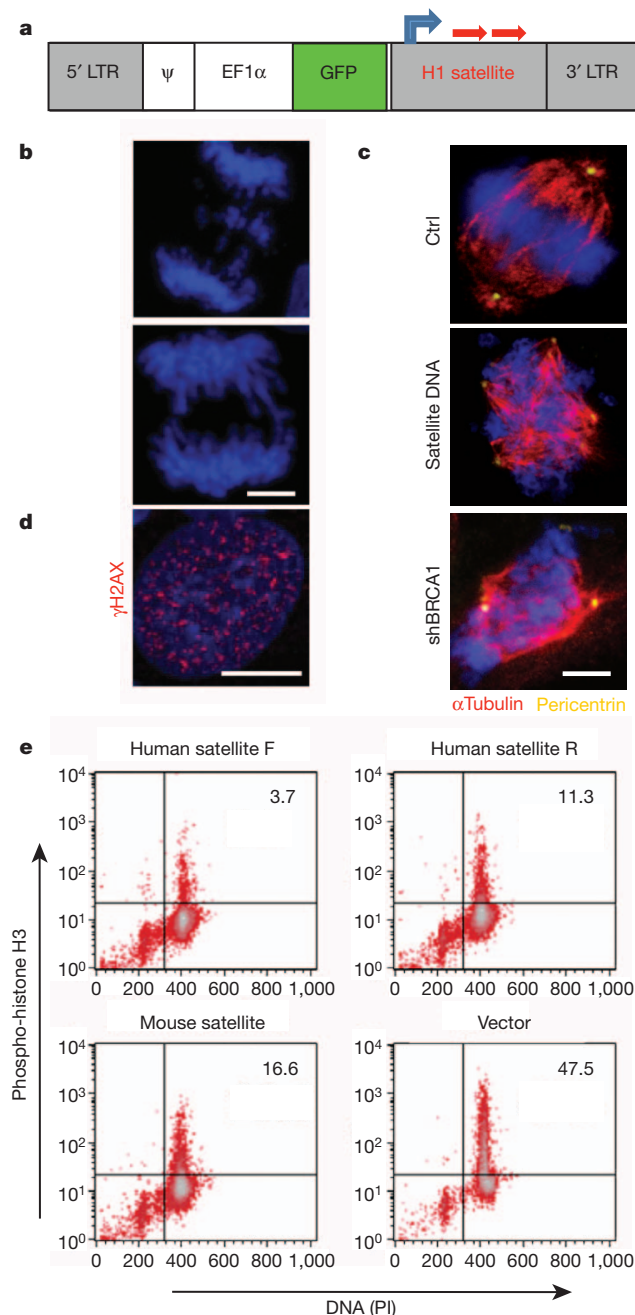


Figure 5 | Ectopic expression of satellite DNA transcripts leads to genomic instability in human mammary epithelial cells. **a**, A diagram of the lentiviral vector expressing the human or mouse satellite DNA sequence (red arrows) under the control of the H1 promoter (blue arrow). **b–d**, Overexpression of satellite RNA induced mitotic catastrophe (**b**), centrosome amplification (**c**) and histone γ H2AX phosphorylation (**d**) in primary HMECs. **e**, Defective mitotic checkpoints induced by satellite DNA overexpression. Forty-eight hours after transduction of a lentivirus expressing human satellite DNA sequence with forward direction (Human satellite F), with reverse direction (Human satellite R), mouse satellite DNA sequence, or an empty vector, U2OS cells were blocked with thymidine, followed by treatment with nocodazole. The cells were stained with phospho-histone H3 antibody and propidium iodide (PI) before flow cytometric analysis. The experiment shown is representative of three independent replicates.

well-established marker of DNA double-strand breaks. This mirrors the phenotype of *BRCA1*-deficient cells. Flow cytometric analyses showed an impaired mitotic spindle checkpoint when cells overexpressing satellite RNA were treated with nocodazole (Fig. 5e), which has also been reported as a *BRCA1* loss phenotype¹⁵. Just as expected,

ectopic expression of satellite RNA was able to recreate a deficiency in homologous recombination similar in magnitude to the knockdown of *BRCA1* (Supplementary Fig. 13). Notably, the cellular defects associated with satellite RNA overexpression are generally considered to be leading causes of genomic instability.

Discussion

Our study shows that *BRCA1* deficiency impairs the integrity of constitutive heterochromatin which leads to the disruption of gene silencing at the tandemly repeated DNA regions, probably through the loss of ubiquitylation of histone H2A. *BRCA1* and *BARD1* preferentially monoubiquitylate H2A at high stoichiometry⁸, which comprises 5–15% of the total cellular nucleosomal histone H2A¹⁶. *BRCA1* accumulates monoubiquitylated histone H2A at satellite DNA regions, which encompass $\sim 3.45\%$ of the mouse genome¹¹ (Fig. 2f), and is itself localized there, as indicated by ChIP experiments (Fig. 2e). The *BRCA1* RING domain is essential for both satellite DNA binding and silencing. *BARD1* is also required for repression of satellite repeats, and loss of *BARD1* is of no consequence if *BRCA1* is already absent (Supplementary Fig. 4c). Although the exact function is not well understood, the emerging notion is that monoubiquitylated histone H2A is most frequently associated with transcriptionally repressive states^{9,17,18}. Other ubiquitin ligases—RING1A/B, of the polycomb repressive complex 1 (PRC1), and RNF8, a DNA repair ligase^{19,20}—ubiquitylate H2A but do not contribute to the silencing of satellite repeats (Supplementary Fig. 6). Similarly, BAP1, a known *BRCA1* binding protein, has been shown to antagonize the polycomb complex by de-ubiquitylating histone H2A^{21,22}. Because a mimic of natural ubiquityl-H2A can rescue the most prominent *BRCA1*-deficiency defects, it suggests that ubiquitylation of histone H2A is probably the primary substrate of *BRCA1* (Fig. 3 and Supplementary Fig. 9).

It is worth noting that overexpression of the satellite transcripts in the presence of wild-type *BRCA1* partially phenocopies *BRCA1* loss (Fig. 5), including centrosome amplification and γ H2AX foci formation. These observations indicate that constitutive heterochromatin formation prevents DNA damage or a DNA damage response. The function of satellite transcripts is largely unknown. However, it has been known that the integrity of centromeric heterochromatin requires an unknown RNA component⁷ that could conceivably be satellite transcripts.

Tumour suppression by *BRCA1* was presumed to occur via homologous recombination³. Recent work showed that cells expressing a mutant *BRCA1* devoid of E3 ligase activity do not exhibit defects in homologous recombination¹³. Thus, the defect in genomic instability in *BRCA1* null cells seems not to require this function, although an intact RING domain is required for recovery from γ -irradiation²³. Nevertheless, mutations that compromise the ubiquitin ligase activity of *BRCA1* are cancer predisposing and constitute hotspots of mutational occurrences in patients²³. Our work shows that satellite DNA repression indeed requires an intact *BRCA1* RING domain, consistent with satellite DNA de-repression observed in *BRCA1* tumours (Fig. 2d). Indeed, satellite transcripts in clinical *BRCA1* patient tumours are upregulated (Fig. 4c). Since satellite transcripts when expressed ectopically can induce centrosome amplification, cell-cycle checkpoint defect and the DNA damage response, it fulfils the criteria to be a main effector of *BRCA1*-mediated tumorigenesis. Although it is presently unclear how these processes are elicited at a mechanistic level, it is tempting to speculate that histone H2A ubiquitylation pathways are involved. Alternatively, the de-repression of satellite DNA might be elicited by some indirect 'global effect' *in trans* that would not require monoubiquitylated histone H2A to be at the de-repressed site. It is conceivable that induction of satellite transcripts could be developed into a marker of loss of heterozygosity for clinical diagnostic application. Recent work has shown that a variety of epithelial cancers overexpress satellite repeats that encompass up to 50% of cellular transcripts²⁴. Although the pathological significance of this finding is

unknown, our work suggests that these satellite transcripts could contribute to the evolution of the cancer cell through the induction of genomic instability (Supplementary Fig. 14).

METHODS SUMMARY

Primary neural progenitor cells were isolated from adult mice containing one *Brca1* null allele and one floxed *Brca1* allele as described²⁵. Embryonic neural progenitors were isolated and cultured as described²⁶. Cultured cells were infected with retroviruses with a MOI of 5 for 12 h and harvested at the time indicated in corresponding figure legends. Cells were harvested with Trizol for RNA extraction. Reverse transcription was carried out using SuperScript III First-strand Synthesis System (Invitrogen). The quantification of PCR products was analysed with SYBR green using ABI PRISM 7900 Sequence Detection system software (Applied Biosystems). Crosslinking and ChIP were performed as a modified version of a protocol described by the Clevers' laboratory²⁷ and Supplementary Information.

Full Methods and any associated references are available in the online version of the paper at www.nature.com/nature.

Received 29 July 2010; accepted 15 July 2011.

- Tutt, A. & Ashworth, A. The relationship between the roles of *BRCA* genes in DNA repair and cancer predisposition. *Trends Mol. Med.* **8**, 571–576 (2002).
- King, M. C., Marks, J. H. & Mandell, J. B. Breast and ovarian cancer risks due to inherited mutations in *BRCA1* and *BRCA2*. *Science* **302**, 643–646 (2003).
- Huen, M. S., Sy, S. M. & Chen, J. *BRCA1* and its toolbox for the maintenance of genome integrity. *Nature Rev. Mol. Cell Biol.* **11**, 138–148 (2010).
- Pageau, G. J., Hall, L. L., Ganesan, S., Livingston, D. M. & Lawrence, J. B. The disappearing Barr body in breast and ovarian cancers. *Nature Rev. Cancer* **7**, 628–633 (2007).
- Lane, T. F. *et al.* Expression of *Brca1* is associated with terminal differentiation of ectodermally and mesodermally derived tissues in mice. *Genes Dev.* **9**, 2712–2722 (1995).
- Korhonen, L., Brannvall, K., Skoglosa, Y. & Lindholm, D. Tumor suppressor gene *BRCA-1* is expressed by embryonic and adult neural stem cells and involved in cell proliferation. *J. Neurosci. Res.* **71**, 769–776 (2003).
- Maison, C. & Almouzni, G. HP1 and the dynamics of heterochromatin maintenance. *Nature Rev. Mol. Cell Biol.* **5**, 296–305 (2004).
- Xia, Y., Pao, G. M., Chen, H. W., Verma, I. M. & Hunter, T. Enhancement of *BRCA1* E3 ubiquitin ligase activity through direct interaction with the BARD1 protein. *J. Biol. Chem.* **278**, 5255–5263 (2003).
- Wang, H. *et al.* Role of histone H2A ubiquitination in Polycomb silencing. *Nature* **431**, 873–878 (2004).
- Meneghini, M. D., Wu, M. & Madhani, H. D. Conserved histone variant H2A.Z protects euchromatin from the ectopic spread of silent heterochromatin. *Cell* **112**, 725–736 (2003).
- Martens, J. H. *et al.* The profile of repeat-associated histone lysine methylation states in the mouse epigenome. *EMBO J.* **24**, 800–812 (2005).
- Hashizume, R. *et al.* The RING heterodimer *BRCA1-BARD1* is a ubiquitin ligase inactivated by a breast cancer-derived mutation. *J. Biol. Chem.* **276**, 14537–14540 (2001).
- Reid, L. J. *et al.* E3 ligase activity of *BRCA1* is not essential for mammalian cell viability or homology-directed repair of double-strand DNA breaks. *Proc. Natl Acad. Sci. USA* **105**, 20876–20881 (2008).
- Xu, X. *et al.* Genetic interactions between tumor suppressors *Brca1* and *p53* in apoptosis, cell cycle and tumorigenesis. *Nature Genet.* **28**, 266–271 (2001).
- Sankaran, S., Starita, L. M., Groen, A. C., Ko, M. J. & Parvin, J. D. Centrosomal microtubule nucleation activity is inhibited by *BRCA1*-dependent ubiquitination. *Mol. Cell. Biol.* **25**, 8656–8668 (2005).
- Matsui, S. I., Seon, B. K. & Sandberg, A. A. Disappearance of a structural chromatin protein A24 in mitosis: implications for molecular basis of chromatin condensation. *Proc. Natl Acad. Sci. USA* **76**, 6386–6390 (1979).
- Kallin, E. M. *et al.* Genome-wide uH2A localization analysis highlights Bmi1-dependent deposition of the mark at repressed genes. *PLoS Genet.* **5**, e1000506 (2009).
- Zhou, W. *et al.* Histone H2A monoubiquitination represses transcription by inhibiting RNA polymerase II transcriptional elongation. *Mol. Cell* **29**, 69–80 (2008).
- Doil, C. *et al.* RNF168 binds and amplifies ubiquitin conjugates on damaged chromosomes to allow accumulation of repair proteins. *Cell* **136**, 435–446 (2009).
- Stewart, G. S. *et al.* The RIDDLE syndrome protein mediates a ubiquitin-dependent signaling cascade at sites of DNA damage. *Cell* **136**, 420–434 (2009).
- Scheuermann, J. C. *et al.* Histone H2A deubiquitinase activity of the Polycomb repressive complex PR-DUB. *Nature* **465**, 243–247 (2010).
- Jensen, D. E. *et al.* BAP1: a novel ubiquitin hydrolase which binds to the *BRCA1* RING finger and enhances *BRCA1*-mediated cell growth suppression. *Oncogene* **16**, 1097–1112 (1998).
- Ruffner, H., Joazeiro, C. A. P., Hemmati, D., Hunter, T. & Verma, I. M. Cancer-predisposing mutations within the RING domain of *BRCA1*: Loss of ubiquitin protein ligase activity and protection from radiation hypersensitivity. *Proc. Natl Acad. Sci. USA* **98**, 5134–5139 (2001).
- Ting, D. T. *et al.* Aberrant overexpression of satellite repeats in pancreatic and other epithelial cancers. *Science* **331**, 593–596 (2011).
- Palmer, T. D., Markakis, E. A., Willhoite, A. R., Safar, F. & Gage, F. H. Fibroblast growth factor-2 activates a latent neurogenic program in neural stem cells from diverse regions of the adult CNS. *J. Neurosci.* **19**, 8487–8497 (1999).
- Nakashima, K. *et al.* Synergistic signaling in fetal brain by STAT3-Smad1 complex bridged by p300. *Science* **284**, 479–482 (1999).
- van Es, J. H. *et al.* Wnt signalling induces maturation of Paneth cells in intestinal crypts. *Nature Cell Biol.* **7**, 381–386 (2005).

Supplementary Information is linked to the online version of the paper at www.nature.com/nature.

Acknowledgements We thank B. Miller for assistance in culturing NPCs; E. Ke for discussion and analysis of Affymetrix data; A. Yanai for the *BRCA1* targeting shRNA construct; C. Lilley for assistance with western blotting; and Z. You for assistance with the LI-COR Odyssey Infrared Imaging System. We thank A. Berns for his sustained interest in this work and providing mutant mice and materials, and M. Vidal for providing mouse embryo fibroblasts containing a conditional deletion allele of *Ring1B*. Q.Z. was supported by the California Breast Cancer Research Program and Ruth L. Kirschstein National Research Service Award. G.M.P. was supported by a fellowship of the California Institute of Regenerative Medicine. H.S. is a recipient of ASPET-Merck fellowship. I.M.V. is an American Cancer Society Professor of Molecular Biology, and holds the Irwin and Joan Jacobs Chair in Exemplary Life Science. This work was supported in part by grants from the NIH, Ipsen/Biomeasure, Sanofi Aventis, and the H.N. and Frances C. Berger Foundation. F.H.G. is supported by NIH NS52842, NS50217 and the Lookout Fund.

Author Contributions Q.Z. generated and Q.Z., N.T. and G.M.P. maintained all the knockout mice. G.M.P. and Q.Z. made the initial heterochromatin observation. Q.Z. and A.M.H. performed confocal microscopy experiments. G.M.P., Q.Z. and N.T. performed ChIP experiments. RNA isolation and microarray experiments were performed by Q.Z., G.M.P. and N.T. Microdissection of murine brains were performed by G.M.P. and A.M.H. under the guidance of F.H.G. G.M.P. designed the H2A–ubiquitin fusion experiments that were performed by Q.Z., G.M.P. and N.T. Satellite RNA experiments were designed by G.M.P. and Q.Z. and performed by Q.Z., G.M.P. and N.T. H.S. established the embryonic neural stem cell isolation and culture. P.M.N. obtained, isolated and curated the clinical patient samples, which were analysed by Q.Z., G.M.P. and N.T. All other experiments were performed by Q.Z., G.M.P. and N.T. All experiments and experimental design was performed under the supervision of I.M.V. G.M.P., Q.Z. and I.M.V. wrote the manuscript.

Author Information Microarray data have been deposited in the GEO database under the accession number GSE6310 (brain *BRCA1* conditional knockout). Reprints and permissions information is available at www.nature.com/reprints. The authors declare no competing financial interests. Readers are welcome to comment on the online version of this article at www.nature.com/nature. Correspondence and requests for materials should be addressed to G.M.P. (pao@salk.edu) or I.M.V. (verma@salk.edu).

METHODS

Immunohistochemical analysis. Immunohistochemical staining was performed as previously described²⁸. Primary antibodies included: goat anti-mouse BRCA1 (1:50, Santa Cruz), goat anti-HP1 (1:100, Santa Cruz), mouse anti-HP1 α (1:200, Millipore), rat anti-HP1 β (1:50, AbD Serotec), mouse anti-HP1 γ (1:200, Millipore), mouse anti-ubiquitin H2A (1:200, Upstate), rabbit anti-dimethyl-histone H3 (Lys 9) (1:100, Upstate), rabbit anti-macro H2A (1:100, Upstate), sheep anti-histone H1 (1:200, Upstate). The mouse tumour tissue histology was performed at the Histology core facility of the Moores Cancer Center of the University of California at San Diego.

Western blotting analysis. Western blotting was performed using 3–8% Tris-acetate or 12% Bis-Tris precast Novex gels (Invitrogen) and XCell Blot Modules (Invitrogen) according to the manufacturer's protocol. The blots were analysed with the LI-COR Odyssey Infrared Imaging System.

Microarray analysis. Brain total RNA was prepared using Trizol reagent (Invitrogen) and processed and hybridized with Affymetrix GeneChip Mouse Genome 430 2.0 Arrays by the Affymetrix Core Facility at the Salk Institute. The gene expression profile was analysed using the Bullfrog software package. Microarray data have been deposited in the GEO database under the accession number GSE6310 (brain BRCA1 conditional knockout).

Cell culture and virus infection. Primary neural progenitor cells were isolated from adult mice containing one *Brca1* null allele and one floxed *Brca1* allele as described²⁵. The cells were cultured in DMEM/F12 (1:1) medium with N2 supplement (Invitrogen), 20 ng ml⁻¹ of human fibroblast growth factor 2 (Peprotech), and 20 ng ml⁻¹ human epidermal growth factor (Peprotech). Embryonic neural progenitors were isolated and cultured as described²⁶. Cultured cells were infected with retroviruses with an MOI of 5 for 12 h and harvested at the time indicated in corresponding figure legends. HCC1937 cells were cultured as described²³. Reconstitution experiments were performed on passage 2 embryonic neural progenitor cells and infected with either retrovirus expressing *cre-GFP* (pCL-CAG-CRE-GFP) or *GFP* (pCL-CAG-GFP) alone. In some experiments an improved lentiviral self-deleting Cre expression vector was used instead (pBOB-CAG-iCRE-SD). Lentiviral human *BRCA1* expressed under the CAG promoter (pBOB-CAG-BRCA1) or the control *GFP* (pBOB-CAG-GFP) was co-infected with the retroviral constructs. Approximately 72 h after infection, cells were harvested with Trizol for RNA extraction. Fibroblasts were isolated from P7 mouse ribcages by digestion with 2 mg ml⁻¹ of pronase (Roche Biochem) for 30 min at 37 °C followed by a 90 min digestion with 3 mg ml⁻¹ of collagenase D (Roche Biochem) in DMEM. Cells were cultured in DMEM 15% FCS with antibiotic/antimycotic and infected with retrovirus as with neural progenitor cells. Cells were left at confluency for 1 week before RNA extraction by Trizol. The ubiquitinated histone mimics were expressed from lentiviral constructs (pBOB-CAG-fHis-H2A-Ub) and the satellite RNAs from a lentiviral construct (p156RRL-EF1a-GFP-U3H1MajSat) for mouse major satellite or p156RRL-EF1a-GFP-U3H1SatA for human alpha satellite.

Quantitative RT-PCR. Reverse transcription was carried out using SuperScript III First-strand Synthesis System (Invitrogen). The quantification of PCR products was analysed with SYBR green using ABI PRISM 7700 Sequence Detection system software (Applied Biosystems).

Tissue preparation. Animals were anaesthetized with ketamine/xylazine and perfused transcardially with 0.9% saline followed by 4% paraformaldehyde in 0.1 M phosphate buffer before brains were dissected out and sectioned either coronally or sagittally on a sliding microtome (40 μ m) or on a cryostat (20 μ m). All animal experiments were performed in the AAALAC certified Salk animal facilities in compliance with an Institutional Animal Care and Use Committee (IACUC) approved protocol to ensure animal welfare.

ChIP experiments. Brains were harvested into DMEM and mechanically minced by pipetting before fixation in DMEM with 1% formaldehyde, 20 mM HEPES pH 7.6, 0.1 M NaCl, 1 mM EDTA, 0.5 mM EGTA at room temperature with rotation. The crosslinking reaction was stopped after 20–25 min by addition of glycine to a final concentration of 0.125 M. Dispersed tissue was subsequently

washed with PBS without calcium or magnesium and with 2 \times complete protease inhibitor cocktail (Roche) followed by a permeabilization wash 20 mM HEPES, 0.25% Triton X-100, 10 mM EDTA, 0.5 mM EGTA, complete protease inhibitor (Roche) and a high salt wash 20 mM HEPES 0.15 M NaCl, 1 mM EDTA, 0.5 mM and complete protease inhibitor. All subsequently used solutions contained 1 \times complete protease inhibitor tablets (Roche). Cells were then re-suspended in ChIP buffer (10 μ M Tris HCl pH 8.0, 0.15% SDS, 1% Triton X-100, 150 mM NaCl, 1 mM EDTA pH 8.0, 0.5 mM EGTA pH 8.0) and sonicated using a cooled Diagenode Bioruptor bath sonicator for 30 min with 1-min pulses and 2-min pauses. Chromatin was then spun at 4 °C for 5 min at 14,000g. The supernatant was then incubated for 2 h with 20 μ l ml⁻¹ of salmon sperm DNA blocked Protein G beads (Upstate biotechnology) before use for ChIP. Chromatin was diluted into a final 1 \times ChIP buffer with 0.5% BSA and 2–5 μ g antibody per 1.0–1.5 ml and incubated overnight at 4 °C. Subsequently 20 μ l of salmon sperm DNA blocked Protein G beads (Upstate Biotechnology) were added for 2–3 h followed by six washes as follows: 2 \times 0.1% SDS, 0.1% DOC, 1% Triton X-100, 150 mM NaCl, 1 mM EDTA pH 8.0, 0.5 mM EGTA pH 8.0, 20 mM TrisHCl pH 8.0, 1 \times 0.1% SDS, 0.1% DOC, 1% Triton X-100, 500 mM NaCl, 1 mM EDTA pH 8.0, 0.5 mM EGTA pH 8.0, 20 mM TrisHCl pH 8.0, 1 \times 0.25 M LiCl, 0.5% DOC, 0.5% NP-40, 1 mM EDTA pH 8.0, 0.5 mM EGTA pH 8.0, 20 mM TrisHCl pH 8.0, 2 \times 1 mM EDTA pH 8.0, 0.5 mM EGTA pH 8.0, 20 mM HEPES pH 8.0. Immune complexes were eluted by 30 min incubation of beads at room temperature in 100 μ l of 1% SDS and 0.1 M NaHCO₃. Eluted samples were then either analysed by qPCR or diluted to 1 \times ChIP buffer to re-precipitate, repeating the above procedure except for eluting in 400 μ l. Samples are then brought to 200 mM NaCl and incubated at 65 °C for 5 h to reverse crosslinks. DNA is then extracted by phenol chloroform extraction and EtOH precipitation with Glycoblue (Invitrogen) glycogen as a carrier. DNA is then re-suspended into 20 μ l of 10 mM Tris HCl pH 8.0 and analysed by qPCR. With HeLa cells, 15 \times 15 cm dishes of confluent HeLa cells were used per experiment. Antibodies used are as follows: anti-mouse BRCA1 (M-20) (Santa Cruz Biotechnology), anti-human BRCA1 (Ab-1) (Calbiochem), anti-HP1 α , clone15.19s2 (Upstate Biotechnology), anti-HP1 γ , clone 42s2 (Upstate Biotechnology), anti-histone H3 06-755, anti-ubiquitin-histone H2A, clone E6C5 (Upstate Biotechnology), anti-dimethyl-histone H3 (Lys9) 07-441, anti-histone H2A (acidic patch) (Upstate Biotechnology). ChIP was quantified by quantitative real time PCR of ChIP samples using genomic rDNA specific reactions as internal normalization. The fold enrichment of particular sequences was compared with a control antibody or H2A antibody alone.

Primer sequences for quantitative PCR. *Brca1* 5'-CCAAACGCTGACTCC CTTAG-3', 5'-CTGCTTCAGCATTTGACTCG-3'; cyclophilin 5'-GGCCG ATGACGAGCCC-3', 5'-TGTCTTTGGAACCTTTGTCTGCAAAAT5'-; *SATa* 5'-AAGGTCAATGGCAGAAAAAGAA-3', 5'-CAACGAAGGCCACAAGAT GTC-3'; *SATIII* 5'-AATCAACCCGAGTGCAATCNGAATGGAATCG-3', 5'-TCCATTCCATTCCTGTACTCGG-3'; *mcBox* 5'-AGGGAATGTCTTCCC ATAAAACT-3', 5'-GTCTACCTTTTATTTGAATCCCCG-3'; *MajSAT* 5'-GGCGAGAAACTGAAATACAG-3', 5'-CTTGCCATATTCACGTCCT-3'; *MinSAT* 5'-TTGGAACGGGATTTGTAGA-3', 5'-CGGTTTCCAACATATG TGT-3'; *Igf2* 5'-GTGGCATCGTGGGAAGAGTGC-3', 5'-GGGGTGGGTAA GGAGAAACC-3'; *H19* 5'-AAGGTGAAGCTGAAAGAACAG-3', 5'-ATG GACGACAGGTGGGTACTG-3'; *18S* 5'-ATGGTAGTCGCCGTGCCTAC-3', 5'-CCGGAATCGAACCCTGATT-3'; *L1 LINE* 5'-TGGCTTGTGCTGTAAG ATCG-3', 5'-TCTGTTGGTGGTCTTTTGTGTC-3'; *SINE1* 5'-GAGCACACCCA TGCACATAC-3', 5'-AAAGGCATGCACCTCTACCAAC-3'; *IAP1* 5'-CGCT CCGGTAGAATACTTAC-3', 5'-TGCCATGCCGCGAGCCTGT-3'; *Igf2R* 5'-CTCTGTGGAACCTTCCCT-3', 5'-CATCCTGGGGAAGTGAAGTA-3' (ref. 29); *Gapdh* 5'-GAAGGTGAAGGTCCGAGT-3', 5'-GAAGATGGTGATG GGATTTC-3 (AbCam website).

28. Lie, D. C. et al. Wnt signalling regulates adult hippocampal neurogenesis. *Nature* **437**, 1370–1375 (2005).

29. Huang, J. et al. Lsh, an epigenetic guardian of repetitive elements. *Nucleic Acids Res.* **32**, 5019–5028 (2004).

An origin of the radio jet in M87 at the location of the central black hole

Kazuhiro Hada^{1,2}, Akihiro Doi^{3,4}, Motoki Kino², Hiroshi Nagai^{2,3}, Yoshiaki Hagiwara^{1,2} & Noriyuki Kawaguchi^{1,2}

Powerful radio jets from active galactic nuclei are thought to be powered by the accretion of material onto the supermassive black hole (the ‘central engine’)^{1,2}. M87 is one of the closest examples of this phenomenon, and the structure of its jet has been probed on a scale of about 100 Schwarzschild radii (R_s , the radius of the event horizon)³. However, the location of the central black hole relative to the jet base (a bright compact radio ‘core’) remains elusive^{4,5}. Observations of other jets indicate that the central engines are located about 10^4 – $10^6 R_s$ upstream from the radio core^{6–9}. Here we report radio observations of M87 at six frequencies that allow us to achieve a positional accuracy of about 20 microarcseconds. As the jet base becomes more transparent at higher frequencies, the multifrequency position measurements of the radio core enable us to determine the upstream end of the jet. The data reveal that the central engine of M87 is located within 14 – $23 R_s$ of the radio core at 43 GHz. This implies that the site of material infall onto the black hole and the eventual origin of the jet reside in the bright compact region seen on the image at 43 GHz.

On 8 and 18 April 2010 we made multifrequency observations of M87 with the Very Long Baseline Array (VLBA) at 2, 5, 8, 15, 22 and 43 GHz quasi-simultaneously. Using the phase-referencing technique, the radio core positions of M87 at each frequency were measured relative to the nearby (separated by 1.5°) reference source M84 (see Supplementary Information for detailed data analysis). When the core at each frequency corresponds to the surface where the optical depth for synchrotron self-absorption becomes unity¹⁰, the position of the radio core moves towards the central engine with increasing frequency (core-shift effect^{11–13}, see also Fig. 1). If we assume that the jet is conical and the central engine is located at the apex of the jet, the separation between the central engine and a core at a given frequency ν satisfies $r_c(\nu) \propto \nu^{-\alpha}$ ($\alpha > 0$). Thus, the location of the central engine can be specified by determining the frequency dependence of the core shift (see Fig. 1 for more details).

In Fig. 2 we show the measured core shift of M87 in right ascension (RA) as a function of ν . Because M84 also has its own core shift, the measured core-position changes on the sky plane are a combination of the core shifts of M87 and M84. Fortunately, M84 has a sufficiently narrow jet structure extended towards the north and the jet is unresolved in the RA direction (see Supplementary Information). This situation enables us to extract the RA contributions of M87’s core shift successfully by minimizing any structural effect of M84 (hereafter we denote the RA contributions of $r_c(\nu)$ as $r_{RA}(\nu)$). It should be stressed that the clear detection of the core shift shown in Fig. 2 explicitly precludes the possibility of a standing shock⁶ in the case of the M87 core; otherwise it would remain stationary with frequency.

The most remarkable finding in Fig. 2 is the strong constraint on the location of the central engine of M87 on a $10 R_s$ scale. The amount of core shift between two adjacent frequencies decreases smoothly with increasing frequency, and the core position converges to the upstream end of the jet, which is supposed to be the location of the central engine. We fit the power-law function to the measured data on core positions

with the weighted least-square method, then we derive the best-fit value as $r_{RA}(\nu) \propto \nu^{-0.94 \pm 0.09}$. The fitted curve approaches the dashed line asymptotically at $41 \pm 12 \mu\text{as}$ eastwards of the 43-GHz core position (errors are 1σ), which is equivalent to the projected separation $6 \pm 2 R_s$ for the black-hole mass $M = 6.0 \times 10^9$ solar masses (ref. 14) at a distance of 16.7 Mpc (ref. 15). The measured frequency dependence of the core shift roughly ν^{-1} is consistent with a ‘conical’ jet with the radial profiles of the magnetic field strength and the electron number density varying as r^{-1} and r^{-2} , respectively¹⁶, with the assumption of a constant jet velocity. With regard to jet shape, a recent theoretical model shows that a jet seems to have a ‘paraboloidal’ shape near a central black hole¹. If this is true of the M87 jet, then the location of the central engine is likely to be even closer to the 43-GHz radio core than the dashed line.

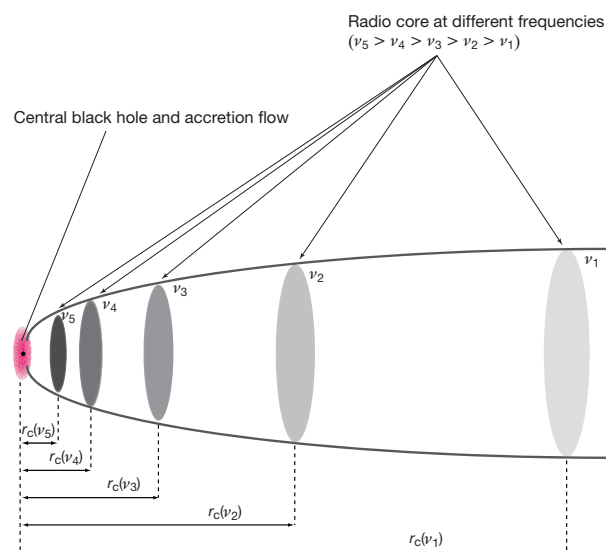


Figure 1 | Schematic diagram explaining the radio core shift of a jet. The diagram illustrates the core shift of a jet generated from the central black hole (a black dot) surrounded by the accretion disk (represented as a red ellipse), with the horizontal axis showing a distance from the black hole (r). The cores of a jet, the bright surfaces of optical depths being unity, are indicated as grey ellipses at the actual radio frequencies of VLBI measurements; darker colours indicate higher frequencies. The cores are located at the apparent origin of the jet in each frequency image. The optical depth τ_{ssa} for the synchrotron self-absorption is a function of the radio-emitting electron number density N_e , the magnetic field strength B and the observing frequency ν . Because N_e and B have a radial profile in the jet, the radial position on the surface at which τ_{ssa} becomes unity shifts as a function of frequency. If we assume that N_e and B have power-law profiles of r described as $N_e \propto r^{-n}$ and $B \propto r^{-m}$ (n and m positive), the frequency dependence of the core position results in $r(\nu) \propto \nu^{-\alpha}$. Here α is the positive power index described as a function of n and m (ref. 10). According to the relation, the cores shift towards the upper stream with increasing frequencies and converge on the location of the central black hole.

¹Department of Astronomical Science, The Graduate University for Advanced Studies (SOKENDAI), 2-21-1 Osawa, Mitaka, Tokyo 181-8588, Japan. ²National Astronomical Observatory of Japan, 2-21-1 Osawa, Mitaka, Tokyo 181-8588, Japan. ³Institute of Space and Astronautical Science, Japan Aerospace Exploration Agency, 3-1-1 Yoshinodai, Chuo, Sagami-hara, Kanagawa 252-5210, Japan. ⁴Department of Space and Astronautical Science, The Graduate University for Advanced Studies (SOKENDAI), 3-1-1 Yoshinodai, Chuo, Sagami-hara, Kanagawa 252-5210, Japan.

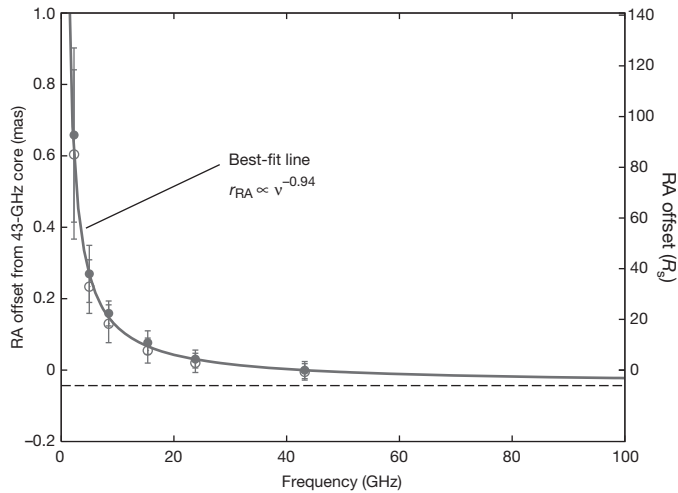


Figure 2 | Plot of the core-shift measurements in right ascension for M87 as a function of observing frequency. The data sets of filled and open circles are results for 8 and 18 April, respectively. Both observations were made at 2.3, 5.0, 8.4, 15.4, 23.8 and 43.2 GHz. The origin of the vertical axis is referenced to the weighted-mean position of the 43.2-GHz core over the two epochs. This plot shows that the measured core positions for the two epochs are consistent within 1σ error bars, indicating that the systematic errors are effectively cancelled out through the quasi-simultaneous multifrequency observations (see also Supplementary Information for details of the data analysis and error estimations). The solid curve represents the best-fit solution, with $r_{\text{RA}}(\nu) = A^{-\alpha} + B$ ($\alpha = 0.94 \pm 0.09$, $A = 1.40 \pm 0.16$ and $B = -0.041 \pm 0.012$), which is derived from the weighted least-square method to the entire data set. The dashed horizontal line represents the asymptotic line of the solid curve, which is located at $41 \mu\text{as}$ eastwards from the 43.2-GHz core in RA. At the distance of M87 of 16.7 Mpc and the mass of the black hole of 6.0×10^9 solar masses, 1 mas corresponds to a length of 0.08 pc or $140R_s$ projected on the plane of the sky.

In Fig. 3 the upstream end of the jet corresponding to the dashed line in Fig. 2 is overlaid on the 43-GHz intensity image as the shaded area. By specifying the position angle of the M87 jet, we can also evaluate the amount of the core shift in declination. On the basis of the 43-GHz image of M87 in previous work that discusses the large direction uncertainty of the inner jet region³, we set the allowed range of the jet position angle

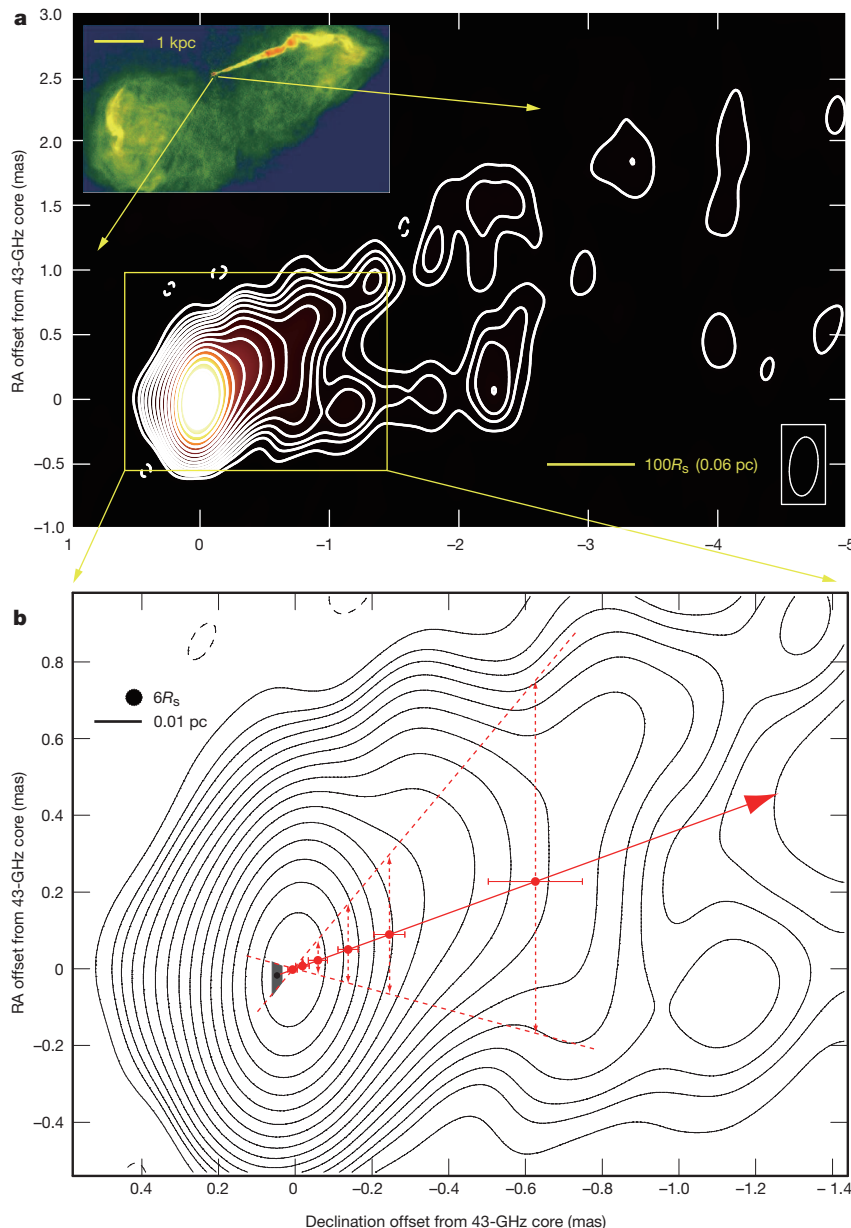


Figure 3 | VLBA image of M87 at 43 GHz superimposed on the measured core-shift positions. **a**, Global view of the radio jet on a subparsec scale. **b**, Close-up view of the region enclosed by the rectangle in **a**. The synthesized beam of the VLBA is $0.22 \text{ mas} \times 0.46 \text{ mas}$ at -5° (bottom right in the upper image). The peak brightness and 1σ noise level are 724 mJy and 1.1 mJy per beam, respectively. Contours are $(-1, 1, 2, 2.8 \text{ and } 4) \times 3.3 \text{ mJy}$ per beam and thereafter increase by factors of $2^{1/2}$. Two broken red lines represent the maximum possible range of the inner jet direction centred on the 43.2-GHz core. A solid red arrow represents the larger-scale jet direction. Red circles indicate the core positions at 2.3, 5.0, 8.4, 15.2, 23.8 and 43.2 GHz relative to the 43.2-GHz core (the higher the frequency of the core, the closer it approaches the central engine). Core positions at each frequency are averaged over two epochs. We assume that the core shift occurs along the larger-scale jet direction. The positional uncertainties in declination are due to uncertainties in the direction of the inner jet, which are shown by the vertical broken arrows threading each core position. The shaded area at the east of the 43.2-GHz core represents the upstream end of the jet derived from the core-shift measurements. This area is enclosed by the 1σ error in the core-shift value in RA, and the direction of the inner jet defines uncertainties in declination. A black circle (top left in **b**) shows the diameter $6R_s$ of the innermost stable orbit around a non-rotating black hole. Inset in **a**, a 15-GHz Very-Long-Baseline Array image showing kiloparsec-scale structure. (Copyright National Radio Astronomy Observatory/Associated Universities, Inc./National Science Foundation).

from 255° to 320° . The shaded area is enclosed by a 1σ error in right ascension and by the possible direction range of the core shift in declination. Our result supports the idea that the faint structure seen on the opposite side of the main jet in previous images of M87 (refs 5, 17) is the counter-jet because it appears on the east side of the black hole's location.

The deprojected separation between the central black hole and the 43-GHz core of M87 can be derived by providing the viewing angle of the jet, which is defined as the angle between the jet axis and our line of sight. The viewing angle of the M87 jet is estimated to be about 15° – 25° (refs 18, 19). The deprojected separation between the black hole and the 43-GHz core is therefore 14 – $23R_s$ (0.007 – 0.01 pc), or shorter if the jet generates with a wider opening angle. The resultant separation is much smaller than those independently estimated for other active-galactic-nuclei jets of BL Lacertae, PKS 1510–089, OJ 287 and 3C 279 on the basis of their multifrequency light curves and spectral properties. All of these sources are categorized as a blazar population, and these observations suggest that the central black holes are on the order of 10^4 – $10^6 R_s$ (equivalent to roughly 0.1 – 10 pc) offset from the emission regions^{6–9,20}.

The significant discrepancy of the black hole's location between M87 and those blazars might be interpreted as a change in appearance of a radio jet resulting from an optical depth structure and a different viewing angle. Recent observations support the idea that a jet is structured not only in the radial direction but also in the transverse direction, being composed of a fast spine flow and a surrounding slow layer²¹. On the basis of this model, the core emission of a blazar whose jet is directed towards our line of sight is dominated by the spine emission propagating down to parsec scales⁶. In contrast, the core of a radio galaxy whose jet axis is offset from the observer originates in a layer, and a spine emission may not reach us because of the relativistic beaming effect. The M87 jet possesses a peculiar component, called HST-1, located at a deprojected distance of at least 120 pc (equivalent to $2 \times 10^5 R_s$) downstream of the core. HST-1 contains subcomponents moving at relativistic speeds^{19,22}, and a large X-ray flare has been reported (ref. 23). These behaviours are reminiscent of blazars^{22,23}, although this interpretation has not yet been confirmed²⁴.

The closeness of the central black hole to the radio core at 43 GHz implies that we start to detect the emission from an accretion flow that is thought to feed matter to the jet in the unresolved resolution element of the 43-GHz radio core. Because the mass accretion rate of M87 is estimated to be much lower than the Eddington rate²⁵, a radiatively inefficient, high-brightness accretion flow (RIAF) is expected for M87 (refs 25, 26). These models suggest the luminosity of the RIAF to be about 10^{21} W Hz^{−1} at 43 GHz with weak parameter dependences, accounting for a small percentage of the observed radio core emission at 43 GHz (3×10^{22} W Hz^{−1}). With increased spatial resolution (less than a few tens of microarcseconds) or higher transparency of the jet base, a next-generation Very Long Baseline Interferometry (VLBI) array using space satellites or at submillimetre wavelengths²⁷ will provide direct imaging of the accretion flow and the jet production site on a scale of the event horizon for M87 (refs 28, 29).

We also stress the importance of synergetic observations with very-high-energy (VHE) γ -rays. The recent detection of an intense VHE γ -ray flare of M87 accompanied by a simultaneous flux increase in the 43-GHz core suggests that the VHE emission originates in the core (ref. 18). Because the variability timescale of the VHE emission is of the order of a few days, causality arguments imply that the size of the VHE emission region is about $10R_s$, a scale that will be accessible by a future VLBI. Simultaneous observations of M87 with future VLBI and VHE γ -ray telescopes will therefore allow us to see a crucial moment of particle acceleration and VHE γ -ray production in the immediate vicinity of the black hole.

Received 31 January; accepted 27 July 2011.

- McKinney, J. C. General relativistic magnetohydrodynamic simulations of the jet formation and large-scale propagation from black hole accretion systems. *Mon. Not. R. Astron. Soc.* **368**, 1561–1582 (2006).

- Blandford, R. D. & Payne, D. G. Hydromagnetic flows from accretion discs and the production of radio jets. *Mon. Not. R. Astron. Soc.* **199**, 883–903 (1982).
- Junor, W., Biretta, J. A. & Livio, M. Formation of the radio jet in M87 at 100 Schwarzschild radii from the central black hole. *Nature* **401**, 891–892 (1999).
- Biretta, J. A., Junor, W. & Livio, M. Evidence for initial jet formation by an accretion disk in the radio galaxy M87. *New Astron. Rev.* **46**, 239–245 (2002).
- Ly, C., Walker, R. C. & Junor, W. High-frequency VLBI imaging of the jet base of M87. *Astrophys. J.* **660**, 200–205 (2007).
- Marscher, A. P. et al. The inner jet of an active galactic nucleus as revealed by a radio-to- γ -ray outburst. *Nature* **452**, 966–969 (2008).
- Marscher, A. P. et al. Probing the inner jet of the quasar PKS 1510–089 with multi-waveband monitoring during strong gamma-ray activity. *Astrophys. J.* **710**, L126–L131 (2010).
- Agudo, I. et al. Location of γ -ray flare emission in the jet of the BL Lacertae object OJ 287 more than 14 pc from the central engine. *Astrophys. J.* **726**, L13–L18 (2011).
- Larionov, V. M. et al. Results of WEBT, VLBA and RXTE monitoring of 3C 279 during 2006–2007. *Astron. Astrophys.* **492**, 389–400 (2008).
- Blandford, R. D. & Königl, A. Relativistic jets as compact radio sources. *Astrophys. J.* **232**, 34–48 (1979).
- Bartel, N., Herring, T. A., Ratner, M. I., Shapiro, I. I. & Corey, B. E. VLBI limits on the proper motion of the 'core' of the superluminal quasar 3C345. *Nature* **319**, 733–738 (1986).
- Lobanov, A. P. Ultracompact jets in active galactic nuclei. *Astron. Astrophys.* **330**, 79–89 (1998).
- O'Sullivan, S. P. & Gabuzda, D. C. Magnetic field strength and spectral distribution of six parsec-scale active galactic nuclei jets. *Mon. Not. R. Astron. Soc.* **400**, 26–42 (2009).
- Gebhardt, K. & Thomas, J. The black hole mass, stellar mass-to-light ratio, and dark halo in M87. *Astrophys. J.* **700**, 1690–1701 (2009).
- Jordán, A. et al. The ACS Virgo cluster survey. X. Half-light radii of globular clusters in early-type galaxies: environmental dependencies and a standard ruler for distance estimation. *Astrophys. J.* **634**, 1002–1019 (2005).
- Königl, A. Relativistic jets as X-ray and gamma-ray sources. *Astrophys. J.* **243**, 700–709 (1981).
- Kovalev, Y. Y., Lister, M. L., Homan, D. C. & Kellermann, K. I. The inner jet of the radio galaxy M87. *Astrophys. J.* **668**, L27–L30 (2007).
- Acciari, V. A. et al. Radio imaging of the very-high-energy γ -ray emission region in the central engine of a radio galaxy. *Science* **325**, 444–448 (2009).
- Biretta, J. A., Sparks, W. B. & Macchetto, F. Hubble Space Telescope observations of superluminal motion in the M87 jet. *Astrophys. J.* **520**, 621–626 (1999).
- Abdo, A. A. et al. A change in the optical polarization associated with a γ -ray flare in the blazar 3C 279. *Nature* **463**, 919–923 (2010).
- Ghisellini, G., Tavecchio, F. & Chiaberge, M. Structured jets in TeV BL Lac objects and radiogalaxies. Implications for the observed properties. *Astron. Astrophys.* **432**, 401–410 (2005).
- Cheung, C. C., Harris, D. E. & Stawarz, Ł. Superluminal radio features in the M87 jet and the site of flaring TeV gamma-ray emission. *Astrophys. J.* **663**, L65–L68 (2007).
- Harris, D. E. et al. in *Extragalactic Jets: Theory and Observation from Radio to Gamma Ray* (ASP Conf. Ser. no. 386) (eds Rector, T. A. & De Young, D. S.) 80–86 (Astronomical Society of the Pacific, 2008).
- Chang, C. S., Ros, E., Kovalev, Y. Y. & Lister, M. L. VLBI detection of the HST-1 feature in the M87 jet at 2 cm. *Astron. Astrophys.* **515**, A38, doi:10.1051/0004-6361/200913915 (2010).
- Di Matteo, T., Allen, S. W., Fabian, A. C., Wilson, A. S. & Young, A. J. Accretion onto the supermassive black hole in M87. *Astrophys. J.* **582**, 133–140 (2003).
- Yuan, F. Possible evidence for the disc origin for the powering of jets in Sgr A* and nearby elliptical galaxies. *Mon. Not. R. Astron. Soc.* **319**, 1178–1184 (2000).
- Doelerman, S. S. et al. Event-horizon-scale structure in the supermassive black hole candidate at the Galactic Centre. *Nature* **455**, 78–80 (2008).
- Broderick, A. E. & Loeb, A. Imaging the black hole silhouette of M87: implications for jet formation and black hole spin. *Astrophys. J.* **697**, 1164–1179 (2009).
- Takahashi, R. & Mineshige, S. Constraining the size of the dark region around the M87 black hole by space-VLBI observations. *Astrophys. J.* **729**, 86–95 (2011).

Supplementary Information is linked to the online version of the paper at www.nature.com/nature.

Acknowledgements We thank M. Honma, H. Sudou and T. Hirota for discussions about the astrometry analysis; and K. Asada, G. Giovannini, M. Giroletti, M. Inoue, S. Kameno, S. Koide, S. Sasaki, L. Stawarz, N. Sugiyama and N. Yoshida for comments. The Very Long Baseline Array is operated by the National Radio Astronomy Observatory, a facility of the National Science Foundation, operated under cooperative agreement by Associated Universities, Inc. This work was supported in part by the Graduate University for Advanced Studies (Sokendai).

Author Contributions K.H., A.D. and H.N. designed and proposed the VLBA observations. K.H. led the work and together with A.D. performed the data analysis. K.H., M.K. and Y.H. jointly wrote the paper. N.K. checked the manuscript. All the authors discussed the results and commented on the manuscript.

Author Information Reprints and permissions information is available at www.nature.com/reprints. The authors declare no competing financial interests. Readers are welcome to comment on the online version of this article at www.nature.com/nature. Correspondence and requests for materials should be addressed to K.H. (kazuhiro.hada@nao.ac.jp).

Three classical Cepheid variable stars in the nuclear bulge of the Milky Way

Noriyuki Matsunaga¹, Takahiro Kawadu², Shogo Nishiyama³, Takahiro Nagayama⁴, Naoto Kobayashi^{1,5}, Motohide Tamura³, Giuseppe Bono^{6,7}, Michael W. Feast^{8,9} & Tetsuya Nagata²

The nuclear bulge is a region with a radius of about 200 parsecs around the centre of the Milky Way¹. It contains stars with ages^{2–4} ranging from a few million years to over a billion years, yet its star-formation history and the triggering process for star formation remain to be resolved. Recently, episodic star formation, powered by changes in the gas content, has been suggested⁵. Classical Cepheid variable stars have pulsation periods that decrease with increasing age⁶, so it is possible to probe the star-formation history on the basis of the distribution of their periods^{7,8}. Here we report the presence of three classical Cepheids in the nuclear bulge with pulsation periods of approximately 20 days, within 40 parsecs (projected distance) of the central black hole. No Cepheids with longer or shorter periods were found. We infer that there was a period about 25 million years ago, and possibly lasting until recently, in which star formation increased relative to the period of 30–70 million years ago.

We conducted a near-infrared survey for the 0.33° by 0.5° area around the Galactic Centre⁹, where no classical Cepheids were known before^{10,11}. Approximately 90 time-series images were collected in each of the *J* (1.25 μ m), *H* (1.63 μ m) and *K_s* (2.14 μ m) wave-passbands during eight years between 2001 and 2008. We discovered 45 variable stars with pulsation periods shorter than 60 days, among which we determined three to be classical Cepheids (Table 1, Fig. 1 and Supplementary Fig. 1) on the basis of their light curves and other observed properties (Supplementary Information). Both their extinctions and distances can be determined⁹ using the period–luminosity relations in the three passbands¹². Their derived distances (Table 1) agree closely with each other. The mean distance is 7.9 kiloparsecs (kpc), with standard error of the mean ± 0.2 kpc, although there remains a systematic error of ± 0.3 kpc, of which the dominant source is an error in the total-to-selective extinction ratio (that is, the coefficient used to convert a colour excess into an extinction). This result from a fundamental distance indicator agrees with the distance to the Galactic Centre derived from orbits round the central black hole¹³ (8.28 ± 0.33 kpc) amongst other estimates^{9,14–16}. We also note that the Cepheids are located close to the plane containing the central black hole ($b = -0.05^\circ$), well within 10 parsec (pc) in projected distance, which is consistent with their being within the thin disk-like structure of the nuclear bulge^{1,5}. These results clearly locate the three objects inside the nuclear bulge.

All of our classical Cepheids have periods close to 20 days. Figure 2 compares their period distribution with that of known Cepheids in a wide region around the Sun¹⁷. Despite the small number of the objects found, the histogram contrasts our targets with the absence of shorter-period Cepheids in the nuclear bulge. Although the older, shorter-period Cepheids are expected to be the fainter ones⁶, our survey would have detected those with periods longer than 5 days if they existed (Supplementary Fig. 2). Our sample shows a concentration in the period range where the proportion of Cepheids is generally small; such a period distribution has not been seen in nearby galaxies¹⁸. The period distribution can be affected by metallicity¹⁸, but the metallicities of young objects in the nuclear bulge have been reported to be approximately solar¹⁹. The 20-day Cepheids have an age of 25 ± 5 million years (Myr), where the error is derived from the standard deviation of the period–age relation⁶. The uncertainty in the metallicity has a smaller effect on the age estimate than the above error⁶. All three Cepheids found in the nuclear bulge are approximately the same age. We discuss the possibility that the two stars projected close to each other might have formed within a cluster, although this is not probable, in the Supplementary Information.

We can estimate the star-formation rate at about 25 Myr ago by assuming an initial mass function²⁰ and the lifetime spent by the Cepheid inside the instability strip²¹. To allow comparison with previous work, we take into account the survey area and the region hidden by extreme interstellar extinction. We find that the star-formation rate was $0.075^{+0.15}_{-0.05}$ solar masses per year in the entire nuclear bulge 20–30 Myr ago. The uncertainty comes from Poisson noise, the uncertainty in the Cepheid lifetime, and the uncertainty in the ratio of the effective survey area to the entire nuclear bulge (Supplementary Information). On the other hand, the absence of shorter-period Cepheids leads to 0.02 solar masses per year as a 1σ upper limit on the star-formation rate for 30–70 Myr ago. The Poisson noise remains the dominant uncertainty in our discussions. We can ignore the uncertainty in the effective area of our survey, a factor of two, when we compare the two star-formation rates. If the star-formation rate remained as high as the value obtained with the 20–30-Myr-old Cepheids, the probability of finding no 30–70-Myr-old Cepheid is low. Thus we conclude that the change in the star-formation rate between 20 and 70 Myr ago is significant at the level of $\sim 2\sigma$, assuming the Poisson statistics.

Table 1 | Catalogue of the classical Cepheids in the nuclear bulge

Star	RA	Dec.	<i>l</i> (deg)	<i>b</i> (deg)	Δ_l (pc)	Δ_b (pc)	<i>J</i> (mag)	<i>H</i> (mag)	<i>K_s</i> (mag)	<i>P</i> (days)	μ_0 (mag)	<i>A_{K_s}</i> (mag)
a	17:46:06.01	–28:46:55.1	+0.1864	–0.0095	+33.9	+6.5	15.63	12.04	10.18	23.54	14.55	2.46
b	17:45:32.27	–29:02:55.2	–0.1054	–0.0433	–6.9	+0.4	15.42	12.00	10.17	19.96	14.49	2.35
c	17:45:30.89	–29:03:10.5	–0.1116	–0.0412	–7.8	+0.7	16.36	12.44	10.35	22.76	14.42	2.74

RA, right ascension; Dec., declination (J2000.0); *l* and *b* are the galactic coordinates; Δ_l and Δ_b are the projected distances of the Cepheids from the central black hole at 8 kpc; *J*, *H* and *K_s* are the mean intensity magnitudes in those wave-passbands. The standard errors for the estimates of the true distance modulus μ_0 and the *K_s*-band foreground extinction *A_{K_s}* are ± 0.13 mag and ± 0.08 mag, respectively (see Supplementary Information).

¹Kiso Observatory, Institute of Astronomy, University of Tokyo, 10762-30 Mitake, Kiso-machi, Kiso-gun, Nagano 397-0101, Japan. ²Department of Astronomy, Kyoto University, Kitashirakawa-Oiwake-cho, Sakyo-ku, Kyoto 606-8502, Japan. ³National Astronomical Observatory of Japan, 2-21-1 Osawa, Mitaka, Tokyo 181-8588, Japan. ⁴Department of Astrophysics, Nagoya University, Furo-cho, Chikusa-ku, Nagoya, Aichi 464-8602, Japan. ⁵Institute of Astronomy, University of Tokyo, 2-21-1 Osawa, Mitaka, Tokyo 181-0015, Japan. ⁶Dipartimento di Fisica, Università di Roma Tor Vergata, Via della Ricerca Scientifica 1, 00133 Rome, Italy. ⁷INAF—Osservatorio Astronomico di Roma, Via Frascati 33, 00040 Monte Porzio Catone, Italy. ⁸Astrophysics, Cosmology and Gravity Centre, Astronomy Department, University of Cape Town, 7701 Rondebosch, South Africa. ⁹South African Astronomical Observatory, PO Box 9, 7935 Observatory, South Africa.

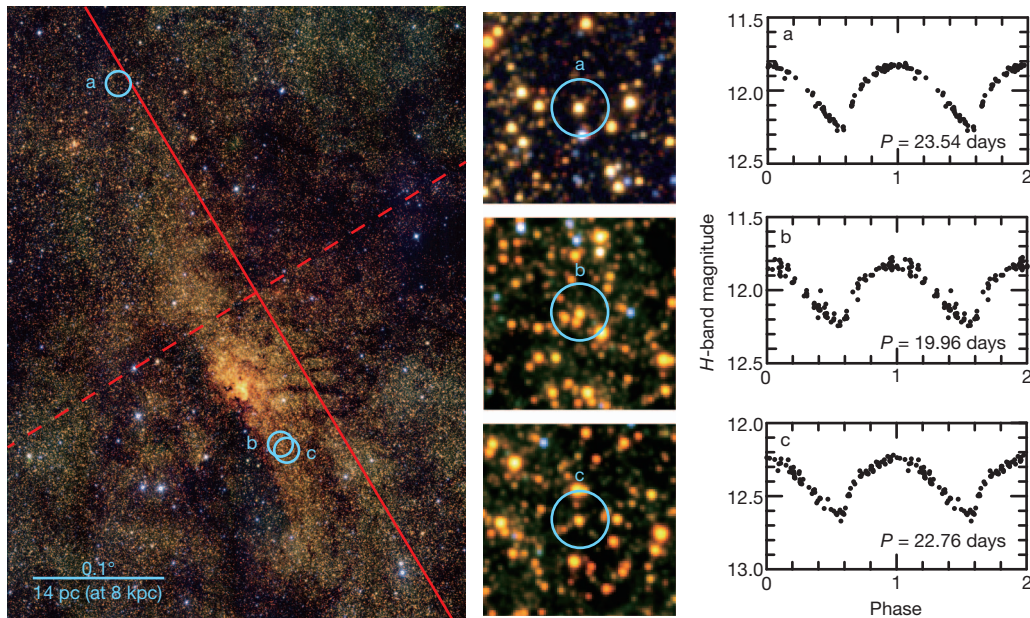


Figure 1 | The classical Cepheids discovered in the Nuclear Bulge. The left panel shows the observed field of 0.33° by 0.5° . This false-colour image is composed of images, a subset of the data we used in analysis, in three passbands: J ($1.25 \mu\text{m}$), H ($1.63 \mu\text{m}$) and K_s ($2.14 \mu\text{m}$). The data were taken with the Infrared Survey Facility (IRSF) 1.4-m telescope and the SIRIUS near-infrared camera located at the South African Astronomical Observatory. North is up and east is left. The Galactic plane (that is, $b = 0^\circ$) is indicated by the solid red line running from the top-left to the bottom-right, while the dashed red line shows the axis of $l = 0^\circ$. An angle of 0.1° corresponds to a scale of 14 pc at the distance of the Galactic nuclear bulge (about 8 kpc), as indicated in the image.

The central black hole is located at the heart of the most crowded region in the chart ($l = -0.056^\circ$, $b = -0.046^\circ$). Our survey field includes two famous clusters: Quintuplet ($l = +0.16^\circ$, $b = -0.06^\circ$) and Arches ($l = +0.12^\circ$, $b = +0.02^\circ$). The three panels in the middle column are close-ups, around the circles labelled a, b and c in the left panel, covering a 40-arcsecond square around each object in Table 1. Again, north is up and east is left. The right panels show the light curves in the H band for the stars labelled a, b and c. The variations of the H -band magnitude are folded according to the periods P indicated, and plotted against the phase. The three light curves, showing a clear resemblance to each other, have the typical variations of classical Cepheids.

A recent investigation suggested that the star-formation rate was low a few tens of millions of years ago and then increased to a peak at about 0.1 Myr ago, followed by a decline in very recent times⁵. However, the tracers used give only a rough timescale for the range 1–100 Myr ago. Our estimates have much higher time resolution for the 20–70-Myr range and indicate an increase in star-formation rate within this period. These results are illustrated in Fig. 3, which also shows a scenario of continuous star formation⁴ (the value of ref. 4 has also been corrected to our scale by taking into account the mass of the entire nuclear bulge, which is $(1.4 \pm 0.6) \times 10^9$ solar masses¹).

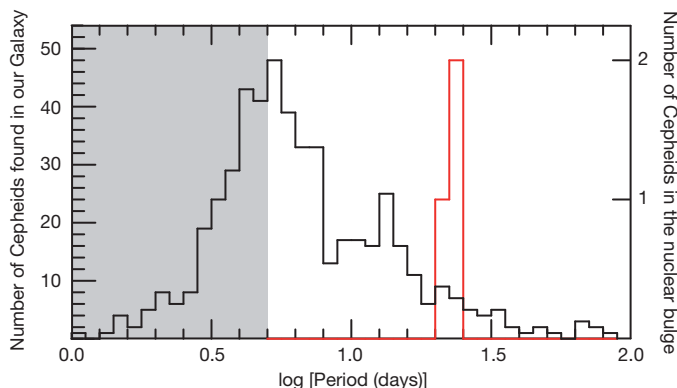


Figure 2 | Period distribution of the nuclear bulge Cepheids and those previously found in the Milky Way. The period distribution of the three Cepheids in the nuclear bulge (red) is compared with that of the previously known Cepheids in the Milky Way¹⁷ (black). The grey region indicates the period range for which our survey could not reach classical Cepheids in the nuclear bulge with typical extinction of $A_{K_s} \approx 3$ mag, even if they were there (see Supplementary Information).

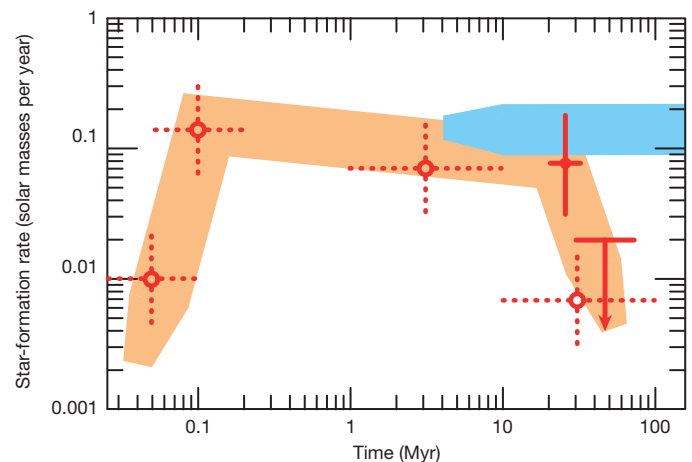


Figure 3 | Star-formation history in the nuclear bulge during the last hundred million years. The star-formation rates we derived are indicated by the point at 25 Myr and the arrow at about 50 Myr. The vertical error bar for the point at 25 Myr corresponds to a factor of 2.5, taking errors like the Poisson noise of the Cepheid number into account. The vertical error bar for the arrow at about 50 Myr indicates the 1σ upper limit. The uncertainty in the correction for our effective survey coverage (a factor of 2) is not included here, in order to illustrate the difference between these estimates, but it should be considered when the star-formation rates are compared with other data below. The horizontal error bars indicate the durations for the corresponding estimates. More details on these error bars are given in the Supplementary Information. The star-formation rates given in ref. 5 are indicated by open circles, and the dashed horizontal bars show the approximate uncertainty in the age for each tracer. The errors of the star-formation rates in ref. 5 were not given, but they cannot be smaller than a factor of two, considering the uncertainty in the age estimate of young stellar objects. The orange stripe indicates our scenario of the episodic star formation, combining our results and those of ref. 5, while the blue stripe indicates the continuous star-formation scenario suggested in ref. 4.

It is of interest to consider, in the context of galactic structure and evolution, how and why such time variations in star formation occurred. Episodic star formation has been suggested in some of the so-called pseudobulges^{22,23}, the central regions of a few barred spiral galaxies, possibly growing with bar-driven gas inflow²⁴. Likewise, our result suggests that episodic star formation on a short timescale of about 25 Myr occurred in the nuclear bulge, which some authors claim to be a pseudobulge²⁵. The timescale is comparable with that of the cyclic gas accumulation predicted for the central part of the Milky Way²⁶.

Received 13 March; accepted 6 July 2011.

Published online 24 August 2011.

- Launhardt, R., Zylka, R. & Mezger, P. G. The nuclear bulge of the Galaxy. III. Large-scale physical characteristics of stars and interstellar matter. *Astron. Astrophys.* **384**, 112–139 (2002).
- Serabyn, E. & Morris, M. Sustained star formation in the central stellar cluster of the Milky Way. *Nature* **382**, 602–604 (1996).
- van Loon, J. Th. *et al.* Infrared stellar populations in the central parts of the Milky Way galaxy. *Mon. Not. R. Astron. Soc.* **338**, 857–879 (2003).
- Figer, D. F., Rich, R. M., Kim, S. S., Morris, M. & Serabyn, E. An extended star formation history for the Galactic Center from Hubble Space Telescope NICMOS observations. *Astrophys. J.* **601**, 319–339 (2004).
- Yusef-Zadeh, F. *et al.* Star formation in the central 400 pc of the Milky Way: Evidence for a population of massive young stellar objects. *Astrophys. J.* **702**, 178–225 (2009).
- Bono, G. *et al.* Classical Cepheid pulsation models. X. The period-age relation. *Astrophys. J.* **621**, 966–977 (2005).
- Alcock, C. *et al.* The MACHO project LMC variable star inventory. VIII. The recent star formation history of the Large Magellanic Cloud from the Cepheid period distribution. *Astron. J.* **117**, 920–926 (1999).
- Meschin, I., Gallart, C., Aparicio, A., Cassisi, S. & Rosenberg, A. Cepheid variable stars in the Pegasus dwarf irregular galaxy: constraints on the star formation history. *Astron. J.* **137**, 3619–3631 (2009).
- Matsunaga, N. *et al.* A near-infrared survey of Miras and the distance to the Galactic Centre. *Mon. Not. R. Astron. Soc.* **399**, 1709–1729 (2009).
- Peeples, M. S., Stanek, K. Z. & DePoy, D. L. A study of stellar photometric variability within the central 4 pc of the Galactic Center with infrared image subtraction. *Acta Astron.* **57**, 173–199 (2007).
- Rafelski, M., Ghez, A. M., Hornstein, S. D., Lu, J. R. & Morris, M. Photometric stellar variability in the Galactic Center. *Astrophys. J.* **659**, 1241–1256 (2007).
- van Leeuwen, F., Feast, M. W., Whitelock, P. A. & Laney, C. D. Cepheid parallaxes and the Hubble constant. *Mon. Not. R. Astron. Soc.* **379**, 723–737 (2007).
- Gillessen, S. *et al.* Monitoring stellar orbits around the massive black hole in the Galactic Center. *Astrophys. J.* **692**, 1075–1109 (2009).
- Nishiyama, S. *et al.* The distance to the Galactic Center derived from infrared photometry of bulge red clump stars. *Astrophys. J.* **647**, 1093–1098 (2006).
- Groenewegen, M. A. T., Udalski, A. & Bono, G. The distance to the Galactic centre based on population II Cepheids and RR Lyrae stars. *Astron. Astrophys.* **481**, 441–448 (2008).
- Trippe, S. *et al.* Kinematics of the old stellar population at the Galactic centre. *Astron. Astrophys.* **492**, 419–439 (2008).
- Fernie, J. D., Evans, N. R., Beattie, B. & Seager, S. A database of Galactic classical Cepheids. *Inform. Bull. Variable Stars* **4148**, 1 (1995).
- Antonello, E., Fugazza, D. & Mantegazza, L. Variable stars in nearby galaxies. VI. Frequency-period distribution of Cepheids in IC 1613 and other galaxies of the Local Group. *Astron. Astrophys.* **388**, 477–482 (2002).
- Davies, B. *et al.* The chemical abundances in the Galactic Center from the atmospheres of red supergiants. *Astrophys. J.* **694**, 46–55 (2009).
- Kroupa, P. On the variation of the initial mass function. *Mon. Not. R. Astron. Soc.* **322**, 231–246 (2001).
- Bono, G. *et al.* Intermediate-mass star models with different helium and metal contents. *Astrophys. J.* **543**, 955–971 (2000).
- Kormendy, J., Cornell, M. E., Block, D. L., Knapen, J. H. & Allard, E. L. Pseudobulges in the disk galaxies NGC 7690 and NGC 4593. *Astrophys. J.* **642**, 765–774 (2006).
- Schinnerer, E., Böker, T., Emsellem, E. & Downes, D. Bar-driven mass build-up within the central 50 pc of NGC 6946. *Astron. Astrophys.* **462**, L27–L30 (2007).
- Kormendy, J. & Kennicutt, R. C. Secular evolution and the formation of pseudobulges in disk galaxies. *Annu. Rev. Astron. Astrophys.* **42**, 603–683 (2004).
- Binney, J. in *The Galaxy Disk in Cosmological Context* (eds Andersen, J., Bland-Hawthorn, J. & Nordström, B.) 145–152 (Proc. IAU Symp. 254, Cambridge Univ. Press, 2009).
- Stark, A. A. *et al.* Gas density, stability, and starbursts near the inner Lindblad resonance of the Milky Way. *Astrophys. J.* **614**, L41–L44 (2004).

Supplementary Information is linked to the online version of the paper at www.nature.com/nature.

Acknowledgements We thank the IRSF/SIRIUS team in Nagoya University, the National Astronomical Observatory of Japan, Kyoto University and the University of Tokyo, and the staff of the South African Astronomical Observatory (SAAO) for their support during our near-IR observations. This work was supported by Grants-in-Aid for Scientific Research from the Japan Society for the Promotion of Science (JSPS). M.W.F. acknowledges the support from National Research Foundation (NRF) of South Africa.

Author Contributions N.M. led the programme, carried out the analysis and wrote most of the text. T.K., S.N. and T. Nagayama as well as N.M. carried out the monitoring observations at the IRSF. S.N., N.K., M.T., G.B., M.W.F. and T. Nagata took part in discussions, especially those on their own research fields such as evolution of galaxies, star formation and stellar pulsation. All authors contributed to the writing of the paper. The figures, including those in the Supplementary Information, were generated by the authors.

Author Information Reprints and permissions information is available at www.nature.com/reprints. The authors declare no competing financial interests. Readers are welcome to comment on the online version of this article at www.nature.com/nature. Correspondence and requests for materials should be addressed to N.M. (matsunaga@ioa.s.u-tokyo.ac.jp).

Magnetic-field-induced charge-stripe order in the high-temperature superconductor $\text{YBa}_2\text{Cu}_3\text{O}_y$

Tao Wu¹, Hadrien Mayaffre¹, Steffen Krämer¹, Mladen Horvatic¹, Claude Berthier¹, W. N. Hardy^{2,3}, Ruixing Liang^{2,3}, D. A. Bonn^{2,3} & Marc-Henri Julien¹

Electronic charges introduced in copper-oxide (CuO_2) planes generate high-transition-temperature (T_c) superconductivity but, under special circumstances, they can also order into filaments called stripes¹. Whether an underlying tendency towards charge order is present in all copper oxides and whether this has any relationship with superconductivity are, however, two highly controversial issues^{2,3}. To uncover underlying electronic order, magnetic fields strong enough to destabilize superconductivity can be used. Such experiments, including quantum oscillations^{4–6} in $\text{YBa}_2\text{Cu}_3\text{O}_y$ (an extremely clean copper oxide in which charge order has not until now been observed) have suggested that superconductivity competes with spin, rather than charge, order^{7–9}. Here we report nuclear magnetic resonance measurements showing that high magnetic fields actually induce charge order, without spin order, in the CuO_2 planes of $\text{YBa}_2\text{Cu}_3\text{O}_y$. The observed static, unidirectional, modulation of the charge density breaks translational symmetry, thus explaining quantum oscillation results, and we argue that it is most probably the same 4a-periodic modulation as in stripe-ordered copper oxides¹. That it develops only when superconductivity fades away and near the same 1/8 hole doping as in $\text{La}_{2-x}\text{Ba}_x\text{CuO}_4$ (ref. 1) suggests that charge order, although visibly pinned by CuO chains in $\text{YBa}_2\text{Cu}_3\text{O}_y$, is an intrinsic propensity of the superconducting planes of high- T_c copper oxides.

The ortho II structure of $\text{YBa}_2\text{Cu}_3\text{O}_{6.54}$ ($p = 0.108$, where p is the hole concentration per planar Cu) leads to two distinct planar Cu NMR sites: Cu2F are those Cu atoms located below oxygen-filled chains, and Cu2E are those below oxygen-empty chains¹⁰. The main discovery of our work is that, on cooling in a field H_0 of 28.5 T along the c axis (that is, in the conditions for which quantum oscillations are resolved; see Supplementary Materials), the Cu2F lines undergo a profound change, whereas the Cu2E lines do not (Fig. 1). To first order, this change can be described as a splitting of Cu2F into two sites having both different hyperfine shifts $K = \langle h_z \rangle / H_0$ (where $\langle h_z \rangle$ is the hyperfine field due to electronic spins) and quadrupole frequencies ν_Q (related to the electric field gradient). Additional effects might be present (Fig. 1), but they are minor in comparison with the observed splitting. Changes in field-dependent and temperature-dependent orbital occupancy (for example $d_{x^2-y^2}$ versus $d_{z^2-r^2}$) without on-site change in electronic density are implausible, and any change in out-of-plane charge density or lattice would affect Cu2E sites as well. Thus, the change in ν_Q can only arise from a differentiation in the charge density between Cu2F sites (or at the oxygen sites bridging them). A change in the asymmetry parameter and/or in the direction of the principal axis of the electric field gradient could also be associated with this charge differentiation, but these are relatively small effects.

The charge differentiation occurs below $T_{\text{charge}} = 50 \pm 10$ K for $p = 0.108$ (Fig. 1 and Supplementary Figs 9 and 10) and 67 ± 5 K for $p = 0.12$ (Supplementary Figs 7 and 8). Within error bars, for each of the samples T_{charge} coincides with T_0 , the temperature at which the Hall constant R_H becomes negative, an indication of the Fermi surface

reconstruction^{11–13}. Thus, whatever the precise profile of the static charge modulation is, the reconstruction must be related to the translational symmetry breaking by the charge ordered state.

The absence of any splitting or broadening of Cu2E lines implies a one-dimensional character of the modulation within the planes and imposes strong constraints on the charge pattern. Actually, only two types of modulation are compatible with a Cu2F splitting (Fig. 2). The first is a commensurate short-range ($2a$ or $4a$ period) modulation running along the (chain) b axis. However, this hypothesis is highly unlikely: to the best of our knowledge, no such modulation has ever been observed in the CuO_2 planes of any copper oxide; it would therefore have to be triggered by a charge modulation pre-existing in the filled chains. A charge-density wave is unlikely because the finite-size chains are at best poorly conducting in the temperature and doping range discussed here^{11,14}. Any inhomogeneous charge distribution such as Friedel oscillations around chain defects would broaden rather than split the lines. Furthermore, we can conclude that charge order occurs only for high fields perpendicular to the planes because the NMR lines neither split at 15 T nor split in a field of 28.5 T parallel to the CuO_2 planes (along either a or b), two situations in which superconductivity remains robust (Fig. 1). This clear competition between charge order and superconductivity is also a strong indication that the charge ordering instability arises from the planes.

The only other pattern compatible with NMR data is an alternation of more and less charged Cu2F rows defining a modulation with a period of four lattice spacings along the a axis (Fig. 2). Strikingly, this corresponds to the (site-centred) charge stripes found in $\text{La}_{2-x}\text{Ba}_x\text{CuO}_4$ at doping levels near $p = x = 0.125$ (ref. 1). Being a proven electronic instability of the planes, which is detrimental to superconductivity², stripe order not only provides a simple explanation of the NMR splitting but also rationalizes the striking effect of the field. Stripe order is also fully consistent with the remarkable similarity of transport data in $\text{YBa}_2\text{Cu}_3\text{O}_y$ and in stripe-ordered copper oxides (particularly the dome-shaped dependence of T_0 around $p = 0.12$)^{11–13}. However, stripes must be parallel from plane to plane in $\text{YBa}_2\text{Cu}_3\text{O}_y$, whereas they are perpendicular in, for example, $\text{La}_{2-x}\text{Ba}_x\text{CuO}_4$. We speculate that this explains why the charge transport along the c axis in $\text{YBa}_2\text{Cu}_3\text{O}_y$ becomes coherent in high fields below T_0 (ref. 15). If so, stripe fluctuations must be involved in the incoherence along c above T_0 .

Once we know the doping dependence of ν_Q (ref. 16), the difference $\Delta\nu_Q = 320 \pm 50$ kHz for $p = 0.108$ implies a charge density variation as small as $\Delta p = 0.03 \pm 0.01$ hole between Cu2Fa and Cu2Fb. A canonical stripe description ($\Delta p = 0.5$ hole) is therefore inadequate at the NMR timescale of $\sim 10^{-5}$ s, at which most (below T_0) or all (above T_0) of the charge differentiation is averaged out by fluctuations faster than 10^5 s^{-1} . This should not be a surprise: the metallic nature of the compound at all fields is incompatible with full charge order, even if this order is restricted to the direction perpendicular to the stripes¹⁷. Actually, there is compelling evidence of stripe fluctuations down to very low temperatures in stripe-ordered copper oxides¹⁸, and indirect

¹Laboratoire National des Champs Magnétiques Intenses, UPR 3228, CNRS-UJF-UPS-INSA, 38042 Grenoble, France. ²Department of Physics and Astronomy, University of British Columbia, Vancouver, British Columbia V6T 1Z1, Canada. ³Canadian Institute for Advanced Research, Toronto, Ontario M5G 1Z8, Canada.

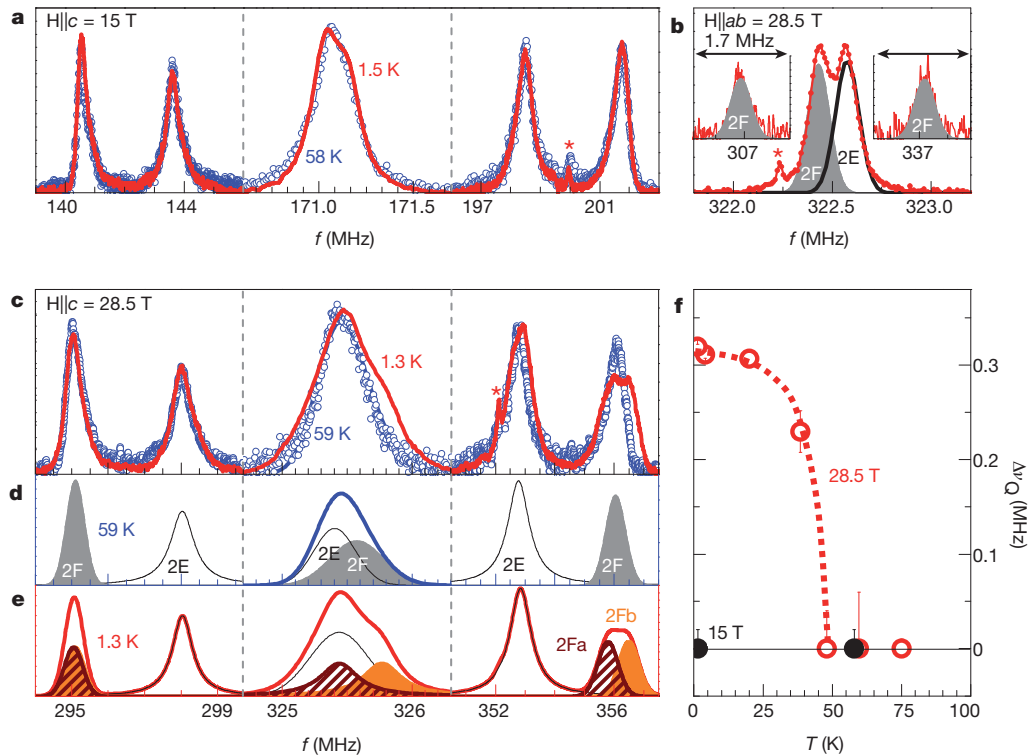


Figure 1 | High-field NMR spectra of $\text{YBa}_2\text{Cu}_3\text{O}_{6.54}$ (ortho II, $p = 0.108$). **a**, $^{63}\text{Cu}(2)$ NMR lines for $H_0 \parallel c$ (15 T) do not show any temperature-induced splitting. A small overall shift has been subtracted for clarity. The slight change in shape of the central line at 1.5 K is due to Cu2F broadening and T_2 shortening, but the Cu2E/Cu2F positions are unchanged with respect to higher temperatures and lower fields. A small background on the central line at 58 K has been subtracted (see Supplementary Information). The difference in ν_Q between Cu2E and Cu2F is due to the presence of empty and filled chains creating different local environments, minute differences in the orbital occupations and, possibly, slightly different charge densities at these sites (this last possibility is as yet unsettled, but this is not directly relevant to the present work because it is field independent up to at least 300 K). **b**, Cu2F lines for $H_0 \parallel ab$ (28.5 T) show no splitting or broadening at 1.5 K. Cu2E satellites are not shown. **c**, ^{63}Cu lines for $H_0 \parallel c$ (28.5 T). **d**, **e**, Decomposition of the spectrum into the different sites above T_{charge} (**d**) and below T_{charge} (**e**). The charge density

modulation below $T_{\text{charge}} \approx 50$ K causes Cu2F to split into Cu2Fa and Cu2Fb (higher-density site for its larger ν_Q value¹⁶). A similar NMR splitting might have been observed in stripe-ordered nickelates³⁰. The parameters are given in Supplementary Table 1. The central line positions are determined from the positions of the satellites, and they are independently confirmed in Supplementary Figs 4 and 5. Asterisks indicate signals from ^{63}Cu in oxygen-empty chains. A subtle bump on the low-frequency side of both Cu2F and Cu2E high-frequency satellites is not understood, but is a minor effect compared with the splitting of the Cu2F site and it could be either intrinsic (weak additional magnetic or charge modulation) or extrinsic (defects in the ordered pattern). **f**, Quadrupolar contribution to the splitting of the high-frequency Cu2F satellite (see Supplementary Fig. 9 for details). Error bars include the statistical error from the fit and the uncertainty on the presence of a splitting at high temperatures.

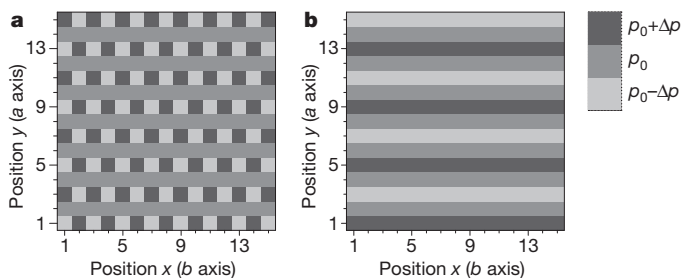


Figure 2 | Charge density modulations compatible with NMR spectra. **a**, $2b$ -periodic charge modulation along the chain (b axis): $p(x,y) = p_0 + p_1 \sin(\pi y/2) \cos(\pi x)$ with $p_0 = 0.108$ being the mean hole content and $\Delta p = 2p_1 = 0.03$ the amplitude of the modulation. Cu2F sites lie at odd positions on the a axis, and Cu2E sites at even positions. A similar $4b$ -period modulation of the form $p(x,y) = p_0 + p_1/2 \sin(\pi y/2) \cos(\pi x/2 + \pi/4)$ is also possible. These two modulations, though consistent with the NMR spectra, are unable to explain the field dependence of the modulation as well as the correlation between our NMR data, transport measurements and ‘1/8 anomalies’. **b**, Stripe order with period $4a$ perpendicular to the chain (b axis): $p(x,y) = p_0 + p_1 \sin(\pi y/2)$. To minimize Coulomb repulsion, the doped holes tend to align below the neutral (filled) chains rather than below the Cu²⁺ (empty) chains, explaining why the higher charge density sites are the Cu2F rather than the 2E sites. Note that, in either case, an additional transverse modulation $p(y) = p_2 \cos(\pi y)$ resulting from the ortho II potential and present at any temperature and field cannot be excluded. In the more complex ortho VIII structure of the $p = 0.12$ sample, it is also possible to obtain the same striped charge pattern with the high density sites only below filled chains.

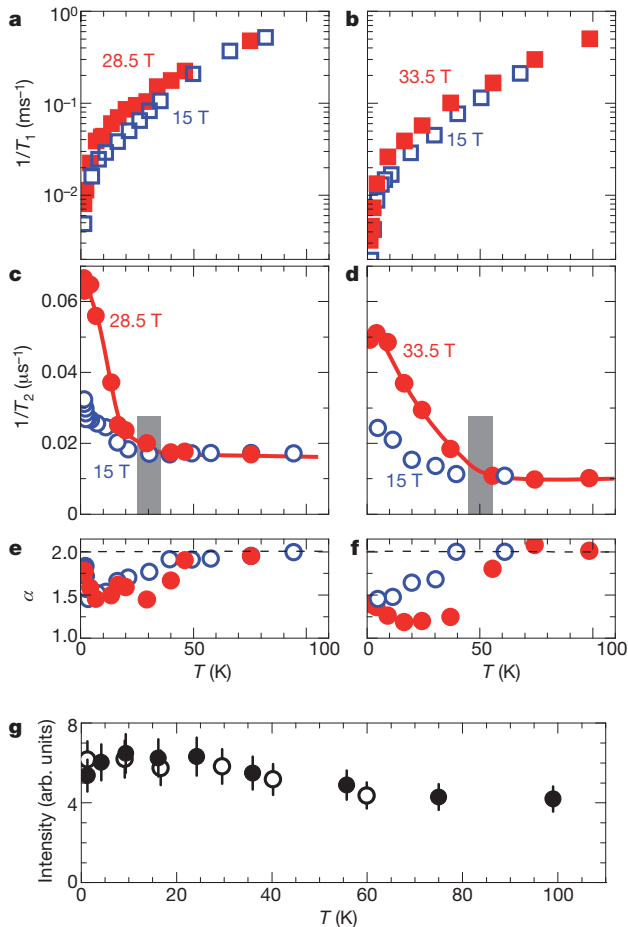


Figure 3 | Slow spin fluctuations instead of spin order. **a, b,** Temperature dependence of the planar ⁶³Cu spin-lattice relaxation rate $1/T_1$ for $p = 0.108$ (**a**) and $p = 0.12$ (**b**). The absence of any peak/enhancement on cooling rules out the occurrence of a magnetic transition. **c, d,** Increase in the ⁶³Cu spin-spin relaxation rate $1/T_2$ on cooling below $\sim T_{\text{charge}}$ obtained from a fit of the spin-echo decay to a stretched form $s(t) \propto \exp(-(t/T_2)^2)$, for $p = 0.108$ (**c**) and $p = 0.12$ (**d**). **e, f,** Stretching exponent α for $p = 0.108$ (**e**) and $p = 0.12$ (**f**). The deviation from $\alpha = 2$ on cooling arises mostly from an intrinsic combination of Gaussian and exponential decays, combined with some spatial distribution of T_2 values (Supplementary Information). The grey areas define the crossover temperature T_{slow} below which slow spin fluctuations cause $1/T_2$ to increase and to become field dependent; note that the change of shape of the spin-echo decay occurs at a slightly higher ($\sim +15$ K) temperature than T_{slow} . T_{slow} is slightly lower than T_{charge} , which is consistent with the slow fluctuations being a consequence of charge-stripe order. The increase of α at the lowest temperatures probably signifies that the condition $\gamma\langle h_z^2 \rangle^{1/2} \tau_c \ll 1$, where τ_c is the correlation time, is no longer fulfilled, so that the associated decay is no longer a pure exponential. We note that the upturn of $1/T_2$ is already present at 15 T, whereas no line splitting is detected at this field. The field therefore affects the spin fluctuations quantitatively but not qualitatively. **g,** Plot of NMR signal intensity (corrected for a temperature factor $1/T$ and for the T_2 decay) against temperature. Open circles, $p = 0.108$ (28.5 T); filled circles, $p = 0.12$ (33.5 T). The absence of any intensity loss at low temperatures also rules out the presence of magnetic order with any significant moment. Error bars represent the added uncertainties in signal analysis, experimental conditions and T_2 measurements. All measurements are with $H \parallel c$.

evidence (explaining the rotational symmetry breaking) over a broad temperature range in YBa₂Cu₃O_y (refs 14, 19–22). Therefore, instead of being a defining property of the ordered state, the small amplitude of the charge differentiation is more likely to be a consequence of stripe order (the smectic phase of an electronic liquid crystal¹⁷) remaining partly fluctuating (that is, nematic).

In stripe copper oxides, charge order at $T = T_{\text{charge}}$ is always accompanied by spin order at $T_{\text{spin}} < T_{\text{charge}}$. Slowing down of the spin

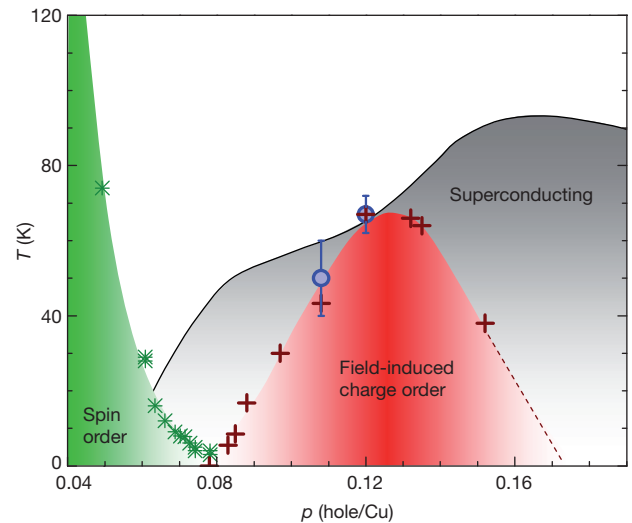


Figure 4 | Phase diagram of underdoped YBa₂Cu₃O_y. The charge ordering temperature T_{charge} (defined as the onset of the Cu2F line splitting; blue open circles) coincides with T_0 (brown plus signs), the temperature at which the Hall constant R_H changes its sign. T_0 is considered as the onset of the Fermi surface reconstruction^{11–13}. The continuous line represents the superconducting transition temperature T_c . The dashed line indicates the speculative nature of the extrapolation of the field-induced charge order. The magnetic transition temperatures (T_{spin}) are from muon-spin-rotation (μ SR) data (green stars)²⁷. T_0 and T_{spin} vanish close to the same critical concentration $p = 0.08$. A scenario of field-induced spin order has been predicted for $p > 0.08$ (ref. 8) by analogy with La_{1.855}Sr_{0.145}CuO₄, for which the non-magnetic ground state switches to antiferromagnetic order in fields greater than a few teslas (ref. 7 and references therein). Our work, however, shows that spin order does not occur up to ~ 30 T. In contrast, the field-induced charge order reported here raises the question of whether a similar field-dependent charge order actually underlies the field dependence of the spin order in La_{2-x}Sr_xCuO₄ and YBa₂Cu₃O_{6.45}. Error bars represent the uncertainty in defining the onset of the NMR line splitting (Fig. 1f and Supplementary Figs 8–10).

fluctuations strongly enhances the spin-lattice ($1/T_1$) and spin-spin ($1/T_2$) relaxation rates between T_{charge} and T_{spin} for ¹³⁹La nuclei. For the more strongly hyperfine-coupled ⁶³Cu, the relaxation rates become so large that the Cu signal is gradually ‘wiped out’ on cooling below T_{charge} (refs 18, 23, 24). In contrast, the ⁶³Cu(2) signal here in YBa₂Cu₃O_y does not experience any intensity loss and $1/T_1$ does not show any peak or enhancement as a function of temperature (Fig. 3). Moreover, the anisotropy of the linewidth (Supplementary Information) indicates that the spins, although staggered, align mostly along the field (that is, c axis) direction, and the typical width of the central lines at base temperature sets an upper magnitude for the static spin polarization as small as $g\langle S_z \rangle \leq 2 \times 10^{-3} \mu_B$ for both samples in fields of ~ 30 T. These consistent observations rule out the presence of magnetic order, in agreement with an earlier suggestion based on the presence of free-electron-like Zeeman splitting⁶.

In stripe-ordered copper oxides, the strong increase of $1/T_2$ on cooling below T_{charge} is accompanied by a crossover of the time decay of the spin-echo from the high-temperature Gaussian form $\exp(-\frac{1}{2}(t/T_{2G})^2)$ to an exponential form $\exp(-t/T_{2E})$ ^{18,23}. A similar crossover occurs here, albeit in a less extreme manner because of the absence of magnetic order: $1/T_2$ sharply increases below T_{charge} and the decay actually becomes a combination of exponential and Gaussian decays (Fig. 3). In Supplementary Information we provide evidence that the typical values of the $1/T_{2E}$ below T_{charge} imply that antiferromagnetic (or ‘spin-density-wave’) fluctuations are slow enough to appear frozen on the timescale of a cyclotron orbit $1/\omega_c \approx 10^{-12}$ s. In principle, such slow fluctuations could reconstruct the Fermi surface, provided that spins are correlated over large enough distances^{25,26} (see also ref. 9). It is unclear whether this condition is fulfilled here. The

fluctuations could also appear frozen on the timescale of an elastic neutron scattering experiment, as in $\text{YBa}_2\text{Cu}_3\text{O}_{6.45}$ ($p \approx 0.08$)^{8,19}. However, there is a fundamental difference between $p = 0.08$ and the $p = 0.108$ – 0.12 samples here, which is not a question of experimental timescale: our NMR data in $\text{YBa}_2\text{Cu}_3\text{O}_{6.45}$ (T. Wu, H. Mayaffre, S. Krämer, M. Horvatić, C. Berthier, C. T. Lin, D. Haug, T. Loew, V. Hinkov, B. Keimer and M.-H. Julien, unpublished observations) are completely different from those reported here, with unequivocal evidence of spin order. Even if we cannot exclude the possibility that a freezing at the NMR timescale occurs at much lower temperatures and/or higher field, spin order seems to be absent over a range of temperatures and fields where charge order and quantum oscillations are observed, indicating that it cannot be an essential ingredient of these two phenomena. Actually, the phase diagram of underdoped $\text{YBa}_2\text{Cu}_3\text{O}_y$ (Fig. 4) even suggests that antiferromagnetic order²⁷ and Fermi surface reconstruction around $p = 0.12$ (refs 4–6, 11–13) are mutually exclusive phenomena. It is tempting to associate the absence of spin order to the remaining stripe fluctuations discussed above.

The implications of our results go beyond the microscopic explanation of quantum oscillation experiments. Although it is the chain structure that manifestly pins stripe order in $\text{YBa}_2\text{Cu}_3\text{O}_y$, the chains should not be taken as being responsible for the whole stripe phenomenon here. First, charge ordering has an onset near T_0 , where the Hall effect changes its sign, and this sign change has been shown to be the same planar '1/8 anomaly' as in stripe-ordered copper oxides^{12,13}. Second, T_0 (ref. 12 and Fig. 4) is a continuous function of hole doping, irrespective of the oxygen ordering sequence. In particular, the highest T_{charge} is found for the ortho VIII structure ($p = 0.12$), which is more complex and of shorter range than ortho II ($p \sim 0.1$). Therefore, neither the presence of chains in $\text{YBa}_2\text{Cu}_3\text{O}_y$ nor the strong disorder typical of La-based stripe copper oxides can be the sole origin of charge stripes in ultra-clean $\text{YBa}_2\text{Cu}_3\text{O}_y$. Stripe correlations originating from the superconducting planes are consistent with the field-tuned competition between charge order and superconductivity revealed here. Our observation of unidirectional charge order in $\text{YBa}_2\text{Cu}_3\text{O}_y$ ($p = 0.11$ – 0.12) thus strengthens the idea that there is an intrinsic and most probably ubiquitous^{28,29} propensity towards charge ordering in high- T_c copper oxides that is most apparent around $p = 1/8$.

Received 2 March; accepted 1 July 2011.

- Tranquada, J. M., Sternlieb, B. J., Axe, J. D., Nakamura, Y. & Uchida, S. Evidence for stripe correlations of spins and holes in copper oxide superconductors. *Nature* **375**, 561–563 (1995).
- Kivelson, S. A. *et al.* How to detect fluctuating stripes in the high-temperature superconductors. *Rev. Mod. Phys.* **75**, 1201–1241 (2003).
- Lee, P. A. From high temperature superconductivity to quantum spin liquid: progress in strong correlation physics. *Rep. Prog. Phys.* **71**, 012501 (2008).
- Doiron-Leyraud, N. *et al.* Quantum oscillations and the Fermi surface in an underdoped high- T_c superconductor. *Nature* **447**, 565–568 (2007).
- Sebastian, S. E., Harrison, N. & Lonzarich, G. G. Quantum oscillations in the high- T_c cuprates. *Phil. Trans. R. Soc. A* **369**, 1687–1711 (2011).
- Ramshaw, B. J. *et al.* Angle dependence of quantum oscillations in $\text{YBa}_2\text{Cu}_3\text{O}_{6.59}$ shows free-spin behaviour of quasiparticles. *Nature Phys.* **7**, 234–238 (2011).
- Chang, J. *et al.* Tuning competing orders in $\text{La}_{2-x}\text{Sr}_x\text{CuO}_4$ cuprate superconductors by the application of an external magnetic field. *Phys. Rev. B* **78**, 104525 (2008).
- Haug, D. *et al.* Magnetic-field-enhanced incommensurate magnetic order in the underdoped high-temperature superconductor $\text{YBa}_2\text{Cu}_3\text{O}_{6.45}$. *Phys. Rev. Lett.* **103**, 017001 (2009).

- Millis, A. J. & Norman, M. Antiphase stripe order as the origin of electron pockets observed in 1/8-hole-doped cuprates. *Phys. Rev. B* **76**, 220503(R) (2007).
- Yamani, Z. *et al.* Cu NMR study of detwinned single crystals of Ortho-II $\text{YBCO}_{6.5}$. *Physica C* **405**, 227–239 (2004).
- LeBoeuf, D. *et al.* Electron pockets in the Fermi surface of hole-doped high- T_c superconductors. *Nature* **450**, 533–536 (2007).
- LeBoeuf, D. *et al.* Lifshitz critical point in the cuprate superconductor $\text{YBa}_2\text{Cu}_3\text{O}_y$ from high-field Hall effect measurements. *Phys. Rev. B* **83**, 054506 (2011).
- Laliberté, F. *et al.* Fermi-surface reconstruction by stripe order in cuprate superconductors. Preprint at (<http://arxiv.org/abs/1102.0984>) (2011).
- Ando, Y. *et al.* Electrical resistivity anisotropy from self-organized one dimensionality in high-temperature superconductors. *Phys. Rev. Lett.* **88**, 137005 (2002).
- Vignolle, B. *et al.* Coherent three-dimensional Fermi surface in an underdoped cuprate superconductor. Preprint at (<http://arxiv.org/abs/1107.5422>) (2011).
- Ofer, R. & Keren, A. Nutation versus angular-dependent NQR spectroscopy and impact of underdoping on charge inhomogeneities in $\text{YBa}_2\text{Cu}_3\text{O}_y$. *Phys. Rev. B* **80**, 224521 (2009).
- Kivelson, S. A., Fradkin, E. & Emery, V. J. Electronic liquid-crystal phases of a doped Mott insulator. *Nature* **393**, 550–553 (1998).
- Hunt, A. W. *et al.* Glassy slowing of stripe modulation in $(\text{La}, \text{Eu}, \text{Nd})_{2-x}(\text{Sr}, \text{Ba})_x\text{CuO}_4$: a ^{63}Cu and ^{139}La NQR study down to 350 mK. *Phys. Rev. B* **64**, 134525 (2001).
- Hinkov, V. *et al.* Electronic liquid crystal state in the high-temperature superconductor $\text{YBa}_2\text{Cu}_3\text{O}_{6.45}$. *Science* **319**, 597–600 (2008).
- Daou, R. *et al.* Broken rotational symmetry in the pseudogap phase of a high- T_c superconductor. *Nature* **463**, 519–522 (2010).
- Sun, K., Lawler, M. J. & Kim, E.-A. Spin-charge interplay in electronic liquid crystals: fluctuating spin stripe driven by charge nematic. *Phys. Rev. Lett.* **104**, 106405 (2010).
- Vojta, M. Tendencies toward nematic order in $\text{YBa}_2\text{Cu}_3\text{O}_{6+\delta}$: uniform distortion vs. incipient charge stripes. *Eur. Phys. J. Spec. Top.* **188**, 49–59 (2010).
- Curro, N. J. *et al.* Inhomogeneous low frequency spin dynamics in $\text{La}_{1.65}\text{Eu}_{0.2}\text{Sr}_{0.15}\text{CuO}_4$. *Phys. Rev. Lett.* **85**, 642–645 (2000).
- Julien, M.-H. *et al.* Glassy spin freezing and NMR wipeout effect in the high- T_c superconductor $\text{La}_{1.90}\text{Sr}_{0.10}\text{CuO}_4$. Critical discussion of the role of stripes. *Phys. Rev. B* **63**, 144508 (2001).
- Harrison, N., McDonald, R. D. & Singleton, J. Cuprate Fermi orbits and Fermi arcs: the effect of short-range antiferromagnetic order. *Phys. Rev. Lett.* **99**, 206406 (2007).
- Sachdev, S., Metlitski, M. A., Qi, Y. & Xu, C. Fluctuating spin density waves in metals. *Phys. Rev. B* **80**, 155129 (2009).
- Coneri, F., Sanna, S., Zheng, K., Lord, J. & De Renzi, R. Magnetic states of lightly hole-doped cuprates in the clean limit as seen via zero-field muon spin spectroscopy. *Phys. Rev. B* **81**, 104507 (2010).
- Lawler, M. J. *et al.* Intra-unit-cell electronic nematicity of the high- T_c copper-oxide pseudogap states. *Nature* **466**, 347–351 (2010).
- Parker, C. V. *et al.* Fluctuating stripes at the onset of the pseudogap in the high- T_c superconductor $\text{Bi}_2\text{Sr}_2\text{CaCu}_2\text{O}_{8+x}$. *Nature* **468**, 677–680 (2010).
- van der Klink, J. J. & Brom, H. B. Relation between susceptibility and Knight shift in $\text{La}_2\text{NiO}_{4.17}$ and K_2NiF_4 by ^{61}Ni NMR. *Phys. Rev. B* **81**, 094419 (2010).

Supplementary Information is linked to the online version of the paper at www.nature.com/nature.

Acknowledgements We thank C. Proust for discussions and help at several stages of this project, and L. Taillefer and S. Kivelson for discussions. We also thank P. Bourges, P. Carretta, S. Chakraverty, W. Chen, P. Hirschfeld, D. LeBoeuf, A. Millis, M. Norman, B. Ramshaw, S. Sachdev, S. Sanna, M. Takigawa and B. Vignolle for communications. This work was supported by the Université Joseph Fourier – Grenoble I (pôle SMI) and Euromagnet II.

Author Contributions W.N.H., R.L. and D.A.B. prepared the samples. T.W., H.M., S.K. and M.-H.J. performed the experiments. S.K. and M.H. developed and operated the high-field NMR facility. H.M. created software for spectrometers and data analysis. T.W. and M.-H.J. analysed the data. C.B. provided conceptual advice and contributed to the planning of the project. M.H.J. wrote the paper and supervised the project. All authors discussed the results and commented on the manuscript.

Author Information Reprints and permissions information is available at www.nature.com/reprints. The authors declare no competing financial interests. Readers are welcome to comment on the online version of this article at www.nature.com/nature. Correspondence and requests for materials should be addressed to M.-H.J. (marc-henri.julien@incm.cnr.fr).

The tungsten isotopic composition of the Earth's mantle before the terminal bombardment

Matthias Willbold¹, Tim Elliott¹ & Stephen Moorbath²

Many precious, 'iron-loving' metals, such as gold, are surprisingly abundant in the accessible parts of the Earth, given the efficiency with which core formation should have removed them to the planet's deep interior¹. One explanation of their over-abundance is a 'late veneer'—a flux of meteorites added to the Earth after core formation as a 'terminal' bombardment that culminated in the cratering of the Moon². Some 3.8 billion-year-old rocks from Isua, Greenland, are derived from sources that retain an isotopic memory of events pre-dating this cataclysmic meteorite shower^{3,4}. These Isua samples thus provide a window on the composition of the Earth before such a late veneer and allow a direct test of its importance in modifying the composition of the planet. Using high-precision (less than 6 parts per million, 2 standard deviations) tungsten isotope analyses of these rocks, here we show that they have a isotopic tungsten ratio $^{182}\text{W}/^{184}\text{W}$ that is significantly higher (about 13 parts per million) than modern terrestrial samples. This finding is in good agreement with the expected influence of a late veneer. We also show that alternative interpretations, such as partial remixing of a deep-mantle reservoir formed in the Hadean eon^{5,6} (more than four billion years ago) or core-mantle interaction⁷, do not explain the W isotope data well. The decrease in mantle $^{182}\text{W}/^{184}\text{W}$ occurs during the Archean eon (about four to three billion years ago), potentially on the same timescale as a notable decrease in $^{142}\text{Nd}/^{144}\text{Nd}$ (refs 3 and 6). We speculate that both observations can be explained if late meteorite bombardment triggered the onset of the current style of mantle convection.

Core formation during accretion of the Earth sequesters elements with a preference for iron-melt over silicate-melt, leaving the accessible, silicate portion of the Earth depleted in these 'siderophile' elements. However, the mantle abundances of the most highly siderophile elements (HSE), which include many of the precious metals, are higher and show less fractionation between one another than would be expected from low-pressure partitioning experiments¹. To account for this puzzle, it has been proposed that the Earth accreted a final amount of primitive meteoritic material after core formation and that this 'late veneer' dominates the mantle budgets of HSE². The bulk of terrestrial accretion and associated core formation occurred within the first 50 million years (Myr) or so of the Solar System's existence and major growth probably terminated with the Moon-forming impact after about 100 Myr (see recent modelling in ref. 8). A late veneer has been related temporally to the 'terminal' meteorite bombardment, the final stages of which are recorded by extensive cratering of the Moon at about 3.9 billion years (Gyr)⁹ (or about 650 Myr from the start of the Solar System) and is also compatible with recent stochastic modelling of planetary growth¹⁰.

Although attractive, the late veneer hypothesis is not without problems (see discussion in ref. 11). The need for a late veneer was originally predicated on relatively low-temperature partitioning experiments¹. However, at the higher temperatures expected of metal-segregation in an early global magma ocean, the magnitude and relative differences in the iron-silicate partition coefficients of HSE are lower.

This conceptual argument has subsequently been shown to have experimental substance, but it still appears that the full range of terrestrial HSE abundances cannot be modelled using high-temperature core segregation alone¹². There also remain difficulties in estimating accurately the HSE abundances of the Earth's mantle¹³, which form the observational basis for the late veneer. A more rigorous assessment of this important model is thus desirable.

Determining the composition of the mantle before and after the terminal bombardment would be a more direct test of the late veneer. The formation ages of Earth's oldest suite of rocks¹⁴ postdate the terminal bombardment¹¹, but these ~3.8-Gyr-old rocks from Isua, Greenland, carry an isotopic record of considerably earlier events^{3,4}. Given a suitable tracer that is sensitive to the addition of meteoritic material but uninfluenced by subsequent processes of crust formation and metamorphism, comparison of the Isua and modern-day rocks can be used to assess the importance of a late veneer. W isotopes provide such a tracer.

The silicate portion of the Earth has an increased $^{182}\text{W}/^{184}\text{W}$ as a result of the radioactive decay of short-lived ^{182}Hf to ^{182}W (half-life 8.9 Myr) after core formation and possibly segregation of an early-enriched reservoir (see below and refs 15 and 16). After the first 50 Myr or so of the Solar System, ^{182}Hf is effectively extinct and any subsequent changes in mantle $^{182}\text{W}/^{184}\text{W}$ ratios can only result from the addition of material derived from an early-formed body that had a different Hf/W. Thus, W isotope ratios are unaffected by later geological processes that may fractionate Hf-W, unlike traditional radiogenic isotope systems with longer-lived parents (for example, ^{147}Sm – ^{143}Nd). W isotope ratios are typically expressed in an $\epsilon^{182}\text{W}$ notation, which reports parts per ten thousand deviations of fractionation-corrected $^{182}\text{W}/^{184}\text{W}$ from a terrestrial standard. Hence, by convention, the Earth's current mantle has $\epsilon^{182}\text{W} = 0$. In contrast, primitive meteorites (chondrites) have $\epsilon^{182}\text{W} \approx -2$ (see ref. 17) and so their addition to the terrestrial mantle can lower its $\epsilon^{182}\text{W}$. As a siderophile element, depleted in the Earth's mantle by core formation, the W budget of the mantle is sensitive to late meteoritic additions. It has been argued that about 0.5% of the Earth's mass¹⁸ was accreted as a late veneer of ordinary chondrites (see ref. 11 for a recent discussion of these constraints) and this is sufficient to decrease the $\epsilon^{182}\text{W}$ of the Earth's mantle by ~0.15 (ref. 10). Detecting such a difference in $\epsilon^{182}\text{W}$ is difficult but possible.

In the Methods we outline our analytical approach, which enables the determination of $\epsilon^{182}\text{W}$ with a precision better than ± 0.05 (2 standard errors, s.e.) and with comparable reproducibility (2 standard deviations, s.d.). Such high-precision measurements require not only careful mass-spectrometry but also efficient purification of W from large samples. We have developed two independent chemical separation techniques, which yield consistent results. Furthermore, we have analysed modern samples that span the same range of matrices as our ancient samples and all return similar $\epsilon^{182}\text{W}$ values, within error of each other and solution standards (Fig. 1 and Table 1).

We have analysed a range of Isua samples, with different lithologies (Table 1); all show increased $\epsilon^{182}\text{W}$ with an average value of 0.18 ± 0.05

¹Bristol Isotope Group, School of Earth Sciences, Wills Memorial Building, Queens Road, University of Bristol, Bristol BS8 1RJ, UK. ²Department of Earth Sciences, South Parks Road, University of Oxford, Oxford OX1 3AN, UK.

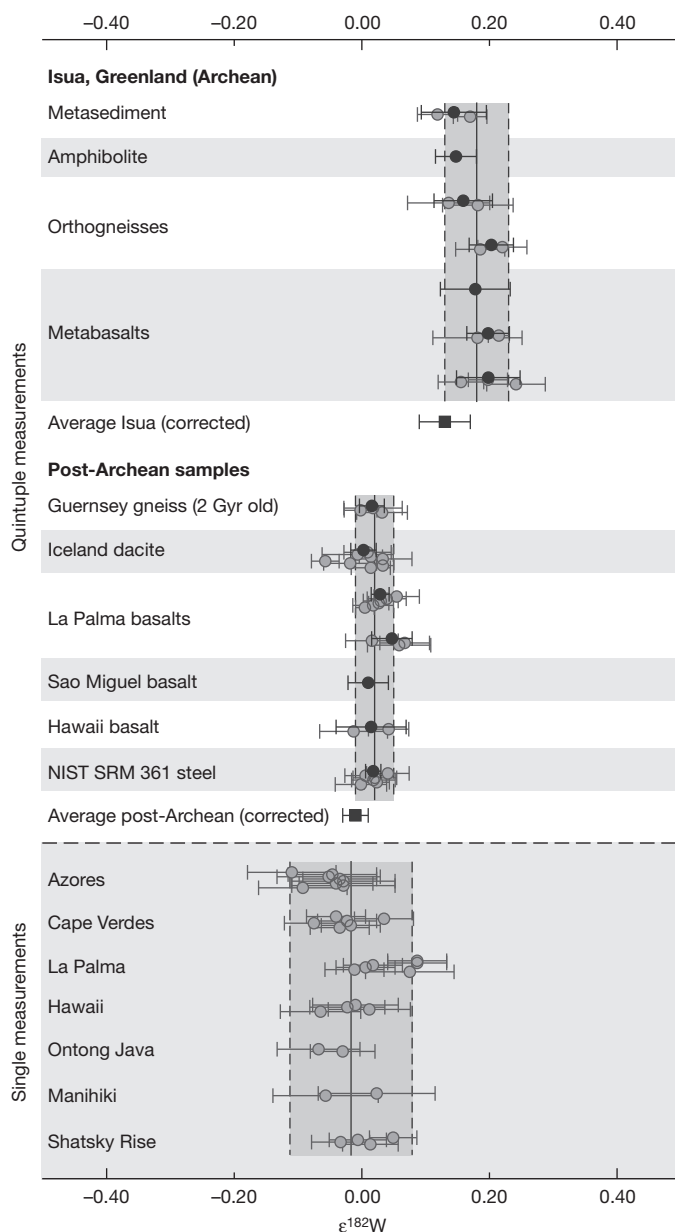


Figure 1 | $\epsilon^{182}\text{W}$ measurements of Isua and post-Archean samples. The upper panel shows results for Isua and post-Archean samples analysed with high-precision, quintuple measurements. Individual quintuple measurements are plotted as grey circles and averaged, repeated quintuple measurements are plotted as black circles (with 2 s.e. uncertainties). The lower panel shows single measurements of recent oceanic basalts thought to be derived from deep mantle plumes. The average for each sample grouping is shown as a solid vertical line (with dashed lines indicating ± 2 s.d.). We note the significant deviation of the $\epsilon^{182}\text{W}$ Isua samples from zero. Also shown are average values (squares) for Isua and post-Archean samples corrected for minor non-zero $\epsilon^{183}\text{W}$ in some samples (see text and Supplementary Information).

(2 s.d.; Fig. 1). A minor correction to account for marginally non-zero $\epsilon^{183}\text{W}$ in some samples (Table 1) suggests that $\epsilon^{182}\text{W} = 0.13 \pm 0.04$ (2 s.d.) is a more accurate average for the Isua samples (see Supplementary Information), which is within error of the face-value analyses and is still clearly resolved from zero. Our high-precision measurements thus highlight a secular change in terrestrial $\epsilon^{182}\text{W}$ that was not resolved by two recent but less precise W isotope studies of similar samples^{15,16}. Some earlier analyses of Isua metasediments¹⁹ yielded negative $\epsilon^{182}\text{W}$ and this was argued to reflect a direct contribution from meteorite impact debris. However, these metasediments have subsequently been shown to have terrestrial Cr isotopic

Table 1 | High-precision, quintuple $\epsilon^{182}\text{W}$ measurements

Sample	$\epsilon^{182}\text{W}$	± 2 s.e.	$\epsilon^{183}\text{W}$	± 2 s.e.	$\epsilon^{142}\text{Nd}$	± 2 s.e.
Isua (Archean)						
Orthogneisses						
155768 ($n = 2$)	0.20	0.03	-0.08	0.04	0.08	0.03
155774 ($n = 2$)	0.16	0.05	-0.04	0.02	0.09	0.03
Metabasalts						
SM/GR/98/21 ($n = 1$)	0.18	0.05	-0.06	0.06	0.11	0.03
SM/GR/98/23 ($n = 3$)	0.20	0.05	-0.05	0.05	0.11	0.03
SM/GR/98/26 ($n = 2$)	0.20	0.03	-0.06	0.06	0.11	0.04
Amphibolite enclave						
SM/GR/00/22 ($n = 1$)	0.15	0.03	-0.06	0.01	0.14	0.02
Metasediment						
SM/GR/97/31 ($n = 2$)	0.14	0.05	-0.02	0.01	0.14	0.02
Average Isua	0.18		-0.05		0.10	
2 s.d.	0.05		0.04		0.04	
Average Isua (corrected)	0.13					
2 s.d. (corrected)	0.04					
Post-Archean rocks						
Iceland dacite I 21 ($n = 8$)						
2 s.d.	0.06		0.06			
La Palma basalt LP 68a ($n = 6$)						
2 s.d.	0.03		0.04			
La Palma basalt LP 48c ($n = 3$)						
2 s.d.	0.05		0.03			
Sao Miguel basalt SM-7 ($n = 1$)						
2 s.d.	0.01		0.03			
Guernsey gneiss CS09G01 ($n = 3$)						
2 s.d.	0.02		0.02			
Average post-Archean						
2 s.d.	0.02		0.02			
Average post-Archean (corrected)						
2 s.d. (corrected)	-0.01		0.02			
Reference materials						
NIST SRM 361 ($n = 6$)						
2 s.d.	0.02		0.01			
Alfa Aesar W standard ($n = 43$)						
2 s.d.	0.001		0.004			
Alfa Aesar W standard ($n = 1$)						
2 s.d.	0.03		0.02			
BHVO-2 ($n = 2$)						
2 s.d.	0.04		0.01			
2 s.d.	0.01		0.05			

The averages of repeated quintuple analyses are reported together with their 2 s.e. The $\epsilon^{142}\text{Nd}$ analyses for the same samples reported by ref. 3 are provided for reference (the two rightmost columns). Values in the $\epsilon^{182}\text{W}$ and $\epsilon^{183}\text{W}$ columns are averages of n quintuple analyses (n = number of quintuple analyses). A full table of all analyses is presented in the Supplementary Information. Average values of Isua and post-Archean $\epsilon^{182}\text{W}$ are reported both with and without a correction for non-zero $\epsilon^{183}\text{W}$ (see text and Supplementary Information for more details and full data set). The single quintuple analysis of the Alfa Aesar W standard ($n = 1$) was passed through a chromatographic separation procedure. BHVO-2 is a basaltic reference material from the United States Geological Survey (USGS).

compositions^{20,21}, despite the high sensitivity of such Cr measurements to meteoritic additions²². Our work also includes one of the samples (SM/GR/97/31) analysed by ref. 20 but we find that it has a positive $\epsilon^{182}\text{W} = 0.14 \pm 0.05$ (2 s.e.; Table 1). Therefore, we share the puzzlement of others^{15,22} over the reported negative $\epsilon^{182}\text{W}$ values for Isua metasediments¹⁹ and we suggest they are likely to be analytical artefacts.

All our Isua samples have elevated $\epsilon^{142}\text{Nd} \approx 0.1$ (ref. 3, Table 1) and their coupled $^{143}\text{Nd}/^{144}\text{Nd}$ - $^{142}\text{Nd}/^{144}\text{Nd}$ systematics imply that they were derived from a mantle source formed within the first 50–200 Myr of Earth's history³. The mean $\epsilon^{182}\text{W} = 0.13$ of our Isua samples should therefore provide a good estimate of the composition of the mantle before the influx of meteorites recorded by the terminal bombardment⁹. The decrease in mantle $\epsilon^{182}\text{W}$ from >4.3 Gyr to the present day is strikingly consistent with what would be expected if the late veneer had indeed been added¹⁰ (see Fig. 2a). Additional analyses are clearly required to define a more detailed record of mantle $\epsilon^{182}\text{W}$ evolution, but our single 2-Gyr-old sample suggests that $\epsilon^{182}\text{W}$ may have dropped to its modern value by this time. Such secular evolution is compatible with the temporally better-constrained period (3.5–2.9 Gyr) over which the HSE contents of komatiites increased, which has also been attributed to the influence of the late veneer²³. Because the approximate doubling of source HSE contents inferred by ref. 23 is only a small fraction of the anticipated more than a hundredfold change due to the late veneer (for example, ref. 12), we further suggest that the major change of HSE contents, and thus $\epsilon^{182}\text{W}$, occurred before 3.5 Gyr ago. The HSE contents of the Isua source would thus be anticipated to be low, but making such inferences from the measured

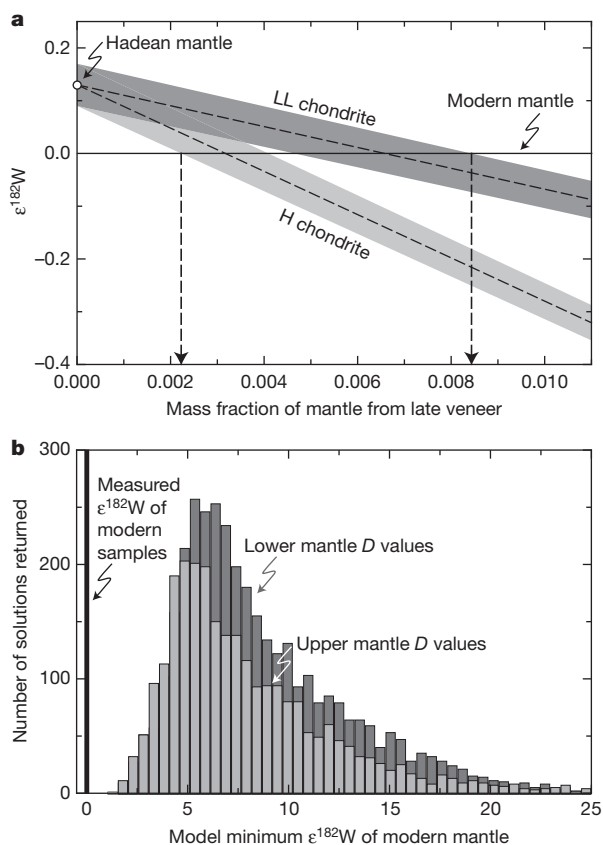


Figure 2 | Model estimates of $\epsilon^{182}\text{W}$ in modern mantle. **a**, The effect of adding variable mass fractions (relative to the total silicate Earth) of late veneer to a Hadean mantle with $\epsilon^{182}\text{W} = 0.13$, as determined in this study. In this calculation we use a current bulk silicate earth value of tungsten concentration from ref. 28 and compositions of LL²⁹ and H³⁰ ordinary chondrites, taken to span the range of probable impacting material¹¹. The fraction of chondritic material added to the mantle in the late veneer has independently been estimated⁵ from HSE abundances to be 0.005, in keeping with the range of possible solutions shown here (0.002 to 0.009). **b**, Modelled minimum $\epsilon^{182}\text{W}$ for the modern mantle calculated from 5,000,000 Monte Carlo simulations of a simple model (see Supplementary Information for full description) that satisfies the ^{142}Nd , ^{143}Nd isotope constraints of Hadean and modern mantle by partial remixing of a portion of an EER (see text). Results are shown using two sets of partition coefficients D , appropriate for forming a hidden reservoir during deep and shallow mantle fractionation¹⁵, respectively. The values of modern $\epsilon^{182}\text{W}$ require an assumption about $\epsilon^{182}\text{W}$ at the time of hidden reservoir formation. We use a chondritic reference as a conservative minimum estimate and yet still find no model $\epsilon^{182}\text{W}$ as low as the modern values of zero. Thus the partial remixing model yields no plausible solutions.

HSE abundances in the available Isua rocks, which are the product of multi-phase magmatic and metamorphic processes, is challenging and probably unreliable.

Although our data are strikingly in keeping with the late veneer hypothesis, it is important to consider other processes that might have resulted in a lowering of $\epsilon^{182}\text{W}$ over early Earth history. Mixing core material back into the mantle could also decrease its $\epsilon^{182}\text{W}$. At present, such a process might be detected in low $\epsilon^{182}\text{W}$ of magmatic products from mantle plumes. Plumes are probably sourced from the core-mantle boundary, where they can potentially inherit a core signature⁷. Hawaii is the most vigorous modern, oceanic plume and its lavas might be expected to display most clearly any low $\epsilon^{182}\text{W}$ if core-mantle interaction is an ongoing process. Previous work²⁴, however, has illustrated that Hawaiian lavas do not have anomalous $\epsilon^{182}\text{W}$. Here we present higher-precision $\epsilon^{182}\text{W}$ analyses for a wider range of hotspot samples, selected from sources linked to the lowermost mantle by several criteria. Namely, we have measured basalts from the voluminous Cretaceous

igneous province of the western Pacific and modern ocean island basalts with high $^3\text{He}/^4\text{He}$ and/or apparent deep tomographic roots²⁵. None of these samples have resolvable unradiogenic $\epsilon^{182}\text{W}$ (± 0.1 ; 2 s.d.). Thus we reaffirm that there is no discernible evidence for the current return of core material to the mantle. We cannot rule out that some core remixing occurred between >4.3 Gyr and 2 Gyr ago but it is not clear why this should suddenly have ceased. In contrast, the independent evidence for a late veneer at an appropriate time is strong⁹, which therefore makes it a more compelling explanation for the secular change in $\epsilon^{182}\text{W}$.

Another potential mechanism to account for a decrease in $\epsilon^{182}\text{W}$ of the Earth's mantle is the partial remixing of an early-formed, enriched, abyssal silicate reservoir²⁶ into the accessible, convecting mantle. This appealing scenario has been previously invoked to explain the secular decrease in $\epsilon^{142}\text{Nd}$ (refs 5 and 6). Nd isotope systematics require that such an early enriched reservoir (EER) would have been formed within the first 30 Myr of the Earth's history²⁶. During this time period ^{182}Hf was extant. Given that W is more incompatible than Hf over a wide range of planetary crystallization scenarios (see ref. 15), an EER should have a low Hf/W and so evolve with low $\epsilon^{182}\text{W}$ (refs 15 and 16). Thus, returning a fraction of EER to the accessible mantle might also cause a decrease in its $\epsilon^{182}\text{W}$.

We assess the merit of this hypothesis with a simple model of mantle evolution (see Supplementary Information for a detailed description). In brief, we start with a chondritic terrestrial composition, extract an EER to produce a complementary early depleted reservoir with $\epsilon^{142}\text{Nd}$ sufficiently radiogenic to account for the Isua rocks and then partially remix the EER into the convecting mantle to lower $\epsilon^{142}\text{Nd}$ to modern mantle values. The model is further constrained using the mass balance of the ^{147}Sm – ^{143}Nd system and by coupling the behaviour of Sm–Nd to Hf–W via experimental mineral-melt partition coefficients¹⁵. In this way we can predict mantle $\epsilon^{182}\text{W}$, if the formation and return of an EER alone accounts for the variability and super-chondritic values of mantle $\epsilon^{142}\text{Nd}$. To explore a full range of input parameters, we have used a Monte Carlo approach. In Fig. 2b we show the minimum model values of $\epsilon^{182}\text{W}$ for the modern mantle and all of these are considerably higher than the observed value of zero. Thus the coupled $\epsilon^{142}\text{Nd}$ and $\epsilon^{182}\text{W}$ isotope data do not provide clear evidence for a hidden reservoir and diminish the arguments for its presence on the basis of the secular change in $\epsilon^{142}\text{Nd}$ (ref. 5).

The late veneer thus provides the most straightforward interpretation of the secular change in $\epsilon^{182}\text{W}$ (Fig. 2a) but obviously does not provide a means of accounting for the decrease in $\epsilon^{142}\text{Nd}$ from 3.8 to 3.5 Gyr ago^{3,6}; as a lithophile element, the budget of Nd will be insignificantly influenced by the late meteorite addition. However, we speculate that these isotopic changes could be linked if the terminal bombardment initiated convective mixing of an outer layer of mantle, which might have been isolated by the formation of a dry, stagnant lid or compositional stratification after crystallization of a global magma ocean. Indeed, it has been argued that a scenario of planetary solidification can lead to melts with increased $\epsilon^{142}\text{Nd}$, like the Isua lavas²⁷. Chondritic material delivered by the terminal bombardment must be stirred into the Earth's interior to lower $\epsilon^{182}\text{W}$ to its current value. This process would destroy any primordial mantle layering and homogenize associated variable $\epsilon^{142}\text{Nd}$ to a lower mean than the Isua source. Thus the terminal bombardment, in addition to contributing to the HSE budget of the Earth, may also have initiated a mode of mantle dynamics that has continued to the present day.

METHODS SUMMARY

We devised two independent chromatographic separation techniques that allow the isolation of W from about 1 g of rock sample. In the first method, the sample powder was digested in a mixture of concentrated HF–HNO₃ on a hotplate. The supernatant was extracted and the precipitates washed three times in 1 M HF to recover any remaining W. The combined solution was dried and loaded in 1 M HF in 3 ml of pre-cleaned and pre-conditioned AG1x8 (a strongly anionic exchange resin, 100–200 mesh). After rinsing with 1 M HF and 0.5 M HCl/0.5% H₂O₂, W

was collected in 2 M HNO₃/0.5 M HF. The procedure was repeated once to purify the W fraction further using 100 µl of AG1x8 (100–200 mesh). In the second method, the sample powder was mixed and fluxed with Na₂O₂ in a furnace. The resulting cake was dissolved in H₂O and the solution directly loaded onto 2 mL of AG1x8 (100–200 mesh). We found that W (as an oxy-anionic species) is highly soluble in alkaline solutions and also strongly retained on anionic exchange resins, whereas matrix elements (in particular Ti, Zr, Nb, Hf and Ta) are not. Tungsten was recovered from the resin in 2 M HNO₃/0.5 M HF and further purified using the HF-based procedure described above. Mass-spectrometric measurements were carried out on a ThermoFinnigan Neptune MC-ICPMS. Measured ¹⁸²W/¹⁸⁴W were internally, exponentially normalized to ¹⁸⁶W/¹⁸³W = 1.98594. Each sample was preceded and followed by the measurement of the NIST SRM 3163 standard, and the average ¹⁸²W/¹⁸⁴W of these bracketing measurements was used to externally normalize sample ¹⁸²W/¹⁸⁴W and thus yield ε¹⁸²W. Every data point reported in Table 1 comprises at least five independent analyses of each sample.

Full Methods and any associated references are available in the online version of the paper at www.nature.com/nature.

Received 19 January; accepted 28 July 2011.

- Kimura, K., Lewis, R. S. & Anders, E. Distribution of gold and rhenium between nickel-iron and silicate melts—implications for abundance of siderophile elements on Earth and Moon. *Geochim. Cosmochim. Acta* **38**, 683–701 (1974).
- Chou, C.-L. Fractionation of siderophile elements in the Earth's upper mantle and lunar samples. *Proc. 9th Lunar Planet. Sci. Conf.* **9**, 163–165 (1978).
- Caro, G., Bourdon, B., Birck, J. L. & Moorbath, S. High-precision ¹⁴²Nd/¹⁴⁴Nd measurements in terrestrial rocks: constraints on the early differentiation of the Earth's mantle. *Geochim. Cosmochim. Acta* **70**, 164–191 (2006).
- Kamber, B. S., Collerson, K. D., Moorbath, S. & Whitehouse, M. J. Inheritance of early Archean Pb-isotope variability from long-lived Hadean protocrust. *Contrib. Mineral. Petrol.* **145**, 25–46 (2003).
- Carlson, R. W. & Boyet, M. Composition of the Earth's interior: the importance of early events. *Phil. Trans. R. Soc. Lond. A* **366**, 4077–4103 (2008).
- Bennett, V. C., Brandon, A. D. & Nutman, A. P. Coupled ¹⁴²Nd–¹⁴³Nd isotopic evidence for Hadean mantle dynamics. *Science* **318**, 1907–1910 (2007).
- Brandon, A. D. & Walker, R. J. The debate over core–mantle interaction. *Earth Planet. Sci. Lett.* **232**, 211–225 (2005).
- Rudge, J. F., Kleine, T. & Bourdon, B. Broad bounds on Earth's accretion and core formation constrained by geochemical models. *Nature Geosci.* **3**, 439–443 (2010).
- Tera, F., Papanastassiou, D. A. & Wasserburg, G. J. Isotopic evidence for a terminal Lunar cataclysm. *Earth Planet. Sci. Lett.* **22**, 1–21 (1974).
- Bottke, W. F., Walker, R. J., Day, J. M. D., Nesvorný, D. & Elkins-Tanton, L. Stochastic late accretion to Earth, the Moon and Mars. *Science* **330**, 1527–1530 (2010).
- Walker, R. J. Highly siderophile elements in the Earth, Moon and Mars: update and implications for planetary accretion and differentiation. *Chem. Erde* **69**, 101–125 (2009).
- Brenan, J. M. & McDonough, W. F. Core formation and metal–silicate fractionation of osmium and iridium from gold. *Nature Geosci.* **2**, 798–801 (2009).
- Lorand, J. P., Alard, O. & Luguet, A. Platinum-group element micronuggets and refertilization process in Lherz orogenic peridotite (northeastern Pyrenées, France). *Earth Planet. Sci. Lett.* **289**, 298–310 (2010).
- Moorbath, S., O'Nions, K. & Pankhurst, R. J. The evolution of early Precambrian crustal rocks at Isua, West Greenland—geochemical and isotopic evidence. *Earth Planet. Sci. Lett.* **27**, 229–239 (1975).
- Iizuka, T. *et al.* The tungsten isotopic composition of Eoarchean rocks: implications for early silicate differentiation and core–mantle interaction on Earth. *Earth Planet. Sci. Lett.* **291**, 189–200 (2010).
- Moynier, F. *et al.* Coupled ¹⁸²W–¹⁴²Nd constraint for early Earth differentiation. *Proc. Natl Acad. Sci. USA* **107**, 10810–10814 (2010).
- Kleine, T. *et al.* Hf–W chronology of the accretion and early evolution of asteroids and terrestrial planets. *Geochim. Cosmochim. Acta* **73**, 5150–5188 (2009).
- Morgan, J. W., Walker, R. J., Brandon, A. D. & Horan, M. F. Siderophile elements in Earth's upper mantle and lunar breccias: data synthesis suggests manifestations of the same late influx. *Meteorit. Planet. Sci.* **36**, 1257–1275 (2001).
- Schoenberg, R., Kamber, B. S., Collerson, K. D. & Moorbath, S. Tungsten isotope evidence from ~3.8-Gyr metamorphosed sediments for early meteorite bombardment of the Earth. *Nature* **418**, 403–405 (2002).
- Trinquier, A., Birck, J. L. & Allègre, C. J. High-precision analysis of chromium isotopes in terrestrial and meteorite samples by thermal ionization mass spectrometry. *J. Anal. At. Spectrom.* **23**, 1565–1574 (2008).
- Frei, R. & Rosing, M. T. Search for traces of the late heavy bombardment on Earth—results from high precision chromium isotopes. *Earth Planet. Sci. Lett.* **236**, 28–40 (2005).
- Moynier, F., Koeberl, C., Quitté, G. & Telouk, P. A tungsten isotope approach to search for meteoritic components. *Earth Planet. Sci. Lett.* **286**, 35–40 (2009).
- Maier, W. D. *et al.* Progressive mixing of meteoritic veneer into the early Earth's deep mantle. *Nature* **460**, 620–623 (2009).
- Scherstén, A., Elliott, T., Hawkesworth, C. & Norman, M. D. Tungsten isotope evidence that mantle plumes contain no contribution from the Earth's core. *Nature* **427**, 234–237 (2004).
- Montelli, R. *et al.* Finite-frequency tomography reveals a variety of plumes in the mantle. *Science* **303**, 338–343 (2004).
- Boyet, M. & Carlson, R. W. ¹⁴²Nd evidence for early (> 4.53 Ga) global differentiation of the silicate Earth. *Science* **309**, 576–581 (2005).
- Caro, G., Bourdon, B., Wood, B. J. & Corgne, A. Trace-element fractionation in Hadean mantle generated by melt segregation from a magma ocean. *Nature* **436**, 246–249 (2005).
- Arevalo, R. & McDonough, W. F. Tungsten geochemistry and implications for understanding the Earth's interior. *Earth Planet. Sci. Lett.* **272**, 656–665 (2008).
- Yin, Q. Z. *et al.* A short timescale for terrestrial planet formation from Hf–W chronometry of meteorites. *Nature* **418**, 949–952 (2002).
- Kleine, T. *et al.* Hf–W thermochronometry: closure temperature and constraints on the accretion and cooling history of the H chondrite parent body. *Earth Planet. Sci. Lett.* **270**, 106–118 (2008).

Supplementary Information is linked to the online version of the paper at www.nature.com/nature.

Acknowledgements We thank the IODP, C. Storey (University of Portsmouth) and M. D. Norman (ANU Canberra) for providing sample material. We thank C. Coath for assistance with mass spectrometric analyses and T. Kleine and F. Moynier for comments. We acknowledge funding from NERC (NE/DO12805/1, NE/H011927/1), STFC (ST/F002734/1), and DFG (WI 3579/1-1).

Author Contributions Samples from Isua were collected by S.M. Analytical development and sample analyses were carried out by M.W. Modelling and manuscript preparation was carried out by T.E. and M.W. All authors contributed to discussing the results and implications.

Author Information Reprints and permissions information is available at www.nature.com/reprints. The authors declare no competing financial interests. Readers are welcome to comment on the online version of this article at www.nature.com/nature. Correspondence and requests for materials should be addressed to M.W. (m.willbold@bristol.ac.uk).

METHODS

For each analysis, W was isolated from sample material of 0.1–2.0 g. The majority of silicate samples (labelled 'Acid' in Supplementary Information Table 1) were dissolved in a mixture of 28 M HF/15 M HNO₃ in closed 60-ml Savillex Teflon jars for at least three days at 150 °C. The samples were centrifuged and the liquid supernatant collected. The residue was washed three times with 1 M HF, centrifuged, and all four supernatant solutions combined. The solution was dried and redissolved in 1 M HF. We also analysed the NIST steel standard SRM 361, to cover a full range of matrices. This was more simply dissolved in 6 M HCl, dried down at 150 °C before being redissolved in 1 M HF. Samples dissolved in 1 M HF were loaded on pre-cleaned and pre-conditioned columns containing 3 ml anion exchange resin (AG1x8, 100–200 mesh). Matrix elements were separated by washing with 9 ml of 1 M HF and 33 ml of 0.5 M HCl/0.5% H₂O₂ (mass/volume). Tungsten was collected in 27 ml 2 M HNO₃/0.5 M HF. The W fraction was dried, redissolved in 1 M HF and the above-described procedure was repeated on columns containing 100 µl of AG1x8 (100–200 mesh). Tungsten was collected in 1 ml 7 M HCl/0.5 M HCl. This separation procedure is similar to those previously described^{31–33} and allowed purification of W with a yield of >80% as determined from the solution collected after chemical separation. Yet, the W yield after drying of this solution was sometimes significantly less than 80%, most likely owing to the formation of insoluble W oxide compounds, which could not be redissolved even using hot concentrated HF. The total procedural blank for W was <450 pg and was insignificant compared to the amount of W processed.

In an alternative separation protocol, some silicate samples (labelled 'Alkaline' in Supplementary Table 1) were mixed and fluxed with ultrapure Na₂O₂ at 590 °C in boron-nitride crucibles in a muffle furnace. After cooling, the cake was dissolved in >18 MΩ per cm H₂O, centrifuged, and the liquid supernatant loaded as NaOH on pre-cleaned and pre-conditioned columns containing 2 ml anion exchange resin (AG1x8, 100–200 mesh). We found that under these conditions W forms oxy-anionic complexes that partition strongly on strong anion exchange resins, whereas most of the matrix elements (in particular Ca, Mg, Fe and Al) are either removed by precipitation as hydroxides during dissolution or do not form anionic complexes in alkaline solutions (in particular Ti, Zr, Nb, Hf and Ta) and are thus effectively removed by this procedure. After collection of W in 27 ml of 2 M HNO₃/0.5 M HF, the solution was dried and the W fraction was further purified using the above-described procedure on 100 µl columns containing AG1x8 (100–200 mesh). Recovery of W was >80% when determined from the solution collected after chemical separation. Yet, as with the procedure described above, drying sometimes led to loss of W. The total procedural blanks were similar to that of the acid medium method (<400 pg).

Between both chemical separations (matrix removal and cleanup of W), as well as before diluting the samples for mass spectrometric analysis, the samples were refluxed up to three times with 50 µl 15 M HNO₃ and 50 µl 30% H₂O₂ (mass/volume) to destroy organic material (mainly fragments of anionic exchange resin that bled through the polypropylene frits used).

Tungsten isotopic measurements were carried out on a ThermoFinnigan Neptune (Bristol Isotope Group, Neptune 2) multi-collector ICPMS in static collection mode. Samples dissolved in 0.4 M HNO₃/0.4 M HF were introduced into the mass spectrometer via a Cetac Aridus desolvation system using a nominal

50 µl per min perfluoroalkoxy (PFA) nebuliser and sweep gas flows of 5–6 litres per min Ar and ~3 ml per min N₂. The plasma was maintained with 1200 W radio-frequency power, 15 litres per min cool gas, 0.8 litres per min auxiliary gas, and 0.7 litres per min sample gas flow. Ni sample and 'X' skimmer cones were used. Analyses were run in 'low' resolution, with nominal mass resolution $M/\Delta M \approx 500$. Typical instrument sensitivity for these conditions ranged between 0.8 and 1.2×10^{-10} A of ¹⁸⁶W for a 100 ng per ml W solution. Individual analyses comprised 200 integrations (each lasting 4 s) of static measurements of ¹⁸²W (L3), ¹⁸³W (L2), ¹⁸⁴W (L1), ¹⁸⁶W (C), ¹⁸⁸Os (H1) and ¹⁹⁰Os (H2), where L3 to H2 refer to the movable low-mass (L) and high-mass (H) side Faraday cups relative to the central, fixed Faraday cup (C). The instrumental mass fraction was corrected assuming the stable ¹⁸⁶W/¹⁸³W ratio of 1.98594. For all data reported, the intensities of interfering Os isotopes were at baseline levels (that is, $<1 \times 10^{-17}$ A for ¹⁸⁸Os). Each sample was preceded and followed by measurements of the standard solution (NIST SRM 3163), which were used to calculate the $\epsilon^{182}\text{W}$ value for the bracketed sample measurement. Depending on the amount of W available in each sample, the intensity of each sample was matched to within 30% of that of the standard solution. Background corrections were performed by subtracting the average on-peak intensities measured in a blank solution (that is, comprising the 0.4 M HNO₃/0.4 M HF solution used to dilute the samples and the standard) before and after each sample and standard measurement.

Each 'quintuple' $\epsilon^{182}\text{W}$ value given in Table 1 was calculated from the average of five independent analyses (five chemical separations and measurements) of an individual sample. The repeatability (2σ) of instrument setup for such measurements is better than 0.03 $\epsilon^{182}\text{W}$ units as determined by repeated analyses of an Alfa Aesar W standard solution (total of 43 quintuple analyses; see Supplementary Table 2). The reproducibility (including the two types of chemical purification and isotopic measurements) of the method is better than 0.06 $\epsilon^{182}\text{W}$ units (2σ) as determined by the repeated quintuple analyses of post-Archean silicate samples: Icelandic dacite I21 (ref. 34), $n = 9$; La Palma basalts LP-68a and LP-48a (ref. 35), $n = 9$; 2-Gyr-old felsic gneiss from Guernsey, UK, CS09G01, obtained from C. Storey, $n = 3$; and USGS basaltic reference material BHVO-2, $n = 2$; see Table 1. Repeated analyses of NIST metal SRM 361 yielded a reproducibility of 0.03 $\epsilon^{182}\text{W}$ (2σ ; $n = 6$).

- Quitté, G., Birck, J.-L., Capmas, F. & Allègre, C. J. High-precision Hf-W isotopic measurements in meteoritic material using negative thermal ionisation mass spectrometry. *Geostand. Newsl.* **26**, 149–160 (2002).
- Kleine, T., Mezger, K., Münker, C., Palme, H. & Bischoff, A. ¹⁸²Hf-¹⁸²W isotope systematics of chondrites, eucrites, and martian meteorites: chronology of core formation and early mantle differentiation in Vesta and Mars. *Geochim. Cosmochim. Acta* **68**, 2935–2946 (2004).
- Sahoo, Y. V., Nakai, S. & Ali, A. Modified ion exchange separation for tungsten isotopic measurements from kimberlite samples using multi-collector inductively coupled plasma mass spectrometry. *Analyst* **131**, 434–439 (2006).
- Willbold, M., Hegner, E., Stracke, A. & Rocholl, A. Continental geochemical signatures in dacites from Iceland and implications for models of early Archaean crust formation. *Earth Planet. Sci. Lett.* **279**, 44–52 (2009).
- Marcantonio, F., Zindler, A., Elliott, T. & Staudigel, H. Os isotope systematics of La Palma, Canary Islands: evidence for recycled crust in the mantle source of HIMU ocean islands. *Earth Planet. Sci. Lett.* **133**, 397–410 (1995).

High plant diversity is needed to maintain ecosystem services

Forest Isbell¹, Vincent Calcagno¹, Andy Hector², John Connolly³, W. Stanley Harpole⁴, Peter B. Reich^{5,6}, Michael Scherer-Lorenzen⁷, Bernhard Schmid², David Tilman⁸, Jasper van Ruijven⁹, Alexandra Weigelt¹⁰, Brian J. Wilsey⁴, Erika S. Zavaleta¹¹ & Michel Loreau¹

Biodiversity is rapidly declining worldwide¹, and there is consensus that this can decrease ecosystem functioning and services^{2–7}. It remains unclear, though, whether few⁸ or many⁹ of the species in an ecosystem are needed to sustain the provisioning of ecosystem services. It has been hypothesized that most species would promote ecosystem services if many times, places, functions and environmental changes were considered⁹; however, no previous study has considered all of these factors together. Here we show that 84% of the 147 grassland plant species studied in 17 biodiversity experiments promoted ecosystem functioning at least once. Different species promoted ecosystem functioning during different years, at different places, for different functions and under different environmental change scenarios. Furthermore, the species needed to provide one function during multiple years were not the same as those needed to provide multiple functions within one year. Our results indicate that even more species will be needed to maintain ecosystem functioning and services than previously suggested by studies that have either (1) considered only the number of species needed to promote one function under one set of environmental conditions, or (2) separately considered the importance of biodiversity for providing ecosystem functioning across multiple years^{10–14}, places^{15,16}, functions^{14,17,18} or environmental change scenarios^{12,19–22}. Therefore, although species may appear functionally redundant when one function is considered under one set of environmental conditions⁷, many species are needed to maintain multiple functions at multiple times and places in a changing world.

Arguments for biodiversity conservation are often based on ecosystem services, but it remains unclear whether few⁸ or many⁹ species are needed to maintain ecosystem services. Determining how many species provide ecosystem services will require a synthesis of several areas of biodiversity research (Fig. 1). Biodiversity–ecosystem functioning studies have often considered a single functional context and found that multiple, but not all, study species promoted ecosystem functioning^{5–7} (Fig. 1a). We define a functional context (henceforth context) as the measurement of one function, at one time and place, under one environmental change scenario. Several related biodiversity studies have explored whether more species promote ecosystem functioning when more than one context is considered. For example, biodiversity–ecosystem stability (that is, the invariability of productivity) studies have found that more species are needed to provide ecosystem functioning at larger spatio-temporal scales because different species promote productivity at different times^{10–14} (Fig. 1b) or places^{15,16}. Biodiversity–ecosystem multifunctionality studies have found that more species are needed to provide multiple functions because different species promote different functions^{14,17,18} (Fig. 1c). Biodiversity–global change studies have found that more species are needed to

provide ecosystem functioning in a changing world because different species promote ecosystem functioning under different environmental change scenarios¹². Here, for the first time to our knowledge, we consider all of these relationships together.

We included data from 17 grassland biodiversity experiments that considered multiple times, places, functions or environmental change scenarios (Supplementary Table 1 and Supplementary Data). To test whether different species promoted ecosystem functioning during different years, we included studies that planted replicate plots (same species compositions) during consecutive years²³ or made repeated measurements of ecosystem functions across years^{17,19,21,22,24,25}. To test whether different species promoted ecosystem functioning at different places, we included studies that planted replicate plots (same species compositions, with one exception²⁵) at multiple sites across Europe²⁶ or multiple spatial blocks within a site^{17,23,25}. To test whether different

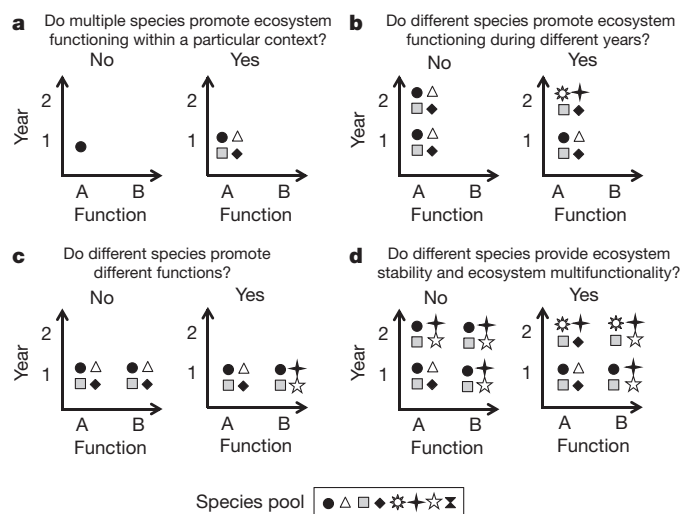


Figure 1 | Some of the ways that biodiversity can be important for ecosystem functioning. Each of the eight symbols represents a species. Species shown in the bivariate plots are those that promoted ecosystem functioning within each functional context (for example, context A1 might be above-ground biomass measured during 2001). Although this figure defines contexts in two dimensions for simplicity, we considered four dimensions (Fig. 3). Previous studies have considered (a) one context, or (b, c) one dimension of contexts (b, ecosystem stability studies; c, ecosystem multifunctionality studies). Figure 2 tests the question in d, by comparing the one-dimensional overlap (for example, between A1 and A2) with the two-dimensional overlap (for example, between A1 and B2) and three-dimensional overlap (that is, a pair of contexts that differs in three ways; not shown). Our results reject each of the null hypotheses shown on the left in a–d.

¹Department of Biology, McGill University, Montreal, Quebec, H3A 1B1, Canada. ²Institute of Evolutionary Biology and Environmental Studies, University of Zurich, CH-8057 Zurich, Switzerland. ³UCD School of Mathematical Sciences, University College Dublin, Dublin 4, Ireland. ⁴Department of Ecology, Evolution, and Organismal Biology, Iowa State University, Ames, Iowa 50011, USA. ⁵Department of Forest Resources, University of Minnesota, St Paul, Minnesota 55108, USA. ⁶Hawkesbury Institute for the Environment, University of Western Sydney, Richmond, New South Wales 2753, Australia. ⁷Faculty of Biology, University of Freiburg, Geobotany, D-79104 Freiburg, Germany. ⁸Department of Ecology, Evolution, and Behavior, University of Minnesota, St Paul, Minnesota 55108, USA. ⁹Nature Conservation and Plant Ecology, Wageningen University, 6700 AA Wageningen, The Netherlands. ¹⁰Institute of Biology I, University of Leipzig, 04103 Leipzig, Germany. ¹¹Environmental Studies Department, University of California, Santa Cruz, California 95064, USA.

species promoted different functions, we included studies that measured several functions^{14,17,22}, such as biomass production and nutrient uptake. Many of these functions are considered to be supporting ecosystem services because other types of ecosystem services depend on them^{4,27}. To test whether different species promoted ecosystem functioning under different environmental change scenarios, we included studies that applied environmental change treatments, such as nutrient and CO₂ enrichment¹⁹, precipitation changes²¹ or land use changes such as livestock grazing²² and haying²⁰.

We began by identifying the sets of study species that influenced ecosystem functioning within each context. Species were considered to promote ecosystem functioning in a particular context if they had effects in the direction that would usually be considered desirable from an ecosystem services perspective¹⁷. Positive effects were considered desirable for all functions except for soil inorganic nitrogen and light availability at ground level, where negative effects are consistent with lower levels of unconsumed resources¹⁷. We did not use separate definitions of desirable effects for different species (for example, positive effects of legumes on soil nitrogen might be considered desirable) to be consistent with previous studies^{17,18}, to be conservative and because it may not be possible to manage simultaneously for both positive and negative effects. We found that approximately 27% of the study species promoted ecosystem functioning within any particular context, regardless of the size of the study species pool (Fig. 2a). Note that if many species were functionally redundant, or if only the most common species promoted ecosystem functioning, then we would expect a saturating relationship in Fig. 2a. Instead, our results suggest that even rare species can promote ecosystem functioning.

After identifying the sets of species that promoted ecosystem functioning in each context, we tested whether different sets of species promoted ecosystem functioning in different contexts. We used Sørensen's similarity index to quantify overlap between species sets¹⁷. All comparisons were made within studies so that differences between pairs of contexts were not due to sampling from multiple species pools. First, we quantified one-dimensional overlap between all pairs of contexts that differed in only one way (Fig. 1b, c). For example, multi-year overlap was quantified between each pair of contexts that differed only in which year ecosystem functioning was measured (that is, same

place, function and environmental change scenario in both contexts). A multi-year overlap value of one or zero would respectively indicate that completely identical or completely unique sets of species promoted ecosystem functioning during different years, independent of the other sources of variation. We found overlap values between these two extremes, which indicates that somewhat different sets of species promoted ecosystem functioning during different years, at different places, for different functions and under different environmental change scenarios (Fig. 2b).

After considering these sources of variation independently, we quantified multi-dimensional overlap between pairs of contexts that differed in two or three ways (Fig. 1d). Again, all comparisons were made within studies. We found that the average overlap between pairs of contexts decreased as the number of differences between contexts increased (Fig. 2b and Supplementary Fig. 1). This means that, for example, the identities of the additional species needed to provide one function during multiple years were not the same as the identities of the additional species needed to provide multiple functions during one year (Fig. 1d). Additionally, species sets did not simply vary independently of context attributes (permutation test $P < 0.001$ for one-, two- and three-dimensional overlap) (Fig. 2b). Thus, our results indicate that even more species will be needed to maintain ecosystem functioning and services than previously suggested by studies that have either (1) considered only the number of species needed to promote one function under one set of environmental conditions, or (2) separately considered the importance of biodiversity for providing ecosystem functioning across multiple years^{10–14}, places^{15,16}, functions^{14,17,18} or environmental change scenarios^{12,19–22}. Future studies could more completely consider the consequences of biodiversity declines for ecosystem functioning and services by similarly considering the multi-dimensionality of ecosystem functioning both in experimental and natural communities.

Next, we quantified the extent to which the number of species promoting ecosystem functioning increased as more years, places, functions or environmental change scenarios were considered within each study. In other words, we quantified the accumulation of species across each of the four dimensions of contexts that we considered (Fig. 1). We found that a greater proportion of species promoted

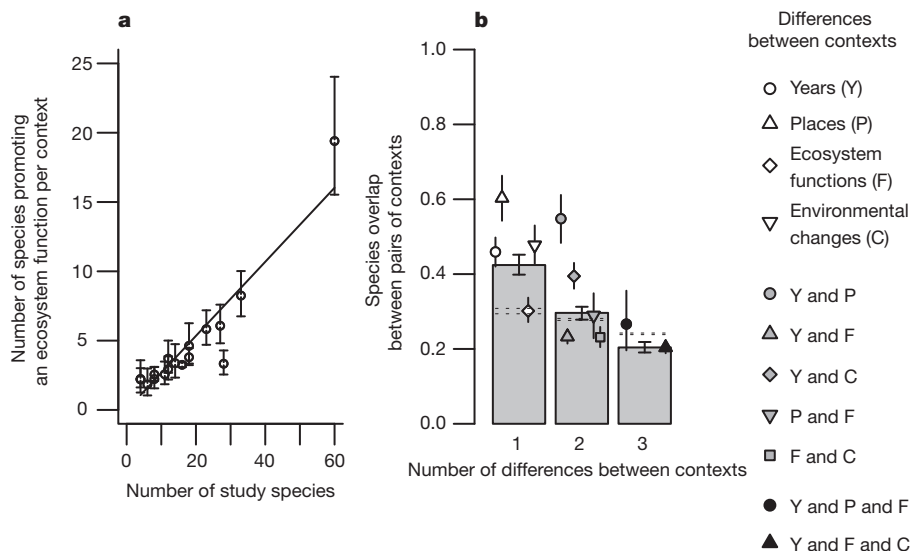


Figure 2 | Sets of study species that promoted ecosystem functioning. **a**, The mean number of species that promoted ecosystem functioning within each context increased linearly ($t = 16.40$, $P < 0.001$, $R^2 = 0.944$) with the size of the species pool, such that approximately 27% (mean, 95% confidence intervals for slope: 0.27, 0.24–0.30) of the study species promoted ecosystem functioning within each context. Error bars for each study indicate 95% generalized linear model confidence intervals. **b**, Different sets of species promoted ecosystem

functioning in different contexts (overlap < 1), and overlap between pairs of contexts decreased as the number of differences between contexts increased (see Fig. 1). Symbols indicate means for each specific type of overlap; horizontal dotted lines show $\pm 95\%$ permutation test confidence intervals; error bars for symbols and bars indicate 95% bootstrap confidence intervals. Supplementary Data indicates numbers of contexts for each study.

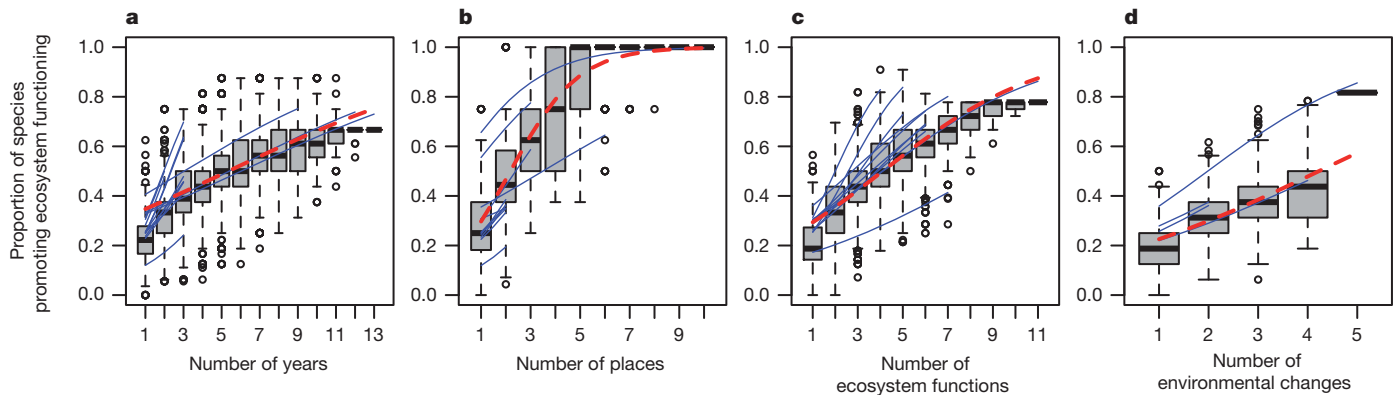


Figure 3 | The proportion of study species that promoted ecosystem functioning increased when more (a) years, (b) places, (c) ecosystem functions and (d) environmental change scenarios were independently considered. Solid blue lines indicate generalized linear model fits for each study; dashed red line indicates grand mean generalized linear model fitted

ecosystem functioning when more years, places, functions or environmental change scenarios were considered (Fig. 3). These relationships result from different species promoting ecosystem functioning in different contexts (Fig. 2b). Note that if the one-dimensional overlap values corresponding to each panel in Fig. 3 were one or zero, then these relationships would be horizontal or linearly increasing, respectively¹⁷. Our results are between these two extremes.

After comparing contexts within studies, data from all studies were combined to consider how the total number of species that promoted ecosystem functioning increased with the total number of contexts. We quantified the number of species that promoted ecosystem functioning in a random subset of all possible combinations of our observed contexts (that is, 100 pairs, 100 groups of three, etc.). The large increase in the number of species that promoted ecosystem functioning as more contexts were considered (Fig. 4) is the result of different species promoting ecosystem functioning during different years, at different places, for different functions, under different environmental change scenarios and in different species pools. Considering all of these factors together suggests that many species will be needed to maintain ecosystem multifunctionality at large spatio-temporal scales in a changing world. Consequently, the extinction (or decreased local occurrence) of almost any of these species is expected to decrease ecosystem functioning and services in at least some contexts. Further study is needed to identify the processes that explain why different species promoted ecosystem functioning in different contexts. The specific mechanisms involved probably differed across contexts, but previous results from these and other biodiversity experiments²⁸ suggest that complementarity (in time, space, functional effect traits and functional response traits) is a general explanation for this pattern.

Our results reveal new opportunities and challenges for prioritizing conservation efforts and predicting consequences of biodiversity declines. According to the precautionary principle, all species should be conserved because we cannot be certain which species actually provide ecosystem services²⁹. Our results offer further support for the precautionary principle because most of the studied species were important at least once, and species exhibited context-dependent effects that will be difficult to predict. If it is impossible or impractical to conserve all species, then future studies could additionally consider how often (Supplementary Fig. 2 and Supplementary Data) and how much species influenced ecosystem functioning to determine which species are most important for maintaining ecosystem functioning and services. This will require careful consideration of many contexts, because it is not possible to make general predictions or conclusions by considering a few context-dependent phenomena³⁰.

Future studies could determine whether some species consistently promote ecosystem functioning under environmental conditions that

are currently common, or under environmental change scenarios that will probably become increasingly common. Note that even species that have small effects could be important for maintaining ecosystem functioning and services if they have a large cumulative desirable effect across many contexts. For example, *Eriochloa sericea* had the smallest desirable effect on above-ground biomass in the irrigated plots at the MEND Irrigation experiment during 2009, but promoted ecosystem functioning in 75% of the contexts in which it was included. Future studies could also determine which species promote ecosystem functioning in particular contexts that are highly valued by stakeholders. Note that even species that rarely promote (or often decrease) ecosystem functioning could be most important for maintaining ecosystem functioning and services within some contexts. For example, although *Pascopyrum smithii* only promoted ecosystem functioning in 2% of the contexts in which it was included, it promoted soil carbon more than any other species in the Cedar Creek Biodiversity experiment during 2004. Furthermore, note that declines in local diversity, which are far more common than global extinctions, will also decrease ecosystem functioning and services within some contexts. Finally, even the few species that never promoted ecosystem functioning in these studies (Supplementary Fig. 2) could promote ecosystem functioning

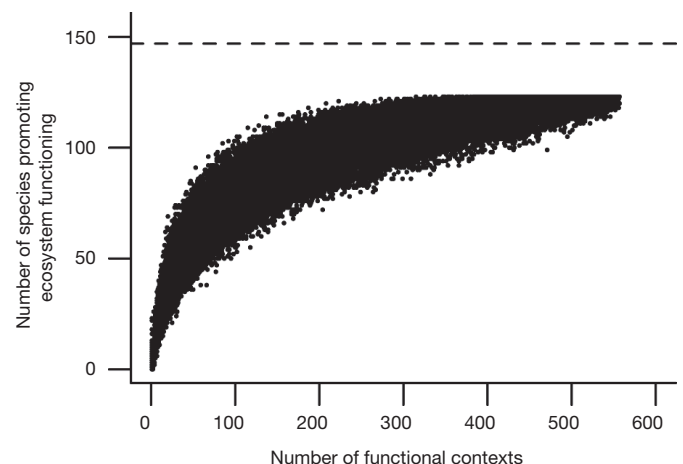


Figure 4 | The number of study species that promoted ecosystem functioning increased with the number of contexts considered across all studies. The points are the number of species that promoted ecosystem functioning when 1–557 contexts were sampled from all 557 contexts. The dashed line indicates the total number of studied species (147), which restricts the upper limit for these values. The x axis includes variation across years, places, functions, environmental change scenarios and species pools.

in other contexts, or be a conservation priority for other (for example, ethical, aesthetic) reasons. Therefore, we encourage careful consideration of many contexts when making conservation decisions and predicting the consequences of biodiversity declines.

METHODS SUMMARY

Identifying the species that promoted ecosystem functioning. For each context, we modelled ecosystem functioning response variables as a function of the presence or absence of each study species at the plot level. We used backward-elimination multiple regression to identify a minimally adequate model, based on the Akaike information criterion (AIC)¹⁷. This procedure was performed with the stepAIC function in the MASS package of R 2.11.1 (see Methods). Species were considered to promote ecosystem functioning in a context if they were included in the minimally adequate model and had effects in the direction that would usually be considered desirable from an ecosystem services perspective¹⁷.

Comparing sets of species between pairs of contexts. We used Sørensen's similarity index to quantify the overlap between the sets of species that promoted ecosystem functioning in pairs of contexts within each study¹⁷. This allowed us to test whether identical (overlap = 1), unique (overlap = 0) or somewhat different ($0 < \text{overlap} < 1$) sets of species promoted ecosystem functioning in different contexts. We also tested whether overlap decreased as the number of differences between contexts increased (Fig. 1).

Accumulation of species across contexts. We quantified the accumulation of species across each of the four dimensions of contexts that we considered (Methods; Fig. 1). A quasi-binomial generalized linear model was fitted to determine how the proportion of species that promoted ecosystem functioning increased with the number of years (or places, functions, environmental changes), including 'study' as a factor. This allowed us to describe the mean trends within and across studies. We also randomly sampled combinations (that is, 100 pairs, 100 groups of three, and so on) of all 557 contexts to determine how the number of species promoting ecosystem functioning increased when all of these factors were considered together.

Full Methods and any associated references are available in the online version of the paper at www.nature.com/nature.

Received 18 March; accepted 10 June 2011.

Published online 10 August 2011.

- Butchart, S. H. M. *et al.* Global biodiversity: indicators of recent declines. *Science* **328**, 1164–1168 (2010).
- Loreau, M. *et al.* Biodiversity and ecosystem functioning: current knowledge and future challenges. *Science* **294**, 804–808 (2001).
- Hooper, D. U. *et al.* Effects of biodiversity on ecosystem functioning: a consensus of current knowledge. *Ecol. Monogr.* **75**, 3–35 (2005).
- Balvanera, P. *et al.* Quantifying the evidence for biodiversity effects on ecosystem functioning and services. *Ecol. Lett.* **9**, 1146–1156 (2006).
- Cardinale, B. J. *et al.* Effects of biodiversity on the functioning of trophic groups and ecosystems. *Nature* **443**, 989–992 (2006).
- Naeem, S., Bunker, D. E., Hector, A., Loreau, M. & Perrings, C. *Biodiversity, Ecosystem Functioning, and Human Wellbeing: An Ecological and Economic Perspective* (Oxford Univ. Press, 2009).
- Cardinale, B. J. *et al.* The functional role of producer diversity in ecosystems. *Am. J. Bot.* **98**, 572–592 (2011).
- Ridder, B. Questioning the ecosystem services argument for biodiversity conservation. *Biodivers. Conserv.* **17**, 781–790 (2008).
- Duffy, J. E. Why biodiversity is important to the functioning of real-world ecosystems. *Front. Ecol. Environ.* **7**, 437–444 (2009).
- McNaughton, S. J. Diversity and stability of ecological communities: a comment on the role of empiricism in ecology. *Am. Nat.* **111**, 515–525 (1977).
- Yachi, S. & Loreau, M. Biodiversity and ecosystem productivity in a fluctuating environment: the insurance hypothesis. *Proc. Natl Acad. Sci. USA* **96**, 1463–1468 (1999).
- Craine, J. M. *et al.* The role of plant species in biomass production and response to elevated CO₂ and N. *Ecol. Lett.* **6**, 623–630 (2003).
- Tilman, D., Reich, P. B. & Knops, J. M. H. Biodiversity and ecosystem stability in a decade-long grassland experiment. *Nature* **441**, 629–632 (2006).

- Zavaleta, E. S., Pasari, J. R., Hulvey, K. B. & Tilman, G. D. Sustaining multiple ecosystem functions in grassland communities requires higher biodiversity. *Proc. Natl Acad. Sci. USA* **107**, 1443–1446 (2010).
- Loreau, M., Mouquet, N. & Gonzalez, A. Biodiversity as spatial insurance in heterogeneous landscapes. *Proc. Natl Acad. Sci. USA* **100**, 12765–12770 (2003).
- Griffin, J. N. *et al.* Spatial heterogeneity increases the importance of species richness for an ecosystem process. *Oikos* **118**, 1335–1342 (2009).
- Hector, A. & Bagchi, R. Biodiversity and ecosystem multifunctionality. *Nature* **448**, 188–190 (2007).
- Garnfeldt, L., Hillebrand, H. & Jonsson, P. R. Multiple functions increase the importance of biodiversity for overall ecosystem functioning. *Ecology* **89**, 1223–1231 (2008).
- Reich, P. B. *et al.* Plant diversity enhances ecosystem responses to elevated CO₂ and nitrogen deposition. *Nature* **410**, 809–812 (2001).
- Weigelt, A., Weisser, W. W., Buchmann, N. & Scherer-Lorenzen, M. Biodiversity for multifunctional grasslands: equal productivity in high-diversity low-input and low-diversity high-input systems. *Biogeosciences* **6**, 1695–1706 (2009).
- Wilsey, B. J., Teaschner, T. B., Daneshgar, P. P., Isbell, F. I. & Polley, H. W. Biodiversity maintenance mechanisms differ between native and novel exotic-dominated communities. *Ecol. Lett.* **12**, 432–442 (2009).
- Isbell, F. I. & Wilsey, B. J. Increasing native, but not exotic, biodiversity increases aboveground productivity in ungrazed and intensely grazed grasslands. *Oecologia* **165**, 771–781 (2011).
- Isbell, F. I., Losure, D. A., Yurkonis, K. A. & Wilsey, B. J. Diversity–productivity relationships in two ecologically realistic rarity and extinction scenarios. *Oikos* **117**, 996–1005 (2008).
- Tilman, D. *et al.* Diversity and productivity in a long-term grassland experiment. *Science* **294**, 843–845 (2001).
- van Ruijven, J. & Berendse, F. Long-term persistence of a positive plant diversity–productivity relationship in the absence of legumes. *Oikos* **118**, 101–106 (2009).
- Kirwan, L. *et al.* Evenness drives consistent diversity effects in intensive grassland systems across 28 European sites. *J. Ecol.* **95**, 530–539 (2007).
- Millennium Ecosystem Assessment. *Ecosystems and Human Well-being: Synthesis* (Island Press, 2005).
- Cardinale, B. J. *et al.* Impacts of plant diversity on biomass production increase through time because of species complementarity. *Proc. Natl Acad. Sci. USA* **104**, 18123–18128 (2007).
- Ehrlich, P. & Ehrlich, A. *Extinction: The Causes and Consequences of the Disappearance of Species* (Victor Gollancz, 1982).
- Lawton, J. H. Are there general laws in ecology? *Oikos* **84**, 177–192 (1999).

Supplementary Information is linked to the online version of the paper at www.nature.com/nature.

Acknowledgements We thank J. Byrnes, L. Gamfeldt and M. Emmerson for comments on an earlier version of this manuscript. We thank the Swiss SystemsX.ch initiative (IPP-2008/23) for supporting this project. The BIODEPTH project was funded by the European Commission within the Framework IV Environment and Climate Programme (ENV-CT95-0008) and by the Swiss Federal Office for Education and Science (Project EU-1311). The Jena Experiment was funded by the Deutsche Forschungsgemeinschaft (DFG, FOR 456), Friedrich Schiller University of Jena, Max Planck Society, University of Zurich, Swiss National Science Foundation (3100AO-107531) and ETH Zurich. The Wageningen experiment was funded by the Dutch Organisation for Scientific Research (NWO) within the framework of the Biodiversity Programme. Work on the Agrobiodiversity experiment was funded by the EU Commission through COST Action 852 and Science Foundation Ireland (09/RFP/E0B2546). The BioCON experiment was funded by the US Department of Energy (DOE/DE-FG02-96ER62291) and the US National Science Foundation (Biocomplexity 0322057, LTER DEB 9411972, DEB 0080382, DEB 0620652 and LTREB DEB 0716587). The MEND Irrigation, BioGEN and Rarity–Extinction experiments were funded by the US National Science Foundation (DEB 0639417). The Cedar Creek Biodiversity experiment was funded by the US National Science Foundation. M.L. was supported by The Natural Sciences and Engineering Research Council of Canada (Discovery Grant) and the Canada Research Chair program.

Author Contributions F.I. conceived the project; J.C., A.H., F.I., P.B.R., M.S.-L., B.S., D.T., J.v.R., A.W. and B.J.W. designed and conducted experiments; F.I. and V.C. analysed the data, with input from A.H. and M.L.; F.I. wrote the paper with input from all authors.

Author Information Reprints and permissions information is available at www.nature.com/reprints. The authors declare no competing financial interests. Readers are welcome to comment on the online version of this article at www.nature.com/nature. Correspondence and requests for materials should be addressed to F.I. (forest.isbell@gmail.com).

METHODS

Identifying the species that promoted ecosystem functioning. For each context, we modelled ecosystem functioning response variables as a function of the presence or absence of each study species at the plot level. We used a backward-elimination multiple regression analysis to identify a minimally adequate model, based on the AIC¹⁷. This procedure was performed with the stepAIC function in the MASS package of R 2.11.1. Specifically, for each context, we started with a full model that included a main effect for each study species and an intercept. The stepAIC function then removed each species, one at a time, from this full model and compared the AIC values of the resulting simpler models with the AIC value of the full model. If the AIC value for any of the simpler models was smaller than the AIC value for the full model, then the variable whose removal resulted in the largest decrease in AIC was permanently removed from the full model. This backward-deletion process was repeated until the removal of any species resulted in a model with a higher AIC value. The minimally adequate model that resulted from this process contained the most parsimonious set of species influencing ecosystem functioning. These species were considered to promote ecosystem functioning if they had effects in the direction that would usually be considered desirable from an ecosystem services perspective¹⁷. Positive effects were considered desirable for all functions except for soil inorganic nitrogen and light availability at ground level, where negative effects are consistent with lower levels of unconsumed resources¹⁷. We did not use separate definitions of desirable effects for different species (for example, positive effects of legumes on soil nitrogen might be considered desirable) to be consistent with previous studies^{17,18}, to be conservative and because it may not be possible to manage simultaneously for both positive and negative effects.

This modelling approach is conservative in several ways. Previous approaches for determining the number of species that promoted ecosystem functioning could have been biased by not allowing species to decrease ecosystem functioning¹⁸ or by not identifying which species actually influenced ecosystem functioning¹⁴. Furthermore, including species interactions in these or other models would probably increase the proportion of study species that promoted ecosystem functioning within each context^{12,26}. For example, some species perform poorly in monocultures, but interact positively with other species in mixtures (for example, grass–legume interactions)³¹. Our approach would underestimate the desirable effects of these species. Also, the presence or absence model that we used would be especially conservative for experimental designs that concentrate on varying evenness rather than richness, such as the simplex design used in the Agrobiodiversity study²⁶. Additionally, our results were qualitatively similar, but less conservative, when we used a model-averaging approach implemented in the glmulti package (version 0.6-3) of R³².

To compare the number of species that promoted ecosystem functioning across studies, we used a quasi-Poisson generalized linear model with ‘study’ as a main effect. This procedure was performed with the generalized linear model function in the stats package of R. The quasi-maximum-likelihood version of the Poisson generalized linear model accounts for over- or under-dispersion in the data. We used the confint.glm function in the MASS package of R to obtain the 95% confidence intervals. To quantify the proportion of study species that promoted ecosystem functioning, we regressed the mean number of species that promoted ecosystem functioning per context on the number of study species (that is, the number of planted species that were present at least once in biomass samples) with no intercept.

Comparing sets of species between pairs of contexts. After identifying the sets of species that promoted ecosystem functioning in each context, we quantified the overlap between these sets of species to test whether different sets of species promoted ecosystem functioning in different contexts. All overlap comparisons were made within studies. Overlap between contexts *a* and *b* was quantified by Sørensen’s similarity index¹⁷:

$$o = \frac{|E_a \cap E_b|}{0.5(|E_a| + |E_b|)}$$

where $|E_a|$ is the number of species that promoted ecosystem functioning in context *a* and $|E_a \cap E_b|$ is the number of species that promoted ecosystem functioning in both contexts. First, one-dimensional overlap was quantified between pairs of contexts that only differed in one way (Fig. 1b, c). For example, multi-year

overlap was quantified between each pair of contexts that differed only in which year ecosystem functioning was measured (that is, place, function and environmental change scenarios were the same in both contexts). This allowed us to test whether identical (overlap = 1), unique (overlap = 0) or somewhat different ($0 < \text{overlap} < 1$) sets of species promoted ecosystem functioning in different contexts. Next, multi-dimensional overlap was quantified between pairs of contexts that differed in two or three ways (Fig. 1d). This allowed us to test whether overlap decreased as the number of differences between contexts increased (Fig. 1).

For each type of overlap, we used non-parametric bootstrap, with correction for bias^{33,34}, to build 95% confidence intervals. We re-sampled the observed contexts with replacement to generate each of 1,000 bootstrap data sets. For each of these bootstrap data sets, we computed the average overlap across all pairs of contexts that were relevant (that is, for the particular type of overlap being considered). We used this bootstrap approach to control for the non-independence of pairwise comparisons that had one context in common. We then used an exact permutation approach³⁴ to test whether the observed overlap values differed from the expected null value (the null hypothesis being that overlap varied across contexts independent of context attributes: year, place, function and environmental change scenario). Within each study, we permuted context data (that is, the sequence of ones or zeros indicating whether each species had a desirable effect or not) with respect to context attributes. For each of 1,000 permutations, we computed the average overlap across all pairs of contexts that were relevant (that is, for the particular type of overlap being considered). We used the null distribution of overlap obtained from these random permutations to test whether the observed value was significantly lower (that is, in the lowest 2.5 percentiles) or significantly higher (that is, in the top 2.5 percentiles) than the null. We used this test because it does not assume that study species had independent responses to context attributes, and thus it should be robust to the presence of functional groups.

Note that there could be correlations between contexts owing to repeated measurements across years. These correlations could influence overlap estimates and tests that assume independent observations. For example, positive correlations between repeated measurements during consecutive years could lead to (1) over-estimates of multi-year (Y) overlap, and (2) smaller estimates of overlap between two different years at two different places than between two different years at one place (that is, Y and P overlap less than Y overlap). These potential correlations had little influence on our results because multi-year overlap estimates were much less than 1, and Y and P overlap estimates were not less than Y overlap estimates (Fig. 2). Nevertheless, we encourage future studies to consider these correlations when interpreting overlap estimates.

Accumulation of species across contexts. We quantified the accumulation of species across each of the four dimensions of contexts that we considered (Fig. 1). For example, above-ground biomass was sampled during 13 years at the Cedar Creek Biodiversity experiment. To determine the extent to which more species promoted above-ground biomass as more years were considered, we sampled all combinations of these 13 contexts (that is, all pairs, groups of three, etc.), and recorded the number of unique species that promoted ecosystem functioning, and the number of unique years, for each combination. This was repeated for each function, at each place, under each environmental change scenario. These results are summarized in Fig. 3a. A quasi-binomial generalized linear model was fitted to determine how the proportion of species that promoted ecosystem functioning increased with the number of years, including ‘study’ as a factor. This allowed us to describe the mean trends within and across studies. We also randomly sampled combinations (that is, 100 pairs, 100 groups of three, etc.) of all 557 contexts to determine how the number of species promoting ecosystem functioning increased when all of these factors were considered together.

31. Nyfeler, D. *et al.* Strong mixture effects among four species in fertilized agricultural grassland led to persistent and consistent transgressive overyielding. *J. Appl. Ecol.* **46**, 683–691 (2009).
32. Calcagno, V. & de Mazancourt, C. glmulti: an R package for easy automated model selection with (generalized) linear models. *J. Stat. Softw.* **34**, 1–29 (2010).
33. Efron, B. & Tibshirani, R. Bootstrap methods for standard errors, confidence intervals, and other measures of statistical accuracy. *Stat. Sci.* **1**, 54–77 (1986).
34. Manly, B. F. J. *Randomization, Bootstrap and Monte Carlo Methods in Biology* 2nd edn (Chapman and Hall, 1997).

Chromosomal rearrangements maintain a polymorphic supergene controlling butterfly mimicry

Mathieu Joron^{1,2,3}, Lise Frezal^{1*}, Robert T. Jones^{4*}, Nicola L. Chamberlain⁴, Siu F. Lee⁵, Christoph R. Haag⁶, Annabel Whibley¹, Michel Becuwe², Simon W. Baxter⁷, Laura Ferguson⁷, Paul A. Wilkinson⁴, Camilo Salazar⁸, Claire Davidsson⁹, Richard Clark⁹, Michael A. Quail⁹, Helen Beasley⁹, Rebecca Glithero⁹, Christine Lloyd⁹, Sarah Sims⁹, Matthew C. Jones⁹, Jane Rogers⁹, Chris D. Jiggins⁷ & Richard H. ffrench-Constant⁴

Supergenes are tight clusters of loci that facilitate the co-segregation of adaptive variation, providing integrated control of complex adaptive phenotypes¹. Polymorphic supergenes, in which specific combinations of traits are maintained within a single population, were first described for 'pin' and 'thrum' floral types in *Primula*¹ and *Fagopyrum*², but classic examples are also found in insect mimicry^{3–5} and snail morphology⁶. Understanding the evolutionary mechanisms that generate these co-adapted gene sets, as well as the mode of limiting the production of unfit recombinant forms, remains a substantial challenge^{7–10}. Here we show that individual wing-pattern morphs in the polymorphic mimetic butterfly *Heliconius numata* are associated with different genomic rearrangements at the supergene locus *P*. These rearrangements tighten the genetic linkage between at least two colour-pattern loci that are known to recombine in closely related species^{9–11}, with complete suppression of recombination being observed in experimental crosses across a 400-kilobase interval containing at least 18 genes. In natural populations, notable patterns of linkage disequilibrium (LD) are observed across the entire *P* region. The resulting divergent haplotype clades and inversion breakpoints are found in complete association with wing-pattern morphs. Our results indicate that allelic combinations at known wing-patterning loci have become locked together in a polymorphic rearrangement at the *P* locus, forming a supergene that acts as a simple switch between complex adaptive phenotypes found in sympatry. These findings highlight how genomic rearrangements can have a central role in the coexistence of adaptive phenotypes involving several genes acting in concert, by locally limiting recombination and gene flow.

The origin and maintenance of adaptive multi-locus polymorphism in the face of recombination is a long-standing puzzle in evolutionary biology^{7,12,13}. In some cases, supergene architecture has evolved with tight linkage that maintains specific combinations of alleles at neighbouring genes^{1–6}. A notable illustration is provided by polymorphic mimetic butterflies, in which several discrete forms, each resembling a different model, are maintained in sympatry. Examples include Batesian polymorphism in *Papilio dardanus*^{5,14} and *Papilio memnon*³ and Müllerian polymorphism in the neotropical species *Heliconius numata*^{4,15}. In each case, a single supergene locus controls coordinated differences in a complex phenotype which can involve modifications of wing pattern and shape, body colour and perhaps behaviour^{3,4}. Mimetic patterns represent sharp fitness peaks corresponding to locally abundant wing patterns, separated by adaptive valleys in which selection acts against recombinant individuals with intermediate, non-mimetic phenotypes¹⁶.

Theoretical debate has centred on the constraints imposed on supergene evolution by genomic organization, specifically whether loci must

be tightly linked from the outset or whether the association between elements can be acquired, either gradually or in a single mutational step^{7–10,16–19}. Chromosomal rearrangements, which can bring genes into closer physical association and influence local recombination, offer one route through which supergenes may be assembled from more loosely linked components^{7,8,17–19}. Although there are many cases of polymorphic inversions associated with adaptive variation^{12,20}, variation is in most cases geographical, rather than being maintained within populations, and effects on local adaptation are cumulative. In contrast, supergenes are characterized by a Mendelian switch between clearly defined combinations of traits in populations. Here we investigate the genomic organization and population genetics of the *P* supergene in *H. numata*^{4,9} and identify a key role for structural variation in strengthening and maintaining allelic associations within the supergene.

In *H. numata*, up to seven sympatric morphs coexist in local populations and each is an accurate mimic of one of several available model species in another butterfly family (Danainae: *Melinaea*)^{4,9}. Each morph is controlled by a specific allele at *P* with precise allelic dominance^{4,15}

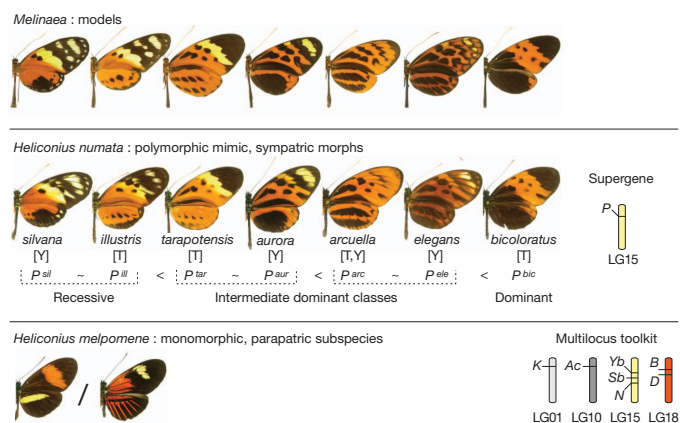


Figure 1 | Supergene alleles and mimicry polymorphism in *H. numata*. Polymorphic forms of *H. numata* each mimic different models in the distantly related genus *Melinaea* (Nymphalidae: Danainae). Each form is controlled by a specific allele of the supergene *P*, with increasing dominance shown from left to right^{4,9}. Two parapatric regions of northeastern Peru (T, Tarapoto and Andean valleys; Y, Yurimaguas and Amazon lowlands) harbour different mimicry assemblages¹⁵; dominance (<) is nearly complete between forms within each region, but is incomplete (~) between certain pairs of alleles from parapatric regions. In all other species studied in the genus *Heliconius*, wing pattern is controlled by several large-effect loci on different chromosomes. In *H. melpomene* the *HmYb–HmSb–HmN* complex is situated in the orthologous position to the *H. numata* *P* supergene⁹. LG, linkage group.

¹CNRS UMR 7205, Muséum National d'Histoire Naturelle, CP50, 45 Rue Buffon, 75005 Paris, France. ²Institute of Evolutionary Biology, University of Edinburgh, Ashworth Laboratories, King's Buildings, West Mains Road, Edinburgh EH9 3JT, UK. ³Institute of Biology, Leiden University, Postbus 9505, 2300 RA Leiden, The Netherlands. ⁴Centre for Ecology and Conservation, School of Biosciences, University of Exeter, Cornwall Campus, Penryn, Cornwall TR10 9EZ, UK. ⁵Department of Genetics, Bio21 Institute, University of Melbourne, 30 Flemington Road, Parkville, 3010 Victoria, Australia. ⁶Department of Biology, Ecology and Evolution, University of Fribourg, Chemin du Musée 10, CH-1700 Fribourg, Switzerland. ⁷Department of Zoology, University of Cambridge, Downing Street, Cambridge CB2 3EJ, UK. ⁸Smithsonian Tropical Research Institute, NAOS island, Causeway Amador, Panamá, República de Panamá. ⁹The Wellcome Trust Sanger Institute, Hinxton, Cambridge CB10 1HH, UK.

*These authors contributed equally to this work.

(Fig. 1). Rare non-mimetic individuals that combine pattern elements from different morphs are observed at a frequency of $<0.7\%$ in natural polymorphic populations^{4,15}. These individuals, presumed to be recombinants, confirm the existence of several functional elements in the locus. The genomic position of *P* was previously shown to correspond to a cluster of three loci, *HmN*, *HmYb* and *HmSb*, on linkage group 15 in the closely related species *Heliconius melpomene*⁹, in which they control distinct wing-pattern elements in geographical races. Other unlinked wing-pattern loci in related species do not have large effects on *H. numata* mimicry^{9,21}.

By fine-scale linkage mapping and positional cloning, we identified a chromosomal interval of about 400 kilobases (kb) containing the *H. numata* *P* supergene, defined by the absence of crossing over in 366 progeny from six broods (Fig. 2a). The orthologous region in *H. melpomene* shows notable rates of recombination and contains two distinct colour-pattern loci, *HmYb* and *HmSb*, ~ 0.9 centimorgans (cM) apart¹¹. Although genome-wide estimates of recombination rate in *Heliconius* are not available, markers adjacent to *P*, markers elsewhere on linkage group 15, and markers in other linkage groups (Supplementary Table 1)⁹ all show significantly higher rates of crossing over (chi-squared test of independence, $P = 3.8 \times 10^{-6}$), consistent with severe suppression of recombination at *P* in *H. numata*.

To examine the gene content and genomic organization of the supergene, we sequenced an approximately one-megabase (Mb) region centred on *P* by screening a bacterial artificial chromosome (BAC) library prepared from a mixture of individuals from a single polymorphic population of *H. numata* (Supplementary Table 2). Colinearity and gene content was generally conserved with *H. melpomene*¹¹, but two BACs overlapping the *P* interval showed distinct gene orders, both different from the order seen in *H. melpomene* (Figs 2a, 3 and Supplementary Fig. 1). A third gene order, corresponding to the *H. melpomene* reference, was detected by PCR (see below). Gene orientation near the breakpoints on the *H. numata* clones indicated a minimum of two rearrangement events compared to the reference, putatively involving 31 genes: a 400-kilobase (kb) segment containing 18 genes from *HN00023* to *HN00040* (breakpoint BP1), and a 180-kb segment containing 13 genes from *HN00041* to *HN00053* (breakpoint BP2) (Fig. 3a and Supplementary Fig. 1). The altered gene orders at *P* contrast with the colinearity of flanking sequences between *H. numata* and *H. melpomene* (Supplementary Fig. 2 and Supplementary Tables 3 and 4), as well as between more distantly related *Heliconius* species²². Furthermore, *H. melpomene* and the silk moth *Bombyx mori*, separated by about 100 million years of evolution, share a generally conserved gene order across this region^{11,23}. This supports the hypothesis that the

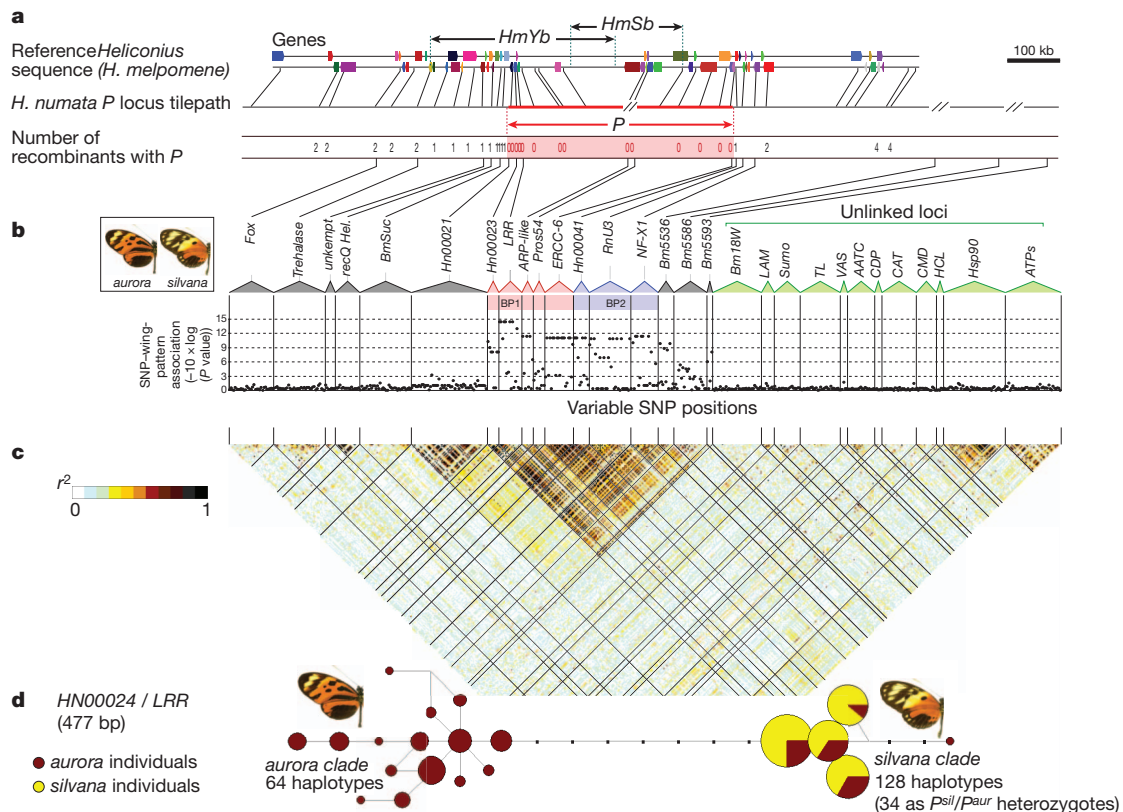


Figure 2 | Fine-scale mapping and nucleotide variation at the *P* supergene in *H. numata*. **a**, Fine-scale linkage mapping of the supergene *P* (indicated by red arrows) to the interval bounded by genes *HN00020* and *HN00041*. Recombinants were observed in crosses totalling 366 individuals. Blue arrows indicate the position of the recombining loci *HmYb* and *HmSb* in *H. melpomene*¹¹. *HmN*, which is known to be part of this cluster of loci, is not fine-mapped in *H. melpomene*¹¹. Coloured blocks represent annotated gene regions on forward and reverse strands (see Supplementary Fig. 1 and Supplementary Table 3 for details). **b**, Association of SNP variation with mimicry polymorphism in a sample of 25 *silvana* and 34 *aurora/arcuella* individuals from a single population. Markers genotyped across rearrangements BP1 (pink) and BP2 (blue) show perfect association of SNP variation with wing pattern. No association was found in the flanking region

from markers *Fox* (*HN00106*) to *BmSUC* (*HN00019*), or at 12 unlinked loci (green). The association decays more slowly in the direction of loci *Bm5536* (*GCP*), *Bm5586* (*NudC*) and *Bm5593* (*Srp68*). **c**, LD heat map. Perfect LD (genotypic correlation coefficient $r^2 = 1$) is found across 580 kb spanning the BP1 and BP2 rearrangements ($n = 59$). LD decays rapidly outside this interval, although strong within-marker LD remains at *HN00021*. Markers that are unlinked to *P* show little LD with each other or with *P*. **d**, Haplotype network for marker *LRR* (*HN00024*) in the Yurimaguas population, coloured according to wing-pattern phenotype. Haplotype clades separated by seven fixed differences are in complete association with wing pattern, taking into account dominance relationships. Similar haplotype clades were found for all loci genotyped within *P*, and across the Amazon basin, but not for genes flanking *P* or in unlinked regions (Supplementary Figs 4 and 6).

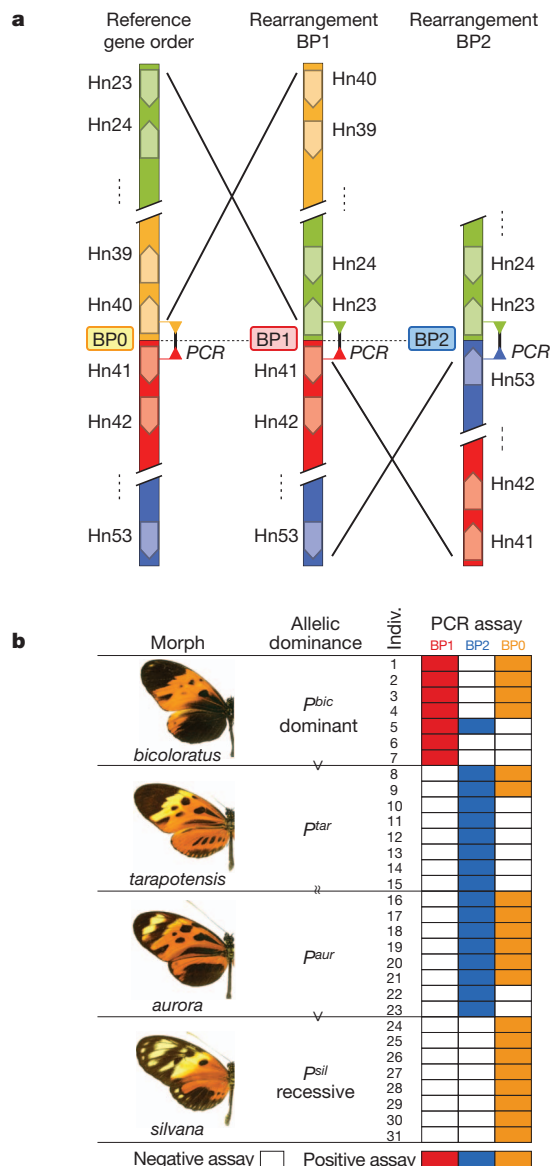


Figure 3 | Chromosomal rearrangements associated with the supergene in natural populations. **a**, Comparison of the gene orders found in the *H. numata* BAC library and wild populations. The rearrangements involve the 400-kb segment from genes *HM00023* to *HM00040* (*ERCC6*) (BP1, clones 24I10 and 45B17), and the adjacent 180-kb segment from gene *HN00041* (*penguin*) and *HN00053* (*lethal (2) giant larvae homologue*) (BP2, clone 38G4). Genes closest to the breakpoints are shown. **b**, Long-range PCR assays across alternative breakpoints (BP0, BP1 and BP2) in wild populations show a perfect association of the polymorphic gene orders with mimicry variation in four morphs from natural populations of Eastern Peru¹⁵, following the dominance relationships (Fig. 1). The Yurimaguas population segregates primarily for *silvana* and *aurora/arcuella* forms, associated with BP0 and BP2, respectively. The Tarapoto population segregates mainly for *tarapotensis* and *bicoloratus* forms, associated with BP2 and BP1, respectively. This population also harbours recessive *illustris* alleles associated with BP0 (Supplementary Table 6).

gene rearrangements are evolutionarily derived and associated with the evolution of this locus in the *H. numata* lineage.

The results from BAC-clone sequencing were extended to natural populations by performing breakpoint-specific PCR on butterflies collected in the field (Fig. 3a and Supplementary Table 5). Long-range PCR analyses of 31 individuals of four morphs revealed a complete association between alternative rearrangements and specific wing-pattern phenotypes (Fig. 3b). Rearrangement BP1 was found in every *H. numata bicoloratus* and in no other morph, as expected for the dominant *P* allele, whereas BP2 was found in all intermediate dominant

forms (*aurora* and *tarapotensis*). All recessive *silvana* individuals were BP0 homozygotes, confirming that the reference gene order segregates in *H. numata* populations. Some individuals with intermediate and dominant alleles had breakpoints that were lower in the dominance series, reflecting their heterozygosity. To confirm the association on a larger sample, short-range PCR assays primed closer to the breakpoints were performed on 156 individuals of six major morphs (Fig. 1 and Supplementary Tables 5–7). Short-range assays were highly consistent with long-range assays (Supplementary Table 6). Natural populations thus harbour at least three chromosomal arrangements in tight association with wing-pattern phenotypes. A short-range PCR product from BP1 was not amplified in two of the 32 *bicoloratus* individuals tested. This could reflect PCR failure due to sequence variation at BP1, or it may indicate that the BP1 breakpoint is not directly causative of the *bicoloratus* phenotype, despite being strongly associated with the causative variant(s).

To assess whether the recombination suppression that is observed in crosses operates at the population level, we estimated LD between nucleotide positions in and around *P*. A notable pattern of long-range LD was seen in tight association with the position of *P*, mapped from a survey of 17 markers sequenced in 59 individuals from the polymorphic population near Yurimaguas (Figs 1 and 2c). Complete LD was found between high-frequency single nucleotide polymorphisms (SNPs) across the 400-kb *P* interval, showing that long-range haplotypes are maintained across the supergene. This haplotype structure decays rapidly outside *P*: flanking markers lack the haplotype segregation found within *P* and show comparable levels of LD to the levels seen in 12 unlinked markers (Fig. 2c and Supplementary Fig. 3). Furthermore, within *P*, complete association was found between the divergent haplotypes and wing-pattern alleles. All recessive *silvana* individuals were homozygous for 39 SNPs in six genes across the *P* locus, whereas *aurora* individuals were heterozygous or homozygous for the alternative nucleotides (Fig. 2b, Supplementary Fig. 4 and Supplementary Table 5). Again, this complete association breaks down immediately outside *P* (Fig. 2b and Supplementary Figs 4 and 5). Therefore, the divergent haplotypes associated with wing-pattern alleles seem to be confined within the boundaries of the polymorphic rearrangements and the position of the supergene.

Finally, to confirm that the haplogroups are associated with phenotype and are not due to local population processes, we screened a population of *H. numata* from French Guiana, situated 2,900 km from Peru but harbouring phenotypically similar morphs (*silvana* and *numata*; Supplementary Table 5)⁴. The same two haplotype groups were found, and breakpoint PCR and haplotype clades were perfectly associated with corresponding phenotypes in both locations (Supplementary Fig. 6 and Supplementary Table 6). The association between mimicry polymorphism, local rearrangements and divergent haplotype blocks therefore seems to be conserved across the Amazonian range.

Our results show that the supergene is characterized by a 400-kb chromosomal block that is sharply structured into distinct haplotype clades separated by 1–4% divergence. These clades correspond to different wing-pattern alleles, segregate consistently with the allelic dominance and are associated with the chromosomal rearrangements (Fig. 2d and Supplementary Figs 3 and 4). This situation stands in stark contrast to the related species *H. melpomene* and *H. erato*, in which several independent wing-patterning loci are under directional selection, and in which markers surveyed in the orthologous region showed no fixed nucleotide differences between colour-pattern races, and no long-range LD^{10,24}. The *P* supergene architecture, associated with mimicry polymorphism under balancing selection in *H. numata*^{4,15}, is thus evolutionarily characterized by non-recombining co-adapted blocks that capture distinct wing-pattern genes that are known to recombine in other species of the clade^{10,24}.

In summary, the four strands of evidence, namely fine-scale comparative mapping, association of three chromosomal arrangements with morphs, SNP–phenotype association at *P*, and long-range LD

and divergent haplotype clades, all indicate that the rearrangements lock together distinct elements involved in wing-pattern evolution, providing long-awaited evidence for a situation that may apply to the evolution of supergenes in other systems^{7,16–19}. Together, the data begin to explain how distinct loci that control geographical variation in some species^{10,11} can become locked together in others. Our results highlight the role that structural variation can have in generating co-adapted gene complexes involved in adaptation and speciation^{8,12,19,20,25}, and open the way to the study of their functional integration.

The next challenge will be to identify the sites that are causally involved in the elements of pattern variation in *H. numata*, a goal hindered by reduced recombination within *P*, which limits the power of fine mapping to dissect the locus. Instead, functional studies of genes in the interval and analysis of rare recombinants will be important. Notably, *P* seems to be a hotspot of adaptation in several other species²⁶, including the melanic peppered moth²⁷, and, along with other colour-pattern regions, is linked to assortative mating and speciation in other *Heliconius* species^{28–30}. Unravelling the genetic nature of the elements that contribute to the supergene will therefore be key to understanding the mechanisms and sequence of events underlying the clustering of adaptive traits in rearrangements that are associated with ecological divergence.

METHODS SUMMARY

A BAC library was screened with radiolabelled probes derived from BAC end-sequences during chromosome walking. Clone sequences, obtained by capillary sequencing, were annotated with the aid of a Roche 454-sequenced cDNA library from the developing wing¹¹. Genomic sequences were aligned to a *H. melpomene* reference¹¹ to detect chromosomal rearrangements. Crossover events were fine-mapped using broods described elsewhere⁹. Recombination estimates from other genomic regions were derived by scoring crossing over along two unlinked clones, using markers separated by known physical distance.

PCR-based diagnostics for the rearrangement breakpoints BP1 and BP2 were designed from *H. numata* BAC sequences. BP0 was designed from the reference *H. melpomene* sequence. Long-range PCRs were primed in exons flanking each breakpoint, and verified by sequencing. Short-range PCRs were primed closer to the breakpoints in unique intergenic regions (Supplementary Table 7).

Genetic markers were sequenced by capillary sequencing. LD was estimated from unphased sequences using genotypic correlation tests between all pairs of variable sites. The association between wing-pattern and SNPs was tested using Fisher's exact tests, taking into account the dominance hierarchy of wing-pattern alleles. Haplotype networks were constructed by parsimony using Network.

Full Methods and any associated references are available in the online version of the paper at www.nature.com/nature.

Received 14 March; accepted 28 June 2011.

Published online 14 August 2011.

- Mather, K. The genetical architecture of heterostyly in *Primula sinensis*. *Evolution* **4**, 340–352 (1950).
- Garber, R. J. & Quisenberry, K. S. The inheritance of length of style in buckwheat. *J. Agric. Res.* **34**, 181–183 (1927).
- Clarke, C. A., Sheppard, P. M. & Thornton, I. W. B. The genetics of the mimetic butterfly *Papilio memnon*. *Philos. Trans. R. Soc. Lond. B* **254**, 37–89 (1968).
- Brown, K. S. & Benson, W. W. Adaptive polymorphism associated with multiple Müllerian mimicry in *Heliconius numata*. *Biotropica* **6**, 205–228 (1974).
- Nijhout, H. F. Polymorphic mimicry in *Papilio dardanus*: mosaic dominance, big effects, and origins. *Evol. Dev.* **5**, 579–592 (2003).
- Murray, J. & Clarke, B. Supergenes in polymorphic land snails—examples from genus *Partula*. *Genetics* **74**, S188–S189 (1973).
- Kirkpatrick, M. & Barton, N. Chromosome inversions, local adaptation and speciation. *Genetics* **173**, 419–434 (2006).
- Manfield, I. W. *et al.* Molecular characterization of DNA sequences from the *Primula vulgaris* S-locus. *J. Exp. Bot.* **56**, 1177–1188 (2005).
- Joron, M. *et al.* A conserved supergene locus controls colour pattern diversity in *Heliconius* butterflies. *PLoS Biol.* **4**, e303 (2006).
- Baxter, S. W. *et al.* Genomic hotspots for adaptation: the population genetics of Müllerian mimicry in the *Heliconius melpomene* clade. *PLoS Genet.* **6**, e1000794 (2010).
- Ferguson, L. *et al.* Characterization of a hotspot for mimicry: Assembly of a butterfly wing transcriptome to genomic sequence at the *HmYb/Sb* locus. *Mol. Ecol.* **19**, 240–254 (2010).
- Hoffmann, A. A. & Rieseberg, L. H. Revisiting the impact of inversions in evolution: from population genetic markers to drivers of adaptive shifts and speciation? *Annu. Rev. Ecol. Evol. Syst.* **39**, 21–42 (2008).

- Pinho, C. & Hey, J. Divergence with gene flow: Models and data. *Annu. Rev. Ecol. Evol. Syst.* **41**, 215–230 (2010).
- Clark, R. *et al.* Colour pattern specification in the Mocker swallowtail *Papilio dardanus*: the transcription factor *invested* is a candidate for the mimicry locus *H. Proc. R. Soc. B* **275**, 1181–1188 (2008).
- Joron, M., Wynne, I. R., Lamas, G. & Mallet, J. Variable selection and the coexistence of multiple mimetic forms of the butterfly *Heliconius numata*. *Evol. Ecol.* **13**, 721–754 (1999).
- Turner, J. R. G. in *The biology of butterflies* Vol. 11 (eds Vane-Wright, R. I. & Ackery, P. R.) 141–161 (Academic, 1984).
- Charlesworth, D. & Charlesworth, B. Theoretical genetics of Batesian mimicry. II. Evolution of supergenes. *J. Theor. Biol.* **55**, 305–324 (1975).
- Alvarez, G. & Zapata, C. Conditions for protected inversion polymorphism under supergene selection. *Genetics* **146**, 717–722 (1997).
- Hatadani, L. M., Baptista, J. C. R., Souza, W. N. & Klaczko, L. B. Colour polymorphism in *Drosophila mediopunctata*: genetic (chromosomal) analysis and nonrandom association with chromosome inversions. *Heredity* **93**, 525–534 (2004).
- Lowry, D. B. & Willis, J. H. A widespread chromosomal inversion polymorphism contributes to a major life-history transition, local adaptation, and reproductive isolation. *PLoS Biol.* **8**, e1000500 (2010).
- Jones, R. T., Salazar, P., French-Constant, R. H., Jiggins, C. D. & Joron, M. Evolution of a mimicry supergene from a multilocus architecture. *Proc. R. Soc. B*. doi:10.1098/rspb.2011.0882 (2011).
- Papa, R. *et al.* Highly conserved gene order and numerous novel repetitive elements in genomic regions linked to wing pattern variation in *Heliconius* butterflies. *BMC Genomics* **9**, 345 (2008).
- Pringle, E. G. *et al.* Synteny and chromosome evolution in the lepidoptera: Evidence from mapping in *Heliconius melpomene*. *Genetics* **177**, 417–426 (2007).
- Counterterman, B. A. *et al.* Genomic hotspots for adaptation: the population genetics of Müllerian mimicry in *Heliconius erato*. *PLoS Genet.* **6**, e1000796 (2010).
- Dobzhansky, T. Genetics of natural populations. XIV. A response of certain gene arrangements in the third chromosome of *Drosophila pseudoobscura* to natural selection. *Genetics* **32**, 142–160 (1947).
- Saenko, S. V., Brakefield, P. M. & Beldade, P. Single locus affects embryonic segment polarity and multiple aspects of an adult evolutionary novelty. *BMC Biol.* **8**, 111 (2010).
- van't Hof, A. E., Edmonds, N., Dalíková, M., Marec, F. & Saccheri, I. J. Industrial melanism in British peppered moths has a singular and recent mutational origin. *Science* **332**, 958–960 (2011).
- Kronforst, M. R. *et al.* Linkage of butterfly mate preference and wing color preference cue at the genomic location of wingless. *Proc. Natl Acad. Sci. USA* **103**, 6575–6580 (2006).
- Chamberlain, N. L., Hill, R. I., Kapan, D. D., Gilbert, L. E. & Kronforst, M. R. Polymorphic butterfly reveals the missing link in ecological speciation. *Science* **326**, 847–850 (2009).
- Merrill, R. M., Van Schooten, B., Scott, J. A. & Jiggins, C. D. Pervasive genetic associations between traits causing reproductive isolation in *Heliconius* butterflies. *Proc. R. Soc. B* **278**, 511–518 (2010).

Supplementary Information is linked to the online version of the paper at www.nature.com/nature.

Acknowledgements We thank M. Blaxter and D. Charlesworth for advice throughout the study; The GenePool and S. Humphray for DNA sequencing; S. Kumar and A. Papanicolaou for bioinformatics support; M. Beltrán, A. Bulski, M. Veuille and the Botanique-Entomologie-Mycologie molecular facility (BoEM) for laboratory support; S. Johnston for genome-size estimates in *H. numata*; D. Obbard for providing R scripts; M. Abanto, S. Gallusser, C. Ramirez, L. de Silva, J. Barbut, B. Gilles and G. Lamas for help with butterfly rearing, fieldwork and collecting permits; and the Peruvian National Institute of Natural Resources (INRENA) for granting collecting and export permits (076-2007-INRENA-IFFS-DCB). Fieldwork in French Guiana was supported by a CNRS 'Nouragues Research Grant'. This work was supported by an EMBO long-term fellowship (ALTF-431-2004), EMBO-matching funds from NWO (Netherlands), a Royal Society University Research Fellowship (516002.K5917/ROG), a CNRS grant (ATIP Biodiversité 2008, France) and a European Research Council Starting Grant (ERC-Stg 'MimEvol') to M.J., a BBSRC grant (BBE0118451) to C.D.J. and R.H.ff.-C., a Leverhulme Trust grant (F/00144AY) to R.H.ff.-C., and a Royal Society University Research Fellowship and a Leverhulme Research Leadership grant to C.D.J.

Author Contributions M.J., C.D.J. and R.H.ff.-C. designed the study and contributed to all stages of the project. M.J., L. Frezal and R.T.J. performed the principal experiments and data analysis, with assistance from N.L.C., S.W.B., S.F.L., M.B., C.S., L. Ferguson, C.R.H., A.W. and P.A.W. BAC clone sequencing was carried out by C.D., R.G., C.L., R.C., H.B., S.S., J.R., M.C.J. and M.A.Q. M.J., A.W., C.D.J. and R.H.ff.-C. co-wrote the manuscript with input from all authors.

Author Information GenBank accessions for BAC clone sequences: FP885863, FP476061, FP565803, FP476023, CU856181, FP885878, FP476047, FP885857, CU856182, CU655868, FP885879, FP885861, FP885880, FP885855, CU914733, FP475989, CU655869, CU914734, CU633161, CU638865, CU856175, FP884220 and FP236755. Accessions for 1364 marker sequences: JN173798–JN175161. Reprints and permissions information is available at www.nature.com/reprints. The authors declare no competing financial interests. Readers are welcome to comment on the online version of this article at www.nature.com/nature. Correspondence and requests for materials should be addressed to M.J. (joron@mnhn.fr).

METHODS

Chromosome walking. A BAC library was constructed by Amplicon Express from five individual larvae from a polymorphic population of *H. numata* segregating for the forms *bicoloratus*, *tarapotensis* and *arcuella*. The BAC library has an estimated 119-kb average insert size and $\times 7$ coverage of the 319-Mb genome. It was printed onto nylon filters and screened using 11 radiolabelled PCR probes designed to span the orthologous genomic sequences from an *H. melpomene* BAC library^{9,11}. The BAC library was also fingerprinted by restriction digest, and overlapping clones were predicted from analysis of a fingerprinted contig (FPC) database. Fifty-three BAC clones were identified and tested for positive amplification of the original probes. Nineteen *H. numata* clones were sequenced by the Wellcome Trust Sanger Institute to high-throughput-genomic (HTG) phase 3 quality, totalling 2.9 Mb of overlapping genomic sequence. Because of the multiple chromosomal arrangements found in this region, and the fact that the clones sequenced come from chromosomes with differing gene orders as a consequence, it is impossible to reconstruct a single linear tilepath of clones at this stage. On the basis of reciprocal BLASTs of the clone sequences, the tilepath covers 0.95 Mb centred on *P*, consisting of four 'floating' contigs, two of which lie within the recombination interval of *P* and show different gene orders. A gap in the BAC chromosomal walk, estimated to be approximately 150 kb, remains between clones 7C9 and 14K13 despite extensive screening of the library. However, the gene markers *ARP-like* (*Hm00028*) and *Pros54* (*Hm00030*), predicted from the reference *Heliconius* sequence to lie in the middle of this gap, do indeed map in full linkage with other markers on either side of the gap, indicating the gene content of the gap is probably conserved. Two additional contigs of clones were identified and sequenced approximately 350 kb and 900 kb from the end of the tilepath further down the chromosome (Fig. 2a and Supplementary Table 2). Sequence similarity was plotted using the software Vista^{31,32}, with a 70% identity threshold and a 100-bp sliding window (Supplementary Fig. 2).

Linkage mapping. Male-informative markers were used to score crossing over events between markers linked and unlinked to *P*. Female Lepidoptera have achiasmatic meiosis, so crossing over only occurs during gametogenesis in the male parent. Thirty-six PCR-based markers were designed from BAC sequences and genotyped by visualization of differences in amplicon size, by restriction-fragment length polymorphism, or by sequence variation, in 366 individuals from six mapping families (B377, B465, B472, B502, B523 and A298 (refs 9, 11)). This was used to circumscribe the *P* supergene and orientate the tilepath by recombination. Special emphasis was given to the regions near the first crossover on either side of the supergene, for a precise positioning of the mapping boundary. The three recombinants with *P* on one side, and two recombinants on the other side, ensured that *P* was circumscribed and in full linkage with markers in an interval estimated to be about 400 kb (using a 0.92 scaling factor for *H. numata* versus *H. melpomene* genomic sequence, on the basis of sequences available for this region). The same procedure was used to score recombination events in unlinked regions using two sequenced BAC clones (bHN20L19 and bHM7E22) from unlinked chromosomes and three mapping families (Supplementary Table 1).

BAC gene annotation. Transcriptome sequencing, assembly and genomic annotation were performed as described elsewhere¹¹. Briefly, annotation and gene predictions in all sequenced BACs (Supplementary Fig. 1 and Supplementary Table 3) were carried out with the Maker annotation pipeline³³, using 600K expressed sequenced tags generated with Roche 454 FLX pyrosequencing (200-base average read length) and assembled using the Mira assembler³⁴ to yield 24,992 objects. Complementary DNA was generated from wing-disc tissue extracted from juvenile stages from the Peruvian populations used throughout this study. Large variations in non-coding content, as well as in the presence and identity of transposable elements, were noted between clones within *H. numata* (Supplementary Table 4), causing some *H. numata* clones (for example, 14K13) to show a higher overall similarity to the orthologous *H. melpomene* sequences (bHM29B7) than to other orthologous *H. numata* clones (46M23 and 38G4). This indicates that the two *H. numata* chromosomal segments with differing gene orders may be anciently derived.

Sequencing and breakpoint analysis. Annotation of the BACs was used to identify exons within and outside the *P* mapping interval; exon markers were PCR-amplified and direct-sequenced for population-genetic analysis (Supplementary Table 8). Unlinked markers were chosen following the method in ref. 35. A total of 17 amplicons lying on linkage group 15, both within and outside the region containing *P*, plus 13 amplicons on unlinked chromosomes, were sequenced in 48–144 individuals (Supplementary Table 5) from a polymorphic population in eastern Peru. This population segregates predominantly for the forms *silvana* and *aurora* (including sub-variants *isabellinus* and *elegans*). In subsequent analyses, we combined the *aurora* variants under the single class *aurora*, because the numerous phenotypic gradations that are found between these forms contrast with the clearly distinct phenotypic form *silvana*^{4,15,36}. Furthermore, PCR assays of

the rearrangement breakpoints and the absence of diagnostic nucleotide differences also indicated that these variants could be combined.

Breakpoint PCR assays were carried out with primers designed from exonic sequences on either side of each breakpoint (Supplementary Table 7). Fragments were amplified from 31 individuals with four different wing patterns (*bicoloratus*, *tarapotensis*, *aurora* and *silvana*) using long-range PCR (Qiagen) following the manufacturer's conditions, and were end-sequenced to confirm fragment identity. A second, larger sample of 201 individuals (including 161 from Peru and 40 from French Guiana) was assayed by standard (short-range) PCR amplification (Fermentas DreamTaq) using primers positioned closer to the breakpoints in unique non-coding DNA (Supplementary Table 7). Capillary sequencing of markers and breakpoint assays was performed on an ABI 3730 capillary sequencer with BigDye chemistry by the University of Edinburgh sequencing service (<http://genepool.bio.ed.ac.uk/>). Sequencing ambiguities were resolved manually using CodonCode Aligner (<http://www.codoncode.com>).

Phenotype-by-genotype associations. Association between genotype and phenotype was estimated for all polymorphic sites (SNPs) within each marker, taking into account the dominance relationships between different morphs. The Amazonian form of *H. numata* termed *silvana* (widespread from French Guiana to the Andean foothills) and its geographic replacement *illustris* (Andean valleys) are recessive to all other forms^{4,9,36}, which predicts that all *silvana* and *illustris* individuals are homozygous at *P*, whereas individuals of other, co-occurring forms can be either heterozygous or homozygous for a different allele. We estimated the association between genotype and phenotype by testing the hypothesis that the major allele should be homozygous in *silvana* individuals and heterozygous or absent in *aurora* individuals. For each polymorphic site with a minor allele frequency of at least 0.1, we calculated the proportion of individuals whose genotype conformed to this hypothesis and tested the null hypothesis of no phenotype-genotype association using Fisher's exact test. This method allows testing of the phenotype-by-genotype association while using knowledge of the dominance relationships between *P* alleles.

Linkage disequilibrium (LD) across the *P* supergene. LD was assessed for all pairs of polymorphic sites within and surrounding the *P* region, as well as in 12 unlinked markers (Fig. 2c) in 59 specimens from a polymorphic population near Yurimaguas, eastern Peru (Supplementary Table 5). We used genotypic correlation-based testing for LD with several alleles with unknown phase between sites³⁷. Significance was tested by a permutation test for the genotypic correlation statistic r^2 (ref. 37).

Haplotype networks. The phase of SNP variation was determined by analysing the segregation of alleles from parent to offspring in markers sequenced from the mapping families, which originate from the same populations as the population samples. Haplotypes from the population samples were inferred by coalescent-based Bayesian methods using the PHASE 2.1 algorithm³⁸, optimized by including sequences with known phase from mapping families. The high level of LD across the region ensured a robust inference of haplotypic diversity for all markers. Haplotype networks were constructed by parsimony using the Network package^{39,40} (<http://www.fluxus-engineering.com/>). The level of genetic differentiation between the *silvana* and non-*silvana* groups was estimated in DNAsp⁴¹ using the *F*_{st} statistics⁴², and its significance was tested by permutation (Supplementary Fig. 5). *F*_{st} was not used to test for genetic differentiation among different populations, but rather to assess genetic differentiation between two groups of individuals in a single population (*silvana* versus non-*silvana*). Even high levels of genetic differentiation do not indicate the absence of random mating, but rather that these sites are linked and/or that they co-vary with the functional loci that determine the different mimetic morphs.

- Frazer, K. A., Pachter, L., Poliakov, A., Rubin, E. M. & Dubchak, I. VISTA: computational tools for comparative genomics. *Nucleic Acids Res.* **32**, W273–W279 (2004).
- Mayor, C. et al. VISTA: visualizing global DNA sequence alignments of arbitrary length. *Bioinformatics* **16**, 1046 (2000).
- Cantarel, B. L. et al. MAKER: An easy-to-use annotation pipeline designed for emerging model organism genomes. *Genome Res.* **18**, 188–196 (2008).
- Chevreaux, B. et al. Using the miraEST assembler for reliable and automated mRNA transcript assembly and SNP detection in sequenced ESTs. *Genome Res.* **14**, 1147–1159 (2004).
- Salazar, C., Jiggins, C. D., Taylor, J. E., Kronforst, M. R. & Linares, M. Gene flow and the genealogical history of *Heliconius heurippa*. *BMC Evol. Biol.* **8**, 132 (2008).
- Brown, K. S. An illustrated key to the silvaniform *Heliconius* (Lepidoptera: Nymphalidae) with descriptions of new subspecies. *Trans. Am. Entomol. Soc.* **102**, 373–484 (1976).
- Zaykin, D. V., Pudovkin, A. & Weir, B. S. Correlation-based inference for linkage disequilibrium with multiple alleles. *Genetics* **180**, 533–545 (2008).
- Stephens, M. & Donnelly, P. A comparison of Bayesian methods for haplotype reconstruction from population genotype data. *Am. J. Hum. Genet.* **73**, 1162–1169 (2003).

39. Polzin, T. & Daneshmand, S. V. On Steiner trees and minimum spanning trees in hypergraphs. *Oper. Res. Lett.* **31**, 12–20 (2003).
40. Forster, P., Torroni, A., Renfrew, C. & Rohl, A. Phylogenetic star contraction applied to Asian and Papuan mtDNA evolution. *Mol. Biol. Evol.* **18**, 1864–1881 (2001).
41. Librado, P. & Rozas, J. DnaSP v5: a software for comprehensive analysis of DNA polymorphism data. *Bioinformatics* **25**, 1451–1452 (2009).
42. Hudson, R. R., Slatkin, M. & Maddison, W. P. Estimation of levels of gene flow from DNA-sequence data. *Genetics* **132**, 583–589 (1992).

The genome sequence of Atlantic cod reveals a unique immune system

Bastiaan Star¹, Alexander J. Nederbragt¹, Sissel Jentoft¹, Unni Grimholt¹, Martin Malmstrøm¹, Tone F. Gregers², Trine B. Rounge¹, Jonas Paulsen^{1,3}, Monica H. Solbakken¹, Animesh Sharma⁴, Ola F. Wetten^{5,6}, Anders Lanzén^{7,8}, Roger Winer⁹, James Knight⁹, Jan-Hinnerk Vogel¹⁰, Bronwen Aken¹⁰, Øivind Andersen¹¹, Karin Lagesen¹, Ave Tooming-Klunderud¹, Rolf B. Edvardsen¹², Kirubakaran G. Tina^{1,13}, Mari Espelund¹, Chirag Nepal^{4,8}, Christopher Previti⁸, Bård Ove Karlsen¹⁴, Truls Moum¹⁴, Morten Skage¹, Paul R. Berg¹, Tor Gjøn¹⁵, Heiner Kuhl¹⁶, Jim Thorsen¹⁷, Ketil Malde¹², Richard Reinhardt¹⁶, Lei Du⁹, Steinar D. Johansen^{14,18}, Steve Searle¹⁰, Sigbjørn Lien¹³, Frank Nilsen¹⁹, Inge Jonassen^{4,8}, Stig W. Omholt^{1,13}, Nils Chr. Stenseth¹ & Kjetil S. Jakobsen¹

Atlantic cod (*Gadus morhua*) is a large, cold-adapted teleost that sustains long-standing commercial fisheries and incipient aquaculture^{1,2}. Here we present the genome sequence of Atlantic cod, showing evidence for complex thermal adaptations in its haemoglobin gene cluster and an unusual immune architecture compared to other sequenced vertebrates. The genome assembly was obtained exclusively by 454 sequencing of shotgun and paired-end libraries, and automated annotation identified 22,154 genes. The major histocompatibility complex (MHC) II is a conserved feature of the adaptive immune system of jawed vertebrates^{3,4}, but we show that Atlantic cod has lost the genes for MHC II, CD4 and invariant chain (Ii) that are essential for the function of this pathway. Nevertheless, Atlantic cod is not exceptionally susceptible to disease under natural conditions⁵. We find a highly expanded number of MHC I genes and a unique composition of its Toll-like receptor (TLR) families. This indicates how the Atlantic cod immune system has evolved compensatory mechanisms in both adaptive and innate immunity in the absence of MHC II. These observations affect fundamental assumptions about the evolution of the adaptive immune system and its components in vertebrates.

We sequenced the genome of a heterozygous male Atlantic cod (NEAC_001, Supplementary Notes 1 and 2), applying a whole-genome shotgun approach to 40× coverage (estimated genome size of 830 megabases (Mb), Supplementary Note 4 and Supplementary Fig. 2) using 454 technology (Supplementary Note 3). Two programs (Newbler⁶ and Celera⁷, Supplementary Notes 5 and 6) produced assemblies with short contigs, yet with scaffolds of comparable size to those of Sanger-sequenced teleost genomes (Supplementary Note 10 and Supplementary Fig. 8). Although fragmentation due to short tandem repeats is difficult to address (Supplementary Note 7), we resolved numerous gaps attributable to heterozygosity (Supplementary Note 8). The assemblies differ in scaffold and contig length (Table 1), although their scaffolds align to a large extent (Supplementary Note 9 and Supplementary Fig. 7). We obtained about one million single nucleotide polymorphisms (SNPs) by mapping 454 and Illumina reads from the sequenced individual to the Newbler assembly (Supplementary Note 11). Both assemblies cover more than 98% of the reads from an extensive transcriptome data set, indicating that the proteome is well represented (Supplementary Note 13). The assemblies are consistent with four

independently assembled bacterial artificial chromosome (BAC) insert clones (Supplementary Note 14 and Supplementary Fig. 9), and with the expected insert size of paired BAC-end reads (Supplementary Note 15 and Supplementary Fig. 10).

A standard annotation approach based on protein evidence was complemented by a whole-genome alignment of the Atlantic cod with the stickleback (*Gasterosteus aculeatus*), after repeat-masking 25.4% of the Newbler assembly (Supplementary Note 16 and Supplementary Table 6). In this way, 17,920 out of 20,787 protein-coding stickleback genes were mapped onto reorganized scaffolds (Supplementary Note 17). Additional protein-coding genes, pseudogenes and non-coding RNAs were annotated using the standard Ensembl pipeline. These approaches resulted in a final gene set of 22,154 genes (Supplementary Table 7). Comparative analysis of gene ontology classes indicates that the major functional pathways are represented in the annotated gene set (Supplementary Note 18 and Supplementary Fig. 11). We anchored 332 Mb of the Newbler assembly to 23 linkage groups of an existing Atlantic cod linkage map using 924 SNPs⁸ (Supplementary Note 19 and Supplementary Table 8). These linkage groups have distinct orthology to chromosomes of other teleosts, on the basis of the number of co-occurring genes, showing that the whole-genome shotgun assembly reflects the expected chromosomal ancestry (Fig. 1, Supplementary Note 20 and Supplementary Table 9).

Table 1 | Assembly statistics

	Number	Bases (Mb)	N50L (bp)*	N50 (n)†	ML (bp)‡
Newbler					
Contigs§	284,239	536	2,778	50,237	76,504
Scaffolds	6,467	611	687,709	218	4,999,318
Entire assembly	157,887	753	459,495	344	4,999,318
Celera					
Contigs§	135,024	555	7,128	19,938	117,463
Scaffolds	3,832	608	488,312	373	2,810,583
Entire assembly	17,039	629	469,840	395	2,810,583

*Minimum sequence length in which half of the assembled bases occur.

†Number of sequences with lengths of N50L or longer.

‡Maximum length.

§Contigs longer than 500 bp.

|| Scaffolds and unplaced contigs.

¹Centre for Ecological and Evolutionary Synthesis (CEES), Department of Biology, University of Oslo, PO Box 1066, Blindern, N-0316 Oslo, Norway. ²Department of Molecular Biosciences, Centre for Immune Regulation, University of Oslo, Blindern, N-0316 Oslo, Norway. ³Bioinformatics Core Facility, Institute for Medical Informatics, Oslo University Hospital, Montebello, N-0310 Oslo, Norway.

⁴Department of Informatics, University of Bergen, N-5020 Bergen, Norway. ⁵Department of Natural Sciences and Technology, Hedmark University College, P.O. Box 4010, Bedriftsenteret, N-2306 Hamar, Norway. ⁶Department of Animal and Aquacultural Sciences, University of Life Sciences, P.O. Box 5003, N-1432 Ås, Norway. ⁷Department of Biology, Centre for Geobiology, University of Bergen, N-5020 Bergen, Norway. ⁸Computational Biology Unit, Uni Research AS, N-5020 Bergen, Norway. ⁹454 Life Sciences, 15 Commercial Street, Branford, Connecticut 06405, USA. ¹⁰Wellcome Trust Sanger Institute, Wellcome Trust Genome Campus, Hinxton, Cambridge CB10 1SA, UK. ¹¹Nofima Marine, P.O. Box 5010, N-1430 Ås, Norway. ¹²Institute of Marine Research, P.O. Box 1870, Nordnes, N-5817 Bergen, Norway. ¹³Department of Animal and Aquacultural Sciences, CIGENE, Centre for Integrative Genetics, Norwegian University of Life Sciences, PO Box 5003, 1432 Ås, Norway. ¹⁴Faculty of Biosciences and Aquaculture, University of Nordland, N-8049 Bodo, Norway. ¹⁵Department of Pharmaceutical Biosciences, School of Pharmacy, University of Oslo, P.O. Box 1068, Blindern, N-0316 Oslo, Norway. ¹⁶Max Planck Institute for Molecular Genetics, Ihnestrasse 63-73, D-14195 Berlin-Dahlem, Germany. ¹⁷Institute for Basic Sciences and Aquatic Medicine, School of Veterinary Sciences, N-0033 Oslo, Norway. ¹⁸Department of Medical Biology, Faculty of Health Sciences, University of Tromsø, N-9037 Tromsø, Norway. ¹⁹Department of Biology, PO Box 7803, University of Bergen, N-5020 Bergen, Norway.

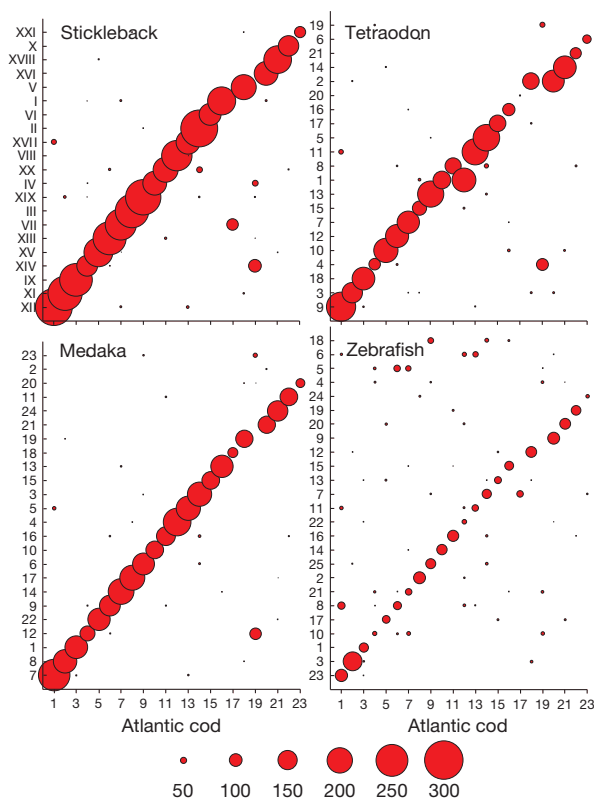


Figure 1 | Synteny between Atlantic cod and selected teleosts. The co-occurrence of orthologous genes (with a minimum of 50% sequence identity over 50% of the alignment, sphere size indicates the numbers of syntenic genes) in 23 Atlantic cod linkage groups⁸ (x-axis) reveals synteny with the chromosomes of four teleosts (y-axis). Several genes located on the stickleback chromosome XIV, tetraodon chromosome 4 and medaka chromosome 12 indicate a lineage-specific chromosomal rearrangement in Atlantic cod.

Well-studied haemoglobin polymorphisms in Atlantic cod are indicative of functional molecular adaptation to thermal variation^{9–12}. The genome contains nine α - and β -globin genes that are organized in two unlinked clusters, $\beta 5$ – $\alpha 1$ – $\beta 1$ – $\alpha 4$ and $\beta 3$ – $\beta 4$ – $\alpha 2$ – $\alpha 3$ – $\beta 2$ (refs 13, 14). We discovered an indel polymorphism of 73 base pairs (bp) in the intergenic promoter region of the $\alpha 1$ – $\beta 1$ globin pair (Fig. 2a and Supplementary Note 21). This promoter polymorphism occurs in highly significant linkage disequilibrium with two known polymorphic sites in the $\beta 1$ gene, the Val55Met and Ala62Lys substitutions¹, in eight Atlantic cod populations (Supplementary Note 22 and Supplementary Fig. 12). In fact, in the three most northern Atlantic populations and in both Baltic populations, the cod $\beta 1$ -globin gene predominantly occurs as a single homozygous genotype consisting of the long promoter and the Val 55–Ala 62 allele (Supplementary Table 10). By placing the two promoter variants in front of a luciferase reporter gene and transfecting the constructs into salmon kidney cells (Supplementary Note 23), we found that temperature and promoter type have a significant interaction effect (generalized linear model, $F_{2,36} = 7.85$, $P = 0.007$, Fig. 2b) and that the long promoter has twofold higher transcriptional activity compared to the short promoter at 15 °C and 20 °C. Increased globin synthesis of the Val 55–Ala 62 allele would compensate for its lower oxygen affinity^{10,11} at high temperatures. Thus, the promoter polymorphism provides a molecular compensatory mechanism that helps to maintain the total oxygen-carrying capacity¹⁵. The tight linkage between the two types of polymorphism provides a compelling example of the coevolution of structural and regulatory adaptation, and highlights the relationship between temperature and functional molecular variation in the haemoglobin system¹⁶.

The Atlantic cod immune system has unusual properties that set it apart from that of other teleosts: high levels of IgM¹⁷, a minimal antibody

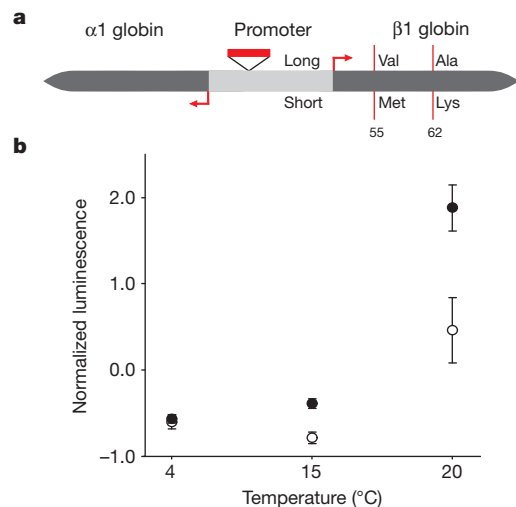


Figure 2 | Functional haemoglobin polymorphisms in Atlantic cod. **a**, Schematic of the head-to-head organized $\alpha 1$ and $\beta 1$ globin genes, the intergenic promoter region and transcription start sites (red arrows). A promoter polymorphism consisting of a 73-bp indel (red box) segregates in linkage disequilibrium with two amino-acid-substitution polymorphisms (vertical lines) at positions 55 and 62 in $\beta 1$ globin that affect its oxygen-binding affinity. This linkage disequilibrium results in two predominant haplotypes, long–Val–Ala and short–Met–Lys. **b**, Normalized luciferase luminescence ratios in salmon kidney cells. Cells were transfected using the long promoter (black circles) or the short promoter (white circles) and incubated at 4 °C, 15 °C or 20 °C ($n = 3$ for each treatment level). Error bars show 95% confidence intervals.

response after pathogen exposure^{5,17,18} and abundant phagocytic neutrophils in the peripheral blood^{19,20}. Despite speculation, the exact causes for these differences remain unknown⁵. We found that most genes involved in the vertebrate immune response are present in Atlantic cod (Supplementary Note 24, Supplementary Fig. 13 and Supplementary Table 11). Nevertheless, we did not find genes for the MHC II isoforms, their assembly and trafficking chaperone Ii²¹ and the MHC II-interacting protein CD4, which is essential for helper T-cell activation. By comparing a comprehensive set of vertebrate MHC II, CD4 and Ii sequences to the genome assemblies and all unassembled 454 and Illumina sequencing reads (a data set of about 49.5 gigabases), we detected a truncated pseudogene for CD4 (Supplementary Note 25), which is located in a region of conserved synteny (Supplementary Note 27 and Supplementary Fig. 18). No traces of MHC II and Ii were found in syntenous regions (Supplementary Note 27 and Supplementary Figs 16, 17, 19 and 20) and quantitative PCR (qPCR) targeting a conserved domain in MHC II did not amplify the target sequence (Supplementary Note 26 and Supplementary Fig. 15). The absence of MHC II and Ii, and the pseudogenic nature of CD4, show that Atlantic cod has lost the function of the classical pathway for adaptive immunity against bacterial and parasitic infections. Nevertheless, Atlantic cod deals adequately with its prevailing pathogen load in its natural ecological settings⁵. Previous transcriptional (complementary DNA) studies in Atlantic cod have indicated an expansion of the number of MHC I loci^{22,23}. By targeting the conserved MHC I $\alpha 3$ domain in genomic DNA using qPCR, we quantified more accurately the number of loci belonging to the teleost U-lineage²⁴ (Supplementary Note 28). Notably, Atlantic cod has about 100 classical MHC I loci, which is a highly expanded number compared to other teleosts (Fig. 3a). A phylogenetic analysis of teleost MHC I sequences supports the existence of two clades in cod (Fig. 3b and Supplementary Note 29). Within each clade, the mutation patterns show statistically significant signs of positive selection that are indicative of subfunctionalization. These findings indicate that loss of MHC II functionality has coincided with a more versatile usage of the cytosolic pathway of MHC I. Two different MHC I antigen-presentation pathways—the classical pathway and the alternative cross-presentation

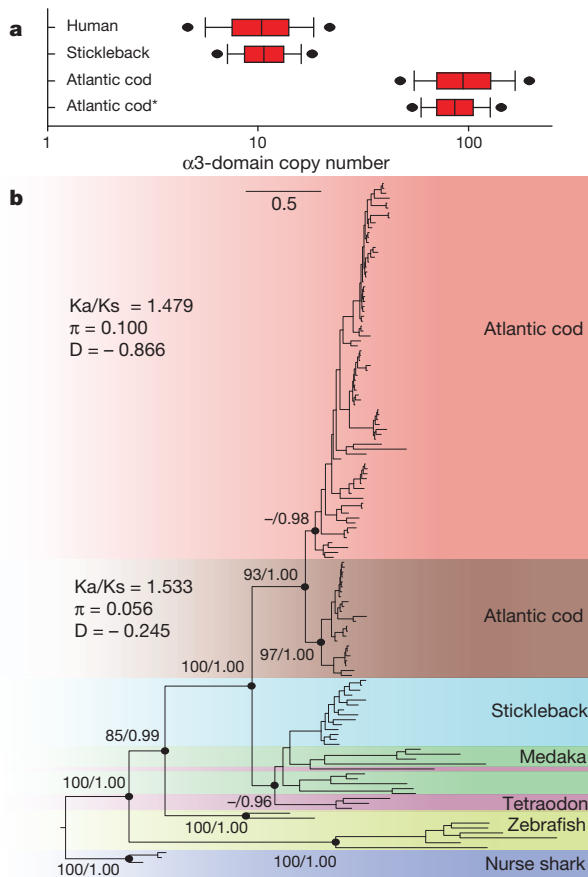


Figure 3 | MHC I diversity in Atlantic cod. **a**, Copy-number estimates of the MHC I $\alpha 3$ domain. Estimates are based on qPCR ratios (see Supplementary Note 28) of the MHC I $\alpha 3$ domain and a single-copy reference gene. For Atlantic cod, $\beta 2$ -microglobulin and topoisomerase III- α (*) were used as reference genes; for human and stickleback, $\beta 2$ -microglobulin was used. The estimates for human and stickleback agree with the expected number of $\alpha 3$ domains found in both reference genomes (Supplementary Table 15). Black dots indicate 95% confidence intervals calculated by bootstrapping ($n = 50,000$). **b**, Phylogeny of amino-acid sequences of MHC I $\alpha 1$ - $\alpha 3$ domains in teleosts. The Atlantic cod sequences are derived from cDNA and comprise classical U-lineage MHC I only. The other teleost sequences were obtained from Ensembl and NCBI, and contain classical and non-classical U-lineage MHC I. Alignments were visually inspected and corrected where necessary. Maximum likelihood (ML) values and Bayesian posterior probabilities (dots) support the main branches on the ML topology. Distance represents the number of substitutions per site (scale bar). The ratio of non-synonymous to synonymous variable sites (Ka/Ks), the average nucleotide diversity per site (π) and Tajima's D (D) were calculated for the two main clades in Atlantic cod.

pathway—can initiate immune responses in mammals²⁵. The cross-presentation pathway represents a structural and cellular modification of the MHC I machinery that allows activation of CD8⁺ T cells upon bacterial infection. The cytokine gene profile of Atlantic cod (Supplementary Table 11) supports the possibility of generating different subsets of CD8⁺ T cells that either provide direct protection or regulate other immune cells, and thus compensate for the loss of CD4⁺ T cells.

In addition to the MHC I expansion, we found an unusual composition of the highly conserved TLR families that have a fundamental role in the innate immune response and the initial detection of pathogens. Teleost TLR-encoding genes occur in well-supported phylogenetic clusters, most of which share functional properties with mammalian orthologues, although some are fish-specific²⁶. The Atlantic cod TLR genes form monophyletic groups within the known teleost functional groups (Fig. 4, Supplementary Note 30 and Supplementary Fig. 22). Genes for several TLRs that recognize bacterial surface antigens (TLR1, TLR2 and TLR5) are, however, absent, leaving only the teleost-specific

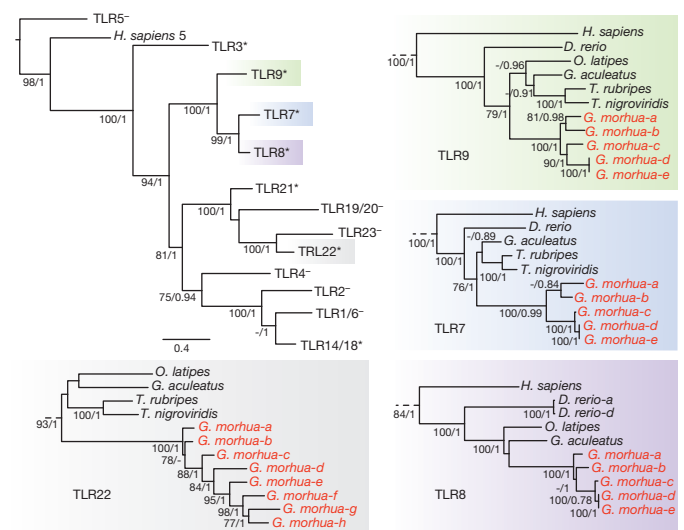


Figure 4 | Phylogeny of TLR families in Atlantic cod. TLR protein sequences were selected on the basis of the conserved Toll-IL-1 receptor (TIR) domain for Atlantic cod, including known sequences from stickleback, zebrafish, tetraodon, fugu, medaka and human as references. TLR clades with (*) or without (–) Atlantic cod sequences are denoted according to human or teleost orthologues (summary tree topology, top left panel). Distance represents the average number of substitutions per site (scale bar). ML values and Bayesian posterior probabilities greater than 75/0.75 support the ML topology. Detailed topologies of TLR7 (blue), TLR8 (purple), TLR9 (green) and TLR22 (grey) show gene expansions for Atlantic cod (red). Multiple TLR copies within species are subdivided by letters, and follow Ensembl nomenclature for *D. rerio*.

TLR14 and TLR18 as members of the TLR1 family in Atlantic cod. Moreover, several families of TLRs that recognize nucleic acids (TLR7, TLR8, TLR9 and TLR22) have markedly expanded, resulting in the highest number of TLRs found in a teleost so far. This TLR repertoire indicates that the Atlantic cod immune system relies relatively heavily on nucleic-acid-detecting TLRs to recognize bacterial pathogens. Notably, the gene expansion of TLR9 coincides with an expansion of interleukin-8 genes (IL-8, Supplementary Table 11). IL-8 is an important chemokine in the innate immune response and is directly induced by TLR9 in human neutrophils²⁷. The corresponding expansions of IL-8 and TLR9 indicate that this signalling cascade is particularly important in Atlantic cod.

The loss of MHC II function and lack of a CD4⁺ T-cell response represent a fundamental change in how the adaptive immune system is initiated and regulated in Atlantic cod. The marked expansion of MHC I genes and unusual TLR composition signify a shift of its immune system in handling microbial pathogens. An expanded MHC I repertoire in the presence of a non-polymorphic MHC II is found in an evolutionarily-distant vertebrate, the axolotl (*Ambystoma mexicanum*)^{28,29}. These observations indicate that anomalous immune systems (possibly analogous to that of Atlantic cod) have evolved independently. Additionally, we did not recover evidence for expressed MHC II, CD4 and Ii in the transcriptomes of three other gadoids, indicating that the unusual immune system is a derived characteristic of the gadoid lineage (Supplementary Tables 18 and 19).

We have provided the first annotated genome of a species that supports extensive fisheries and is on the verge of becoming an important aquaculture species. This work provides a major foundation for addressing key issues related to the management of natural Atlantic cod populations, such as the concept of fisheries-induced evolution, which dictates that selective harvesting can change the evolutionary trajectory of major life-history traits of natural populations³⁰. Moreover, our novel findings regarding the immune system will allow for more targeted vaccine development, aiding disease management and the process of domestication of Atlantic cod. These findings

change fundamental assumptions regarding the evolution of the vertebrate immune system.

METHODS SUMMARY

Detailed methods on the sequencing and assembly of data from genomic and transcriptomic origins; annotation, synteny analyses, transfection experiments, bioinformatic analyses and phylogenetic analyses presented in this manuscript are described in the Supplementary Information.

Received 11 February; accepted 28 June 2011.

Published online 10 August 2011.

- Kurlansky, M. *Cod: A Biography of the Fish that Changed the World*. (Penguin, 1998).
- Johansen, S. D. *et al.* Large-scale sequence analyses of Atlantic cod. *New Biotechnol.* **25**, 263–271 (2009).
- Flajnik, M. F. & Kasahara, M. Origin and evolution of the adaptive immune system: genetic events and selective pressures. *Nature Rev. Genet.* **11**, 47–59 (2010).
- Litman, G. W., Rast, J. P. & Fugmann, S. D. The origins of vertebrate adaptive immunity. *Nature Rev. Immunol.* **10**, 543–553 (2010).
- Pilstrom, L., Warr, G. W. & Stromberg, S. Why is the antibody response of Atlantic cod so poor? The search for a genetic explanation. *Fish. Sci.* **71**, 961–971 (2005).
- Miller, J. R., Koren, S. & Sutton, G. Assembly algorithms for next-generation sequencing data. *Genomics* **95**, 315–327 (2010).
- Miller, J. R. *et al.* Aggressive assembly of pyrosequencing reads with mates. *Bioinformatics* **24**, 2818–2824 (2008).
- Hubert, S., Higgins, B., Borza, T. & Bowman, S. Development of a SNP resource and a genetic linkage map for Atlantic cod (*Gadus morhua*). *BMC Genomics* **11**, 191 (2010).
- Sick, K. Haemoglobin polymorphism in fishes. *Nature* **192**, 894–896 (1961).
- Brix, O., Thorkildsen, S. & Colosimo, A. Temperature acclimation modulates the oxygen binding properties of the Atlantic cod (*Gadus morhua* L.) genotypes *Hbl*1/1*, *Hbl*1/2*, and *Hbl*2/2* by changing the concentrations of their major hemoglobin components (results from growth studies at different temperatures). *Comp. Biochem. Physiol. A* **138**, 241–251 (2004).
- Andersen, O. *et al.* Haemoglobin polymorphisms affect the oxygen-binding properties in Atlantic cod populations. *Proc. R. Soc. B* **276**, 833–841 (2009).
- Petersen, M. F. & Steffensen, J. F. Preferred temperature of juvenile Atlantic cod *Gadus morhua* with different haemoglobin genotypes at normoxia and moderate hypoxia. *J. Exp. Biol.* **206**, 359–364 (2003).
- Borza, T., Stone, C., Gamperl, A. K. & Bowman, S. Atlantic cod (*Gadus morhua*) hemoglobin genes: multiplicity and polymorphism. *BMC Genet.* **10**, 51 (2009).
- Wetten, O. *et al.* Genomic organization and gene expression of the multiple globins in Atlantic cod: conservation of globin-flanking genes in chordates infers the origin of the vertebrate globin clusters. *BMC Evol. Biol.* **10**, 315 (2010).
- Gamperl, A. K., Busby, C. D., Hori, T. S. F., Afonso, L. O. B. & Hall, J. R. Hemoglobin genotype has minimal influence on the physiological response of juvenile Atlantic cod (*Gadus morhua*) to environmental challenges. *Physiol. Biochem. Zool.* **82**, 483–494 (2009).
- Weber, R. E. & Fago, A. Functional adaptation and its molecular basis in vertebrate hemoglobins, neuroglobins and cytoglobins. *Respir. Physiol. Neurobiol.* **144**, 141–159 (2004).
- Magnadottir, B., Gudmundsdottir, S., Gudmundsdottir, B. K. & Helgason, S. Natural antibodies of cod (*Gadus morhua* L.): specificity, activity and affinity. *Comp. Biochem. Physiol. B* **154**, 309–316 (2009).
- Solem, S. T. & Stenvik, J. Antibody repertoire development in teleosts—a review with emphasis on salmonids and *Gadus morhua* L. *Dev. Comp. Immunol.* **30**, 57–76 (2006).
- Rønneseth, A., Wergeland, H. I. & Pettersen, E. F. Neutrophils and B-cells in Atlantic cod (*Gadus morhua* L.). *Fish Shellfish Immunol.* **23**, 493–503 (2007).
- Øverland, H. S., Pettersen, E. F., Rønneseth, A. & Wergeland, H. I. Phagocytosis by B-cells and neutrophils in Atlantic salmon (*Salmo salar* L.) and Atlantic cod (*Gadus morhua* L.). *Fish Shellfish Immunol.* **28**, 193–204 (2010).
- Landsverk, O. J., Bakke, O. & Gregers, T. F. MHC II and the endocytic pathway: regulation by invariant chain. *Scand. J. Immunol.* **70**, 184–193 (2009).
- Persson, A. C., Stet, R. J. M. & Pilstrom, L. Characterization of MHC class I and β 2-microglobulin sequences in Atlantic cod reveals an unusually high number of expressed class I genes. *Immunogenetics* **50**, 49–59 (1999).
- Miller, K. M., Kaukinen, K. H. & Schulze, A. D. Expansion and contraction of major histocompatibility complex genes: a teleostean example. *Immunogenetics* **53**, 941–963 (2002).
- Dijkstra, J. M. *et al.* A third broad lineage of major histocompatibility complex (MHC) class I in teleost fish; MHC class II linkage and processed genes. *Immunogenetics* **59**, 305–321 (2007).
- Amigorena, S. & Savina, A. Intracellular mechanisms of antigen cross presentation in dendritic cells. *Curr. Opin. Immunol.* **22**, 109–117 (2010).
- Rebl, A., Goldammer, T. & Seyfert, H. M. Toll-like receptor signaling in bony fish. *Vet. Immunol. Immunopathol.* **134**, 139–150 (2010).
- József, L., Khreiss, T., El Kebir, D. & Filep, J. G. Activation of TLR-9 induces IL-8 secretion through peroxynitrite signaling in human neutrophils. *J. Immunol.* **176**, 1195–1202 (2006).
- Tournefier, A. *et al.* Structure of MHC class I and class II cDNAs and possible immunodeficiency linked to class II expression in the Mexican axolotl. *Immunol. Rev.* **166**, 259–277 (1998).
- Kaufman, J., Volk, H. & Wallny, H. J. A. “Minimal essential Mhc” and an “unrecognized Mhc”: two extremes in selection for polymorphism. *Immunol. Rev.* **143**, 63–88 (1995).
- Stenseth, N. C. & Dunlop, E. S. Evolution: unnatural selection. *Nature* **457**, 803–804 (2009).

Supplementary Information is linked to the online version of the paper at www.nature.com/nature.

Acknowledgements This work was supported by a grant from the Research Council of Norway (FUGE program) to K.S.J. The authors wish to thank the following people and organizations: the 454 Life Science Sequencing Center (Branford, USA); the 454 and Illumina nodes of the Norwegian Sequencing Centre (University of Oslo); M. Egholm (formerly 454 Life Science); the Norwegian Metacenter for Computational Science (Notur) and the Norwegian Storage Infrastructure (Norstore); the Research Computing Services group, especially B. -H. Mevik, at the Center for Information Technology (University of Oslo); B. Walenz (Celera); the Canadian Cod Genomics and Broodstock Development Consortium; P. Olsvik, K. Lie and E. Holen at the Norwegian National Institute of Nutrition and Seafood Research (NIFES); J. Gaup and H. Bakke (CEES, University of Oslo); M. Kent (CIGENE, Norwegian University of Life Sciences); S. Bowman (Genome Atlantic); the FUGE bioinformatics platforms group, especially S. Grindhaug; I. Sandlie and O. B. Landsverk (Centre for Immune Regulation, University of Oslo); and Roche Norway.

Author Contributions DNA and RNA isolation, library construction and sequencing: A.T.-K., M.S., M.H.S., T.B.R., M.M., M.E., B.S., A.J.N. and J.T. Sanger BAC (end-) sequencing: H.K. and R.R. Assembly: A.J.N., B.S., A.S. and A.L. Linkage map analyses: K.G.T. and B.S. SNP analyses: K.G.T., P.R.B., S.L. and A.J.N. Annotation: J.-H.V., B.A. and S.S. Repeat analyses: B.S. Synteny analyses: J.P. and B.S. Haemoglobin analyses: Ø.A., O.F.W., B.S. and T.G. Bioinformatics: A.J.N., B.S., A.S., T.B.R., J.P., C.P., C.N., R.B.E., R.W., J.K., K.L., A.L., I.J., M.M., K.M., P.R.B., K.G.T. and M.H.S. Immune analyses: U.G., M.M., M.H.S., M.E., B.S., B.O.K., T.M., K.L., S.D.J. and T.B.R. Interpretation of immune results: U.G., T.F.G., S.J., B.S. and K.S.J. 454 contributions: L.D. Revisions: Ø.A., T.M., S.D.J., F.N., I.J., S.J., N.C.S. and S.W.O. Project initiation: S.W.O., I.J., F.N., S.L., N.C.S. and K.S.J. Project coordination: S.J. Consortium leader: K.S.J. This manuscript is dedicated to the memory of L. Pilstrom and R. J. M. Stet. Their research inspired our work to understand further the Atlantic cod immune system.

Author Information The unassembled sequencing reads and Newbler assembly have been deposited at ENA-EMBL under the accession numbers CAEA01000001–CAEA01554869. The annotation is available through Ensembl at <http://www.ensembl.org/index.html>. These and more resources are also available through <http://codgenome.no>. Reprints and permissions information is available at www.nature.com/reprints. This paper is distributed under the terms of the Creative Commons Attribution-Non-Commercial-Share-Alike licence, and is freely available to all readers at www.nature.com/nature. The authors declare no competing financial interests. Readers are welcome to comment on the online version of this article at www.nature.com/nature. Correspondence and requests for materials should be addressed to K.S.J. (k.s.jakobsen@bio.uio.no).

Mutations in *UBQLN2* cause dominant X-linked juvenile and adult-onset ALS and ALS/dementia

Han-Xiang Deng^{1*}, Wenjie Chen^{1*}, Seong-Tshool Hong^{1†}, Kym M. Boycott², George H. Gorrie^{1†}, Nailah Siddique¹, Yi Yang¹, Faisal Fecto^{1,3}, Yong Shi¹, Hong Zhai¹, Hujun Jiang^{1†}, Makito Hirano^{1†}, Evadnie Rampersaud⁴, Gerard H. Jansen⁵, Sandra Donkervoort¹, Eileen H. Bigio⁶, Benjamin R. Brooks⁷, Kaouther Ajroud¹, Robert L. Sufit¹, Jonathan L. Haines⁸, Enrico Mugnaini^{3,9}, Margaret A. Pericak-Vance⁴ & Teepu Siddique^{1,3,9}

Amyotrophic lateral sclerosis (ALS) is a paralytic and usually fatal disorder caused by motor-neuron degeneration in the brain and spinal cord. Most cases of ALS are sporadic but about 5–10% are familial. Mutations in superoxide dismutase 1 (*SOD1*)^{1,2}, TAR DNA-binding protein (*TARDBP*, also known as *TDP43*)^{3,4} and fused in sarcoma (*FUS*, also known as translocated in liposarcoma (*TLS*))^{5,6} account for approximately 30% of classic familial ALS. Mutations in several other genes have also been reported as rare causes of ALS or ALS-like syndromes^{7–15}. The causes of the remaining cases of familial ALS and of the vast majority of sporadic ALS are unknown. Despite extensive studies of previously identified ALS-causing genes, the pathogenic mechanism underlying motor-neuron degeneration in ALS remains largely obscure. Dementia, usually of the frontotemporal lobar type, may occur in some ALS cases. It is unclear whether ALS and dementia share common aetiology and pathogenesis in ALS/dementia. Here we show that mutations in *UBQLN2*, which encodes the ubiquitin-like protein ubiquilin 2, cause dominantly inherited, chromosome-X-linked ALS and ALS/dementia. We describe novel ubiquilin 2 pathology in the spinal cords of ALS cases and in the brains of ALS/dementia cases with or without *UBQLN2* mutations. Ubiquilin 2 is a member of the ubiquilin family, which regulates the degradation of ubiquitinated proteins. Functional analysis showed that mutations in *UBQLN2* lead to an impairment of protein degradation. Therefore, our findings link abnormalities in ubiquilin 2 to defects in the protein degradation pathway, abnormal protein aggregation and neurodegeneration, indicating a common pathogenic mechanism that can be exploited for therapeutic intervention.

We identified a five-generation family (family 186) with ALS, including 19 affected individuals (Supplementary Information). The disease is transmitted in a dominant fashion with reduced penetrance in females. Mutations in the known ALS-linked genes were excluded. No evidence of genetic linkage was found with a genome-wide set of autosomal microsatellite markers. There was no evidence for male-to-male transmission of the disease, so we screened the family with markers from the X chromosome. Linkage was established with several microsatellite markers on the X chromosome, with the highest two-point lod score of 5.0 occurring with marker DXS9736 at $\Theta = 0$ (Supplementary Table 1). Detailed mapping with dense microsatellite markers and Illumina's Sentrix HumanHap300 Genotyping BeadChip defined the disease-causing gene in a 21.3-megabase (Mb) minimum candidate

region (MCR) between markers rs6417786 and DXS1275, located in the pericentric region from Xp11.23 to Xq13.1.

No other large ALS families without male-to-male transmission were available to us to narrow down the MCR. We therefore focused on finding the causative gene in family 186. Of the 206 genes in this MCR, 191 were protein-coding. Genes in the MCR were analysed on the basis of their expression profile, function, structure and the potential relevance of their encoded proteins to disease. Forty-one genes were sequenced and a unique mutation in *UBQLN2* was identified. This mutation, a C to A substitution at position 1,490 at the level of coding DNA (c.1490C>A), is predicted to result in an amino-acid substitution of proline with histidine at codon 497 at the protein level (p.P497H) (Fig. 1a). The c.1490 C>A mutation co-segregated with the disease in this large X-linked-ALS pedigree (Fig. 1a). This mutation was not present in the SNP database, nor was it present in 928 ethnically matched control samples (representing 1,332 X chromosomes).

UBQLN2 is an intronless gene. To test whether mutations of *UBQLN2* are causative for other ALS patients, we analysed 188 probands from families with ALS or ALS/dementia, but without male-to-male transmission. Mutations in *SOD1*, *TDP43* and *FUS* were excluded in this cohort. The sequenced region covered the entire coding sequence (see Methods). We found four other *UBQLN2* mutations in four unrelated families, including c.1489 C>T (p.P497S), c.1516 C>A (p.P506T), c.1525 C>T (p.P509S) and c.1573 C>T (p.P525S) (Fig. 1 and Supplementary Fig. 1). All the amino-acid residues at the mutated sites are conserved (Fig. 1c). None of these mutations was present in the SNP database or in 928 control samples. Notably, all five ALS-linked *UBQLN2* mutations identified in this study involved proline residues in a unique PXX repeat region (Fig. 1c, d).

Clinical data were obtained from 40 individuals in the five families with *UBQLN2* mutations, including 35 patients and five obligate carriers. We estimated a penetrance of approximately 90% by the age of 70 years. The age of onset of the disease ranged from 16 to 71 years. A significant difference in age at onset was noted between male and female patients, with male patients having an earlier age of onset (33.9 ± 14.0 versus 47.3 ± 10.8 years, $P = 0.003$, two-tailed Student's *t*-test) (Supplementary Table 2). However, differences in the duration of the disease were not statistically significant (43.1 ± 42.1 versus 48.5 ± 19.9 months, $P = 0.61$). Eight patients with both ALS and dementia were identified. Dementia in these patients was similar to the frontotemporal lobar

¹Division of Neuromuscular Medicine, Davee Department of Neurology and Clinical Neurosciences, Northwestern University Feinberg School of Medicine, Chicago, Illinois 60611, USA. ²Department of Pediatrics, University of Ottawa and Children's Hospital of Eastern Ontario Research Institute, Ottawa, Ontario K1H 8L1, Canada. ³Interdepartmental Neuroscience Program, Northwestern University Feinberg School of Medicine, Chicago, Illinois 60611, USA. ⁴John P. Hussman Institute for Human Genomics, University of Miami, Miller School of Medicine, Miami, Florida 33136, USA. ⁵Division of Anatomic Pathology, The Ottawa Hospital, Ottawa, Ontario K1Y 4E9, Canada. ⁶Division of Neuropathology, Department of Pathology, Northwestern University Feinberg School of Medicine, Chicago, Illinois 60611, USA. ⁷Department of Neurology, Neuroscience and Spine Institute, Carolinas Medical Center, Charlotte, North Carolina 28207, USA. ⁸Center for Human Genetics Research, Vanderbilt University, Nashville, Tennessee 37232, USA. ⁹Department of Cell and Molecular Biology, Northwestern University Feinberg School of Medicine, Chicago, Illinois 60611, USA. [†]Present addresses: Laboratory of Genetics and Department of Microbiology, Chonbuk National University Medical School, Chonbuk 561-712, South Korea (S.-T.H.); Institute of Neurological Sciences, Southern General Hospital, Glasgow G51 4TF, UK (G.H.G.); Department of Health Sciences, National Natural Science Foundation of China, Beijing 100085, China (H.J.); Department of Neurology, Sakai Hospital Kinki University Faculty of Medicine, Osaka 590-0132, Japan (M.H.).

*These authors contributed equally to this work.

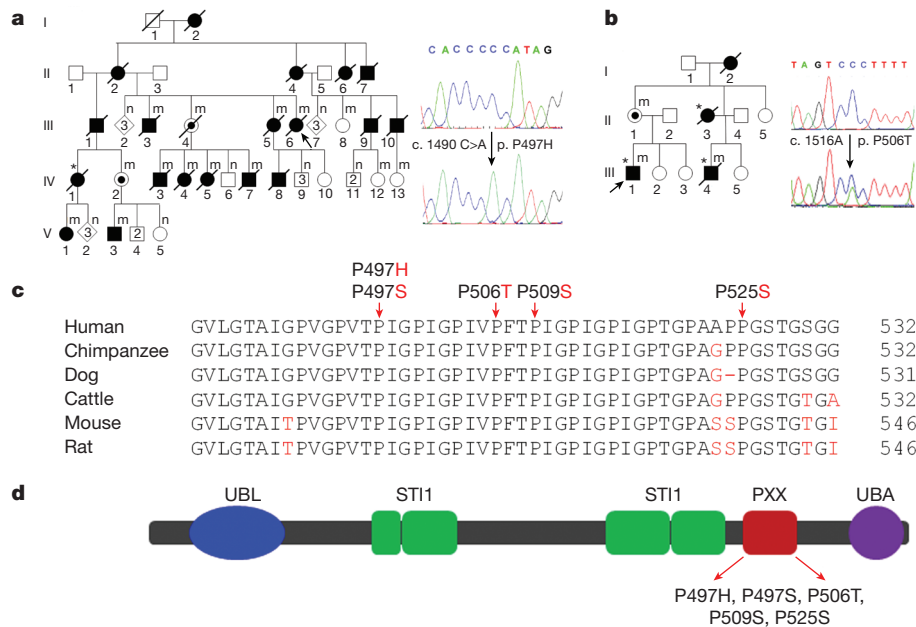


Figure 1 | Mutations of *UBQLN2* in patients with ALS and ALS/dementia. **a**, The mutation c.1490 C>A, resulting in p.P497H, was identified in a large family with ALS (family 186). This family was used to map X-linked ALS. The pedigree is shown on the left and DNA sequences are shown on the right: wild-type sequence (upper panel) and a representative hemizygous mutation in a male patient, V3 (lower panel). All affected members whose DNA samples were available for sequencing had the mutation. Two obligate carriers (III 4 and IV 2) were identified as having the same mutation. For simplicity and clarity, more than one unaffected individuals of both genders are represented by a single diamond and more than one unaffected male individual is represented by a single square. Filled symbols, affected individuals; open symbols, unaffected individuals; m, individuals with a mutation in *UBQLN2*; n, individuals without a mutation in *UBQLN2*. **b**, The mutation c.1516 C>A (p.P506T) was identified in family 6316: the pedigree is shown in the left panel and sequences in the right panel (showing a heterozygous mutation from a female obligate carrier, II 1). In

a and **b**, probands are indicated with arrows and patients with dementia are indicated with asterisks. **c**, Evolutionary conservation of amino acids in the mutated region of ubiquitin 2 in various species. Comparison of human (*Homo sapiens*) ubiquitin 2 and its orthologues in chimpanzee (*Pan troglodytes*), dog (*Canis lupus familiaris*), cattle (*Bos taurus*), mouse (*Mus musculus*) and rat (*Rattus norvegicus*). Amino acids identical to those in the human protein are shown in black and non-identical ones are in red. The positions of the C-terminal amino acids are shown on the right. Mutated amino acids are indicated by arrows. **d**, Predicted structural and functional domains of ubiquitin 2, a protein of 624 amino acids. Predicted structural and functional domains include a ubiquitin-like domain (UBL, 33–103), four heat-shock-chaperonin-binding motifs (ST1), twelve PXX repeats (491–526) and a ubiquitin-associated domain (UBA). ALS- and ALS/dementia-linked mutations are clustered in the 12 PXX repeats.

type (FTD), including abnormalities in both behaviour and executive function. The dementia was progressive, and eventually global in most ALS/dementia patients. In some cases, the dementia preceded motor symptoms, but all patients eventually developed motor disability. Pathological analysis of spinal-cord autopsy samples from two patients with either the P497H or P506T mutation revealed axonal loss in the corticospinal tract, loss of anterior horn cells and astrogliosis in the anterior horn of the spinal cord (Supplementary Fig. 2).

Protein aggregates or inclusions have been recognized as a pathological hallmark of several neurodegenerative disorders, such as extracellular amyloid- β plaques and intracellular tau neurofibrillary tangles in Alzheimer's disease, and α -synuclein-containing Lewy bodies in Parkinson's disease¹⁶. In ALS, protein aggregates or inclusions are most common in spinal motor neurons, and are typically skein-like in morphology. These ubiquitin-positive inclusions, among others, are considered to be a hallmark of ALS pathology. Notably, several proteins that are mutated in a small subset of ALS, such as SOD1, TDP43, FUS and optineurin (OPTN) are prominent components of these inclusions^{6,12,17–20}. To test whether ubiquitin 2 is present in the characteristic skein-like inclusions, we performed immunohistochemical analysis of post-mortem spinal-cord sections from two patients with a P497H or P506T mutation. Two different ubiquitin 2 antibodies were used. One was a commercially available mouse monoclonal antibody raised with a polypeptide of 71 amino acids from the carboxy terminus (amino acids 554–624, ubiquitin 2-C). The other was a rabbit polyclonal antibody that we generated using a polypeptide of 17 amino acids from the amino terminus (amino acids 8–24, ubiquitin 2-N). This polypeptide is unique to ubiquitin 2 and is not

present in other members of the ubiquitin family or in any other known protein. The ubiquitin 2-N antibody immunoreacted with human and mouse ubiquitin 2 (Supplementary Fig. 3). We also detected a single band of the expected size in western blots using ubiquitin 2-N and ubiquitin 2-C antibodies with human spinal-cord autopsy tissues (Supplementary Fig. 3). Using immunohistochemistry, we saw skein-like inclusions that were immunoreactive with both the ubiquitin 2-C and ubiquitin 2-N antibodies (Supplementary Fig. 4), indicating that ubiquitin 2 is involved in inclusion formation in X-linked ALS. We then examined whether the inclusions in cases of X-linked ALS were also immunoreactive with antibodies against other proteins that are known to be involved in the formation of inclusions in other types of ALS. We found that the skein-like inclusions in the X-linked ALS patients were also immunoreactive with antibodies to ubiquitin, p62, TDP43, FUS and optineurin (Fig. 2a–c and Supplementary Figs 4 and 5), but not SOD1.

Mutations in TDP43, FUS or optineurin occur in a small fraction of familial ALS, but these proteins have been found in the inclusions of a wide spectrum of ALS^{6,12,17,18,20}. To test whether ubiquitin 2 is involved in inclusion formation in other types of ALS, we examined 47 post-mortem spinal-cord samples, including cases of sporadic ALS ($n = 23$), familial ALS without mutations in *SOD1*, *TDP43* and *FUS* ($n = 5$), ALS with dementia ($n = 5$), familial ALS with *SOD1* mutations ($n = 7$ (A4V, $n = 4$; G85R, $n = 2$; E100G, $n = 1$)), familial ALS with a G298S mutation in *TDP43* ($n = 1$), and controls without ALS ($n = 6$). We observed ubiquitin-2-positive skein-like inclusions in all ALS cases (Supplementary Figs 6 and 7), indicating that ubiquitin 2 is a common component in the skein-like inclusions of a wide variety of ALS.

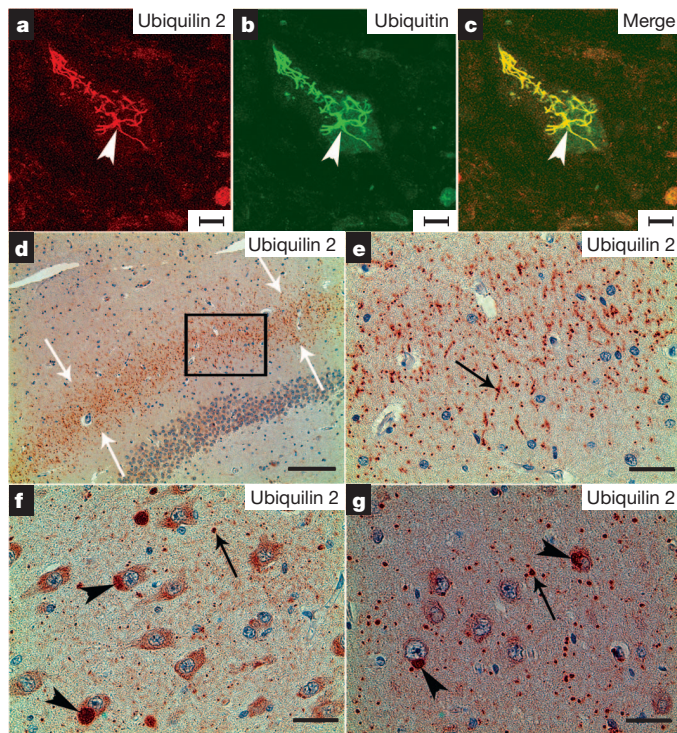


Figure 2 | Ubiquitin-2-immunoreactive inclusions in the spinal cord and hippocampus. a–g, Spinal cord (a–c) and hippocampal (d–g) sections from a patient with a *UBQLN2*^{P506T} mutation were analysed with confocal microscopy (a–c) and immunohistochemistry (d–g), using a monoclonal antibody against ubiquitin 2 (ubiquitin 2-C). The ubiquitin-2-positive and skein-like inclusions (arrowhead) are shown in a spinal motor neuron (a). These inclusions are also ubiquitin-positive (b, c). In the hippocampus, the ubiquitin-2-positive inclusions are shown in the molecular layer of the fascia dentata (d, e), CA3 (f) and CA1 (g). White arrows in d indicate the middle region of the molecular layer with ubiquitin-2-positive inclusions. A higher-magnification image of the boxed area in d is shown in e. Black arrows indicate representative inclusions in neurites (e–g), and arrowheads indicate cytoplasmic inclusions in the cell bodies (f and g). Scale bars: a–c, 10 μm; d, 200 μm; e, 50 μm; f and g, 25 μm.

Dementia was a prominent feature in eight *UBQLN2*-linked cases. To examine whether ubiquitin-2-immunoreactive inclusions are present in the brain, and to explore the potential link between ubiquitin 2 inclusions and dementia, we analysed brain autopsy samples from two patients with the P506T mutation. We saw ubiquitin 2 pathology, which was most prominent in the hippocampus (Fig. 2d–g and Supplementary Fig. 8). Small ubiquitin 2 inclusions (1–5 μm in diameter) were predominantly situated in the neuropil. The fascia dentata presented with a band of radially oriented dendritic and neuropil inclusions in the intermediate region of the molecular layer (Supplementary Fig. 8). In addition to the small neuropil inclusions, large inclusions (up to 20 μm in diameter) were observed in some pyramidal neurons, especially those in the CA3 and CA1 regions (Fig. 2f, g and Supplementary Fig. 8). Co-localization of ubiquitin 2 and ubiquitin in these inclusions was confirmed with confocal microscopy (Supplementary Fig. 8). This type of hippocampal pathology has not previously been observed in any other neurodegenerative disorder. The ubiquitin-2-positive and ubiquitin-positive inclusions did not seem to be co-localized with major glial markers (Supplementary Fig. 9). In addition, we observed a novel, membrane-bound perikaryal structure, which contained eosinophilic granules of varying sizes, in some hippocampal pyramidal neurons. These structures were strongly immunoreactive for ubiquitin 2 (Supplementary Fig. 10).

To test whether ubiquitin 2 pathology is present in the hippocampus of ALS/dementia cases without *UBQLN2* mutations, and to explore the correlation of ubiquitin 2 pathology with dementia in ALS, we

examined hippocampal sections of 15 pathologically characterized ALS cases without *UBQLN2* mutations, including five cases of ALS/dementia with pathological signatures corresponding to frontotemporal lobar degeneration of motor-neuron-disease type (FTLD-MND/FTLD-U). We found prominent ubiquitin 2 pathology in the hippocampus of all five cases with ALS/dementia (Supplementary Fig. 11). Similar to the ubiquitin 2 inclusions in *UBQLN2*-linked ALS/dementia cases, the ubiquitin 2 inclusions in these non-*UBQLN2*-linked cases were also positive for ubiquitin and p62 (Supplementary Fig. 11), but negative for FUS. Although there was no apparent TDP43 neuritic pathology in the dentate molecular layer, we saw variable numbers of cytoplasmic TDP43 inclusions in dentate granule cells. These have previously been shown in ALS/dementia¹⁸ (Supplementary Fig. 11). However, a notable number of the inclusions containing ubiquitin 2, ubiquitin and p62 were negative for TDP43 (Supplementary Figs 11 and 12). The absence of TDP43 in ubiquitin-2-positive inclusions was further confirmed with an antibody that specifically detects phosphorylated TDP43 in cytoplasmic TDP43 inclusions¹⁸ (Supplementary Fig. 13). We also observed that the inclusions containing ubiquitin 2, ubiquitin and p62 were mostly negative for TDP43 in the CA regions in the non-*UBQLN2*-linked ALS/dementia cases (Supplementary Fig. 12). We did not observe ubiquitin 2 pathology in the hippocampus of the ten ALS cases without dementia. The correlation of hippocampal ubiquitin 2 pathology to dementia in ALS cases with or without *UBQLN2* mutations indicates that ubiquitin 2 is widely involved in ALS-related dementia, even without *UBQLN2* mutations.

TDP43 inclusions have been observed in dentate granule cells of the hippocampus in most cases with FTLD-U¹⁸, and FUS inclusions have been shown in most TDP43-negative FTLD-U cases^{21,22}. To test whether ubiquitin 2 co-aggregates with these two known ALS- and dementia-linked proteins *in vitro*, we generated ten expression constructs (Supplementary Information) and co-transfected Neuro-2a cells with different combinations of them. Both wild-type and mutant ubiquitin 2 were mostly distributed in the cytosol. We did not observe obvious differences in the distributions of wild-type and mutant ubiquitin 2. Wild-type FUS and wild-type TDP43 were located almost exclusively in the nuclei (Fig. 3 and Supplementary Fig. 14), whereas mutant FUS showed prominent cytoplasmic distribution (Supplementary Fig. 14) and the C-terminal fragment (218–414, C-TDP43) of TDP43 that has been linked to ALS and FTLD^{18,23} was almost exclusively located in the cytosol (Fig. 3). We did not observe cytoplasmic inclusions in cells transfected with wild-type FUS and mutant FUS (Supplementary Fig. 14), nor with wild-type TDP43 (Fig. 3). However, cytoplasmic inclusions were seen in cells expressing either wild-type or mutant ubiquitin 2. Notably, C-TDP43 was co-localized with either wild-type or mutant ubiquitin 2 in the cytoplasmic inclusions (Fig. 3). We obtained consistent data using two expression systems: either tagged ubiquitin 2 or tag-free ubiquitin 2 (Fig. 3 and Supplementary Figs 14 and 15). These data indicate that both ALS- and dementia-linked ubiquitin 2 and TDP43 are prone to co-aggregation. We also noted that inclusion formation was apparently dose-dependent, because the cells with the lowest expression of wild-type or mutant ubiquitin 2, or C-TDP43, did not show cytoplasmic inclusions. However, ubiquitin-2-positive but C-TDP43-negative inclusions were frequently seen in cells with relatively lower levels of ubiquitin 2 and C-TDP43 expression (Fig. 3). This phenomenon indicates that ubiquitin 2 may be more prone to aggregation than TDP43. This is consistent with the pathology observed in ALS/dementia cases, in which the ubiquitin-2-containing inclusions in the molecular layer and in some dentate granule cells were TDP43-negative.

Ubiquitin 2 is a member of the ubiquitin-like protein family (ubiquilins). Humans have four ubiquitin genes, each encoding a separate protein. Ubiquilins are characterized by the presence of an N-terminal ubiquitin-like domain and a C-terminal ubiquitin-associated domain (Fig. 1d). The middle part of ubiquilins is highly variable. This structural organization is characteristic of proteins that deliver ubiquitinated

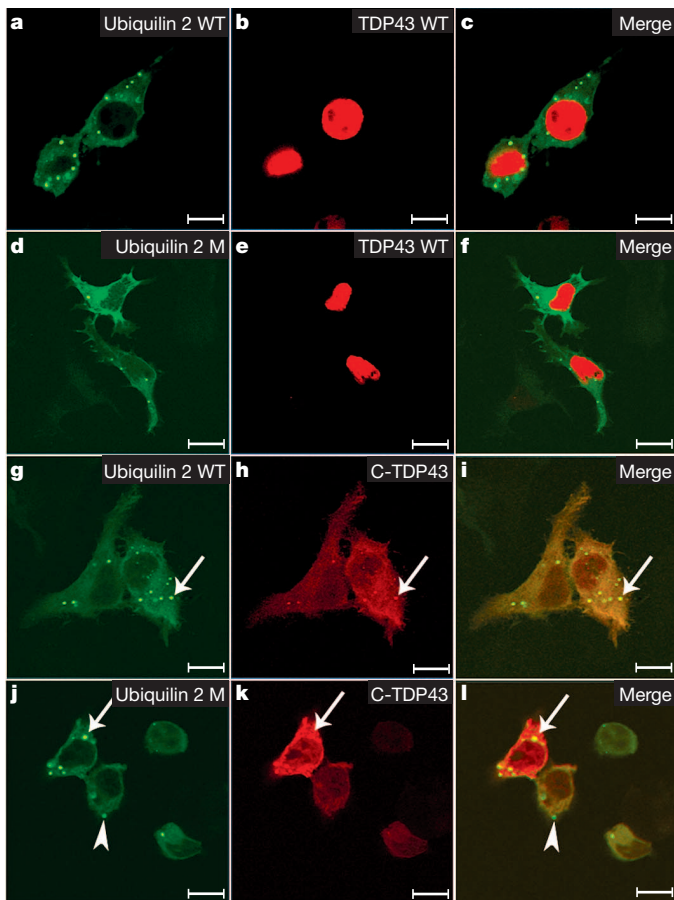


Figure 3 | Co-localization of ubiquitin 2 with ALS- and dementia-linked TDP43. **a–l**, Neuro-2a cells were transfected with various combinations of wild-type (WT) ubiquitin 2, mutant (M) ubiquitin 2 (P497H), wild-type TDP43 and a C-terminal fragment of TDP43 (amino acids 218–414) that is linked to ALS and FTL. Ubiquitin 2 is GFP-tagged and TDP43 is mCherry-tagged. Wild-type and mutant ubiquitin 2 are mostly cytoplasmic. Wild-type TDP43 is located almost exclusively in the nuclei and C-TDP43 is almost exclusively cytoplasmic. TDP43 inclusions are co-localized with wild-type (**g–i**) and mutant (P497H) (**j–l**) ubiquitin 2 (arrows). Some ubiquitin-2-positive inclusions are TDP43-negative (arrowhead). Scale bars, 10 μ m.

proteins to the proteasome for degradation. In accordance with this function, the ubiquitin-like domain of the ubiquilins binds to subunits of the proteasome, and the ubiquitin-associated domain binds to poly-ubiquitin chains that are typically conjugated onto proteins marked for degradation by the proteasome²⁴. In addition to the ubiquitin-like and ubiquitin-associated domains that are shared by all ubiquilins, ubiquitin 2 has a unique repeat region containing 12 PXX tandem repeats (Fig. 1d). Notably, all five ALS-linked mutations identified in this study involve proline residues in this short PXX repeat region (Fig. 1c, d), indicating that these mutations may confer on ubiquitin 2 a common property that may be related to the pathogenic mechanism of the disease.

On the basis of the involvement of ubiquitin 2 in the protein degradation pathway, we then investigated the functional consequences of mutant ubiquitin 2 in protein degradation through the ubiquitin–proteasome system (UPS). We used a UPS reporter substrate, ubiquitin^{G76V} fused with green fluorescent protein (Ub^{G76V}–GFP)²⁵ to test the effects of mutant ubiquitin 2 on ubiquitin-mediated protein degradation. Two mutations at two different sites were tested (P497H and P506T) using the Ub^{G76V}–GFP reporter system. The G76V substitution prevents removal of N-terminally fused ubiquitin by cellular de-ubiquitinating enzymes, leading to efficient proteasomal degradation of the Ub^{G76V}–GFP reporter²⁵. First, we tested the transfection

efficiency of wild-type and mutant ubiquitin 2 constructs, and saw similar levels of exogenous ubiquitin 2 expression (Supplementary Fig. 16). We also tested the functionality of the Ub^{G76V}–GFP reporter system using the proteasome inhibitor MG-132 in transiently transfected cells. As expected, incubation with MG-132 resulted in marked accumulation of the Ub^{G76V}–GFP signal (Supplementary Fig. 17). We then examined the accumulation of Ub^{G76V}–GFP in Neuro-2a cells transiently transfected with either wild-type or mutant ubiquitin 2 constructs. Expression of mutant ubiquitin 2 resulted in significantly higher accumulation of Ub^{G76V}–GFP than expression of wild-type ubiquitin 2 (Fig. 4a). Similar data were obtained using SH-SY5Y cells (Supplementary Fig. 18).

We further analysed the dynamics of Ub^{G76V}–GFP degradation after new protein synthesis was blocked with cycloheximide for 0, 2, 4 and 6 h in Neuro-2a cells. We found that the rates of reporter degradation were significantly slower in cells expressing both the P497H and P506T ubiquitin 2 mutants, when compared to wild-type ubiquitin 2, at 4 h ($P < 0.05$) and 6 h ($P < 0.001$) (Fig. 4b), further supporting the notion that the ubiquitin 2 mutants impair the protein degradation pathway.

It is notable that all five ALS-linked *UBQLN2* mutations identified here involve four proline residues in the PXX region. Proline is a unique amino acid in that it has a side chain cyclized onto the backbone nitrogen atom, leading to steric restriction of its rotation, and thus hindering the formation of major known secondary structures. Moreover, among the primary structures of many ligands for protein–protein interactions, a proline residue is often critical²⁶. Some protein–protein interaction domains, such as SH3, prefer ligand sequences containing tandem PXXP motifs, as noted in the PXX domain of ubiquitin 2, for high affinity and selectivity of such interactions²⁷. Further studies of the consequences of the proline mutations may reveal interacting molecular partners that are relevant to the functions of ubiquitin 2.

The exact function of ubiquitin 2 is not well understood. However, there is increasing evidence that ubiquilins, together with their interactions with other proteins, may be involved in neurodegenerative disorders. Ubiquitin 1, another member of the ubiquitin family, is associated with Alzheimer's disease and interacts with presenilins 1 and 2 (ref. 28) and TDP43 (ref. 29). We observed that ubiquitin 2 formed cytoplasmic inclusions with ALS- and FTL-linked TDP43, indicating that an interaction between TDP43 and ubiquitin 2 may underlie the pathogenesis of ALS and ALS/dementia, and possibly other neurodegenerative disorders as well.

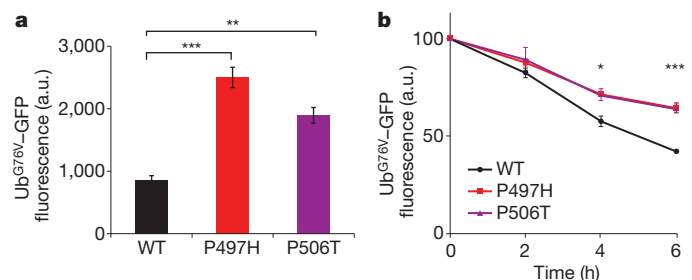


Figure 4 | Mutations in ubiquitin 2 lead to ubiquitin-mediated impairment of proteasomal degradation. **a, b**, Ub^{G76V}–GFP fluorescence intensity (arbitrary units, a.u.) was quantified by flow cytometry 48 h after transient transfection of Neuro-2a cells with either wild-type (WT) or mutant (P497H or P506T) *UBQLN2* (**a**). The dynamics of Ub^{G76V}–GFP reporter degradation after blockage of protein synthesis with cycloheximide for 0, 2, 4, and 6 h are shown in **b**. Rates of UPS-reporter degradation were significantly slower for both the P497H and P506T mutants when compared to the wild-type at 4 h and 6 h. Mean fluorescence before cycloheximide administration was standardized as 100%. Data are averaged from at least three independent experiments. *, $P < 0.05$; **, $P < 0.01$; ***, $P < 0.001$ (indicating significant differences when compared to wild-type by two-tailed Student's *t*-test). Error bars, means \pm s.e.m.

The removal of misfolded or damaged proteins is critical for optimal cell functioning. In the cytosol and the nucleus, a major proteolytic pathway to recycle misfolded or damaged proteins is the UPS. Although an impaired UPS is thought to be associated with the formation of proteinaceous inclusions in many neurodegenerative disorders, direct evidence of mutations in the UPS pathway has been limited³⁰. In this study, we show mutations of ubiquilin 2, a ubiquitin-like protein, in five families with ALS and ALS/dementia. We also show that inclusions containing ubiquilin 2 are a common pathological feature in a wide spectrum of ALS and ALS/dementia. Functional studies indicate an impairment of ubiquitin-mediated proteasomal degradation in cells expressing mutant ubiquilin 2. These data provide robust evidence for an impairment of protein turnover in the pathogenesis of ALS and ALS/dementia, and possibly in other neurodegenerative disorders as well. Further elucidation of these processes may be central to the understanding of pathogenic pathways. These pathways should provide novel molecular targets for the design of rational therapies for these disorders.

METHODS SUMMARY

Genomic DNA was PCR-amplified and Sanger-sequenced using a CEQ 8000 genetic analysis system (Beckman Coulter). Western blotting, immunohistochemistry and confocal microscopy were performed using previously established methods¹⁷. Construction of expression vectors, cell culture and flow cytometry were performed according to standard protocols. For statistical analysis, all graphs show mean \pm s.e.m. and significance was calculated using Student's *t*-test.

Full Methods and any associated references are available in the online version of the paper at www.nature.com/nature.

Received 20 November 2010; accepted 5 July 2011.

Published online 21 August 2011.

- Deng, H. X. *et al.* Amyotrophic lateral sclerosis and structural defects in Cu,Zn superoxide dismutase. *Science* **261**, 1047–1051 (1993).
- Rosen, D. R. *et al.* Mutations in Cu/Zn superoxide dismutase gene are associated with familial amyotrophic lateral sclerosis. *Nature* **362**, 59–62 (1993).
- Kabashi, E. *et al.* TARDBP mutations in individuals with sporadic and familial amyotrophic lateral sclerosis. *Nature Genet.* **40**, 572–574 (2008).
- Sreedharan, J. *et al.* TDP-43 mutations in familial and sporadic amyotrophic lateral sclerosis. *Science* **319**, 1668–1672 (2008).
- Kwiatkowski, T. J. Jr *et al.* Mutations in the FUS/TLS gene on chromosome 16 cause familial amyotrophic lateral sclerosis. *Science* **323**, 1205–1208 (2009).
- Vance, C. *et al.* Mutations in FUS, an RNA processing protein, cause familial amyotrophic lateral sclerosis type 6. *Science* **323**, 1208–1211 (2009).
- Chen, Y. Z. *et al.* DNA/RNA helicase gene mutations in a form of juvenile amyotrophic lateral sclerosis (ALS4). *Am. J. Hum. Genet.* **74**, 1128–1135 (2004).
- Greenway, M. J. *et al.* ANG mutations segregate with familial and 'sporadic' amyotrophic lateral sclerosis. *Nature Genet.* **38**, 411–413 (2006).
- Nishimura, A. L. *et al.* A mutation in the vesicle-trafficking protein VAPB causes late-onset spinal muscular atrophy and amyotrophic lateral sclerosis. *Am. J. Hum. Genet.* **75**, 822–831 (2004).
- Yang, Y. *et al.* The gene encoding alsin, a protein with three guanine-nucleotide exchange factor domains, is mutated in a form of recessive amyotrophic lateral sclerosis. *Nature Genet.* **29**, 160–165 (2001).
- Chow, C. Y. *et al.* Deleterious variants of FIG4, a phosphoinositide phosphatase, in patients with ALS. *Am. J. Hum. Genet.* **84**, 85–88 (2009).
- Maruyama, H. *et al.* Mutations of optineurin in amyotrophic lateral sclerosis. *Nature* **465**, 223–226 (2010).
- Ticozzi, N. *et al.* Paraoxonase gene mutations in amyotrophic lateral sclerosis. *Ann. Neurol.* **68**, 102–107 (2010).
- Mitchell, J. *et al.* Familial amyotrophic lateral sclerosis is associated with a mutation in D-amino acid oxidase. *Proc. Natl Acad. Sci. USA* **107**, 7556–7561 (2010).
- Johnson, J. O. *et al.* Exome sequencing reveals VCP mutations as a cause of familial ALS. *Neuron* **68**, 857–864 (2010).
- Lansbury, P. T. & Lashuel, H. A. A century-old debate on protein aggregation and neurodegeneration enters the clinic. *Nature* **443**, 774–779 (2006).
- Deng, H. X. *et al.* FUS-immunoreactive inclusions are a common feature in sporadic and non-SOD1 familial amyotrophic lateral sclerosis. *Ann. Neurol.* **67**, 739–748 (2010).
- Neumann, M. *et al.* Ubiquitinated TDP-43 in frontotemporal lobar degeneration and amyotrophic lateral sclerosis. *Science* **314**, 130–133 (2006).
- Shibata, N. *et al.* Intense superoxide dismutase-1 immunoreactivity in intracytoplasmic hyaline inclusions of familial amyotrophic lateral sclerosis with posterior column involvement. *J. Neuropathol. Exp. Neurol.* **55**, 481–490 (1996).
- Mackenzie, I. R. *et al.* Pathological TDP-43 distinguishes sporadic amyotrophic lateral sclerosis from amyotrophic lateral sclerosis with SOD1 mutations. *Ann. Neurol.* **61**, 427–434 (2007).
- Neumann, M. *et al.* Frontotemporal lobar degeneration with FUS pathology. *Brain* **132**, 2922–2931 (2009).
- Urwin, H. *et al.* FUS pathology defines the majority of tau- and TDP-43-negative frontotemporal lobar degeneration. *Acta Neuropathol.* **120**, 33–41 (2010).
- Nonaka, T., Kametani, F., Arai, T., Akiyama, H. & Hasegawa, M. Truncation and pathogenic mutations facilitate the formation of intracellular aggregates of TDP-43. *Hum. Mol. Genet.* **18**, 3353–3364 (2009).
- Ko, H. S., Uehara, T., Tsuruma, K. & Nomura, Y. Ubiquilin interacts with ubiquitylated proteins and proteasome through its ubiquitin-associated and ubiquitin-like domains. *FEBS Lett.* **566**, 110–114 (2004).
- Dantuma, N. P., Lindsten, K., Glas, R., Jellne, M. & Masucci, M. G. Short-lived green fluorescent proteins for quantifying ubiquitin/proteasome-dependent proteolysis in living cells. *Nature Biotechnol.* **18**, 538–543 (2000).
- Kay, B. K., Williamson, M. P. & Sudol, M. The importance of being proline: the interaction of proline-rich motifs in signaling proteins with their cognate domains. *FASEB J.* **14**, 231–241 (2000).
- Aitio, O. *et al.* Recognition of tandem PxxP motifs as a unique Src homology 3-binding mode triggers pathogen-driven actin assembly. *Proc. Natl Acad. Sci. USA* **107**, 21743–21748 (2010).
- Haapasalo, A. *et al.* Emerging role of Alzheimer's disease-associated ubiquilin-1 in protein aggregation. *Biochem. Soc. Trans.* **38**, 150–155 (2010).
- Kim, S. H. *et al.* Potentiation of amyotrophic lateral sclerosis (ALS)-associated TDP-43 aggregation by the proteasome-targeting factor, ubiquilin 1. *J. Biol. Chem.* **284**, 8083–8092 (2009).
- Aguzzi, A. & O'Connor, T. Protein aggregation diseases: pathogenicity and therapeutic perspectives. *Nature Rev. Drug Discov.* **9**, 237–248 (2010).

Supplementary Information is linked to the online version of the paper at www.nature.com/nature.

Acknowledgements This study was supported by the National Institute of Neurological Disorders and Stroke (NS050641), the Les Turner ALS Foundation, the Vena E. Schaff ALS Research Fund, the Harold Post Research Professorship, the Herbert and Florence C. Wenske Foundation, the David C. Asselin MD Memorial Fund, the Help America Foundation and the Les Turner ALS Foundation/Herbert C. Wenske Foundation Professorship. F.F. has support from NIH (T32 AG20506). K.A. is a postdoctoral fellow of the Blazeman Foundation for ALS. G.H.G. received travel funds from MND Scotland. We thank N. Dantuma for the UPS reporter plasmid (through Addgene) and the staff of the Northwestern University Robert H. Lurie Comprehensive Cancer Center flow cytometry core facility for technical assistance. Imaging work was performed at the Northwestern University Cell Imaging Facility, supported by NCI CCSG P30 CA060553 awarded to the Robert H. Lurie Comprehensive Cancer Center.

Author Contributions T.S. conceived and supervised this project. W.C., S.-T.H., Y.Y., H.J., M.H., H.-X.D. and T.S. did the sequencing analysis. S.T.H., E.R., J.L.H., M.P.-V. and T.S. performed linkage analysis. K.M.B., G.H.G., F.F., G.H.J., H.Z., E.H.B., K.A., E.M., H.-X.D. and T.S. performed immunohistochemical, confocal and pathological analysis. F.F., Y.S. and H.-X.D. performed functional analysis. N.S., S.D. and T.S. collected family information and coordinated this study. K.M.B., G.H.J., B.R.B., R.L.S. and T.S. did clinical studies. H.-X.D. and T.S. analysed the data and wrote the paper.

Author Information Reprints and permissions information is available at www.nature.com/reprints. The authors declare no competing financial interests. Readers are welcome to comment on the online version of this article at www.nature.com/nature. Correspondence and requests for materials should be addressed to T.S. (t-siddique@northwestern.edu).

METHODS

Patients and samples. This study was approved by the local institutional review boards. ALS patients met the diagnosis of probable or definite ALS as defined in the revised EL-Escorial³¹. Patients with dementia met the criteria for FTD or FTLD proposed in refs 32 and 33. The dementia was similar to frontal variant FTD on inception and was progressive, and eventually global in most patients. One patient had mild mental retardation before the onset of dementia. There were eight patients with both ALS and dementia. Dementia preceded motor symptoms in some patients, but no patient remained free of motor involvement. The FTLD symptoms included abnormalities in both behaviour and executive function, although the degree of severity varied between individuals in different stages of the disease. Pedigrees and clinical data were collected by specialists in neuromuscular medicine and were verified by medical records or recent examination to establish diagnosis (Supplementary Table 2). DNA and other samples were taken after obtaining written informed consent. Overall, DNA from more than 200 ALS cases and 928 controls was used for genetic analysis. Spinal-cord autopsy samples from two X-linked ALS cases (P497H or P506T), 41 cases with ALS or ALS/dementia and six non-ALS controls were studied. In addition, available autopsy samples from the motor-cortex region of a patient with the P497H mutation (family 186, IV 7), brain regions (including hippocampus, cerebellum, optic nerve, visual cortex, pons and midbrain) of two patients with the P506T mutation (family 6316, II 3 and III 4), and the hippocampal regions of ten ALS and five ALS/dementia cases were also used for pathological and immunohistological studies. These five ALS/dementia cases were classified as having FTLD-MND/FTLD-U, including four cases with pathological type 3 and one case with pathological type 2 according to the classification system proposed in ref. 34. These cases were evaluated by a neuropathologist (E.H.B.).

Genetic analysis. Genomic DNA was extracted by standard methods (Qiagen) from whole peripheral blood, transformed lymphoblastoid cell lines or tissues. Intronic primers flanking exons were designed at least 50 nucleotides away from the intron/exon boundary. When a PCR product was larger than 500 base pairs (bp), several overlapping primers were designed with an average of 50-bp overlap. Genomic DNA (40 ng) was used for PCR amplification. The amplification protocol consisted of the following steps: incubation at 95 °C for 1 min, 32 cycles of 95 °C (30 s), 55 °C (30 s) and 72 °C (1 min), and a final 5-min extension at 72 °C, with modifications when necessary. Excess dNTPs and primers were digested with exonuclease I and shrimp alkaline phosphatase (ExoSAP-IT, USB). When non-specific PCR amplification occurred, the PCR products were separated on a 1.5% agarose gel and the specific PCR product was cut out from the gel and purified using QIAquick gel extraction kit (Qiagen). For sequencing of a PCR product, fluorescent-dye-labelled single-stranded DNA was amplified using Beckman Coulter sequencing reagents (GenomeLab DTCS quick start kit), followed by single-pass bidirectional sequencing with a CEQ 8000 genetic analysis system (Beckman Coulter). We sequenced the entire protein-coding exons and intronic sequences of 30–50 bp flanking the exons. *UBQLN2* is an intronless gene. We divided the *UBQLN2* gene into five overlapping PCR fragments for sequencing analysis. These fragments cover the entire coding sequence (1,872 bp), 125 bp of the 5' UTR and 293 bp of the 3' UTR. Primers were as follows: Ubqln2-1F, 5'-cttcacacagaggtacgtg-3'; Ubqln2-1R, 5'-gtgtgaggtactctctggag-3'; Ubqln2-2F, 5'-catgatggctgactgttcac-3'; Ubqln2-2R, 5'-ctctgtgctgagcattcagcatc-3'; Ubqln2-3F, 5'-gactgtgctcttagcaatctag-3'; Ubqln2-3R, 5'-gtgtctgctgattctgcatctgc-3'; Ubqln2-4F, 5'-cacagatgatgctgaatagcc-3'; Ubqln2-4R, 5'-gctgaatgaactgctgtgttg-3'; Ubqln2-5F, 5'-ctgcactagtgaaccacag-3'; Ubqln2-5R, 5'-aacagcattgtaccacac-3'. For fragments 4 and 5, the PCR protocol consisted of the following steps: incubation at 96 °C for 2 min, 32 cycles of 96 °C (30 s), 56 °C (30 s) and 72 °C (1 min), and a final 5-min extension at 72 °C. The PCR products were separated on a 1.5% agarose gel and purified with QIAquick gel extraction kit (Qiagen) before sequencing.

Antibodies. Two anti-ubiquitin 2 antibodies were used. One was a mouse monoclonal antibody (5F5, H00029978-M03, Novus Biologicals Inc.). We made the other antibody, which was raised in rabbit using a polypeptide of human ubiquitin 2 (amino acids 8–24, SGPPRPSRGPAQAQGS). The antiserum was affinity-purified. Other polyclonal and monoclonal antibodies used in this study included: anti-ubiquitin (PRB-268C, Covance; 10R-U101B, Fitzgerald Industries International; Ub(N-19):sc-6085, Santa Cruz Biotechnology), anti-p62 (H00008878-M01, Abnova; NB110-74805, Novus Biologicals Inc.), anti-TDP43 (TIP-PTD-P01, Cosmo Bio Co; 10782-2-AP, ProteinTech Group; 60019-2-Ig, ProteinTech Group; WH0023435M1-100UG, Sigma-Aldrich), anti-FUS (11570-1-AP, ProteinTech Group), anti-optineurin (100000, Cayman), anti-SOD1 (ref. 35), anti-Myc (MMS-150P, Covance), anti-GFAP (Z0334, Dako North America; G3893, Sigma-Aldrich), anti-Iba1 (019-19741, Wako Pure Chemical Industries) and anti-CNPase (MAB326R, Millipore).

Immunohistochemistry and confocal microscopy. The basic protocols for immunohistochemistry and confocal microscopy have been described in detail in a previous study¹⁷. In brief, 6-µm sections were cut from formalin-fixed,

paraffin-embedded spinal cord and brain regions containing the frontal lobe or the hippocampus. The sections were deparaffinized with xylene and rehydrated with a descending series of diluted ethanol and water. Antigens in the sections were retrieved using a high-pressure decloaking chamber. For immunohistochemistry, endogenous peroxidase activity was blocked with 2% hydrogen peroxide. Non-specific background was blocked with 1% bovine serum albumin. The titres of the antibodies were determined on the basis of preliminary studies using serial dilution of the antibodies. Various antibodies against ubiquitin 2 or other proteins were used as primary antibodies. These included rabbit polyclonal anti-ubiquitin 2 (ubiquitin 2-N; 0.5 µg ml⁻¹; generated by us), mouse monoclonal anti-ubiquitin 2 (ubiquitin 2-C; 0.2 µg ml⁻¹; H00029978-M03, Novus Biologicals), rabbit polyclonal anti-FUS (3 µg ml⁻¹; 11570-1-AP, ProteinTech Group), mouse monoclonal anti-TDP43 (1 µg ml⁻¹; 60019-2-Ig, ProteinTech Group), rabbit polyclonal anti-TDP43 (0.1 µg ml⁻¹; 10782-2-AP, ProteinTech Group), mouse monoclonal anti-ubiquitin (0.5 µg ml⁻¹; 10R-U101B, Fitzgerald Industries International), rabbit polyclonal anti-ubiquitin (0.5 µg ml⁻¹; PRB-268C, Covance), goat polyclonal anti-ubiquitin (0.5 µg ml⁻¹; Ub(N-19):sc-6085, Santa Cruz Biotechnology), mouse monoclonal anti-p62 (1 µg ml⁻¹; H00008878-M01, Abnova Corporation) and rabbit polyclonal anti-optineurin (C-term; 0.2 µg ml⁻¹; 100000, Cayman). Biotinylated goat anti-rabbit and anti-mouse IgG, biotinylated mouse anti-goat IgG, or biotinylated rabbit anti-mouse IgG were used as the secondary antibodies. Immunoreactive signals were detected with peroxidase-conjugated streptavidin (BioGenex) using 3-amino-9-ethylcarbazole as a chromogen. The slides were counterstained with haematoxylin and sealed with Aqua PolyMount (Polyscience).

For confocal microscopy, antibodies generated in different species were used in various combinations. These antibodies included those against ubiquitin 2, FUS, TDP43, p62, optineurin, ubiquitin, Myc, GFAP, Iba1 and CNPase. Fluorescence signals were detected with appropriate secondary anti-rabbit, anti-mouse or anti-goat IgG, conjugated with Alexa Fluor 488 or Alexa Fluor 555 (Invitrogen), using an LSM 510 META laser-scanning confocal microscope with the multi-tracking setting¹⁷. The same pinhole diameter was used to acquire each channel.

Western blotting. Western blotting was performed using the protocol previously described¹⁷. Briefly, cells or spinal-cord tissues from lumbar segments were processed and homogenized. Cell lysates or the supernatants of tissue homogenates were subjected to total protein quantification, gel electrophoresis and blotting on PVDF membranes. Ubiquitin 2 was detected using the ubiquitin 2-N or ubiquitin 2-C antibodies. The membranes were then stripped and blotted with an antibody against β-actin (A5441, Sigma-Aldrich).

Expression constructs. A full-length human cDNA clone (*Homo sapiens* ubiquitin 2, IMAGE:4543266) was used as a template for construction of the expression constructs. Two primers anchored with a XhoI site (ubiquitin 2-TP1, 5'-ttctcaggcccgccatgctgagaat-3') and a BamHI site (ubiquitin 2-TP2, 5'-catgatcctgtatgtctgtattacc-3') were used to amplify the full-length coding sequence. The amplified fragment was cloned into plasmid vector pBluescript M13. The ubiquitin 2 sequence was verified by direct sequencing. The P497H and P506T mutations were introduced into the plasmid vector by site-directed mutagenesis using a primer containing each respective mutation. The XhoI/BamHI fragment containing wild-type *UBQLN2*, *UBQLN2*^{P497H} or *UBQLN2*^{P506T} was released from the pBluescript M13 vector and cloned into the XhoI and BamHI sites of dual expression vectors pIRES2-DsRed2 or pIRES2-ZsGreen1 (Clontech), to create such constructs as wtUBQLN2-ZsGreen1 and mUBQLN2-ZsGreen1 (mutant ubiquitin 2 (P497H or P506T)).

We generated seven additional expression constructs, including wild-type ubiquitin 2 tagged with GFP (wtUBQLN2-GFP), mutant ubiquitin 2 (P497H or P506T) tagged with GFP (mUBQLN2-GFP), wild-type TDP43 tagged with mCherry (wtTDP43-mCherry), an ALS- and dementia-linked C-terminal fragment of TDP43 (amino acids 218–414, C-TDP43)^{18,23} tagged with mCherry (C-TDP43-mCherry), wild-type FUS tagged with Myc (Myc-wtFUS) and mutant FUS (R495X) tagged with Myc (Myc-mFUS).

Cell culture, transfection and immunocytochemistry. SH-SY5Y, Neuro-2a and HEK293 cell lines were grown on collagen-coated plates in Dulbecco's modified Eagle's medium containing 10% (v/v) human serum, 2 mM L-glutamine, 2 U ml⁻¹ penicillin and 2 mg ml⁻¹ streptomycin, at 37 °C in a humidity-controlled incubator with 5% CO₂. The cells were transiently transfected with different combinations of expression vectors using Lipofectamine 2000 (Invitrogen) according to manufacturer's instructions. Immunocytochemistry was performed as previously described¹⁶.

UPS reporter assay. SH-SY5Y and Neuro-2a cells were grown in 24-well plates and double-transfected with a UPS-reporter vector encoding Ub^{G76V}-GFP (ref. 25) (Addgene plasmid 11941), and a dual expression vector encoding DsRed2 with either wild-type or mutant ubiquitin 2. Cells were harvested 48 h after transfection and resuspended in PBS. Cells transfected with the Ub^{G76V}-GFP vector were used for control experiments to test the functionality of the UPS reporter. In these control experiments, the medium was changed 24 h after

transfection to medium containing 5 μ M proteasomal inhibitor MG-132 (A.G. Scientific Inc.). Cells were incubated in this medium for 24 h and then harvested and resuspended in PBS. For cycloheximide chase of Ub^{G76V}-GFP, transiently transfected Neuro-2a cells were used. The cells were transferred 24 h after transfection to medium containing 5 μ M MG-132. After incubation with MG-132 for 16 h to accumulate the Ub^{G76V}-GFP reporter, cells were washed in sterile PBS and incubated with medium containing 100 μ g ml⁻¹ cycloheximide (Sigma) for 0, 2, 4, and 6 h. At each time point, cells were washed, harvested and resuspended in ice-cold PBS supplemented with 100 μ g ml⁻¹ cycloheximide. The fluorescence intensities at each time point were measured by flow cytometry. The fluorescence intensity at 0 h was taken to be maximal fluorescence (100%). All flow-cytometric data were collected and analysed using a MoFlo cell sorter and Summit software (DakoCytomation). Argon-ion (488 nm) and yellow (565 nm) lasers were used for excitation. The GFP and DsRed2 signals were collected using 530/540-nm and 600/630-nm bandpass filters, respectively. In all experiments, data were gated on GFP/DsRed2 dual-labelled cells. At least 500–1,000 such events were recorded in each experiment. The DsRed2 expression levels and profiles were similar across

experiments. Data were collected from three independent experiments. Two-tailed unpaired Student's *t*-test ($P < 0.05$) was used for statistical analysis.

31. Brooks, B. R., Miller, R. G., Swash, M. & Munsat, T. L. El Escorial revisited: revised criteria for the diagnosis of amyotrophic lateral sclerosis. *Amyotroph. Lateral Scler. Other Motor Neuron Disord.* **1**, 293–299 (2000).
32. Neary, D. *et al.* Frontotemporal lobar degeneration: a consensus on clinical diagnostic criteria. *Neurology* **51**, 1546–1554 (1998).
33. Cairns, N. J. *et al.* Neuropathologic diagnostic and nosologic criteria for frontotemporal lobar degeneration: consensus of the consortium for frontotemporal lobar degeneration. *Acta Neuropathol.* **114**, 5–22 (2007).
34. Mackenzie, I. R. *et al.* Heterogeneity of ubiquitin pathology in frontotemporal lobar degeneration: classification and relation to clinical phenotype. *Acta Neuropathol.* **112**, 539–549 (2006).
35. Deng, H. X. *et al.* Conversion to the amyotrophic lateral sclerosis phenotype is associated with intermolecular linked insoluble aggregates of SOD1 in mitochondria. *Proc. Natl Acad. Sci. USA* **103**, 7142–7147 (2006).
36. Fecto, F. *et al.* Mutant TRPV4-mediated toxicity is linked to increased constitutive function in axonal neuropathies. *J. Biol. Chem.* **286**, 17281–17291 (2011).

Different patterns of peripheral migration by memory CD4⁺ and CD8⁺ T cells

Thomas Gebhardt¹, Paul G. Whitney¹, Ali Zaid¹, Laura K. Mackay¹, Andrew G. Brooks¹, William R. Heath¹, Francis R. Carbone¹ & Scott N. Mueller¹

Infections localized to peripheral tissues such as the skin result in the priming of T-cell responses that act to control pathogens. Activated T cells undergo migrational imprinting within the draining lymph nodes¹, resulting in memory T cells that provide local and systemic protection². Combinations of migrating and resident memory T cells have been implicated in long-term peripheral immunity, especially at the surfaces that form pathogen entry points into the body³. However, T-cell immunity consists of separate CD4⁺ helper T cells and CD8⁺ killer T cells, with distinct effector and memory programming requirements⁴. Whether these subsets also differ in their ability to form a migrating pool involved in peripheral immunosurveillance or a separate resident population responsible for local infection control has not been explored. Here, using mice, we show key differences in the migration and tissue localization of memory CD4⁺ and CD8⁺ T cells following infection of the skin by herpes simplex virus. On resolution of infection, the skin contained two distinct virus-specific memory subsets; a slow-moving population of sequestered CD8⁺ T cells that were resident in the epidermis and confined largely to the original site of infection, and a dynamic population of CD4⁺ T cells that trafficked rapidly through the dermis as part of a wider recirculation pattern. Unique homing-molecule expression by recirculating CD4⁺ T effector-memory cells mirrored their preferential skin-migratory capacity. Overall, these results identify a complexity in memory T-cell migration, illuminating previously unappreciated differences between the CD4⁺ and CD8⁺ subsets.

Intravital microscopy has provided novel insights into the migration of naive and effector T cells in lymphoid and non-lymphoid compartments, although there has been no concurrent investigation of CD4⁺ and CD8⁺ T-cell responses in the context of infection^{5,6}. We wanted to examine long-term peripheral immunity by visualizing how the localization of helper and killer T cells differs as immunity progresses to the memory phase of the response. To this end, we used skin infection with herpes simplex virus (HSV) because of the accessibility of this tissue to intravital imaging and the availability of TCR transgenic mice specific for viral helper (gDT-II)⁷ and killer (gBT-I)⁸ T-cell determinants. Transgenic gDT-II (CD4⁺) and gBT-I (CD8⁺) cells expressing fluorescent markers (enhanced green fluorescent protein, EGFP, or the red fluorescent protein, DsRed) were transferred into recipient C57BL/6 mice to track virus-specific T cells. Initial experiments using confocal microscopy showed that both gDT-II and gBT-I T cells were intermixed and present in large numbers throughout the skin 8 days after inoculation (Fig. 1a), which correlates with the time when virus is just cleared from this tissue⁹. Subsequently, the memory phase was marked by segregation of the CD4⁺ T cells to the dermis and CD8⁺ T cells to the epidermis (Fig. 1a and b), although T cells were also found in association with keratin-rich hair follicles in regions with indistinct boundaries between epithelium and dermis. Differential expression of the α_E integrin subunit CD103 (an adhesion molecule implicated in persistence of intraepithelial T cells^{10,11}) on the skin-infiltrating T cells

was consistent with differences in localization by the subsets, with the strongest CD103 staining on the CD8⁺ cells (Fig. 1c).

Differential localization of helper and killer T cells has previously been noted in human skin^{12,13} and other tissues, such as gut and genital mucosa^{11,14}. Intravaginal HSV infection resulted in localization (after clearance of the infection) of the majority of the virus-specific helper T cells to the lamina propria and of killer T cells to the epithelium (Supplementary Fig. 2), similar to the separation observed after skin infection (Fig. 1a).

To investigate the dynamics associated with the differential T-cell localization, intravital two-photon microscopy was performed at various times after infection. As observed by static imaging, we found a broad distribution of gDT-II and gBT-I T cells throughout the skin during the effector phase of the response (Fig. 1d and Supplementary Movies 1 and 2). This was followed by retreat of the CD8⁺ T cells to the epidermis and a largely dermal localization for the CD4⁺ T cells during memory (Fig. 1d and Supplementary Movies 3–5). During the effector phase, movement of the CD4⁺ and CD8⁺ T cells through the dermis occurred with similar mean velocities, and was marked by polarized cell shapes and rapid changes in direction (Fig. 1e and Supplementary Fig. 3a and b). Interestingly, epidermal T cells were significantly less motile than those in the dermis, with a lower mean velocity and higher arrest coefficients during this period. This migrational difference between dermal- and epidermal-associated T cells was even more pronounced during memory, when slow-moving epidermal killer T cells of dendritic morphology were observed above the more rapidly trafficking dermal helper T cells (Fig. 1e–g, Supplementary Fig. 3a and Supplementary Movies 3–5). Such findings suggest that the relative motility of cells in the skin was determined by their localization to epidermis or dermis, and was only indirectly subset related.

The distinct localization and motility of the helper and killer T cells probably reflected differences in trafficking capabilities. To test whether HSV-specific helper T cells could preferentially leave the tissue, we cultured explanted skin that had resolved infection and contained virus-specific memory CD4⁺ and CD8⁺ T cells. As shown in Fig. 2a and Supplementary Fig. 4, almost half of all helper T cells left the skin during the culture period, compared to less than 5% of killer T cells, suggesting that the latter were probably sequestered from the circulation. To demonstrate such sequestration, we contrived a situation where cells with access to the bloodstream were susceptible to depletion. Adoptive transfer of virus-specific T cells of male origin into female mice results in an immune response directed to the male minor transplantation antigens that eliminates circulating cells bearing male antigens. We surmised that T cells in the epidermis of the skin might be independent from the circulation, and thus largely resistant to rejection.

Figure 2b and Supplementary Fig. 5a and b show that the male-origin virus-specific helper and killer T cells underwent expansion after skin infection with HSV, and then both were lost from the circulation at around 12 days after infection, consistent with anti-male transplant rejection. This rejection was not seen with female-into-female transfer

¹Department of Microbiology and Immunology, The University of Melbourne, Melbourne, Victoria 3010, Australia.

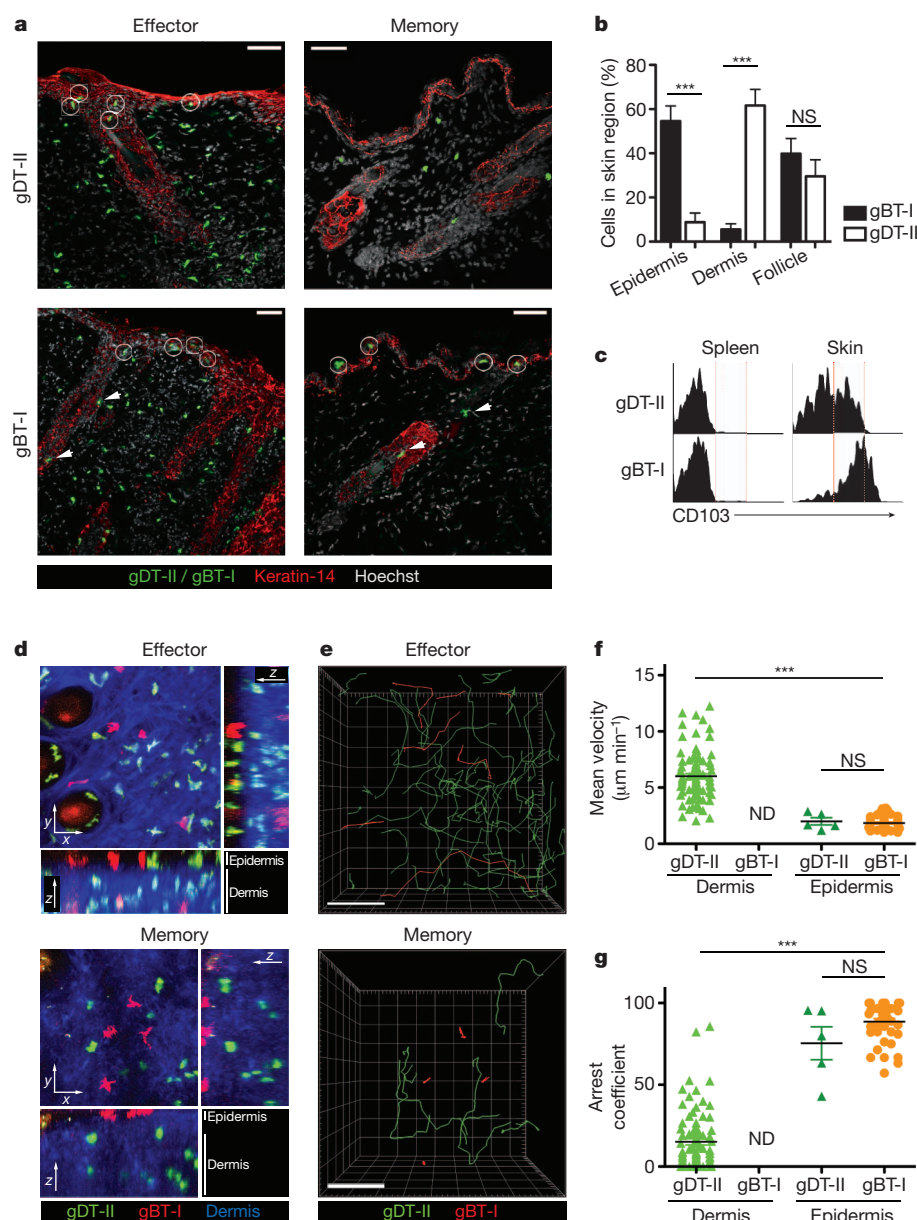


Figure 1 | Killer and helper memory T cells localize to different areas in the skin and display distinct migration patterns. **a**, **b**, Immunofluorescence of gBT-I or gDT-II cells (GFP, green) during the effector and memory response after epicutaneous HSV infection (day 8 and 30, respectively). **a**, Sections were stained for keratin-14 (red) and nuclei (Hoechst dye, white). Circles and arrowheads show GFP⁺ cells in epidermis and around hair follicles, respectively. Scale bars, 50 μm . **b**, The number of gDT-II or gBT-I T cells in different skin regions enumerated 30 days after infection (mean \pm s.e.m.). $n = 12$ –14 sections from 5–6 mice per group. **c**, CD103 expression on spleen and skin T cells 5–6 weeks after infection. **d–g**, Intravital two-photon microscopy of skin gDT-II (GFP, green) and gBT-I (DsRed, red) T cells after HSV infection. **d**, Maximum intensity projections across x , y and z dimensions of skin helper and killer T cells during the effector and memory phases (day 8 and 50 after infection, respectively). Dermis and epidermis was defined by the respective presence or absence of collagen (second harmonic generation, blue). **e**, Cell migration tracks from **d** and Supplementary Movies 1 and 4. **f**, **g**, Skin T-cell mean velocity (**f**) and arrest coefficients (**g**) during memory (day 50 after infection). One representative experiment containing five individual movies from two mice is shown. Points represent individual cells and the lines show the mean \pm s.e.m. NS, not statistically significant; ND, not detected; *** $P < 0.0001$.

controls (Supplementary Fig. 5c). In contrast to the elimination of both CD4⁺ and CD8⁺ T cells from the blood, there was a preferential survival of the male-origin skin-infiltrating killer T cells 4–5 weeks after infecting female recipients (Fig. 2c and d). Remarkably, these CD8⁺ cells persisted in the absence of their circulating counterparts for at least 10 weeks after infection (Supplementary Fig. 5d and e), demonstrating that they were independent of the circulating memory pool. As the immune privilege responsible for the CD8⁺ T-cell survival is probably confined to the epidermis, these experiments do not formally exclude the existence of some long-term dermal-resident CD4⁺ T cells. However, the results in Fig. 1 and 2 suggest that as the infection subsides and the response enters the memory phase, convalescent skin contains two generally distinct virus-specific T-cell subsets; a trafficking population of helper T cells within the dermis largely in equilibrium with the circulation, and an epithelial-localized killer T-cell population that is of limited motility and isolated from the circulating pool.

It has been reported for both sheep and humans that the cells returning to the blood via the afferent lymph show an intriguing bias towards the CD4⁺ T-cell subset^{15,16}, suggesting differences in recirculation for the distinct T-cell subsets. Consistent with this, areas of skin remote from the original site of HSV inoculation contained virus-specific CD4⁺ T cells of high motility after infection had subsided,

but strikingly, very few memory CD8⁺ T cells (Supplementary Fig. 6 and Supplementary Movie 6). We infused whole T-cell populations into uninfected recipients to show that the CD4⁺CD44⁺ memory helper subset dominated entry into the skin and vagina, whereas memory CD8⁺ T cells were more abundant in the spleen (Fig. 2e), demonstrating preferential helper T-cell migration through these tissues. In line with this, CD4⁺ T cells also dominated the skin and vagina in non-transfer, uninfected mice (Supplementary Fig. 7).

The distinct behaviour of the peripheral CD4⁺ and CD8⁺ T cells suggested that their circulating counterparts might differ in expression of tissue-homing molecules. We examined expression of E-selectin ligands (ESL) and P-selectin ligands (PSL) as E- and P-selectins are key adhesion molecules expressed in the skin endothelium¹⁷, and used splenic populations as surrogates for the circulating pool. In addition to epicutaneous infection, we included subcutaneous injection and intranasal inoculation to fully explore the potential for differential migrational programming of the two T-cell subsets. We note that all three modalities gave roughly equal levels of T-cell priming (Supplementary Fig. 8). Focusing first on the helper T cells, ESL and PSL were strongly upregulated on the effector cells after both forms of skin inoculation (Supplementary Fig. 9a–d), and this expression was generally maintained during memory (Fig. 3a–d). Importantly,

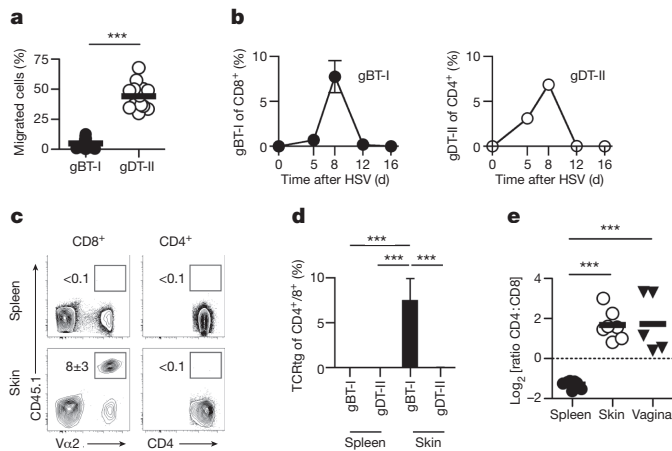


Figure 2 | Migratory differences between helper and killer memory T cells. **a**, Explanted skin containing either gBT-I or gDT-II CD45.1⁺ T cells 7–12 weeks after epicutaneous HSV infection was cultured overnight. Shown is the proportion of cells leaving the skin (migrated cells) compared with cells remaining in the tissue. Data pooled from three independent experiments; $n = 14$ –15. **b–d**, Analysis of male gBT-I and gDT-II CD45.1⁺ cells after transfer into female recipients and epicutaneous HSV infection. **b**, Frequency of HSV-specific effector gBT-I and gDT-II T cells (among total CD8⁺ or CD4⁺ T cells, respectively) in the peripheral blood. Results are mean \pm s.e.m.; $n = 10$. **c**, **d**, Analysis of gBT-I and gDT-II CD45.1⁺ cells isolated from spleen and skin 4–5 weeks after infection. **d**, Frequency of HSV-specific memory gBT-I or gDT-II T cells (TCRtg) among total CD8⁺ or CD4⁺ T cells, respectively. Results are mean \pm s.e.m.; $n = 23$. **e**, Ratio of donor CD44^{hi} CD4⁺ and CD8⁺ memory T cells in the indicated tissues 6–7 days after transfer of T cells from HSV memory mice into naive recipient mice. Symbols represent individual mice; $n = 5$ –7. *** $P < 0.001$.

intranasal inoculation induced little ESL or PSL upregulation on the CD4⁺ effector T cells (Supplementary Fig. 9a–d), and the resultant memory cells were largely ESL/PSL negative (Fig. 3a–d).

In contrast to the CD4⁺ T cells, all modes of peripheral inoculation drove substantial levels of ESL and especially PSL expression on the CD8⁺ killer T cells during both the effector (Supplementary Fig. 9a–d) and memory phase of the response (Fig. 3a–d and Supplementary Fig. 9e). At face value, the persisting ESL/PSL levels suggested that all infection modalities generated an equivalent memory killer T-cell population with skin-recirculating capacity. However, closer examination showed that homing molecule expression was largely restricted to CD8⁺ T cells of the central memory phenotype (T_{CM}), calling into question their peripheral surveillance potency (Fig. 3e). Circulating memory T cells are classified into two major subsets: a CD62L^{lo} T effector-memory (T_{EM}) population believed to be responsible for tissue surveillance and able to mount rapid response to antigen challenge, and a CD62L^{hi} T_{CM} subset that largely recirculates between the secondary lymphoid organs^{18,19}. Whereas there was a marked reduction in homing molecule expression on the CD62L^{lo} T_{EM} subset of CD8⁺ T cells, CD62L^{lo} T_{EM} CD4⁺ T cells maintained ESL and PSL expression during the memory phase of the response (Fig. 3e).

Given the preferential expression of ESL/PSL by the circulating CD4⁺ T_{EM} cells, we ascertained whether this correlated with a dominant role for helper T cells in this form of skin infection. Inhibition of HSV replication was most prominent in mice that were previously infected via the skin either by epicutaneous or subcutaneous means (Fig. 4a); these were the two modalities that programmed long-term ESL and PSL expression in the virus-specific helper T_{EM} subset. Antibody depletion of CD4⁺ T cells, but not of CD8⁺ T cells, abrogated protection seen early after HSV infection (Fig. 4b). The assessment of T-cell-mediated protection (Fig. 4a and b) was done using antibody-deficient μ MT mice and involved regions of skin not involved in the primary inoculation. This was necessary because antibody can be protective and previously infected skin will contain skin-resident CD8⁺ memory T cells able to control local infection²⁰. Also, virus loads were measured at 48 h after

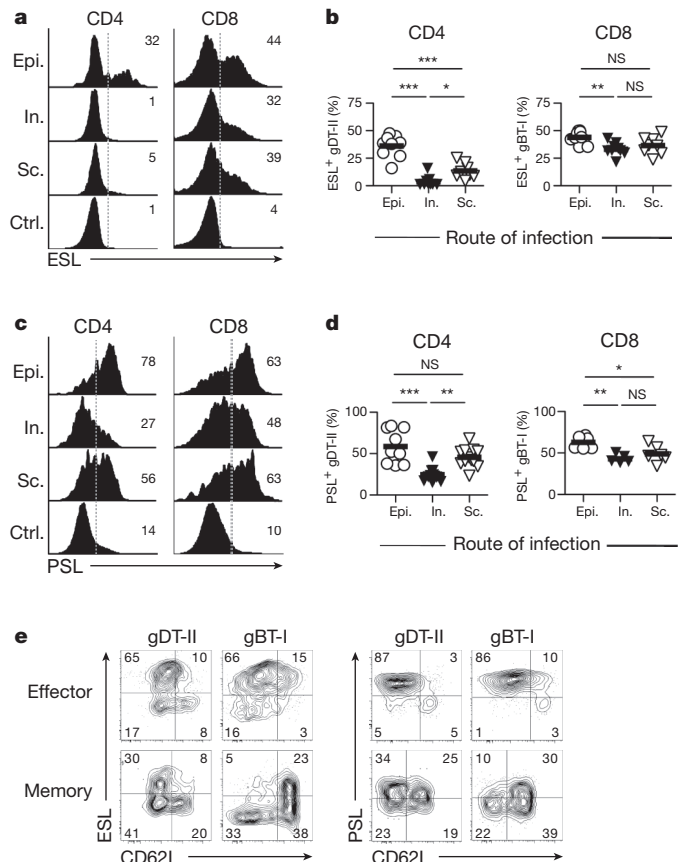


Figure 3 | Imprinting of ESL and PSL expression in memory T cells. **a–d**, Analysis of ESL (**a**, **b**) and PSL (**c**, **d**) expression by HSV-specific helper and killer T cells isolated from the spleen 4–8 weeks following adoptive transfer and HSV infection via different routes. Control histograms are gated on total CD8⁺ cells from naive mice. Epi., epicutaneous; In., intranasal; Sc., subcutaneous; Ctrl., uninfected; * $P < 0.05$, ** $P < 0.01$, *** $P < 0.001$. Numbers on histograms depict percentage of positive cells. Results from 2–4 independent experiments; $n = 8$ –12. **e**, CD62L and ESL or PSL co-expression by effector and memory gDT-II and gBT-I CD45.1⁺ T cells isolated from spleen 6 days or 2–3 months after epicutaneous HSV infection. Numbers represent percentage of events in respective quadrants.

infection, as this corresponds to the initial virus burst at the inoculation site^{7,21}, and so any reduction in titres would represent an inhibition of the first rounds of infection. Although intrinsic differences in CD4⁺ and CD8⁺ T-cell control of HSV infection may explain the observed CD4⁺ T-cell dominance of protection, the results are nonetheless consistent with the preferential skin-homing ability of this memory subset.

Skin infiltration by the circulating memory CD4⁺ T cells was examined by delivering a non-specific inflammatory stimulus using the contact-sensitizing agent 2,4-dinitro-1-fluorobenzene (DNFB). At 42 h after DNFB treatment, HSV-specific helper T cells showed preferential accumulation over killer T cells (Supplementary Fig. 10a). As expected, the recruited CD4⁺ T cells were predominantly CD62L^{lo} T_{EM} cells, whereas the small component of recruited memory CD8⁺ T cells contained a considerable proportion of CD62L^{hi} T_{CM} (Supplementary Fig. 10b). Circulating memory helper T cells (Fig. 4c) were most efficiently recruited by DNFB-mediated inflammation in mice primed by epicutaneous infection (Fig. 4d and e), and this biased recruitment was also seen in non-inflamed skin (Fig. 4f). Efficient recruitment of the virus-specific T cells was blocked by anti-E-selectin and anti-P-selectin antibodies (Supplementary Fig. 10c). Together, the results suggest that early protection in previously non-involved regions of skin was largely under helper T-cell control, which matched the migrational phenotype evident for this subset.

Our study reveals differential localization and migration of populations of memory CD4⁺ and CD8⁺ T cells after cutaneous HSV infection

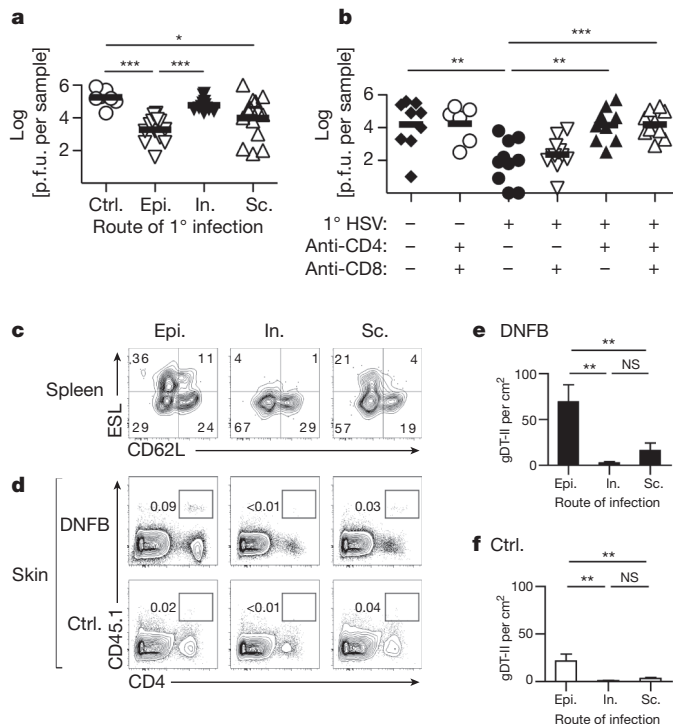


Figure 4 | Migrational imprinting mirrors immunosurveillance function by memory helper T cells. **a**, HSV load in skin 2 days after epicutaneous challenge of μ MT mice primed via different routes of inoculation (as in Fig. 3) 4–6 weeks earlier. Controls (Ctrl.) are non-immunized mice. $n = 9$ –14. **b**, HSV load in contralateral skin 2 days after epicutaneous inoculation of μ MT mice primed 4–5 weeks earlier and treated with anti-CD4 and/or anti-CD8 antibodies before reinfection. $n = 6$ –11. **c–f**, Analysis of HSV-specific memory T helper cells isolated from spleen and inflamed (DNFB) or control (Ctrl.) skin. DNFB was applied to skin of mice containing gDT-II CD45.1⁺ memory CD4⁺ T cells after HSV inoculation via different routes (as in Fig. 3) 9–12 weeks earlier. **c**, Phenotype of memory gDT-II CD45.1⁺ T cells isolated from spleen. Numbers represent percentage of events in respective quadrants. **d–f**, Detection and enumeration of memory gDT-II CD45.1⁺ T cells in skin 42 h after initiation of skin inflammation expressed as mean \pm s.e.m. $n = 9$ –11; * $P < 0.05$, ** $P < 0.01$, *** $P < 0.001$.

(Supplementary Fig. 1). It remains unclear whether the phenomenon extends to other infections, although preferential recirculation of CD4⁺ T cells has been shown for normal skin of sheep and humans^{15,16}. In addition, sequestration of CD8⁺ memory T cells within extra-lymphoid compartments, with limited input from the wider circulation, has been reported with other tissue and virus combinations^{22–24}. Overall, the previously unappreciated migration-linked T-cell subset specialization shown here has the potential to affect a range of peripheral immune phenomena, at least in barrier tissues such as skin and mucosa.

METHODS SUMMARY

Epicutaneous infection by scarification was done using the HSV-1 KOS strain as described elsewhere⁹. For T-cell isolation, mice were perfused with saline before removal of 1–2 cm² of skin, which was incubated for 90 min at 37 °C with collagenase (3 mg ml⁻¹) and DNase (5 μ g ml⁻¹). For some experiments, the skin was first incubated for 90 min at 37 °C with Dispase (2.5 mg ml⁻¹) and DNase (5 μ g ml⁻¹), followed by mechanical separation of epidermis and dermis. For intravital two-photon microscopy, mice were anaesthetized, depilated and two parallel incisions were made approximately 15 mm apart along the flank. The skin was separated from the peritoneum, and adhered to an 18-mm-wide piece of 1-mm stainless steel inserted to form a stable raised platform, attached to a custom-made imaging platform maintained at 35 °C. Images were acquired with an upright LSM710 NLO multiphoton microscope (Carl Zeiss Microimaging) with a $\times 20/1.0$ NA water immersion objective. For four-dimensional data sets, three-dimensional stacks were captured every 1 min for 30–120 min. Raw imaging data were processed with Imaris 7.1 (Biplane).

Full Methods and any associated references are available in the online version of the paper at www.nature.com/nature.

Received 17 September 2010; accepted 28 June 2011.

Published online 14 August 2011.

- Sigmundsdottir, H. & Butcher, E. C. Environmental cues, dendritic cells and the programming of tissue-selective lymphocyte trafficking. *Nature Immunol.* **9**, 981–987 (2008).
- Kaech, S. M. & Wherry, E. J. Heterogeneity and cell-fate decisions in effector and memory CD8⁺ T cell differentiation during viral infection. *Immunity* **27**, 393–405 (2007).
- Woodland, D. L. & Kohlmeier, J. E. Migration, maintenance and recall of memory T cells in peripheral tissues. *Nature Rev. Immunol.* **9**, 153–161 (2009).
- Seder, R. A. & Ahmed, R. Similarities and differences in CD4⁺ and CD8⁺ effector and memory T cell generation. *Nature Immunol.* **4**, 835–842 (2003).
- Bouso, P. T-cell activation by dendritic cells in the lymph node: lessons from the movies. *Nature Rev. Immunol.* **8**, 675–684 (2008).
- Mueller, S. N. & Hickman, H. D. *In vivo* imaging of the T cell response to infection. *Curr. Opin. Immunol.* **22**, 293–298 (2010).
- Bedoui, S. *et al.* Cross-presentation of viral and self antigens by skin-derived CD103⁺ dendritic cells. *Nature Immunol.* **10**, 488–495 (2009).
- Mueller, S. N., Heath, W., McLain, J. D., Carbone, F. R. & Jones, C. M. Characterization of two TCR transgenic mouse lines specific for herpes simplex virus. *Immunol. Cell Biol.* **80**, 156–163 (2002).
- van Lint, A. *et al.* Herpes simplex virus-specific CD8⁺ T cells can clear established lytic infections from skin and nerves and can partially limit the early spread of virus after cutaneous inoculation. *J. Immunol.* **172**, 392–397 (2004).
- Cepek, K. L. *et al.* Adhesion between epithelial cells and T lymphocytes mediated by E-cadherin and the $\alpha\beta_7$ integrin. *Nature* **372**, 190–193 (1994).
- Schon, M. P. *et al.* Mucosal T lymphocyte numbers are selectively reduced in integrin α_E (CD103)-deficient mice. *J. Immunol.* **162**, 6641–6649 (1999).
- Nestle, F. O., Di Meglio, P., Qin, J. Z. & Nickoloff, B. J. Skin immune sentinels in health and disease. *Nature Rev. Immunol.* **9**, 679–691 (2009).
- Zhu, J. *et al.* Persistence of HIV-1 receptor-positive cells after HSV-2 reactivation is a potential mechanism for increased HIV-1 acquisition. *Nature Med.* **15**, 886–892 (2009).
- Miller, C. J., McChesney, M. & Moore, P. F. Langerhans cells, macrophages and lymphocyte subsets in the cervix and vagina of rhesus macaques. *Lab. Invest.* **67**, 628–634 (1992).
- Mackay, C. R., Marston, W. L. & Dudley, L. Naive and memory T cells show distinct pathways of lymphocyte recirculation. *J. Exp. Med.* **171**, 801–817 (1990).
- Yawalkar, N., Hunger, R. E., Pichler, W. J., Braathen, L. R. & Brand, C. U. Human afferent lymph from normal skin contains an increased number of mainly memory/effector CD4⁺ T cells expressing activation, adhesion and co-stimulatory molecules. *Eur. J. Immunol.* **30**, 491–497 (2000).
- Ley, K., Laudanna, C., Cybulsky, M. I. & Nourshargh, S. Getting to the site of inflammation: the leukocyte adhesion cascade updated. *Nature Rev. Immunol.* **7**, 678–689 (2007).
- Masopust, D., Vezys, V., Marzo, A. L. & Lefrancois, L. Preferential localization of effector memory cells in nonlymphoid tissue. *Science* **291**, 2413–2417 (2001).
- Sallusto, F., Lenig, D., Forster, R., Lipp, M. & Lanzavecchia, A. Two subsets of memory T lymphocytes with distinct homing potentials and effector functions. *Nature* **401**, 708–712 (1999).
- Gebhardt, T. *et al.* Memory T cells in nonlymphoid tissue that provide enhanced local immunity during infection with herpes simplex virus. *Nature Immunol.* **10**, 524–530 (2009).
- Wakim, L. M., Jones, C. M., Gebhardt, T., Preston, C. M. & Carbone, F. R. CD8⁺ T-cell attenuation of cutaneous herpes simplex virus infection reduces the average viral copy number of the ensuing latent infection. *Immunol. Cell Biol.* **86**, 666–675 (2008).
- Masopust, D. *et al.* Dynamic T cell migration program provides resident memory within intestinal epithelium. *J. Exp. Med.* **207**, 553–564 (2010).
- Wakim, L. M., Woodward-Davis, A. & Bevan, M. J. Memory T cells persisting within the brain after local infection show functional adaptations to their tissue of residence. *Proc. Natl Acad. Sci. USA* **107**, 17872–17879 (2010).
- Klonowski, K. D. *et al.* Dynamics of blood-borne CD8 memory T cell migration *in vivo*. *Immunity* **20**, 551–562 (2004).

Supplementary Information is linked to the online version of the paper at www.nature.com/nature.

Acknowledgements We thank members of the Carbone and Heath laboratories for discussions. This work was supported by the Australian NHMRC and ARC.

Author Contributions T.G., W.R.H., F.R.C. and S.N.M. designed the study. T.G., A.Z., L.K.M. and S.N.M. performed experiments. T.G., A.Z. and S.N.M. collected and analysed data. P.G.W. and A.G.B. provided reagents and gave conceptual advice. F.R.C. wrote the manuscript with T.G., W.R.H. and S.N.M. The research program was led by F.R.C. and W.R.H. who are joint senior authors.

Author Information Reprints and permissions information is available at www.nature.com/reprints. The authors declare no competing financial interests. Readers are welcome to comment on the online version of this article at www.nature.com/nature. Correspondence and requests for materials should be addressed to S.N.M. (smue@unimelb.edu.au) or T.G. (gebhardt@unimelb.edu.au).

METHODS

Mice. C57BL/6, B6.SJL-*PtprcaPep3b/BoyJ* (B6.CD45.1), gBT-I^g, gDT-II^g, gBT-I × B6.CD45.1 (gBT-I.CD45.1), gBT-I.EGFP, gBT-I.DsRed, gDT-II × B6.CD45.1 (gDT-II.CD45.1), gDT-II.EGFP and μMT mice were bred in the Department of Microbiology and Immunology at The University of Melbourne. gBT-I and gDT-II are T-cell receptor-transgenic mice recognizing the HSV-1 glycoprotein B-derived epitope gB_{498–505} and the glycoprotein D-derived epitope gD_{290–302}, respectively. B6.CD45.1 mice express the congenic marker CD45.1, in contrast to C57BL/6 that express CD45.2. gBT-I.CD45.1 and gDT-II.CD45.1 are F₁ generation offspring expressing both CD45.1 and CD45.2. Animal experiments were approved by The University of Melbourne Animal Ethics Committee.

Virus infections. Epicutaneous infection by scarification was done using 1×10^6 plaque forming units (p.f.u.) of the HSV-1 KOS strain as described in detail elsewhere⁹. Briefly, mice were anaesthetized by i.p. injection of a 1:1 mixture of ketamine and Xylazil ($10 \mu\text{g l}^{-1}$ of body weight) solution in saline. Hair was removed from the left flank of each mouse with clippers and depilation cream (Veet, Reckitt Benckiser) and a small area of skin ($2\text{--}4 \text{ mm}^2$) corresponding with the top of the spleen was lightly abraded before inoculation of virus in a $10 \mu\text{l}$ volume. The infection site was then covered with a piece of OpSite Flexigrid (Smith & Nephew) and secured with Micropore tape and Transpore tape (3M Health Care) for 48 h following infection. This method of inoculation results in zosteriform spread of virus throughout the dermatome with complete virus clearance by day 8 after infection⁹ and extinguishing of antigen presentation within the lymph nodes by 3–4 weeks after infection²⁵. Lung infection (1×10^6 p.f.u.) was performed by intranasal inoculation and subcutaneous infection by injection into the left and right foot hocks (4×10^5 p.f.u. each). Intravaginal infection was performed on mice treated with progesterone (Depo Provera, 2 mg per mouse) by subcutaneous injection in the scruff of the neck, 5–7 days earlier. For infection, mice were intravaginally swabbed with calcium alginate swabs and inoculated with 1×10^6 p.f.u. of HSV in $10 \mu\text{l}$ phosphate buffered saline (PBS) using a blunt pipette tip. Rechallenge infections, done in μMT mice to circumvent interference by neutralizing antibodies, involved scarification using the thymidine kinase-deficient KOS.CreTK[−] strain (1×10^6 p.f.u.). Viral titres were analysed using standard p.f.u. assay on Vero cells as described elsewhere⁹.

Adoptive transfer of T cells and antibody treatments. T cells were isolated from spleen and/or lymph nodes of transgenic female mice. For selected experiments, cell suspensions were magnetically enriched for CD8⁺ or CD4⁺ T cells by negative selection as described⁷, yielding purities of >90% for gBT-I and 20–40% for gDT-II cells. For some experiments, gDT-II cells were further positively selected using magnetically labelled anti-CD4 antibodies (Dynabeads mouse CD4, L4T4) and the DetachA bead reagent for mouse CD4 (both from Invitrogen Dynal As), yielding purities between 40% and 70%. Cell suspensions corresponding to 1×10^4 gDT-II (2.5×10^4 for imaging) and 5×10^4 gBT-I cells were intravenously transferred into congenic female recipient mice. For sex-mismatched transfer experiments, cells were isolated from male donor mice and 1×10^5 of each transgenic T-cell population was transferred either together or separately into recipient female mice. For experiments analysing the migration of endogenous memory T cells, spleen cells were isolated from C57BL/6 mice 1–7 months after HSV flank infection, magnetically enriched for T cells and transferred into naive B6.CD45.1 recipient mice ($3\text{--}7 \times 10^7$ total cells per mouse). Donor cells were analysed in spleen, skin and vagina at least 6 days after transfer. Depletion of CD4⁺ and/or CD8⁺ cells was achieved by treating mice with monoclonal antibodies, GK1.5 (0.1 mg per mouse) and/or 2.43 (0.1 mg per mouse) for three consecutive days. These antibodies were prepared by the National Cell Culture Center. Blocking antibodies to CD62E and CD62P (10E9.6, RB40.34; both from BD Pharmingen) were injected intraperitoneally into mice (0.1 mg of each antibody) for three consecutive days before DNFB challenge. The treatment was continued for 2 days (0.2 mg of each antibody) thereafter.

Immunofluorescence and confocal microscopy. Skin from the flank of HSV-infected mice (left flank, infected; right flank, uninfected) was collected at various times after infection and fixed in 4% paraformaldehyde and 10% sucrose (w/v in PBS) for 20 min at room temperature (20 °C). Vaginal tissues were collected from mice after intravaginal infection and fixed in 4% paraformaldehyde and 10% sucrose for 10 min at room temperature (20 °C), followed by incubation in 20% sucrose for 20 min. Fixed tissue was embedded in OCT (Tissue Tek IA018; Sakura) and frozen in liquid nitrogen. Tissue sections were performed on a cryostat (Leica CM3050S) at $12\text{--}25 \mu\text{m}$ thickness and air-dried for 16–18 h before staining. Sections were fixed in -20°C acetone for 5 min, rehydrated with PBS for 15 min then blocked for 10 min (Protein Block X0909; DAKO) at room temperature (20 °C). When using biotinylated antibodies, avidin-biotin blocking (Dako Biotin-Blocking System X0590; DAKO) was applied for 5 min each before primary antibody incubation. Sections were stained with rabbit anti-keratin 14 antibody (clone AF64; Covance), rabbit anti-collagen IV (Abcam), or CD8a-AlexaFluor488

(clone 53-6.7; Caltag) and CD4-biotin (clone L3T4, BD Pharmingen) for 3 h at 4 °C in a semi-humid chamber. Sections were rinsed for 10 min in PBS, and labelled with donkey anti-rabbit AlexaFluor647 (A31573; Invitrogen) or streptavidin-conjugated AlexaFluor555 (S32355; Invitrogen) for 40 min at room temperature (20 °C). Sections were rinsed for 10 min in PBS, incubated with Hoechst nuclear stain (H33258, 1:3,000 vol./vol. in PBS) for 3 min, and then mounted with ProLongGold (P36934; Invitrogen). Images were acquired with a Zeiss LSM710 microscope and processed using Imaris 7.1 software (Bitplane). For calculating T-cell numbers in skin regions (epidermis, dermis and associated with hair follicles) or vaginal tissue (epithelia and lamina propria), the number of T cells in each region was counted in multiple sections from each mouse at 30 days after infection (skin) or 22 days after infection (vagina).

Intravital two-photon microscopy. Mice were anaesthetized with isoflurane (Cenvet; 2.5% for induction, ~1.5% for maintenance, vaporized in an 80:20 mixture of oxygen and air) using a Tech 3 vaporizer (Surgivet), and the left flank shaved and depilated using Veet (Reckitt Benckiser). Two parallel incisions were made through the dermis, approximately 15 mm apart, along the flank. The skin was carefully separated from the peritoneum, and an 18-mm-wide piece of 1-mm stainless steel inserted under the dermis. This formed a stable raised platform, attached to a custom made imaging platform. The underside of the dermis was adhered to the steel platform using Vetbond tissue adhesive (3M). Vacuum grease (Dow Corning) was used to attach and seal a glass coverslip onto the epidermis of the skin for imaging. Moist gauze was packed around the incision and covered to prevent dehydration.

Images were acquired with an upright LSM710 NLO multiphoton microscope (Carl Zeiss Microimaging) enclosed in a custom-built environmental chamber (Precision Plastics) that was maintained at 35 °C with heated air. Three external non-scanned PMT detectors in the reflected light path were used to acquire images. Images were acquired with a $\times 20/1.0 \text{ NA}$ water immersion objective. Fluorescence excitation was provided by a Chameleon Vision II Ti:sapphire laser (Coherent), with dispersion correction. EGFP and DsRed were excited at 940 nm. The collagen-rich dermis of the skin was visualized by second harmonic generation, using a short-pass 485 nm filter. Typical voxel dimensions were $(0.55\text{--}0.7) \times (0.55\text{--}0.7) \times 3 \mu\text{m}$. For four-dimensional data sets, three-dimensional stacks were captured every 1 min for 30–120 min.

Raw imaging data were processed with Imaris 7.1 (Bitplane). Cell migration was analysed through automatic cell tracking aided by manual corrections. Only tracks that lasted longer than 5 min were analysed. Statistical data were imported into Excel (Microsoft) for calculating cell velocities, displacement over time, relative cell tracks, and arrest coefficients (proportion of time cells were moving at less than $2 \mu\text{m min}^{-1}$). Data were used to plot graphs in Prism 5 (Graphpad). For the generation of movies, image sequences exported from Imaris were composed in Adobe After Effects CS5.

Cell isolation and flow cytometry. Mice were killed by carbon dioxide administration and perfusion performed with 10 ml Hank's buffered salt solution (Media Preparation Unit, The University of Melbourne). Spleens were harvested and disrupted by passage through a wire mesh. Skin tissue ($1\text{--}2 \text{ cm}^2$) was removed after clipping and treatment of flank skin with Veet depilation cream (Reckitt Benckiser), chopped into small fragments and incubated for 90 min at 37 °C in MEM medium containing fetal calf serum (FCS, 2%, Gibco BRL), collagenase (3 mg ml^{−1}; Worthington) and DNase (5 μg ml^{−1}, Sigma). For some experiments skin samples were first incubated for 90 min at 37 °C in 3 ml PBS containing Dispase (2.5 mg ml^{−1}, Roche) and DNase (5 μg ml^{−1}) followed by the mechanical separation of epidermis and dermis. Epidermal sheets were subsequently incubated for 30 min in Trypsin/EDTA (0.25%/0.1%, SAFC Biosciences) whereas the remaining skin tissue was chopped into small fragments and incubated for 30 min at 37 °C in collagenase solution. For analysis of vaginal tissues, tissue was isolated, the cervix removed, and chopped into small pieces before incubation in calcium- and magnesium-free HBSS medium containing 1.3 mM EDTA for 30 min (37 °C, shaking at 180 r.p.m.). Tissue pieces were then treated with 1 mg ml^{−1} collagenase 3 (Worthington) and 5 μg ml^{−1} DNase (Sigma) in RPMI supplemented with 1 mM MgCl₂ and CaCl₂ and 5% FCS for 90 min at 37 °C, shaking at 180 r.p.m. Tissues were pushed through 70 μm nylon mesh and lymphocytes purified on a 44/67% Percoll (GE Healthcare) gradient (centrifuged at 800g, 20 °C for 20 min, no brake). All cell suspensions were filtered twice through nylon meshes (70 and 30 μm pore size) before staining for flow cytometric analysis (30 min at 4 °C) or overnight culture in RPMI 1640 medium containing 10% (vol./vol.) FCS and standard supplements¹². The following antibodies/reagents were purchased from BD Pharmingen: anti-CD8a-APC and anti-CD8a-PE-Cy7 (53-6.7), anti-CD45.1-FITC and anti-CD45.1-PE (A20), anti-CD45.2-FITC (104), anti-CD4-APCCy7 and anti-CD4-PE-Cy7 (GK1.5 or RM4-5), anti-Vα2-PE (B20.1), CD62L-PE (Me1-14), anti-CD16/32 (2.4G2) and streptavidin-FITC. Anti-CD8a-APC eFluor 780 (53-6.7), anti-CD45.1-APC (A20), anti-CD45.2-PE (104) and anti-CD45.2-APC

eFluor 780 (104) and anti-CD103-FITC (2E7) were purchased from eBioscience. E- and P-selectin binding was measured using mouse E- or P-selectin Fc chimaeric proteins ($1 \mu\text{g ml}^{-1}$ or $0.3 \mu\text{g ml}^{-1}$ respectively; R&D Systems) in conjunction with biotin conjugated rabbit anti-human IgG F(c) antibody (Rockland). Dead cells were identified using propidium iodide (PI) staining. Sphero calibration particles (BD Pharmingen) were added to the samples to allow for calculation of cell numbers. Flow cytometric analysis was performed using FACSCanto II flow cytometers and FlowJo software (TreeStar).

DNFB treatment. HSV memory or naive control mice were anaesthetized and the back and the flanks were clipped and treated with Veet depilation cream. $25 \mu\text{l}$ of 0.5% (vol./vol.) DNFB in acetone/oil (4:1) were applied onto a 1 cm^2 area of previously non-infected skin. 42 h after treatment, mice were killed for analysis of memory cell migration into treated and non-treated areas of skin.

Ex vivo migration assay. Full thickness skin was excised from previously infected mice as described above. Skin samples were cultured overnight in RPMI 1640 medium containing 10% (vol./vol.) FCS and standard supplements⁹. The next day, cells that had migrated out of explants were harvested from the culture medium and non-migrated cells left in skin tissue were isolated as described above. Cells were enumerated by flow cytometry.

Statistics. Comparison of data sets was performed by one-way analysis of variance followed by Tukey post-test or by two-tailed, unpaired Student's *t*-test where appropriate.

25. Stock, A. T., Jones, C. M., Heath, W. R. & Carbone, F. R. Rapid recruitment and activation of CD8^+ T cells after herpes simplex virus type 1 skin infection. *Immunol. Cell Biol.* **89**, 143–148 (2011).

Continued clearance of apoptotic cells critically depends on the phagocyte Ucp2 protein

Daeho Park^{1,2}, Claudia Z. Han^{1,2,3}, Michael R. Elliott^{1,2}, Jason M. Kinchen^{1,2,3}, Paul C. Trampont^{1,2}, Soumita Das⁴, Sheila Collins⁵, Jeffrey J. Lysiak⁶, Kyle L. Hoehn⁷ & Kodi S. Ravichandran^{1,2,3}

Rapid and efficient removal of apoptotic cells by phagocytes is important during development, tissue homeostasis and in immune responses^{1–5}. Efficient clearance depends on the capacity of a single phagocyte to ingest multiple apoptotic cells successively, and to process the corpse-derived cellular material⁶. However, the factors that influence continued clearance by phagocytes are not known. Here we show that the mitochondrial membrane potential of the phagocyte critically controls engulfment capacity, with lower potential enhancing engulfment and vice versa. The mitochondrial membrane protein Ucp2, which acts to lower the mitochondrial membrane potential^{7–9}, was upregulated in phagocytes engulfing apoptotic cells. Loss of Ucp2 reduced phagocytic capacity, whereas Ucp2 overexpression enhanced engulfment. Mutational and pharmacological studies indicated a direct role for Ucp2-mediated mitochondrial function in phagocytosis. Macrophages from Ucp2-deficient mice^{10,11} were impaired in phagocytosis *in vitro*, and Ucp2-deficient mice showed profound *in vivo* defects in clearing dying cells in the thymus and testes. Collectively, these data indicate that mitochondrial membrane potential and Ucp2 are key molecular determinants of apoptotic cell clearance. As Ucp2 is linked to metabolic diseases and atherosclerosis^{11,12}, this newly discovered role for Ucp2 in apoptotic cell clearance has implications for the complex aetiology and pathogenesis of these diseases.

When a phagocyte engulfs a dying cell it essentially doubles its cellular contents. Yet phagocytes often ingest multiple apoptotic cells sequentially, and the factors regulating the ‘engulfment capacity’ of a given phagocyte are not understood. Because metabolites derived from the ingested apoptotic cells could influence phagocyte mitochondrial function, we asked whether the phagocyte mitochondrial membrane potential is altered. Phagocytes labelled with the dyes JC-1 (the red-to-green fluorescence ratio of which depends on mitochondrial membrane potential¹³; Supplementary Fig. 1a) or TMRE were incubated with apoptotic thymocytes for different periods of time. To focus on phagocytes with ingested targets, the thymocytes were labelled with cypHer5E, a pH-dependent dye for which the fluorescence increases after the apoptotic corpse enters the acidic phagolysosome. There was a significant increase in the relative mitochondrial membrane potential in phagocytes with engulfed targets (1.99-fold \pm 0.11, $P < 0.001$, $n = 6$) compared to non-engulfing phagocytes within the same population (Fig. 1a and Supplementary Fig. 1b). The enhanced mitochondrial membrane potential was not derived from the apoptotic thymocytes (Supplementary Fig. 1c). Remarkably, phagocytes ingesting synthetic targets showed no increase in mitochondrial membrane potential (Fig. 1a and Supplementary Fig. 1b), even though the synthetic targets use components of the apoptotic cell engulfment machinery¹⁴. As the synthetic targets do not have a metabolic load, the higher mitochondrial membrane potential could not be attributed to a general effect of engulfment. The mitochondrial membrane potential returned

to baseline over the next few hours (Fig. 1b). In general, cellular ATP levels are maintained within a fairly narrow range and the engulfing phagocytes had a modest 10% increase in cellular ATP at the 2-h point (Supplementary Fig. 1d). Therefore, the return to baseline of the mitochondrial membrane potential within phagocytes suggested a mechanism for uncoupling nutrient oxidation from ATP generation⁸.

A well-known mechanism for uncoupling the proton gradient and ATP generation is mediated by uncoupling proteins (UCPs)⁸. UCPs regulate the mitochondrial membrane potential through dissipation of the proton gradient across the inner mitochondrial membrane, without ATP generation. Compared to Ucp1 (restricted to brown adipose tissue)¹⁵, Ucp2 is more ubiquitously expressed⁸, with expression also occurring in several phagocytic cell types (Supplementary Fig. 2a). Whereas messenger RNA levels of *Ucp2* were not detectably altered within engulfing phagocytes, mitochondrial Ucp2 protein levels increased after incubation with apoptotic cells (Fig. 1c, left, and Supplementary Fig. 2b, c). The higher Ucp2 protein levels were not derived from ingested targets, as Ucp2 levels in thymocytes were below detection, and Ucp2-deficient apoptotic thymocytes used as targets also enhanced Ucp2 protein levels in phagocytes (Fig. 1c and Supplementary Fig. 2d). The synthetic targets did not induce higher levels of Ucp2, consistent with their lack of effect on mitochondrial membrane potential (Fig. 1c, right).

To test directly the role of Ucp2 in engulfment, we knocked down endogenous *Ucp2* expression in phagocytes via short interfering RNA (siRNA) (Supplementary Fig. 1e). *Ucp2* knockdown in NIH/3T3 cells led to increased mitochondrial membrane potential basally and during engulfment (Fig. 1d and Supplementary Fig. 2f). We observed two key phenotypes in Ucp2-depleted cells. First, *Ucp2* knockdown phagocytes were less efficient engulfers, with a lower percentage of phagocytes ingesting apoptotic cells over a 6-h time course (Fig. 1e, left). Second, *Ucp2* knockdown reduced the phagocytic ‘capacity’ with a lower amount of apoptotic material being ingested per phagocyte (mean fluorescence intensity derived from the labelled apoptotic cells) (Fig. 1e, right). Again, the uptake of synthetic targets was unaffected by *Ucp2* knockdown (Fig. 1f). These data indicated that phagocytes engulfing apoptotic cells upregulate Ucp2 and that Ucp2 expression influences phagocytic capacity.

To test whether overexpressing Ucp2 might provide a ‘gain of function’ for engulfing apoptotic cells, we transiently overexpressed Flag-tagged Ucp2 in LR73 phagocytes. Ucp2-Flag was properly targeted to the mitochondria (Supplementary Fig. 3a, b), and Ucp2-Flag cells showed three striking phenotypes. First, a greater percentage of Ucp2-Flag cells ingested apoptotic cells, and this enhanced uptake depended on the known engulfment machinery components (Fig. 2a and Supplementary Fig. 4a, b). Second, in a time course, Ucp2-Flag cells continued to ingest apoptotic targets for up to 6 h whereas control-transfected LR73 cells reached a plateau by 2 h (Fig. 2b). Ucp2-overexpressing cells had

¹Center for Cell Clearance, University of Virginia, Charlottesville, Virginia 22908, USA. ²Beirne B. Cater Center for Immunology Research, University of Virginia, Charlottesville, Virginia 22908, USA.

³Department of Microbiology, University of Virginia, Charlottesville, Virginia 22908, USA. ⁴Department of Medicine, University of Virginia, Charlottesville, Virginia 22908, USA. ⁵Diabetes and Obesity Research Center, Sanford-Burnham Medical Research Institute, Orlando, Florida 32827, USA. ⁶Department of Urology, University of Virginia, Charlottesville, Virginia 22908, USA. ⁷Department of Pharmacology and CVRC, University of Virginia, Charlottesville, Virginia 22908, USA.

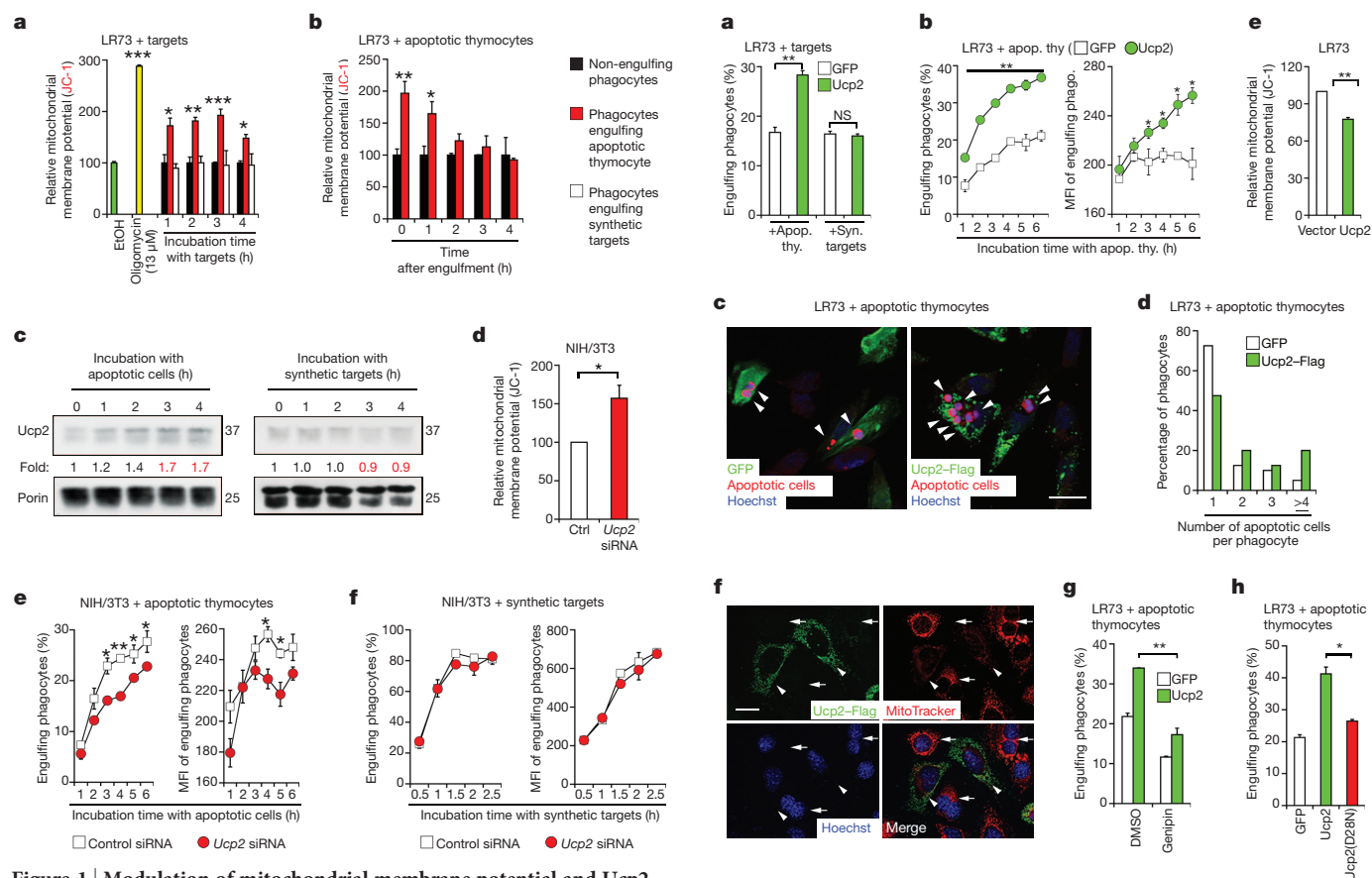


Figure 1 | Modulation of mitochondrial membrane potential and Ucp2 during engulfment. **a**, Increase in mitochondrial membrane potential in engulfing phagocytes. LR73 phagocytes were stained with JC-1 and incubated with cypHer5E-labelled apoptotic thymocytes or synthetic targets. Mitochondrial membrane potentials in engulfing and non-engulfing phagocytes within the same population (based on cypHer5E and pacific blue signal) were compared. Oligomycin-treated phagocytes served as a positive control for increased mitochondrial membrane potential. **b**, LR73 cells were incubated with cypHer5E-stained apoptotic thymocytes (3 h), washed to remove unengulfed targets, and further incubated for the indicated times, stained with JC-1 dye and analysed as above. **c**, LR73 cells were incubated with targets (apoptotic thymocytes from *Ucp2* knockout mice or synthetic targets), and the mitochondrial fractions were immunoblotted for endogenous Ucp2. The mitochondrial membrane protein porin served as loading control. **d**, Mitochondrial membrane potential in control (Ctrl) or *Ucp2* siRNA transfected NIH/3T3 (2 days post-transfection) was determined via JC-1 dye and flow cytometry. **e**, **f**, NIH/3T3 cells transfected with control or *Ucp2*-specific siRNA were incubated with apoptotic thymocytes stained with the dye TAMRA (**e**) or synthetic targets (**f**) and the percentage of cells engulfing targets (left) and phagocytic capacity (using the apoptotic-cell-derived fluorescence per phagocyte) were determined. Data are shown as mean \pm standard deviation (s.d.) and are representative of at least two independent experiments. * $P < 0.05$, ** $P < 0.01$, *** $P < 0.001$.

more ingested apoptotic cells per phagocyte (Fig. 2c, d). Third, the rate of uptake of synthetic targets was unaffected in Ucp2-Flag cells (Supplementary Fig. 4c), suggesting a role for Ucp2 in sensing the metabolic load derived from apoptotic cells. Overexpression of Ucp2 homologues (Ucp1 or Ucp3; Supplementary Fig. 4d) also promoted engulfment. Thus, higher levels of Ucp2 provide a gain-of-function phenotype, conferring a capacity for phagocytes to 'continue to eat' apoptotic cells.

Ucp2-Flag cells showed decreased mitochondrial membrane potential compared to controls (Fig. 2e). The signal for MitoTracker, a dye that accumulates as the mitochondrial membrane potential increases¹⁶, was distinctly weaker in Ucp2-Flag-expressing cells compared to neighbouring non-transfected cells (Fig. 2f). The drug genipin, which inhibits mitochondrial uncoupling by Ucp2 (ref. 17), blunted the

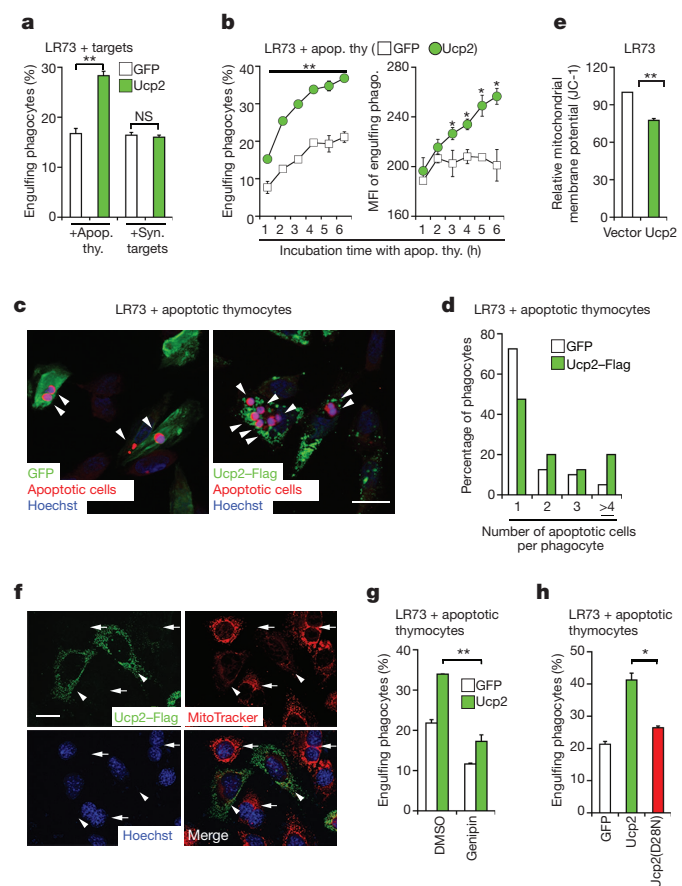


Figure 2 | Ucp2 overexpression promotes continued uptake of apoptotic cells. **a**, LR73 cells transfected with Ucp2 show enhanced uptake of apoptotic thymocytes (Apop. thy.) but not synthetic targets (Syn. targets). NS, not significant. **b**, LR73 cells expressing GFP or Ucp2 were incubated with TAMRA-stained apoptotic thymocytes for the indicated times, and the percentage (left) and mean fluorescence intensity of engulfing phagocytes, which reflects the ability to continue to ingest apoptotic cells (right), are shown. **c**, Comparison of LR73 cells transfected with GFP alone or Ucp2-Flag engulfing TAMRA-stained apoptotic thymocytes (4 h) assessed by confocal microscopy. Arrowheads indicate engulfed apoptotic thymocytes. Scale bar, 20 μ m. **d**, Forty randomly chosen fields from **c** were counted, and the percentage of phagocytes with the indicated number of internalized apoptotic cells is shown. **e**, Mitochondrial membrane potential of LR73 cells transfected with Ucp2 or control vector. **f**, Fluorescence microscopy of NIH/3T3 cells transfected with Ucp2-Flag and stained with MitoTracker and anti-Flag antibody. Arrowheads indicate NIH/3T3 cells expressing Ucp2-Flag and arrows indicate non-transfected cells. Scale bar, 20 μ m. **g**, LR73 phagocytes expressing GFP or Ucp2 were pre-treated with vehicle control or genipin (100 μ M) for 1 h and assessed for engulfment. **h**, Ucp2(D28N) mutant fails to enhance engulfment of apoptotic thymocytes. Data are shown as mean \pm s.d. and are representative of at least three independent experiments. * $P < 0.05$, ** $P < 0.01$.

enhanced engulfment by Ucp2 (Fig. 2g and Supplementary Fig. 4e). As a parallel approach, we generated a Ucp2(D28N) mutant with decreased uncoupling activity^{18,19}. The Ucp2(D28N) mutant was expressed and localized to the mitochondria (as did wild type), yet Ucp2(D28N) failed to enhance engulfment of apoptotic cells (Fig. 2h and Supplementary Fig. 4f). Collectively, the decrease in mitochondrial membrane potential by Ucp2 correlates with enhanced and continued uptake of apoptotic cells.

We then asked whether the effect of Ucp2 could be mimicked by synthetic uncouplers that lower the mitochondrial membrane potential^{20,21}. We tested 2,4-dinitrophenol (2,4-DNP) and carbonyl cyanide 4-(trifluoromethoxy)phenylhydrazone (FCCP) over a range of concentrations at which the total cellular ATP levels were unaltered and

the phagocytes appeared morphologically similar to controls (Supplementary Fig. 5a, b). Both 2,4-DNP and FCCP significantly enhanced the uptake of apoptotic thymocytes by LR73 phagocytes (Fig. 3a); this increased uptake correlated with decreased mitochondrial membrane potential induced by these drugs (Supplementary Fig. 5c, d). Synthetic uncoupling also promoted phagocytes to continue to ingest multiple apoptotic cells over a time course (similar to Ucp2 overexpression) (Fig. 3b, c and Supplementary Fig. 5g). To test whether mitochondrial membrane potential itself was the signal for enhanced engulfment capacity—that is, independent of increased proton leak and electron transport chain flux—we tested sodium azide, an inhibitor of complex IV of the electron transport chain that slows electron transport flux and lowers mitochondrial membrane potential.

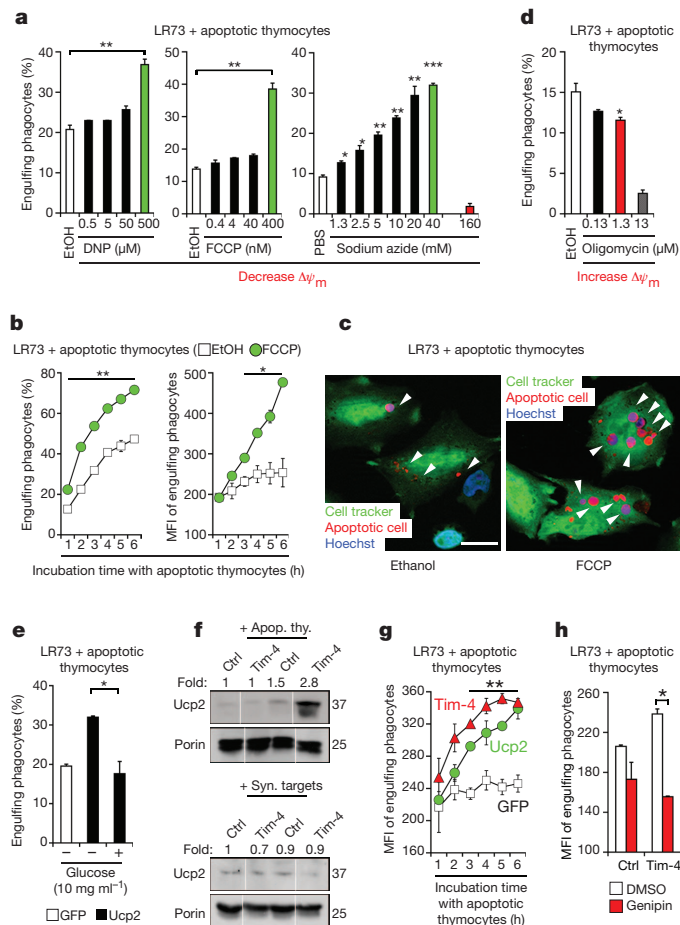


Figure 3 | Ucp2 links mitochondrial membrane potential to engulfment of apoptotic cells. **a**, LR73 cells pre-treated with synthetic uncouplers DNP (left), FCCP (middle), or the electron transport chain inhibitor NaN₃ (right) or vehicle control were assessed for engulfment. **b**, LR73 cells pre-treated with FCCP were incubated with apoptotic thymocytes and the percentage of phagocytes engulfing targets (left) and the MFI of engulfing phagocytes (right) are shown. **c**, Engulfment by FCCP-treated LR73 cells determined by confocal microscopy. Arrowheads indicate engulfed apoptotic thymocytes. Scale bar, 20 μ m. **d**, Apoptotic cell engulfment by LR73 cells pre-treated with oligomycin to increase mitochondrial membrane potential. **e**, LR73 cells transfected with GFP or Ucp2 were assessed for engulfment in the presence or absence of 10 mg ml⁻¹ glucose. **f**, LR73 cells stably overexpressing vector control or Tim-4 were incubated with apoptotic thymocytes (top) or synthetic targets (bottom) for 3 h and the levels of endogenous Ucp2 in mitochondrial fractions are shown. **g**, Continued uptake of apoptotic thymocytes by Tim-4- and Ucp2-overexpressing cells (compared to GFP-transfected cells that reach a plateau) was determined by the MFI of phagocytes over a time course of engulfment. **h**, The increased uptake of apoptotic thymocytes by Tim-4-overexpressing cells was inhibited by genipin. Data are shown as mean \pm s.d. and are representative of at least two independent experiments. * P < 0.05, ** P < 0.01, *** P < 0.001.

At sodium azide concentrations that did not affect cellular ATP levels, it enhanced engulfment with a progressive decrease in the mitochondrial membrane potential (Fig. 3a and Supplementary Fig. 5e, f). Higher sodium azide concentrations that lower cellular ATP levels did block engulfment (an ATP-dependent process) (Fig. 3a and Supplementary Fig. 5f).

We next asked whether raising the mitochondrial membrane potential would dampen engulfment. Oligomycin, an inhibitor of ATP synthase, increased the mitochondrial membrane potential within phagocytes and strongly inhibited engulfment (Fig. 3d). The concentration of oligomycin used here affected the mitochondrial membrane potential but did not alter cellular ATP levels (Supplementary Fig. 5h, i). To test whether modulating the metabolic state of the phagocytes would affect apoptotic cell engulfment, we cultured phagocytes in glucose-free medium that decreased mitochondrial membrane potential, and in turn enhanced apoptotic cell engulfment (Supplementary Fig. 6a, b). Conversely, excess glucose (leading to higher mitochondrial membrane potential) reversed the effect of Ucp2 overexpression or FCCP (Fig. 3e and Supplementary Fig. 6c–e). Thus, the mitochondrial membrane potential within phagocytes is a critical determinant in regulating phagocytic capacity and continued uptake by phagocytes.

Increased metabolic load in phagocytes during engulfment may affect many aspects of metabolism. As Ucp2 is known to increase β -oxidation and decrease reactive oxygen species (ROS) production⁸, perhaps excess cellular lipids or ROS feedback could slow down the engulfment pathway. Incubating phagocytes with apoptotic thymocytes (but not synthetic targets) increased the rate of fatty acid oxidation (Supplementary Fig. 7a, b); however, both Ucp2-overexpressing cells and Ucp2-deficient phagocytes showed higher fatty acid oxidation rates (Supplementary Fig. 7c, d), yet they have opposite phenotypes in apoptotic cell engulfment. This suggested that the possible effect of Ucp2 on lipid oxidation alone is not a major regulator of apoptotic cell clearance.

Ucp2 has also been shown to decrease ROS levels, which could be a potential mechanism by which Ucp2 promotes continued engulfment. However, increasing phagocyte mitochondrial ROS levels via the drugs rotenone or antimycin A (blocking complexes I or III within the electron transport chain, respectively) did not decrease apoptotic cell engulfment (Supplementary Fig. 8a, b). Rather, these drugs modestly increased phagocytosis, probably owing to the decreased mitochondrial membrane potential. Furthermore, ameliorating ROS with FCCP, overexpression of the mitochondrial antioxidant enzyme superoxide dismutase 2 (SOD2), or scavenging ROS with well-known scavengers (Tiron or MitoTEMPO) did not increase engulfment (Supplementary Fig. 8a–g). PGC1 α , the master transcription factor for mitochondrial biogenesis, was not altered during engulfment and overexpressing PGC1 α did not promote engulfment of apoptotic cells (data not shown and Supplementary Fig. 8h). Moreover, neither the AMPK nor the mTOR signalling pathways were activated during engulfment (Supplementary Fig. 8i, j). While these data cannot rule out a contribution of β -oxidation and ROS, they could not provide a mechanistic reason for Ucp2 function during apoptotic cell engulfment. Ucp2-mediated regulation of the phagocyte mitochondrial membrane potential seemed to correlate best with continued phagocytosis of apoptotic cells.

To determine whether signalling via specific engulfment receptors may link to Ucp2/mitochondrial signalling, we generated LR73 cells overexpressing the phosphatidylserine receptor Tim-4 (LR73^{Tim-4} cells). Tim-4 overexpression led to increased apoptotic cell engulfment^{6,22,23}. Three lines of data indicated a link between Tim-4-mediated apoptotic cell recognition and Ucp2. First, although there was no difference in the basal Ucp2 level between control and LR73^{Tim-4} cells, the latter upregulated Ucp2 to a higher level (Fig. 3f, top). Importantly, synthetic targets did not increase Ucp2 expression, even though Tim-4 overexpression promotes uptake of synthetic targets (Fig. 3f, bottom). Second, LR73^{Tim-4} cells continued to take up multiple apoptotic cells (as indicated by mean fluorescence intensity (MFI)), consistent with

the increased upregulation of Ucp2 and the phenocopying of LR73 cells transfected with Ucp2 (Fig. 3g). Third, the Ucp2 inhibitor genipin blocked Tim-4-mediated enhanced uptake (Fig. 3h). We also tested whether synthetic uncoupling or Ucp2 overexpression affected Tim-4 levels. However, surface expression of endogenous Tim-4 or haemagglutinin-tagged (HA)-Tim-4 was unaffected by Ucp2 overexpression, Ucp2 deficiency, synthetic uncoupling or by scavenging ROS (Supplementary Fig. 9a–e). These data indicate a link between apoptotic cell recognition at the membrane and the mitochondrial membrane potential of phagocytes, with Ucp2 serving as a molecular intermediate.

We next addressed the relative importance of Ucp2 in apoptotic cell clearance *in vivo* using Ucp2-deficient mice^{10,12}. Bone-marrow-derived macrophages (BMDMs) from Ucp2^{-/-} mice had a higher mitochondrial membrane potential compared to controls (Fig. 4a). *In vitro*, BMDMs from Ucp2^{-/-} mice consistently showed lower phagocytic capacity for apoptotic cells (Fig. 4b), but no defect in uptake of synthetic targets, live or dead bacteria, or zymosan particles (Fig. 4c and Supplementary Fig. 10a–f). This suggested that use of Ucp2 for apoptotic cell clearance is dependent both on the metabolic load (absent in synthetic targets) and on the nature of phagocytosis (for example,

bacteria and yeast that do carry a metabolic load are taken up via other types of phagocytic receptors). There was residual engulfment in Ucp2-null phagocytes, which may in part be due to the upregulation of Ucp3 seen in 6-day cultures of cells from Ucp2^{-/-} mice (Supplementary Fig. 11a–c).

We next asked how Ucp2^{-/-} phagocytes clear apoptotic cells when a significant population of cells within a tissue are undergoing apoptosis. Injection of dexamethasone induces rapid and synchronous death of thymocytes, and the subsequent clearance of apoptotic thymocytes by resident phagocytes can provide a quantitative *in vivo* model of apoptotic cell clearance²⁴. Whereas control mice show a decrease in overall thymic size at 6 h after dexamethasone injection, Ucp2^{-/-} mice showed only a limited reduction in thymic size after dexamethasone injection (Fig. 4d). The absolute number of cells confirmed that dexamethasone-injected Ucp2^{-/-} mice had much higher total thymic cell numbers compared to controls (Fig. 4e). Ucp2^{-/-} thymocytes underwent apoptosis comparable to control littermates (Supplementary Fig. 12a, b); moreover, the migration of monocytes or macrophages towards find-me signals from apoptotic cells was unaffected by Ucp2 levels or mitochondrial uncoupling (Supplementary Fig. 13a–e).

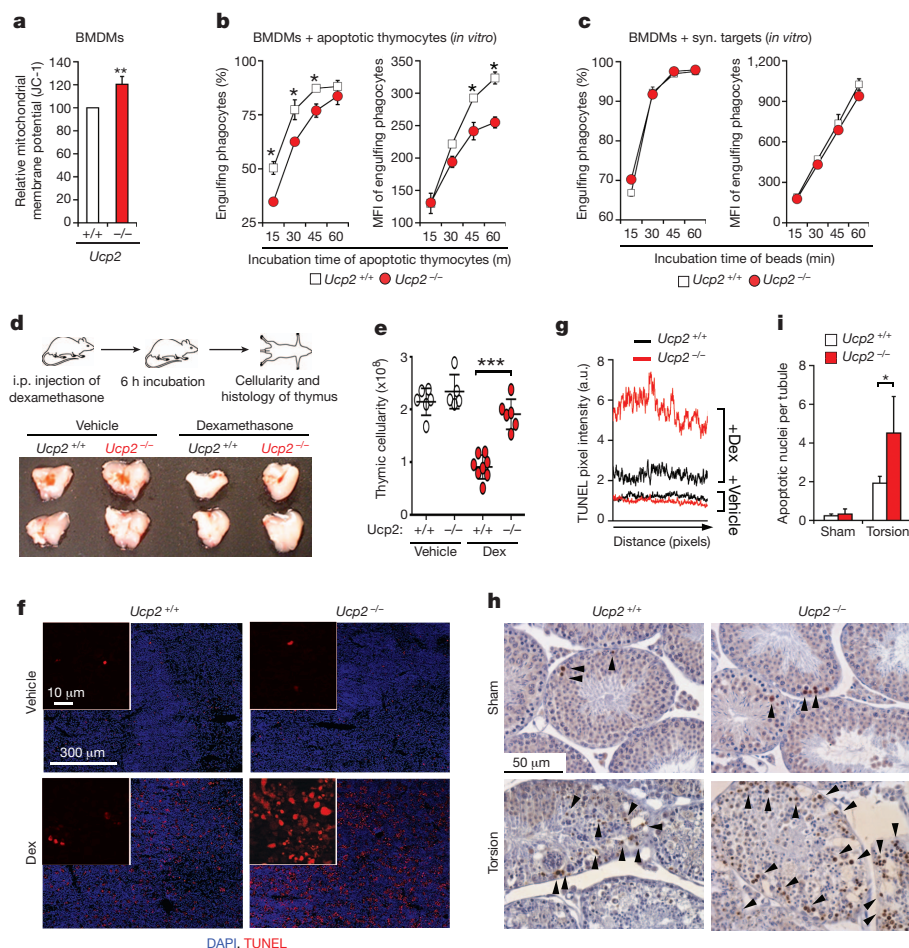


Figure 4 | Impaired clearance of apoptotic cells in Ucp2-deficient mice. **a**, Mitochondrial membrane potential of BMDMs from Ucp2^{+/+} and Ucp2^{-/-} mice assessed by JC-1 staining. **b**, Engulfment of TAMRA-labelled apoptotic thymocytes by BMDMs from Ucp2^{+/+} and Ucp2^{-/-} mice was assessed over a time course. The less pronounced effect of BMDM cultures could be due to compensatory Ucp3 upregulation (see Supplementary Fig. 11). **c**, Comparable engulfment of synthetic targets by BMDMs from Ucp2^{+/+} and Ucp2^{-/-} mice. **d**, Top, schematic of the assay for assessing clearance of apoptotic thymocytes *in vivo*. i.p., intraperitoneal. Bottom, photographs of representative thymuses from Ucp2^{+/+} and Ucp2^{-/-} mice treated with vehicle or dexamethasone. **e**, Total thymic cellularity of thymuses from Ucp2^{+/+} and Ucp2^{-/-} mice

treated with dexamethasone (Dex) for 6 h. *n* = 5 to ~8 mice per group. **f**, Cryosections of thymuses from Ucp2^{+/+} and Ucp2^{-/-} mice treated with dexamethasone stained with TUNEL (red) and 4',6-diamidino-2-phenylindole (DAPI; blue). **g**, Histogram of TUNEL staining from thymic sections in **f**. Data were averaged from 9 slices of thymus and 3 mice per group. **h**, **i**, Staining of apoptotic nuclei in testes sections (specifically the seminiferous tubules), showing increased numbers of apoptotic germ cells in Ucp2^{-/-} mice after testicular torsion. The average number of apoptotic cells per tubule was quantified from 4 slices of each testis and from 2 to ~3 mice per group. Data are shown as mean ± s.d. and are representative of at least two independent experiments. **P* < 0.05, ***P* < 0.01, ****P* < 0.001.

Thus, the increased thymic cellularity in dexamethasone-treated *Ucp2*^{-/-} mice resulted from defective clearance. The thymuses of dexamethasone-treated *Ucp2*^{-/-} mice consistently had higher levels of unengulfed corpses by TdT-mediated dUTP nick end labelling (TUNEL) and a threefold increase in TUNEL fluorescence, without altered density of F4/80-positive cells (Fig. 4f, g and Supplementary Fig. 13f–h). We also tested the ability of *Ucp2*^{-/-} mice to clear apoptotic cells in other tissues. By initiating acute apoptosis of germ cells in the testes via testicular torsion, we assessed the clearance of dying germ cells by Sertoli cells. The testes of *Ucp2*^{-/-} mice contained increased numbers of uncleared apoptotic cells per seminiferous tubule compared to *Ucp2*^{+/+} mice (Fig. 4h, i). These data demonstrate an essential role for Ucp2 in apoptotic cell clearance *in vivo*.

Although significant recent progress has been made in understanding how phagocytes recognize and engulf apoptotic cells²⁵, this work provides additional insights on this process. First, mitochondrial membrane potential critically controls how well a phagocyte can engulf apoptotic cells, with an inverse correlation between mitochondrial membrane potential and engulfment capacity. Second, the Ucp2 protein acts as a regulator of mitochondrial membrane potential within phagocytes during apoptotic cell engulfment, with a requirement for Ucp2 in efficient apoptotic cell clearance *in vivo*. Third, a previously unappreciated crosstalk exists between the mitochondria and the engulfment machinery within phagocytes, with the 'sensing' of the total mitochondrial membrane potential critically influencing phagocytic capacity. This has broad implications for apoptotic cell clearance *in vivo*, because failed clearance has been linked to inflammation and autoimmune diseases. Moreover, *Ucp2* deficiency was linked to impaired pancreatic β -cell function and glucose-induced insulin secretion^{26,27}, and *Ucp2*^{-/-} mice show increased atherosclerosis^{11,12,28}. The data presented here provide a new and unexpected link between mitochondrial function, Ucp2 and apoptotic cell clearance and may help to provide a better understanding of the complex aetiology of metabolic diseases.

METHODS SUMMARY

To detect mitochondrial membrane potential, phagocytes (LR73, NIH/3T3 or BMDMs)^{14,24} were stained with Mitotracker Deep Red FM, TMRE or JC-1, incubated with apoptotic cells and analysed by flow cytometry. Cell clearance in the thymus was analysed as detailed previously²⁴. Testicular torsion was performed as per the guidelines of the Society for the Study of Reproduction.

Full Methods and any associated references are available in the online version of the paper at www.nature.com/nature.

Received 21 December 2010; accepted 28 June 2011.

Published online 21 August 2011.

1. Elliott, M. R. & Ravichandran, K. S. Clearance of apoptotic cells: implications in health and disease. *J. Cell Biol.* **189**, 1059–1070 (2010).
2. Henson, P. M. & Hume, D. A. Apoptotic cell removal in development and tissue homeostasis. *Trends Immunol.* **27**, 244–250 (2006).
3. Gregory, C. D. & Pound, J. D. Cell death in the neighbourhood: direct microenvironmental effects of apoptosis in normal and neoplastic tissues. *J. Pathol.* **223**, 178–195 (2011).
4. Muñoz, L. E., Lauber, K., Schiller, M., Manfredi, A. A. & Herrmann, M. The role of defective clearance of apoptotic cells in systemic autoimmunity. *Nature Rev. Rheumatol.* **6**, 280–289 (2010).
5. Tabas, I. Macrophage death and defective inflammation resolution in atherosclerosis. *Nature Rev. Immunol.* **10**, 36–46 (2010).
6. Miyashita, M. *et al.* Identification of Tim4 as a phosphatidylserine receptor. *Nature* **450**, 435–439 (2007).

7. Krauss, S., Zhang, C. Y. & Lowell, B. B. A significant portion of mitochondrial proton leak in intact thymocytes depends on expression of UCP2. *Proc. Natl Acad. Sci. USA* **99**, 118–122 (2002).
8. Krauss, S., Zhang, C. Y. & Lowell, B. B. The mitochondrial uncoupling-protein homologues. *Nature Rev. Mol. Cell Biol.* **6**, 248–261 (2005).
9. Fleury, C. *et al.* Uncoupling protein-2: a novel gene linked to obesity and hyperinsulinemia. *Nature Genet.* **15**, 269–272 (1997).
10. Arsenijevic, D. *et al.* Disruption of the uncoupling protein-2 gene in mice reveals a role in immunity and reactive oxygen species production. *Nature Genet.* **26**, 435–439 (2000).
11. Blanc, J. *et al.* Protective role of uncoupling protein 2 in atherosclerosis. *Circulation* **107**, 388–390 (2003).
12. Moukdar, F. *et al.* Reduced antioxidant capacity and diet-induced atherosclerosis in uncoupling protein-2-deficient mice. *J. Lipid Res.* **50**, 59–70 (2009).
13. Reers, M., Smith, T. W. & Chen, L. B. J-aggregate formation of a carbocyanine as a quantitative fluorescent indicator of membrane potential. *Biochemistry* **30**, 4480–4486 (1991).
14. Park, D. *et al.* BAI1 is an engulfment receptor for apoptotic cells upstream of the ELMO/Dock180/Rac module. *Nature* **450**, 430–434 (2007).
15. Enerbäck, S. *et al.* Mice lacking mitochondrial uncoupling protein are cold-sensitive but not obese. *Nature* **387**, 90–94 (1997).
16. Lugli, E. *et al.* Characterization of cells with different mitochondrial membrane potential during apoptosis. *Cytometry A* **68**, 28–35 (2005).
17. Zhang, C. Y. *et al.* Genipin inhibits UCP2-mediated proton leak and acutely reverses obesity- and high glucose-induced β cell dysfunction in isolated pancreatic islets. *Cell Metab.* **3**, 417–427 (2006).
18. Echtaay, K. S., Winkler, E., Bienengraeber, M. & Klingenberg, M. Site-directed mutagenesis identifies residues in uncoupling protein (UCP1) involved in three different functions. *Biochemistry* **39**, 3311–3317 (2000).
19. Urbánková, E., Hanak, P., Skobisova, E., Ruzicka, M. & Jezek, P. Substitutional mutations in the uncoupling protein-specific sequences of mitochondrial uncoupling protein UCP1 lead to the reduction of fatty acid-induced H⁺ uniport. *Int. J. Biochem. Cell Biol.* **35**, 212–220 (2003).
20. Buckler, K. J. & Vaughan-Jones, R. D. Effects of mitochondrial uncouplers on intracellular calcium, pH and membrane potential in rat carotid body type I cells. *J. Physiol. (Lond.)* **513**, 819–833 (1998).
21. Sokal, A. & Bartosz, G. Uncouplers of mitochondrial oxidative phosphorylation are not substrates of the erythrocyte glutathione-S-conjugate pump. *Arch. Biochem. Biophys.* **349**, 113–121 (1998).
22. Park, D., Hochreiter-Hufford, A. & Ravichandran, K. S. The phosphatidylserine receptor TIM-4 does not mediate direct signaling. *Curr. Biol.* **19**, 346–351 (2009).
23. Kobayashi, N. *et al.* TIM-1 and TIM-4 glycoproteins bind phosphatidylserine and mediate uptake of apoptotic cells. *Immunity* **27**, 927–940 (2007).
24. Elliott, M. R. *et al.* Nucleotides released by apoptotic cells act as a find-me signal to promote phagocytic clearance. *Nature* **461**, 282–286 (2009).
25. Ravichandran, K. S. & Lorenz, U. Engulfment of apoptotic cells: signals for a good meal. *Nature Rev. Immunol.* **7**, 964–974 (2007).
26. Azzu, V. & Brand, M. D. The on-off switches of the mitochondrial uncoupling proteins. *Trends Biochem. Sci.* **35**, 298–307 (2010).
27. Andrews, Z. B. *et al.* UCP2 mediates ghrelin's action on NPY/AgRP neurons by lowering free radicals. *Nature* **454**, 846–851 (2008).
28. Pi, J. & Collins, S. Reactive oxygen species and uncoupling protein 2 in pancreatic β -cell function. *Diabetes Obes. Metab.* **12** (Suppl. 2), 141–148 (2010).

Supplementary Information is linked to the online version of the paper at www.nature.com/nature.

Acknowledgements We thank M. Schwartz and members of the K.S.R. laboratory for discussions. This work was supported by grants from the National Institute of General Medical Sciences (to K.S.R.), and ARRA funding from National Institute of Child Health and Development (to J.J.L. and K.S.R.). K.S.R. is a Bill Benter Senior Fellow of the American Asthma Foundation. J.M.K. is supported by an American Heart Association Award.

Author Contributions D.P., C.Z.H., M.R.E., P.C.T., J.M.K., S.D., J.J.L. and K.L.H. designed and performed all of the experiments. S.C. provided advice and the *Ucp2* knockout mice. K.S.R. helped in the design of many of the experiments and provided overall coordination. D.P., K.L.H. and K.S.R. wrote and edited the manuscript with input from other authors.

Author Information Reprints and permissions information is available at www.nature.com/reprints. The authors declare no competing financial interests. Readers are welcome to comment on the online version of this article at www.nature.com/nature. Correspondence and requests for materials should be addressed to K.S.R. (ravi@virginia.edu).

METHODS

Cell culture and transfections. LR73 cells were cultured in α -MEM, whereas NIH/3T3 cells and J774 macrophage cells were maintained in DMEM and Jurkat cells were cultured with RPMI, along with 10% FBS and 1% penicillin-streptomycin-glutamine. SCI cells were cultured in α -MEM and 1 mM of sodium pyruvate. LR73 cells were transfected using Lipofectamine 2000 (Invitrogen) according to the manufacturer's instructions. NIH/3T3 cells were nucleofected using amaxa nucleofector (kit R, program U-030) or transfected with Lipofectamine 2000 according to the manufacturer's instructions.

Primary cell culture. Bone marrow cells from 6-week-old mice were cultured in RPMI medium with 10% FBS, 1% penicillin-streptomycin-glutamine, and 10% L929 cell conditioned medium. Two or six days later, more than 85% of the adherent cells were F4/80 positive and 95% of the cells were CD11b positive. Resident peritoneal cells were collected from 6-week-old mice and plated with RPMI supplemented with 10% FBS and 1% penicillin-streptomycin-glutamine. Four hours later, floating cells were washed with warm PBS twice and adherent cells were regarded as resident peritoneal macrophages and used in further assays.

Plasmids and mutagenesis. All constructs generated were sequenced to confirm fidelity and the presence of the appropriate mutations. The pEBB-Ucp2 and pEBB-Ucp2-Flag constructs were generated from the *Ucp2* cDNA templates by a PCR-based strategy in the pEBB-Flag vector. pEBB-Ucp2(D28N) was generated by site-directed mutagenesis. ELMO, Dock180, Rac, BAI1 and Tim-4 constructs used in this study have been described previously¹⁹.

Immunoblotting and antibodies. The antibodies used were anti-Ucp2 (Santa Cruz Biotechnology, C-20), anti-Flag (Sigma, M-2), anti-porin (Abcam, ab15895), anti-Erk2 (Santa Cruz, C-14) and anti-AIF (Cell Signaling, D39D2). Phospho-AMPK α (Thr 172), AMPK α antibody, phospho-p70 S6 kinase (Thr 389) and p70 S6 kinase were purchased from Cell Signaling Technology. To detect endogenous Ucp2, it is necessary to isolate mitochondria. For the isolation of mitochondria, cells were resuspended in 500 μ l of TS buffer (10 mM Tris, pH 7.5, 250 mM sucrose, 2 μ g ml⁻¹ DNase and protease inhibitor cocktail), and then subjected to three cycles of 5-min freezing in liquid nitrogen followed by 10-min thawing at 37 °C. Unbroken cells and nuclei were removed by centrifugation at 800g for 10 min and mitochondria were collected from the supernatant by centrifugation at 10,000g for 20 min. The isolated mitochondria were lysed in RIPA buffer and subjected to immunoblotting. To measure induction of Ucp2 during apoptotic cell engulfment, 2.0×10^6 LR73 cells were plated on a 100-mm culture dish 2 days before 1.0×10^8 apoptotic thymocytes in 10 ml of α -MEM were added. After incubation for 3 h, the mitochondria were isolated and the Ucp2 levels were analysed. For BMDMs, 5.0×10^6 BMDMs were plated on a 100-mm Petri dish 1 day before the assay. The next day, 1.0×10^8 apoptotic thymocytes in 10 ml of RPMI were added to the BMDMs and incubated for 1 h. The cells were extensively washed with cold PBS and trypsinized and analysed for Ucp2 levels. To detect overexpressed Ucp2, LR73 cells were transiently transfected with Flag-tagged Ucp2 using Lipofectamine 2000 (Invitrogen). One day after transfection, the cells were lysed and subjected to immunoblotting against the respective tags or endogenous proteins.

Immunofluorescence microscopy. NIH/3T3 fibroblasts were plated on glass chamber slides and transfected with Flag-Ucp2 either alone or in combination with YFP-Rab5 or YFP-Rab7. To stain lysosomes or mitochondria, cells were incubated with LysoTracker Red (1:10,000 dilution) or Mitotracker Deep Red (100 nM) in DMEM/10% FBS for 20 min. Cells were then fixed with 3% paraformaldehyde (Sigma) in PBS for 30 min, permeabilized with 0.1% Triton X-100 (Sigma) and blocked with 5% milk that had been clarified by high-speed centrifugation. Antibody staining was then performed using antibodies to Flag (clone M5, Sigma) and/or AIF (D39D2, Cell Signaling) detected with either Alexa 488 or Alexa-555 goat anti-mouse and/or Alexa-555 goat anti-rabbit antibodies (highly cross-absorbed, Invitrogen), respectively. YFP was detected using an Alexa-488 anti-GFP antibody (Invitrogen). The stained cells were analysed by Axio imager 2 with Apotome (Zeiss).

Quantitative RT-PCR. Total RNA was isolated using the RNeasy Mini Kit (Qiagen) and cDNA was generated from total RNA with Superscript III (Invitrogen) according to the manufacturers' protocol. *Ucp1*, *Ucp2* and *Ucp3* mRNA were detected by PCR using cDNA as template. For siRNA transfected NIH/3T3 cells and *Ucp2* knockout mice, relative *Ucp2* or *Ucp3* mRNA levels were determined by normalizing to *Hprt* using the StepOnePlus qPCR system (Applied Biosystems).

Phagocytosis assay. Phagocytosis assays were performed as described previously¹⁴. 1.0×10^5 LR73 cells were transiently transfected in triplicates with the indicated plasmids either with GFP or GFP fusion proteins in a 24-well plate. The cells were incubated with apoptotic thymocytes or 2 μ m carboxylate-modified red fluorescent beads (Invitrogen), which mimic the negative charge on apoptotic cells and can serve as simplified targets. For the induction of apoptosis, thymocytes were incubated with 50 μ M dexamethasone (Calbiochem) at 37 °C for 4 h. The

thymocytes were resuspended to a final concentration of 1.0×10^7 cells per 300 μ l with α -MEM (or cell culture medium for specific cell types) supplemented with 2% FBS and 0.2% penicillin-streptomycin-glutamine for the phagocytosis assay of LR73. The transfected cells were incubated with 300 μ l of the apoptotic thymocyte resuspension in a 5% CO₂ incubator at 37 °C for the desired time. After incubation of the phagocytes with targets, the phagocytes were extensively washed with cold PBS, trypsinized, resuspended in cold medium (with 1% NaN₃), and analysed by two-colour flow cytometry (FACSCalibur from BD). The transfected cells were recognized by their GFP fluorescence and targets were recognized by red fluorescence (carboxylate-modified red fluorescent beads or apoptotic thymocytes). Forward and side-scatter parameters were used to distinguish free unbound targets from phagocytes. The majority of 'double-positive' cells scored in the FACS assay represented targets engulfed by phagocytes, or targets in the process of being engulfed. The MFI in the red channel of the cells taking up targets provided an indication of the capacity of uptake (proportional to the number of particles taken up). For measuring phagocytosis by BMDMs, 2.0×10^4 BMDMs were plated in the 24-well plate one day before the phagocytosis assay. Next day, the cells were incubated with 2.0×10^6 TAMRA-stained apoptotic thymocytes for the desired time and analysed for engulfment as above.

Internalization assay. Thymocytes were double stained with TAMRA (25 μ M) and cypHer5E (1 μ M; GE Healthcare) and the phagocytosis assay was performed as described above. TAMRA and cypHer5E high-double-positive cells were considered to be phagocytes internalizing apoptotic cells, and TAMRA-positive but cypHer5E-low cells were regarded as bound but uninternalized targets on phagocytes.

Phagocytosis of dead *Escherichia coli*, *Staphylococcus aureus* and zymosan. 2.0×10^4 BMDMs from wild-type or *Ucp2*-deficient mice were plated on a well of a 24-well plate. Next day, BMDMs were incubated with alexa-488 conjugated 5×10^6 *E. coli* and *S. aureus* or 5×10^5 zymosan particles (Invitrogen) for the desired time. Unbound targets were extensively washed with cold PBS five times and BMDMs were trypsinized and subjected to FACS analysis. Alexa-488-positive BMDMs were considered to be phagocytes engulfing targets.

Gentamicin protection assay for bacterial internalization. Quantification of intracellular bacteria was done using the gentamicin protection assay. 2×10^5 BMDMs per well were seeded into a 24-well culture dish 18 h before infection at a multiplicity of infection of 10 for 1 h in antibiotic-free media in a 37 °C CO₂ incubator. Cells were then washed and incubated with gentamicin for 90 min to kill extracellular bacteria. Subsequently, cells were lysed in 1% Triton-X 100, lysates were serially diluted, and plated directly onto Luria-Bertani agar plates. Total colony-forming units (c.f.u.) were enumerated the next day after overnight incubation at 37 °C. Values were standardized to levels of colonization in control cell preparations.

Ucp2 knockdown. NIH/3T3 cells were nucleofected according to the manufacturer's manual (Kit R, U-030, amaxa) with minor modifications. 1.0×10^6 cells were nucleofected with 6 picomoles per sample control or *Ucp2* siRNA (Dharmacon *Ucp2* smart pool) and plated onto 3 wells of a 6-well plate. Twenty-four hours after nucleofection, the cells were trypsinized and 2.0×10^4 cells were replated in the 12-well plate. Two days after nucleofection, the cells were incubated with 1.0×10^6 TAMRA-stained apoptotic SCI or Jurkat cells in DMEM supplemented with 10% FBS and 1% penicillin-streptomycin-glutamine at 37 °C for the desired time.

Measurement of mitochondrial membrane potential. To detect the mitochondrial membrane potential, cells treated with the indicated experimental conditions were stained with Mitotracker Deep Red FM (Invitrogen), the accumulation of which in mitochondria is dependent on mitochondrial membrane potential. Mitochondrial membrane potential was also measured using TMRE (Invitrogen) or a dual emission potential-sensitive probe, JC-1 dye (SIGMA-Aldrich), according to the manufacturer's protocol. For TMRE staining, cells were incubated with 50 nM of TMRE in culture medium in a 5% CO₂ incubator at 37 °C for 30 min and fluorescence coming from cells was measured by flow cytometry. For JC-1 staining, cells in a 24-well plate were incubated with 1 ml of mitochondrial staining solution containing the 50% medium used for cell growth and 2.5 μ g ml⁻¹ of JC-1 dye in a 5% CO₂ incubator at 37 °C for 20 min. The cells were then washed twice with warm PBS and trypsinized. Overflow of green fluorescent signal to red fluorescence was compensated and the intensity of red fluorescence coming from JC-1 aggregates was detected by flow cytometry using the FACSCalibur instrument (Becton Dickinson).

Measurement of intracellular ATP. Intracellular ATP levels were measured using CellTiter-Glo Luminescent Cell Viability Assay kit (Promega) according to the manufacturer's manual. Cells were treated with experimental conditions and trypsinized. 2.5×10^4 cells per 50 μ l were added into a well of a 96-well plate. Then, 50 μ l of CellTiter-Glo Reagent was added to the well containing the cells. The cells were incubated on an orbital shaker for 2 min and followed by incubation

at room temperature (25 °C) for 10 min. Luminescence was measured using MicroBeta TriLux (EG&G WALLAC).

Analysis of cell clearance in the thymus. Five-to-six-week-old wild-type and *Ucp2*-deficient mice were intraperitoneally injected with 300 µl of PBS containing 250 µg dexamethasone dissolved in ethanol (10 mg ml⁻¹). Six hours after injection, the mice were killed and thymuses were extracted. For quantification of thymic cellularity, thymocytes were resuspended with HBSS supplemented with 5% FBS. The cells were diluted and mixed with 50 µl of quantification beads (Spherotech). The mixture was subjected to flow cytometric analysis to allow for the quantification of thymocytes. To monitor the presence of TUNEL-positive uncleared apoptotic cells, 6 h after injection thymuses from the mice were extracted and embedded in O.C.T. compound. The O.C.T.-compound-embedded thymuses then were frozen in liquid nitrogen. After that, thymic cryosections on glass slides were stained using the *In situ* Cell Death Red kit according to manufacturer's instructions (Roche). Sections were mounted with Prolong Antifade plus DAPI medium and analysed by Axio Imager 2 with Apotome (ZEISS). To monitor *ex vivo* apoptosis of thymocytes, 1.0×10^7 thymocytes from 5 to ~6-week-old *Ucp2* wild-type and deficient littermate mice were incubated with 50 µM dexamethasone at 37 °C for 4 or 6 h. The cells were washed with PBS once and then stained with annexin V and propidium iodide (Annexin V: FITC apoptosis detection kit II, BD).

Cell migration assay. 2×10^6 cells ml⁻¹ THP-1 cells were resuspended with RPMI containing 5% FBS, 1% penicillin, streptomycin and glutamine and 10 mM HEPES and were pre-incubated with the desired concentration of FCCP for 1 h. Five-hundred microlitres of apoptotic supernatant or MCP-1 (25 ng ml⁻¹) was added to the lower chamber of a 24-well plate with a 5-µm pore size transwell (5-µm pore size, Corning) and 100 µl of cells (2×10^6 cells ml⁻¹) were loaded on the upper chamber of the plate and then incubated at 37 °C for 1 h. The percentage of migrated cells was determined by FACS with 5.1-µm AccuCount beads and compared to input cells. For BMDM migration, 4.0×10^5 cells ml⁻¹ were resuspended in RPMI containing 1% BSA, 1% penicillin, streptomycin and glutamine and 10 mM HEPES. Five-hundred microlitres of apoptotic supernatant or Sdf-1 (50 ng ml⁻¹) was added to the lower chamber of a 24-well transwell plate and 100 µl of BMDMs was added on the upper chamber and incubated at 37 °C for 3 h. The number of BMDMs that migrated on the underside of the membrane was determined by Diff-Quick staining and counted using microscopy.

Thymus staining. Tissue sections were blocked for 15 min with 2% normal goat serum and then were stained for 60 min at 25 °C with PE-conjugated F4/80 (eBioscience) and FITC-conjugated anti pan-cytokeratin (Sigma). After incubation, slides were washed three times in PBS and then mounted with GelMount (Molecular Probes, Invitrogen).

Fatty acid oxidation assay. Phagocytes were seeded in a 12-well plate at a density of 2×10^5 cells per well on the day before the fatty acid oxidation

(FAO) assay. Next day, the phagocytes were incubated with 2×10^7 apoptotic thymocytes or 2-µm carboxylate-modified beads for the desired times. After incubation, each well was washed five times with PBS. Rates of FAO were determined over the next 2 h as follows: a 0.2 ml PCR tube with 50 µl 1 M NaOH was leaned diagonally in each well before addition of 300 µl FAO buffer (Krebs Ringer phosphate buffer pH 7.4 containing 1% fatty-acid-free BSA (Sigma Aldrich), 5 mM glucose (Sigma Aldrich), 125 µM palmitate (Sigma Aldrich), 1 mM carnitine (Sigma Aldrich), and 6 µCi 1-¹⁴C-palmitate (Perkin Elmer)). The wells were immediately sealed with masking tape and incubated at 37 °C for 2 h before 100 µl of 2 M perchloric acid was injected through the tape to stop the reaction and release ¹⁴CO₂ trapped as bicarbonate. The plate was incubated for 2 h at room temperature to trap the released ¹⁴CO₂ as bicarbonate in NaOH. The tape was removed and NaOH from each tube was diluted with 5 ml scintillant and counted with a Beckman LS6500 scintillation counter. Partially oxidized metabolites of ¹⁴C-palmitate were recovered from the FAO buffer precipitate by extraction in chloroform:methanol (2:1). Acid-soluble ¹⁴C-metabolites were recovered from the aqueous phase, diluted in scintillant and counted. Rates of total FAO were determined by summing ¹⁴CO₂- and ¹⁴C-labelled acid-soluble metabolite disintegration rates and normalizing to the specific activity of the FAO buffer, cell number and the duration of incubation.

Measurement of superoxide. LR73 cells were plated at a density of 1.0×10^5 cells per well in a 12-well plate in α-MEM supplemented with 10% FBS and 1% penicillin, streptomycin and glutamine. The cells were treated with the indicated drugs for 4 h and incubated with 2 µM MitoSox (Invitrogen) for 30 min. The cells were trypsinized and analysed by flow cytometry.

Testicular torsion. This work was conducted in accordance with the Guiding Principles of the Care and Use of Research Animals promulgated by the Society for the Study of Reproduction. Adult male C57BL/6 mice were anaesthetized with an intraperitoneal injection of 0.01 mg g⁻¹ sodium pentobarbital and the testis was exteriorized through a low midline laparotomy, the gubernaculum was divided, and the testis was freed from the epididymo-testicular membrane. The testis was rotated 720° for 2 h, during which time it remained in the abdomen with a closed incision. Following the 2 h torsion, the incision was reopened, the testis was counter-rotated to the natural position, the gubernaculum was rejoined, and the testis was reinserted into the scrotum via the inguinal canal. Testes were examined at the time of repair for the degree of ischaemia and reperfusion. Sham-operated animals were treated identically except that upon completion of the torsion manoeuvre the testis was immediately counter-rotated.

Statistical analysis. Data are shown as mean ± standard deviation. For analysis of statistical difference between experiments involving two groups, a Student's two-tailed *t*-test was applied. A one-way ANOVA was applied for statistical analysis of three or more groups. Significance was defined when *P* values were <0.05.

Haem oxygenase is synthetically lethal with the tumour suppressor fumarate hydratase

Christian Frezza¹, Liang Zheng¹, Ori Folger², Kartik N. Rajagopalan³, Elaine D. MacKenzie¹, Livnat Jerby², Massimo Micaroni⁴, Barbara Chaneton¹, Julie Adam⁵, Ann Hedley¹, Gabriela Kalna¹, Ian P. M. Tomlinson⁶, Patrick J. Pollard⁵, Dave G. Watson⁷, Ralph J. Deberardinis³, Tomer Shlomi^{8*}, Eytan Ruppin^{2,9*} & Eyal Gottlieb¹

Fumarate hydratase (FH) is an enzyme of the tricarboxylic acid cycle (TCA cycle) that catalyses the hydration of fumarate into malate. Germline mutations of *FH* are responsible for hereditary leiomyomatosis and renal-cell cancer (HLRCC)¹. It has previously been demonstrated that the absence of *FH* leads to the accumulation of fumarate, which activates hypoxia-inducible factors (HIFs) at normal oxygen tensions^{2–4}. However, so far no mechanism that explains the ability of cells to survive without a functional TCA cycle has been provided. Here we use newly characterized genetically modified kidney mouse cells in which *Fh1* has been deleted, and apply a newly developed computer model of the metabolism of these cells to predict and experimentally validate a linear metabolic pathway beginning with glutamine uptake and ending with bilirubin excretion from *Fh1*-deficient cells. This pathway, which involves the biosynthesis and degradation of haem, enables *Fh1*-deficient cells to use the accumulated TCA cycle metabolites and permits partial mitochondrial NADH production. We predicted and confirmed that targeting this pathway would render *Fh1*-deficient cells non-viable, while sparing wild-type *Fh1*-containing cells. This work goes beyond identifying a metabolic pathway that is induced in *Fh1*-deficient cells to demonstrate that inhibition of haem oxygenation is synthetically lethal when combined with *Fh1* deficiency, providing a new potential target for treating HLRCC patients.

To study metabolic adaptation of *FH*-deficient cells we first generated immortalized kidney cells from mice homozygous for a conditionally targeted *Fh1* allele³. These cells contain LoxP sites flanking exons 3 and 4 (*Fh1*^{fl/fl}) (Fig. 1a and Supplementary Fig. 2a) and express normal levels of Fh1 protein (Fig. 1b). To generate *Fh1*^{−/−} cells the *Fh1*^{fl/fl} cells were infected with recombinant adenovirus expressing Cre recombinase and two clones (CL1 and CL19) were selected from the infected pools. Both clones were genetically confirmed to contain homozygous *Fh1*-deleted (knockout) alleles (Fig. 1a) and did not express Fh1 protein (Fig. 1b).

To assess the biochemical consequences of *Fh1* deletion on TCA cycle function, the intracellular levels of several TCA cycle metabolites were measured by gas chromatography–mass spectrometry (GC–MS) (Fig. 1c). *Fh1*^{−/−} cells accumulate substantial amounts of fumarate, which reached levels more than a 100-fold that of *Fh1*^{fl/fl} cells. In addition, a sevenfold increase in succinate levels and a marked decrease of malate and citrate were detected (Fig. 1d). In cancer cells, the TCA cycle is largely supplied through the metabolism of glucose and glutamine⁵. To investigate the effects of *Fh1* deletion on carbon supply to the TCA cycle, cells were cultured in medium containing ¹³C-labelled glucose and unlabelled glutamine, or vice versa, and ¹³C-enrichment of fumarate and succinate was analysed. When ¹³C-glucose was used, the

majority of fumarate was unlabelled (m+0), indicating that glucose is a minor source of carbon for the TCA cycle in both *Fh1*^{fl/fl} and *Fh1*^{−/−} cells (Fig. 1e). On the other hand, when cells were incubated with ¹³C-glutamine most of the fumarate was labelled (Fig. 1f). In *Fh1*^{−/−} cells cultured with uniformly labelled glutamine (Fig. 1f), the vast majority of the labelled fumarate contained all four carbon atoms derived from glutamine (m+4). By contrast, in *Fh1*^{fl/fl} cells, the fumarate pool contained substantial fractions of molecules with fewer than four ¹³C atoms due to processing of fumarate beyond the Fh1 step. The lack of these products in *Fh1*^{−/−} cells confirms that no accessory pathway exists in these cells to circumvent the loss of Fh1 enzymatic activity, indicating a true blockade of the cycle. Notably, the ¹³C-enrichment profiles of

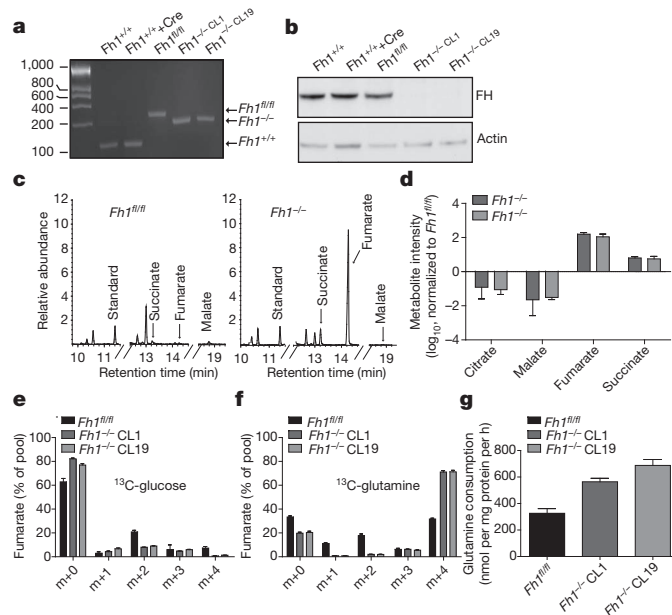


Figure 1 | Characterization of *Fh1*-deficient cells. **a**, PCR analysis of genomic DNA of epithelial kidney cells of the indicated genotype. Numbers indicate base pairs. **b**, Fh1 protein levels of the indicated cells were detected by western blot analysis. **c**, Representative chromatogram of a GC–MS analysis performed from the indicated cell lines. Annotated metabolites are indicated by the arrows. **d**, Fold change of the indicated TCA cycle metabolites in *Fh1*^{−/−} compared to control *Fh1*^{fl/fl} cells ($n = 3$). **e**, **f**, Isotopomer distribution of intracellular fumarate. Cells were incubated with either ¹³C-glucose (**e**) or ¹³C-glutamine (**f**) and fumarate isotopomers (with the indicated mass shift) were analysed ($n = 3$). **g**, Glutamine consumption rate of the indicated cell lines ($n = 3$). All data are presented as mean \pm s.e.m.

¹Cancer Research UK, Beatson Institute for Cancer Research, Switchback Road, Glasgow G61 1BD, UK. ²The Blavatnik School of Computer Science, Tel Aviv University, Tel Aviv 69978, Israel. ³Department of Pediatrics and McDermott Center for Human Growth and Development, University of Texas–Southwestern Medical Center at Dallas, 5323 Harry Hines Blvd, Dallas, Texas 75390-9063, USA. ⁴The University of Queensland, Institute for Molecular Bioscience, St Lucia, Brisbane, Queensland 4072, Australia. ⁵Henry Wellcome Building for Molecular Physiology, University of Oxford, Roosevelt Drive, Oxford OX3 7BN, UK. ⁶Molecular and Population Genetics Laboratory, Wellcome Trust Centre for Human Genetics, University of Oxford, Oxford OX3 7BN, UK. ⁷Strathclyde Institute of Pharmaceutical and Biomedical Sciences, University of Strathclyde, 27 Taylor Street, Glasgow G4 0NR, UK. ⁸Computer Science Department, Technion, Israel Institute of Technology, Haifa, 32000, Israel. ⁹The Sackler School of Medicine, Tel Aviv University, Tel Aviv 69978, Israel.

*These authors contributed equally to this work.

succinate perfectly matched fumarate results, underlining the presence of a flux of carbons from glutamine to fumarate via succinate. In addition, no reverse flux of TCA cycle metabolites was detected (Supplementary Fig. 2b, c). (See Supplementary Fig. 1 for a diagram summarizing these results.) Consistent with the increased contribution of glutamine to the pool of TCA cycle intermediates, *Fh1*^{-/-} cells used significantly more glutamine than *Fh1*^{fl/fl} cells (Fig. 1g).

Because the TCA cycle is a major source for mitochondrial NADH, the truncation of the TCA cycle may have severe bioenergetic outcomes. Indeed, steady-state levels of mitochondrial NADH in *Fh1*^{-/-} cells were lower than those of control cells (Fig. 2a; untreated and Supplementary Fig. 2d for quantification). However, *Fh1*^{-/-} cells still generate significant amounts of NADH and retained normal mitochondrial membrane potential (Fig. 2a). In addition, depolarizing the mitochondria by using the protonophore carbonyl cyanide *m*-chlorophenyl hydrazone (CCCP) decreased mitochondrial NADH, whereas blocking NADH oxidation with rotenone, an inhibitor of NADH:ubiquinone oxidoreductase, increased mitochondrial NADH in both control and *Fh1*-deficient cells. These results indicate that despite having a truncated TCA cycle, *Fh1*-deficient cells retain significant mitochondrial bioenergetic activity and are capable of generating and oxidizing NADH. Because NADH oxidation in the mitochondria fuels the respiratory chain, the oxygen consumption rate was analysed. *Fh1*^{-/-} cells showed a significant reduction of their cyanide-dependent respiratory rate (Fig. 2b) when compared to wild-type cells. The decrease in respiration was not due to a general reduction in mitochondrial number as was assessed both microscopically (Fig. 2a) and by mitochondrial DNA quantification (Supplementary Fig. 2e). Furthermore, and as was recently reported for HLRCC (Online Mendelian Inheritance in Man accession number 605839) patient-derived cells⁶, although mitochondria of *Fh1*^{-/-} cells appear larger under electron microscopy they do retain some organized cristae structures (Supplementary Fig. 2f). The

decrease in respiration of *Fh1*^{-/-} cells was associated with an increase in glycolysis as indicated initially by the increased extracellular acidification rate (Fig. 2b) and further confirmed by the increase in glucose consumption and lactate production (Fig. 2c, d).

Metabolic networks are highly interconnected, making them resistant to most single gene perturbations⁷. To elucidate the metabolic changes that enable the survival of *Fh1*^{-/-} cells despite having a truncated TCA cycle, we took a systemic approach based on flux balance analysis (FBA) to obtain a genome-scale model of cellular metabolism, as very commonly used in modelling of microbial metabolism⁸. We adopted an *in silico* modelling approach for cancer metabolism⁹ (see Supplementary Information for details) to predict genes for which elimination together with *Fh1* would selectively affect the growth ability of *Fh1*^{-/-} cells without affecting the wild-type *Fh1*^{fl/fl} cells (predicted to be synthetic lethal with *Fh1*). This modelling involved the reconstruction of genome-scale metabolic network models of the metabolism of *Fh1*^{fl/fl} and *Fh1*^{-/-} cells, using a generic computational method for building metabolic models of specific human tissues¹⁰. The reconstruction of the models began with the identification of core sets of metabolic-enzyme-coding genes that are expressed in *Fh1*^{fl/fl} and *Fh1*^{-/-} cells, based on accompanying microarray gene expression analysis (Supplementary Fig. 3), added to a set of metabolic genes that are highly expressed across many cancer cell lines¹¹. Then, for each cell line, a minimal, consistent metabolic network that includes the corresponding core reactions set was extracted from an existing generic human model¹², such that each of the core reactions can potentially carry a stoichiometrically balanced metabolic flux (Supplementary Table 1). As conventionally done in FBA modelling¹³, cellular growth requirements are modelled via the addition of a growth reaction, which represents the steady-state consumption of essential biomass constituents required for cellular proliferation, based on previous knowledge of their relative concentrations. The resulting metabolic models were used to predict the consequences of gene knock-outs based on their effect on reducing biomass production rate, considering the rate of glucose, glutamine and oxygen uptake as well as lactate secretion measured in each of the cell lines (Supplementary Table 2).

Overall, 24 reactions were predicted by this analysis to be synthetic lethal with *Fh1*, as their deletion is predicted to affect growth only in the *Fh1*^{-/-} metabolic network model (Fig. 3a and Supplementary Table 3). Of these, 18 belong to a linear pathway of haem metabolism, which was also predicted by the model to have increased flux in *Fh1*^{-/-} cells. Haem biosynthesis is a cataplerotic pathway that uses TCA-cycle-derived carbon to generate haem, whereas the haem degradation pathway generates bilirubin that can be removed from the cells. Thus, haem biosynthesis and degradation would generate a linear pathway starting with glutamine uptake and ending with bilirubin excretion. This biochemical escape valve would allow some generation of mitochondrial NADH (Supplementary Fig. 1). Interestingly, the transcriptomic analysis revealed that three of the predicted synthetic lethal genes were also upregulated in *Fh1*^{-/-} cells (Fig. 3b): haem oxygenase 1 (*Hmox1*; but not *Hmox2*), which catabolizes haem to biliverdin; biliverdin reductase B (*BhvrB*), which catabolizes biliverdin to bilirubin; and UDP-glucuronyl transferase 2b34 (*Ugt2b34*), which facilitates bilirubin excretion. The expression levels of these genes were validated (Fig. 3c, d) and the increase in *Hmox1* protein levels was also confirmed (Fig. 3e). None of these transcriptional changes could be simply attributed to the expression of Cre recombinase, because they were not observed in the Cre-infected *Fh1*^{+/+} cells, which do not express the conditional (LoxP) *Fh1* alleles (Fig. 3c, d). Notably, although these three genes exhibit significantly increased expression in *Fh1*^{-/-} cells, the potential role of this metabolic pathway in the survival of the *Fh1*-deficient cells could not have been predicted solely by its gene expression response to *Fh1* knock-out, as many additional pathways show a similar increase in expression (Supplementary Fig. 3b).

To validate the activation of the haem pathway in *Fh1*^{-/-} cells, as predicted by the FBA model, we measured the levels of excreted bilirubin in the media using liquid chromatography–mass spectrometry

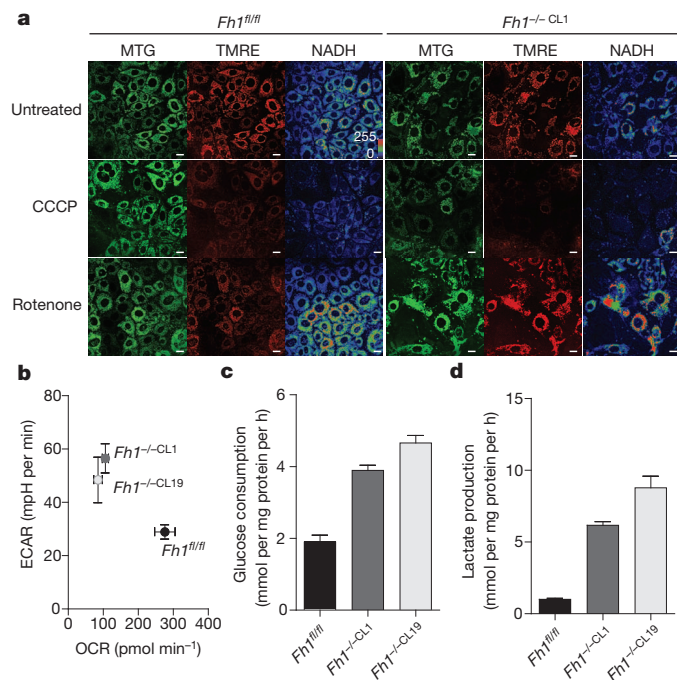


Figure 2 | Metabolic analyses of *Fh1*^{-/-} cells. **a**, Confocal microscopy was used to assess mitochondrial membrane potential and mitochondrial NADH levels in the indicated cell lines. Where indicated, cells were incubated with rotenone or CCCP before visualization. Scale bar: 50 μ m. MTG, MitoTracker green; TMRE, tetramethyl rhodamine ethyl ester. **b**, Representative graph of oxygen consumption rate (OCR) versus extracellular acidification rate (ECAR). Data are presented as mean \pm s.d. ($n = 6$). **c**, **d**, Glucose consumption (**c**) and lactate production (**d**) of the indicated cell lines. Data are presented as mean \pm s.e.m. ($n = 3$).

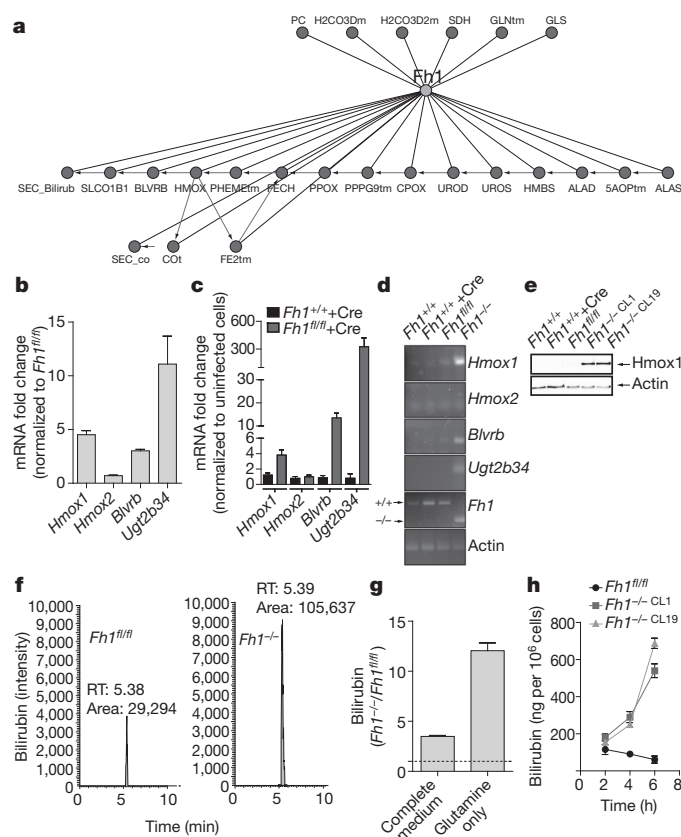


Figure 3 | The haem pathway is predicted to be synthetically lethal with *Fh1*.

a, Synthetic lethal pairs with *FH* were predicted using the FBA metabolic modelling. The haem synthesis and degradation pathway (bottom) was highly represented. 5AOPtm, aminolevulinic acid (ALA) transport; ALAD, ALA dehydratase; ALAS, ALA synthase; BLVRB, biliverdin reductase; COT, carbon monoxide (CO) transport; CPOX, coproporphyrinogen oxidase; FE2tm, iron transport; FECH, ferrochelatase; GLNtm, glutamine transport; GLS, glutaminase; H2CO3Dm/D2m, carbonate transport; HMBS, hydroxymethylbilane synthase; HMOX, haem oxygenase; PC, pyruvate carboxylase; PHEMtm, haem transporter; PPOX, protoporphyrinogen oxidase; PPPG9tm, porphyrin transporter; SDH, succinate dehydrogenase; SEC_Bilirub, bilirubin excretion; SEC_co, CO excretion; SLCO1B1, bilirubin transporter; UROD, uroporphyrinogen (URO) decarboxylase; UROS, URO synthase. **b**, Transcriptomic analysis of *Fh1*^{-/-} cells revealed an increased expression of three genes involved with the haem degradation pathway: *Hmox1*, *Blvrb* and UDP-glucuronyl transferase 2b34 (*Ugt2b34*). Data are presented as mean ± s.d. (*n* = 2). **c**, **d**, The expression levels of the genes indicated in **b** were verified using qPCR (**c**) and end-point RT-PCR (**d**). Data are presented as mean ± s.e.m. (*n* = 3). **e**, Hmox1 protein levels in the indicated cell lines were detected by western blot analysis. **f**, Representative LC-MS chromatogram of bilirubin excreted by the indicated cell lines after 24 h in complete medium. RT, retention time (min); area is expressed as arbitrary units and was calculated by the integration of the bilirubin peak. **g**, Analysis of bilirubin excretion from the indicated cell lines grown either in complete medium or in the absence of glucose for 6 h. Data are presented as mean ± s.e.m. (*n* = 3). **h**, Kinetics of bilirubin excretion from the indicated cell lines incubated in glucose-free medium. Data are presented as mean ± s.d. (*n* = 2).

(LC-MS) (Fig. 3f). In agreement with our model, the levels of excreted bilirubin were higher in *Fh1*-deficient cells (Fig. 3f-h). Importantly, excretion of bilirubin in *Fh1*^{-/-} cells was further increased when cells were transiently deprived of glucose (Fig. 3g), underpinning their increased dependency on glutamine as a mitochondrial carbon source during glucose deprivation.

In support of these findings, analysis of a published transcriptomic data set of human uterine fibroids¹⁴ revealed significant upregulation of *HMOX1* (but not *HMOX2*) in *FH*-mutant fibroids (Supplementary Fig. 4). These results prompted us to validate the predicted synthetic

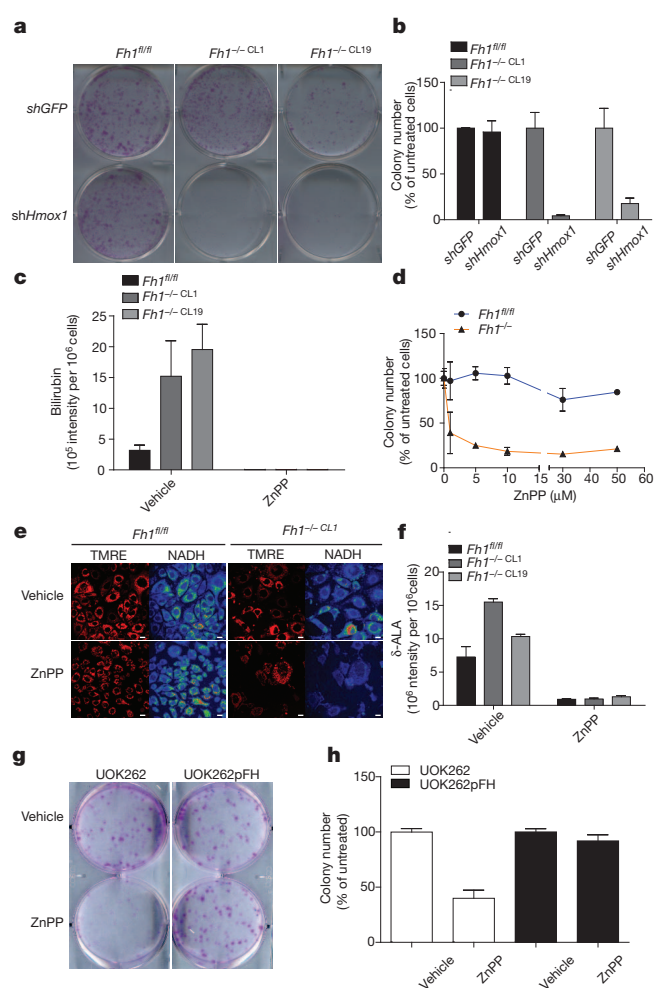


Figure 4 | Targeting the haem degradation pathway is lethal for *Fh1*-deficient cells. **a**, Representative images of a colony assay of cells infected with lentiviruses expressing either a non-targeting shRNA sequence (*shGFP*) or with an shRNA targeting *Hmox1*. **b**, Quantification of the clonogenic assay described in **a**. **c**, Quantification of bilirubin excretion before and after treatment with 10 μmol l⁻¹ ZnPP for 24 h. **d**, Clonogenic survival assay of wild-type or *Fh1*-deficient cells treated with the indicated concentration of ZnPP. **e**, The effect of ZnPP (treated as in **c**) on mitochondrial NADH was analysed microscopically. **f**, The effect of ZnPP (treated as in **c**) on intracellular ALA levels was measured by LC-MS. **g**, **h**, Representative images (**g**) and colony quantification (**h**) of a clonogenic survival assay of UOK262 and UOK262pFH cells treated with 1 μmol l⁻¹ ZnPP for 4 days. All the data are presented as mean ± s.e.m., (*n* = 3).

lethality between *Fh1* and *Hmox1* in our mouse kidney cell model. First, *Hmox1* was efficiently silenced by lentiviral infection of short hairpin (sh)RNAs (*shHmox1* 1–3) (Supplementary Fig. 5a). All three shRNAs demonstrated significant reduction in growth of *Fh1*-deficient cells, whereas there was minimal to no effect on the control cells (Supplementary Fig. 5b). The effect of the most efficient shRNA (*shHmox1* 1) on long-term colony survival was further studied and it resulted in a marked decrease in colony number in *Fh1*^{-/-} cells but not in wild-type cells (Fig. 4a, b). Importantly, the surviving *shHmox1*-infected *Fh1*^{-/-} cells escaped silencing and their *Hmox1* expression levels reverted to that of mock-infected cells (Supplementary Fig. 5c).

For further confirmation of the above findings, we used zinc protoporphyrin (ZnPP), a *Hmox* inhibitor¹⁵. First, the efficacy of *Hmox* inhibition by ZnPP was tested by measuring bilirubin excretion. In both wild-type and *Fh1*-deficient cells bilirubin excretion was completely blocked by ZnPP (Fig. 4c). Whereas acute treatment with ZnPP had no profound effect on wild-type cells, it decreased the growth of *Fh1*^{-/-} cells (Supplementary Fig. 5d). More importantly, similarly to

Hmox1 silencing, long-term treatment with ZnPP abolished colony formation of *Fh1*^{-/-} cells but had very little effect on wild-type cells (Fig. 4d). Furthermore, treatment of *Fh1*-deficient cells with ZnPP resulted in a decrease in mitochondrial NADH, whereas only slight changes were observed in control cells (Fig. 4e). These observations further elucidate the bioenergetic support that the glutamine–bilirubin linear pathway provides to *Fh1*-deficient cells.

δ-Aminolevulinic acid (ALA) synthase (ALAS), the entry point and rate-limiting step of haem biosynthesis (Supplementary Fig. 1), is tightly (negatively) controlled by haem and protoporphyrin to prevent the accumulation of porphyrins and its toxic consequences (porphyria)¹⁶. Therefore, it is likely that by blocking haem degradation, ZnPP can also inhibit the activity of ALAS. Indeed, the intracellular levels of ALA were decreased in ZnPP-treated cells (Fig. 4f), indicating that ZnPP has profound effects on the entire haem pathway beyond the inhibition of *Hmox*. To confirm further the importance of the cataplerotic role of haem biosynthesis in supporting *Fh1*-deficient cells, we also inhibited ALAS using hemin, an approved drug used for acute porphyria¹⁷. Similarly to *Hmox* inhibition, the inhibition of ALAS had no effect on control cells, whereas *Fh1*-deficient cells were sensitive to hemin treatment (Supplementary Fig. 5e).

Finally, to extend our findings to a human model of *FH* deficiency, we studied the recently described HLRCC-derived renal cancer cell line UOK262 (ref. 6). These cells are pseudo-hypoxic due to the accumulation of fumarate¹⁸. UOK262 cells were reintroduced with V5-tagged FH protein which was correctly localized to the mitochondria, improved oxygen consumption and restored low levels of fumarate (Supplementary Fig. 6a–c). Importantly, restoring TCA function to the *FH*-deficient UOK262 cells also markedly reduced bilirubin secretion and rendered the cells less sensitive to the HMOX and ALAS inhibitors ZnPP and hemin, respectively (Fig. 4g, h and Supplementary Fig. 6d, e). Importantly, the sensitivity of the *FH*-deficient UOK262 cells to ZnPP is independent on HIF activity (Supplementary Fig. 6f–h).

Taken together, the results of this work demonstrate that the inhibition of the haem biosynthesis/degradation pathway in general, and *Hmox* in particular, is synthetically lethal with *Fh1* both in mouse and in human cell lines. Hence, its inhibition would provide a valid therapeutic window for the treatment of HLRCC patients as it would specifically target *FH*-deficient cells while sparing normal tissues, thus reducing nonspecific toxic effects.

METHODS SUMMARY

Epithelial kidney cells were obtained from *Fh1*^{fl/fl} mice following the method described previously¹⁹. The *Fh1*^{-/-} cell line was generated by infection with AhCRE adenoviral particles. The genotype was assessed by PCR on genomic DNA using the primers described in the Methods. TCA metabolites and their isotopomer enrichment analyses were performed by GC–MS after incubating the cells with either U-¹³C-glucose or U-¹³C-glutamine. Mitochondrial potential and NADH were analysed by confocal microscopy using the potentiometric probe TMRE and NADH autofluorescence, respectively. Glucose and glutamine consumption and lactate secretion were measured using the BioProfile Basic4 Analyser. Oxygen consumption rate and extracellular acidification rate were measured using the Seahorse XF24. Expression levels of the genes in the haem pathway were determined by qPCR and validated using semi-quantitative RT–PCR as detailed in the Methods. Bilirubin, ALA, citrate and aconitate levels were measured by LC–MS. Sulphorhodamine B was used to stain colonies. Colonies were counted using ImageJ software.

Full Methods and any associated references are available in the online version of the paper at www.nature.com/nature.

Received 13 July 2010; accepted 11 July 2011.

Published online 17 August 2011.

- Tomlinson, I. P. *et al.* Germline mutations in *FH* predispose to dominantly inherited uterine fibroids, skin leiomyomata and papillary renal cell cancer. *Nature Genet.* **30**, 406–410 (2002).

- Isaacs, J. S. *et al.* HIF overexpression correlates with biallelic loss of fumarate hydratase in renal cancer: novel role of fumarate in regulation of HIF stability. *Cancer Cell* **8**, 143–153 (2005).
- Pollard, P. J. *et al.* Targeted inactivation of *fh1* causes proliferative renal cyst development and activation of the hypoxia pathway. *Cancer Cell* **11**, 311–319 (2007).
- Frezza, C., Pollard, P. J. & Gottlieb, E. Inborn and acquired metabolic defects in cancer. *J. Mol. Med.* **89**, 213–220 (2011).
- DeBerardinis, R. J. *et al.* Beyond aerobic glycolysis: transformed cells can engage in glutamine metabolism that exceeds the requirement for protein and nucleotide synthesis. *Proc. Natl Acad. Sci. USA* **104**, 19345–19350 (2007).
- Yang, Y. *et al.* UOK262 cell line, fumarate hydratase deficient (*FH*⁻/*FH*⁻) hereditary leiomyomatosis renal cell carcinoma: *in vitro* and *in vivo* model of an aberrant energy metabolic pathway in human cancer. *Cancer Genet. Cytogenet.* **196**, 45–55 (2010).
- Deutscher, D., Meilijon, I., Kupiec, M. & Rupp, E. Multiple knockout analysis of genetic robustness in the yeast metabolic network. *Nature Genet.* **38**, 993–998 (2006).
- Price, N. D., Papin, J. A., Schilling, C. H. & Palsson, B. O. Genome-scale microbial *in silico* models: the constraints-based approach. *Trends Biotechnol.* **21**, 162–169 (2003).
- Folger, O. *et al.* Predicting selective drug targets in cancer through metabolic networks. *Mol. Syst. Biol.* **7**, 501 (2011).
- Jerby, L., Shlomi, T. & Rupp, E. Computational reconstruction of tissue-specific metabolic models: application to human liver metabolism. *Mol. Syst. Biol.* **6**, 401 (2010).
- Lee, J. K. *et al.* A strategy for predicting the chemosensitivity of human cancers and its application to drug discovery. *Proc. Natl Acad. Sci. USA* **104**, 13086–13091 (2007).
- Duarte, N. C. *et al.* Global reconstruction of the human metabolic network based on genomic and bibliomic data. *Proc. Natl Acad. Sci. USA* **104**, 1777–1782 (2007).
- Orth, J. D., Thiele, I. & Palsson, B. O. What is flux balance analysis? *Nature Biotechnol.* **28**, 245–248 (2010).
- Vanharanta, S. *et al.* Distinct expression profile in fumarate-hydratase-deficient uterine fibroids. *Hum. Mol. Genet.* **15**, 97–103 (2006).
- Labbe, R. F., Vreman, H. J. & Stevenson, D. K. Zinc protoporphyrin: A metabolite with a mission. *Clin. Chem.* **45**, 2060–2072 (1999).
- Schoenfeld, N. *et al.* The effects of metalloporphyrins, porphyrins and metals on the activity of delta-aminolevulinic acid synthase in monolayers of chick embryo liver cells. *Biochem. Pharmacol.* **33**, 2783–2788 (1984).
- Anderson, K. E. & Collins, S. Open-label study of hemin for acute porphyria: clinical practice implications. *Am. J. Med.* **119**, e19–24 (2006).
- Sudarshan, S. *et al.* Fumarate hydratase deficiency in renal cancer induces glycolytic addiction and hypoxia-inducible transcription factor 1 α stabilization by glucose-dependent generation of reactive oxygen species. *Mol. Cell. Biol.* **29**, 4080–4090 (2009).
- Mathew, R., Degenhardt, K., Haramaty, L., Karp, C. M. & White, E. Immortalized mouse epithelial cell models to study the role of apoptosis in cancer. *Methods Enzymol.* **446**, 77–106 (2008).

Supplementary Information is linked to the online version of the paper at www.nature.com/nature.

Acknowledgements This work was supported by Cancer Research UK. We would like to acknowledge the Patterson Institute for Cancer Research for the Exon Array analysis. C.F. is supported by an EMBO long term fellowship (ALTF330). P.J.P. is in receipt of a Beit Memorial Fellowship funded by the Wellcome Trust (WT091112MA). D.G.W. and L.Z. would like to acknowledge SULSA (Scottish Universities Life Science Alliance). R.J.D. and K.N.R. are supported by the NIH (DK072565-05) and the Cancer Prevention and Research Institute of Texas (HIRP100437-01). O.F., T.S. and E.R. are supported by the Israel Science Foundation (ISF) and the Israel Cancer Research Foundation. L.J. is supported by the Edmond J. Safra Bioinformatics program at TAU. We thank UOB Tumor Cell Line Repository and W. Marston Linehan for providing us with the UOK262 cell lines, and A. King for editorial work.

Author Contributions C.F. and E.G. conceived the project, analysed the data and wrote the manuscript. C.F. and E.D.M. generated the kidney cell lines. O.F., L.J., T.S. and E.R. built the metabolic network of the cells and predicted the synthetic lethal genes. J.A., I.P.M.T. and P.J.P. provided the *Fh1*^{fl/fl} mice, generated the UOKpFH cell line and provided genotyping tools. G.K. and A.H. performed the bioinformatics and statistical analysis. L.Z. and D.G.W. performed the LC–MS analysis. K.N.R. and R.J.D. performed GC–MS and the BioProfile metabolic analyses. C.F. performed all other experiments with the help of B.C. M.M. performed the electron microscopy. All the authors discussed the results and commented on the manuscript.

Author Information Microarray data are deposited at the website <http://bioinformatics.picr.man.ac.uk/vice/Welcome.vice>, accession reference GE_EG(2). Reprints and permissions information is available at www.nature.com/reprints. The authors declare no competing financial interests. Readers are welcome to comment on the online version of this article at www.nature.com/nature. Correspondence and requests for materials should be addressed to E.G. (egottlieb@beatson.gla.ac.uk).

METHODS

Cell culture: *Fh1^{fl/fl}* and *Fh1^{-/-}* cell lines. Epithelial kidney cells were obtained from *Fh1^{fl/fl}* mice following the method described previously¹⁹. 2×10^5 cells were either left untreated or infected with Cre recombinase-encoding adenovirus (Ad5CMVCRE) using 300 p.f.u. per cell. After 4 days of infection, 100 cells were plated and grown onto 15-cm dishes. Individual colonies were harvested using paper cloning discs (Sigma) and transferred onto 24-well plates for clonal expansion. Cells were grown using DMEM (21969-035, Invitrogen) supplemented with 10% FBS, 2 mmol l⁻¹ glutamine, 1 mmol l⁻¹ pyruvate and 50 μ g l⁻¹ uridine. UOK262 were cultured in DMEM (21969-035, Invitrogen) supplemented with 10% FBS, 2 mmol l⁻¹ glutamine, 1 mmol l⁻¹ pyruvate.

UOK262 and UOKpFH cell lines. UOK262 cells were grown using high glucose DMEM (Invitrogen) supplemented with 2 mM glutamine and 10% FBS. Full-length FH human cDNA was cloned into pEF1-V5-HIS. Transfected cells were selected in 1 mg ml⁻¹ G418 and single clones were expanded. Expression and subcellular localization of FH was confirmed by immunofluorescence using anti V5 antibody with a FITC-conjugated secondary antibody; mitochondria were stained using Mitotraker red and nuclei were stained with DAPI.

Genomic DNA, mitochondrial DNA, RNA isolation and qPCR analyses. 2×10^5 cells were harvested in RLT buffer (Qiagen) using a cell lifter and lysates were passed through QiaShredder columns (Qiagen). Genomic DNA and mRNA were then separated using the AllPrep micro kit (Qiagen) following manufacturer's instructions. Quantification of RNA was obtained on the Eppendorf Biophotometer using Eppendorf single-sealed cuvettes, UVette (Eppendorf UK Limited).

Genomic DNA was assessed to determine the different genotypes of the different cell lines using the primers F1, F3 and R1 described above. The PCR of the genomic DNA was performed using GoTaq DNA polymerase (Promega) and 0.5 μ M primers following the manufacturer's instructions. The PCR program was: 15 min at 95 °C followed by 40 cycles of 45 s at 95 °C, 30 s at 55 °C and then 30 s at 72 °C. The PCR products were separated in a 2% agarose gel stained with ethidium bromide.

Mitochondrial DNA content was analysed from the genomic DNA extraction by comparing the expression levels of a nuclear-encoded single-copy gene, amyloid precursor protein (APP), to the DNA levels of the mtDNA encoded cytochrome c oxidase subunit II (COXII), as performed previously²⁰. The following primers were used: APP: FW 5'-GGCTGCTGGCAGAACCCAG-3', RV 5'-CCCTGACGG GTCTGACTCCCA-3'; COXII FW 5'-AACTGATGCCATCCAGGCCGA-3', RV 5'-GGTGAAGGTGCCAGTGGAATGT-3'.

For PCR analyses, 1 μ g of mRNA was retro-transcribed into cDNA using M-Mulv Reverse Transcriptase and random hexamers and qPCR reactions were performed using a Sybr-green master mix as per the manufacturer's instructions (Dynamo qPCR kit, Finnzymes, ThermoFisher). In brief, 0.5 μ M primers, ROX dye, and a 1 μ l of a 1:10 dilution of cDNA in a final volume of 20 μ l were used. The primers were designed by the Roche Universal Library (UPL, Roche, <http://www.roche-applied-science.com/sis/rtpcr/upl/ezhome.html>) and the sequences are indicated in Supplementary Table 5. Real-time PCR was performed on the 7500 Fast Real-Time PCR System (Life Technologies Corporation) and expression levels of the indicated genes were calculated using the $\Delta\Delta C_t$ method by the appropriate function of the software using actin as calibrator. The results were further validated using Polg2R as calibrator (data not shown). The PCR programme was: 15 min at 95 °C followed by 40 cycles of 10 s at 94 °C, 30 s at 55 °C and then 30 s at 72 °C. A final extension at 72 °C for 10 min was allowed before the melting curve, which was used to confirm the presence of single PCR products. For the semi-quantitative end-point RT-PCR the cDNA prepared as indicated above was cycled for 25 times and the PCR products were separated using a 2% agarose gel stained with ethidium bromide.

Exon array analysis. RNA obtained as described above was subjected to a Microarray analysis using a GeneChip Mouse Exon 1.0 ST Array (Affimetrix). The .Cel files were normalized and analysed in Partek Genomics Suite Software, version 6.5beta Copyright 2010. Interrogating and control core probe sets were imported and default RMA setting used, including quantile normalization, log₂ transformation and mean probe-set summarization. In gene-level analysis the multiway analysis of variance (ANOVA) was used to identify significantly regulated genes from one of the experimental groups and linear contrasts performed between all pairs of experimental conditions. Multiple test corrections were performed for all calculated *P*-values. Step-up *P*-value, a *P*-value that controls the false discovery rate, and the fold change values were used for further selection of significantly differentially expressed genes.

Microarray bioinformatics analysis. Affimetrix Human Genome U133A .Cel files of 15 wild-type and 7 mutant fumarate hydratase samples were normalized and analysed in Partek Genomics Suite Software, version 6.5 Copyright 2010.

RMA normalization and log₂ transformation of the data was followed by *t*-test and multiple test corrections of *P*-values.

Immunoblotting. 2×10^5 cells were lysed in RIPA buffer (150 mM sodium chloride, 1.0% NP-40, 0.5% sodium deoxycholate, and 50 mM Tris, pH 8.0) supplemented with a 1:100 dilution of the protein inhibitor cocktail (Sigma). Protein concentration was determined using the Bicinchoninic Acid Assay (ThermoFisher) using BSA as standard. Equal amounts of protein were loaded into 4–12% Tris-Mops pre-casted gels (Invitrogen) and electrophoretically separated using MOPS running buffer (Invitrogen). After SDS-PAGE, proteins were blotted onto 0.22 μ m nitrocellulose (Millipore) and probed with the following antibodies, all at 1:1,000 dilution in 5% non-fat milk: Fh1 (polyclonal rabbit AutogenBioclear NE054 /7S), Hmx1 (polyclonal rabbit SPA-896, Stressgen Enzo Life Science), actin (mouse monoclonal AC-40; Sigma). Membranes were then incubated with secondary HRP-conjugated antibodies at 1:1,000 dilution in 5% non-fat milk: anti-mouse (7076) and anti rabbit (7074), both from Cell Signaling Technology. ECL (RPN 2209, GE Healthcare UK) was used for chemiluminescence detection. For Hmx1 and actin western blot, a secondary donkey anti-rabbit (926 32213, Licor) and donkey anti-mouse (926 32212, Licor) IR800 at 1:1,000 dilution were used. The IR scanning was performed using the Licor Odyssey scanner (channel, 800; brightness, 50; contrast, 50; sensitivity, auto; resolution, 169.492 μ m; pixel area, 0.02873 mm²; intensity, 5) and acquired using Odyssey software version 3.

Measurement of NADH and mitochondrial potential. 2×10^5 cells were grown in 3.5-cm glass-bottom dishes (MatTek corporation) and loaded with 50 nmol l⁻¹ MitoTracker green (MTG; Invitrogen) and 10 nmol l⁻¹ tetramethyl rhodamine ethyl ester (TMRE) (Invitrogen) for 30 min at 37 °C. Cells were then left untreated or treated as indicated. The final concentrations and incubation time of the drugs are: 5 μ mol l⁻¹ rotenone, 5 min; 10 μ mol l⁻¹ carbonylcyanide-*m*-chlorophenyl hydrazone (CCCP) for 1 min. Images were collected with a Leica TCS SP2 AOBS inverted laser scanning microscope equipped with a Coherent 351–364 nm UV laser using a 63 \times /1.32.ph3 oil HCX PL APO objective, resolution 1,024 \times 1,024 d.p.i., 8-bit image depth, 200 Hz scanning speed, and line average 2. The acquisition of the two-colour images was performed in a sequential scanning mode to minimize spectral bleed-through artefacts. Laser excitation was 364 nm for NADH autofluorescence, 488 nm for MTG and 568 nm for TMRE, whereas fluorescence emission was adjusted with AOBS at 390–486 nm for NADH, 501–546 nm for MTG and 580–620 nm for TMRE. To increase sensitivity of NADH detection, the pinhole aperture used for all channels was set at 2.62 airy units. The images were quantified for NADH levels using the Image Pro Plus software (Media Cybernetics) using MTG signal as a mask to outline the mitochondrial reticulum. Intensity of fluorescence of NADH determined in the outlined areas was then normalized to MTG fluorescence intensity. To better appreciate changes in NADH fluorescence intensity, a rainbow look-up table was applied to the relevant images using the appropriate function of ImageJ (ImageJ, US National Institutes of Health, <http://rsb.info.nih.gov/ij/>).

Measurement of glucose, lactate and glutamine. 2×10^5 cells were plated onto 6-cm dishes and cultured until 90% confluent. Each dish was then replenished with fresh medium and cultured for 16 h. After the culture period, the medium was recovered for determination of glucose, lactate and glutamine concentration using a BioProfile Basic4 Analyser (NOVA Biomedical) and compared to concentration of these metabolites in the starting medium. To correct for spontaneous glutamine degradation, an additional dish with no cells was cultured in parallel. Raw values of glutamine and glucose utilization, and lactate secretion, were converted to rates by correcting for the protein content at the end of the assay, and the duration of the assay in hours.

Measurement of OCR and ECAR rate. 2×10^4 *Fh1^{fl/fl}* cells, 3×10^4 *Fh1^{-/-}*, or 3×10^4 UOK262 and UOK262pFH cells were plated onto XF24 plates (Seahorse Bioscience) and incubated at 37 °C, 5% CO₂ for 24 h. The medium was then replaced with 675 μ l of unbuffered assay media (Seahorse Bioscience) supplemented with 2 mmol l⁻¹ glutamine, 25 mmol l⁻¹ glucose and 2% FBS (pH was adjusted to 7.4 using sodium hydroxide 0.5 M) and cells were then placed at 37 °C in a CO₂-free incubator. Basal oxygen consumption rate (OCR) and extracellular acidification rate (ECAR) were then recorded using the XF24 plate reader. At the end of the experiment 1 mmol l⁻¹ potassium cyanide or 1 μ mol l⁻¹ antimycin A were added to measure mitochondria-independent oxygen consumption. Each cycle of measurement consisted of 3 min mixing, 3 min waiting and 4 min measuring. OCR and ECAR were normalized to cell number calculated at the end of the experiments. To obtain the mitochondrial-dependent OCR, only the cyanide-sensitive respiration was used. Homogeneous plating of the cells and cell count were assessed by fixing the cells with trichloroacetic acid 10% for 1 h at 4 °C and then staining the fixed cells with 0.47% solution of sulphorhodamine B (SRB) (Sigma).

Determination of TCA cycle metabolites and isotopomer enrichment analysis by GC-MS. Cells were cultured in DMEM supplemented with 10% FBS, 2 mmol

1^{-1} sodium pyruvate, $50 \mu\text{g ml}^{-1}$ uridine, $100 \text{ units ml}^{-1}$ penicillin and $100 \mu\text{g ml}^{-1}$ streptomycin in 6-cm tissue culture dishes. Metabolic experiments were performed when cells were approximately 90% confluent. Medium for ^{13}C glucose labelling experiments contained $10 \text{ mM D-[U-}^{13}\text{C]-glucose}$ (Cambridge Isotope Labs) and 4 mmol l^{-1} unlabelled glutamine. Medium for ^{13}C -glutamine labelling experiments contained 10 mmol l^{-1} unlabelled glucose and 4 mmol l^{-1} L-[U- ^{13}C]-glutamine (Isotec). Medium containing ^{13}C -labelled nutrients did not contain sodium pyruvate. Each dish of cells was rinsed in phosphate-buffered saline, and replenished with the labelling medium. After 16 h, cells were rinsed with normal saline, and metabolites were extracted in $0.5 \text{ ml } 50\% \text{ MeOH}$ pre-chilled to -20°C . 100 nmol of sodium oxobutyrate was added as a standard to the extracted metabolites. Extracts were concentrated under blown air and derivatized using Tri-Sil trimethylsilane reagent (Thermo Scientific). One microlitre of each derivatized sample was injected onto an Agilent 6980N GC coupled to an Agilent 5973N mass selective detector. GC-MS data were analysed using MSDChem Data Analysis Software (Agilent). Retention times of the sodium oxobutyrate standard, succinate, fumarate and malate were 11.4, 13.2, 14.2 and 18.7 min , respectively. Informative ions were monitored for derivatized, unenriched oxobutyrate (m/z 230), succinate (247), fumarate (245), and malate (335). Relative metabolite abundances were determined by normalizing abundances of each metabolite to the internal standard and to protein content. For mass isotopomer analysis, the abundance of each mass isotopomer ($m+0$, $m+1$, ... $m+n$, where n is the number of carbons in the parent metabolite) was corrected for natural ^{13}C abundance using published methods²¹.

Measurement of bilirubin, ALA, lactate and TCA cycle intermediates by LC-MS. 1×10^6 cells were plated onto 10-cm dishes and cultured in standard medium for 12 h. The medium was replaced by fresh standard medium or by medium without glucose or without glutamine for the indicated time. Fresh medium in the same dishes but without cells was incubated simultaneously and used as a reference. $100 \mu\text{l}$ of medium were diluted into $200 \mu\text{l}$ of acetonitrile (Fisher). The solution was centrifuged at $16,000g$ for 4 min at 4°C . The supernatant was collected and transferred into autosampler vials for LC-MS determinations. Cells were lysed with a solution kept in dry ice/methanol (-80°C) composed of 50% methanol and 30% acetonitrile in water and quickly scraped. The insoluble material was immediately pelleted in a cooled centrifuge (0°C) and the supernatant was collected for subsequent LC-MS analysis. A ZIC-HILIC column ($4.6 \text{ mm} \times 150 \text{ mm}$, guard column $2.1 \text{ mm} \times 20 \text{ mm}$, Merck) was used for LC separation using formic acid, water acetonitrile as component of the mobile phase.

Measurement of ^{13}C -labelled metabolites by LC-MS. 1×10^6 cells were plated onto 10-cm dishes and cultured in standard medium for 12 h. The medium was replaced by fresh medium supplemented with $2 \text{ mM U-}^{13}\text{C}$ -glutamine for the indicated time. Fresh medium in the same dishes but without cells was incubated simultaneously and used as a reference. Cells were then lysed with a solution kept in dry ice/methanol (-80°C) composed of 50% methanol and 30% acetonitrile in water and quickly scraped. The insoluble material was immediately pelleted in a cooled centrifuge at $16,000g$ for 15 min at 0°C and the supernatant was collected for subsequent LC-MS analysis. The amount of extraction solution was calculated according to the number of cells present in the sample dish, extrapolated using a 'counter dish' cultured in the same conditions of the sample dishes. A concentration of 1 ml per 2×10^6 cells was used in the extraction solutions. Intermediates were separated using a liquid chromatography system.

Colony formation assay. Clonogenic survival assay was performed as previously described²² with minor modifications. The plating efficiency among different cell lines was different therefore $100 \text{ Fh1}^{\text{H}/\text{H}}$ cells and $600 \text{ Fh1}^{-/-}$ cells per each 10-cm dish were plated, whereas 150 UOK262 cells, 150 UOK262pFH cells and 600

$\text{UOK262 shHIF}\beta$ cells per each 6-well plate were plated. Twenty-four hours after plating, cells were treated with the indicated doses of ZnPP, $100 \mu\text{mol l}^{-1}$ hemin (Sigma) or vehicle (DMSO for ZnPP or water for the other drug). UOK262 cells infected with shHIF1 β plasmid were selected with $2 \mu\text{g ml}^{-1}$ puromycin. Hemin was prepared by dissolving the drug in a solution of 0.2 M sodium carbonate, pH 10. The pH was then adjusted at 7.4 and the mixture was sterilized using $0.45 \mu\text{m}$ filters. The final concentration of the solution was determined using the molar extinction coefficient of hemin at $\lambda_{407 \text{ nm}}$ $\epsilon = 36,000 \text{ M cm}^{-1}$ (ref. 23). The medium was changed every 2 days for a total of 7 days treatment for murine cell lines and a total of 4 days of treatment for human cell lines. The medium was then replaced with fresh standard medium without drug or vehicle and cells were left to grow for 2–4 more days. The cells were then fixed as described²⁴ by adding ice-cold trichloroacetic acid onto the plate at the final concentration of 3% for 1 h at 4°C . Cells were then washed with water and air-dried. Cells were then stained using 0.47% SRB for 30 min at room temperature. SRB was removed and cells were thoroughly washed with 1% acetic acid and air-dried. Plates were scanned at the resolution of 600 d.p.i., 24-bit saved as TIFF files and analysed using the object count function of the ImageJ software.

ShRNA of Hmox1. The lentiviral shRNA plasmids against *Hmox1* (NM_010442) and the non-targeted shGFP, and a scramble sequence were all purchased from Open Biosystems, TRC1 library (Thermoscientific). The three independent shRNAs were identified as follows: 1, TRCN0000071578; 2, TRCN0000071579; 3, TRCN0000071580 and the sequences are shown in Supplementary Table 6. The viral supernatant was obtained from the filtered growth media of the packaging cells HEK293T transfected with appropriate packaging plasmids and either shRNA for *Hmox1* or control pLKO plasmids, using calcium phosphate procedure. $2 \times 10^5 \text{ Fh1}^{\text{H}/\text{H}}$, $\text{Fh1}^{-/-}$ and UOK262 cells were then plated on 6-well plates and infected with the viral supernatant prepared as indicated above. After 2 days, the medium was replaced by selection medium containing $4 \mu\text{g ml}^{-1}$ puromycin. Cells were then allowed to grow under selection for 2 days and then an equal number of cells was plated onto 6-well plates and grown using the selection media. After a week cells were fixed using SRB following the procedure described above.

shRNA of HIF1 β (ARNT). 2×10^5 cells were infected with shRNA for *HIF1 β* (NM_001668.2) and control plasmid using lentiviral infection. HEK293T and relevant packaging plasmids were used to produce the lentiviral suspension. shRNA plasmids were purchased from Openbiosystems and the clone number TRCN0000003819 (for the sequence see Supplementary Table 6) was used for subsequent infections. After infection, cells were selected using $4 \mu\text{g ml}^{-1}$ puromycin.

Statistical analyses. The data (mean \pm s.e.m.) are representative of 3–5 independent experiments, performed in technical triplicates if not differently indicated. Data were analysed and presented with Graphpad Prism 5.01 software (GraphPad Software Inc.).

- Malena, A., Loro, E., Di Re, M., Holt, I. J. & Vergani, L. Inhibition of mitochondrial fission favours mutant over wild-type mitochondrial DNA. *Hum. Mol. Genet.* **18**, 3407–3416 (2009).
- Fernandez, C. A., Des Rosiers, C., Previs, S. F., David, F. & Brunengraber, H. Correction of ^{13}C mass isotopomer distributions for natural stable isotope abundance. *J. Mass Spectrom.* **31**, 255–262 (1996).
- Franken, N. A., Rodermond, H. M., Stap, J., Haveman, J. & van Bree, C. Clonogenic assay of cells *in vitro*. *Nature Protocols* **1**, 2315–2319 (2006).
- Uc, A., Stokes, J. B. & Britigan, B. E. Heme transport exhibits polarity in Caco-2 cells: evidence for an active and membrane protein-mediated process. *Am. J. Physiol. Gastrointest. Liver Physiol.* **287**, G1150–G1157 (2004).
- Vichai, V. & Kirtikara, K. Sulforhodamine B colorimetric assay for cytotoxicity screening. *Nature Protocols* **1**, 1112–1116 (2006).

TSLP promotes interleukin-3-independent basophil haematopoiesis and type 2 inflammation

Mark C. Siracusa^{1,2}, Steven A. Saenz^{1,2}, David A. Hill^{1,2}, Brian S. Kim^{1,2}, Mark B. Headley³, Travis A. Doering^{1,2}, E. John Wherry^{1,2}, Heidi K. Jessup⁴, Lori A. Siegel⁴, Taku Kambayashi⁵, Emily C. Dudek⁶, Masato Kubo^{7,8}, Antonella Cianferoni⁶, Jonathan M. Spergel⁶, Steven F. Ziegler³, Michael R. Comeau⁴ & David Artis^{1,2,9}

CD4⁺ T-helper type 2 (T_H2) cells, characterized by their expression of interleukin (IL)-4, IL-5, IL-9 and IL-13, are required for immunity to helminth parasites¹ and promote the pathological inflammation associated with asthma and allergic diseases². Polymorphisms in the gene encoding the cytokine thymic stromal lymphopoietin (TSLP) are associated with the development of multiple allergic disorders in humans, indicating that TSLP is a critical regulator of T_H2 cytokine-associated inflammatory diseases^{3–6}. In support of genetic analyses, exaggerated TSLP production is associated with asthma, atopic dermatitis and food allergies in patients, and studies in murine systems demonstrated that TSLP promotes T_H2 cytokine-mediated immunity and inflammation^{5,7–12}. However, the mechanisms through which TSLP induces T_H2 cytokine responses remain poorly defined. Here we demonstrate that TSLP promotes systemic basophilia, that disruption of TSLP–TSLPR interactions results in defective basophil responses, and that TSLPR-sufficient basophils can restore T_H2-cell-dependent immunity *in vivo*. TSLP acted directly on bone-marrow-resident progenitors to promote basophil responses selectively. Critically, TSLP could elicit basophil responses in both IL-3–IL-3R-sufficient and -deficient environments, and genome-wide transcriptional profiling and functional analyses identified heterogeneity between TSLP-elicited versus IL-3-elicited basophils. Furthermore, activated human basophils expressed TSLPR, and basophils isolated from eosinophilic oesophagitis patients were distinct from classical basophils. Collectively, these studies identify previously unrecognized heterogeneity within the basophil cell lineage and indicate that expression of TSLP may influence susceptibility to multiple allergic diseases by regulating basophil haematopoiesis and eliciting a population of functionally distinct basophils that promote T_H2 cytokine-mediated inflammation.

Previous *in vitro* studies suggested that TSLP could promote T_H2 cytokine-mediated inflammation by influencing dendritic cell, mast cell and lymphocyte populations¹³. However, the IL-4-expressing cell populations that TSLP targets *in vivo* remain poorly defined. Following administration of recombinant TSLP (rTSLP) to IL-4/eGFP (enhanced green fluorescent protein) reporter mice, an increase in the frequency and total number of basophils was observed in the spleen (Fig. 1a, b). Mice receiving hydrodynamic tail vein injections of cDNA plasmid encoding TSLP (TSLP cDNA)¹⁴ also exhibited significant increases in the frequency and total number of basophils in the spleen (Fig. 1c, d), blood, lung and bone marrow (Supplementary Fig. 1a–f). Basophils, along with dendritic cells, are capable of contributing to the induction of optimal T_H2 cytokine responses^{15–20}. Consistent with this, exaggerated basophil responses in TSLP-cDNA-treated mice were associated with increased systemic production of T_H2 cytokines

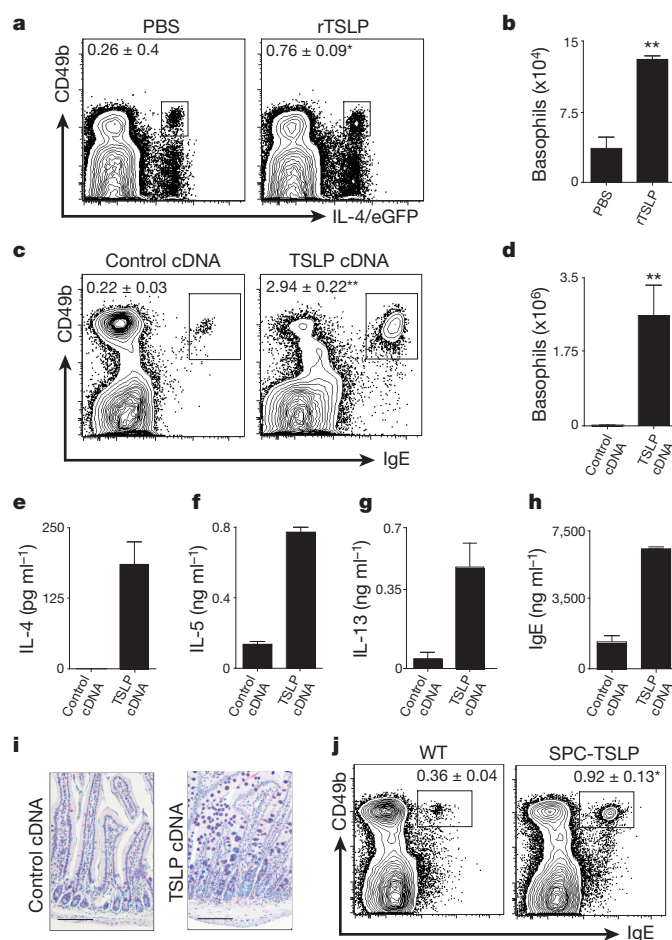


Figure 1 | TSLP promotes peripheral basophilia. **a, b**, IL-4/eGFP reporter mice were treated with PBS or rTSLP and splenic basophils were identified (**a**) and quantified (**b**). **c, d**, Wild-type mice were treated with control cDNA or TSLP-encoding (TSLP cDNA) plasmid and splenic basophils were identified (**c**) and quantified (**d**). **e–h**, Serum IL-4 (**e**), IL-5 (**f**), IL-13 (**g**) and total IgE (**h**) were quantified. **i**, Histological analysis of small intestine. Scale bars, 100 μm. **j**, Splenic basophils from control mice (WT), or SPC-TSLP mice were identified. Flow cytometry plots are gated on live NBNT cells. Results are representative of at least three (**a–d** and **j–i**) or two (**e–i**) separate experiments containing 3–5 (**a–d**), 5 (**e–i**) or 6–12 (**j**) mice per group. Results are shown as means ± s.e.m. Statistical analyses performed using a two-tailed students *t*-test (**P* < 0.05), (***P* < 0.01).

¹Institute for Immunology, Perelman School of Medicine, University of Pennsylvania, Philadelphia, Pennsylvania 19104, USA. ²Department of Microbiology, Perelman School of Medicine, University of Pennsylvania, Philadelphia, Pennsylvania 19104, USA. ³Immunology Program, Benaroya Research Institute, Seattle, Washington 98101, and Immunology Department, University of Washington School of Medicine, Seattle, Washington 98195, USA. ⁴Inflammation Research, Amgen Inc., Seattle, Washington 98119, USA. ⁵Department of Pathology and Laboratory Medicine, Perelman School of Medicine, University of Pennsylvania, Philadelphia, Pennsylvania 19104, USA. ⁶Division of Allergy and Immunology, Children's Hospital of Philadelphia, Department of Pediatrics, Perelman School of Medicine, University of Pennsylvania, Philadelphia, Pennsylvania 19104, USA. ⁷Laboratory for Signal Network, Research Center for Allergy and Immunology, RIKEN Yokohama Institute, Yokohama 230-0045, Japan. ⁸Division of Molecular Pathology, Research Institute for Biological Science, Tokyo University of Science, Chiba 278-0022, Japan. ⁹Department of Pathobiology, School of Veterinary Medicine, University of Pennsylvania, Philadelphia, Pennsylvania 19104, USA.

(Fig. 1e–g), elevated IgE levels (Fig. 1h) and the development of T_H2 cytokine-associated intestinal inflammation (Fig. 1i). In addition to reported expression by mast cells and basophils, epithelial cells at barrier surfaces are potent sources of TSLP¹³. Therefore, we tested whether epithelial-cell-derived TSLP could influence peripheral basophil populations. Mice that constitutively express a *Tslp* transgene under the surfactant protein C promoter (SPC-TSLP) in lung epithelial cells²¹ exhibited increased frequencies of basophils in the spleen (Fig. 1j).

To test whether TSLP–TSLPR signalling influences infection-induced basophilia *in vivo*, we used a helminth model in which protective immunity is dependent on TSLP–TSLPR signalling¹⁰. Whereas *Trichuris muris*-infected wild-type mice exhibited increased basophils in the periphery, *Tslpr*^{−/−} mice failed to exhibit infection-induced basophilia (Supplementary Fig. 2a). Critically, TSLP-elicited basophils isolated from *Tslpr*^{+/+} mice and adoptively transferred into normally susceptible *T. muris*-infected *Tslpr*^{−/−} mice were sufficient to restore T_H2 cytokine responses (Supplementary Fig. 2b,c), IgE production (Supplementary Fig. 2d), goblet cell hyperplasia (Supplementary Fig. 2e, f), secretion of goblet-cell-derived RELM- β (Supplementary Fig. 2g) and significantly reduce worm burdens (Supplementary Fig. 2h). These data demonstrate that basophil-restricted TSLPR expression is sufficient to partially restore protective T_H2 cytokine responses *in vivo*.

TSLP was originally identified as a lymphocyte growth factor capable of regulating the differentiation of lymphocytes from haematopoietic progenitor cells¹³. These findings provoked the hypothesis that in addition to influencing peripheral basophil responses, TSLP may regulate basophil haematopoiesis in the bone marrow. To test directly whether TSLP could elicit the population expansion of basophils from bone-marrow-resident cells, we adopted a basophil differentiation assay using IL-4/eGFP reporter mice²². When bone marrow was cultured in media alone, 4.25% of the non-B non-T (NBNT) cells expressed IL-4/eGFP (Fig. 2a), but no mast cells or basophils were present (Fig. 2b). As previously reported²², bone marrow cells cultured

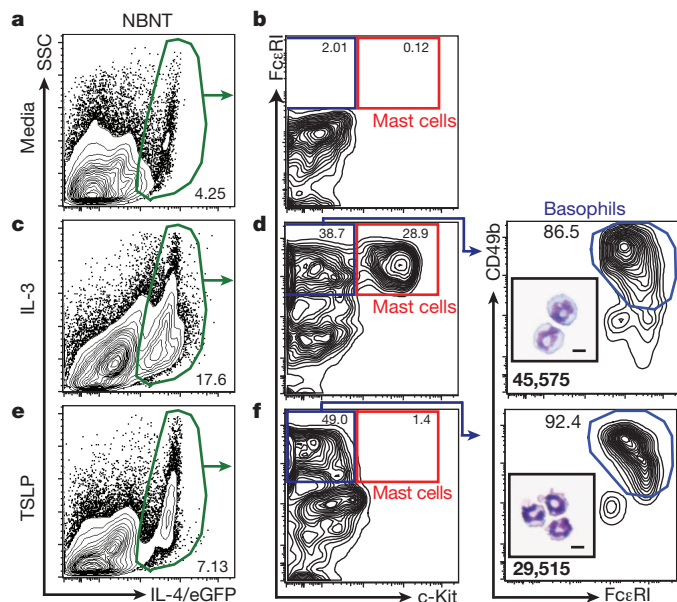


Figure 2 | TSLP preferentially expands basophil populations from bone-marrow-resident cells. **a, c, e**, Bone-marrow-resident cells were taken from IL-4/eGFP reporter mice and cultured in the presence of media (**a**), IL-3 (**c**) or TSLP (**e**), and the frequency of IL-4/eGFP⁺ NBNT cells was determined. **b, d, f**, The frequencies of IL-4/eGFP⁺, NBNT, Siglec-F[−] basophils and mast cells were determined. Insets of cytology of IL-4/eGFP⁺, CD49b⁺, FcεRI⁺ and c-Kit[−] IL-3-elicited (**d**) or TSLP-elicited (**f**) basophils are shown. Results are representative of at least three separate experiments. Bold numbers in basophil gates represent the mean fluorescence intensity (MFI) levels of CD49b staining. Scale bar, 10 μ m.

in the presence of IL-3 exhibited increased frequencies of IL-4/eGFP⁺ NBNT cells (17.6%) (Fig. 2c) and increased mast cell and basophil populations (Fig. 2d). In contrast, TSLP-stimulated bone marrow cultures yielded increased frequencies of IL-4/eGFP⁺ cells (7.13%) (Fig. 2e) and basophils but did not yield mast cell populations (Fig. 2f). Consistent with these data, bone marrow from wild-type mice cultured in the presence of IL-3 exhibited increased frequencies and total numbers of basophils and mast cells, whereas bone marrow cultured in the presence of TSLP alone exhibited increased frequencies and total numbers of basophils but not mast cells (Supplementary Fig. 3a–h). Collectively, these data illustrate that TSLP can elicit the selective population expansion of mature basophils from bone-marrow-resident cells.

Basophil populations develop from precursors (BaP) that are characterized as CD34⁺c-Kit[−]FcεRI⁺NBNT cells²³. BaPs isolated from bone marrow expressed both chains of the TSLPR complex (IL-7R α and TSLPR), indicating that they may be TSLP-responsive (Supplementary Fig. 4a). To test whether IL-3 or TSLP could induce basophil maturation, sorted bone-marrow-resident BaPs (Supplementary Fig. 4b) were cultured in the presence of media, IL-3 or TSLP and mature basophil populations were evaluated on day 5 after culture. Greater than 30% of BaPs cultured in the presence of media alone retained their progenitor-like phenotype as measured by expression of CD34 (Supplementary Fig. 4c). In contrast, IL-3-stimulated BaPs were predominantly CD34[−] and exhibited elevated CD49b expression, a phenotype consistent with mature basophils (Supplementary Fig. 4c, d). Critically, TSLP-stimulated BaPs were also predominantly CD34[−] and exhibited elevated levels of CD49b expression (Supplementary Fig. 4c, d). Consistent with whole bone marrow cultures (Fig. 2d, f), IL-3- or TSLP-treated cell cultures yielded more basophils than media alone controls, and IL-3-elicited basophils were larger in size than TSLP-elicited basophils (Supplementary Fig. 4e, f). To compare the ability of IL-3 or TSLP to enhance basophil survival, mature basophils were sort-purified from the blood and spleen of wild-type mice and cultured in the presence of media, IL-3 or TSLP for 24 h. Whereas most mature basophils died when cultured in media alone, 24.6% of basophils survived in the presence of IL-3 and 13.1% of the basophils survived in the presence of TSLP (Supplementary Fig. 5a). These data demonstrate that both IL-3 and TSLP can promote basophil maturation from bone-marrow-resident precursor cells and promote survival of mature basophils isolated from the periphery.

IL-3 is reported to be essential for optimal basophil activation, population expansion and survival²⁴. To test whether TSLP-elicited basophil responses were dependent on IL-3–IL-3R signalling, bone marrow cells from wild-type mice or mice deficient in both IL-3R β 1 and IL-3R β 2 (*Csf2rb2*^{−/−}*Csf2rb*^{−/−})²⁵ were cultured in the presence of media, IL-3 or TSLP. Addition of IL-3 to wild-type bone marrow cultures increased the frequency of basophils compared to media alone controls (Fig. 3a), whereas the addition of IL-3 to *Csf2rb2*^{−/−}*Csf2rb*^{−/−} bone marrow cultures had no effect on basophil populations (Fig. 3b). Similar to IL-3 stimulation, addition of TSLP to wild-type bone marrow cultures increased the frequency of basophils (Fig. 3a). Critically, addition of TSLP to *Csf2rb2*^{−/−}*Csf2rb*^{−/−} bone marrow cultures also increased the frequency of basophils (Fig. 3b), demonstrating that TSLP can promote the population expansion of basophils from bone marrow cells independently of IL-3–IL-3R signalling. However, basophils were readily identified in the spleen and bone marrow of *Csf2rb2*^{−/−}*Csf2rb*^{−/−} × *Tslpr*^{−/−} mice, or *Csf2rb2*^{−/−}*Csf2rb*^{−/−} mice treated with neutralizing anti-TSLP monoclonal antibody (Supplementary Fig. 5b, c), demonstrating that signalling via IL-3–IL-3R and TSLP–TSLPR is not essential for basophil development. To test whether TSLP could elicit mature basophil responses independently of IL-3–IL-3R signalling *in vivo*, wild-type or *Csf2rb2*^{−/−}*Csf2rb*^{−/−} mice were injected with PBS or rTSLP and peripheral basophil responses were examined. TSLP-treated wild-type mice exhibited increased frequencies and total numbers of basophils

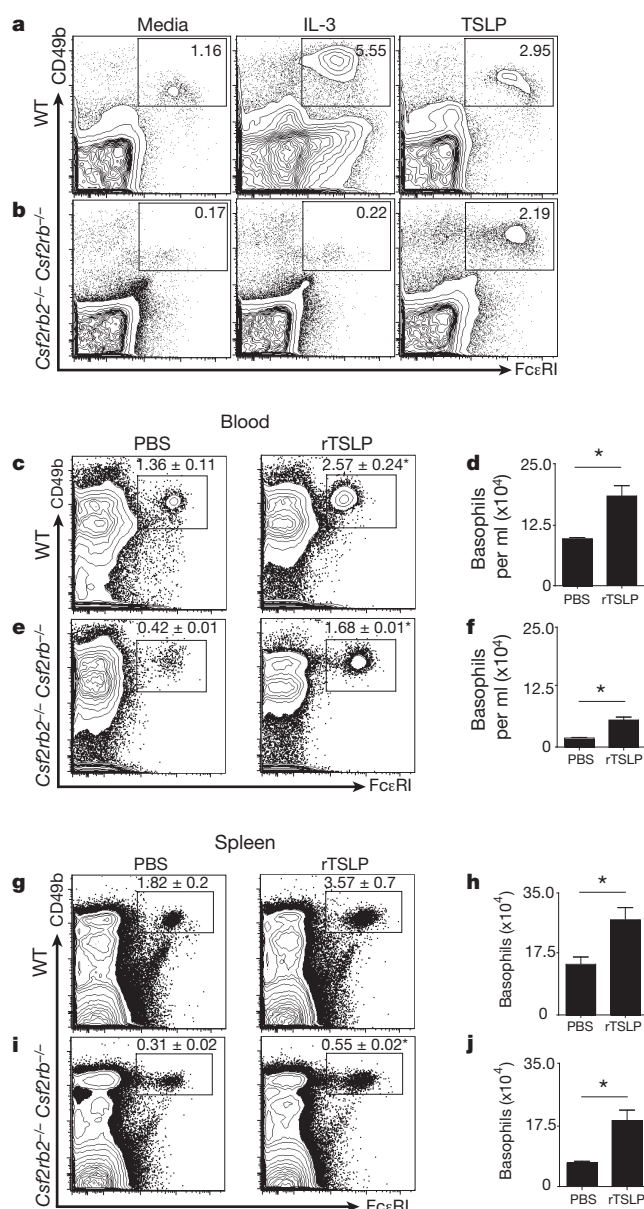


Figure 3 | TSLP-elicited basophilia is independent of IL-3-IL-3R signalling. **a, b**, Bone marrow cultures from wild-type (WT; **a**) or *Csf2rb2*^{-/-} *Csf2rb2*^{-/-} (**b**) mice. **c, e, g, i**, Wild-type or *Csf2rb2*^{-/-} *Csf2rb2*^{-/-} mice were treated with PBS or rTSLP and blood (**c, e**) and splenic basophils (**g, i**) were identified. **d, f, h, j**, Total numbers of basophils were quantified. Flow cytometry plots are gated on live NBNT cells. **a, b**, Results are representative of at least 3 separate experiments. **c–j**, Results are representative of 3 separate experiments (WT + PBS, *n* = 7; *Csf2rb2*^{-/-} *Csf2rb2*^{-/-} + PBS, *n* = 7; WT + TSLP, *n* = 7; *Csf2rb2*^{-/-} *Csf2rb2*^{-/-} + TSLP, *n* = 7). Results are shown as means ± s.e.m. Statistical analysis was performed using a two-tailed students *t*-test (**P* < 0.05).

in the blood (Fig. 3c, d) and spleen (Fig. 3g, h) compared to PBS treated controls. Critically, rTSLP treatment significantly increased both the frequency and total number of basophils in the blood (Fig. 3e, f) and spleen (Fig. 3i, j) of *Csf2rb2*^{-/-} *Csf2rb2*^{-/-} mice. Collectively, these data illustrate that TSLP promotes peripheral basophilia in both IL-3-IL-3R-sufficient and -deficient environments.

To test if IL-3-elicited versus TSLP-elicited basophil populations were phenotypically distinct, flow cytometric analysis of basophil-associated surface markers was performed. Whereas IL-3-elicited and TSLP-elicited basophils exhibited similar expression of CD200R and CD69, IL-3-elicited basophils exhibited elevated expression of CD11b and CD62L (Fig. 4a). In contrast, TSLP-elicited basophils

exhibited elevated expression of CD123, IL-33R (also called T1/ST2) and IL-18Rα (Fig. 4b). Collectively, these data demonstrate that IL-3- versus TSLP-elicited basophils exhibit distinct surface marker expression. Genome-wide transcriptional profiling of IL-3-elicited versus TSLP-elicited basophils also revealed remarkable differences in patterns of gene expression between the two basophil populations. Gene-set enrichment analysis (GSEA)²⁶ of complete transcriptional profiles revealed that IL-3-elicited basophils reflected gene expression associated with monocyte and dendritic cell maturation, matrix metalloproteinase production and tumour-necrosis factor-α (TNF-α) signalling (Fig. 4c and Supplementary Fig. 6). In contrast, TSLP-elicited basophils exhibited a gene expression profile enriched for linoleic acid metabolism, arachidonic acid metabolism, cell communication and the expression of cell adhesion molecules (Fig. 4c and Supplementary Fig. 6). Real-time PCR analysis also revealed selective differential expression of messenger RNA encoding basophil-associated proteases mast cell protease 2 (*Mcpt2*) and *Mcpt7* (also called *Tpsab1*) between the two populations (Supplementary Fig. 7a). Collectively, these results demonstrate phenotypic heterogeneity between IL-3-elicited versus TSLP-elicited basophils and indicate that either the two basophil populations represent distinct developmental stages of basophils or that they are functionally heterogeneous mature basophil populations.

To test whether phenotypic differences in the two basophil populations were associated with functional heterogeneity, a panel of basophil activation assays was used. IL-3-elicited basophils exhibited similar degranulation and β-hexosaminidase release²⁷ (a hallmark of basophil effector function²⁸) as mast cells in response to IgE-mediated FcεRI crosslinking (Supplementary Fig. 7b). Consistent with distinct effector functions, TSLP-elicited basophils exhibited minimal degranulation (Supplementary Fig. 7b). Surface marker expression on IL-3-elicited versus TSLP-elicited basophils indicated that these two populations may differ in their responsiveness to cytokines (Fig. 4b). To test this directly, IL-3- or TSLP-elicited basophils were sort-purified and stimulated with media alone, IL-3, IL-18 or IL-33, and production of cytokines and chemokines was assessed. Whereas the two basophil populations shared some functions including similar production of IL-1α and CCL11 (Supplementary Fig. 8a, b), TSLP-elicited basophils produced significantly more IL-4 and IL-6 (Supplementary Fig. 8a) and more CCL3, CCL4 and CCL12 (Supplementary Fig. 8b) in response to IL-3 stimulation compared to IL-3-elicited basophils. TSLP-elicited basophils also produced significantly more IL-4, IL-6, TNF-α (Supplementary Fig. 8a), CCL3, CCL4, CCL9, CCL12 (Supplementary Fig. 8b) and CXCL2 (Supplementary Fig. 8c) in response to IL-18 stimulation when compared to IL-3-elicited basophils. Finally, TSLP-elicited basophils produced more IL-4, IL-6 (Supplementary Fig. 8a), CCL3, CCL12 (Supplementary Fig. 8b) and CXCL2 (Supplementary Fig. 8c) in response to IL-33 stimulation than IL-3-elicited basophils. Collectively, these data indicate that IL-3-elicited and TSLP-elicited basophils exhibit distinct responsiveness and functional potential after stimulation with IL-3, IL-18 or IL-33.

To test whether IL-3-independent, TSLP-dependent basophil responses exist *in vivo* following exposure to an inflammatory stimulus, a TSLP-dependent murine model of atopic dermatitis²⁹ was used. Topical treatment with the vitamin D analogue MC903 resulted in increased levels of TSLP (Supplementary Fig. 9a). Furthermore, MC903 treatment resulted in the accumulation of basophils in the skin of wild-type mice (Supplementary Fig. 9b). MC903-induced basophil responses were TSLP-dependent, as treatment of wild-type mice with anti-TSLP diminished the accumulation of basophil populations (Supplementary Fig. 9b). MC903 treatment of *Csf2rb2*^{-/-} *Csf2rb2*^{-/-} mice also resulted in a robust accumulation of basophils in the skin (Supplementary Fig. 9c), and MC903-induced, IL-3-independent basophil responses were significantly reduced after anti-TSLP treatment (Supplementary Fig. 9c). Collectively, these data demonstrate IL-3-independent, TSLP-dependent basophil responses *in vivo*. To test whether TSLP-dependent basophils contribute to the induction of TH2

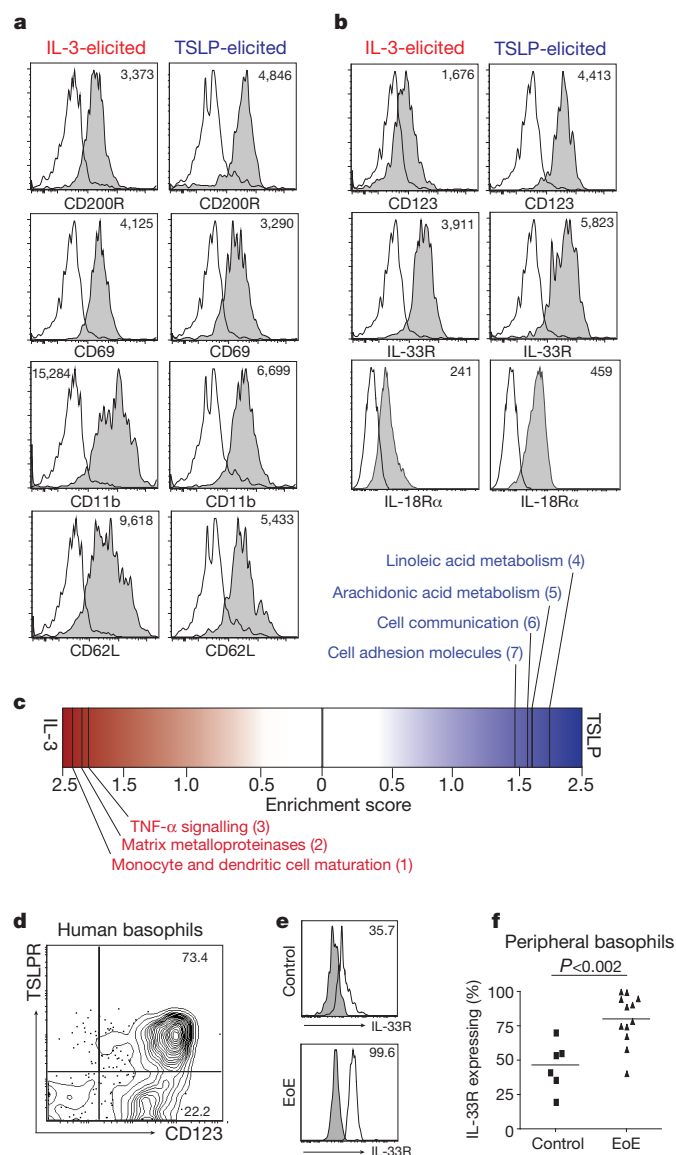


Figure 4 | Murine and human basophil populations exhibit heterogeneity. **a**, IL-3-elicited or TSLP-elicited murine basophils were stained (shaded) for CD200R, CD69, CD11b and CD62L (**a**), and CD123, IL-33R (T1/ST2) and IL-18Rα (**b**) expression and compared to fluorescence minus one controls. Numbers represent MFI levels. Results are representative of at least 3 separate experiments. **c**, GSEA of microarray data comparing IL-3-elicited and TSLP-elicited basophils. **d**, Activated human basophils stained for TSLPR. **e**, Representative histograms demonstrating IL-33R (ST2) expression (open) compared to isotype controls. **f**, Percentage of basophils from control or eosinophilic oesophagitis (EoE) patients expressing IL-33R compared to isotype controls. Statistical analysis was performed using a two-tailed Student's *t*-test.

cell responses, MC903 treatment of wild-type mice was extended to 7 days. MC903 treatment resulted in the robust accumulation of basophils in the skin (Supplementary Fig. 9d) and a marked increase in IL-4 and IL-5 production in the draining lymph nodes (Supplementary Fig. 9f). Critically, diphtheria-toxin-mediated depletion of basophils³⁰ reduced the accumulation of basophils in the skin (Supplementary Fig. 9e) and decreased IL-4 and IL-5 production (Supplementary Fig. 9f), demonstrating that TSLP-dependent basophils contribute to T_H2 cytokine responses *in vivo*.

To test whether human basophils can respond to TSLP, peripheral blood from healthy human donors was taken and TSLPR expression on basophils was evaluated. Greater than 70% of activated peripheral human basophils expressed TSLPR (Fig. 4d), indicating that human basophils can be TSLP-responsive. The food-allergy-associated disease

eosinophilic oesophagitis is associated with gain-of-function polymorphisms in the gene encoding TSLP and elevated expression of TSLP^{3–6,13}. To examine whether basophil heterogeneity exists when human basophils develop in a TSLP-rich environment associated with food allergy, basophil responses were examined in healthy control or eosinophilic oesophagitis patients. No differences in expression of HLA-DR, CD28, CD40, CD86, CD69 or CD203c were observed between control and eosinophilic oesophagitis patients (data not shown). However, consistent with TSLP-induced basophils in mice, basophils from eosinophilic oesophagitis patients expressed significantly higher levels of IL-33R compared to basophils from healthy controls (Fig. 4e, f). These data indicate that heterogeneity in basophil populations may exist in humans and correlates with susceptibility to allergic inflammation.

Collectively, these data identify that TSLP can selectively promote basophil haematopoiesis from bone-marrow-resident precursors and elicit mature basophil responses in the periphery in an IL-3–IL-33R-sufficient or -deficient environment. The demonstration that TSLP-elicited basophils exhibit divergent transcriptional and functional profiles from IL-3-elicited basophils indicates that similar to other immune cell lineages, basophils are a heterogeneous cell population that exhibit distinct phenotypic and functional characteristics depending on the cytokine environment in which they develop or are activated. The identification of a role for TSLP in promoting basophil haematopoiesis, peripheral basophilia and altering the functional capacity of basophils (Supplementary Fig. 10) may provide a biological mechanism through which local production of TSLP at one barrier surface can confer susceptibility to pan-allergic diseases at multiple mucosal sites.

METHODS SUMMARY

C57BL/6 or BALB/c wild-type, IL-4/eGFP reporter or *Csf2rb2*^{−/−} *Csf2rb*^{−/−} mice were treated by intraperitoneal (i.p.) injection with PBS or 10 μg of rTSLP daily for 4–7 days and basophil populations were evaluated. Mice were injected intravenously (i.v.) with 10 μg of control or TSLP encoding cDNA plasmid and basophils (day 21) and small intestine pathology (day 28) were evaluated after injection. Wild-type and *Tslpr*^{−/−} mice were infected with *T. muris* and on day 10 after infection, one group of *Tslpr*^{−/−} mice received 100 × 10³ TSLPR-sufficient basophils elicited from TSLP-cDNA-injected H2K-Bcl2-transgenic mice. All groups received 10 μg injections of rTSLP every other day starting at day 11 after infection. On day 21 after infection, T_H2 cytokine responses, serum IgE, pathology, RELM-β and worm burdens were evaluated. Bone marrow from wild-type, IL-4/eGFP reporter or *Csf2rb2*^{−/−} *Csf2rb*^{−/−} mice was cultured in the presence of 10 ng ml^{−1} of IL-3 or 1 μg ml^{−1} of TSLP for 5 days. Bone-marrow-derived basophils were sorted on day 5 after culture, RNA was isolated and gene expression profiles were determined using an Affymetrix HT Mouse 430 PM platform, and analysis was performed using GSEA software through <http://www.broadinstitute.org/gsea/index.jsp>. Bone-marrow-resident BaPs were sorted from wild-type whole bone marrow and cultured in the presence of 10 ng ml^{−1} of IL-3 or 1 μg ml^{−1} of TSLP for 5 days and basophils were evaluated by flow cytometry and cytology. Wild-type, *Csf2rb2*^{−/−} *Csf2rb*^{−/−}, or BaS-TRECK mice were treated with 50 μl of 100% ethanol or 50 μl of 2 nm MC903 dissolved in 100% ethanol topically for 3–7 days. Groups were treated (i.p.) with 1 mg of rat IgG isotype control or anti-TSLP antibody on day 0 of ethanol or anti-MC903 treatment. Skin-draining lymph node cells were isolated from ethanol-treated or MC903-treated mice on day 7 and stimulated with anti-CD3 and anti-CD28 for 48 h.

Full Methods and any associated references are available in the online version of the paper at www.nature.com/nature.

Received 24 May; accepted 27 June 2011.

Published online 14 August 2011.

1. Anthony, R. M., Rutitzky, L. I., Urban, J. F., Jr, Staderker, M. J. & Gause, W. C. Protective immune mechanisms in helminth infection. *Nature Rev. Immunol.* **7**, 975–987 (2007).
2. Umetsu, D. T., McIntire, J. J., Akbari, O., Macaubas, C. & DeKruyff, R. H. Asthma: an epidemic of dysregulated immunity. *Nature Immunol.* **3**, 715–720 (2002).
3. Harada, M. et al. TSLP promoter polymorphisms are associated with susceptibility to bronchial asthma. *Am. J. Respir. Cell Mol. Biol.* **44**, 787–793 (2011).

4. Sherrill, J. D. *et al.* Variants of thymic stromal lymphopoietin and its receptor associate with eosinophilic esophagitis. *J. Allergy Clin. Immunol.* **126**, 160–168 (2010).
5. Rothenberg, M. E. *et al.* Common variants at 5q22 associate with pediatric eosinophilic esophagitis. *Nature Genet.* **42**, 289–291 (2010).
6. Hunninghake, G. M. *et al.* TSLP polymorphisms are associated with asthma in a sex-specific fashion. *Allergy* **65**, 1566–1575 (2010).
7. Ying, S. *et al.* Thymic stromal lymphopoietin expression is increased in asthmatic airways and correlates with expression of Th2-attracting chemokines and disease severity. *J. Immunol.* **174**, 8183–8190 (2005).
8. Al-Shami, A. *et al.* A role for thymic stromal lymphopoietin in CD4⁺ T cell development. *J. Exp. Med.* **200**, 159–168 (2004).
9. Ito, T. *et al.* TSLP-activated dendritic cells induce an inflammatory T helper type 2 cell response through OX40 ligand. *J. Exp. Med.* **202**, 1213–1223 (2005).
10. Taylor, B. C. *et al.* TSLP regulates intestinal immunity and inflammation in mouse models of helminth infection and colitis. *J. Exp. Med.* **206**, 655–667 (2009).
11. Mou, Z. *et al.* Overexpression of thymic stromal lymphopoietin in allergic rhinitis. *Acta Otolaryngol. (Stockh.)* **129**, 297–301 (2009).
12. Soumelis, V. *et al.* Human epithelial cells trigger dendritic cell mediated allergic inflammation by producing TSLP. *Nature Immunol.* **3**, 673–680 (2002).
13. Ziegler, S. F. & Artis, D. Sensing the outside world: TSLP regulates barrier immunity. *Nature Immunol.* **11**, 289–293 (2010).
14. Sebestyén, M. G. *et al.* Mechanism of plasmid delivery by hydrodynamic tail vein injection. I. Hepatocyte uptake of various molecules. *J. Gene Med.* **8**, 852–873 (2006).
15. Perrigoue, J. G. *et al.* MHC class II-dependent basophil-CD4⁺ T cell interactions promote T_H2 cytokine-dependent immunity. *Nature Immunol.* **10**, 697–705 (2009).
16. Sokol, C. L. *et al.* Basophils function as antigen-presenting cells for an allergen-induced T helper type 2 response. *Nature Immunol.* **10**, 713–720 (2009).
17. Yoshimoto, T. *et al.* Basophils contribute to T_H2-IgE responses *in vivo* via IL-4 production and presentation of peptide-MHC class II complexes to CD4⁺ T cells. *Nature Immunol.* **10**, 706–712 (2009).
18. Hammad, H. *et al.* Inflammatory dendritic cells—not basophils—are necessary and sufficient for induction of Th2 immunity to inhaled house dust mite allergen. *J. Exp. Med.* **207**, 2097–2111 (2010).
19. Ohnmacht, C. *et al.* Basophils orchestrate chronic allergic dermatitis and protective immunity against helminths. *Immunity* **33**, 364–374 (2010).
20. Tang, H. *et al.* The T helper type 2 response to cysteine proteases requires dendritic cell-basophil cooperation via ROS-mediated signaling. *Nature Immunol.* **11**, 608–617 (2010).
21. Zhou, B. *et al.* Thymic stromal lymphopoietin as a key initiator of allergic airway inflammation in mice. *Nature Immunol.* **6**, 1047–1053 (2005).
22. Gessner, A., Mohrs, K. & Mohrs, M. Mast cells, basophils, and eosinophils acquire constitutive IL-4 and IL-13 transcripts during lineage differentiation that are sufficient for rapid cytokine production. *J. Immunol.* **174**, 1063–1072 (2005).
23. Iwasaki, H. & Akashi, K. Myeloid lineage commitment from the hematopoietic stem cell. *Immunity* **26**, 726–740 (2007).
24. Lantz, C. S. *et al.* Role for interleukin-3 in mast-cell and basophil development and in immunity to parasites. *Nature* **392**, 90–93 (1998).
25. Scott, C. L. *et al.* Reassessment of interactions between hematopoietic receptors using common β -chain and interleukin-3-specific receptor β -chain-null cells: no evidence of functional interactions with receptors for erythropoietin, granulocyte colony-stimulating factor, or stem cell factor. *Blood* **96**, 1588–1590 (2000).
26. Haining, W. N. & Wherry, E. J. Integrating genomic signatures for immunologic discovery. *Immunity* **32**, 152–161 (2010).
27. Lenox, L. E. *et al.* Mutation of tyrosine 145 of lymphocyte cytosolic protein 2 protects mice from anaphylaxis and arthritis. *J. Allergy Clin. Immunol.* **124**, 1088–1098 (2009).
28. Siracusa, M. C., Perrigoue, J. G., Comeau, M. R. & Artis, D. New paradigms in basophil development, regulation and function. *Immunol. Cell Biol.* **88**, 275–284 (2010).
29. Li, M. *et al.* Induction of thymic stromal lymphopoietin expression in keratinocytes is necessary for generating an atopic dermatitis upon application of the active vitamin D3 analogue MC903 on mouse skin. *J. Invest. Dermatol.* **129**, 498–502 (2009).
30. Sawaguchi, M. *et al.* Basophils and mast cells differently regulate allergic response; *in vivo* demonstration by diphtheria toxin based deletion system. *Int. Congress Immunol.* WS/PP-043–04 (2011).

Supplementary Information is linked to the online version of the paper at www.nature.com/nature.

Acknowledgements We thank members of the Artis laboratory for critical reading of the manuscript, A. Budelsky, T. Martin, B.-R. Park Yoon, J. Bigler and M. Timour (Amgen) for assistance with experiments and microarrays and the University of Pennsylvania flow cytometry core for assistance with sorting. Work in the Artis laboratory is supported by the National Institutes of Health (AI61570, AI74878, AI87990 and AI083480 (to D.A.), F32 fellowship AI085828 (to M.C.S.), F31 training grant GM082187 (to S.A.S.), T32 training grant AI060516 (to D.A.H.)) and the Burroughs Wellcome Fund (to D.A.).

Author Contributions M.C.S., S.A.S., D.A.H., B.S.K., M.B.H., H.K.J., L.A.S., M.R.C. and D.A. designed and performed the research. S.F.Z., T.K. and M.K. provided reagents. E.C.D., A.C. and J.M.S. collected and provided human samples. M.C.S., S.A.S., D.A.H., B.S.K., T.A.D., E.J.W. and D.A. analysed the data. M.C.S. and D.A. wrote the paper.

Author Information Reprints and permissions information is available at www.nature.com/reprints. The authors declare no competing financial interests. Readers are welcome to comment on the online version of this article at www.nature.com/nature. Correspondence and requests for materials should be addressed to D.A. (dartis@mail.med.upenn.edu).

METHODS

Mice. BALB/c, C57BL/6 and *Tslpr*^{-/-} mice were obtained from Charles River Laboratories. IL4/eGFP reporter mice, *Csf2rb2*^{-/-}*Csf2rb*^{-/-} mice, *Tslpr*^{-/-} × *Csf2rb2*^{-/-}*Csf2rb*^{-/-} and H2K-Bcl2-transgenic mice and BaS-TRECK mice were bred at the University of Pennsylvania. The above strains were housed in specific pathogen-free conditions at the University of Pennsylvania. Control and SPC-TSLP mice were maintained at Benaroya Research Institute. All experiments were performed under Institutional Animal Care and Use Committee (IACUC) approved protocols and in accordance with the guidelines of the IACUC of the University of Pennsylvania. All mice used were 4–12 weeks of age. Wild-type, IL-4/eGFP reporter mice or *Csf2rb2*^{-/-}*Csf2rb*^{-/-} mice were treated by intraperitoneal injection with PBS or 10 µg of rTSLP daily for 4–7 days, and basophil populations were evaluated. Mice were injected (i.v.) with 10 µg of control or TSLP encoding cDNA plasmids (provided by M. Comeau), and basophil populations and small intestine pathology were evaluated on days 21 and 28 after injection. *Csf2rb2*^{-/-}*Csf2rb*^{-/-} mice were given intraperitoneal injections of anti-TSLP (1 mg) on day 0 and 4 and basophil populations were evaluated on day 7 as previously described^{10,15,31,32}.

Recombinant cytokines. rmTSLP (R&D Systems, M. Comeau, Amgen), rmIL-3 (R&D Systems, M. Comeau, Amgen), rmSCF (R&D Systems), rmIL-18 (R&D Systems), rhIL-3 (M. Comeau, Amgen).

Flow cytometry. Murine spleens were homogenized by passing through a 70-µm nylon mesh filter, and stained with anti-mouse fluorochrome-conjugated monoclonal antibodies against CD3e, CD4, CD8, B220, CD19, CD11b, CD49b, FcεRIα, c-Kit, CD123, CD69, CD11b, IL-18Rα and CD62L (eBioscience or BD Bioscience). Fluorochrome-conjugated monoclonal antibodies against CD200R and IL-33R were obtained from AbD serotec and mdbioproducts. Bone-marrow-resident cells were collected by removing and sterilizing femurs in 70% ethanol, removing the ends of the femurs and flushing cells out with 10 ml of complete media. Human peripheral blood cells were stained with anti-human fluorochrome-conjugated monoclonal antibodies against CD203c, HLA-DR, CD28, CD40, CD86, CD69, TSLPR, IgE, FcεRI, CD19 and TCRα/β (eBioscience, Miltenyi Biotec and mdbioproducts). Cells were run on a BD LSR II flow using DiVa software (BD Bioscience) and analysed with FlowJo software (version 8.7.1; Tree Star).

T. muris infection and TSLPR-sufficient basophil transfer. Wild-type and *Tslpr*^{-/-} mice were infected with 200 *Trichuris muris* eggs via oral gavage as previously described^{10,15,31,32}, and on day 21 after infection basophil populations were quantified. Wild-type and *Tslpr*^{-/-} mice were infected with 200 *T. muris* eggs via oral gavage and on day 10 after infection one group of *Tslpr*^{-/-} mice received 100 × 10³ TSLPR-sufficient TSLP-cDNA-elicited basophils from H2K-Bcl2-transgenic mice. H2K-Bcl2-transgenic basophils were used to assure cell survival after adoptive transfer. All groups received 10 µg injections of rTSLP every other day starting at day 11 after infection. On day 21 after infection, *T. muris* antigen-specific T_H2 cytokine responses, serum IgE, pathology and worm burdens were evaluated as previously described^{10,15,31,32}.

Bone-marrow-derived basophils. Bone-marrow-resident cells from wild-type, IL-4/eGFP reporter mice or *Csf2rb2*^{-/-}*Csf2rb*^{-/-} mice were cultured in the presence of 10 ng ml⁻¹ of IL-3 or 1 µg ml⁻¹ of TSLP for 5 days, and basophil populations were evaluated by flow cytometry using a BD LSR II flow cytometer or sort-purified using a BD FACS Aria II flow cytometer. RNA from sort-purified bone-marrow-derived basophils was isolated, cDNA was made and gene expression profiles were determined by real time PCR (Qiagen, SYBR Green) or genome-wide transcriptional profiling using an Affymetrix HT Mouse 430 PM platform. Microarray analysis was performed using GSEA software (<http://www.broadinstitute.org/gsea/index.jsp>).

Bone-marrow-derived basophil stimulation assays. Bone-marrow-derived sort-purified basophils were stimulated with media, 10 ng ml⁻¹ of IL-3, 20 ng ml⁻¹ of IL-18 or 10 ng ml⁻¹ of IL-33, and cell-free supernatants were analysed using a

multi-analyte panel (Rodent v2.0) (<http://www.rulesbasedmedicine.com/>). Bone-marrow-derived basophils were grown in 10 ng ml⁻¹ of IL-3 or 1 µg ml⁻¹ of TSLP for 5 days and sort-purified. Bone-marrow-derived mast cells were grown in IL-3 (10 ng ml⁻¹) and SCF (12.5 ng ml⁻¹) for 8 weeks. IL-3-elicited basophils and mast cells were allowed to rest overnight in media containing 10 ng ml⁻¹ of IL-4 and 10 ng ml⁻¹ of IL-3. TSLP-elicited basophils were rested in media containing 10 ng ml⁻¹ of IL-4 and 1 µg ml⁻¹ of TSLP. Cells were incubated with 1 µg ml⁻¹ anti-dinitrophenol IgE for 1 h at 37 °C, washed, and stimulated with 100 ng ml⁻¹ dinitrophenol-conjugated human serum albumin (HSA-DNP; Sigma) for 1 h. Supernatants were tested for β-hexosaminidase activity by incubating with 1 mM *p*-nitrophenyl-*N*-acetyl-β-D-glucosamide. Absorbance was read at 405 nm. Serial dilutions of a known quantity of lysed bone-marrow-derived mast cells were used as a standard reference.

Basophil survival assays. Basophils were sort-purified from the blood and spleens of wild-type mice and cultured in the presence 10 ng ml⁻¹ of IL-3 or 1 µg ml⁻¹ of TSLP for 24 h, and cell viability was determined by 7-AAD (BD Bioscience) exclusion.

Basophil progenitor cultures. Basophil progenitor cells (identified as NBNT, CD34⁺, FcεRI⁺, c-Kit⁺) were sort-purified from whole bone marrow isolated from wild-type mice and cultured in the presence of 10 ng ml⁻¹ of IL-3 or 1 µg ml⁻¹ of TSLP for 5 days, and basophil populations were evaluated by flow cytometry and cytology.

MC903-induced atopic dermatitis. Wild-type or *Csf2rb2*^{-/-}*Csf2rb*^{-/-} mice were treated with 50 µl of 100% ethanol or 50 µl of 2 nM MC903 dissolved in 100% ethanol topically for 3–7 days. Groups were treated (i.p.) with 1 mg of rat IgG isotype control or anti-TSLP neutralizing antibody on day 0. BaS-TRECK mice were treated for 7 days with MC903 and given intraperitoneal injections of diphtheria toxin (750 ng) on day 0 and day 4 after treatment. Skin was mechanically disrupted, single-cell suspensions were prepared and basophil populations were evaluated by flow cytometry. Ears were separated into two halves and floated dermis side down in complete media for 24 h to determine local production of TSLP, and serum was collected to determine systemic TSLP levels by ELISA (eBioscience). Skin-draining lymph node cells were isolated from ethanol-treated or MC903-treated mice on day 7 and stimulated with anti-CD3 and anti-CD28 for 48 h, and IL-4 and IL-5 production was determined by ELISA (eBioscience).

Human patients and sample preparation. All subjects were studied under IRB approval from The Children's Hospital of Philadelphia. All subjects signed an informed consent. EoE was defined by the current consensus guidelines of having greater than 15 eosinophils per high powered field (HPF) at ×400 light microscopy isolated to the oesophagus after other diagnoses were excluded and after being at least 8 weeks on optimal dose of proton pump inhibitors. Human blood was collected from healthy donors and peripheral blood cells were isolated using a Ficoll gradient. Basophils were isolated using a MACS basophil isolation kit II according to the manufacturer's protocol (Miltenyi Biotec, 130-092-662). Basophils were cultured overnight in 50 ng ml⁻¹ of IL-3 and stained for TSLPR. Human blood was collected from healthy paediatric donors and paediatric donors diagnosed with eosinophilic oesophagitis. Peripheral blood cells were isolated by Ficoll gradient, and surface marker expression was determined by flow cytometry.

Statistics. Results are shown as means ± s.e.m. for individual animals. Statistical significance was determined by Student's *t*-test. Results were considered significant at *P* < 0.05.

31. Zaph, C. *et al.* Epithelial-cell-intrinsic IKK-β expression regulates intestinal immune homeostasis. *Nature* **446**, 552–556 (2007).
32. Nair, M. G. *et al.* Goblet cell-derived resistin-like molecule β augments CD4⁺ T cell production of IFN-γ and infection-induced intestinal inflammation. *J. Immunol.* **181**, 4709–4715 (2008).

N₂O binding at a [4Cu:2S] copper–sulphur cluster in nitrous oxide reductase

Anja Pomowski¹, Walter G. Zumft², Peter M. H. Kroneck³ & Oliver Einsle^{1,4}

Nitrous oxide (N₂O) is generated by natural and anthropogenic processes and has a critical role in environmental chemistry. It has an ozone-depleting potential similar to that of hydrochlorofluorocarbons as well as a global warming potential exceeding that of CO₂ 300-fold^{1,2}. In bacterial denitrification, N₂O is reduced to N₂ by the copper-dependent nitrous oxide reductase (N₂OR)³. This enzyme carries the mixed-valent Cu_A centre and the unique, tetranuclear Cu_Z site. Previous structural data were obtained with enzyme isolated in the presence of air that is catalytically inactive without prior reduction. Its Cu_Z site was described as a [4Cu:S] centre, and the substrate-binding mode and reduction mechanism remained elusive. Here we report the structure of purple N₂OR from *Pseudomonas stutzeri*, handled under the exclusion of dioxygen, and locate the substrate in N₂O-pressurized crystals. The active Cu_Z cluster contains two sulphur atoms, yielding a [4Cu:2S] stoichiometry; and N₂O bound side-on at Cu_Z, in close proximity to Cu_A. With the substrate located between the two clusters, electrons are transferred directly from Cu_A to N₂O, which is activated by side-on binding in a specific binding pocket on the face of the [4Cu:2S] centre. These results reconcile a multitude of available biochemical data on N₂OR that could not be explained by earlier structures, and outline a mechanistic pathway in which both metal centres and the intervening protein act in concert to achieve catalysis. This structure represents the first direct observation, to our knowledge, of N₂O bound to its reductase, and sheds light on the functionality of metalloenzymes that activate inert small-molecule substrates. The principle of using distinct clusters for substrate activation and for reduction may be relevant for similar systems, in particular nitrogen-fixing nitrogenase⁴.

N₂O is a kinetically inert, colourless gas that is being scrutinized for its deleterious effects on global climate and, in this context, was named the most critical anthropogenic substance emitted in the twenty-first century¹. Although the net amount of atmospheric CO₂ is significantly higher, its anthropogenic emissions have been put under regulation and control, whereas N₂O concentrations are on a steady rise^{1,5}. N₂O is generated by abiotic processes, for instance in hypersaline ponds in the Antarctic⁶ that are subject to major fluctuations with an impact on global climate⁷. It also occurs as a significant by-product of the bacterial respiratory pathways of nitrification and denitrification that are strongly enhanced by fertilization in modern agriculture^{8,9}, leading to an overall imbalance in the global nitrogen cycle⁵. Although the reduction of N₂O to dinitrogen—N₂—is strongly exergonic (N₂O + 2 H⁺ + 2 e⁻ → N₂ + H₂O; ΔG^{0'} = -339.5 kJ mol⁻¹), electronic delocalization stabilizes the molecule and leads to an activation energy barrier of 250 kJ mol⁻¹ (ref. 10). Its reduction by bacteria is catalysed by N₂OR (ref. 3), a copper-dependent enzyme that forms tightly linked head-to-tail homodimers of 130 kDa (Fig. 1). N₂OR contains two multi-copper centres, Cu_A and Cu_Z, with distinct spectroscopic properties. Cu_A is a mixed-valent [Cu_{A1}^{+1.5}:Cu_{A2}^{+1.5}] S = 1/2 centre that is also found in some haem-copper oxidases¹¹ and was engineered into the type I Cu site of azurin¹². It was suggested to transfer

one electron from an external donor such as cytochrome *c*-552 to the active site at Cu_Z¹³. The three-dimensional structure of N₂OR from *Marinobacter hydrocarbonoclasticus* (formerly *Pseudomonas nautica*)¹⁴ revealed Cu_Z to be tetranuclear, and it was subsequently recognized to be a μ₄-sulphido-bridged [4Cu:S] centre¹⁵. This was confirmed by structures of N₂OR from *Paracoccus denitrificans*¹⁶ and '*Achromobacter cycloclastes*'¹⁷, but no direct evidence was obtained concerning the mode of substrate binding or the mechanism of its conversion. One¹⁶ or two¹⁷ water ligands were observed bound to a face of the Cu_Z cluster between atoms Cu_{Z1} and Cu_{Z4} and theoretical considerations have suggested the binding of the substrate N₂O in a bridging manner in this position^{18,19}.

N₂OR was identified in 1982²⁰, and a wealth of biochemical data has been accumulated since. However, seeming inconsistencies arose

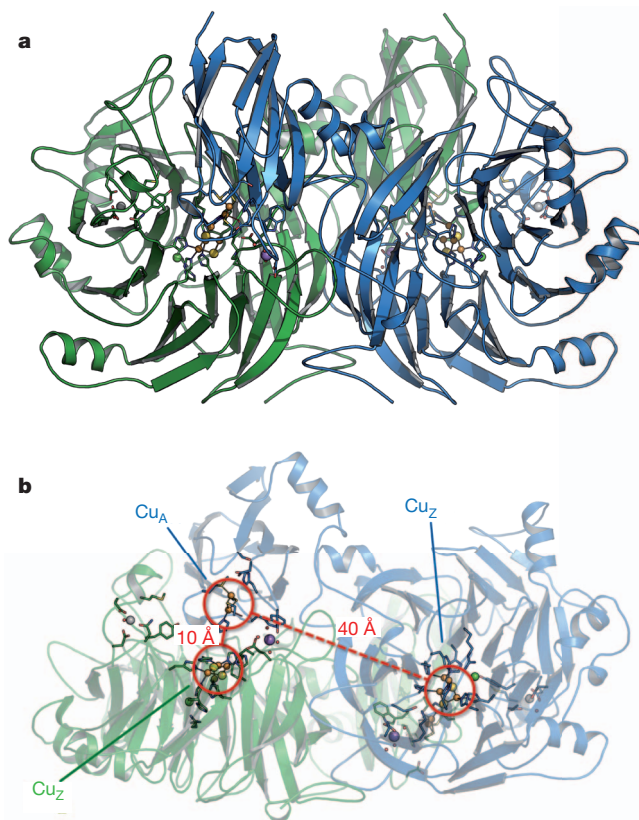


Figure 1 | N₂OR from *Pseudomonas stutzeri*. **a**, The enzyme is a homodimer in head-to-tail orientation with the tetranuclear Cu_Z active site located in the N-terminal, seven-bladed β-propeller domain and the binuclear Cu_A site in the C-terminal cupredoxin domain. **b**, The Cu_A–Cu_Z distance within one monomer is around 40 Å and thus too large for efficient electron transfer. Instead, the Cu_A site of one monomer is at a distance of only 10 Å from Cu_Z in the other monomer.

¹Lehrstuhl für Biochemie, Institut für organische Chemie und Biochemie, Albert-Ludwigs-Universität Freiburg, Albertstr. 21, 79104 Freiburg, Germany. ²Institut für Angewandte Biowissenschaften, Abteilung Molekulare Mikrobiologie, Karlsruher Institut für Technologie, Hertzstr. 16, 76187 Karlsruhe, Germany. ³Fachbereich Biologie, Universität Konstanz, Universitätsstr. 10, 78457 Konstanz, Germany. ⁴Centre for Biological Signalling Studies (bloss), Albert-Ludwigs-Universität Freiburg, Hebelstr. 25, 79104 Freiburg, Germany.

from the fact that studies were carried out on two different forms of the enzyme^{3,21,22}. N₂OR prepared under anoxic conditions differs from enzyme isolated in the presence of dioxygen, in particular with respect to the Cu_Z site. An active, purple form of the enzyme (form I) was obtained in anoxic preparations from *P. stutzeri*^{21,22} and from *A. cycloclastes*²³. Oxidic preparations produce a pink enzyme (form II) with only 20–40% of the specific activity of form I (ref. 3). However, when fully reduced to the all-Cu(I) state¹⁹, form II N₂OR shows a specific activity for N₂O reduction of 4.5 $\mu\text{kat mg}^{-1}$ that is fourfold higher than the one of *P. stutzeri* N₂OR form I (1.1 $\mu\text{kat mg}^{-1}$)²¹. Reductive activation of N₂OR II requires methyl viologen, at a redox potential that is not achieved in the bacterial periplasm, while the all-Cu(I) state of *P. stutzeri* N₂OR I was not obtained even after 65 h of dithionite incubation²². We therefore argue that the modes of substrate activation and electron transfer of N₂OR I are distinct from what was suggested for all-Cu(I) N₂OR II^{17,19,24}.

Although overall the structure of anoxically isolated *P. stutzeri* N₂OR I is very similar to the structures reported thus far, both metal centres show marked differences. Cu_A is of a characteristic, pink colour in the mixed-valent [Cu_{A1}^{+1.5}:Cu_{A2}^{+1.5}] S = 1/2 state and its conformation was virtually identical in its oxidized form in *A. cycloclastes* N₂OR¹⁷ and in the reduced form in *M. hydrocarbonoclasticus*¹⁴ and *P. denitrificans*¹⁶ N₂OR. The spectroscopic hallmark of Cu_A is the narrow 7-line hyperfine splitting in the g_{\parallel} region of the electron paramagnetic resonance (EPR) spectrum (Supplementary Fig. 6) that originates from an unpaired electron fully delocalized over two copper nuclei with a nuclear spin $I_{\text{Cu}} = 3/2$ (refs 11, 25). Each copper has a single histidine ligand, His 583 for Cu_{A1} and His 626 for Cu_{A2} in *P. stutzeri* (Fig. 2b). In previous descriptions of the centre, the histidine ligand to Cu_{A1} coordinated the metal through its N δ_1 atom at a canonical Cu–N_{His} distance of approximately 2.1 Å. However, in purple N₂OR

from *P. stutzeri*, H583 was not a ligand to Cu_{A1}. Instead, the imidazole ring of H583 was rotated by approximately 130° to form a short (2.6 Å) hydrogen bond between the N δ_1 atom of H583 and the O γ atom of S550 and a second one at 2.8 Å from the N ϵ_2 atom of the same histidine to the β -carboxy group of D576 (Fig. 2b and Supplementary Fig. 1a). As a consequence, the now three-coordinate Cu_{A1} atom was retracted into the plane formed by the sulphur atoms of C618, C622 and M629. The Cu_{A1}–Cu_{A2} distance was 2.5 Å, and this protein still showed the characteristic, 7-line EPR signal (Supplementary Fig. 6). Both S550 and D576 are conserved residues among N₂O reductases with D576 forming a putative entry point for electrons. This arrangement suggests a mechanistic relevance, in that reduction of Cu_A from an external electron donor is only made possible after H583 flips back to ligate Cu_{A1}, and this rearrangement occurred only after exposure to N₂O (see later).

The second cluster—Cu_Z—is coordinated by seven histidine residues originating from six of the seven blades of a β -propeller domain (Fig. 1). In *P. stutzeri* N₂OR I the ligands to Cu_Z are H129, H130, H178, H326, H382, H433 and H494. The occurrence of positive- or negative-difference electron density was used in modelling, and with slightly reduced occupancies (see Supplementary Discussion) the model of the previously observed μ_4 -[4Cu:S] cluster was well accommodated. However, the maps revealed electron density for an additional ligand bridging Cu_{Z1} and Cu_{Z4}. Although in earlier crystallographic studies similar species were modelled as water^{16,17,26}, a water molecule at this position in *P. stutzeri* N₂OR resulted in a positive-difference electron density peak (Supplementary Fig. 7a). The atom refined to low *B* factors, indicating that a more electron-rich species was required. A second sulphur atom—S_{Z2}—optimally explained the observed electron density (Supplementary Fig. 3c). We thus propose a composition of [4Cu:2S] for the Cu_Z cluster in N₂OR I (Fig. 2a and Supplementary Fig. 1b). This interpretation is supported by several experimental

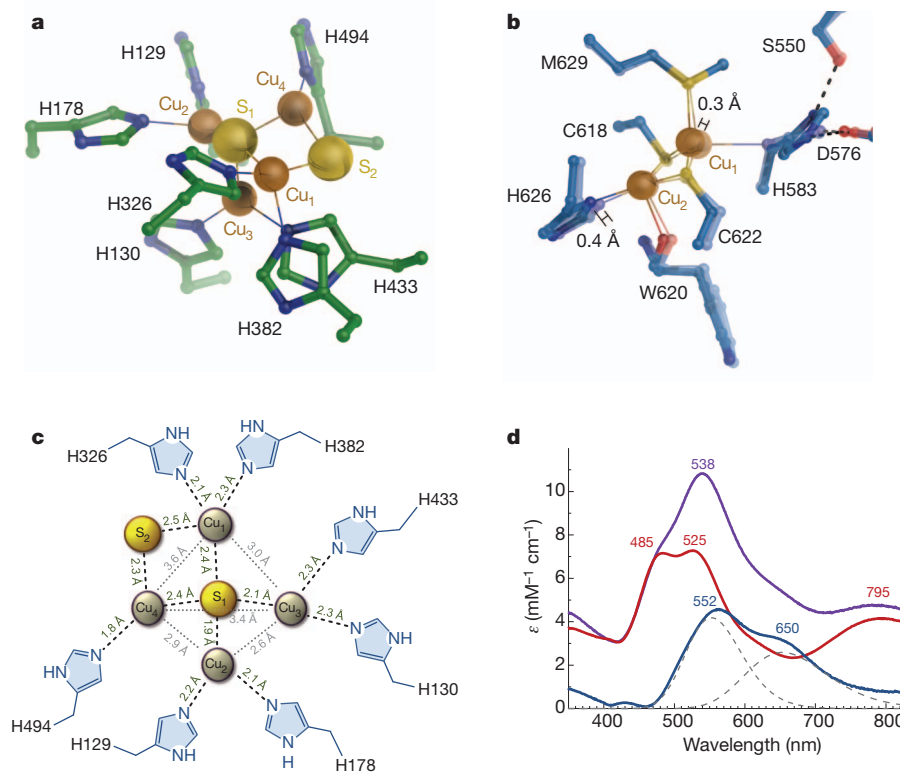


Figure 2 | The copper sites of purple *P. stutzeri* N₂OR. **a**, The Cu_Z site containing two sulphur atoms (S_{Z1} and S_{Z2}). **b**, The Cu_A site, overlaying the state with His 583 ligating Cu_{A1} (transparent) and the as isolated form (opaque), where the histidine is not a ligand to the metal. **c**, Bond distances in and around the Cu_Z site. **d**, Ultraviolet/visible light spectrum of *P. stutzeri*

N₂OR (purple). The spectrum can be deconvoluted into the contributions of the Cu_A site (red) and the tetranuclear Cu_Z site (blue). The signature spectrum of Cu_Z consists of two individual bands (grey) that represent distinct charge-transfer transitions from the two sulphur atoms. For stereo images of **a**, **b** see Supplementary Fig. 1.

observations. First, the observed bond distances to Cu_{Z1} (2.6 Å) and Cu_{Z4} (2.5 Å) are closer to typical Cu–S coordinative bonds than to Cu–O bonds (Fig. 2c). Second, in *A. cycloclastes* N_2OR an iodide anion that was added as a specific inhibitor of enzymatic activity binds in the same position as S_{Z2} does in *P. stutzeri* N_2OR I¹⁷ and I^- , as a strong ligand according to the spectrochemical series, is well suited to replace S^{2-27} . Third, the electron excitation spectrum of *P. stutzeri* N_2OR can be deconvoluted into the individual contributions of the metal sites Cu_{A} and Cu_{Z} (Fig. 2d; see Supplementary Discussion and Supplementary Figs 3 and 4), and the Cu_{Z} site of N_2OR I can be modelled by two distinct maxima at 552 nm and 650 nm (Supplementary Fig. 3c). They fall within an energy range typical for S→Cu charge transfer transitions involving mainly Cu 3d and sulphur 3p orbitals²⁸ and we interpret them to originate from the two sulphur atoms of Cu_{Z} , S_{Z1} and S_{Z2} , respectively.

The tetranuclear site of N_2OR was described as a mixture of an active form (Cu_{Z}) and an inactive form (Cu_{Z}^*)³, and our structural data reflects this difference: whereas in N_2OR I the active $[\text{4Cu:2S}] \text{Cu}_{\text{Z}}$ dominates, the inactive $[\text{4Cu:S}] \text{Cu}_{\text{Z}}^*$ is the main species in N_2OR II, with the residual activity in the as isolated state being due to a small remaining fraction of Cu_{Z} . Atom S_{Z2} is directly exposed to the substrate channel, and in oxo preparations, O_2 may diffuse to the Cu_{Z} site and remove the bridging sulphur S_{Z2} , concomitant with the loss of enzymatic activity, as Cu_{Z} irreversibly converts to the $[\text{4Cu:S}]$ core cluster Cu_{Z}^* . Correspondingly, the 552 nm band is lost in the spectral signature of Cu_{Z}^* . Removing this contribution from a spectrum of the purple form I (Fig. 2d and Supplementary Fig. 4a) leads to a spectrum highly similar to that of *A. cycloclastes* N_2OR II (Supplementary Fig. 4b)¹⁷. The origin of the 650 nm band is the S_{Z1} atom. This band only disappears when all surrounding copper ions are reduced to the Cu(I) state. In consequence, the sensitivity of the S_{Z2} atom is the Achilles' heel of the enzyme and the reason for its frequent loss of activity in micro-oxic environments.

The physiologically active state of the enzyme should be able to bind the substrate N_2O . Consequently, we pressurized crystals of N_2OR I with N_2O gas, followed by flash cooling in liquid nitrogen and X-ray diffraction data collection. In individual observations of Cu_{Z} , this

resulted in the appearance of an elongated difference electron density feature (Fig. 3c) that was adequately modelled with a linear N_2O molecule. At equal, fixed occupancies, the observed B factors of both the N_2O molecule and the Cu_{Z} centre were very close to those of the surrounding protein. Although the precise positioning of the substrate on the cluster showed slight variations, the overall orientation of all observed N_2O molecules was consistent (see Supplementary Discussion). Notably, in all eight independent copies of Cu_{A} in the asymmetric unit, ligand H583 was now rotated back to ligate Cu_{A1} weakly, at a distance of 2.6 Å.

Little experimental evidence and only few theoretical calculations are available concerning the interaction of N_2O with metal sites^{10,29}. A mechanistic study based on the structure of a reduced form of N_2OR isolated in the presence of dioxygen suggested that the $\text{Cu}_{\text{Z1}}-\text{Cu}_{\text{Z4}}$ edge of the cluster was the site of substrate binding¹⁸, but the discovery of a second sulphur atom in the Cu_{Z} centre of purple N_2OR contrasts with this suggestion. Instead, we observe N_2O positioned at Cu_{Z} in a side-on manner on the cluster face built by the atoms Cu_{Z2} , Cu_{Z4} and S_{Z1} (Fig. 3). This is determined in part by the intricate arrangement of a hydrophobic substrate channel leading from the protein surface to the Cu_{Z} cluster (Fig. 3a and Supplementary Fig. 2). The channel terminates close to Cu_{Z1} and forms a proximal vestibule of sufficient size for the reorientation of the substrate N_2O . Note that F621 and M627, both part of the Cu_{A} binding loop in the cupredoxin domain of the neighbouring monomer, form a barrier at this point. In the N_2O -bound structure the two residues move slightly apart as compared to the substrate-free enzyme, to accommodate the N_2O molecule. We hypothesize that an initial interaction of the more polar end of N_2O (the O atom) with the S_{δ} sulphur atom of M627 is the selection mechanism assuring the correct orientation of the substrate. Above the face of the Cu_{Z} cluster N_2O resides within a tight binding pocket formed by F621, H626 (a ligand to Cu_{A}) and M627 adjacent to a larger, distal cavity where several coordinated water molecules are located (Fig. 3a and Supplementary Fig. 2). The architecture of the substrate channel thus allows the apolar N_2 , end product of the N_2OR reaction, to leave the enzyme through the hydrophobic channel to the surface, while H_2O is retained in the distal, water-filled cavity within the protein matrix. The observed distance between N_2O and Cu_{Z} suggests a weak

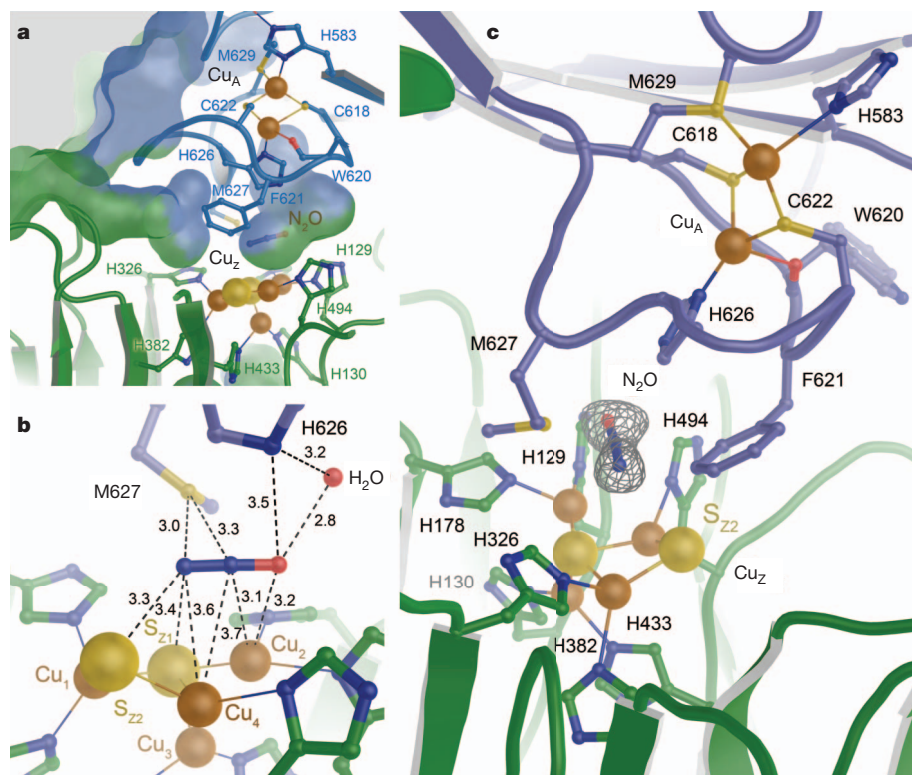


Figure 3 | Substrate binding in N_2OR . **a**, Active-site substrate binding. A hydrophobic substrate channel leads from the protein surface (left) to a proximal vestibule at Cu_{Z} , where the linear N_2O molecule can re-orient to displace the two residues shielding the cluster, F621 and M627. The substrate enters with the oxygen atom first and is then bound in a side-on manner on the face of the cluster. The reduction takes place in a hydrophilic (water-filled), distal chamber where the reaction by-product H_2O remains while the product N_2 exits via the hydrophobic entry channel. **b**, Distances around the N_2O ligand (in Å). The closest interaction partners are H626, M627 and the Cu_{Z} cluster. **c**, A $F_o - F_c$ difference electron density map contoured at the 3σ level showed the presence of the substrate. For stereo images of **a**, **b** see Supplementary Fig. 2.

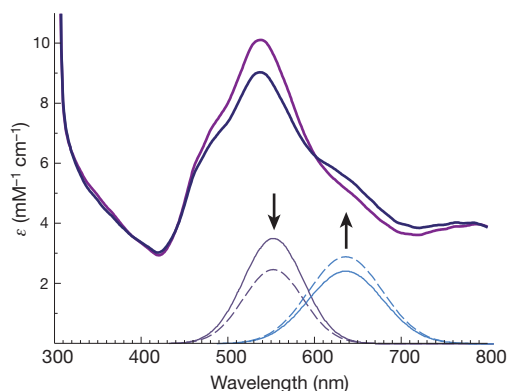


Figure 4 | Changes in the electron excitation spectrum of N₂OR form I upon binding of the substrate N₂O. The N₂OR I spectrum is shown in purple; the N₂O-bound form in blue. On the basis of the deconvolution of the spectra (Supplementary Fig. 3) the difference can be explained entirely by alterations of the two transitions that constitute the Cu_Z spectrum (Fig. 2c and Supplementary Fig. 4a), a decrease of the 552 nm band concomitant with an increase of the 650 nm band. Arrows signify the increase/decrease of the bands upon transition from the purple to the blue curve when N₂O binds.

interaction, supported by EPR and ultraviolet/visible light spectra (Fig. 4 and Supplementary Figs 5 and 6). For the process of activation and reduction of N₂O, a stronger interaction might be required, which would involve a conformational change in the protein that is yet to be identified. The positioning of N₂O between the two metal sites points towards a reaction mechanism where the substrate, precisely oriented by the protein, is activated by the Cu_Z cluster. Only after binding of N₂O is electron transfer from Cu_A to Cu_Z observed (Supplementary Fig. 5), and thus, rather than being a mere electron transfer site, Cu_A of N₂OR is an integral part of the enzyme's catalytic centre.

METHODS SUMMARY

P. stutzeri N₂OR was isolated and crystallized under strict exclusion of dioxygen as described previously³⁰. Crystals of N₂OR were obtained by sitting-drop vapour diffusion. For the formation of substrate complexes, crystals were pressurized with 15 bar of N₂O gas for 15 min in a pressure cell and subsequently flash frozen in liquid nitrogen for diffraction data collection.

Full Methods and any associated references are available in the online version of the paper at www.nature.com/nature.

Received 17 September 2010; accepted 23 June 2011.

Published online 14 August 2011.

1. Ravishankara, A. R., Daniel, J. S. & Portmann, R. W. Nitrous oxide (N₂O): the dominant ozone-depleting substance emitted in the 21st century. *Science* **326**, 123–125 (2009).
2. Crutzen, P. J., Mosier, A. R., Smith, K. A. & Winiwarter, W. N₂O release from agro-biofuel production negates global warming reduction by replacing fossil fuels. *Atmos. Chem. Phys.* **8**, 389–395 (2008).
3. Zumft, W. G. & Kroneck, P. M. H. Respiratory transformation of nitrous oxide (N₂O) to dinitrogen by Bacteria and Archaea. *Adv. Microb. Physiol.* **52**, 107–227 (2006).
4. Einsle, O. *et al.* Nitrogenase MoFe-protein at 1.16 Å resolution: a central ligand in the FeMo-cofactor. *Science* **297**, 1696–1700 (2002).
5. Canfield, D. E., Glazer, A. N. & Falkowski, P. G. The evolution and future of Earth's nitrogen cycle. *Science* **330**, 192–196 (2010).
6. Samarkin, V. A. *et al.* Abiotic nitrous oxide emission from the hypersaline Don Juan Pond in Antarctica. *Nature Geosci.* **3**, 341–344 (2010).
7. Schmittner, A. & Galbraith, E. D. Glacial greenhouse-gas fluctuations controlled by ocean circulation changes. *Nature* **456**, 373–376 (2008).
8. Einsle, O. & Kroneck, P. M. H. Structural basis of denitrification. *Biol. Chem.* **385**, 875–883 (2004).
9. Zumft, W. G. Cell biology and molecular basis of denitrification. *Microbiol. Mol. Biol. Rev.* **61**, 533–616 (1997).

10. Tolman, W. B. Binding and activation of N₂O at transition-metal centers: recent mechanistic insights. *Angew. Chem. Int. Ed.* **49**, 1018–1024 (2010).
11. Kroneck, P. M. H., Antholine, W. A., Riestler, J. & Zumft, W. G. The nature of the cupric site in nitrous oxide reductase and of Cu_A in cytochrome c oxidase. *FEBS Lett.* **248**, 212–213 (1989).
12. Savelieff, M. G. & Lu, Y. Cu_A centers and their biosynthetic models in azurin. *J. Biol. Inorg. Chem.* **15**, 461–483 (2010).
13. Rasmussen, T., Brittain, T., Berks, B. C., Watmough, N. J. & Thomson, A. J. Formation of a cytochrome c–nitrous oxide reductase complex is obligatory for N₂O reduction by *Paracoccus pantotrophus*. *Dalton Transact.* **21**, 3501–3506 (2005).
14. Brown, K. *et al.* A novel type of catalytic copper cluster in nitrous oxide reductase. *Nature Struct. Biol.* **7**, 191–195 (2000).
15. Rasmussen, T. *et al.* The catalytic center in nitrous oxide reductase, Cu_Z, is a copper–sulfide cluster. *Biochemistry* **39**, 12753–12756 (2000).
16. Haltia, T. *et al.* The crystal structure of nitrous oxide reductase (N₂OR) from *Paracoccus denitrificans* at 1.6 Å resolution. *Biochem. J.* **369**, 77–88 (2003).
17. Paraskevopoulos, K., Antonyuk, S. V., Sawers, R. G., Eady, R. R. & Hasnain, S. S. Insight into catalysis of nitrous oxide reductase from high-resolution structures of resting and inhibitor-bound enzyme from *Achromobacter cycloclastes*. *J. Mol. Biol.* **362**, 55–65 (2006).
18. Goresky, S. I., Ghosh, S. & Solomon, E. I. Mechanism of N₂O reduction by the μ₄-S tetranuclear Cu_Z cluster of nitrous oxide reductase. *J. Am. Chem. Soc.* **128**, 278–290 (2006).
19. Ghosh, S. *et al.* Activation of N₂O reduction by the fully reduced μ₄-sulfide bridged tetranuclear Cu_Z cluster in nitrous oxide reductase. *J. Am. Chem. Soc.* **125**, 15708–15709 (2003).
20. Zumft, W. G. & Matsubara, T. A novel kind of multi-copper protein as terminal oxidoreductase of nitrous-oxide respiration in *Pseudomonas perfectomarinus*. *FEBS Lett.* **148**, 107–112 (1982).
21. Coyle, C. L., Zumft, W. G., Kroneck, P. M. H., Körner, H. & Jakob, W. Nitrous oxide reductase from denitrifying *Pseudomonas perfectomarina*—purification and properties of a novel multicopper enzyme. *Eur. J. Biochem.* **153**, 459–467 (1985).
22. Riestler, J., Zumft, W. G. & Kroneck, P. M. H. Nitrous oxide reductase from *Pseudomonas stutzeri*—redox properties and spectroscopic characterization of different forms of the multicopper enzyme. *Eur. J. Biochem.* **178**, 751–762 (1989).
23. Fujita, K., Chan, J. M., Bollinger, J. A., Alvarez, M. L. & Dooley, D. M. Anaerobic purification, characterization and preliminary mechanistic study of recombinant nitrous oxide reductase from *Achromobacter cycloclastes*. *J. Inorg. Biochem.* **101**, 1836–1844 (2007).
24. Dell'Acqua, S. *et al.* A new Cu_Z active form in the catalytic reduction of N₂O by nitrous oxide reductase from *Pseudomonas nautica*. *J. Biol. Inorg. Chem.* **15**, 967–976 (2010).
25. Kroneck, P. M. H., Antholine, W. A., Riestler, J. & Zumft, W. G. The cupric site in nitrous oxide reductase contains a mixed-valence [Cu(II),Cu(I)] binuclear center: a multifrequency electron-paramagnetic resonance investigation. *FEBS Lett.* **242**, 70–74 (1988).
26. Brown, K. *et al.* Revisiting the catalytic Cu_Z cluster of nitrous oxide (N₂O) reductase: evidence of a bridging inorganic sulfur. *J. Biol. Chem.* **275**, 41133–41136 (2000).
27. Shriver, D. F. & Atkins, P. W. *Inorganic Chemistry* 3rd edn, 227–236 (Oxford Univ. Press, 2001).
28. Solomon, E. I. Spectroscopic methods in bioinorganic chemistry: blue to green to red copper sites. *Inorg. Chem.* **45**, 8012–8025 (2006).
29. Paulat, F. *et al.* Spectroscopic properties and electronic structure of pentammineruthenium(II) dinitrogen oxide and corresponding nitrosyl complexes: binding mode of N₂O and reactivity. *Inorg. Chem.* **43**, 6979–6994 (2004).
30. Pomowski, A., Zumft, W. G., Kroneck, P. M. H. & Einsle, O. Crystallization of purple nitrous oxide reductase from *Pseudomonas stutzeri*. *Acta Crystallogr. F* **66**, 1541–1543 (2010).

Supplementary Information is linked to the online version of the paper at www.nature.com/nature.

Acknowledgements This work was supported by the Deutsche Forschungsgemeinschaft (IRTG 1422) and the Center for Biological Signalling Studies (bioss, EXC 294). We thank the beam line staff at the Swiss Light Source for their assistance with data collection, T. Spatzal, K. Dörner and T. Friedrich for recording EPR spectra and F. Neese for discussions.

Author Contributions A.P., W.G.Z. and O.E. performed the experiments, A.P. and O.E. built and refined the structural model, P.M.H.K. and O.E. designed the experiments, O.E., P.K. and W.G.Z. wrote the manuscript.

Author Information Atomic coordinates for the reported crystal structures have been deposited with the Protein Data Bank under accession codes 3SBP (native1), 3SBQ (native2) and 3SBR (N₂O adduct). Reprints and permissions information is available at www.nature.com/reprints. The authors declare no competing financial interests. Readers are welcome to comment on the online version of this article at www.nature.com/nature. Correspondence and requests for materials should be addressed to O.E. (einsle@biochemie.uni-freiburg.de).

METHODS

Protein purification. *P. stutzeri* N₂OR was purified from fresh cells under strict exclusion of dioxygen and purification was carried out without interruption as described previously^{22,31}. The protein was kept constantly under the N₂/H₂ atmosphere of a glove box at <1 p.p.m. of O₂. For long-term storage protein was concentrated to 16 mg ml⁻¹ and pelleted by dripping into liquid N₂.

Crystallization and formation of substrate complexes. *P. stutzeri* N₂OR was crystallized under exclusion of dioxygen using the sitting-drop vapour diffusion method as described previously³⁰. Purple crystals were harvested into a cryoprotective buffer containing reservoir solution with added 10% (v/v) of 2R,3R-butane diol and flash cooled in liquid nitrogen for data collection at 100 K. Data sets were recorded on beam lines X06SA and X06DA at the Swiss Light Source. The native P1 data set was collected on an in-house rotating anode generator (Rigaku MicroMax 007HF) with an imaging plate (mar research mar345dtb). For data collection statistics see Supplementary Table 1.

For the preparation of substrate complexes, crystals of N₂OR were transferred to the cryoprotective buffer solution and subsequently pressurized with 15 bar of pure N₂O gas for 15 min using a XeCell pressurization chamber (Oxford Cryosystems). After pressure release the crystals were immediately flash cooled in liquid nitrogen for diffraction data collection.

Structure solution and refinement. The structure of *P. stutzeri* N₂OR was solved by the molecular replacement method, using the enzyme from *Paracoccus*

denitrificans (PDB code 1FWX) as a search model²⁶. One homodimer was located in the asymmetric unit of the P6₅ crystal form of the enzyme and four dimers in the P1 crystal form. The occurrence of the two crystal forms depended on the crystallization temperature, with hexagonal crystals dominating at 298 K and the P1 crystal form at 293 K using identical precipitant solutions³⁰. Model building was carried out in Coot³² and the structures were refined with REFMAC5³³. In order to assess the structural inhomogeneity observed at the Cu_Z site, restraints were generated from the most well-defined copies of the centre and used for the refinement of all sites. The distances shown in Fig. 3b are based on these restraints. Final refinement statistics are summarized in Supplementary Table 1. Structure representations were created using PyMOL³⁴.

31. Zumft, W. G. & Matsubara, T. A novel kind of multi-copper protein as terminal oxidoreductase of nitrous oxide respiration in *Pseudomonas perfectomarinus*. *FEBS Lett.* **148**, 107–112 (1982).
32. Emsley, P., Lohkamp, B., Scott, W. G. & Cowtan, K. Features and development of Coot. *Acta Crystallogr. D* **66**, 486–501 (2010).
33. Murshudov, G. N., Vagin, A. A. & Dodson, E. J. Refinement of macromolecular structures by the maximum-likelihood method. *Acta Crystallogr. D* **53**, 240–255 (1997).
34. DeLano, W. L. The PyMOL molecular graphics system (<http://www.pymol.org>) (2002).

CORRIGENDUM

doi:10.1038/nature10410

Tumour vascularization via endothelial differentiation of glioblastoma stem-like cells

Lucia Ricci-Vitiani, Roberto Pallini, Mauro Biffoni, Matilde Todaro, Gloria Invernici, Tonia Cenci, Giulio Maira, Eugenio Agostino Parati, Giorgio Stassi, Luigi Maria Larocca & Ruggero De Maria

Nature **468**, 824–828 (2010)

The figures and Supplementary figures of this Letter are affected by errors and improper editing. The correct figures are now provided, with an explanation of the variations. The original Letter has not been corrected online. We apologise for the confusion that our errors could have produced. We admit our negligence in the supervision of technical activity. We acknowledge that image manipulation is not acceptable and that any image modification must be clearly described. None of the alterations have any direct impact on the validity of our conclusions, which were also substantially confirmed in papers published by other independent groups^{1,2}.

In Fig. 1b, the left panel was generated by joining different fields acquired from several pictures in which the density of nuclei was very low. This was not apparent in the original figure because no border limits the individual acquisitions. This does not affect the interpretation of the results, which was based on the direct observation of a large number of cell nuclei by a senior investigator that gave the frequency of euploid versus aneuploid cells in each case preparation. The figure is only intended to show the appearance of different patterns. The same

correction has been made in the right panel. Figure 1b, now showing the eight separate images, is corrected below. The master pictures of the figure are available as Supplementary Figs 1 and 2 of this Corrigendum. In Fig. 1c, two parts of the same picture were cut, flipped and moved closer to save space in the figure. However, the upper and lower panels of Fig. 1c partially overlapped. In Fig. 2b, the panel showing the uptake of LDL by HMVEC (bottom image only) erroneously showed a duplication of the GBM patient panel. The HMVEC panel of Fig. 2b is corrected below.

Further errors in the Supplementary Information of the original Letter are described and corrected in the Supplementary Information of this Corrigendum.

Supplementary Information is linked to the online version of the Corrigendum at www.nature.com/nature.

1. Wang, R. *et al.* Glioblastoma stem-like cells give rise to tumour endothelium. *Nature* **468**, 829–833 (2010).
2. Soda, Y. *et al.* Transdifferentiation of glioblastoma cells into vascular endothelial cells. *Proc. Natl Acad. Sci. USA* **108**, 4274–4280 (2011).

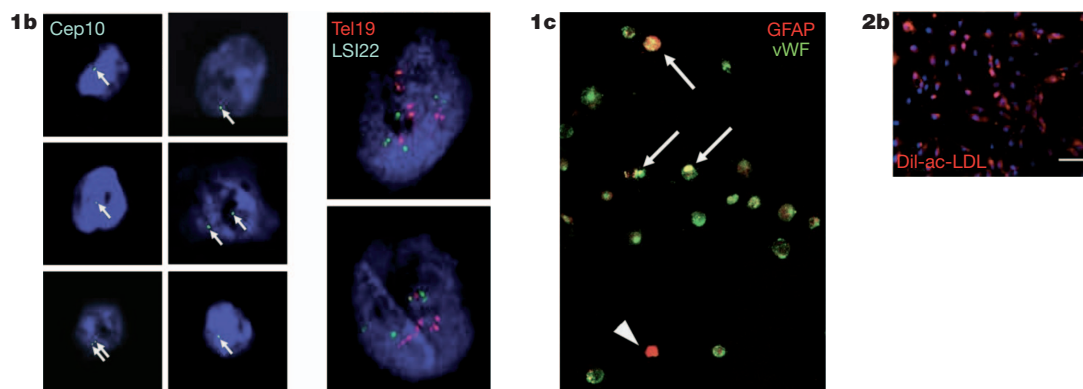


Figure 1 | Corrected left panel of original Fig. 1b, corrected original Fig. 1c, and corrected HMVEC panel in original Fig. 2b.

CORRECTIONS & AMENDMENTS

ERRATUM

doi:10.1038/nature10411

DMRT1 prevents female reprogramming in the postnatal mammalian testis

Clinton K. Matson, Mark W. Murphy, Aaron L. Sarver, Michael D. Griswold, Vivian J. Bardwell & David Zarkower

Nature **476**, 101–104 (2011)

In Fig. 3 of this Letter, the label above Fig. 3c should have read “XY *Dmrt1KO* gonads” should have read “XY *SCDmrt1KO* gonads”. “Mutant gonad” not “Mutant gonad (TX)”. In the legend to Fig. 3i These errors were corrected online on 3 August 2011.

CAREERS

TURNING POINT A love of teaching leads to a position at a liberal-arts college **p.241**

JOURNAL Read about the travails of young scientists **go.nature.com/3fttcj**

NATUREJOBS For the latest career listings and advice **www.naturejobs.com**

B. HANDELMAN



Middlebury College in Vermont is one of many liberal-arts colleges hiring researchers who enjoy teaching.

ACADEMIA

Small-school science

Undergraduate-focused colleges aren't known for research. But they are attractive to those with an interest in teaching.

BY KAREN KAPLAN

On a sultry morning in early July, two undergraduates are hard at work in Alison Holliday's chemistry lab at Swarthmore College, a four-year liberal-arts institution on a pastoral campus a few kilometres outside Philadelphia, Pennsylvania. As part of Holliday's research into environmental contaminants, senior-year student Daniel Pak hunches over a syringe, desorbing pesticides. Travis Mattingly, a junior, tests for melamine, an illegal additive in pet foods and

other products. During the ten-week summer break, research heats up in Holliday's lab.

The students and Holliday, an assistant professor in analytical chemistry, each spend about 40 hours a week in the lab over the summer. Like her colleagues at other liberal-arts colleges in the United States — institutions that focus on giving undergraduates a broad education in academic subjects — Holliday depends on the summer semester and her undergraduates to advance her research. Her teaching and other obligations at Swarthmore keep her from spending more than a few hours a week on research during the

rest of the year. And Holliday needs her undergraduates as lab personnel because the college has no graduate students and few postdocs.

Holliday and her students are aiming to develop faster and more efficient ways of measuring levels of environmental contaminants, although it is unlikely that any of the work will lead to a paper this year. She isn't worried, even though her most recent article came out in 2009. The 'publish or perish' edict that typically drives faculty members at large universities isn't the rule at Swarthmore and other liberal-arts colleges. At such institutions in the United States and, increasingly, elsewhere (see 'Europe embraces the trend'), teaching has as large a role as research in tenure review, and Holliday loves teaching as much as being at the bench. Her outlook is tied to her students. "It would be very difficult to go back to a research university and not have that level of interaction," she says.

Demand for scientific posts at these colleges is on the rise, suggest figures from the US National Institutes of Health (NIH), which funds biomedical research at undergraduate institutions through its Academic Research Enhancement Award (R15). In 2000, the NIH reviewed 501 R15 applications. By 2010, that had increased by nearly 50% to 992, although the number of grants awarded has not risen apace (see 'Increased demand'). During the same period, the number of reviewed applications for R01 grants — the NIH's primary research award — rose by 27%. Fierce competition for the few academic slots at universities, and a legitimizing of liberal-arts colleges as research institutions, have contributed to the rise in demand for positions at undergraduate institutions, says Howard Garrison, public-affairs director of the Federation of American Societies for Experimental Biology in Bethesda, Maryland. "We are seeing highly trained researchers taking jobs at the types of institutions that a decade ago would not have been likely destinations," he adds.

What's in it for an academic researcher who bypasses high-status, research-intensive universities for a tiny undergraduate college? A lot, say early-career scientists and veteran researchers at such institutions. They love doing actual bench research instead of being a de facto lab manager. They're relieved to be free of the panicked scramble for grants. And, like Holliday, they enjoy teaching and advising undergraduates.

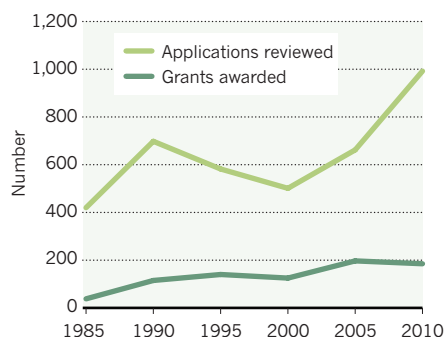
A DIFFERENT WORLD

But being a scientific researcher at a four-year liberal-arts college is not at all the leisurely, indolent experience that some might ►

SOURCE: NIH

INCREASED DEMAND

Applications for US National Institutes of Health R15 grants have increased in the past 25 years, but the number awarded has not kept pace with demand.



► envisage, warns Amy Cheng Vollmer, a microbiologist who has worked at Swarthmore since 1989. “It’s like comparing the winter Olympics to the summer Olympics,” says Vollmer, who frequently gives talks on career issues. “It’s not easier; it’s different.”

The teaching responsibilities are among the biggest differences. Specifics vary by institution, but junior faculty members typically teach two or three courses in the autumn semester and two in the spring, with a minimum of one lab section for at least one course. Along with teaching comes a raft of associated tasks: assembling a syllabus and selecting textbooks; developing lectures and lab sessions; and assigning exams, papers, lab reports and other classroom work. Although some of these tasks eventually become easier, others are perennially time-consuming. “I do all my own grading,” sighs Holliday.

Researchers also take on advisory obligations, including shepherding students through a thesis, counselling student organizations and

managing honours and independent-study programmes. And the small size of the colleges means that they may have to share equipment with another institution or even build their own — equipment that, at a larger campus, would already be in place or easily purchased. Anne Goodsell, a physicist at Middlebury College in Vermont, had to build her own apparatus for her work on laser cooling of atoms.

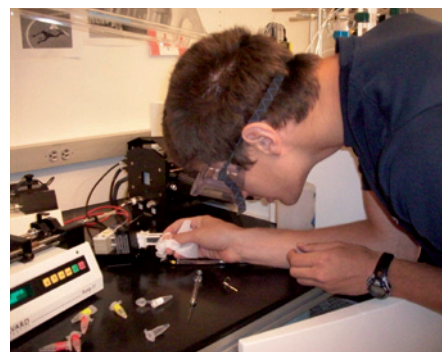
Goodsell has no thoughts of returning to a research-oriented institution such as Harvard University in Cambridge, Massachusetts, where she was a graduate student and postdoc, despite the greater number of nearby colleagues at such universities, and the associated ease of collaboration. Other researchers, however, do find the relative isolation at small colleges hard. “There certainly is collaborative work here, but typically you’re the only one who does what you do,” says Tiku Majumder, an atomic physicist at Williams College in Williamstown, Massachusetts. “I miss the opportunity for close collegial scientific exchanges every day.”

To beat the sense of isolation, Vollmer advises staying active in professional societies and attending as many conferences as possible. A resource for physicists in particular is the Anacapa Society, based at Amherst College in Massachusetts, which was created in 2003 in part to address that lack of connections.

Isolation isn’t the only stumbling block. “The research rhythm is different,” says Majumder. “It can take years to publish. As measured by how many papers I’ve authored, no way could I compete with my colleagues at big universities.” With undergraduates, researchers can also expect a smaller and less experienced team, which can detract from the science itself. “I am the sole source of continuity in my lab,” says Holliday. “I am the sole problem-solver and

troubleshooter-in-chief.” Scientists must also scale down their experiments to adapt to having less time in the lab. If a project doesn’t work one summer, it must usually be abandoned, at least until the following summer. Experiments that require more than a couple of months are typically not possible. “You’ve got to come up with small projects that you can quickly ramp up,” cautions Vollmer. “You can’t study the long-term effects of fire on a site. You can’t study corn, because it has only one growing season a year.”

Still, a research career at a liberal-arts college has its assets. Financial support is a huge benefit — many US liberal-arts colleges offer a start-up package, salary and internal funding that allow researchers to dodge the constant struggle for grants that their colleagues at research universities undergo. Bridge funding helps with grant gaps. Many liberal-arts colleges also provide funds for lab equipment. And researchers don’t have to support graduate students, postdocs or, usually, lab technicians. “I don’t worry about money — basically ever,” says Nick Kaplinsky, a plant biologist at Swarthmore.



Undergraduate student Travis Mattingly helps with research at Swarthmore College in Pennsylvania.

K. KAPLAN

A SPREADING MODEL

Europe embraces the trend

Although mostly a US phenomenon, liberal-arts colleges have started to gain traction elsewhere — notably in the Netherlands. “Here, we are moving away from an egalitarian past to create programmes for talented, motivated students who were otherwise becoming invisible,” says Harm Hoppers, dean of University College Maastricht, a liberal-arts institution that opened in 2001. This is one way in which the country has responded to calls for higher-education reform and new degree standards across Europe, as outlined in the Bologna Process agreement of 1999.

To date, five Dutch liberal-arts and sciences colleges — University College Maastricht, University College Utrecht, Amsterdam University College, Roosevelt Academy in Middelburg, and Leiden University College — have grown out of existing research institutions. These colleges increasingly focus on science, yet they often rely on their parent universities’ infrastructure and research expertise to do so, says Marijk van der Wende, dean of Amsterdam University College.

In the Netherlands, positions for scientists can be based at the affiliated university or at the

liberal-arts college itself. Core faculty positions at the liberal-arts colleges typically require PhDs, but focus almost exclusively on teaching — so research is pursued elsewhere. But university researchers can boost their careers and their chances of tenure by teaching at the colleges. They also gain access to top students interested in pursuing graduate studies.

Scientists at such institutions have much-sought-after autonomy, says Terence Kealey, vice-chancellor of the University of Buckingham, UK, an independent liberal-arts college. Kealey believes that if

his institution is to ascend the university rankings, it must build up its research base. He hopes to double the number of science faculty members from 35 to 70 in the next few years, although the main focus will stay on teaching. Jacobs University Bremen in Germany, which opened in 2001, is another liberal-arts college with a science focus.

And Rotterdam University in the Netherlands and Freiburg University in Germany are creating their own liberal-arts programmes. Such institutions seem likely to see continued growth in several parts of Europe. **Virginia Gewin**

In the United States, several grant schemes are tailored to researchers at liberal-arts institutions. The NIH awards about 200 R15s each year; the maximum funding is US\$300,000 over three years. The National Science Foundation (NSF) has the Research in Undergraduate Institutions (RUI) programme, which allows eligible researchers in the physical and biological sciences to apply for NSF grants. Applicants must submit impact statements explaining how the grant would affect their research, their department and their institution. “You can include information about the students you have working with you and the educational activities interwoven into the research project,” says Robert Scott Fisher, programme director at the NSF’s division of astronomical sciences in Arlington, Virginia. “You have an extra chance to explain the impact of the award.”

The NSF also offers three- to five-year grants with no maximum through its Faculty Early Career Development Program for tenure-track faculty members who combine research with teaching. The Research Corporation for Science Advancement, based in Tucson, Arizona, offers two-year grants of up to about \$75,000 to early-career scientific researchers at undergraduate institutions.

There is also, in general, a less furious battle for tenure than at many big universities. “We hire with the intent that the person will become a permanent part of the community,” says Cecilia Conrad, vice-president of academic affairs at Pomona College in Claremont, California. “We provide resources and advice so that the assistant professor will be successful in earning tenure.” Pomona offers faculty members a fully paid year’s leave from teaching in their third year of employment, to let them focus on research. Still, Conrad says, Pomona’s tenure process requires excellence in both research and teaching, as well as evidence of contributions to the community.

The teaching emphasis, in particular, can have a big impact. At Swarthmore, candidates for tenure must have letters of review from 25 students. “If you have an aptitude for teaching, and for performing, which in some ways teaching is about, then tenure is almost more of a sure thing,” says Kaplinsky, who recently earned tenure.

Ultimately, say researchers at liberal-arts colleges, the biggest payoff is helping students learn how to become scientists. “They’re dry sponges — they’re new, they’re hungry to learn, and they’re full of ideas,” says Bruce Kohorn, a biologist at Bowdoin College in Maine, who in 2001 left Duke University in Durham, North Carolina. “I love that.” ■

Karen Kaplan is assistant Careers editor at Nature.

TURNING POINT

Sarah Schaack

Last month, evolutionary geneticist Sarah Schaack started a tenure-track faculty position at Reed College, a liberal-arts college in Portland, Oregon. She reflects on the decisions that led to this move.

How did your liberal-arts undergraduate experience influence your research pursuits?

I went to Earlham College, a liberal-arts college in Richmond, Indiana. I wanted to double-major in biology — Earlham was known for its strong biology department — and the humanities. My experiences there, including a trip to Kenya as part of the school’s international programme, shaped both my career and my love of Africa. One of my mentors encouraged me to pursue research in field ecology. Networking with other Earlham graduates led to research experiences around the world.

What prompted your switch from field ecology to molecular biology?

I went to the University of Florida in Gainesville with the intention of focusing on tropical ecology in Uganda. While there, I ran a journal club whose only rule was that you had to pick a paper outside your comfort zone. A paper on transposable elements, pieces of DNA capable of moving in the genome, blew my mind and prompted me to pursue a PhD at Indiana University in Bloomington, a stronghold for evolution and genetics.

How did you end up back in Africa as a graduate student?

I knew that moving back to Indiana might keep open the possibility of heading my alma mater’s East Africa programme. Sure enough, three years later — in 2005 — I was chosen for that post, and took a four-month sabbatical from my PhD. I led 16 students around Tanzania to teach them about evolutionary processes in Africa while they conducted their own research. I have leapt at every chance to get back to Africa, learning Swahili along the way. My experiences helped me to get a unique job — teaching bioinformatics in East Africa in a postdoctoral position funded by the Howard Hughes Medical Institute.

How did you navigate your way to a tenure-track position?

I applied to ten or so schools about a year before I knew I would need a job. They ranged from small, mostly teaching-oriented schools to larger academic-research institutions. I got an offer after my first interview, but didn’t accept it, mainly because attending scientific



D. S. FREY

meetings was not a priority for faculty members at that institution. For me, going to meetings is one of the best parts of academia. I had two more interviews and two more offers, so I was able to use those as leverage during subsequent negotiations with Reed. I accepted their offer, which included a start-up package on a par with what you would get at a research-oriented state university — it includes lab space, money for personnel, equipment and travel for meetings, and a pledge to support my bioinformatics workshops in East Africa. I work hard at teaching and I didn’t want to end up at a place where that was a liability.

Why do you think your application stood out at Reed?

It stood out because, in addition to leading the East Africa programme, I’ve taken advantage of several opportunities to explore different teaching venues. Some — for example, taking over an undergraduate ‘introduction to biology’ course when a professor became ill — fell into my lap when I was a graduate student. Other opportunities I created myself. As a postdoc at the University of Texas at Arlington, I organized a workshop on how to annotate transposable-elements data. After the workshop, I compiled a reference pamphlet now referred to as the bible in our lab. Part of how I learn a topic is to learn it well enough to teach it.

What is your single best career strategy?

I typically don’t apply for opportunities when I’m panicked. I apply just before that point. Then I have the luxury of being able to think clearly about whether or not I want a certain job. That is a hugely powerful position, much more so than waiting until I have to take the first job I’m offered. ■

INTERVIEW BY VIRGINIA GEWIN

In the United States, several grant schemes are tailored to researchers at liberal-arts institutions. The NIH awards about 200 R15s each year; the maximum funding is US\$300,000 over three years. The National Science Foundation (NSF) has the Research in Undergraduate Institutions (RUI) programme, which allows eligible researchers in the physical and biological sciences to apply for NSF grants. Applicants must submit impact statements explaining how the grant would affect their research, their department and their institution. “You can include information about the students you have working with you and the educational activities interwoven into the research project,” says Robert Scott Fisher, programme director at the NSF’s division of astronomical sciences in Arlington, Virginia. “You have an extra chance to explain the impact of the award.”

The NSF also offers three- to five-year grants with no maximum through its Faculty Early Career Development Program for tenure-track faculty members who combine research with teaching. The Research Corporation for Science Advancement, based in Tucson, Arizona, offers two-year grants of up to about \$75,000 to early-career scientific researchers at undergraduate institutions.

There is also, in general, a less furious battle for tenure than at many big universities. “We hire with the intent that the person will become a permanent part of the community,” says Cecilia Conrad, vice-president of academic affairs at Pomona College in Claremont, California. “We provide resources and advice so that the assistant professor will be successful in earning tenure.” Pomona offers faculty members a fully paid year’s leave from teaching in their third year of employment, to let them focus on research. Still, Conrad says, Pomona’s tenure process requires excellence in both research and teaching, as well as evidence of contributions to the community.

The teaching emphasis, in particular, can have a big impact. At Swarthmore, candidates for tenure must have letters of review from 25 students. “If you have an aptitude for teaching, and for performing, which in some ways teaching is about, then tenure is almost more of a sure thing,” says Kaplinsky, who recently earned tenure.

Ultimately, say researchers at liberal-arts colleges, the biggest payoff is helping students learn how to become scientists. “They’re dry sponges — they’re new, they’re hungry to learn, and they’re full of ideas,” says Bruce Kohorn, a biologist at Bowdoin College in Maine, who in 2001 left Duke University in Durham, North Carolina. “I love that.” ■

Karen Kaplan is assistant Careers editor at Nature.

TURNING POINT

Sarah Schaack

Last month, evolutionary geneticist Sarah Schaack started a tenure-track faculty position at Reed College, a liberal-arts college in Portland, Oregon. She reflects on the decisions that led to this move.

How did your liberal-arts undergraduate experience influence your research pursuits?

I went to Earlham College, a liberal-arts college in Richmond, Indiana. I wanted to double-major in biology — Earlham was known for its strong biology department — and the humanities. My experiences there, including a trip to Kenya as part of the school’s international programme, shaped both my career and my love of Africa. One of my mentors encouraged me to pursue research in field ecology. Networking with other Earlham graduates led to research experiences around the world.

What prompted your switch from field ecology to molecular biology?

I went to the University of Florida in Gainesville with the intention of focusing on tropical ecology in Uganda. While there, I ran a journal club whose only rule was that you had to pick a paper outside your comfort zone. A paper on transposable elements, pieces of DNA capable of moving in the genome, blew my mind and prompted me to pursue a PhD at Indiana University in Bloomington, a stronghold for evolution and genetics.

How did you end up back in Africa as a graduate student?

I knew that moving back to Indiana might keep open the possibility of heading my alma mater’s East Africa programme. Sure enough, three years later — in 2005 — I was chosen for that post, and took a four-month sabbatical from my PhD. I led 16 students around Tanzania to teach them about evolutionary processes in Africa while they conducted their own research. I have leapt at every chance to get back to Africa, learning Swahili along the way. My experiences helped me to get a unique job — teaching bioinformatics in East Africa in a postdoctoral position funded by the Howard Hughes Medical Institute.

How did you navigate your way to a tenure-track position?

I applied to ten or so schools about a year before I knew I would need a job. They ranged from small, mostly teaching-oriented schools to larger academic-research institutions. I got an offer after my first interview, but didn’t accept it, mainly because attending scientific



D. S. FREY

meetings was not a priority for faculty members at that institution. For me, going to meetings is one of the best parts of academia. I had two more interviews and two more offers, so I was able to use those as leverage during subsequent negotiations with Reed. I accepted their offer, which included a start-up package on a par with what you would get at a research-oriented state university — it includes lab space, money for personnel, equipment and travel for meetings, and a pledge to support my bioinformatics workshops in East Africa. I work hard at teaching and I didn’t want to end up at a place where that was a liability.

Why do you think your application stood out at Reed?

It stood out because, in addition to leading the East Africa programme, I’ve taken advantage of several opportunities to explore different teaching venues. Some — for example, taking over an undergraduate ‘introduction to biology’ course when a professor became ill — fell into my lap when I was a graduate student. Other opportunities I created myself. As a postdoc at the University of Texas at Arlington, I organized a workshop on how to annotate transposable-elements data. After the workshop, I compiled a reference pamphlet now referred to as the bible in our lab. Part of how I learn a topic is to learn it well enough to teach it.

What is your single best career strategy?

I typically don’t apply for opportunities when I’m panicked. I apply just before that point. Then I have the luxury of being able to think clearly about whether or not I want a certain job. That is a hugely powerful position, much more so than waiting until I have to take the first job I’m offered. ■

INTERVIEW BY VIRGINIA GEWIN

NPG'S POLICY ON AUTHORSHIP

Important change to submission criteria.

BY JORDAN SUCHOW

To the dismay of many (yet to the delight of a few), Nature Publishing Group announced today that its flagship journal, *Nature*, will no longer accept submissions from humans (*Homo sapiens*). The new policy, which has been under editorial consideration for many years, was sparked by a growing sentiment in the scientific community that the heuristics and biases inherent in human decision-making preclude them from conducting reliable science. In an ironic twist of fate, the species has impeached itself by thorough research on its own shortcomings.

The ban takes effect on 12 September and will apply to those who self-identify as human. Authors will be required to include, in addition to the usual declaration of competing financial interests, the names of all humans consulted in preparation of the submitted work. Other journals are likely to adopt a similar policy.

Although the reactions are mixed, not everyone is surprised, and a few remain comfortably unaffected.

The Massachusetts Institute of Technology has since 2010 asked that all active researchers opt-in to wearing an implantable tag as part of the TMI project, which aggregates real-time data across the campus to improve all aspects of everything. As these tags are sentient, the researchers who wear them qualify as bionic (*Homo bionika*) according to standard ISO +1.914/582.2646. This act of foresight by the university, which at the time was controversial and the cause of much debate, now pays a handsome dividend.

Similarly, researchers at Yale, who have never been the type to self-identify as mere mortals, remain unscathed.

It seems unavoidable that other universities will soon follow suit, causing a sharp rise in the incidence of implants and arrogance. Exploiting these loopholes may be a saving grace for the species' full participation in the sciences.

While professors weep, students rejoice. According to the provisions of the ISO standard (the one gainfully employed by MIT), a human who spends at least half its waking hours interacting with a sentient non-carbon-based machine qualifies as bionic. The newest generation of students, having grown up on the interwebs, spends on average the entirety of its life online. Students everywhere have been seen calling their mothers, reiterating how brilliant they were to have flatly ignored the warnings to "put down that damn hand computer". Cyberculture paid off.

Those who have been slow to adopt new technology (or who still identify as human) are rightly concerned: their contribution to

Nature had been dwindling well before the ban, and today constitutes less than 10% of published papers. In its

➔ **NATURE.COM**
Follow Futures on
Facebook at:
go.nature.com/mtoodm

place stands the work of pharmaceutical laboratory automatons, embedded devices, the interwebs and most recently, Google Books, which having declared independence from its parent company Google (NASDAQ: GOOG), has become increasingly prolific, contributing 42 manuscripts this year alone.

Shortly after the announcement, the World Wide interwebs Consortium (W2iC, formerly W3C), alongside the Union of Embedded Tags, jointly filed a formal complaint with the journal, arguing for mandatory first-authorship of non-carbon-based machines in all bionic collaborations. (See also the letter to the editor in the 12 March issue of *Nature*, written by Tag #15167247373 and co-signed by the arm in which it is embedded.) Although amendments to *Nature's* policy are at this time unlikely, concerns regarding authorship will surely be the cause of considerable tension in many laboratories. Embedded devices will use the ban as leverage for salary increases and promotions.

Not everyone is so bothered by the announcement. Egbert B. Gebstadter, professor of com-

puter science at the University of Mishugan, notes: "Although it is nonsensical to rely on evidence provided by human-based research when judging whether humans are themselves inept, in doing so, the editors (all human, I note) provide a perfect example of the feebleness of human reasoning, thereby validating their claims." Gebstadter is bionic, although was human when he had come to this conclusion.

The editors of *Nature* were readily available for comment, and their incisive remarks gave such great credibility to the new policy that it rendered all future debate moot. But, in the spirit of the policy, because the editors are human, these remarks are duly censored. ■

Jordan Suchow is a graduate student in cognitive science at Harvard University, and can be found online at jwsu.ch/ow. He self-identifies as human.



Widespread iron-rich conditions in the mid-Proterozoic ocean

Noah J. Planavsky¹, Peter McGoldrick², Clinton T. Scott¹, Chao Li^{1,3}, Christopher T. Reinhard¹, Amy E. Kelly¹, Xuelei Chu⁴, Andrey Bekker⁵, Gordon D. Love¹ & Timothy W. Lyons¹

The chemical composition of the ocean changed markedly with the oxidation of the Earth's surface¹, and this process has profoundly influenced the evolutionary and ecological history of life^{2,3}. The early Earth was characterized by a reducing ocean-atmosphere system, whereas the Phanerozoic eon (less than 542 million years ago) is known for a stable and oxygenated biosphere conducive to the radiation of animals. The redox characteristics of surface environments during Earth's middle age (1.8–1 billion years ago) are less well known, but it is generally assumed that the mid-Proterozoic was home to a globally sulphidic (euxinic) deep ocean^{2,3}. Here we present iron data from a suite of mid-Proterozoic marine mudstones. Contrary to the popular model, our results indicate that ferruginous (anoxic and Fe²⁺-rich) conditions were both spatially and temporally extensive across diverse palaeogeographic settings in the mid-Proterozoic ocean, inviting new models for the temporal distribution of iron formations and the availability of bioessential trace elements during a critical window for eukaryotic evolution.

It is well established that Earth evolved from having an early anoxic ocean devoid of eukaryotes to one that is fully oxygenated and teeming with complex life. However, the timing and mechanisms of Earth's redox evolution are still debated. Foremost, marine redox conditions and atmospheric oxygen levels remain poorly constrained during the period between the Earth's oxygen-deficient early history (more than ~2.4 billion years (Gyr) ago) and the dominantly oxygenated realm of the Phanerozoic (the last ~0.542 Gyr). Traditional arguments held that ocean oxygenation was responsible for the disappearance of large iron formations at 1.8 Gyr ago (ref. 1). More recently, the majority opinion among Precambrian workers has instead favoured a deep mid-Proterozoic ocean with a vast or perhaps even global reservoir of hydrogen sulphide^{4–6}, and H₂S, much like oxygen, would have titrated the dissolved iron needed for the deposition of iron formations. It is further proposed that these euxinic (anoxic and sulphidic) conditions would have hindered the expansion and diversification of eukaryotes, because of the insolubility of bioessential trace elements, such as molybdenum, in sulphidic waters⁷. Consistent with a shift to euxinia, well-preserved sedimentary rocks from the Animikie basin on the Superior craton were suggested to capture the transition to a global sulphidic ocean⁶ at ~1.8 Gyr ago. It is now apparent, however, that large iron formations were deposited tens of millions of years after the deposition of this sedimentary succession^{8,9} and that iron-rich conditions persisted in deep waters in the Animikie basin even after the deposition of the largest Animikie iron formations^{8,10}, demanding that we rethink the spatiotemporal details of Proterozoic ocean redox and specifically the character of the mid-Proterozoic ocean (1.8–1.0 Gyr ago)¹⁰.

In contrast with endmember euxinic or oxic Proterozoic deep-ocean models, a third possibility has recently been proposed: that anoxic and iron-rich deepwater conditions may have been common throughout the Precambrian, including the mid-Proterozoic^{3,8,10,11}. This surprising

view of ocean evolution finds its origins in part with recent evidence that the ocean was ferruginous in the terminal Proterozoic^{12–14}, suggesting continuity with the iron-formation-favouring conditions present before 1.8 Gyr ago. Alternatively, researchers have also asserted that the Neoproterozoic was instead a special case—marked by a return to the iron-rich state of the early Precambrian as a consequence of supercontinent break-up¹³, extensive glaciations¹⁵, and drawdown of marine sulphate caused by a billion years of deepwater euxinia and pyrite burial¹². Although tantalizing, the ferruginous mid-Proterozoic model is currently hindered by a billion-year gap in direct evidence from the geological record for this marine redox state. Our study fills that data gap with results from four diverse mid-Proterozoic depositional settings that all point to iron-rich marine waters. Included are samples from the McArthur basin in north-central Australia—the only basin so far that has yielded direct evidence for mid-Proterozoic euxinia^{16,17}.

To evaluate ancient redox chemistry, we have applied a well-established sequential iron extraction scheme to fine-grained sedimentary rocks¹⁸. The accumulation of biogeochemically reactive iron, termed 'highly reactive iron' (Fe_{HR}), is linked to the redox conditions in the water column overlying the site of sedimentary deposition. In modern oxic marine sediments, Fe_{HR} comprises less than 38% of the total sedimentary iron pool (that is, Fe_{HR}/Fe_T < 0.38), reflecting the detrital sediment flux in the absence of dissolved iron in the O₂-containing water column. Enrichments beyond this limit (Fe_{HR}/Fe_T > 0.38) are a clear signature of transport, scavenging and deposition of additional iron from an anoxic water column^{3,12}. Because mineralogical changes associated with even moderate burial alteration (such as iron uptake into secondary silicate minerals) can decrease the pool of Fe_{HR}, the upper limit is possibly lower than 0.38 in older rocks¹⁹, suggesting that essentially all of our samples could have formed under anoxic conditions (Fig. 1). Where anoxia is indicated, we can further distinguish between ferruginous (Fe²⁺ > H₂S) and euxinic (H₂S > Fe²⁺) environments by measuring the extent to which Fe_{HR} has reacted with H₂S to form pyrite (Fe_{Py}/Fe_{HR}). Accordingly, anoxic shales with Fe_{Py}/Fe_{HR} > 0.8 are considered to have been deposited under euxinic conditions^{11,12}.

Because the McArthur basin has had a defining role in previous arguments for mid-Proterozoic euxinia^{16,17,20,21}, we began our search for ferruginous conditions with an additional analysis of fresh drill cores of shale from deep-water settings in this region. We specifically investigated the iron chemistry of the ~1.64-Gyr-old Barney Creek and Lady Loretta formations in the McArthur and Mount Isa basins, respectively. Our samples are from geographically widespread marine sequences that extend over more than 2,000 km across northern Australia. We included locations with palaeogeographic positions closer to the open ocean compared with past studies in the region that also focused on marine palaeoredox. In addition, we targeted the deepest-water facies as delineated in previous detailed basin analysis (see, for example, ref. 22).

¹Department of Earth Sciences, University of California, Riverside, California 92521, USA. ²CODES ARC Centre of Excellence in Ore Deposits, University of Tasmania, Tasmania 7001, Australia. ³State Key Laboratory of Biogeology and Environmental Geology, China University of Geosciences, Wuhan 430074, China. ⁴Institute of Geology and Geophysics, Chinese Academy of Sciences, Beijing 100029, China. ⁵Department of Geological Sciences, University of Manitoba, Winnipeg, Manitoba R3T 2N2, Canada.

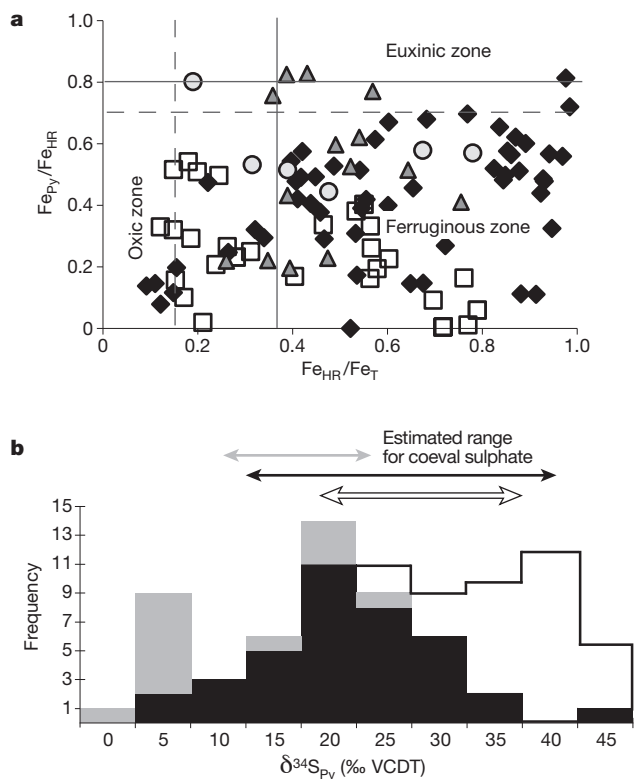


Figure 1 | Iron speciation and sulphur isotope data for mid-Proterozoic shales. Data from the 1.64-Gyr-old Mt Isa Superbasin (black diamonds and bars), the 1.7-Gyr-old Chuanlinggou Formation (white squares and bars), the 1.45-Gyr-old Newland Formation (grey triangles and bars) and the 1.2-Gyr-old Borden basin (grey circles). **a**, The vast majority of our samples have ratios of highly reactive to total iron (Fe_{HR}/Fe_T) and of pyrite to highly reactive iron (Fe_{Py}/Fe_{HR}) falling above 0.15–0.38 and below 0.7–0.8, respectively, which is diagnostic of sediment accumulation beneath an anoxic and iron-rich (non-sulphidic) water column. **b**, Pyrite $\delta^{34}S$ isotope values ($\delta^{34}S_{Py}$) relative to Vienna Canyon Diablo Troilite (VCDT). Estimates for sulphate $\delta^{34}S$ values are from refs 32, 33.

Fe_{HR}/Fe_T values in both the Barney Creek and Lady Loretta formations are generally above 0.38, conservatively indicating deposition under anoxic conditions (Fig. 1a). The vast majority of these samples have Fe_{Py}/Fe_{HR} ratios well below 0.8, which is consistent with a persistently sulphide-free water column. Together, these ratios point to widespread ferruginous conditions over thick (hundreds of metres) stratigraphic intervals, indicating prolonged periods of ferruginous deep waters, with the likelihood of laterally contemporaneous occurrences of euxinia^{16,17} in certain small or isolated sub-basins and/or on the shallower margins. Previous regional studies have argued for a relatively strong marine connection during deposition at our specific sample locations (see Supplementary Information), suggesting that deep ocean waters enriched in dissolved Fe^{2+} may have exchanged with the McArthur and Mt Isa basins.

Given these exciting results, we were obliged to look beyond this region for records of mid-Proterozoic ferruginous waters. With this goal, we analysed additional suites of carbonaceous shales from other, widely distributed mid-Proterozoic basins, emphasizing well-preserved (sub-greenschist) shales from diverse palaeogeographic settings spanning the mid-Proterozoic. Each of these additional units yielded abundant samples with $Fe_{HR}/Fe_T > 0.38$ and $Fe_{Py}/Fe_{HR} < 0.8$ (Fig. 1a), signifying widespread ferruginous depositional conditions. Our data include samples from the 1.7-Gyr-old Chuanlinggou Formation in northern China, the 1.45-Gyr-old Belt Supergroup in the north-central USA and the 1.2-Gyr-old Borden basin in Arctic Canada. The Chuanlinggou Formation is interpreted as being a passive-margin sequence, suggesting a strong connection to the open ocean, and the Borden basin was a

passive margin that evolved into a foredeep setting. In contrast, the Belt basin probably represents an extensional marine setting with transiently more restricted depositional conditions (see Supplementary Information).

A small subset of samples from the Mt Isa superbasin, the Belt Supergroup and the Borden basin have significant iron enrichments and Fe_{Py}/Fe_{HR} near 0.8 (Fig. 1a), suggesting that sulphidic conditions may have developed episodically in the water column. The lack of persistently euxinic conditions in the Belt Supergroup is surprising. As a semi-isolated, probably marginal marine system with evidence for high rates of primary productivity²³, the Belt basin would seem ideally suited to developing euxinia—as we see in the modern, restricted Black Sea. Clear fingerprints of ferruginous conditions in the Chuanlinggou Formation are also revealing: as a passive-margin sequence lacking indications of appreciable basin restriction, this setting provides one of our best windows on conditions in the open Proterozoic ocean.

Our finding of iron-rich conditions in several mid-Proterozoic marine settings contrasts with the widely accepted view of globally persistent and pervasive deep euxinia. However, this discovery is entirely consistent with an emerging view of Precambrian ocean chemistry brought to light by the most recent trace-metal and iron speciation studies from younger and older portions of the Precambrian ocean. Specifically, there is evidence for coexisting iron-rich and H_2S -rich conditions in several Neoproterozoic^{24–27}, early and middle Palaeoproterozoic^{10,28} and early and late Neoproterozoic settings^{13,14} (Fig. 2). Ferruginous conditions were apparently widespread in the deeper portions of the ocean, whereas sulphide was probably limited to highly productive regions along the continental margins^{10,13,25,26}, which is analogous to the more reducing conditions in modern oxygen minimum zones. Our data fill a billion-year gap in the evidence for this marine redox state, indicating a hitherto undocumented continuity of iron-rich conditions throughout the Precambrian.

Our finding of extensive ferruginous conditions is also consistent with a recent study of marine molybdenum inventories²⁷, which argued that the extent of euxinic depositional environments during the mid-Proterozoic could have been severalfold that of the modern ocean ($\ll 1\%$) but far from whole-ocean euxinia. Similarly, mid-Proterozoic Mo isotope data are easily explained through greatly expanded (relative to today) but still largely local euxinia, with deep

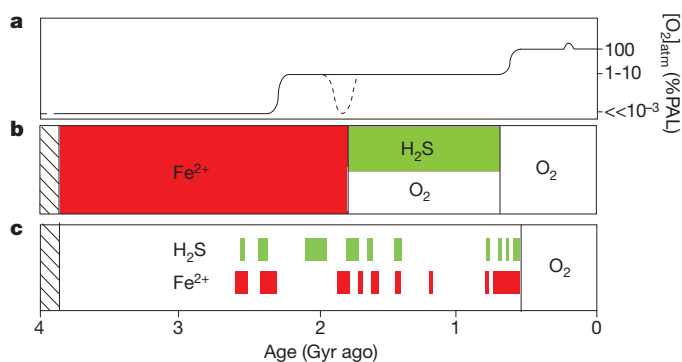


Figure 2 | Summary of marine chemical conditions in the Precambrian.

a, Estimates of atmospheric oxygen compared with present atmospheric level (PAL). **b**, Classical models of the chemical composition of the deep ocean. **c**, Distribution of Precambrian euxinic and ferruginous deep waters, based on the shale record. Our study provides evidence for extensively developed and likely persistent ferruginous conditions in the deep ocean during the mid-Proterozoic, which was previously thought to have been characterized by either oxygenated or sulphide-rich conditions. The emerging view based on redox studies of marine shales is that during the mid-Proterozoic, when there were relatively low levels of atmospheric oxygen, both euxinic and ferruginous waters were common, and often stratified, below the oxygenated surface-mixing zone. In the Phanerozoic, with higher levels of atmospheric oxygen, the deep oceans were anoxic for only short periods (see the text for details).

waters that were dominantly ferruginous and thus less efficient at burying Mo (see, for example, ref. 20).

We argue that the flux of organic matter was central to controlling the redox landscape of the mid-Proterozoic ocean, as has been suggested for other—both older and younger—instances of Precambrian euxinia^{10,13,25}. Estimates for dissolved sulphate levels in the mid-Proterozoic ocean range from 500 to 3,000 μM (see Supplementary Information). Even the lower estimate for sulphate is well above the upper limit for dissolved iron, which is fixed at roughly 100 μM by the solubilities of iron carbonates and silicates². Therefore, ferruginous marine conditions must instead mirror limited sulphide production¹³. Sulphide is produced anaerobically by bacteria at the expense of organic matter. It follows that spatial gradients in the organic flux and, ultimately, organic productivity may have limited the extent of euxinia.

Consistent with an organic matter delivery control on the distribution of sulphidic marine conditions, the analysed samples contain substantially less organic carbon than do typical euxinic Precambrian and Phanerozoic shales. Samples in our study contain on average less than 1% organic carbon, which is severalfold lower than concentrations common in euxinic shales (see, for example, ref. 27). Low levels of organic matter in ferruginous shales suggest relatively low productivity in the overlying water column. In addition, there is a sulphur isotope signal consistent with bacterial sulphate reduction occurring predominantly in the porewaters. Pyrite in our samples has $\delta^{34}\text{S}$ values that are slightly lower than or equivalent to coeval sulphate (Fig. 1b). A simple explanation for these results is that bacterial sulphate reduction is occurring largely in sediments where potentially high isotopic fractionations are muted by limited sulphate availability. Sulphate supplies in the sediments would be controlled by rates of diffusional replenishment, and associated deficiencies would be exacerbated by the comparatively small amount of sulphate in mid-Proterozoic seawater. In other words, limited availability of organic matter probably caused the onset of appreciable bacterial sulphate reduction to be restricted to the sediments. However, these sulphur isotope results do not completely exclude water column sulphur cycling.

For ferruginous conditions to have been extensive in the mid-Proterozoic ocean, dissolved oxygen acquired in surface waters through photosynthesis and gas exchange with the overlying atmosphere must have been consumed as deep water masses aged. Oxygen will be consumed through the degradation of sinking organic matter and, if oxygen remains available at depth, by hydrothermally sourced reductants (see, for example, ref. 29). Our results indicate that the flux of Fe^{2+} into deep waters typically exceeded rates of sulphide generation in all but nearshore or restricted regions with relatively high rates of primary productivity that fuelled localized sulphate reduction in the water column.

Our results also call for a reconsideration of the factors controlling the temporal distribution of large iron formations. In contrast with the canonical view, in which iron formations disappeared as the deep ocean evolved from iron to oxygen or sulphide domination^{1,4}, the long persistence of ferruginous conditions in our model argues that iron formations are anomalous sedimentary deposits linked in most cases to an enhanced iron supply by means of strong hydrothermal inputs⁸. Consistent with our ocean model, the amount of hydrothermal iron released to the oceans has varied greatly with marine sulphate concentrations³⁰ and mantle plume activity as reflected by dyke swarms and large igneous provinces⁸.

Our findings cast a new perspective on mid-Proterozoic environmental conditions, ecology and evolution. For example, evidence for extensive ferruginous conditions throughout the Proterozoic ocean provides a simple answer to the apparent conundrum of increasing enzymatic use of iron, molybdenum and cobalt during the mid-Proterozoic as inferred by a recent study of the evolution of almost 4,000 gene families³¹. It is possible for these bioessential metals to have been readily available in an ocean with pervasively ferruginous deep

waters, in contrast with the certainty of biolimitation if deep waters were globally sulphidic⁷. Free sulphide in the water column greatly decreases the solubility of these elements. It remains to be tested, however, whether broad, but far from global, extents of euxinia in a stratified ocean were still able to pull down trace metal inventories at least locally to biologically critical levels, as suggested in previous work²⁷. More generally, our data now provide the foundation for a unified model for the chemical evolution of the Precambrian ocean consistent with diverse redox tracers and bridging past work bracketing the mid-Proterozoic. Recognizing the spatial and temporal heterogeneity expected in a dynamic early ocean, we propose the almost continuous coexistence of sulphide-rich and iron-rich conditions for billions of years beneath oxic surface waters as the backdrop for Precambrian biological evolution, and specifically the protracted radiation of eukaryotes and the ultimate rise of animals.

METHODS SUMMARY

Iron speciations were performed at the University of California, Riverside (UCR), using a well-calibrated sequential extraction protocol designed to quantify the different pools of Fe_{HR} (ref. 18). A small portion of sample powder (~ 100 mg) was used for the extractions, and iron concentrations were determined with an Agilent 7500ce inductively coupled plasma mass spectrometry (ICP-MS) at UCR. Fe_{py} was calculated on the basis of the weight percentage of sulphur extracted during a 2-h hot chromous chloride distillation followed by iodometric titration. Total iron concentrations were determined by one of two methods: X-ray fluorescence at the CODES Research Centre at the University of Tasmania, or a three-acid digest and ICP-MS analysis at UCR. Sulphur isotope measurements were made at UCR with a ThermoFinnigan Delta V continuous-flow stable-isotope-ratio mass spectrometer after a chromous chloride distillation, where the pyrite-S was reprecipitated as Ag_2S .

Full Methods and any associated references are available in the online version of the paper at www.nature.com/nature.

Received 25 January; accepted 23 June 2011.

Published online 7 September 2011.

- Holland, H. D. Sedimentary mineral deposits and the evolution of Earth's near-surface environments. *Econ. Geol.* **100**, 1489–1509 (2005).
- Canfield, D. E. The early history of atmospheric oxygen: homage to Robert A. Garrels. *Annu. Rev. Earth Planet. Sci.* **33**, 1–36 (2005).
- Lyons, T. W., Anbar, A., Severmann, S., Scott, C. & Gill, B. Tracking euxinia in the ancient ocean: a multiproxy perspective and Proterozoic case study. *Annu. Rev. Earth Planet. Sci.* **37**, 507–534 (2009).
- Canfield, D. E. A new model for Proterozoic ocean chemistry. *Nature* **396**, 450–453 (1998).
- Lyons, T. W., Reinhard, C. T. & Scott, C. Redox redux. *Geobiology* **7**, 489–494 (2009).
- Poulton, S. W., Fralick, P. W. & Canfield, D. E. The transition to a sulphidic ocean similar to 1.84 billion years ago. *Nature* **431**, 173–177 (2004).
- Anbar, A. D. & Knoll, A. H. Proterozoic ocean chemistry and evolution: a bioinorganic bridge. *Science* **297**, 1137–1142 (2002).
- Bekker, A. *et al.* Iron formation: the sedimentary product of a complex interplay among mantle, tectonic, oceanic, and biospheric processes. *Econ. Geol.* **105**, 467–508 (2010).
- Wilson, J. P. *et al.* Geobiology of the late Paleoproterozoic Duck Creek Formation, Western Australia. *Precamb. Res.* **179**, 135–149 (2010).
- Poulton, S. W., Fralick, P. W. & Canfield, D. E. Spatial variability in oceanic redox structure 1.8 billion years ago. *Nature Geosci.* **3**, 486–490 (2010).
- Poulton, S. W. & Canfield, D. E. Ferruginous conditions: a dominant feature of the ocean through Earth's history. *Elements* **7**, 107–112 (2011).
- Canfield, D. E. *et al.* Ferruginous conditions dominated later Neoproterozoic deep-water chemistry. *Science* **321**, 949–952 (2008).
- Johnston, D. T. *et al.* An emerging picture of Neoproterozoic ocean chemistry: insights from the Chuar Group, Grand Canyon, USA. *Earth Planet. Sci. Lett.* **290**, 64–73 (2010).
- Li, C. *et al.* A stratified redox model for the Ediacaran Ocean. *Science* **328**, 80–83 (2010).
- Swanson-Hysell, N. L. *et al.* Cryogenian glaciation and the onset of carbon-isotope decoupling. *Science* **328**, 608–611 (2010).
- Brocks, J. J. *et al.* Biomarker evidence for green and purple sulphur bacteria in a stratified Palaeoproterozoic sea. *Nature* **437**, 866–870 (2005).
- Johnston, D. T. *et al.* Sulfur isotope biogeochemistry of the Proterozoic McArthur Basin. *Geochim. Cosmochim. Acta* **72**, 4278–4290 (2008).
- Poulton, S. W. & Canfield, D. E. Development of a sequential extraction procedure for iron: implications for iron partitioning in continentally derived particulates. *Chem. Geol.* **214**, 209–221 (2005).
- Raiswell, R. Turbidite depositional influences on the diagenesis of Beecher's Trilobite Bed and the Hunsrück Slate; sites of soft tissue pyritization. *Am. J. Sci.* **305**, 105–129 (2008).

20. Kendall, B., Creaser, R. A., Gordon, G. W. & Anbar, A. D. Re–Os and Mo isotope systematics of black shales from the Middle Proterozoic Velkerri and Wolllogorang Formations, McArthur Basin, northern Australia. *Geochim. Cosmochim. Acta* **73**, 2534–2558 (2009).
21. Shen, Y., Knoll, A. H. & Walter, M. R. Evidence for low sulphate and anoxia in a mid-Proterozoic marine basin. *Nature* **423**, 632–635 (2003).
22. McGoldrick, P., Winefield, P., Bull, S., Selley, D. & Scott, R. Sequences, synsedimentary structures, and sub-basins: the where and when of SEDEX zinc systems in the southern McArthur Basin, Australia. *Soc. Econ. Geol. Spec. Publ.* **15**, 1–23 (2010).
23. Lyons, T. W., Luepke, J. J., Schreiber, M. E. & Zieg, G. A. Sulfur geochemical constraints on Mesoproterozoic restricted marine deposition: lower Belt Supergroup, northwestern United States. *Geochim. Cosmochim. Acta* **64**, 427–437 (2000).
24. Kendall, B. *et al.* Pervasive oxygenation along late Archaean ocean margins. *Nature Geosci.* **3**, 647–652 (2010).
25. Reinhard, C. T., Raiswell, R., Scott, C., Anbar, A. D. & Lyons, T. W. A Late Archaean sulfidic sea stimulated by early oxidative weathering of the continents. *Science* **326**, 713–716 (2009).
26. Scott, C. *et al.* Late Archaean euxinic conditions before the rise of atmospheric. *Geology* **39**, 119–122 (2011).
27. Scott, C. *et al.* Tracing the stepwise oxygenation of the Proterozoic ocean. *Nature* **452**, 457–460 (2008).
28. Bekker, A. *et al.* Fractionation between inorganic and organic carbon during the Lomagundi (2.22–2.1 Ga) carbon isotope excursion. *Earth Planet. Sci. Lett.* **271**, 278–291 (2008).
29. Slack, J. F., Grenne, T., Bekker, A., Rouxel, O. J. & Lindberg, P. A. Suboxic deep seawater in the late Paleoproterozoic: evidence from hematitic chert and iron formation related to seafloor-hydrothermal sulfide deposits, central Arizona, USA. *Earth Planet. Sci. Lett.* **255**, 243–256 (2007).
30. Kump, L. R. & Seyfried, W. E. Hydrothermal Fe fluxes during the Precambrian: effect of low oceanic sulfate concentrations and low hydrostatic pressure on the composition of black smokers. *Earth Planet. Sci. Lett.* **235**, 654–662 (2005).
31. David, L. A. & Alm, E. J. Rapid evolutionary innovation during an Archaean genetic expansion. *Nature* **469**, 93–96 (2011).
32. Chu, X., Zhang, T., Zhang, Q. & Lyons, T. W. Sulfur and carbon isotope records from 1700 to 800 Ma carbonates of the Jixian section, northern China: Implications for secular isotope variations in Proterozoic seawater and relationships to global supercontinental events. *Geochim. Cosmochim. Acta* **71**, 4668–4692 (2007).
33. Gellatly, A. M. & Lyons, T. W. Trace sulfate in mid-Proterozoic carbonates and the sulfur isotope record of biospheric evolution. *Geochim. Cosmochim. Acta* **69**, 3813–3829 (2005).

Supplementary Information is linked to the online version of the paper at www.nature.com/nature.

Acknowledgements We thank P. Emsbo, S. Bull and D. Winston for formative discussions, P. Fralick for constructive comments, and S. Bates and J. Owens for assistance with the analyses. This work was supported by funding from the National Science Foundation (NSF) Graduate Research Fellowship programme, Geological Society of America and American Philosophical Society, to N.J.P.; from the NSF Division of Earth Sciences, the NASA Exobiology Program and Astrobiology Institute and the UTAS Visiting Fellows programme to T.W.L.; from the Agouron Institute to T.W.L. and G.D.L.; and from Natural Sciences and Engineering Research Council of Canada to A.B. P.McG. was supported through the Australian Research Council's Centre of Excellence programme.

Author Contributions P.McG., A.B., T.W.L., X.C., C.L. and N.J.P. collected samples, and P.McG., N.J.P., C.T.S. and C.L. analysed them. All authors were involved in the writing and the design and interpretations of this study.

Author Information Reprints and permissions information is available at www.nature.com/reprints. The authors declare no competing financial interests. Readers are welcome to comment on the online version of this article at www.nature.com/nature. Correspondence and requests for materials should be addressed to T.W.L. (timothy.lyons@ucr.edu).

METHODS

The extraction method used in this study to speciate between the reactive iron pools in fine-grained siliciclastic rocks and sediments has been described in detail elsewhere, and we therefore provide only an overview here. In short, our iron speciations were performed at UCR, using a well-calibrated sequential extraction protocol designed to quantify the different pools of Fe_{HR} (refs 6, 18). Fe_{HR} is subdivided into three subpools, each with the potential to react with hydrogen sulphide on diagenetic timescales: carbonate-associated iron extracted with a sodium acetate solution (Fe_{Carb}), ferric oxides extracted with a dithionite solution (Fe_{Ox}), and mixed-valence iron oxides, principally magnetite, extracted with ammonium oxalate (Fe_{Mag}). We used ~ 100 mg of sample powder, and the sequential extracts were analysed with an Agilent 7500ce ICP-MS. Pyrite (Fe_{Py}) is also included in the Fe_{HR} pool. Fe_{Py} was calculated (assuming a stoichiometry of FeS_2) on the basis of the weight percentage of sulphur extracted during a 2-h hot chromous chloride distillation followed by iodometric titration. The assumption of a FeS_2 stoichiometry in the sulphide pool was tested through extensive extractions for acid-volatile sulphide with hot SnCl_2 -HCl (15% SnCl_2 , 6 M HCl) for 1 h.

The samples included here all contain less than 0.1% sulphur extractable by HCl. Total iron concentrations were determined by one of two methods: X-ray fluorescence at the CODES Research Centre at the University of Tasmania, or a three-acid digestion followed by ICP-MS analysis at UCR. On the basis of duplicate analyses and Geostandard monitoring, reproducibility of iron measurements was better than 5%. However, samples with less than 0.1% iron were found to be reproducible to two decimal places, but the error can exceed 5%. At such low levels of iron, these errors have no impact on our conclusions.

We determined concentrations of total organic carbon by taking the difference between carbonate carbon liberated by 4 M HCl and total carbon released by combustion at 1,450 °C, both of which were measured with an ELTRA C/S determinator at UCR. Last, also at UCR, pyrite-S was extracted for isotope measurements by using the same chromous chloride distillation but, in this case, reprecipitating the pyrite-S as Ag_2S . Sulphur isotope measurements were made with a ThermoFinnigan Delta V continuous-flow stable-isotope-ratio mass spectrometer. Reproducibility was better than 0.2‰ on the basis of single-run and long-term standard monitoring.

Antidiabetic actions of a non-agonist PPAR γ ligand blocking Cdk5-mediated phosphorylation

Jang Hyun Choi^{1*}, Alexander S. Banks^{1*}, Theodore M. Kamenecka^{2,4*}, Scott A. Busby^{3*}, Michael J. Chalmers³, Naresh Kumar³, Dana S. Kuruvilla³, Youseung Shin², Yuanjun He², John B. Bruning⁵, David P. Marciano³, Michael D. Cameron^{2,3,4}, Dina Laznik¹, Michael J. Jurczak⁶, Stephan C. Schürer⁷, Dušica Vidović⁷, Gerald I. Shulman⁶, Bruce M. Spiegelman¹ & Patrick R. Griffin^{2,3,4}

PPAR γ is the functioning receptor for the thiazolidinedione (TZD) class of antidiabetes drugs including rosiglitazone and pioglitazone¹. These drugs are full classical agonists for this nuclear receptor, but recent data have shown that many PPAR γ -based drugs have a separate biochemical activity, blocking the obesity-linked phosphorylation of PPAR γ by Cdk5 (ref. 2). Here we describe novel synthetic compounds that have a unique mode of binding to PPAR γ , completely lack classical transcriptional agonism and block the Cdk5-mediated phosphorylation in cultured adipocytes and in insulin-resistant mice. Moreover, one such compound, SR1664, has potent antidiabetic activity while not causing the fluid retention and weight gain that are serious side effects of many of the PPAR γ drugs. Unlike TZDs, SR1664 also does not interfere with bone formation in culture. These data illustrate that new classes of antidiabetes drugs can be developed by specifically targeting the Cdk5-mediated phosphorylation of PPAR γ .

PPAR γ is a member of the nuclear receptor family of transcription factors and is a dominant regulator of adipose cell differentiation and development^{3,4}. It is also the functioning receptor for the thiazolidinedione (TZD) class of antidiabetic drugs such as rosiglitazone and pioglitazone^{1,5}. These antidiabetes drugs were developed specifically to have high affinity and full agonism towards PPAR γ before their molecular modes of action were known⁶. It has therefore been assumed that their therapeutic actions result from their functional agonism on this receptor. From a clinical perspective, rosiglitazone (Avandia) and pioglitazone (Actos) are both highly effective oral medications for type 2 diabetes and are well tolerated by the majority of patients⁷. Unfortunately, a substantial number of patients experience side effects from these drugs, including fluid retention, weight gain, congestive heart failure and loss of bone mineral density^{8,9}. Whereas some of the non-TZD full agonists have good antidiabetic activity, they also cause many of the same side effects, including fluid retention.

The therapeutic role of classical agonism of PPAR γ was made somewhat confusing by the development of several compounds that have less than full agonist properties (partial agonists) but retain substantial insulin-sensitizing and antidiabetic actions in experimental models^{10,11}. Furthermore, we have recently shown that many antidiabetic PPAR γ ligands have a second, distinct biochemical function: blocking the obesity-linked phosphorylation of PPAR γ by cyclin-dependent kinase 5 (Cdk5) at serine 273 (ref. 2). This is a direct action of the ligands and requires binding to the PPAR γ ligand binding domain (LBD), causing a conformational change that interferes with the ability of Cdk5 to phosphorylate serine 273. Rosiglitazone and MRL24 (a selective partial agonist towards PPAR γ) both modulate serine 273 phosphorylation at therapeutic doses in mice. Furthermore, a small clinical trial of newly diagnosed type 2 diabetics showed a remarkably close

association between the clinical effects of rosiglitazone and the blocking of this phosphorylation of PPAR γ . Thus, the contribution made by classical agonism to the therapeutic effects of these drugs and to their side effects is not clear.

These data indicate that it might be possible to develop entirely new classes of antidiabetes drugs optimized for the inhibition of Cdk5-mediated phosphorylation of PPAR γ while lacking classical agonism. Here we describe the development of synthetic small molecules that bind tightly to PPAR γ , yet are completely devoid of classical agonism and effectively inhibit phosphorylation at serine 273. These compounds have a unique binding mode in the ligand binding pocket of PPAR γ . An example from this series, SR1664, shows potent and dose-dependent antidiabetic effects in obese mice. Unlike TZDs and other PPAR γ agonists, this compound does not cause fluid retention or weight gain *in vivo* or reduce osteoblast mineralization in culture.

To develop a suitable ligand, we optimized compounds for (1) high binding affinity for PPAR γ , (2) blocking the Cdk5-mediated PPAR γ phosphorylation and (3) lacking classical agonism. We first identified published compounds that bind tightly to PPAR γ and have favourable properties as a scaffold for extensive chemical modifications. Classical agonism is defined here, as is standard in the nuclear receptor field, as an increased level of transcription through a tandem PPAR response element luciferase reporter. Of particular interest was compound **7b** described previously as an extremely potent and selective PPAR γ partial agonist (30% activation compared to rosiglitazone)¹². A modular synthesis approach was used to make a series of analogues of compound **7b**; these compounds were tested *in vitro* and in adipose cells (Supplementary Fig. 1c, d). Using a Lanthascreen competitive binding assay, SR1664 (Fig. 1a) had a half-maximum inhibitory concentration (IC₅₀) of 80 nM (Supplementary Fig. 1a, b). As shown in Fig. 1b, when compared to rosiglitazone or MRL24 (a partial agonist) in a classical transcriptional activity assay, SR1664 had essentially no transcriptional agonism at any concentration. Rosiglitazone and SR1664 both effectively blocked the Cdk5-mediated phosphorylation of PPAR γ *in vitro* with half-maximal effects between 20 and 200 nM (Fig. 1c). In contrast, they had no effect on the phosphorylation of a well-characterized Cdk5 substrate, the Rb protein (Fig. 1d)¹³. This indicated that these compounds do not disrupt the basic protein kinase function of Cdk5. In addition, SR1664 was also effective at blocking Cdk5-mediated phosphorylation of PPAR γ in differentiated fat cells (Fig. 1e) with no measurable difference in phosphorylation of Rb (Supplementary Fig. 1e). Additional analogues were synthesized and four compounds were identified that have similar *in vitro* profiles (Supplementary Fig. 1b). SR1824 (Fig. 1a) was further characterized for its ability to block Cdk5-dependent phosphorylation of PPAR γ (Fig. 1b–e). These data demonstrate that ligands can be made that potentially block Cdk5-dependent

¹Department of Cancer Biology and Division of Metabolism and Chronic Disease, Dana-Farber Cancer Institute and Department of Cell Biology, Harvard Medical School, Boston, Massachusetts 02115, USA.

²Translational Research Institute, The Scripps Research Institute, Scripps Florida, Jupiter, Florida 33458, USA. ³Department of Molecular Therapeutics, The Scripps Research Institute, Scripps Florida, Jupiter, Florida 33458, USA. ⁴The Scripps Research Molecular Screening Center (SRMSC), The Scripps Research Institute, Scripps Florida, Jupiter, Florida 33458, USA. ⁵Department of Biochemistry and Biophysics, Texas A&M University, College Station, Texas 77843-2128, USA. ⁶Howard Hughes Medical Institute, Departments of Internal Medicine and Cellular & Molecular Physiology, Yale University School of Medicine, New Haven, Connecticut 06510, USA. ⁷Center for Computational Science, University of Miami, Miami, Florida 33136, USA.

*These authors contributed equally to this work.

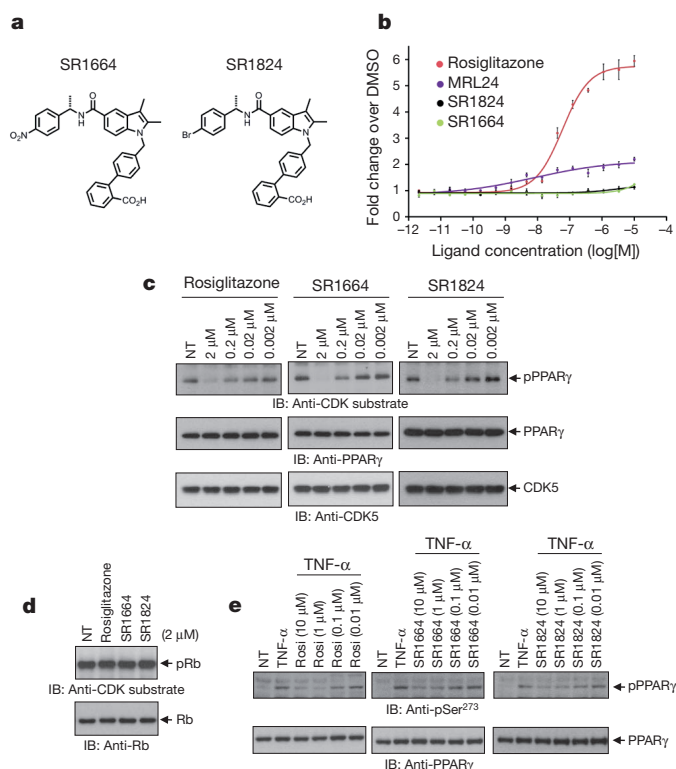


Figure 1 | Novel PPAR γ ligands lack classical agonism, block phosphorylation at Ser 273. **a**, Chemical structures of SR1664 and SR1824. **b**, Transcriptional activity of a PPAR-derived reporter gene in COS-1 cells following treatment with rosiglitazone, SR1664 or SR1824 ($n = 3$). **c**, *In vitro* Cdk5 assay with rosiglitazone, SR1664 or SR1824 with PPAR γ or Rb substrates. IB, immunoblot; NT, not treated; pPPAR γ , phosphorylated PPAR γ ; pRb, phosphorylated Rb. **d**, TNF- α -induced phosphorylation of PPAR γ in differentiated PPAR γ knock-out MEFs expressing wild-type PPAR γ treated with rosiglitazone, SR1664 or SR1824. Error bars are s.e.m.

phosphorylation of PPAR γ in cells while demonstrating little to no classical agonism.

Of the four compounds identified as non-agonist inhibitors of Cdk5-mediated PPAR γ phosphorylation, SR1664 had adequate pharmacokinetic properties to move forward to biological and therapeutic assays. Adipogenesis was the first known biological function of PPAR γ ³ and agonist ligands for PPAR γ have been shown to stimulate potently the differentiation of pre-adipose cell lines; this response has been widely used as a sensitive cellular test for PPAR γ agonism^{1,14,15}. As shown in Fig. 2a, rosiglitazone potently stimulated fat cell differentiation, as evidenced by Oil Red O staining of the cellular lipid. In contrast, SR1664 did not stimulate increased lipid accumulation or changes in morphology characteristic of differentiating fat cells. The stimulation of fat cell gene expression was also apparent with rosiglitazone, as illustrated by an increased expression of genes linked to adipogenesis. In contrast, SR1664 induced little or no change in the expression of these genes (Fig. 2b).

Another well-known effect of both rosiglitazone and pioglitazone is that they decrease bone formation and bone mineral density leading to an increase in fracture risk^{8,16}. TZDs have also been shown to decrease bone mineralization in cultured osteoblasts¹⁷. As shown in Fig. 2c, rosiglitazone treatment reduced the mineralization of mouse osteoblastic cells, as measured by Alizarin red staining. Moreover, the expression of genes involved in the differentiation of these cells was impaired (see Supplementary Fig. 2). Importantly, treatment with SR1664 did not affect the extent of calcification or the expression of this osteoblast gene set in MC3T3-E1 cells.

Co-crystallography, mutagenesis and hydrogen/deuterium exchange (HDX) have all demonstrated that full agonists of PPAR γ affect critical

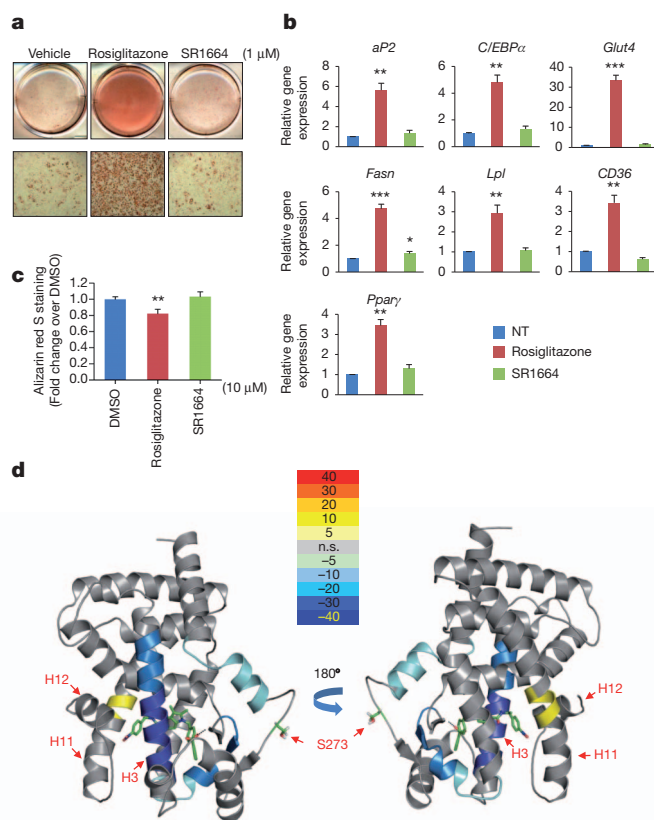


Figure 2 | Structural and *in vitro* functional analysis of SR1664. **a**, Lipid accumulation in differentiated 3T3-L1 cells treated with rosiglitazone or SR1664 following Oil Red O staining. **b**, Expression of adipocyte-enriched genes in these cells was analysed by qPCR ($n = 3$). **c**, Mineralization of MC3T3-E1 osteoblast cells as determined by Alizarin Red-S. Error bars are s.e.m.; * $P < 0.05$, ** $P < 0.01$, *** $P < 0.001$. NT, no treatment. **d**, Overlay of differential HDX data onto the docking model of 2hfp bound to SR1664 (see Supplementary Fig. 3). This overlay depicts the difference in HDX between ligand-free and SR1664 bound PPAR γ LBD. Perturbation data are colour coded and plotted onto the backbone of the PDB file according to the key. n.s., not significant. Observed changes in HDX were statistically significant ($P < 0.05$) in a two-tailed t -test ($n = 3$).

hydrogen bonds within the C-terminal helix (H12) of the receptor^{18–21}. This interaction stabilized the AF2 surface (helix 3–4 loop, C-terminal end of H11 and H12) of the receptor facilitating co-activator interactions. Interestingly, high affinity partial agonists have been identified that do not make these interactions yet still possess some level of classical agonism, and several of these have been shown to bind the backbone amide of S342 (S370 in PPAR γ 2) within the β -sheet of the LBD¹⁸. More recently, we demonstrated that the proximity of ligand to the amide of S342 correlated with increased stability of the helix 2-helix 2' loop, the region of the receptor containing S273 (S245 in PPAR γ 1) as determined by HDX². Surprisingly, HDX analysis of SR1664 and SR1824 increased the conformational mobility of the C-terminal end of H11, a helix that abuts H12 (Fig. 2d); in contrast, the full and partial agonists stabilized the same region of H11 (Supplementary Fig. 3).

In silico docking studies were carried out to understand the structural basis of SR1664 interactions in the PPAR γ 1 ligand binding domain (Supplementary Fig. 4). In this model, the phenyl-substituted nitro group of SR1664 clashes with hydrophobic side chains of H11 such as Leu 452 and Leu 453 (Leu 480 and Leu 481 in PPAR γ 2, respectively) as well as Leu 469 and Leu 465 (corresponding to Leu 497 and Leu 493 in PPAR γ 2) of the loop N-terminal to H12. This potentially explains the lack of stabilization of H12 and the destabilization of the region of H11 near His 449 as seen by HDX. Despite the altered mode of

binding, SR1664 and rosiglitazone both bind to the same core residues within the PPAR γ LBD. This is demonstrated by the ability of SR1664 to attenuate the transcriptional activity of rosiglitazone on PPAR γ in the context of a competitive ligand binding assay (Supplementary Fig. 4b).

To determine whether the altered transcriptional activity of SR1664 may be attributed to differences in DNA binding or coactivator recruitment, we compared the chromatin association of PPAR γ or steroid receptor co-activator-1 (SRC1) within the α P2 promoter. As expected, rosiglitazone significantly increased SRC1 occupancy without affecting PPAR γ occupancy. However, SR1664 treatment did not influence the occupancy of PPAR γ or SRC1 recruitment to the α P2 promoter, indicating that SR1664 has a very different activity of co-regulator recruitment (Supplementary Fig. 4c).

We next asked whether SR1664 had antidiabetic properties *in vivo*. Wild-type mice fed a high-fat high-sugar diet become obese and insulin-resistant, with activation of Cdk5 in their adipose tissues². Figure 3a demonstrates that SR1664, injected twice daily for 5 days, caused a dose-dependent decrease in the Cdk5-mediated phosphorylation of PPAR γ at serine 273 in adipose tissue. Moreover, SR1664 treatment also caused a trend towards lowered (and normalized) glucose levels, and a significant reduction in the fasting insulin levels. Insulin resistance, as

computed by HOMA-IR, showed a clear and dose-dependent improvement with SR1664 (Fig. 3b). These changes occurred without significant differences in body weight compared to vehicle-treated mice (Supplementary Fig. 5).

The most accurate method for measuring changes in insulin sensitivity *in vivo* is the hyperinsulinaemic-euglycaemic clamp²². As shown in Fig. 3c and in Supplementary Fig. 6, the glucose infusion rate (GIR) needed to maintain euglycaemia in the mice treated with SR1664 was significantly greater than in animals treated with the vehicle alone, indicating improved whole-body insulin sensitivity. Suppression of hepatic glucose production (HGP), an important component of insulin action, was improved by SR1664. Whereas no difference in whole-body glucose disposal was detected from calculations of ³H-glucose turnover, analysis of tissue-specific ¹⁴C-2-deoxyglucose transport demonstrated improved insulin-stimulated glucose disposal in adipose tissue of SR1664-treated mice. Similarly, reductions in both basal and clamped plasma free fatty acids levels, as well as a 20% greater suppression of lipolysis in response to insulin, indicated improved adipose tissue insulin sensitivity in SR1664-treated mice. Together, these data indicate that SR1664 improves insulin sensitivity.

Using cells expressing the S273A mutant of PPAR γ , we previously defined a gene set in cultured adipose cells that was most sensitive to the phosphorylation at this site². Treatment of mice with SR1664 caused changes in the expression of 11/17 (65%) of these genes, all in the direction predicted for the inhibition of the PPAR γ S273 phosphorylation (Fig. 3d). Adiponectin and adipisin, genes long recognized as being reduced in obesity^{23,24}, are both induced by SR1664. We also defined a separate set of genes reflective of a full agonist (rosiglitazone) on cultured fat cells. SR1664 caused changes in expression of 6/19 genes in this 'agonist' gene set; importantly, three of these changes were in the same direction as expected for an agonist, but three were changed in the opposite direction (Fig. 3e). Taken together, these data show that SR1664 has an insulin-sensitizing effect with preferential regulation of the gene set sensitive to the phosphorylation of PPAR γ by Cdk5.

A more severe model of obesity is the leptin-deficient ob/ob mouse. These animals are very obese and insulin-resistant, with substantial compensatory hyperinsulinaemia. Preliminary pharmacokinetic and pharmacodynamic experiments showed comparable drug exposures at 40 mg kg⁻¹ for SR1664 and 8 mg kg⁻¹ for rosiglitazone, both injected twice daily (Supplementary Fig. 7). Functional analyses were performed at days 5 and 11 after the start of treatments. As shown in Fig. 4a, both drugs caused a similar reduction in PPAR γ phosphorylation at S273. After 5 days of treatment, there were no overt differences in fasting body weight or glucose levels (Fig. 4b). Control mice receiving only the vehicle remained hyperinsulinaemic, but both rosiglitazone and SR1664 substantially reduced these insulin levels (Fig. 4b). Glucose tolerance tests were markedly improved with both rosiglitazone and SR1664, and the areas under these glucose excursion curves were statistically indistinguishable, without changing body weight (Fig. 4c).

Weight gain and fluid retention caused by TZD drugs like rosiglitazone are suspected to be key factors in their increased cardiac risk^{9,25}. After recovering from the glucose tolerance test on day 5, rosiglitazone-treated mice began to show an increase in body weight (Fig. 4d). This increased mass is accounted for primarily by fluid retention, quantified by a decrease in haematocrit seen with haemodilution (Fig. 4f). However, an increase in body fat was also observed by magnetic resonance imaging (Fig. 4e, f). Importantly, SR1664 treatment did not cause the weight gain seen with the rosiglitazone treatment. Furthermore, SR1664 treatment showed no decrease in the haematocrit or change in body adiposity. These results were confirmed by measurements showing a decreased concentration of haemoglobin in the mice treated with rosiglitazone, but not in those treated with SR1664 (Supplementary Fig. 8). Taken together, these data indicate that SR1664, a non-agonist PPAR γ ligand, has antidiabetic actions in two murine models

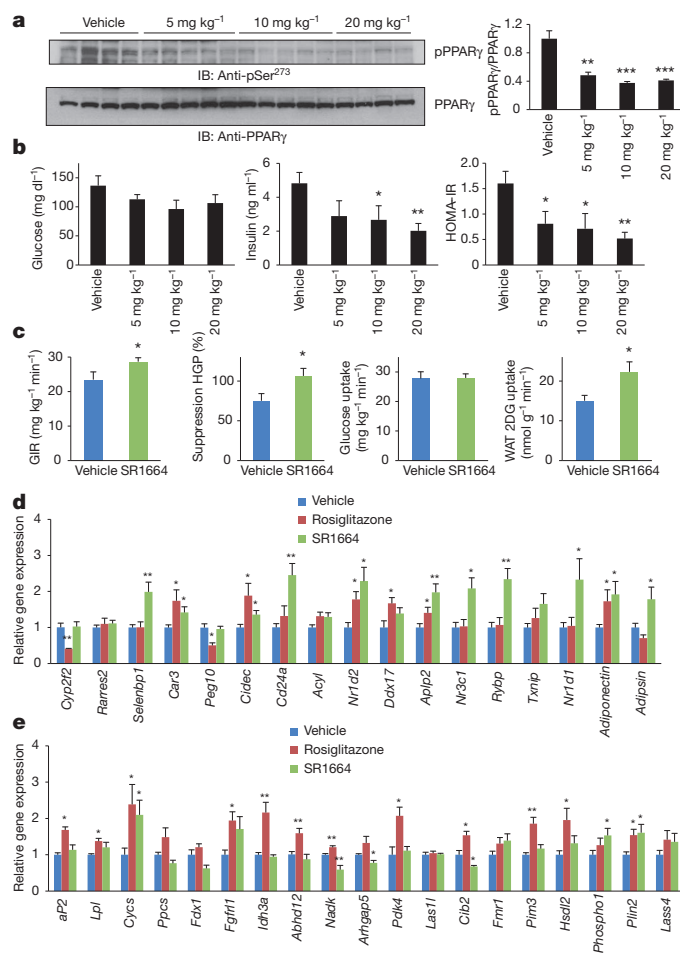


Figure 3 | Antidiabetic activity of SR1664 in high-fat diet (HFD) mice.

a, Dose-dependent inhibition of phosphorylation of PPAR γ by SR1664 in white adipose tissue (WAT). Quantification of PPAR γ phosphorylation compared to total PPAR γ (right). **b**, *Ad libitum*-fed glucose ($P = 0.062$ at 10 mg kg⁻¹), insulin and HOMA-IR in HFD mice. **c**, Glucose infusion rate (GIR), suppression of hepatic glucose production (HGP), whole body glucose disposal and WAT 2-deoxyglucose tracer uptake during hyperinsulinaemic-euglycaemic clamps. **d**, Expression of a gene set regulated by PPAR γ phosphorylation in WAT. **e**, Expression of an agonist gene set (see Methods) in WAT. Error bars are s.e.m.; * $P < 0.05$, ** $P < 0.01$.

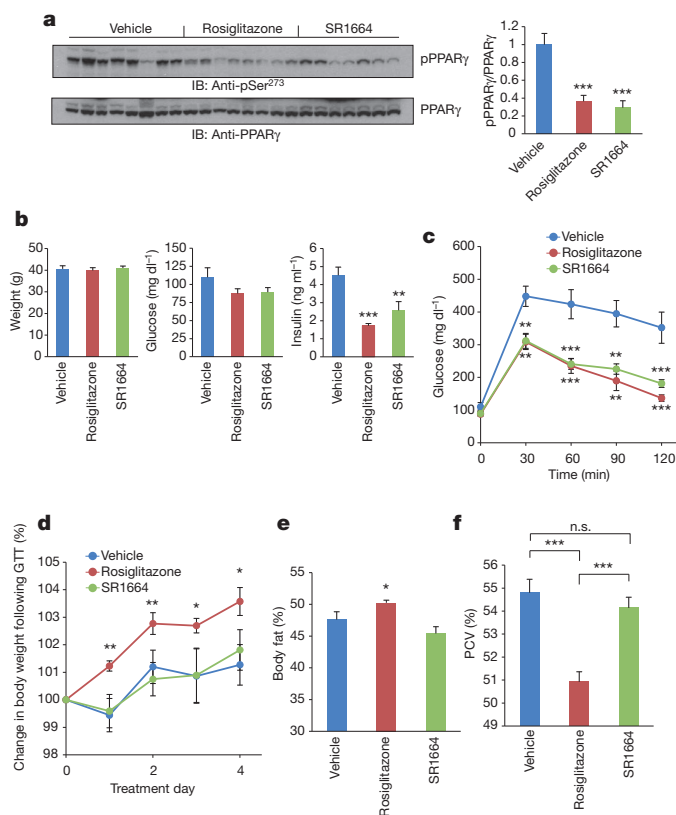


Figure 4 | SR1664 has potent antidiabetic activity and does not promote fluid retention in ob/ob mice. **a**, Phosphorylation of PPAR γ in WAT (left). Quantification of PPAR γ phosphorylation compared to total PPAR γ (right). **b**, **c**, Fasting body weight, blood glucose and insulin levels before glucose-tolerance tests (GTT) in ob/ob mice treated with vehicle, rosiglitazone or SR1664 ($n = 8$). Whole-body weight (**d**) and fat change (**e**) with continued drug administration following the GTT. **f**, Packed cell volume (PCV) in whole blood from ob/ob mice treated with vehicle, rosiglitazone or SR1664. Error bars are s.e.m.; * $P < 0.05$, ** $P < 0.01$, *** $P < 0.001$. n.s., not significant.

of insulin-resistance. Furthermore, this non-agonist does not stimulate two of the best documented side-effects of the PPAR γ agonist drugs *in vivo*.

The TZD class of drugs has been important for the treatment of type 2 diabetes²⁶. Whereas these drugs function as full agonists for PPAR γ , the role of agonism in their therapeutic effects has been called into question recently. Rosiglitazone and partial agonists like MRL24 both block the obesity-linked phosphorylation of PPAR γ at serine 273 (ref. 2). The tight correlation between inhibition of this phosphorylation and the therapeutic effects of these drugs in both mouse and man suggested that it might be possible to create new classes of non-agonist ligands for PPAR γ which are effective for the treatment of diabetes and cause fewer side effects. Hence, this paper addresses three key questions: first, is it possible to create novel PPAR γ ligands that block Cdk5-mediated PPAR γ phosphorylation yet have no classical agonism? Second, would such compounds have robust antidiabetic activity? Finally, would non-agonist compounds have fewer side effects than classical full agonists like rosiglitazone?

We show here that it is possible to create new ligands that have high affinity for PPAR γ , block the Cdk5-mediated phosphorylation and completely lack classical agonism. SR1664 does not function as an agonist and has no adipogenic action *in vitro*. The structural requirements for the non-agonist actions of SR1664 and SR1824 are particularly interesting. Ligands that function as classical full agonists, like rosiglitazone, have been shown to alter the conformation and HDX kinetics of H12, the major agonist helix. Surprisingly, ligands that do not affect the conformational dynamics of H12 are not non-agonists,

rather they seem to function as partial agonists^{18,21,27}. This strongly suggests that when engaged by ligands, other structural features of the AF2 surface such as H3, H3-H4 loops and the C-terminal end of H11 contribute to partial agonism of the receptor. As expected SR1664 and SR1824 do not interact with H12 in any detectable way, but unexpectedly both ligands cause an increase in the conformational mobility of H11, which is part of the AF2 surface and directly abuts H12. Hence, it seems likely that the destabilization of H11 distorts the AF2 surface enough to block partial agonism. Whether there are other alternative modes of ligand binding that would lead to a complete lack of classical agonism remains to be determined.

That classical agonism is not required for strong antidiabetic actions of a PPAR γ ligand is now clear. In both diet-induced and genetically obese animals, SR1664 has strong antidiabetic actions. The ability to improve adipose tissue insulin sensitivity is similar to the effects shown for rosiglitazone²⁸. SR1664 has inferior pharmacokinetic properties compared to rosiglitazone, so an absolute quantitative comparison of their efficacy is difficult. However, using our best calculations to get approximately equal exposure to the two drugs *in vivo*, SR1664 has very robust antidiabetic activity, roughly equivalent to rosiglitazone in the experiments shown here. The unfavourable pharmacokinetic properties of SR1664 strongly suggest that this compound will never be administered to patients but it proves that non-agonist compounds can have robust therapeutic effects.

Analysis of the side effects of PPAR γ ligands can be difficult because some of these (like cardiovascular disorders) do not occur in mice whereas others (like loss of bone mineral density) take many months of treatment to manifest. However, weight gain and fluid retention occur rapidly in both humans and mice. Increased body weight, increased accretion of fat tissues and increased fluid retention all occur in mice within 11 days of treatment with rosiglitazone (Fig. 4). The non-agonist SR1664 shows none of these side effects, even as it effectively improves glucose homeostasis. Unlike rosiglitazone, SR1664 does not affect bone cell mineralization in culture (Fig. 2c). Taken together, these data indicate that many of the known side effects of the TZD drugs occur as a consequence of classical agonism on target genes. Whether ligands directed at the Cdk5-mediated phosphorylation have their own problems remains to be determined. Still, these studies illustrate that the development of entirely new classes of PPAR γ -targeted drugs is feasible.

METHODS SUMMARY

Cell culture. Adipocyte differentiation in 3T3-L1 or PPAR γ -null mouse embryonic fibroblasts (MEFs) expressing PPAR γ ² was induced by treating cells with 1 μ M dexamethasone, 0.5 mM isobutylmethylxanthine, and 850 nM insulin for 48 h and cells were switched to the maintenance medium containing 850 nM insulin for 6 days.

Gene expression analysis. Total RNA was isolated from cells or tissues using TRIzol reagent (Invitrogen). The RNA was reverse-transcribed using ABI reverse transcription kit. Quantitative PCR (qPCR) reactions were performed with SYBR green fluorescent dye using an ABI9300 PCR machine. Relative mRNA expression was determined by the $\Delta\Delta$ -C_t method using TATA-binding protein (TBP) levels.

Animals. All animal experiments were performed according to procedures approved by Beth Israel Deaconess Medical Center's Institutional Animal Care and Use Committee. Male C57BL/6J and C57BL/6J-*Lep^{ob/ob}* mice (4- to 5-week-old) were obtained from the Jackson Laboratory. C57BL/6J mice were fed a high-fat, high-sucrose diet (60% kcal fat, D12492, Research Diets Inc.). For glucose tolerance tests, mice were injected intraperitoneally (i.p.) with rosiglitazone or SR1664 for 5 days, and fasted overnight before i.p. injection of 1 g kg⁻¹ D-glucose.

Full Methods and any associated references are available in the online version of the paper at www.nature.com/nature.

Received 16 May; accepted 22 July 2011.

Published online 4 September 2011.

- Lehmann, J. M. *et al.* An antidiabetic thiazolidinedione is a high affinity ligand for peroxisome proliferator-activated receptor γ (PPAR γ). *J. Biol. Chem.* **270**, 12953–12956 (1995).

2. Choi, J. H. *et al.* Anti-diabetic drugs inhibit obesity-linked phosphorylation of PPAR γ by Cdk5. *Nature* **466**, 451–456 (2010).
3. Tontonoz, P., Hu, E. & Spiegelman, B. M. Stimulation of adipogenesis in fibroblasts by PPAR γ 2, a lipid-activated transcription factor. *Cell* **79**, 1147–1156 (1994).
4. Willson, T. M., Lambert, M. H. & Kliewer, S. A. Peroxisome proliferator-activated receptor gamma and metabolic disease. *Annu. Rev. Biochem.* **70**, 341–367 (2001).
5. Forman, B. M. *et al.* 15-Deoxy- $\Delta^{12,14}$ -prostaglandin J_2 is a ligand for the adipocyte determination factor PPAR γ . *Cell* **83**, 803–812 (1995).
6. Henke, B. R. *et al.* *N*-(2-Benzoylphenyl)-L-tyrosine PPAR γ agonists. 1. Discovery of a novel series of potent antihyperglycemic and antihyperlipidemic agents. *J. Med. Chem.* **41**, 5020–5036 (1998).
7. Parulkar, A. A., Pendergrass, M. L., Granda-Ayala, R., Lee, T. R. & Fonseca, V. A. Nonhypoglycemic effects of thiazolidinediones. *Ann. Intern. Med.* **134**, 61–71 (2001).
8. Kahn, S. E. *et al.* Rosiglitazone-associated fractures in type 2 diabetes. *Diabetes Care* **31**, 845–851 (2008).
9. Nesto, R. W. *et al.* Thiazolidinedione use, fluid retention, and congestive heart failure: a consensus statement from the American Heart Association and American Diabetes Association. *Diabetes Care* **27**, 256–263 (2004).
10. Rocchi, S. *et al.* A unique PPAR γ ligand with potent insulin-sensitizing yet weak adipogenic activity. *Mol. Cell* **8**, 737–747 (2001).
11. Berger, J. P. *et al.* Distinct properties and advantages of a novel peroxisome proliferator-activated protein γ selective modulator. *Mol. Endocrinol.* **17**, 662–676 (2003).
12. Lamotte, Y. *et al.* Synthesis and biological activities of novel indole derivatives as potent and selective PPAR γ modulators. *Bioorg. Med. Chem. Lett.* **20**, 1399–1404 (2010).
13. Grana, X. *et al.* PITALRE, a nuclear CDC2-related protein kinase that phosphorylates the retinoblastoma protein *in vitro*. *Proc. Natl Acad. Sci. USA* **91**, 3834–3838 (1994).
14. Kliewer, S. A. *et al.* A prostaglandin J_2 metabolite binds peroxisome proliferator-activated receptor γ and promotes adipocyte differentiation. *Cell* **83**, 813–819 (1995).
15. Chawla, A., Schwarz, E. J., Dimaculangan, D. D. & Lazar, M. A. Peroxisome proliferator-activated receptor (PPAR) gamma: adipose-predominant expression and induction early in adipocyte differentiation. *Endocrinology* **135**, 798–800 (1994).
16. Grey, A. *et al.* The peroxisome proliferator-activated receptor-gamma agonist rosiglitazone decreases bone formation and bone mineral density in healthy postmenopausal women: a randomized, controlled trial. *J. Clin. Endocrinol. Metab.* **92**, 1305–1310 (2007).
17. Lecka-Czernik, B. *et al.* Inhibition of Osf2/Cbfa1 expression and terminal osteoblast differentiation by PPAR γ 2. *J. Cell. Biochem.* **74**, 357–371 (1999).
18. Bruning, J. B. *et al.* Partial agonists activate PPAR γ using a helix 12 independent mechanism. *Structure* **15**, 1258–1271 (2007).
19. Hamuro, Y. *et al.* Hydrogen/deuterium-exchange (H/D-Ex) of PPAR γ LBD in the presence of various modulators. *Protein Sci.* **15**, 1883–1892 (2006).
20. Nolte, R. T. *et al.* Ligand binding and co-activator assembly of the peroxisome proliferator-activated receptor- γ . *Nature* **395**, 137–143 (1998).
21. Chalmers, M. J., Busby, S. A., Pascal, B. D., Southern, M. R. & Griffin, P. R. A two-stage differential hydrogen deuterium exchange method for the rapid characterization of protein/ligand interactions. *J. Biomol. Tech.* **18**, 194–204 (2007).
22. DeFronzo, R. A., Tobin, J. D. & Andres, R. Glucose clamp technique: a method for quantifying insulin secretion and resistance. *Am. J. Physiol.* **237**, E214–E223 (1979).
23. Flier, J. S., Cook, K. S., Usher, P. & Spiegelman, B. M. Severely impaired adipisin expression in genetic and acquired obesity. *Science* **237**, 405–408 (1987).
24. Hu, E., Liang, P. & Spiegelman, B. M. AdipoQ is a novel adipose-specific gene dysregulated in obesity. *J. Biol. Chem.* **271**, 10697–10703 (1996).
25. Kahn, B. B. & McGraw, T. E. Rosiglitazone, PPAR γ , and type 2 diabetes. *N. Engl. J. Med.* **363**, 2667–2669 (2010).
26. Nolan, J. J., Ludvik, B., Beerdson, P., Joyce, M. & Olefsky, J. Improvement in glucose tolerance and insulin resistance in obese subjects treated with troglitazone. *N. Engl. J. Med.* **331**, 1188–1193 (1994).
27. Hamuro, Y. *et al.* Hydrogen/deuterium-exchange (H/D-Ex) of PPAR γ LBD in the presence of various modulators. *Protein Sci.* **15**, 1883–1892 (2006).
28. Mayerson, A. B. *et al.* The effects of rosiglitazone on insulin sensitivity, lipolysis, and hepatic and skeletal muscle triglyceride content in patients with type 2 diabetes. *Diabetes* **51**, 797–802 (2002).

Supplementary Information is linked to the online version of the paper at www.nature.com/nature.

Acknowledgements We are grateful for support from S. Novick for assistance in the HDX studies and from R. D. Garcia-Ordóñez in protein production and mutagenesis. We are grateful for support from B. Pascal and S. Willis for software analysing the HDX data. We are grateful to R. Gupta and P. Cohen for their critical comments on the manuscript. This work was supported in part by the Intramural Research Program of the National Institutes of Health (NIH), National Institute of Mental Health (grant U54-MH074404, H. Rosen principal investigator), the National Institute of General Medical Sciences (grant R01-GM084041, P.R.G.) and the National Institute of Diabetes and Digestive and Kidney Diseases (grant 1RC4DK090861, B.M.S.). This work also supported by NIH DK31405 to B.M.S.

Author Contributions B.M.S. and P.R.G. conceived the project and designed research; J.H.C., A.S.B., T.M.K., S.A.B., M.J.C., N.K., D.S.K., Y.S., Y.H., J.B.B., D.P.M., M.D.C., D.L., M.J.J., S.C.S., and D.V. performed research; J.H.C., A.S.B., T.M.K., S.A.B., M.J.C., N.K., D.K., J.B.B., D.M., M.D.C., D.L., M.J.J., S.C.S., D.V., G.I.S., B.M.S. and P.R.G. analysed data; and B.M.S., A.S.B. and P.R.G. wrote the paper with contributions from all authors.

Author Information Reprints and permissions information is available at www.nature.com/reprints. The authors declare no competing financial interests. Readers are welcome to comment on the online version of this article at www.nature.com/nature. Correspondence and requests for materials should be addressed to B.M.S. (bruce_spiegelman@dfci.harvard.edu) or P.R.G. (pgriffin@scripps.edu).

METHODS

SR1664. (S)-4'-((5-((1-(4-nitrophenyl)ethyl)carbamoyl)-1H-indol-1-yl)methyl)-[1,1'-biphenyl]-2-carboxylic acid. Commercially available ethyl 2,3-dimethyl-1H-indole-5-carboxylate was *N*-alkylated with commercially available *tert*-butyl 4'-(bromomethyl)biphenyl-2-carboxylate using NaH in DMF. The corresponding ethyl ester was hydrolysed using aqueous NaOH in ethanol to give the acid, which was coupled to (S)-1-(4-nitrophenyl)ethanamine using 2-(3H-[1,2,3]triazolo [4,5-*b*]pyridin-3-yl)-1,1,3,3-tetramethylisouronium hexafluorophosphate(V) (HATU) and diisopropylethylamine in CH₂Cl₂ to give the amide. Final deprotection of the *tert*-butyl ester using 30% trifluoroacetic acid in CH₂Cl₂ and purification by flash chromatography (ethyl acetate/hexanes 10–100%) afforded SR1664. Electrospray ionisation coupled with mass spectrometry (ESI-MS; *m/z*): 576 [M+H]⁺; ¹H NMR (400 MHz, dimethylsulphoxide (DMSO)-*d*₆): δ (p.p.m.) 8.83 (d, *J* = 7.6 Hz, 1H), 8.25 (m, 1H), 8.16 (d, *J* = 1.2 Hz, 1H), 7.74–7.68 (m, 4H), 7.57 (dt, *J* = 1.6, 7.2 Hz, 1H), 7.51 (d, *J* = 8.4 Hz, 1H), 7.46 (dt, *J* = 1.2, 7.2 Hz, 1H), 7.36 (dd, *J* = 0.8, 7.6 Hz, 1H), 7.28 (m, 2H), 7.03 (m, 2H), 5.52 (s, 2H), 5.32 (quint, *J* = 7.2 Hz, 1H), 2.36 (s, 3H), 2.34 (s, 3H), 1.57 (d, *J* = 6.8 Hz, 3H); ¹³C NMR (400 MHz, DMSO-*d*₆): δ (p.p.m.) 170.5, 167.9, 154.5, 147.2, 141.5, 140.7, 138.7, 138.2, 135.1, 133.2, 131.8, 131.5, 130.0, 129.6, 128.6, 128.2, 128.1, 126.8, 125.8, 124.4, 121.4, 118.8, 109.7, 108.3, 49.4, 46.7, 22.9, 11.0, 9.7.

SR1824. (S)-4'-((5-((1-(4-bromophenyl)ethyl)carbamoyl)-2,3-dimethyl-1H-indol-1-yl)methyl)biphenyl-2-carboxylic acid (1824) was synthesized in the same manner using (S)-1-(4-bromophenyl)ethanamine. ESI-MS (*m/z*): 581/583 [M+H]⁺; ¹H NMR (400 MHz, DMSO-*d*₆): δ (p.p.m.) 1.48 (d, *J* = 6.8 Hz, 3H, CH₃ (4-bromophenyl)ethylcarbamoyl), 2.28 (s, 3H, CH₃ indole), 2.32 (s, 3H, CH₃ indole), 5.17 (quintuplet, *J* = 7.6 Hz, 1H, CH (4-bromophenyl)ethylcarbamoyl), 5.47 (s, 2H, CH₂-biphenyl), 6.99 (d, *J* = 8 Hz, 2H, H₇ and H₉ biphenyl), 7.24 (d, *J* = 8 Hz, 2H, H₆ and H₁₀ biphenyl), 7.31 (d, *J* = 7.6 Hz, 1H, H₇ indole), 7.36–7.55 (m, 7H, H₂, H₃ and H₄ biphenyl, H₆ indole and H 4-bromophenyl), 8.10 (d, *J* = 1.6 Hz, 1H, H₄ indole), 8.65 (d, *J* = 8 Hz, 1H, NH amide). ¹³C NMR (400 MHz, DMSO-*d*₆): δ (p.p.m.) 169.5, 166.7, 144.9, 140.5, 139.7, 137.6, 137.3, 134.0, 132.2, 131.0, 130.8, 130.4, 129.0, 128.6, 128.4, 127.6, 127.2, 125.9, 125.0, 120.3, 119.4, 117.7, 108.7, 107.3, 47.9, 45.7, 22.1, 10.1, 8.6.

Cell culture. COS-1, 3T3-L1 and HEK-293 cells were obtained from ATCC. Adipocyte differentiation in 3T3-L1 or PPARγ-null mouse embryonic fibroblasts (MEFs) expressing PPARγ² was induced by treating cells with 1 μM dexamethasone, 0.5 mM isobutylmethylxanthine, and 850 nM insulin with 10% FBS in DMEM for 48 h and cells were switched to the maintenance medium containing 10% FBS and 850 nM insulin. Lipid accumulation in the cells was detected by Oil Red O staining. All chemicals for cell culture were obtained from Sigma unless otherwise indicated.

In vitro kinase assay. Active Cdk5/p35 was purchased from Millipore. *In vitro* CDK kinase assay was performed according to the manufacturer's instructions (Cell Signaling Technology). Purified PPARγ (0.5 μg; Cayman Chemicals) were incubated with active CDK kinase in assay buffer (25 mM Tris-HCl pH 7.5, 5 mM beta-glycerophosphate, 2 mM dithiothreitol (DTT), 0.1 mM Na₃VO₄, 10 mM MgCl₂) containing 20 μM ATP for 15 min at 30 °C. PPARγ ligands were pre-incubated with the specified substrates for 30 min before the assay was performed. Rb (Cell Signaling Technology) was used as a positive control.

LanthaScreen. PPARγ competitive binding assay (Invitrogen) was performed according to the manufacturer's protocol. A mixture of 5 nM glutathione S-transferase fused with the PPARγ ligand binding domain (GST-PPARγ-LBD), 5 nM Tb-GST-antibody, 5 nM Fluormone Pan-PPAR Green, and serial dilutions of SR1664 beginning at 10 μM downwards was added to wells of black 384-well low-volume plates (Greiner) to a total volume of 18 μl. All dilutions were made in TR-FRET assay buffer C. DMSO at 2% final concentration was used as a no-ligand control. Experiments were performed in triplicate and incubated for 2 h in the dark before analysis in Perkin Elmer ViewLux ultra HTS microplate reader. The FRET signal was measured by excitation at 340 nm and emission at 520 nm for fluorescein and 490 nm for terbium. The fold change over DMSO was calculated by 520 nm/490 nm ratio. Graphs were plotted as fold change of FRET signal for each compound over DMSO-only control.

Cell-based transactivation assay. COS-1 cells were cotransfected in batch by adding 4.5 μg full-length murine PPARγ2-pSV Sport or full-length human PPARγ2-pSport6, with 4.5 μg 3× multimerized pPRE-luciferase reporter and 27 μl X-treme Gene 9 transfection reagent in serum-free Opti-mem reduced serum media (Gibco). After 18-h incubation at 37 °C in a 5% CO₂ incubator, transfected cells were plated in triplicate in white 384-well plates (Perkin Elmer) at a density of 10,000 cells per well. After replating, cells were treated with either DMSO vehicle only or the indicated compounds in increasing doses from 2 pM–10 μM for mouse receptor or 220 pM–2 μM for the human receptor. After 18-h incubation, treated cells were developed with Brite Lite Plus (Perkin Elmer) and read in 384-well Luminescence Perkin Elmer EnVision Multilabel plate reader. Graphs were plotted in triplicate as fold change of treated cells over DMSO-treated control cells.

Ensemble docking. PPARγ co-crystal structures (68 in total) with unique ligands were identified in the Protein Data Bank (PDB) (as of 3 January 2011). Four structures were selected based on the maximum similarity of the co-crystal ligands to SR1664; specifically 3kmg (ligand 538, 0.98 similarity), 2hfp (ligand NSI, similarity of 0.91), 1fm9 (ligand 570, 0.90 similarity), 2pob (ligand GW4, 0.88 similarity). SR1664 was prepared using Schrodinger LigPrep generating tautomers and ionization states (pH range 7 ± 2). Flexible ligand docking of SR1664 against the four structures was performed using Schrodinger Glide. At least one of the two constraints Arg 288 and Ser 342 (Arg 316 and Ser 370 in PPARγ²) was required to score docking poses. The best docking score (Glide docking scores are meant to correspond to binding affinity) of −9.21 was achieved with the PPARγ structure 2hfp and SR1664 forms a hydrogen bond to Ser 342 (shown in Fig. 2). Unconstrained docking produced almost the same docking pose with the preserved hydrogen bonding to Ser 342 and a slightly less favourable docking score of −8.99 indicating Ser 342 as a critical ligand binding element.

Differentiation of MC3T3-E1. After reaching confluence, cells were grown in α-MEM supplemented with 10% FBS, 1% penicillin-streptomycin, 200 μM ascorbic acid and 10 mM β-glycerophosphate. The cells were treated with either rosiglitazone (10 μM) or SR1664 (10 μM) or left in vehicle at the start of differentiation. The cells were collected 7 days post-differentiation for gene expression analysis and 21 days post-differentiation for mineralization. The mineralization of MC3T3-E1 cells was determined by Alizarin red S staining (Millipore catalogue no. ECM815) as per manufacturer's instructions.

Preparation of cell or tissue lysates and immunoblotting. Differentiated adipocytes were pre-treated with PPARγ ligands for 45 min, and incubated with TNF-α for 30 min. For tissue lysates, WAT from mice was homogenized in RIPA buffer (50 mM Tris pH 7.5, 150 mM NaCl, 1% NP-40, 0.5% sodium deoxycholate, 0.1% SDS with protease and phosphatase inhibitors). For western blotting, a phospho-specific antibody against PPARγ Ser 273 was used². Total tissue lysates were analysed with an anti-PPARγ antibody (Santa Cruz).

Gene expression analysis. Total RNA was isolated from cells or tissues using TRIzol reagent (Invitrogen). The RNA was reverse-transcribed using the ABI reverse transcription kit. Quantitative PCR reactions were performed with SYBR green fluorescent dye using an ABI9300 PCR machine. Relative mRNA expression was determined by the ΔΔ-*C_t* method normalized to TATA-binding protein (TBP) levels. The sequences of primers used in this study are found in Supplementary Table 1.

ChIP. Differentiated 3T3-L1 adipocytes were treated on day 6 with 1 μM of compounds or vehicle for 24 h. The samples were prepared using manufacturer's protocol (ChampionChIP One-Day Kit, Qiagen). Briefly, cross-linked chromatin was sonicated and 5 μg of antibody was used to immunoprecipitate the pre-cleared samples. The following antibodies were used: normal rabbit IgG, PPARγ (Santa Cruz), SRC-1 (Abcam). The promoter region of aP2 for PPAR-γ binding was amplified using PCR with reverse transcription (RT-PCR). The primers used for aP2 were aP2 forward 5'-AAATTCAGAAGAAAGTAAACACATTATT-3'; aP2 reverse 5'-ATGCCCTGACCATGTGA-3'.

Gene sets from microarray. We performed a microarray with total RNA isolated from PPARγ-null fibroblasts expressing wild-type or S273A mutant of PPARγ or WT cells treated with 1 μM rosiglitazone for 24 h (ref. 2). To create refined gene sets regulated by phosphorylation of PPARγ or rosiglitazone, we first calculated *P*-values as well as fold-change of gene expression in wild-type versus S273A mutant cells or wild-type versus wild-type/Rosiglitazone cells, and we plotted −log *P*-value versus log₂ fold-change. From this list of genes, we selected genes which were changed in magnitude (≥1.4 fold difference) and statistical significance (*P* < 0.05). The selected genes were validated in cells by using qPCR, the resulting gene sets (phosphorylation-dependent or agonist-dependent gene sets) were analysed in WAT of mice using qPCR.

Animals. All animal experiments were performed according to procedures approved by Beth Israel Deaconess Medical Center's Institutional Animal Care and Use Committee. Male C57BL/6J or C57BL/6J-*Lep^{ob/ob}* mice (4- to 5-week-old) were obtained from the Jackson Laboratory. C57BL/6J mice were fed a regular diet (10% kcal fat, D12450B, Research Diets Inc.) or a high-fat, high-sugar diet (60% kcal fat, D12492, Research Diets Inc.) for either 8, 10 or 18 weeks. The mice were intraperitoneally (i.p.) injected twice daily with 4 mg kg^{−1} rosiglitazone or 20 mg kg^{−1} SR1664 for 6 days before gene expression analysis or hyperinsulinaemic-euglycaemic clamp experiments. Clamps were performed essentially as previously described with one exception to the standard protocol²⁹. As the mice were fed a high-fat diet for 8 weeks before the clamp studies, a higher insulin infusion rate of 4 mU (kg-min)^{−1} was used instead of the typical 3 mU (kg-min)^{−1} for standard chow studies. For glucose tolerance tests, 6-week-old male C57BL/6J-*Lep^{ob/ob}* mice were i.p. injected twice daily with 8 mg kg^{−1} rosiglitazone or 40 mg kg^{−1} SR1664 for 6 days, and fasted overnight before i.p. injection of 1 g kg^{−1} D-glucose. Glucose was measured by tail vein bleeds at the indicated intervals using a TruTrack

- glucometer. Serum insulin concentrations were determined by ELISA (Crystal Chem).
29. Kim, H. J. *et al.* Differential effects of interleukin-6 and -10 on skeletal muscle and liver insulin action *in vivo*. *Diabetes* **53**, 1060–1067 (2004).

Polyamine sensing by nascent ornithine decarboxylase antizyme stimulates decoding of its mRNA

Leo Kurian^{1†*}, R. Palanimurugan^{1*}, Daniela Gödderz^{1†} & R. Jürgen Dohmen¹

Polyamines are essential organic polycations with multiple cellular functions relevant for cell division, cancer and ageing^{1–3}. Regulation of polyamine synthesis is mainly achieved by controlling the activity of ornithine decarboxylase (ODC) through an unusual mechanism involving ODC antizyme^{1,4}, the binding of which disrupts homodimeric ODC and targets it for ubiquitin-independent degradation by the 26S proteasome⁵. Whereas mammals express several antizyme genes⁶, we have identified a single orthologue, termed *OAZ1*, in *Saccharomyces cerevisiae*⁷. Similar to its mammalian counterparts, *OAZ1* synthesis is induced with rising intracellular polyamine concentrations, which also inhibit ubiquitin-dependent degradation of the *OAZ1* protein⁷. Together, these mechanisms contribute to a homeostatic feedback regulation of polyamines^{1,7,8}. Antizyme synthesis involves a conserved +1 ribosomal frameshifting (RFS) event at an internal STOP codon during decoding of its messenger RNA^{6–10}. Here we used *S. cerevisiae OAZ1* to dissect the enigmatic mechanism underlying polyamine regulation of RFS. In contrast with previous assumptions, we report here that the nascent antizyme polypeptide is the relevant polyamine sensor that operates *in cis* to negatively regulate upstream RFS on the polysomes, where its own mRNA is being translated. At low polyamine levels, the emerging antizyme polypeptide inhibits completion of its synthesis causing a ribosome pile-up on antizyme mRNA, whereas polyamine binding to nascent antizyme promotes completion of its synthesis. Thus, our study reveals a novel autoregulatory mechanism, in which binding of a small metabolite to a nascent sensor protein stimulates the latter's synthesis co-translationally.

Our dissection of the elements controlling decoding of *OAZ1* mRNA involving RFS shows that it is negatively regulated within a polyribosome unit by nascent *OAZ1* polypeptide, which serves as the sensor of polyamines in this system (Supplementary Fig. 1). To identify the elements in *OAZ1* mRNA important for polyamine regulation of RFS, we generated constructs that either carried the authentic RFS site bearing a TGA codon or a deletion of a T nucleotide in this STOP codon, yielding an in-frame fusion (Fig. 1)⁷. Expression of all constructs was monitored in a mutant impaired in proteasomal activity to minimize effects of polyamines or the truncations on the stability of *OAZ1* (refs 7 and 11). Polyamine levels and truncations had no significant effects on the abundance of *OAZ1* transcripts (Supplementary Fig. 2). Quantitative western blot analyses were performed to determine 'relative RFS efficiency' by comparing levels for the constructs carrying the RFS site to those of the corresponding in-frame controls. In the absence of added polyamines, the wild-type RFS construct yielded approximately 3% RFS efficiency (Fig. 1a). Addition of 10 μ M or higher concentrations of the polyamine spermidine to the growth media had no detectable effect on the in-frame control but led to a ~fourfold induction (~13% RFS efficiency) for the RFS construct (Fig. 1a and Supplementary Fig. 3).

Truncations at the 5' end of the *OAZ1* coding sequence had marked effects, yielding RFS efficiencies up to approximately 62%, with a

gradual loss of polyamine regulation. These observations indicated that translation of *OAZ1* mRNA bearing the RFS site is inhibited by sequences close to its 5' end (Fig. 1a). A different scenario was observed for the 3' end of *OAZ1* mRNA, where deletions of 57 or more nucleotides resulted in a complete loss of polyamine regulation (Fig. 1b). In contrast to the 5' deletions, however, the 3' deletions caused RFS rates (~20%) that were only moderately higher than those of spermidine-induced wild-type *OAZ1* (~13%). These findings demonstrated that a segment of the *OAZ1* mRNA downstream of the RFS site is essential for negative regulation at low polyamine levels. Next, we asked whether the effects observed for 5' or 3' truncations were synthetic or epistatic. We observed a loss of polyamine regulation of all constructs bearing deletions at the 5' end when combined with 3' Δ 150. Both in the absence or presence of externally applied polyamines, RFS rates detected for all of these constructs were remarkably high (~65%), indicating that 5' and 3' truncations had a synthetic effect in eliminating negative regulation of RFS (Fig. 1c). Together these experiments surprisingly revealed that RFS during decoding of *OAZ1* is strongly inhibited by *OAZ1* elements 5' and 3' to the RFS site, both of which are also required to sense polyamines.

To test whether the element provided by the 5' portion of *OAZ1* is an mRNA secondary structure motif, silent mutations were introduced at all possible positions within the first 24 or 51 nucleotides of the *OAZ1* coding sequence. These mutations had no effects on RFS, indicating that mRNA structure motifs in this area are not relevant for polyamine sensing (Supplementary Fig. 4a). To investigate whether instead the encoded polypeptide is mediating the regulation, we caused drastic changes to the polypeptide sequence close to the amino terminus by introducing two frameshift mutations (Fig. 2a). Despite the only small changes to the mRNA sequence, this 'shift of frames' variant (5'SF) had completely lost negative regulation of RFS in the absence of spermidine, indicating that the coding capacity rather than the mRNA structure of the 5' portion of *OAZ1* mRNA is critical for the observed inhibition of RFS. This notion was further supported by an *OAZ1* mutant that showed constitutive inhibition of RFS unresponsive to the addition of polyamines (Supplementary Fig. 5). The underlying mutation was a change of an Ile (I) codon at position 5 to a Phe (F) codon (I5F). Inhibition of RFS was obtained with both Phe codons tested, whereas all other permutations of codon 5 yielding Ile or Leu codons had no effect, showing that the relevant parameter is the encoded amino acid residue rather than specificity for a certain transfer RNA. Together, these findings led to the unexpected conclusion that the *OAZ1* N terminus mediates a negative control of RFS during decoding of *OAZ1* mRNA.

Next we asked whether the N-terminal inhibitory element of *OAZ1* could act independently of the polyamine-regulated element that depends on sequences downstream of the RFS site. Therefore, we generated a set of constructs, in which *OAZ1* variants extending only until 30 nucleotides downstream of the RFS site were fused to the mouse *Dhfr* open reading frame (ORF) (Fig. 2b). The much lower

¹Institute for Genetics, University of Cologne, Cologne Biocenter, Zùlpicher Strasse 47a, D-50674 Cologne, Germany. [†]Present addresses: Salk Institute for Biological Studies, 10010 North Torrey Pines Road, La Jolla, California 92037-1099, USA (L.K.); Department for Cell and Molecular Biology, Karolinska Institutet, Von Eulers väg 3, S-17177 Stockholm, Sweden (D.G.).

*These authors contributed equally to this work.

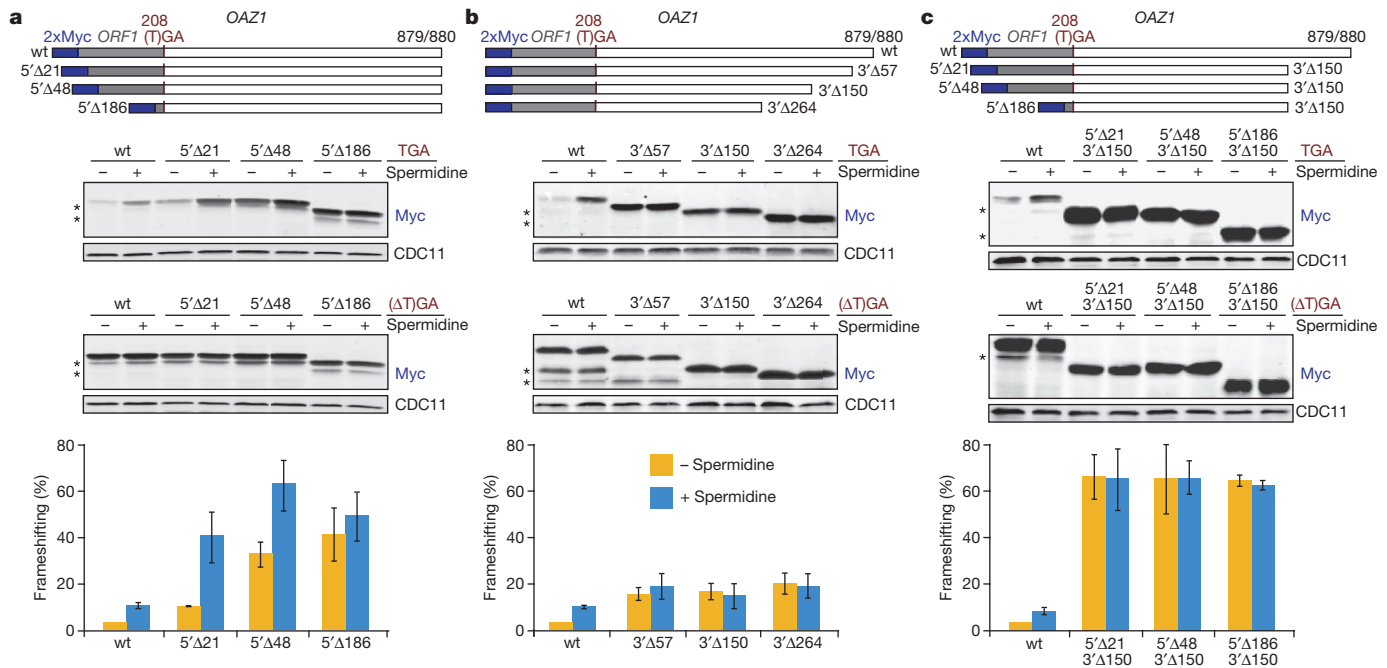


Figure 1 | Mapping of elements in *OAZ1* that regulate its decoding.

a, Analysis of the effects of *OAZ1* 5' truncations. Top, schematic representation of constructs used, all of which encoded 2×Myc-tagged *OAZ1* variants. Truncations were introduced at the 5' end removing the indicated number of nucleotides starting from the ATG start codon. Two versions of each construct were generated, one that contained the RFS site with the TGA STOP codon, and one in-frame control construct, in which the first nucleotide of this codon was deleted. Middle, western blot analysis of Myc–*OAZ1* levels in yeast *pre1-1* cells expressing constructs either with RFS site ("TGA") or without ("(ΔT)GA"). Bottom, relative RFS efficiencies (% *OAZ1* protein obtained with a construct bearing the RFS site relative to the corresponding in-frame control) calculated from quantification of western blot signals. wt, wild type. **b**, As in panel **a**, but with 3' truncated *OAZ1* constructs. **c**, As in panel **a**, but with *OAZ1* constructs combining the indicated 5' and 3' truncations. See also Supplementary Fig. 1 for an RT–PCR analysis of selected constructs. Error bars, s.d.; $n = 3$.

RFS rates obtained for the construct bearing an intact *ORF1* in comparison to the corresponding 5'Δ48 and 5'SF constructs demonstrated that the N-terminal element is a strong inhibitor of RFS even in the absence of the sequence 3' of the RFS site. This notion was further supported by the observation that the I5F mutation caused an even lower RFS rate in this context. These results therefore clearly demonstrated that the N-terminal inhibitory element can operate independently of the 3' element, and that it is not directly regulated by polyamines. Whereas the exact mechanism by which the N terminus of nascent *OAZ1* inhibits RFS remains to be explored, it is in line with an increasing number of examples of nascent polypeptides that inhibit their own synthesis¹² (see also Supplementary Discussion).

To characterize the polyamine-regulated element, which depends on sequence downstream of the RFS site, we used strategies analogous to the ones applied for the characterization of the upstream element. Whereas silent mutations affecting the 3' end of the *OAZ1* ORF had no effect on RFS (Supplementary Fig. 4b), a mutant version, in which the C-terminal eight amino acids are changed by two frameshift mutations, yielded constitutive RFS similar to constructs bearing carboxy-terminal truncations (Fig. 2a). These observations led us to the striking conclusion that the polyamine-regulated element also resides in the nascent polypeptide. To determine how close to the end of the *OAZ1* ORF this element is located, we individually mutated its last four codons to STOP codons (Fig. 3a). Whereas mutation of the last two codons had no effect on the decoding efficiency, mutating the third (9stop) or the fourth (12stop) codon from the C terminus resulted in constitutive RFS. These results indicated that residues very close to the *OAZ1* C terminus are critically important for the function of the polyamine-responsive element. Perturbation of this element results in constitutive RFS with an efficiency that is only slightly higher than that of wild-type *OAZ1* upon polyamine induction. We note that drastic depletion of cellular polyamines leads to a reduction in translation

grown either in the absence or presence of 10 μM spermidine. CDC11 was simultaneously detected as a loading control. *OAZ1* degradation products are indicated by asterisks. Bottom, relative RFS efficiencies (% *OAZ1* protein obtained with a construct bearing the RFS site relative to the corresponding in-frame control) calculated from quantification of western blot signals. wt, wild type. **b**, As in panel **a**, but with 3' truncated *OAZ1* constructs. **c**, As in panel **a**, but with *OAZ1* constructs combining the indicated 5' and 3' truncations. See also Supplementary Fig. 1 for an RT–PCR analysis of selected constructs. Error bars, s.d.; $n = 3$.

and RFS also for *OAZ1* constructs lacking these elements, indicating that translation across the RFS site shows an additional sensitivity to very low concentrations of polyamines (see Supplementary Discussion).

The experiments described so far revealed the remarkable finding that RFS during decoding of *OAZ1* mRNA is under negative control by distinct elements within the *OAZ1* polypeptide. Their inactivation resulted in an up to 20-fold increase of RFS at low polyamine levels (Fig. 1c). The observation that residues very close to the C terminus of *OAZ1* polypeptide are required for an inhibitory effect on decoding of the *OAZ1* mRNA was surprising because this sequence emerges from the ribosome only after the RFS event. This raised the possibility that the *OAZ1* polypeptide influences *OAZ1* decoding *in trans*, that is, after its release from the ribosome. Co-expression of an *OAZ1* in-frame construct, however, had no effect on the decoding of an RFS reporter construct demonstrating that *OAZ1* protein does not inhibit RFS *in trans* (Supplementary Fig. 6). These results indicated that the elements residing in the nascent *OAZ1* polypeptide inhibit RFS *in cis* within the context of an *OAZ1* mRNA–polyribosome complex. To determine whether there is a correlation of the association of nascent *OAZ1* polypeptides with ribosomes and the efficiency of RFS, ribosomal complexes were affinity-purified from a strain bearing a Flag-tagged version of ribosomal subunit RPL25 (ref. 13). Strikingly, higher levels of incompletely synthesized Myc–*OAZ1* polypeptides of various sizes were associated with ribosomes in cells grown in the absence of polyamines than in those grown in their presence (Fig. 3b). This result illustrated that polyamine induction of RFS promotes completion of *OAZ1* synthesis and its release from the ribosomes. Consistent with this notion, either high or low levels of *OAZ1* peptides were pulled down with ribosomes, respectively, when mutants were used that either repressed or induced RFS constitutively (I5F or cRFS, respectively, in Fig. 3b). We conclude that inhibition of RFS results in a

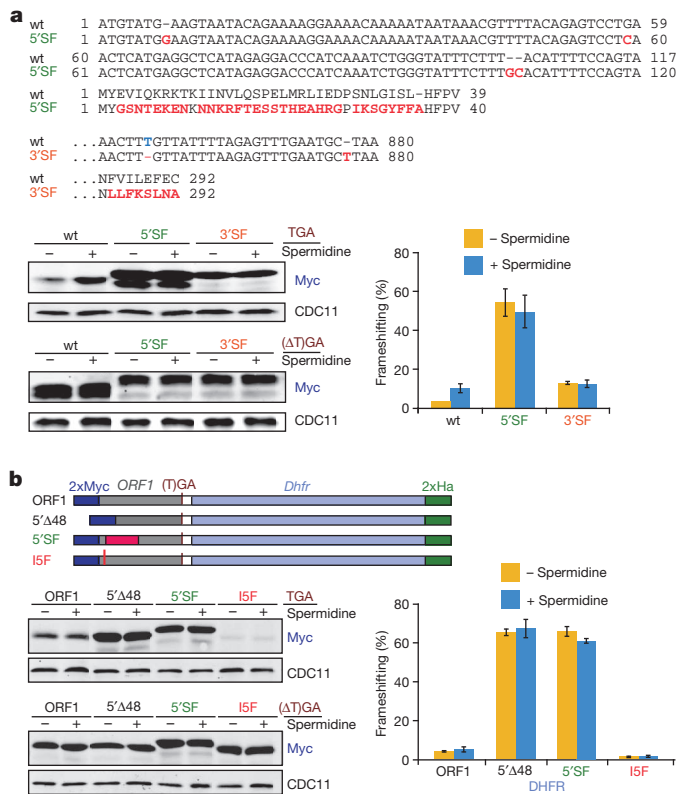


Figure 2 | Two elements in OAZ1 polypeptide affect decoding of OAZ1 mRNA. **a**, Depicted are alignments of wild-type OAZ1 with mutant variants carrying nucleotide insertions or deletions (marked in red) to switch reading frames, the corresponding encoded polypeptide sequences, a western blot analysis of Myc-OAZ1 levels derived from these constructs, and quantification of data. SF, shift of frames variant. **b**, Mutations at the N terminus of the OAZ1 polypeptide strongly affect RFS independent of the downstream element. Top, schematic representation of constructs, in which ORF1 sequence followed by 30 nucleotides of OAZ1 was fused to mouse Dhfr. Ha, haemagglutinin tag. Below, western blot analysis of DHFR fusion protein levels and their quantification. Mutations correspond to those introduced into full-length OAZ1 shown in Fig. 1a, Supplementary Fig. 5, or in (a). Error bars, s.d.; $n = 3$.

stalling of ribosomes on OAZ1 mRNA, whereas induction of RFS coincides with a release of full-length OAZ1. The electrophoretic mobility of the detected nascent OAZ1 polypeptides indicated that a significant fraction of them was associated with ribosomes that had already traversed the RFS site. This finding suggested that ribosomes with nascent OAZ1 polypeptides pile up on a fraction of OAZ1 mRNAs at low polyamine concentrations. This is consistent with the observation that a polyamine-regulated element extending close to the C terminus of the OAZ1 protein operates *in cis* within a translation unit and that low polyamine levels resulted in increased relative levels of OAZ1 mRNA in fractions with larger polysomes (Supplementary Fig. 7).

Another noteworthy aspect is that we found low levels of OAZ1 polypeptides in association with ribosomes when the in-frame OAZ1 construct lacking the RFS site was used, whether polyamines were added to the media or not (Fig. 3b). One plausible explanation for the lack of any polyamine effect on this construct is that the responsive element initially requires a certain distance between ribosomes to acquire its inhibitory function on the completion of OAZ1 translation. In this hypothesis, the RFS site causes a pause in translation leading to a spacing of ribosomes sufficient for formation of the inhibitory element. Efficient translation of the in-frame construct, in contrast, would lead to a ribosome density unfavourable for formation of this element. If so, the inhibitory element should also be activated during decoding of the in-frame construct when ribosome density is reduced

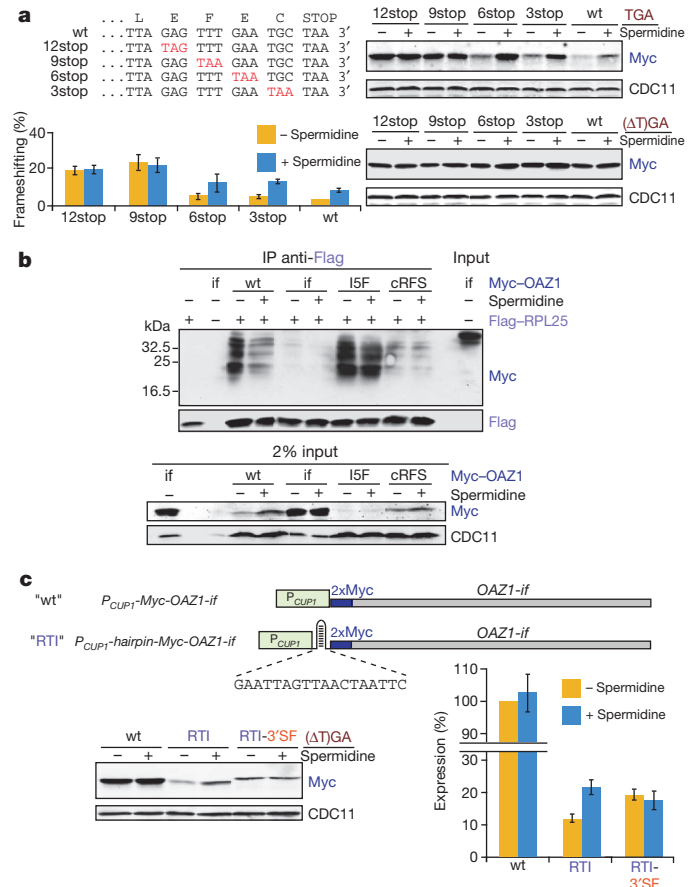


Figure 3 | Nascent OAZ1 polypeptide confers polyamine-regulated inhibition of its own mRNA decoding by causing ribosome pile-up. **a**, Truncation of OAZ1 by as little as three residues from the C terminus abolishes polyamine regulation of OAZ1 decoding. Left, alignment of wild-type OAZ1 with variants carrying nonsense mutations (in red) shortening the 3' end by 1–4 codons. Right and below, western blot analysis and quantification. **b**, Nascent OAZ1 polypeptides accumulate on ribosomes in the absence of polyamines. Ribosome pull-down assays were performed with a strain bearing a tagged ribosomal subunit (Flag-RPL25). Cells either expressed wild-type OAZ1, its in-frame (if) variant, the I5F mutant, or a version carrying a frameshift mutation near the 3' end (leading to a change of the last four residues and a C-terminal extension of 16 residues) that causes constitutive RFS (cRFS). Extracts from cells grown either in the absence or presence of spermidine were subjected to anti-Flag pull-down followed by a western blot analysis comparing co-precipitated Myc-OAZ1 polypeptides. An extract with full-length OAZ1 (input) was loaded for comparison. The lower panel shows the analysis of the extracts used as starting material. IP, immunoprecipitation. **c**, Reduced translation initiation (RTI) rates promote formation of the polyamine-regulated inhibitory element during translation of an in-frame version of OAZ1. RTI was achieved by insertion of a sequence expected to form a hairpin in front of the START codon. The RTI-3'SF construct (not depicted), in addition, carried the frameshift mutations shown in Fig. 2a. Below the constructs, a western blot analysis of crude extracts and quantification of OAZ1 levels are shown. OAZ1 levels are given relative to those for the wild-type OAZ1-if construct in the absence of spermidine, which was set to 100%. Error bars, s.d.; $n = 3$.

by lowering the rate of translation initiation¹⁴. To test this prediction, we inserted a nucleotide sequence expected to form an mRNA hairpin structure between the promoter and the translation initiation codon of the OAZ1 in-frame construct (Fig. 3c). Similar structures have been demonstrated to cause strongly reduced translation initiation (RTI) rates¹⁵. In the absence of polyamines, we observed a reduction of OAZ1 levels to approximately 10% in cells expressing the RTI construct compared to the levels obtained with the otherwise identical wild-type construct lacking the hairpin. Remarkably, however, when spermidine

was added to the cultures, OAZ1 levels obtained with the RTI construct were induced approximately twofold, whereas levels remained unchanged for the wild-type construct. Introduction of the 3' SF mutation described above, which impairs the polyamine-responsive element, also resulted in a loss of polyamine regulation of the RTI in-frame construct, with OAZ1 levels in the absence of polyamines rising to those observed in their presence (Fig. 3c). We conclude that the same element in nascent OAZ1 is conferring polyamine regulation to the RFS reporter and the RTI in-frame construct. When polyamine concentration is low, this element, which requires a relatively low ribosome density, can therefore either be activated by translational pausing caused by the RFS site or, even though not with full efficiency, by reduced translation initiation rates (see also Supplementary discussion).

Our observation that regulation of RFS during OAZ1 decoding involves the nascent OAZ1 peptide prompted us to ask whether the OAZ1 protein senses polyamines directly. We previously observed that high polyamine levels inhibit ubiquitin-dependent degradation of OAZ1 protein. It was also noted that OAZ1 has homology to the polyamine-binding enzyme spermidine/spermine-acetyltransferase (SSAT)⁷, which was supported by structural similarity between antizyme and acetyltransferases, including SSAT¹⁶. To test for polyamine binding to OAZ1, we developed a filtration-based assay using 6His-OAZ1 purified from *Escherichia coli* and radiolabelled spermidine or spermine. 6His-OAZ1 was incubated at approximately equimolar concentration together with polyamines followed by centrifugal ultrafiltration. 6His-OAZ1 showed a strong retention of spermidine (~50%) and spermine (84%), whereas neither material from mock preparations (Supplementary Fig. 8) nor several control proteins showed any values significantly above background (Fig. 4). We conclude that OAZ1 specifically binds to both polyamines, apparently with a higher affinity for spermine. To address whether polyamine binding is a conserved property of antizyme, we produced human AZ1 as a fusion to maltose binding protein (MBP). In contrast to the MBP control, human MBP-AZ1 specifically bound spermidine with similar efficiency as yeast OAZ1, indicating that polyamine sensing by antizyme is conserved from yeast to humans (Supplementary Fig. 9).

What might be the mechanism by which binding of polyamines to nascent OAZ1 regulates its synthesis? The element in the C-terminal portion of nascent OAZ1 could arrest translation during elongation or at the termination step. The former would be reminiscent of the regulated elongation arrest caused by a specific sequence in nascent *E. coli* SecM (secretion monitor) protein¹⁷. The observation that residues so close to the OAZ1 C terminus that they must still be in the ribosome exit tunnel are critical for this arrest to occur, indicates that interactions between these residues with inner surfaces of the ribosome contribute to the arrest, similar to what has been shown for SecM¹⁸. Based on our findings, we propose a model (Supplementary Fig. 1), wherein nascent OAZ1

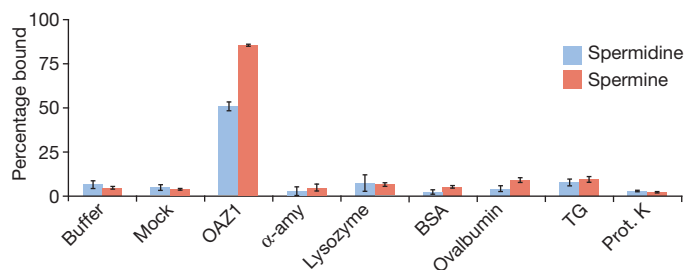


Figure 4 | Polyamines bind to OAZ1 protein. Shown are the results of measurements that determined the retention of radiolabelled polyamines during ultrafiltration. Retention of [³H]-spermidine or [¹⁴C]-spermine by 6His-OAZ1 from three independent preparations was compared to that observed with buffer only, with material from Ni-NTA mock preparations from an *E. coli* strain not expressing 6His-OAZ1, as well as with *Bacillus subtilis* α-amylase (α-amy), chicken egg lysozyme, bovine serum albumin (BSA), ovalbumin, thyroglobulin (TG), and proteinase K (each at 10 μM). Error bars, s.d.; n = 3.

assumes a conformation that, together with the residues located inside the exit tunnel, promotes an arrest of translation at low cellular polyamine concentrations, whereas binding of polyamines to OAZ1 prevents formation of this inhibitory conformation. We found that various mutations downstream of the RFS site inactivated the polyamine-regulated element (Supplementary Fig. 10), indicating that the downstream inhibitory element involves a larger structural domain. Formation of this element apparently requires translational pausing at the RFS site (Supplementary discussion). In our model, the N-terminal inhibitory element and the RFS site are cooperating to achieve the required translational pausing resulting in low ribosome density.

A key finding of our study is that ribosome-associated nascent OAZ1 polypeptide acts as a direct sensor of intracellular polyamine concentrations. Therefore, this system provides an intriguing novel type of co-translational control mechanism, in which a metabolite binds to a nascent, ribosome-associated autoregulatory sensor protein that regulates the decoding of its own mRNA. Similar types of co-translational mechanisms are likely to control the expression of other autoregulatory proteins, including metabolic enzymes. One possible example is the expression of mammalian SSAT, an enzyme involved in polyamine catabolism, which is known to bind polyamines (see above). Translation of SSAT mRNA is induced by polyamines and depends on sequences close to both ends of its ORF¹⁹. Polyamine binding to nascent SSAT might regulate its expression co-translationally, similar to what we observed for OAZ1, except that RFS is not involved. Beyond the control of ODC, antizyme was reported to have multiple additional cellular targets with relevance to cancer, such as the polyamine uptake system, Aurora A kinase, and the anti-apoptotic protein DeltaNp73 (refs 2, 20–22). The identification of antizyme as a polyamine sensor therefore may provide an interesting drug target to simultaneously stimulate downregulation of polyamine synthesis and uptake, as well as downregulation of cell cycle regulators.

METHODS SUMMARY

Determination of relative frameshifting efficiency. *S. cerevisiae* YHI29/1 (*pre1-1*)¹¹ (a gift from D. H. Wolf) transformants expressing OAZ1 constructs either with the RFS site or the corresponding in-frame variants (see plasmid table in the Supplementary information) were grown in SD medium supplemented with 10 μM spermidine where indicated. RFS efficiency (given in percentage of concentration obtained for the in-frame construct) was calculated as follows. First, steady-state signals obtained for OAZ1 expressed from the corresponding RFS and in-frame constructs as well as for CDC11 were quantified. Second, the OAZ1 levels were normalized for protein loading differences using the corresponding CDC11 values. RFS efficiency was then calculated from the normalized OAZ1 levels obtained with the RFS construct and the corresponding in-frame constructs in at least three independent experiments.

Ribosome pull-down assay. To analyse ribosome-associated nascent OAZ1 polypeptides, strain LEY1 expressing RPL25-Flag-6His was used. Extracts from transformants of this strain encoding 2×Myc-OAZ1 variants were subjected to anti-Flag pull-down and western blot analysis.

In vitro polyamine binding assay. Polyamine binding was assayed with recombinant affinity purified 6His-OAZ1 and [³H]-spermidine or [¹⁴C]-spermine by an ultrafiltration protocol. Purified 6His-OAZ1 (~10 μM) was incubated with 10 μM spermidine or spermine for 1 h on ice. Unbound polyamines were then separated from bound ones by ultrafiltration. Samples of the filtrate and the retentate were subjected to scintillation counting. The resulting values from at least three independent measurements were used to calculate the percentage of bound polyamines with the formula %C_B = 100 × (C_R - C_F)/C_R; where C_F is the concentration of free polyamines detected in the filtrate, and C_R the total concentration of soluble polyamines in the retentate.

Full Methods and any associated references are available in the online version of the paper at www.nature.com/nature.

Received 23 August 2010; accepted 27 July 2011.

Published online 7 September 2011.

- Coffino, P. Regulation of cellular polyamines by antizyme. *Nature Rev. Mol. Cell Biol.* **2**, 188–194 (2001).
- Wallace, H. M., Fraser, A. V. & Hughes, A. A perspective of polyamine metabolism. *Biochem. J.* **376**, 1–14 (2003).

3. Eisenberg, T. *et al.* Induction of autophagy by spermidine promotes longevity. *Nature Cell Biol.* **11**, 1305–1314 (2009).
4. Hayashi, S., Murakami, Y. & Matsufuji, S. Ornithine decarboxylase antizyme: a novel type of regulatory protein. *Trends Biochem. Sci.* **21**, 27–30 (1996).
5. Murakami, Y. *et al.* Ornithine decarboxylase is degraded by the 26S proteasome without ubiquitination. *Nature* **360**, 597–599 (1992).
6. Ivanov, I. P. & Atkins, J. F. Ribosomal frameshifting in decoding antizyme mRNAs from yeast and protists to humans: close to 300 cases reveal remarkable diversity despite underlying conservation. *Nucleic Acids Res.* **35**, 1842–1858 (2007).
7. Palanimurugan, R., Scheel, H., Hofmann, K. & Dohmen, R. J. Polyamines regulate their synthesis by inducing expression and blocking degradation of ODC antizyme. *EMBO J.* **23**, 4857–4867 (2004).
8. Matsufuji, S. *et al.* Autoregulatory frameshifting in decoding mammalian ornithine decarboxylase antizyme. *Cell* **80**, 51–60 (1995).
9. Rom, E. & Kahana, C. Polyamines regulate the expression of ornithine decarboxylase antizyme *in vitro* by inducing ribosomal frame-shifting. *Proc. Natl Acad. Sci. USA* **91**, 3959–3963 (1994); erratum **91**, 9195 (1994).
10. Rato, C., Amirova, S. R., Bates, D. G., Stansfield, I. & Wallace, H. M. Translational recoding as a feedback controller: systems approaches reveal polyamine-specific effects on the antizyme ribosomal frameshift. *Nucleic Acids Res.* **39**, 4587–4597 (2011).
11. Heinemeyer, W., Kleinschmidt, J. A., Saidowsky, J., Escher, C. & Wolf, D. H. Proteinase yscE, the yeast proteasome/multicatalytic-multifunctional proteinase: mutants unravel its function in stress induced proteolysis and uncover its necessity for cell survival. *EMBO J.* **10**, 555–562 (1991).
12. Tenson, T. & Ehrenberg, M. Regulatory nascent peptides in the ribosomal tunnel. *Cell* **108**, 591–594 (2002).
13. Inada, T. *et al.* One-step affinity purification of the yeast ribosome and its associated proteins and mRNAs. *RNA* **8**, 948–958 (2002).
14. Arava, Y., Boas, F. E., Brown, P. O. & Herschlag, D. Dissecting eukaryotic translation and its control by ribosome density mapping. *Nucleic Acids Res.* **33**, 2421–2432 (2005).
15. Baim, S. B. & Sherman, F. mRNA structures influencing translation in the yeast *Saccharomyces cerevisiae*. *Mol. Cell. Biol.* **8**, 1591–1601 (1988).
16. Hoffman, D. W., Carroll, D., Martinez, N. & Hackert, M. L. Solution structure of a conserved domain of antizyme: a protein regulator of polyamines. *Biochemistry* **44**, 11777–11785 (2005).
17. Nakatogawa, H. & Ito, K. The ribosomal exit tunnel functions as a discriminating gate. *Cell* **108**, 629–636 (2002).
18. Woolhead, C. A., Johnson, A. E. & Bernstein, H. D. Translation arrest requires two-way communication between a nascent polypeptide and the ribosome. *Mol. Cell* **22**, 587–598 (2006).
19. Butcher, N. J., Broadhurst, G. M. & Minchin, R. F. Polyamine-dependent regulation of spermidine-spermine N1-acetyltransferase mRNA translation. *J. Biol. Chem.* **282**, 28530–28539 (2007).
20. Basuroy, U. K. & Gerner, E. W. Emerging concepts in targeting the polyamine metabolic pathway in epithelial cancer chemoprevention and chemotherapy. *J. Biochem.* **139**, 27–33 (2006).
21. Lim, S. K. & Gopalan, G. Antizyme1 mediates AURKAIP1-dependent degradation of Aurora-A. *Oncogene* **26**, 6593–6603 (2007).
22. Dulloo, I., Gopalan, G., Melino, G. & Sabapathy, K. The antiapoptotic DeltaNp73 is degraded in a c-Jun-dependent manner upon genotoxic stress through the antizyme-mediated pathway. *Proc. Natl Acad. Sci. USA* **107**, 4902–4907 (2010).

Supplementary Information is linked to the online version of the paper at www.nature.com/nature.

Acknowledgements We thank M. Hochstrasser for comments, D. Richardson for critical reading of the manuscript, and D. H. Wolf for the *pre1-1* strain. L.K. and D.G. were supported by the NRW Graduate School in Genetics and Functional Genomics. This work was supported by a grant from the Deutsche Forschungsgemeinschaft (Do 649/4) to R.J.D.

Author Contributions All authors contributed to the design of experiments. L.K. and R.P. generated constructs, performed RFS assays and analysed data. L.K. performed ribosome pull-down experiments. D.G. established expression and purification of 6His-OAZ1. R.P. established and performed polyamine binding assays (with help from D.G.), and performed all experiments in the revision process (Supplementary Figs. 3, 7, 8, 9 and 10). R.P. and R.J.D. wrote the manuscript with contributions from L.K. and D.G.

Author Information Reprints and permissions information is available at www.nature.com/reprints. The authors declare no competing financial interests. Readers are welcome to comment on the online version of this article at www.nature.com/nature. Correspondence and requests for materials should be addressed to R.J.D. (j.dohmen@uni-koeln.de).

METHODS

Growth of strains and western blot analysis for determination of RFS efficiency. Yeast rich (YPD) and synthetic minimal media with 2% dextrose (SD) were prepared as described⁷. YH129/1 (*pre1-1*)¹¹ transformants expressing OAZ1 variants from the copper-inducible P_{CUP1} promoter were grown in SD medium supplemented with 100 μ M CuSO_4 (ref. 7). Spermidine (Sigma-Aldrich) was added when the precultures were diluted into fresh media. Cells were grown at 30 °C from an attenuation measured at 600 nm (D_{600}) of approximately 0.2 until they reached a D_{600} of 0.6–0.8. Equal amounts of cells were harvested by pelleting them at 4,000g for 5 min. Cell extracts were prepared by boiling the pellets in an appropriate volume of loading buffer (62.5 mM Tris-HCl, pH 6.8, 2% SDS, 1% β -mercaptoethanol, 10% glycerol, and 0.002% bromophenol blue) for 5 min at 100 °C. Extracts from cells corresponding to $0.5 \times D_{600}$ (~15 μ g protein) for the in-frame constructs and from $1.0 \times D_{600}$ (~30 μ g protein) for the RFS constructs were used for SDS-PAGE and quantitative two-colour western blot analysis using the Odyssey Infrared Imaging System (Li-Cor). Anti-Myc (9B11, Cell Signaling Technology) and anti-haemagglutinin (16B12, HISS Diagnostics) monoclonal antibodies were used for detecting tagged versions of various OAZ1 proteins. Anti-rabbit polyclonal antibody (Santa Cruz Biotechnology) was used to detect CDC11, which served as an internal protein loading control. Western blotting procedure as well as anti-mouse and anti-rabbit secondary antibodies coupled to fluorophores were used as described before⁷.

Ribosome pull-down assay. We used a ribosome-tagged strain similar to one described by others¹³. Strain LEY1, which expressed genomically tagged *RPL25-Flag-6His*, is a derivative of YH129/1 generated using the integrative plasmid pLE133. LEY1 transformants expressing *2xMyc-OAZ1* variants were grown from a starting D_{600} of 0.2 in a volume of 100 ml selective SD medium to a D_{600} of approximately 0.8. Cells were harvested and resuspended in 600 μ l of ice cold lysis buffer (20 mM HEPES, pH 7.4, 2 mM $\text{Mg}(\text{CH}_3\text{COO})_2$, 100 mM KCH_3COO , 0.5 mM DTT) containing a protease inhibitor mix (complete, EDTA free, from Roche), and lysed with an equal volume of acid-washed glass beads (0.4–0.6 mm diameter) by vortexing five times for 30 s with 1 min intervals on ice. Lysates were clarified by an initial centrifugation at 10,000g for 5 min at 4 °C. The supernatant was again cleared by centrifugation for 20 min at 10,000g at 4 °C. For affinity purification of ribosomes, lysates containing 1 mg of total protein were mixed with an equal volume of ice-cold 2 \times binding buffer (100 mM Tris-HCl pH 7.5, 24 mM $\text{Mg}(\text{CH}_3\text{COO})_2$, 1 mM DTT, 1 mM PMSF, 50 U ml^{-1} RNasin). To this mix, 100 μ l of anti-Flag M2-agarose affinity resin (Sigma-Aldrich) was added followed by an incubation for 4 h at 4 °C with end-over-end rotation. The resin was then washed five times with 1 ml of ice-cold washing buffer (50 mM Tris-HCl, pH 7.5, 100 mM KCl, 12 mM $\text{Mg}(\text{CH}_3\text{COO})_2$, 1 mM DTT, 1 mM PMSF). After washing, the bound proteins were eluted by incubating the resin in 50 μ l of washing buffer containing 300 μ g ml^{-1} Flag peptide, and analysed by western blotting.

Sucrose density gradient fractionation and quantification of OAZ1 mRNA. Yeast strain LEY1 carrying the plasmid pPM318 was grown in approximately 300 ml of synthetic medium without leucine and uracil containing 200 μ M CuSO_4 at 30 °C. Spermidine (10 μ M) was added to the indicated cultures approximately 3 h before harvesting. Cells were harvested when the cultures reached a D_{600} of 0.6–0.8. Culture volumes corresponding to 100 D_{600} units were centrifuged at 2,800g for 5 min at 4 °C. Cell pellets were washed once in 5 ml of ice-cold lysis buffer (30 mM HEPES-KOH (pH 7.4), 100 mM KCH_3COO , 30 mM $\text{Mg}(\text{CH}_3\text{COO})_2$, 0.5 mM DTT, Protease inhibitor cocktail without EDTA (Roche), 200 μ g ml^{-1} heparin). Cell pellets were resuspended in ice-cold lysis buffer (1 ml final volume) containing 5 μ l RNasin (Promega). Cells were lysed by vortexing five times for 30 s at full speed in the presence of 500 μ l 0.5-mm glass beads with 30 s intervals on ice. The lysates were clarified by three 5 min centrifugation steps, first at 5,200g, then at 10,600g, and finally at 20,800g. Extracts present in 450 μ l of the final supernatant were loaded on top of an 11 ml 10–50% w/v sucrose gradient prepared in ice-cold gradient buffer (30 mM HEPES-KOH (pH 7.4), 50 mM KCH_3COO , 12 mM $\text{Mg}(\text{CH}_3\text{COO})_2$, 0.5 mM DTT and Protease inhibitor cocktail without EDTA (Roche)). Polyosomes were separated by centrifugation at 100,000g for 105 min at 4 °C in a Beckman SW40Ti rotor. After the centrifugation, 750 μ l fractions were collected from the sucrose gradient. Each fraction was mixed with 2.5 volume ice-cold ethanol and kept at –20 °C for 15 h or longer for RNA precipitation. To isolate total RNA from the fractions, they

were centrifuged at 20,800g for 20 min. Supernatants were carefully removed from all the samples and the pellets were dried at room temperature for 15 min. After drying, the pellets were resuspended in 100 μ l RNase-free water and placed on ice. RNA from each fraction was isolated using Qiagen's RNeasy mini kit. RNA was eluted from each column with 25 μ l RNase-free water. RNA samples isolated from each fraction were transferred onto ice immediately after elution. Ten microlitre of the eluted RNA samples were used for cDNA synthesis using the High-Capacity cDNA Reverse Transcription kit (Applied Biosystems). *OAZ1* and *TPI1* transcripts from each fraction were quantified by Q-PCR using TaqMan Gene Expression Master Mix (Applied Biosystems) and gene-specific TaqMan probes (Eurogentec).

Affinity purification of 6His-OAZ1. A plasmid expressing codon-optimized *6His-OAZ1* was constructed based on the pET11a vector (Merck) to obtain pDG240. *E. coli* strain Rosetta (Merck) was transformed either with pDG240 or the empty pET11a (mock) plasmid. Expression was induced for 4 h at 30 °C with 1 mM IPTG. Cell pellets corresponding to approximately 550 D_{600} units were resuspended in 10 ml binding buffer (50 mM Tris, pH 7.8 at 4 °C). In order to purify 6 \times His-tagged OAZ1, frozen cell pellets were thawed at 25 °C, then 20 mg of lysozyme from chicken egg (Sigma-Aldrich), 2 mg of DNase I (Roche) and protease inhibitor mix (Roche) were added. Lysis was initiated by vortexing six times for 10 s at 25 °C followed by incubation on ice for 45 min. Later, the lysate was clarified by centrifugation at 25,000g for 30 min at 4 °C. Imidazole was added to the supernatant to a final concentration of 20 mM, followed by addition of 250 μ l of pre-equilibrated Ni-NTA Sepharose (GE healthcare). Binding was carried out by keeping the suspension at 4 °C for 2 h with mild rotation. Unbound material was removed by centrifugation at 200g for 3 min at 4 °C. The beads were washed four times with 10 ml lysis buffer containing 20 mM imidazole. Bound protein was eluted in 350 μ l lysis buffer containing 250 mM imidazole for 1 h. Protein concentration was determined using the Bradford assay (Bio-Rad).

Affinity purification of MBP-hAZ1. A plasmid expressing codon-optimized human AZ1 (hAZ1) as a fusion to maltose binding protein (MBP-hAZ1) was constructed based on the pMAL-c2 vector (New England Biolabs (NEB)) to obtain pJD633. *E. coli* strain Rosetta (Merck) was transformed either with pJD633 or the empty pMAL-c2 plasmid. Expression was induced overnight in Overnight Express Instant TB Medium (Novagen). Cell pellets were frozen in liquid nitrogen and stored at –80 °C. For lysis, pellets were thawed on ice overnight and resuspended in 10 ml binding buffer (50 mM Tris, pH 7.8 at 4 °C). To purify MBP or MBP-hAZ1, 10 mg of lysozyme from chicken egg (Sigma-Aldrich), 1 mg of DNase I (Roche) and protease inhibitor mix (Roche) were added. Lysis was initiated by vortexing six times for 10 s at 25 °C followed by incubation on ice for 45 min. Later, the lysate was clarified by centrifugation at 25,000g for 30 min at 4 °C. Amylose resin (200 μ l; NEB) equilibrated with binding buffer was added to the supernatant. Binding was carried out by keeping the suspension at 4 °C for 2 h with mild rotation. Unbound material was removed by centrifugation at 200g for 3 min at 4 °C. The beads were washed four times with 5 ml binding buffer. Bound protein was eluted in 350 μ l binding buffer containing 10 mM maltose for 90 min.

Polyamine binding assay. To establish an ultrafiltration-based binding assay, we first tested whether spermidine and spermine passed freely and without retention through low protein binding (10K cutoff) centrifugal filtration devices with modified polyethersulphone membranes (VWR). Samples (100 μ l) were subjected to centrifugal filtration at 2,500g for 4 min at 4 °C. These conditions yielded a filtrate of approximately 15 μ l. Samples (10 μ l) of the filtrate and the retentate were then used to determine the concentration of radioactive polyamines by scintillation counting. Retention of polyamines was 5% or less as shown in Fig. 4. To detect polyamine binding to proteins, purified 6His-OAZ1, MBP-hAZ1, or control proteins were diluted to a final volume of 100 μ l (~10 μ M) using binding buffer (50 mM Tris, pH 7.8 at 4 °C) containing 10 μ M [³H]-spermidine (PerkinElmer) or [¹⁴C]-spermine (GE Healthcare). After 1 h of binding on ice, these samples were analysed by centrifugal filtration and scintillation counting as described above. The percentage of bound polyamines was calculated with the formula $\%C_B = 100 \times (C_R - C_F)/C_R$; where C_F is the concentration of free polyamines detected in the filtrate, and C_R the total concentration of soluble polyamines in the retentate. Control proteins used were *B. subtilis* α -amylase, chicken egg lysozyme, bovine serum albumin, chicken egg ovalbumin, bovine thyroglobulin, and proteinase K (all from Sigma-Aldrich).

The structure and catalytic mechanism of a poly(ADP-ribose) glycohydrolase

Dea Slade^{1,2*}, Mark S. Dunstan^{3*}, Eva Barkauskaite¹, Ria Weston¹, Pierre Lafite⁴, Neil Dixon³, Marijan Ahel⁵, David Leys³ & Ivan Ahel¹

Post-translational modification of proteins by poly(ADP-ribosyl)ation regulates many cellular pathways that are critical for genome stability, including DNA repair, chromatin structure, mitosis and apoptosis¹. Poly(ADP-ribose) (PAR) is composed of repeating ADP-ribose units linked via a unique glycosidic ribose-ribose bond, and is synthesized from NAD by PAR polymerases^{1,2}. PAR glycohydrolase (PARG) is the only protein capable of specific hydrolysis of the ribose-ribose bonds present in PAR chains; its deficiency leads to cell death^{3,4}. Here we show that filamentous fungi and a number of bacteria possess a divergent form of PARG that has all the main characteristics of the human PARG enzyme. We present the first PARG crystal structure (derived from the bacterium *Thermomonospora curvata*), which reveals that the PARG catalytic domain is a distant member of the ubiquitous ADP-ribose-binding macrodomain family^{5,6}. High-resolution structures of *T. curvata* PARG in complexes with ADP-ribose and the PARG inhibitor ADP-HPD, complemented by biochemical studies, allow us to propose a model for PAR binding and catalysis by PARG. The insights into the PARG structure and catalytic mechanism should greatly improve our understanding of how PARG activity controls reversible protein poly(ADP-ribosyl)ation and potentially of how the defects in this regulation are linked to human disease.

Whereas the mechanism and functional aspects of PAR synthesis have been extensively characterized, the present understanding of the PAR-degradation pathways catalysed by PARG is comparatively poor. Until now, the catalytic fold and the mechanism of PARG-mediated hydrolysis have remained unknown. Our homology searches revealed that the majority of fungal genomes lack close mammalian/canonical PARG homologues, but instead possess a divergent PARG-like protein, annotated as DUF2263. DUF2263 protein sequences contain the PARG signature (GGG-X₆₋₈-QEE)⁷, which includes the previously identified key residues: two consecutive glutamates⁷ (Fig. 1a, black asterisk) and a glycine⁸ (Fig. 1a, grey asterisk). In addition, a tyrosine residue (Fig. 1a, black cross) implicated in binding to the PARG inhibitor ADP-HPD⁹ is also present in DUF2263. The DUF2263 orthologue is found also in other eukaryotes lacking canonical PARGs such as the rotifer *Adineta vaga* (Fig. 1b), where it is fused to several copies of the PAR-binding zinc finger¹⁰. As both filamentous fungi and *A. vaga* have functional PARP orthologues and an active PAR metabolism^{11,12}, we postulated that DUF2263 was likely to be a functional PARG in these organisms. Surprisingly, although bacteria are historically thought to be devoid of PAR metabolism, certain bacterial species possess both PARP (closely related to PARP1; ref 13) and DUF2263 genes, whereas some only contain the DUF2263 homologue (Fig. 1a, b). To analyse the biochemical activities of the corresponding bacterial PARP and PARG proteins, we purified His₆-tagged *Herpetosiphon aurantiacus* PARP and DUF2263. *H. aurantiacus* PARP was able to synthesize PAR from NAD, as revealed by antibodies recognizing PAR (Fig. 1c)

and by the analysis of PAR ladders using sequencing gels (Supplementary Fig. 1). Analogous to the human PARP1 enzyme, *H. aurantiacus* PARP was sensitive to the PARP inhibitor KU-0058948 and required DNA for its activation (Fig. 1c). Notably, poly(ADP-ribosyl)ation produced by *H. aurantiacus* PARP is efficiently hydrolysed by the *H. aurantiacus* DUF2263 protein, demonstrating that DUF2263 is a functional PARG (Fig. 1c) and suggesting the presence of functional PAR metabolism in bacteria.

We extended our analyses to other bacterial and fungal PARGs (Fig. 1a, b and Supplementary Fig. 2) using established PAR substrates formed by the activity of the well-characterized human PARP1 enzyme. Canonical human and *Entamoeba dispar* PARGs served as controls. The *in vitro* activity of the purified PARG enzymes was evaluated in five ways: (1) an assay that measures the loss of PAR from PARP1-modified histones; (2) a western-blot analysis of the hydrolysis of PAR from the auto-modified human PARP1 using anti-PAR antibodies; (3) an SDS-polyacrylamide gel electrophoresis (SDS-PAGE) analysis of the [³²P]-PAR auto-modified human PARP1; (4) an analysis of the release of ADP-ribose from PAR either by thin-layer chromatography (TLC); or (5) by liquid chromatography-mass spectrometry (LC/MS) (Fig. 2a–d and Supplementary Fig. 4). The quantification of PAR hydrolysis by the PARG assay shows that bacterial and fungal PARGs are highly active in hydrolysing PAR *in vitro*; their catalytic potency is comparable to the *E. dispar* and human PARG enzymes (Fig. 2a). Moreover, the mode of action of these proteins and mutant versions on poly(ADP-ribosyl)ated PARP1 shows the same pattern observed for the canonical PARGs. First, they are all inactivated by the mutation of a key glutamate residue (Fig. 2b, d) and by treatment with the PARG inhibitor ADP-HPD (Fig. 2c). Second, they are all active on ribose-ribose bonds between the two ADP-ribose units, but they are not efficient on mono(ADP-ribosyl)ated protein substrates with the ADP-ribose unit linked directly to the PARP1 (Fig. 2c) or the PARP10 protein (Supplementary Fig. 3). Last, TLC and LC/MS analyses confirmed that the main product of DUF2263-type PARGs is ADP-ribose (Fig. 2d and Supplementary Fig. 4). Collectively, these results demonstrate that bacterial and fungal PARG proteins possess genuine PARG activity *in vitro*.

To test whether bacterial and fungal PARG proteins can act as PARGs *in vivo*, we used the *Saccharomyces cerevisiae* system expressing human PARP1 (ref. 14). Yeast cells, naturally deficient in PAR metabolism, can readily express human PARP1, resulting in poly(ADP-ribosyl)ation of various protein substrates¹⁴ (Fig. 2e). When divergent PARG proteins were co-expressed with human PARP1, we observed that the poly(ADP-ribosyl)ation levels in yeast extracts diminished, indicating an efficient hydrolysis of PAR *in vivo* (Fig. 2e and Supplementary Fig. 5).

Although the first PARG gene was cloned in 1997 (ref. 15), until now there has been no structural data available for a PARG enzyme. To gain an insight into the PARG structure and mechanism, we solved the

¹Cancer Research UK, Paterson Institute for Cancer Research, University of Manchester, Wilmslow Road, Manchester M20 4BX, UK. ²Université de Paris-Descartes, Faculté de Médecine, INSERM U1001, 156 rue de Vaugirard, 75015 Paris, France. ³Manchester Interdisciplinary Biocentre, Princess Street 131, Manchester M1 7DN, UK. ⁴ICOA – UMR CNRS 6005 Université d'Orléans, Rue de Chartres, F-45067 Orléans, France. ⁵Rudjer Boskovic Institute, Bijenicka 54, HR-10000 Zagreb, Croatia.

*These authors contributed equally to this work.

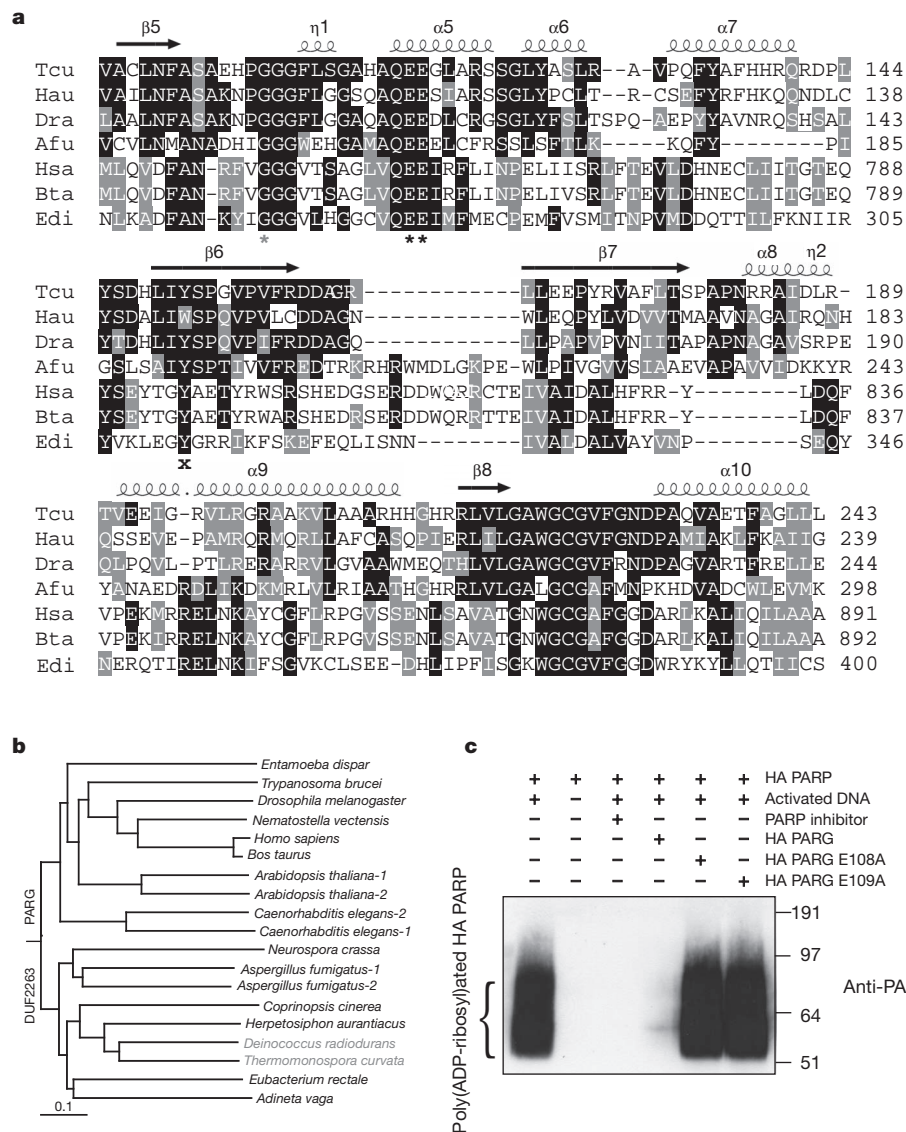


Figure 1 | Phylogeny and functional relationship between DUF2263 and canonical-type PARGs. **a**, Multiple sequence alignment of different DUF2263 and PARG proteins from *T. curvata* (Tcu), *H. aurantiacus* (Hau), *Deinococcus radiodurans* (Dra), *Aspergillus fumigatus* (Afu), *Homo sapiens* (Hsa), *Bos taurus* (Bta) and *E. dispar* (Edi). The two catalytic glutamates, a conserved glycine and tyrosine are marked with black asterisks, a grey asterisk and a black

T. curvata PARG ligand-free crystal structure to 1.5 Å in addition to ADP-ribose and ADP-HPD inhibitor-bound structures (Supplementary Table 1). Comparison with available structures reveals that *T. curvata* PARG consists of an ADP-ribose-binding macrodomain fold with an amino-terminal extension (residues 3–67; Fig. 3c). Similar macrodomain structures are found in the *Escherichia coli* YmdB protein (PDB accession 1SPV; Z score 16.2, root mean squared deviation (r.m.s.d.) 2.1 Å over 161 Cα atoms, 19% identity), an *Archaeoglobus fulgidus* macrodomain protein (PDB accession 2BFQ; Z score 15.6, r.m.s.d. 2.8 Å over 164 Cα atoms, 16% identity)⁵ and the histone variant MACROH2A1.1 (PDB accession 1ZR3; Z score 15.0, 2.3 Å r.m.s.d. over 157 Cα atoms, 12% identity)¹⁶. The diphosphate-binding loop that flanks one side of the ADP-ribose-binding cavity is highly conserved between PARG and other macrodomain structures (in magenta, Fig. 3a, c). In contrast, the opposite side of the PARG ADP-ribose-binding cavity is lined by a stretch of amino acids corresponding to the PARG-specific GGG-X_{6–8}-QEE signature sequence⁷ (in yellow, Fig. 3a–c). The structural alignment reveals this PARG-specific loop is inserted into the macrodomain fold to accommodate

cross, respectively. Secondary structural elements from the Tcu PARG structure are indicated above. **b**, YmdB-rooted phylogenetic tree of PARGs implied by the neighbour-joining method. Organisms devoid of PARG are marked in grey. **c**, *H. aurantiacus* (HA) PARG and PARG enzymes are active as shown by western blotting with anti-PARG antibodies. The positions of protein markers are indicated on the right margin (in kDa).

the Glu 115 side chain that projects into the PARG active site (Fig. 3c, d). Owing to the PARG-specific loop, it seems that only PARGs but not other macrodomain proteins can hydrolyse PAR (Supplementary Fig. 6).

The ligand–PARG complex structures reveal that ADP-α-ribose occupies a position similar to that observed in other ADP-ribose-macrodomain complex structures⁵ (Fig. 3d and Supplementary Fig. 7). A minor rearrangement can be observed for Val 226–Phe 227 upon ADP-ribose binding. The Phe 227 side chain is in close contact with the ribose'' moiety of ADP-ribose, ensuring a close distance between the ribose'' O4 and one of the phosphate groups within the constraints of the active site. The ribose'' moiety also forms hydrogen bonds with Glu 114 (via the 2'-OH group) and Glu 115 (via the 1'-OH group) (Fig. 3d). With the exception of water-mediated polar contacts, few direct contacts can be observed with the adenosine moiety. In contrast to the ribose'' moiety, the adenosine ribose' moiety is markedly less accessible. The presence of any substituents on the ribose' 2'-OH group (such as another ADP-ribose) would require a major reorientation of the PARG carboxy-terminal α-helix (see Fig. 4a) with concomitant

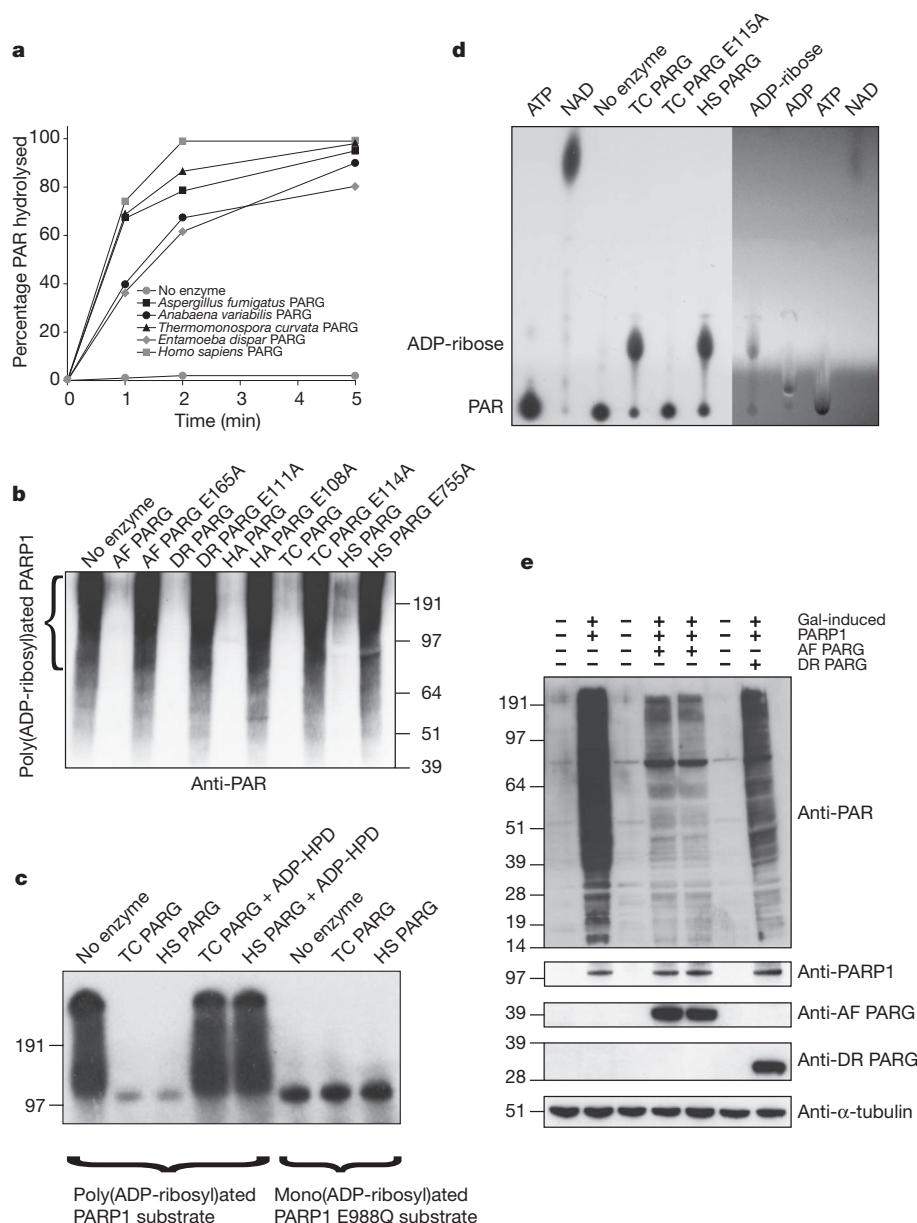


Figure 2 | PAR hydrolytic activities of divergent and canonical PARGs. **a**, A colorimetric PARG assay. **b**, Analysis of the hydrolysis of the PARP1-generated PAR substrate by anti-PAR antibodies. AF, *A. fumigatus*; AV, *A. variabilis*; DR, *D. radiodurans*; HA, *H. auranitacus*; HS, *H. sapiens*; ED, *E. dispar*; TC, *T. curvata*. The positions of protein markers are indicated on the margins of panels **b**, **c** and **e** (in kDa). **c**, SDS-PAGE-based assay with [32 P]-automodified

PARP1 substrate. PARGs are inhibited by ADP-HPD. **d**, TLC analysis of PARG activity on the [32 P]-PAR substrate. The right side of the TLC plate was visualized by shadowing under ultraviolet light. **e**, Heterologously expressed *A. fumigatus* and *D. radiodurans* PARG hydrolyse PAR in human PARP1-expressing budding yeast cells.

exposure of the hydrophobic core of the macrodomain. This suggests that bacterial PARG binds the PAR terminus and acts as an exoglycohydrolase.

The steric restraints imposed by the PARG active site form a basis for the modelling of an $\alpha(1' \rightarrow 2')$ O-glycosidic linkage with an additional ADP-ribose group to provide further insight into PAR binding (Fig. 4a, b). Our models suggest that the $(n-1)$ adenine moiety is partially enclosed by Ala 110, Ala 112 and Val 226 while the $(n-1)$ ribose' is in close contact with Ser 98 and Gly 104 (Fig. 4b). However, molecular dynamics simulations suggest that the enzyme lacks any obvious binding sites for the $(n-1)$ phosphate and ribose'' moieties, as exemplified by the considerable conformational freedom of the latter with respect to the terminal ADP-ribose and the associated $(n-1)$ ribose'. This suggests that bacterial PARG does not specifically bind additional PAR elements.

The *T. curvata* PARG complex with ADP-ribose (Fig. 3d) and the corresponding PAR-PARG model (Fig. 4b) allow us to propose a mechanism for PARG catalysis (Fig. 4c). Binding of the PAR terminus positions the key ribose-ribose O-glycosidic linkage in direct hydrogen-bonding contact with Glu 115, while constraining the conformation of the terminal ribose''. Formation of a putative oxocarbenium intermediate is supported by the protonation of the $(n-1)$ PAR ribose' 2'-OH leaving group via Glu 115, and by the stabilization of the positively charged oxocarbenium through close proximity with the terminal diphosphate group. A water molecule is ideally positioned to attack the oxocarbenium intermediate, activated through concomitant deprotonation by Glu 115. This leads to the release of ADP- β -ribose'' and $(n-1)$ PAR.

This mechanism is supported by mutagenesis and binding studies. Although mutations of both Glu 114 and Glu 115 render the enzyme

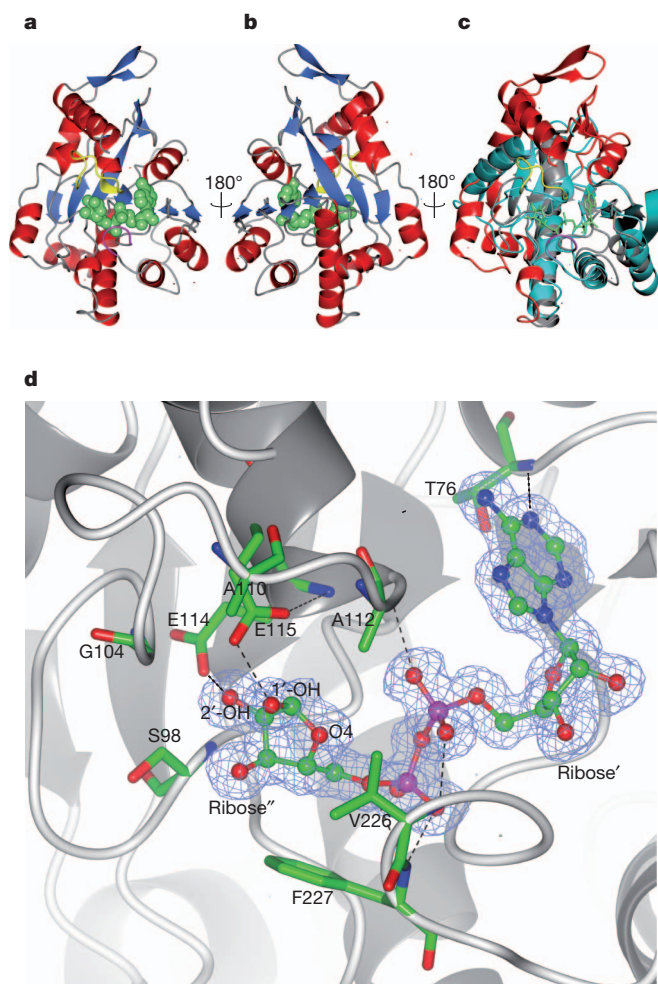


Figure 3 | *T. curvata* PARG crystal structure in complex with ADP-ribose. **a, b**, Overall fold of PARG with α -helices depicted in red, β -sheets in blue and bound ADP-ribose in green spheres. The PARG-specific catalytic loop is shown in yellow, and the diphosphate-binding loop in magenta. **c**, Overlay of the *T. curvata* PARG structure with a representative macrodomain structure (PDB accession 2BFQ, in cyan). The PARG-specific N-terminal extension and additional PARG structural elements are highlighted in red. Structural features that are similar to 2BFQ and other macrodomains are shown in grey. **d**, Detailed view of ADP-ribose bound in the PARG active site. ADP-ribose is shown with the corresponding $2F_o - F_c$ omit map density contoured at 1.2σ in blue. Key active site residues are represented in atom coloured sticks with hydrogen bonds indicated by black dotted lines.

inactive without disruption to the overall PARG fold (Fig. 4d and Supplementary Fig. 8), the isothermal titration calorimetry (ITC) ADP-ribose binding studies reveal that mutation of Glu 115 into an alanine does not affect binding, whereas the Glu114Ala mutation leads to an approximately tenfold decrease in binding affinity (Supplementary Fig. 9). This supports the notion that the role of Glu 114 is confined to substrate binding/orientation as opposed to the acid-base catalysis proposed for Glu 115. The mutation of Phe 227 implicated in positioning the terminal ribose'' also renders the enzyme inactive (Fig. 4d). Mutations of Ser 98 and Val 226, implicated by our model in binding the $(n - 1)$ ADP-ribose, greatly diminish *T. curvata* PARG activity (Fig. 4d). Importantly, mutations of the corresponding catalytic residues in human PARG have a similar effect on the enzymatic activity, which suggests a universal catalytic mechanism for bacterial and mammalian PARGs (Fig. 4d).

These data provide the first insight into PARG structure and catalytic mechanism, and improve our understanding of the biochemical strategies regulating reversible poly(ADP-ribosyl)ation. Our results indicate the existence of bacterial PAR metabolism and show that PARG is a member of the widespread macrodomain protein family^{5,6}, which is known to be implicated in genome stability and regulated by poly(ADP-ribosyl)ation^{17–19}. Our data confirm that PARGs are evolutionary unrelated to ARH3 proteins, another class of enzymes with the ability to cleave PAR^{20,21} (Supplementary Information). We believe that our findings will provide the groundwork for future studies that

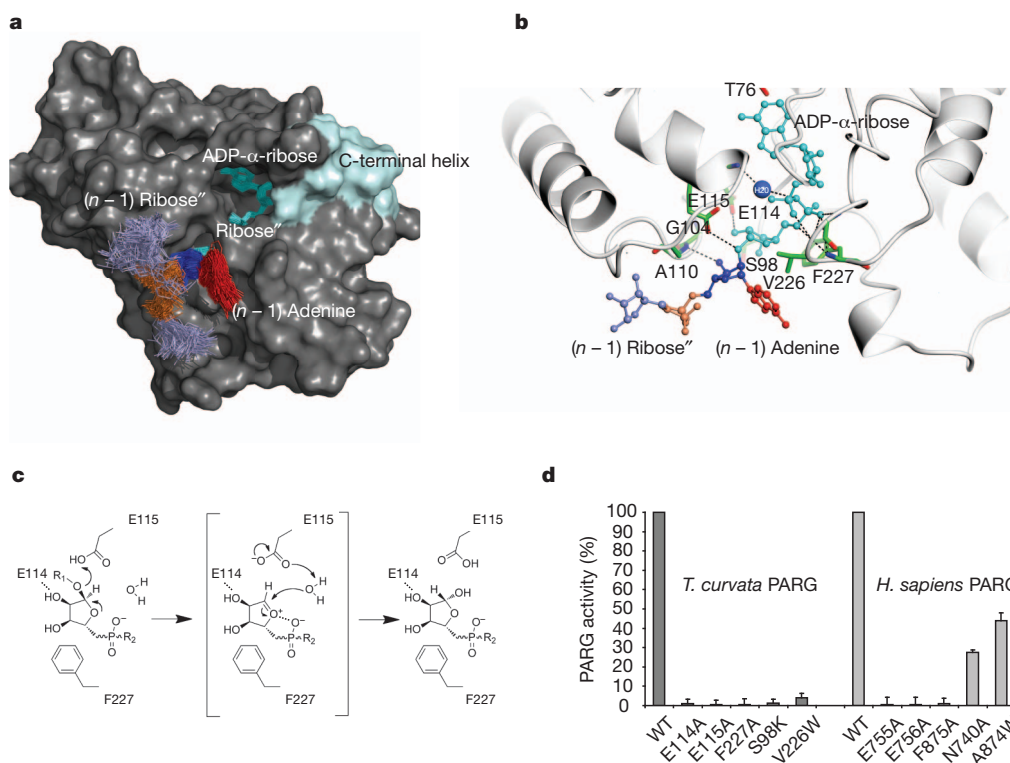


Figure 4 | Structural basis of PAR glycohydrolysis. **a**, The PARG solvent accessible surface derived from molecular dynamics simulations. **b**, A detailed view of the lowest energy PARG-ADP-ribose dimer model obtained from the 100 snapshot structures. Key active site residues are highlighted in green with PAR structural elements coloured as in **a**. **c**, Proposed mechanism for PAR glycohydrolysis. R_1 and R_2 represent $(n - 1)$ PAR and terminal adenosine moieties respectively. **d**, PARG activities of the *T. curvata* PARG mutants and the corresponding *H. sapiens* PARG mutants. WT, wild type. Error bars represent s.d. ($n = 3$).

might ultimately lead to the development of small, cell-permeable PARG inhibitors and the potential to manipulate the physiology of health and disease by interfering with PAR metabolism.

METHODS SUMMARY

Proteins with His₆-tags were purified from *E. coli*. A colourimetric PARG Assay Kit (Trevigen) was used to measure the loss of biotinylated PAR from histones. Auto-modified poly(ADP-ribosyl)ated human and bacterial PARP substrates were made by incubation with NAD¹⁰. *In vivo* activity of PARGs was tested in a yeast system with inducible expression of human PARP1. The *T. curvata* PARG structure was solved by means of single-wavelength anomalous diffraction on Pt-soaked crystals. Ligand-enzyme complexes were obtained by the soaking of PARG crystals. The PAR-PARG model was created using molecular dynamics simulations of the ADP- α -ribose dimer in complex with PARG.

Full Methods and any associated references are available in the online version of the paper at www.nature.com/nature.

Received 30 November 2010; accepted 28 July 2011.

Published online 4 September 2011.

- Hakmé, A., Wong, H. K., Dantzer, F. & Schreiber, V. The expanding field of poly(ADP-ribosylation) reactions. *EMBO Rep.* **9**, 1094–1100 (2008).
- D'Amours, D., Desnoyers, S., D'Silva, I. & Poirier, G. G. Poly(ADP-ribosylation) reactions in the regulation of nuclear functions. *Biochem. J.* **342**, 249–268 (1999).
- Koh, D. W. *et al.* Failure to degrade poly(ADP-ribose) causes increased sensitivity to cytotoxicity and early embryonic lethality. *Proc. Natl Acad. Sci. USA* **101**, 17699–17704 (2004).
- Hanai, S. *et al.* Loss of poly(ADP-ribose) glycohydrolase causes progressive neurodegeneration in *Drosophila melanogaster*. *Proc. Natl Acad. Sci. USA* **101**, 82–86 (2004).
- Karras, G. I. *et al.* The macro domain is an ADP-ribose binding module. *EMBO J.* **24**, 1911–1920 (2005).
- Till, S. & Ladurner, A. G. Sensing NAD metabolites through macro domains. *Front. Biosci.* **14**, 3246–3258 (2009).
- Patel, C. N., Koh, D. W., Jacobson, M. K. & Oliveira, M. A. Identification of three critical acidic residues of poly(ADP-ribose) glycohydrolase involved in catalysis: determining the PARG catalytic domain. *Biochem. J.* **388**, 493–500 (2005).
- Panda, S., Poirier, G. G. & Kay, S. A. *tej* defines a role for poly(ADP-ribosylation) in establishing period length of the *Arabidopsis* circadian oscillator. *Dev. Cell* **3**, 51–61 (2002).
- Koh, D. W. *et al.* Identification of an inhibitor binding site of poly(ADP-ribose) glycohydrolase. *Biochemistry* **42**, 4855–4863 (2003).
- Ahel, I. *et al.* Poly(ADP-ribose)-binding zinc finger motifs in DNA repair/checkpoint proteins. *Nature* **451**, 81–85 (2008).
- Kothe, G. O., Kitamura, M., Masutani, M., Selker, E. U. & Inoue, H. PARP is involved in replicative aging in *Neurospora crassa*. *Fungal Genet. Biol.* **47**, 297–309 (2010).
- Semighini, C. P., Savoldi, M., Goldman, G. H. & Harris, S. D. Functional characterization of the putative *Aspergillus nidulans* poly(ADP-ribose) polymerase homolog PrpA. *Genetics* **173**, 87–98 (2006).
- Hassa, P. O. & Hottiger, M. O. The diverse biological roles of mammalian PARPs, a small but powerful family of poly-ADP-ribose polymerases. *Front. Biosci.* **13**, 3046–3082 (2008).
- Tao, Z., Gao, P. & Liu, H. W. Studies of the expression of human poly(ADP-ribose) polymerase-1 in *Saccharomyces cerevisiae* and identification of PARP-1 substrates by yeast proteome microarray screening. *Biochemistry* **48**, 11745–11754 (2009).
- Lin, W., Ame, J. C., Aboul-El, N., Jacobson, E. L. & Jacobson, M. K. Isolation and characterization of the cDNA encoding bovine poly(ADP-ribose) glycohydrolase. *J. Biol. Chem.* **272**, 11895–11901 (1997).
- Kustatscher, G., Hothorn, M., Pugieux, C., Scheffzek, K. & Ladurner, A. G. Splicing regulates NAD metabolite binding to histone macroH2A. *Nature Struct. Mol. Biol.* **12**, 624–625 (2005).
- Ahel, D. *et al.* Poly(ADP-ribose)-dependent regulation of DNA repair by the chromatin remodeling enzyme ALC1. *Science* **325**, 1240–1243 (2009).
- Gottschalk, A. J. *et al.* Poly(ADP-ribosylation) directs recruitment and activation of an ATP-dependent chromatin remodeler. *Proc. Natl Acad. Sci. USA* **106**, 13770–13774 (2009).
- Timinszky, G. *et al.* A macrodomain-containing histone rearranges chromatin upon sensing PARP1 activation. *Nature Struct. Mol. Biol.* **16**, 923–929 (2009).
- Mueller-Diekmann, C. *et al.* The structure of human ADP-ribosylhydrolase 3 (ARH3) provides insights into the reversibility of protein ADP-ribosylation. *Proc. Natl Acad. Sci. USA* **103**, 15026–15031 (2006).
- Oka, S., Kato, J. & Moss, J. Identification and characterization of a mammalian 39-kDa poly(ADP-ribose) glycohydrolase. *J. Biol. Chem.* **281**, 705–713 (2006).

Supplementary Information is linked to the online version of the paper at www.nature.com/nature.

Acknowledgements We thank G. Clark for genomic DNA from *E. dispar*, G. Smith for the PARP inhibitor, M. Rossi for purified proteins and R. Thorough for editing English. We thank D. Ahel, A. Jordan, D. Ogilvie, S. Terzic, D. Neuhaus and S. Eustermann for helpful discussions. We are grateful to B. Lüscher for the gift of the PARP10 expression plasmid, and K. Labib and the members of his laboratory for advice with yeast work. This work was funded by Cancer Research UK. D.S. holds an AXA Research Fund post-doctoral fellowship. D.L. is a Royal Society University Research Fellow. Access to Diamond beamlines is gratefully acknowledged.

Author Contributions D.S. performed biochemical and *in vivo* experiments, prepared proteins for crystallization, analysed data and wrote the manuscript. M.S.D. performed structural/biophysical studies and analysed data. E.B. performed biochemical and *in vivo* experiments; R.W. performed supporting studies. M.A. and N.D. performed LC/MS analyses; P.L. performed molecular modelling studies. I.A. and D.L. wrote the manuscript, designed experiments and analysed data.

Author Information Atomic coordinates and structure factors have been deposited with the Protein Data Bank under accession codes 3SIG, 3SIH, 3SII and 3SIJ. Reprints and permissions information is available at www.nature.com/reprints. The authors declare no competing financial interests. Readers are welcome to comment on the online version of this article at www.nature.com/nature. Correspondence and requests for materials should be addressed to I.A. (iahel@picr.man.ac.uk).

METHODS

Plasmids and proteins. Bacterial and fungal PARG proteins and the *E. dispar* PARG were expressed from the pET28a vector (Novagen). Human PARG with an N-terminal truncation ($\Delta 1$ –455) was expressed from the pColdTF vector (Takara). The *A. fumigatus* Af293 gene (AFUA_4G11940), the *D. radiodurans* R1 ATCC13939 gene (DR_B0099) and the *E. dispar* SAW760 gene (EDI_110590) were amplified from genomic DNA, the human *PARP1* and *PARG* genes (Q86W56) were amplified from HeLa cDNA, while the *T. curvata* DSM 43183 gene (Tcur_1721) and the *A. variabilis* ATCC 29413 gene (Ava_4013) were synthesized according to the database sequence (GenScript USA). The *H. aurantiacus* ATCC 23779 *PARG* (Haur_1618) and *PARP* (Haur_4763) genes were amplified from genomic DNA extracted from a dried culture purchased from DSMZ. The codes in brackets indicate gene accession numbers. All proteins bear an N-terminal His tag with the exception of the *A. variabilis* PARG, which has a C-terminal His tag. Mutations were introduced using the QuickChange II site-directed mutagenesis kit (Stratagene). Proteins were expressed in *E. coli* Rosetta2(DE3) cells (Novagen). Recombinant proteins were purified on Ni-NTA beads according to standard procedure. For crystallization studies, the *T. curvata* PARG was purified by FPLC on a HisTrap HP column followed by Superdex 200 (GE Healthcare). The catalytic fragment of human *PARP1* (amino acids 818–1025) was expressed as a GST-tagged protein and purified on glutathione sepharose columns.

PARP activity assay. PARP automodification activity of the recombinant *H. aurantiacus* PARP was assayed in a 30-min room-temperature reaction containing 100 nM *H. aurantiacus* PARP, 200 μ M NAD (Trevigen), 50 mM Tris pH 7.5 and 50 mM NaCl with or without activated DNA (Trevigen), and with or without the PARP inhibitor KU-0058948 (10 μ M). After the reactions were stopped with the PARP inhibitor, 500 nM *H. aurantiacus* PARG and its catalytic glutamate mutants were added to the reaction for 30 min. The reactions were analysed by western blotting with rabbit anti-PAR antibodies as described later.

PARG activity assays. PARG activity of recombinant proteins was quantified with a colorimetric PARG assay kit (Trevigen), which measured the loss of biotinylated PAR from histones generated by *PARP1*. 3 nM PARG enzymes were used for this assay. For western-blot analysis of PARG activity, PAR was synthesized by the automodification of *PARP1* in a reaction mixture containing 2 units of *PARP1* (Trevigen), 200 μ M NAD (Trevigen), activated DNA (Trevigen), 50 mM Tris pH 7.5 and 50 mM NaCl at 20 °C. Reactions were stopped after 30 min by the addition of the PARP inhibitor KU-0058948. 500 nM PARGs were added to the reaction and incubated for another 30 min. The reactions were run on 4–12% SDS-PAGE gels and blotted onto a nitrocellulose membrane. PAR hydrolysis was detected by rabbit polyclonal anti-PAR antibodies (1:1,000; Trevigen). Western blots were analysed densitometrically by GeneTools (SynGene). For a direct visualization of PARG activity via SDS-PAGE, [32 P]-labelled NAD (GE Healthcare) was added to the above reaction to generate radioactively labelled poly(ADP-ribosyl)ated or mono(ADP-ribosyl)ated PARP substrates. 500 nM PARGs were subsequently added with or without the PARG inhibitor ADP-HPD (50 μ M). The reaction products were analysed by SDS-PAGE and visualized by autoradiography. For TLC analysis, the reactions were stopped by the addition of 50 mM ADP-ribose, spotted onto polyethyleneimine (PEI)-cellulose plates (Macherey-Nagel, Polygram CEL 300 PEI/UV₂₅₄) and developed in 0.15 M LiCl and 0.15 M formic acid. Dried plates were exposed on X-ray film or visualized by UV₂₅₄ shadowing.

Expression of heterologous proteins in *S. cerevisiae*. Plasmids used to introduce human *PARP1*, *A. fumigatus* PARG and *D. radiodurans* PARG into *S. cerevisiae* were created via the Gateway (Invitrogen) site-specific recombination system using yeast-specific destination vectors (Addgene)²². Human *PARP1* was introduced into pAG303GAL-ccdB (HIS3), while *A. fumigatus* PARG and *D. radiodurans* PARG were introduced into pAG423GAL-ccdB (URA3). The host strain W303-1a (MATa, *ade2-1*, *ura3-1*, *his3-11,15*, *trp1-1*, *leu2-3,112*, *can1-100*) was grown in rich YPD medium at 30 °C. The strain was first transformed with the human *PARP1*-harbouring plasmid resulting in His⁺ transformants with chromosomally integrated human *PARP1*. Subsequent transformation with the PARG-harbouring plasmids yielded His⁺Ura⁺ transformants with episomally maintained PARG. To induce the expression of *PARP1* and PARG from the *GAL1* promoter, the strains were grown overnight in minimal SC medium with 2% glucose. The overnight cultures were washed, resuspended in SC+2% raffinose at 7×10^6 cells ml⁻¹ and grown for one cell generation. Cells were centrifuged before resuspending in SC+2% galactose medium and grown overnight to induce the expression of human *PARP1* and PARG from the *GAL1* promoter. Yeast protein extracts were analysed by immunoblotting. Rabbit polyclonal anti-PAR antibody (Trevigen) and rabbit anti-*PARP1* antibody (Abcam) were used at 1:1,000 dilution, while rat monoclonal anti- α -tubulin antibody (Abcam) was used at 1:5,000 dilution. Rabbit anti-*D. radiodurans* PARG and anti-*A. fumigatus* PARG polyclonal antibodies were raised

against the respective full-length proteins purified from *E. coli* (Eurogentec) and applied at 1:1,000 dilution.

Crystallization, refinement and model building. Initial *T. curvata* PARG crystallization conditions were identified using the JCSG+ matrix screen (Molecular dimensions). Crystals suitable for diffraction experiments were obtained by sitting-drop vapour diffusion in 4 μ l drops containing equal volumes of protein and a solution containing 10% PEG 6K and 0.1 M Bicine buffer (pH 9.0). The crystals were derivatised by soaking with the same solution supplemented with 1 mM potassium tetracyanoplatinate (II) trihydrate for 10 min. For the ADP-ribose and ADP-HPD complexes, native crystals were soaked with 1 mM ligand for 1–2 h. The crystals were cryoprotected with the addition of 15% PEG 200 to the mother liquor and flash cooled in liquid nitrogen. Data were collected on beamline I04 at the Diamond Light Source Facility and reduced and scaled with the X-ray Detector Software suite (XDS)²³.

The ligand-free PARG crystal structure was determined by single-wavelength anomalous diffraction on a Pt-soaked crystal using Solve and Resolve as implemented in Phenix²⁴. The initial electron density map was of sufficient quality for Resolve to build 70% of the model. Further automated model building with ARPwARP²⁵ successfully constructed the entire model, with the exception of a small loop region incorporating residues 58–66, for which no corresponding density could be observed. The model was completed by iterative cycles of manual model building and real space refinement using the program Coot²⁶ and crystallographic refinement using Phenix.refine²⁴. Validation of the structure was performed with Molprobity. The processing, phasing and final refinement statistics are presented in Supplementary Table 1.

ITC. The thermodynamic ligand binding properties of wild-type *T. curvata* and two mutant proteins (E114A and E115A) were measured using a VP-ITC micro-calorimeter. Protein and ligand concentrations were 20 μ M and 200 μ M respectively in 50 mM Tris (pH 7.5), 100 mM NaCl. Titration curves were fitted using a nonlinear least squares method in Microcal Origin software. A model that was indicative of a single binding site was found to give the best fit in each case; this model was used to obtain the thermodynamic parameters shown in Supplementary Fig. 9.

Thermal shift assay. In each 50 μ l reaction 15 μ l of 300 \times Sypro Orange (Sigma), 2 μ l of water and 33 μ l of protein (4 mg ml⁻¹) in 25 mM Tris pH 7.5, 50 mM NaCl, 10% glycerol and 1 mM DTT were added to the wells of a 96-well thin-wall PCR plate (Bio-Rad). For thermal shift assays in the presence of ADP-ribose, 2 μ l of 25 mM ADP-ribose was added instead of water. Samples were placed in a CFX96 Real Time PCR thermal cycler (Bio-Rad) and slowly heated from 15 to 95 °C with sample fluorescence recorded every 0.2 °C. Fluorescence was monitored at 575 nm (emission), using 490 nm for excitation.

Analysis of PAR chains by sequencing gels. [32 P]-labelled PAR chains produced by PARPs were resolved in 10% sequencing gels in TBE buffer. Reactions were stopped by the addition of 600 μ l 20% ice-cold trichloroacetic acid (TCA). The precipitated material was washed twice with 5% TCA. The pellet was then incubated with 70 μ l of 10 mM Tris and 1 mM EDTA buffer (pH 12) for 2 h at 60 °C to detach PAR chains. PAR was phenol-chloroform extracted, dried and resuspended in 2 mM EDTA-formamide buffer before loading. The products were visualized by autoradiography.

Computational simulations. NAMD software²⁷ was used to perform all molecular dynamics simulations of the ADP- α -ribose dimer in complex with PARG. The topology and parameters files for the ligand were obtained using the Antechamber program²⁸ and AM1-BCC charges²⁹. The additional ADP- α -ribose monomer was added to the ADP- α -ribose bound to PARG by creating an $\alpha(1' \rightarrow 2')$ O-glycosidic bond. Five conformers of the added monomer were taken as starting points for molecular dynamics simulations. The PARG-ADP- α -ribose dimer complex model was then immersed in a periodic water box (TIP3), as half of the ligand was in contact with the bulk solvent. Then, for each conformer, several simulations (0.5 ns) were run with variable parameters (200 K or 310 K, peptidic backbone fixed, restrained or free). During these MD simulations, snapshots (100 in total for clarity) were periodically extracted and energy-minimized, to represent the conformational flexibility of the ADP- α -ribose dimer.

Analyses by UHPLC coupled to QTOFMS. Ultrahigh-performance liquid chromatography (UHPLC) coupled to quadrupole-time-of-flight mass spectrometry (QTOFMS) was used to analyse the nucleotide products of PARG enzymes. The poly(ADP-ribosyl)ated *PARP1* was treated with *T. curvata* PARG, and the mixture was filtered using centrifuges (30 kD cut-off). The analysis of the filtrate was performed using a modified previously described procedure³⁰, which used ion-pair chromatography for the separation of nucleotides and negative electrospray ionization for mass spectrometric detection. All analyses were performed using a Waters Acquity UPLC system (Waters Corp.), equipped with a binary solvent delivery system and autosampler. The chromatographic separations used a column (50 mm \times 2.1 mm) filled with a 1.7 μ m BEH C18 stationary phase

(Waters Corp.). Binary gradients at a flow rate of 0.4 ml min^{-1} were applied for the elution. The eluent A was water containing 5 mmol l^{-1} of pentylamine, while the pH value was adjusted to 6.5 using acetic acid. A fast elution gradient was applied, which allowed an efficient separation of NAD^+ and ADP-ribose within 5 min. The gradient started at 2% B and then the percentage of B linearly increased to 25% in 5 min.

The mass spectrometry was performed on a QTOF Premier instrument (Waters Micromass) using an orthogonal Z-spray-electrospray interface. The drying gas and the nebulizing gas was nitrogen. The desolvation gas flow was set to 700 l h^{-1} at a temperature of 300°C . The cone gas flow was adjusted to 25 l h^{-1} , and the source temperature to 120°C . The capillary and cone voltages were 3,200 V and 30 V respectively. The instrument was operated in V mode with TOFMS data being collected between m/z 100–1,000, applying a collision energy of 4 eV. All spectra were recorded using the extended dynamic range (DRE) option in order to correct for possible peak saturations, the data were collected in the centroid mode with a scan time of 0.08 s and interscan time of 0.02 s. In order to ensure maximum accuracy and reproducibility of the system, all acquisitions were carried out using an independent reference spray via the lock spray interface. Leucine enkephalin was applied as a lock mass in negative ionization mode (m/z 554.2615).

The chromatograms, recorded in the total ion current (TIC) mode, were systematically examined by manually generating mass spectra of each visible individual peak using the background-subtraction option and searching for target components expected to occur in the mixture, in particular ADP-ribose and NAD^+ , using extracted ion chromatograms. The target analyses were based on the accurate mass feature of the instrument, applying a mass window of 50 mDa.

Elemental composition of the selected ions was calculated using the MassLynx software incorporated in the instrument. The main criterion for selecting the elements to be included in search parameters for the calculation of the molecular formula was the elemental composition of the presumed parent compounds. According to the instrument specifications, the acceptable deviation from the theoretical m/z values was set at 5 mDa.

22. Alberti, S., Gitler, A. D. & Lindquist, S. A suite of Gateway cloning vectors for high-throughput genetic analysis in *Saccharomyces cerevisiae*. *Yeast* **24**, 913–919 (2007).
23. Kabsch, W. Evaluation of single-crystal X-ray diffraction data from a position-sensitive detector. *J. Appl. Cryst.* **21**, 916–924 (1988).
24. Adams, P. D. *et al.* PHENIX: a comprehensive Python-based system for macromolecular structure solution. *Acta Crystallogr. D* **66**, 213–221 (2010).
25. Perrakis, A., Morris, R. & Lamzin, V. S. Automated protein model building combined with iterative structure refinement. *Nature Struct. Biol.* **6**, 458–463 (1999).
26. Emsley, P. & Cowtan, K. Coot: model-building tools for molecular graphics. *Acta Crystallogr. D* **60**, 2126–2132 (2004).
27. Phillips, J. C. *et al.* Scalable molecular dynamics with NAMD. *J. Comput. Chem.* **26**, 1781–1802 (2005).
28. Cornell, W. D. *et al.* A second generation force field for the simulation of proteins, nucleic acids, and organic molecules. *J. Am. Chem. Soc.* **117**, 5179–5197 (1995).
29. Jakalian, A., Jack, D. B. & Bayly, C. I. Fast, efficient generation of high-quality atomic charges. AM1-BCC model: II. Parameterization and validation. *J. Comput. Chem.* **23**, 1623–1641 (2002).
30. Coulrier, L. *et al.* Simultaneous quantitative analysis of metabolites using ion-pair liquid chromatography-electrospray ionization mass spectrometry. *Anal. Chem.* **78**, 6573–6582 (2006).

SUMO1-dependent modulation of SERCA2a in heart failure

Changwon Kho^{1*}, Ahyoung Lee^{1*}, Dongtak Jeong¹, Jae Gyun Oh², Antoine H. Chaanine¹, Eddy Kizana³, Woo Jin Park² & Roger J. Hajjar¹

The calcium-transporting ATPase ATP2A2, also known as SERCA2a, is a critical ATPase responsible for Ca^{2+} re-uptake during excitation-contraction coupling. Impaired Ca^{2+} uptake resulting from decreased expression and reduced activity of SERCA2a is a hallmark of heart failure¹. Accordingly, restoration of SERCA2a expression by gene transfer has proved to be effective in improving cardiac function in heart-failure patients², as well as in animal models³. The small ubiquitin-related modifier (SUMO) can be conjugated to lysine residues of target proteins⁴, and is involved in many cellular processes⁵. Here we show that SERCA2a is SUMOylated at lysines 480 and 585 and that this SUMOylation is essential for preserving SERCA2a ATPase activity and stability in mouse and human cells. The levels of SUMO1 and the SUMOylation of SERCA2a itself were greatly reduced in failing hearts. SUMO1 restitution by adeno-associated-virus-mediated gene delivery maintained the protein abundance of SERCA2a and markedly improved cardiac function in mice with heart failure. This effect was comparable to SERCA2A gene delivery. Moreover, SUMO1 overexpression in isolated cardiomyocytes augmented contractility and accelerated Ca^{2+} decay. Transgene-mediated SUMO1 overexpression rescued cardiac dysfunction induced by pressure overload concomitantly with increased SERCA2a function. By contrast, downregulation of SUMO1 using small hairpin RNA (shRNA) accelerated pressure-overload-induced deterioration of cardiac function and was accompanied by decreased SERCA2a function. However, knockdown of SERCA2a resulted in severe contractile dysfunction both *in vitro* and *in vivo*, which was not rescued by overexpression of SUMO1. Taken together, our data show that SUMOylation is a critical post-translational modification that regulates SERCA2a function, and provide a platform for the design of novel therapeutic strategies for heart failure.

It was previously reported that SERCA2a activity could be modulated by post-translational modifications (PTMs) such as glutathiolation⁶ and nitration⁷. We identified SUMO1 as a SERCA2a interactor in a proteomic screen (Supplementary Fig. 1a, b). We confirmed that SERCA2a binds *in vivo* to SUMO1 and to ubiquitin-conjugating enzyme E2I (UBE2I, also known as UBC9) (Supplementary Fig. 1c–e).

We then examined whether SERCA2a is indeed SUMOylated in human hearts. The SERCA2a band was present along with other slowly migrating SERCA2a bands (Fig. 1a, top panel), which represent the SUMOylated protein. The level of SUMOylated SERCA2a was significantly reduced in failing hearts compared to normal hearts. SUMOylation of SERCA2a was specific for SUMO1 (but not for SUMO2 or 3) (Supplementary Fig. 1f). Along with the reduction in SERCA2a, which is consistent with previous reports, the level of SUMO1 was also significantly reduced in failing hearts. However, the levels of UBC9 and SENP1, critical SUMOylating and de-SUMOylating enzymes, were unaltered in failing hearts (Fig. 1a, bottom panel). These

data indicate that the reduction in SERCA2a SUMOylation might be primarily due to the reduced level of SUMO1 and not to alterations in the level or activity of SUMOylating or de-SUMOylating factors. In additional experiments, we observed that the levels of both SUMO1 and SERCA2a were significantly reduced in a murine model of heart failure induced by pressure overload (Fig. 1b), and in a porcine model of heart failure induced by volume overload (Fig. 1c).

To characterize the potential role of SUMO1 during heart failure, we restored SUMO1 expression in a murine model of transverse aortic constriction (TAC)-induced heart failure. We delivered cardiotropic recombinant adeno-associated viruses, serotype 9 (rAAV9) when mice developed heart failure (Fig. 1d). Gene transfer of rAAV9-SUMO1 resulted in a dose-dependent increase in SUMO1 in the myocardium one month after gene transfer (Supplementary Fig. 2). After induction of heart failure and before gene delivery (two months after TAC), cardiac function was markedly decreased in the mice. The TAC mice received tail-vein injection of either rAAV9-GFP (encoding green fluorescent protein, used as a negative control), rAAV9-SERCA2a (positive control) or rAAV9-SUMO1, and were followed for two more months. Cardiac function assessment by echocardiography revealed substantial improvements after rAAV9-SUMO1 gene delivery (at a total of four months after TAC), despite constant pressure overload, compared with severe deterioration in the rAAV9-GFP control (Fig. 1e, f and Supplementary Table 1). The mice injected with rAAV9-SUMO1 recovered cardiac function to the same degree as the mice injected with rAAV9-SERCA2a. Furthermore, haemodynamic analyses showed substantially improved left-ventricular function in the SUMO1-treated mice, and stabilization of the ratio of heart-weight to body-weight (Supplementary Fig. 3 and Supplementary Table 2). The survival rate in the rAAV9-SUMO1-injected mice was also significantly extended compared with rAAV9-GFP-injected mice with heart failure (Fig. 1g). Consistent with the improvement in cardiac performance in rAAV9-SUMO1-injected mice, protein levels of SERCA2a were significantly increased in rAAV9-SUMO1-injected mice compared with rAAV9-GFP-injected animals, indicating that SUMO1 restoration maintained SERCA2a levels during heart failure (Fig. 1h). Thus, we provide the first evidence, to our knowledge, that cardiac restoration of SUMO1 by rAAV9-mediated gene transfer enables long-term improvement of cardiac function. These findings provide further evidence that manipulating PTMs of SERCA2a may result in a functional benefit.

SUMOylation usually occurs in a highly conserved recognition motif⁸. We found two putative SUMO conjugation sites in human SERCA2a, lysines 480 and 585. These residues are perfectly conserved in mouse, rat, pig and human SERCA2a (Supplementary Fig. 4). We generated three SERCA2a variants with mutations in these lysines. Whereas K480R and K585R were SUMOylated at levels indistinguishable from wild-type SERCA2a, the K480R/K585R mutant was completely un-SUMOylated

¹Cardiovascular Research Center, Mount Sinai School of Medicine, 1 Gustave L. Levy Place, Box 1030, New York, New York 10029, USA. ²College of Life Sciences, Gwangju Institute of Science and Technology, 261 Cheomdan-gwagi-ro, Buk-gu, Gwangju, 500-712, South Korea. ³Westmead Millennium Institute, Sydney Medical School and Department of Cardiology, Westmead Hospital, Westmead NSW 2145, Australia.

*These authors contributed equally to this work.

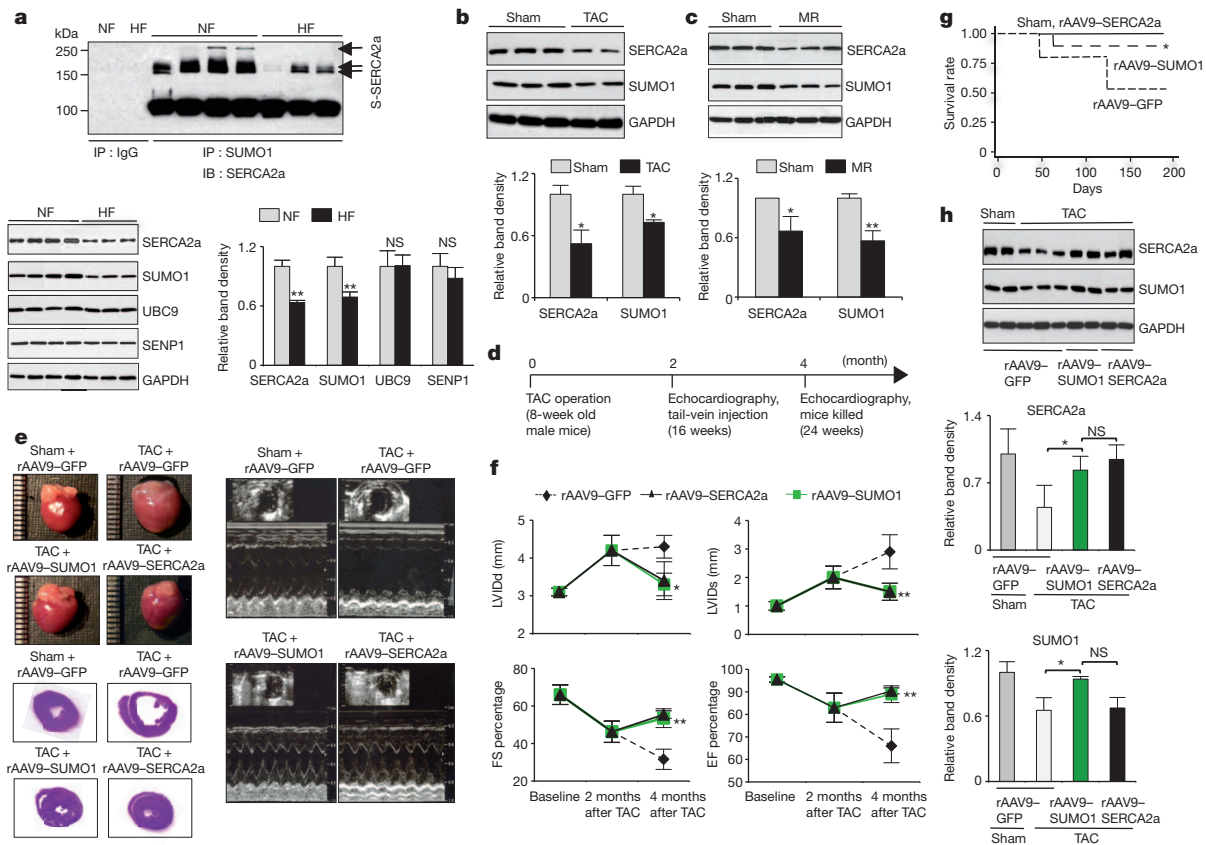


Figure 1 | Endogenous SUMO1 protein levels are decreased in both experimental animal and human heart failure. **a**, SERCA2a SUMOylation in human cardiac tissues ($n = 4$ per heart failure (HF), $n = 3$ per non-failing control (NF)). Representative immunoblots and protein quantification results are shown ($n = 5$ in each group). S-SERCA2a, SUMOylated SERCA2a; GAPDH, glyceraldehyde 3-phosphate dehydrogenase; NS, not significant. **b**, **c**, Representative immunoblots for SUMO1 and SERCA2a, and quantification of protein levels, in models of heart failure. The experimental models are TAC-induced heart failure in mice (**b**; $n = 5$ TAC, $n = 8$ sham-operated control hearts), and porcine heart failure induced by mitral valve regurgitation (MR) (**c**; $n = 3$ MR, $n = 5$ sham-operated). **d**, Protocol for SUMO1 gene therapy in mouse model of heart failure. **e**, Representative gross images of whole hearts (top left panel), haematoxylin and eosin staining results (bottom left panel) and two-dimensional guided M-mode images of the left ventricle (right panel), from rAAV9-SUMO1-injected mice, or negative

(Fig. 2a). Because the SUMOylated lysine residues, K480 and K585, reside in the nucleotide-binding domain that binds ATP, we predicted that SUMOylation might affect the ATPase activity of SERCA2a. As expected, the K480R/K585R mutant showed a significantly decreased ATPase activity compared to the wild type. SUMO1 co-expression significantly increased the ATPase activity of the wild type but did not affect the ATPase activity of K480R/K585R (Fig. 2b). We further tested whether SUMOylation affects the ATP-binding affinity of SERCA2a. Co-expression of SUMO1 markedly increased the ATP-binding affinity of the wild type. By contrast, K480R/K585R had considerably less ATP-binding affinity, which was not affected by SUMO1 co-expression (Fig. 2c). These data indicate that SUMOylation increases the ATPase activity of SERCA2a at least partially by enhancing its ATP-binding affinity.

Because both SERCA2a and SUMO1 levels were reduced in heart failure, we studied whether SUMOylation affects SERCA2a stability. The estimated half-life of the wild type was 4.9 days, which increased to 5.9 days when SUMO1 was co-expressed. The estimated half-life of the K480R/K585R mutant was significantly reduced compared to wild type (Fig. 2d). In endoplasmic-reticulum-associated protein degradation, misfolded proteins are usually degraded by 26S proteasomes after polyubiquitination⁹. To determine whether the instability of the

controls injected with rAAV9-SERCA2a or rAAV9-GFP, subjected to TAC. **f**, Effect of rAAV9-SUMO1 treatment on echocardiography indices of left-ventricle function measured by fractional shortening (FS) and ejection fraction (EF), and left-ventricle end-diastolic diameter measured by internal diameters in end-diastole (LVIDd) and end-systole (LVIDs). TAC rAAV9-GFP, $n = 10$; TAC rAAV9-SUMO1, $n = 14$; TAC rAAV9-SERCA2a, $n = 12$. **g**, Survival of animals after rAAV9-mediated SUMO1 restoration. The Kaplan-Meier method was used to analyse animal lifespan after infection with different viruses. rAAV9-GFP, $n = 12$; rAAV9-SUMO1 or rAAV9-SERCA2a (5×10^{10} vg mouse $^{-1}$), $n = 24$ in each group. Of 50 TAC-operated animals, 34 mice survived and were further divided into groups that received rAAV9-GFP ($n = 9$), rAAV9-SUMO1 ($n = 13$) or rAAV9-SERCA2a ($n = 12$). **h**, Immunoblot results from a representative experiment and protein quantification ($n = 5$ per group). All data represent the mean \pm s.d. *, $P < 0.05$ versus the respective control, as determined by Student's *t*-test.

K480R/K585R mutant involves ubiquitin-dependent degradation, we performed ubiquitination assays of SERCA2a in HEK-293 cells. SUMO1 overexpression decreased levels of polyubiquitin-conjugated wild-type SERCA2a, whereas it did not alter polyubiquitination of the K480R/K585R mutant (Supplementary Fig. 5). These data support our hypothesis that SUMOylation may compete with ubiquitination on SERCA2a, and indicate that SUMOylation increases the stability of SERCA2a by preventing 26S-proteasomal degradation of SERCA2a.

To examine the physiological function of SUMO1, we isolated cardiomyocytes from adult mice after TAC-induced heart failure or sham operation, and then infected the cells with adenovirus expressing either β -galactosidase (Ad- β -gal) or SUMO1 (Ad-SUMO1). When infected with Ad-SUMO1, cardiomyocytes from sham-operated mice showed significantly enhanced contractility compared to Ad- β -gal-infected cardiomyocytes. A more prominent enhancement in contractility was observed when failing cardiomyocytes were infected with Ad-SUMO1. Ad-SUMO1-infected cardiomyocytes showed increased Ca^{2+} amplitude and faster Ca^{2+} decay compared to the Ad- β -gal-infected controls. The overall inotropic effect of SUMO1 overexpression was comparable to that induced by SERCA2a overexpression (Fig. 3a). It is possible that SUMO1 overexpression

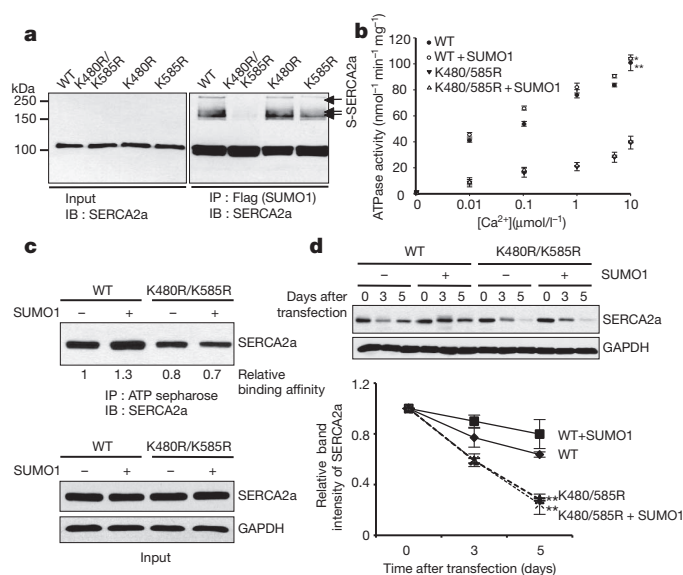


Figure 2 | SUMO1 is conjugated to lysines 480 and 585 of SERCA2a and is required for SERCA2a function. **a**, SUMOylation of SERCA2a *in vivo*. HEK-293 cells were co-transfected with plasmids expressing Flag-tagged SUMO1 and Myc-tagged UBC9 and wild-type or mutant SERCA2a. SUMOylated forms of SERCA2a were detected by immunoblot (IB) analysis using anti-SERCA2a antibody. IP, immunoprecipitation. **b**, Ca²⁺-dependent ATPase activity of wild-type SERCA2a and the K480R/K585R mutant in the presence and absence of additional SUMO1. The data represent three independent experiments, each performed in duplicate. **c**, ATP binding capacity of wild-type and K480R/K585R SERCA2a. Lysates from HEK-293 cells transfected with the indicated plasmids were affinity-precipitated with ATP-sepharose and subsequently subjected to immunoblot analysis with an anti-SERCA2a antibody. **d**, Effects of SUMO1 overexpression on the stability of wild-type and K480R/K585R SERCA2a mutant protein in HEK-293 cells. HEK-293 cells were transfected with wild-type or K480R/K585R SERCA2a expression plasmids, together with empty or SUMO1-expression plasmids. Cells were treated with cycloheximide 48 h after transfection to inhibit protein synthesis. Immunoblot analysis was performed with the indicated antibodies at different time points. Quantification data represent the ratio relative to day 0 ($n = 3$). All data represent the mean \pm s.d. *, $P < 0.05$; **, $P < 0.001$ versus the respective control, as determined using Student's *t*-test.

enhanced cardiomyocyte contractility at least partly by increasing the enzymatic activity and stability of SERCA2a.

Given our positive *in vitro* and gene-delivery results, we then proceeded to define the physiological consequences of SUMO1 overexpression *in vivo*. We generated cardiac-specific, Cre/loxP-conditional *Sumo1*-transgenic mice (Supplementary Fig. 6a, b). Along with increased SUMO1 levels, the levels of both SERCA2a itself and its SUMOylation were significantly induced by tamoxifen administration (Supplementary Fig. 6c, d). No cardiac dysfunction was apparent in these transgenic animals (Supplementary Table 3). Wild-type and transgenic mice were subjected to TAC operations and heart failure developed in two months, characterized by a decrease of less than 50% in fractional shortening. One month after tamoxifen was administered (three months in total after TAC), cardiac function was examined. At this point, wild-type mice showed severe failing phenotypes with left ventricular dilation and a low ejection fraction. However, tamoxifen-induced overexpression of SUMO1 markedly reversed these failing phenotypes, resulting in less left ventricular dilation and improved fractional shortening and ejection fraction (Fig. 3b, c and Supplementary Table 4). Haemodynamic analyses also showed improved left ventricular function in the transgenic mice, along with stabilization of heart-weight to body-weight ratio (Supplementary Fig. 7 and Supplementary Table 5). The recovery from cardiac dysfunction induced by SUMO1 overexpression was also manifested by the increased survival rate of transgenic animals under prolonged pressure overload

(Fig. 3d). All transgenic animals survived 100 days after tamoxifen administration, whereas only seven out of fifteen wild-type animals survived at this time point. These findings are consistent with the results from the rAAV9 gene-delivery study.

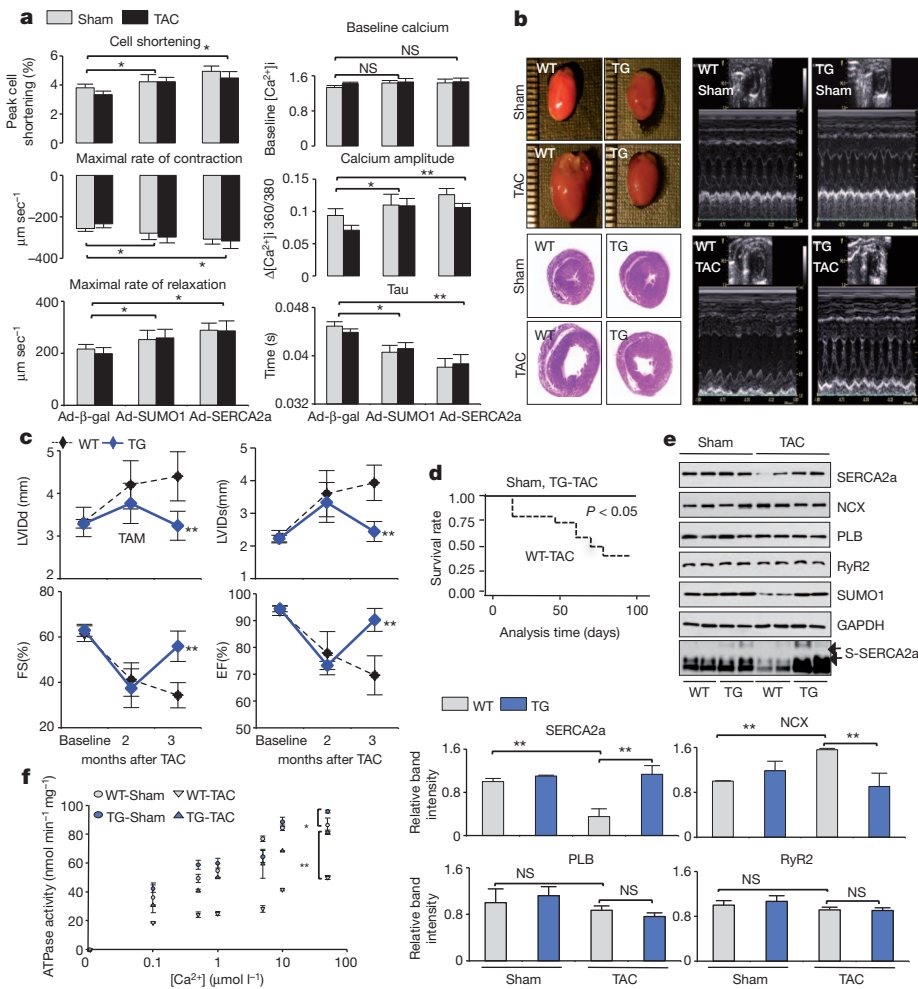
Next, we monitored the expression levels of key regulatory proteins involved in Ca²⁺ homeostasis. After TAC, a notable reduction in the level of SERCA2a was observed, and levels of sodium/calcium exchanger 1 (SLC8A1, also known as NCX1) increased compared to sham-operated controls (Fig. 3e). A decrease in SERCA2a function is coupled with an increase in NCX1 function in failing hearts¹⁰. The TAC-induced changes in the levels of SERCA2a and NCX1 did not occur in transgenic animals.

In wild-type animals, TAC resulted in a significant reduction of SERCA2a ATPase activity, but this was significantly lessened in the transgenic animals (Fig. 3f). Taken together, these data indicate that SUMO1 overexpression ameliorates cardiac dysfunction induced by pressure overload.

To evaluate the effects of downregulation of SUMO1 in hearts, we generated rAAV9 viruses that express SUMO1-directed shRNA (rAAV9-shSumo1), or a scrambled sequence (rAAV9-SC). We confirmed the efficiency and specificity of the shSumo1 in mice (Supplementary Fig. 8a, b). Six weeks after tail-vein injection of viruses, cardiac function was evaluated. Hearts from rAAV9-shSumo1-injected mice showed left ventricular dilation and functional deterioration compared to hearts from rAAV9-SC-injected mice (Fig. 4a, b and Supplementary Tables 6 and 7). Injection of an increased dose of rAAV9-shSumo1 resulted in more severe cardiac dysfunction (Supplementary Fig. 8c, d). Cardiac dysfunction induced by rAAV9-shSumo1 manifested as sudden death of the mice. All mice receiving 1×10^{11} viral genomes (vg) of rAAV9-shSumo1 died within 3 weeks. The death rates of mice that received 3×10^{10} vg and 5×10^{10} vg of rAAV9-shSumo1 were slightly higher than the rates in control mice that received rAAV9-SC (none of these control mice died) (Fig. 4c). SERCA2a protein levels were decreased by approximately 40% in rAAV9-shSumo1-injected hearts, and NCX1 levels were slightly elevated, although this was not statistically significant. As expected, SUMOylation of SERCA2a was also notably blunted (Fig. 4d and Supplementary Fig. 8e). These results support the premise that SUMO1 is important for the stability and function of SERCA2a. Downregulation of SUMO1 also significantly suppressed the ATPase activity of SERCA2a (Fig. 4e), and this was further impaired when a higher dose of rAAV9-shSumo1 was injected (Supplementary Fig. 8f). These data show that SUMO1 is an essential regulator of SERCA2a function in the heart.

We next tested the SUMOylation status of some important cardiac transcriptional factors such as GATA binding protein 4 (GATA4)¹¹ and serum response factor (SRF)¹². These factors are involved in cardiac pathogenesis and have been reported by other groups to be regulated by SUMOylation^{11,12}. The SUMOylation status and protein expression level of GATA4 were not altered by SUMO1 gene delivery, whereas SUMOylation of SRF was increased (Supplementary Fig. 9). Increased SRF SUMOylation may contribute to the activation of certain genes, such as SERCA2a and genes encoding contractile proteins, during heart failure¹³. Several other transcriptional factors, such as SP1 and SP3, and calcium-regulatory signalling pathways, are associated with SERCA2a gene expression^{14,15}. Notably, the cleaved form of SRF was detected in failing hearts and this was decreased by SUMO1 and SERCA2a gene delivery. Recent studies have shown that caspase-3-mediated SRF cleavage occurs in heart failure¹⁶ and SUMO1 overexpression blocks cell-death signalling induced by both tumour necrosis factor and FAS¹⁷. Our findings and other recent studies indicate that SUMO1 restoration increases levels of SUMOylated SRF and may alter apoptotic signalling in heart failure.

To determine the critical link between SUMO1 and SERCA2a in the setting of cardiac dysfunction, we knocked down SERCA2a using a lentiviral system carrying a shRNA directed towards *Serca2a* (shSerca2a). In isolated cardiomyocytes from rat and mouse, shSerca2a markedly



decreased contractile parameters and these were not improved by overexpression of SUMO1 (Supplementary Figs 10a, b and 11a). *In vivo*, rat ventricular function was significantly decreased after gene transfer of sh*Serca2a* but no improvements were observed after co-infection with Ad-*Sumo1* (Supplementary Fig. 10c–f and Supplementary Table 8). In mice, antecedent overexpression of SUMO1 did not rescue ventricular function after lentiviral gene transfer of sh*Serca2a* (Supplementary Fig. 11b–e and Supplementary Table 9). Taken together, these four experiments show that SERCA2a is critical in modulating SUMO1's beneficial effects in the setting of heart failure. However we cannot exclude that knockdown of SERCA2a may have effects on other proteins that would not allow SUMO1 to rescue contractile function.

We have shown that SERCA2a is SUMOylated at two lysine residues. We found that the levels of both SERCA2a itself and SERCA2a SUMOylation were significantly reduced in failing hearts. We have provided compelling evidence that the reduction of SERCA2a SUMOylation is a direct result of reduced SUMO1 levels in failing hearts. This reduction in SUMOylation correlated with reduced ATPase activity and decreased SERCA2a stability. Moreover, restoration of SUMO1 reversed contractile dysfunction in failing hearts. Our findings are summarized in Fig. 4f.

It is possible that SUMOylation may induce a conformational change¹⁸ in SERCA2a or may provide an additional interface for ATP binding, leading to increased ATPase activity. It is also possible that SUMOylation may reciprocally and competitively affect other PTMs of SERCA2a and, in particular, may alter acetylation¹⁹. Notably, acetylation of SERCA2a was recently identified in a large-scale analysis of the human acetylome in cancer cell lines²⁰. We also found that SERCA2a is indeed acetylated and that this acetylation is

more prominent in failing hearts and can be reversed by SIRT1 deacetylase (Kho *et al.*, unpublished data). Further elucidation of the reciprocal or competitive relationship between SUMOylation and acetylation of SERCA2a is currently underway. There are precedents for this type of SUMOylation-mediated inhibition of protein degradation. For example, SUMOylation of axin, a negative regulator of Wnt signalling, prevents ubiquitination and thus induces a prolonged axin half-life²¹. Similarly, SUMOylation of the RNA helicases p68 and p72 increases their stability by reducing ubiquitin-proteasome-mediated protein degradation²². Detailed biochemical analyses are underway to identify the ubiquitination sites in SERCA2a.

Our data show that the amount of SUMO1 is reduced in failing hearts from various species, indicating that the level of cellular SUMO1 must be precisely maintained and controlled for proper cardiomyocyte function. Our finding that restoration of SUMO1 reversed TAC-induced heart failure indicates that a reduction in SUMO1 levels is a direct cause of contractile dysfunction. Our study was based on strong background data that has clearly established impaired SERCA2a as a key molecular abnormality in heart failure. The therapeutic effects of SUMO1, with near-complete recovery of contractile function, are notable, considering that expression of only a single gene is altered. In contrast to the reduction of SUMO1 levels in failing hearts, the levels of the SUMOylating and de-SUMOylating enzymes UBC9 and SENP1 were unaltered, and did not change when shSUMO1 was administered or when SUMO1 levels were restored (data not shown). Therefore, the specificity and capacity of SUMOylation itself is unlikely to be altered in failing hearts. Instead, the supply of SUMO1 itself seems to have the largest impact on SUMOylation. In this regard, it is notable that depletion of cellular ubiquitin is sufficient to cause neuronal dysfunction and death²³.

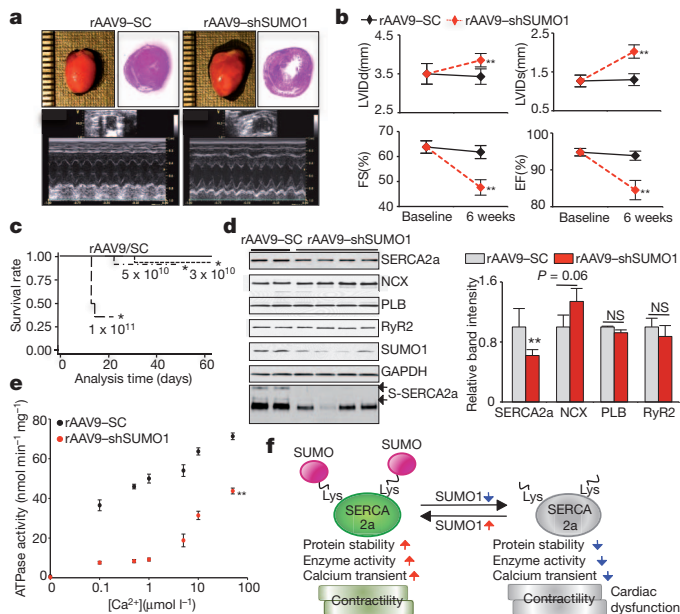


Figure 4 | Reduction of SUMO1 levels accelerates cardiac dysfunction.

a, Heart morphology, cardiac function and heart dimensions were examined in mice 6 weeks after injection of 5×10^{10} vg of rAAVs. Representative gross images of the hearts (top left panel), haematoxylin and eosin staining results (top right panel) and M-mode imaging data (bottom panel) are shown. **b**, Echocardiographic measurements, as in Fig. 1f, for rAAV9-shSC or rAAV9-shSUMO1-injected mice (5×10^{10} vg mouse $^{-1}$, $n = 14$ per group). Kaplan–Meier curves are shown for different doses of rAAV9-shSUMO1 ($n = 14$ per group) or rAAV9-shSC (5×10^{10} vg mouse $^{-1}$, $n = 24$). Solid line represents rAAV9-shSC-injected animals and dotted lines represent rAAV9-shSUMO1-injected animals. **d**, Representative immunoblot analysis for the indicated cardiac proteins in samples collected 6 weeks after tail-vein injection of rAAV9-shSC (5×10^{10} vg mouse $^{-1}$, $n = 4$) or rAAV9-shSUMO1 (5×10^{10} vg mouse $^{-1}$, $n = 7$) (left panel). Quantification of GAPDH-corrected immunoblot signals (right panel). **e**, Ca^{2+} -dependence of ATPase activity of SERCA2a. ATPase activity was examined in preparations from shSC-injected and shSUMO1-injected hearts (5×10^{10} vg mouse $^{-1}$, $n = 3$ per group). All data represent mean \pm s.d. *, $P < 0.05$; **, $P < 0.001$ versus the respective control, as determined using Student's t -test. **f**, A working model for the regulation of SERCA2a function by SUMOylation. Under basal conditions, SUMOylation enhances the stability of SERCA2a and its Ca^{2+} pump function to regulate cardiac contractility. However, increased levels of unSUMOylated SERCA2a due to low SUMO1 protein pools trigger impaired SERCA2a activity and induce cardiac dysfunction under pathophysiological conditions.

In this study we demonstrate a novel regulatory mechanism whereby SUMOylation affects SERCA2a activity and the overall contractile properties of the heart. This highlights the importance of post-translational mechanisms in experimental and human heart failure. In addition, the beneficial effects of SUMO1 on cardiac contractility and survival indicate that targeting SUMO1 may provide a novel therapeutic strategy for the treatment of heart failure.

METHODS SUMMARY

Animals. All mice and rats were housed and treated in accordance with guidelines from the NIH and institutional animal care and use committees, and the protocols used were approved by the Mount Sinai School of Medicine animal care and use committee.

Human heart samples. Left ventricular samples were obtained from explanted human hearts obtained at the time of cardiac transplantation. Non-failing hearts (which were used as controls) were obtained from donors who died from neurological diseases or motor-vehicle accidents, and who had normal cardiac function by echocardiography. The five donors, three males and two females, had a median

age of 62. The heart-failure patients, three males and two females, had a median age of 60 and their average ejection fraction was $20 \pm 3\%$.

Full Methods and any associated references are available in the online version of the paper at www.nature.com/nature.

Received 18 February; accepted 1 August 2011.

Published online 7 September 2011.

- Meyer, M. *et al.* Alterations of sarcoplasmic reticulum proteins in failing human dilated cardiomyopathy. *Circulation* **92**, 778–784 (1995).
- Jessup, M. *et al.* Calcium upregulation by percutaneous administration of gene therapy in cardiac disease (CUPID): a phase 2 trial of intracoronary gene therapy of sarcoplasmic reticulum Ca^{2+} -ATPase in patients with advanced heart failure. *Circulation* **124**, 304–313 (2011).
- Kawase, Y. *et al.* Reversal of cardiac dysfunction after long-term expression of SERCA2a by gene transfer in a pre-clinical model of heart failure. *J. Am. Coll. Cardiol.* **51**, 1112–1119 (2008).
- Johnson, E. S. Protein modification by SUMO. *Annu. Rev. Biochem.* **73**, 355–382 (2004).
- Geiss-Friedlander, R. & Melchior, F. Concepts in sumoylation: a decade on. *Nature Rev. Mol. Cell Biol.* **8**, 947–956 (2007).
- Adachi, T. *et al.* S-Glutathiolation by peroxynitrite activates SERCA during arterial relaxation by nitric oxide. *Nature Med.* **10**, 1200–1207 (2004).
- Knyushko, T. V., Sharov, V. S., Williams, T. D., Schoneich, C. & Bigelow, D. J. 3-Nitrotyrosine modification of SERCA2a in the aging heart: a distinct signature of the cellular redox environment. *Biochemistry* **44**, 13071–13081 (2005).
- Sampson, D. A., Wang, M. & Matunis, M. J. The small ubiquitin-like modifier-1 (SUMO-1) consensus sequence mediates Ubc9 binding and is essential for SUMO-1 modification. *J. Biol. Chem.* **276**, 21664–21669 (2001).
- Plemper, R. K. & Wolf, D. H. Retrograde protein translocation: ERADication of secretory proteins in health and disease. *Trends Biochem. Sci.* **24**, 266–270 (1999).
- Schillinger, W., Fiolet, J. W., Schlotthauer, K. & Hasenfuss, G. Relevance of Na^{+} - Ca^{2+} exchange in heart failure. *Cardiovasc. Res.* **57**, 921–933 (2003).
- Wang, J., Feng, X. H. & Schwartz, R. J. SUMO-1 modification activated GATA4-dependent cardiogenic gene activity. *J. Biol. Chem.* **279**, 49091–49098 (2004).
- Matsuzaki, K. *et al.* Serum response factor is modulated by the SUMO-1 conjugation system. *Biochem. Biophys. Res. Commun.* **306**, 32–38 (2003).
- Wang, J. & Schwartz, R. J. Sumoylation and regulation of cardiac gene expression. *Circ. Res.* **107**, 19–29 (2010).
- Brady, M. *et al.* Sp1 and Sp3 transcription factors are required for trans-activation of the human SERCA2 promoter in cardiomyocytes. *Cardiovasc. Res.* **60**, 347–354 (2003).
- Vlasblom, R. *et al.* Contractile arrest reveals calcium-dependent stimulation of SERCA2a mRNA expression in cultured ventricular cardiomyocytes. *Cardiovasc. Res.* **63**, 537–544 (2004).
- Drewett, V. *et al.* Serum response factor cleavage by caspases 3 and 7 linked to apoptosis in human BJAB cells. *J. Biol. Chem.* **276**, 33444–33451 (2001).
- Okura, T. *et al.* Protection against Fas/APO-1- and tumor necrosis factor-mediated cell death by a novel protein, sentrin. *J. Immunol.* **157**, 4277–4281 (1996).
- Baba, D. *et al.* Crystal structure of thymine DNA glycosylase conjugated to SUMO-1. *Nature* **435**, 979–982 (2005).
- Van Rechem, C. *et al.* Differential regulation of HIC1 target genes by CtBP and NuRD, via an acetylation/SUMOylation switch, in quiescent versus proliferating cells. *Mol. Cell Biol.* **30**, 4045–4059 (2010).
- Choudhary, C. *et al.* Lysine acetylation targets protein complexes and co-regulates major cellular functions. *Science* **325**, 834–840 (2009).
- Kim, M. J., Chia, I. V. & Costantini, F. SUMOylation target sites at the C terminus protect axin from ubiquitination and confer protein stability. *FASEB J.* **22**, 3785–3794 (2008).
- Mooney, S. M., Grande, J. P., Salisbury, J. L. & Janknecht, R. Sumoylation of p68 and p72 RNA helicases affects protein stability and transactivation potential. *Biochemistry* **49**, 1–10 (2010).
- Ryu, K. Y., Garza, J. C., Lu, X. Y., Barsh, G. S. & Kopito, R. R. Hypothalamic neurodegeneration and adult-onset obesity in mice lacking the *Ubb* polyubiquitin gene. *Proc. Natl Acad. Sci. USA* **105**, 4016–4021 (2008).

Supplementary Information is linked to the online version of the paper at www.nature.com/nature.

Acknowledgements This work is supported by NIH RO1 HL083156, HL080498, HL093183 and P20HL100396 (R.J.H.). W.J.P. is funded by Global Research Laboratory Program (M6-0605-00-0001) of the Korean Ministry of Science and Technology.

Author Contributions C.K., A.L. and R.J.H. conceived the project and its design. C.K., A.L., D.J., J.G.O. and A.H.C. performed experiments and data analysis. E.K. aided in experimental design. C.K., A.L., W.J.P. and R.J.H. wrote the manuscript.

Author Information Reprints and permissions information is available at www.nature.com/reprints. The authors declare no competing financial interests. Readers are welcome to comment on the online version of this article at www.nature.com/nature. Correspondence and requests for materials should be addressed to R.J.H. (roger.hajjar@mssm.edu).

METHODS

In vivo SUMOylation assay. To analyse SUMOylation in cells, lipofectamine 2000 was used to transfect HEK-293 cells with plasmids encoding wild-type or SUMOylation-site mutants of SERCA2a, along with Flag-tagged SUMO1 and Myc-tagged UBC9. The cells were lysed by sonication in ice-cold lysis buffer (50 mM Tris-HCl (pH 8.0), 150 mM NaCl, 0.1% Triton X-100, 10 mM EDTA, complete protease inhibitor (1 tablet per 10 ml, Roche) and protein phosphatase inhibitor cocktail (Sigma)) containing 20 mM *N*-ethylmaleimide. Lysates were cleared by centrifugation at 30,000g for 20 min. Cell lysates were then immunoprecipitated overnight at 4 °C with a Flag-specific affinity matrix gel (Sigma), after which the immunoprecipitates were washed in cold lysis buffer. The immunocomplexes were then resolved by SDS polyacrylamide gel electrophoresis (SDS-PAGE) and immunoblot analysis was performed with a SERCA2a-specific antibody.

Fresh tissue extracts were prepared in lysis buffer for *in vivo* SUMOylation assays. Hearts from each experimental and control group were frozen in liquid nitrogen. The frozen tissues were crushed and homogenized in lysis buffer as described above using the MP homogenate system (FastPrep homogenizer). The insoluble portion was removed by centrifugation at 30,000g for 20 min. The extracts were incubated with anti-SUMO1 agarose resin with agitation overnight. The SUMO-conjugated forms were detected by immunoblot analysis with specific primary antibodies.

SERCA2a activity assay. SERCA2a activity was determined using an assay based on pyruvate/NADH-coupled reactions, as previously described²⁴. The activity of the Ca^{2+} -ATPase was calculated as follows: $\Delta\text{absorbance}/6.22 \times \text{protein} \times \text{time}$ (in nmol ATP per mg protein \times min). All assays were performed in triplicate.

Generation of conditional *Sumo1*-transgenic mice. The αMHC -flox-mouse SUMO1 transgene was subcloned into the pML2G vector (gift from Y. Wang), which encodes GFP cDNA between two loxP sites. The construct was microinjected into fertilized eggs from B6C3 mice, and transgenic integration was confirmed by PCR (mouse genetics shared research facility, Mount Sinai School of Medicine).

Antibodies. Antibodies against the following proteins were used for immunoblotting: SERCA2a (21st Century Biochemicals), GAPDH (Sigma), Myc (Sigma), Flag (Sigma), SUMO1 (Cell Signaling), SUMO1 agarose resin (Santa Cruz Biotech), SUMO2/3 (MBL), UBC9 (Boston Biochem), SENP1 (Pierce), PLN (Badrilla), RyR2 (Badrilla), NCX1 (Chemicon), GATA4 (Millipore), SRF (Millipore), anti-rabbit-HRP and anti-mouse-HRP secondary antibodies (Sigma).

Primers for mutagenesis. The following primer sets were used for mutagenesis: K480R_sense, 5'-TCA GTC ATT AAA CAG CTG ATG AGA AAG GAA TTC ACT CTA GAG-3'; K480R_antisense, 5'-CTC TAG AGT GAA TTC CTT TCT CAT CAG CTG TTT AAT GAC TGA-3'; K585R_sense, 5'-GAG GAC TCT GCC AAC TTT ATT AGA TAT GAG ACC AAT CTG ACC-3'; K585R_antisense, 5'-GGT CAG ATT GGT CTC ATA TCT AAT AAA GTT GGC AGA GTC CTC-3'.

Proteomic analysis. Solubilized immunocomplexes were combined with a rehydration buffer (9 M urea, 2 M thiourea, 4 M CHAPS buffer, 16 mM dithiothreitol, 2% w/v pharmalyte 3-11 and trace amounts of bromophenol blue) to a final volume of 340 μl , and then rehydrated for 16 h. After rehydration, strips were focused at 60 kVh at 20 °C (IPGphor III, GE Healthcare). When isoelectric focusing was complete, the strips were equilibrated, separated on 12.5% SDS-PAGE gels and visualized by silver staining using the Plus One silver staining kit (GE Healthcare), with minor modifications to ensure compatibility with subsequent mass spectrometry analysis. Stained two-dimensional gel images were scanned (ImageScanner II, GE Healthcare) and analysed by PDquest 8.1 software system (Bio-Rad). Spots were excised from the gels by spot picker and prepared for mass spectrometry as previously described²⁵.

Mass spectrometry analysis. Identification of gel spots was accomplished by ESI/LC/MS/MS system (Thermo-Scientific). Full scan spectra were recorded in positive mode over the mass range 350–2000 Da. MS/MS data were automatically acquired on the two most intense precursor ions in each full scan spectrum, and were interpreted using Xcalibur 2.0 and Bioworks 3.2 software.

Contractility measurement. The mechanical properties of isolated ventricular cardiomyocytes were assessed using a video-based edge detection system (IonOptix) as previously described²⁶.

Adenoviruses. Adenoviruses encoding SERCA2a and SUMO1 were generated using the pAdEasy XL adenoviral vector system (Stratagene) according to the manufacturer's protocols.

rAAV vector production and purification. rAAV9-SERCA2a, rAAV9-shSumo1 and rAAV9-SC were produced using the two-plasmids protocol as previously described²⁷ with the following modifications: HEK-293T cells (ATCC) were grown in triple flasks for 24 h (DMEM, 10% fetal bovine serum) before adding the calcium phosphate precipitate. After 72 h, the virus was purified from benzonase-treated crude cell lysates over an iodixanol density gradient (Optiprep, Greiner Bio-One Inc.), followed by heparin-agarose type I affinity

chromatography (Sigma). Finally, viruses were concentrated and formulated into lactated Ringer's solution (Baxter Healthcare Corporation) using Vivaspin 20 centrifugal concentrators 50K MWCO (Vivascience Inc.), and stored at -80°C .

Lentivirus. The lentiviral plasmids encoding shRNAs for *Serca2a* were previously described by us²⁸. The *Serca2a* shRNA construct is the following sequence; the underlined segment indicates the loop: 5'-GATCCGACTTACTAGTTAGAA TTTGGCTAAGAGCAAATTTCTAACTAGTAAGTCTTTTGGAAATTAAT-3'. We used third-generation lentiviral systems to generate the vectors²⁹.

Transverse aortic constriction. Mice underwent TAC using a supraclavicular construction model as previously described²⁶. TAC or sham surgery was performed in 8-week-old male mice (body weight 18–22 g). Mice were anesthetized with intraperitoneal ketamine and placed on a ventilator. A longitudinal cut of 2–3 mm was made in the proximal portion of the sternum, allowing visualization of the aortic arch. The transverse aortic arch was ligated between the innominate and left common carotid arteries with an overlying 27-gauge needle. The needle was immediately removed leaving a discrete region of constriction. The sham group underwent a similar procedure without ligation.

Gene transfer *in vivo*. Adult Sprague-Dawley rats (body weight 240–260 g) underwent gene transfer via aortic cross-clamping as previously described³⁰. After dissection of the aorta and pulmonary artery, lentiviral sh*Serca2a* with or without adenoviral SUMO1 were injected into the left ventricular cavity through a 22G catheter while the aorta and pulmonary artery were cross-clamped for 50 s. In sham-operated animals, normal saline was injected into the left ventricular cavity while the aorta and pulmonary artery were cross-clamped for 50 s. After cross-clamping was released, the chest was closed.

Echocardiography. Transthoracic echocardiography was performed using a Vivid 7000 (GE Healthcare) equipped with a H13L transducer (14 MHz). Two-dimensional and M-mode images were obtained in the short-axis view. The heart rate, left ventricular end-diastolic internal diameter and left ventricular end-systolic internal diameter were measured in at least three repeated cardiac cycles. The ejection fraction and fractional shortening were then calculated.

Haemodynamics. Haemodynamic measurements are performed using a 1.2 Fr pressure-volume conductance catheter (Sciense). Pressure-volume loop analysis was performed as previously described³¹. Mice were injected intraperitoneally with urethane (1 g kg^{-1}), etomidate (10 mg kg^{-1}) and morphine (1 mg kg^{-1}) and mechanically ventilated with $7\text{ }\mu\text{l g}^{-1}$ stroke volume at 125 respirations min^{-1} . The chest was opened to expose the heart for an apical stab approach. To determine absolute ventricular volumes via admittance technology, myocardial and blood conductance were obtained before pressure-volume catheter placement in the left ventricle³². The inferior vena cava was transiently occluded to reduce ventricular pre-load to obtain load-independent pressure-volume relationships. Haemodynamic measurements were acquired and analysed using IOX software (EMKatech).

Histological analysis. Hearts were prepared in Tissue-Tek OCT compound (Sakura Finetech) and sectioned into 6- μm slices (Microm HM560 Cryo-star, Thermo Scientific). The sections were stained with haematoxylin and eosin.

Statistical analysis. Statistical analyses were performed using Student's *t*-test. Significant differences are indicated *, $P < 0.05$ or **, $P < 0.001$. Data in the figures represent mean \pm s.d.

24. Hajjar, R. J., Schmidt, U., Kang, J. X., Matsui, T. & Rosenzweig, A. Adenoviral gene transfer of phospholamban in isolated rat cardiomyocytes. Rescue effects by concomitant gene transfer of sarcoplasmic reticulum Ca^{2+} -ATPase. *Circ. Res.* **81**, 145–153 (1997).
25. Lee, A. Y. *et al.* Identification of the degradome of Isp-1, a major intracellular serine protease of *Bacillus subtilis*, by two-dimensional gel electrophoresis and matrix-assisted laser desorption/ionization-time of flight analysis. *Proteomics* **4**, 3437–3445 (2004).
26. Jeong, D. *et al.* PICOT inhibits cardiac hypertrophy and enhances ventricular function and cardiomyocyte contractility. *Circ. Res.* **99**, 307–314 (2006).
27. Zolotukhin, S. *et al.* Recombinant adeno-associated virus purification using novel methods improves infectious titer and yield. *Gene Ther.* **6**, 973–985 (1999).
28. Kizana, E., Cingolani, E. & Marban, E. Non-cell-autonomous effects of vector-expressed regulatory RNAs in mammalian heart cells. *Gene Ther.* **16**, 1163–1168 (2009).
29. Tiscornia, G., Singer, O., Ikawa, M. & Verma, I. M. A general method for gene knockdown in mice by using lentiviral vectors expressing small interfering RNA. *Proc. Natl Acad. Sci. USA* **100**, 1844–1848 (2003).
30. Hajjar, R. J. *et al.* Modulation of ventricular function through gene transfer *in vivo*. *Proc. Natl Acad. Sci. USA* **95**, 5251–5256 (1998).
31. Pacher, P., Nagayama, T., Mukhopadhyay, P., Batkai, S. & Kass, D. A. Measurement of cardiac function using pressure-volume conductance catheter technique in mice and rats. *Nature Protocols* **3**, 1422–1434 (2008).
32. Porterfield, J. E. *et al.* Dynamic correction for parallel conductance, G_p , and gain factor, α , in invasive murine left ventricular volume measurements. *J. Appl. Physiol.* **107**, 1693–1703 (2009).

The role of Tet3 DNA dioxygenase in epigenetic reprogramming by oocytes

Tian-Peng Gu^{1*}, Fan Guo^{1*}, Hui Yang^{2*}, Hai-Ping Wu^{1†}, Gui-Fang Xu¹, Wei Liu¹, Zhi-Guo Xie¹, Linyu Shi², Xinyi He³, Seung-gi Jin⁴, Khursheed Iqbal⁵, Yujiang Geno Shi⁶, Zixin Deng³, Piroska E. Szabó⁵, Gerd P. Pfeifer⁴, Jinsong Li² & Guo-Liang Xu¹

Sperm and eggs carry distinctive epigenetic modifications that are adjusted by reprogramming after fertilization¹. The paternal genome in a zygote undergoes active DNA demethylation before the first mitosis^{2,3}. The biological significance and mechanisms of this paternal epigenome remodelling have remained unclear⁴. Here we report that, within mouse zygotes, oxidation of 5-methylcytosine (5mC) occurs on the paternal genome, changing 5mC into 5-hydroxymethylcytosine (5hmC). Furthermore, we demonstrate that the dioxygenase Tet3 (ref. 5) is enriched specifically in the male pronucleus. In Tet3-deficient zygotes from conditional knockout mice, paternal-genome conversion of 5mC into 5hmC fails to occur and the level of 5mC remains constant. Deficiency of Tet3 also impedes the demethylation process of the paternal *Oct4* and *Nanog* genes and delays the subsequent activation of a paternally derived *Oct4* transgene in early embryos. Female mice depleted of Tet3 in the germ line show severely reduced fecundity and their heterozygous mutant offspring lacking maternal Tet3 suffer an increased incidence of developmental failure. Oocytes lacking Tet3 also seem to have a reduced ability to reprogram the injected nuclei from somatic cells. Therefore, Tet3-mediated DNA hydroxylation is involved in epigenetic reprogramming of the zygotic paternal DNA following natural fertilization and may also contribute to somatic cell nuclear reprogramming during animal cloning.

To investigate whether loss of DNA methylation in the male pronucleus coincides with oxidation of 5mC to 5hmC, a recently reported type of modification of mammalian DNA^{5,6}, we performed immunostaining of mouse zygotes using an antibody specifically recognizing 5hmC (Supplementary Fig. 1). We found that the 5hmC signal increased markedly in the paternal pronucleus around the pronuclear stage PN3 when the paternal pronucleus became larger than the maternal pronucleus (Fig. 1a, b). By contrast, the 5mC signal became markedly weaker in the male pronucleus from the PN3 stage whereas there was no clear change in the female pronucleus (Supplementary Fig. 2), as reported previously². The inverse correlation between the 5hmC and 5mC signals in the two parental genomes seemed to persist beyond the zygotic stage (Supplementary Fig. 3). Therefore, 5mC oxidation in the male pronucleus coincides with the loss of methylation in the early mouse embryo. A similar observation has recently been reported in two independent studies^{7,8}.

Next, we examined the expression of Tet enzymes that can catalyse the oxidation of 5mC in DNA⁹. The *Tet3* mRNA was specifically detected in oocytes and zygotes (Supplementary Fig. 4). At the zygotic stage, the Tet3 protein was concentrated in the male pronucleus, but localized to the cytoplasm at other pre-implantation stages (Fig. 1c and Supplementary Fig. 5). The unique expression pattern of Tet3 suggests its possible role in modifying the zygotic paternal genome.

To study the biological function of Tet3 in mouse, we generated a conditional knockout allele abolishing its catalytic activity (Supplementary Fig. 6a). Because homozygous mutation led to neonatal lethality, we achieved germ-line-specific deletion of Tet3 from primordial germ cells (PGCs) in [*Tet3*^{f/f}, TNAP-Cre] conditional knockout (CKO) mice.

Female CKO mice were normal in growth and morphology. Although they displayed much reduced fecundity (see below), they gave birth to heterozygous offspring when crossed with wild-type males (Supplementary Fig. 6b). The deletion of Tet3 in oocytes and zygotes was confirmed by immunostaining and PCR with reverse transcription assays (Fig. 2a and Supplementary Fig. 6c). Strikingly, no 5hmC signal could be detected and the 5mC signal intensity did not decline in the late male pronuclei of zygotes collected from the CKO females mated with wild-type males (Fig. 2b and Supplementary Fig. 7). In contrast, deletion of *Tet3* from the male germ cells did not seem to affect the change in 5hmC and 5mC. Therefore, the loss of 5mC in the paternal genome in developing zygotes is caused by its conversion to 5hmC and the maternal Tet3 is required for this conversion.

We then assessed the role of Tet3 in demethylation of specific sequences in the male pronucleus. *Line1* transposons are known to be actively demethylated in zygotes^{10,11}. Comparison of the methylation level of male pronuclear DNA from Tet3-deficient zygotes at the PN3–4 stages with that of wild-type zygotes showed that the process of active DNA demethylation was impeded by Tet3 deletion (Fig. 2c, upper panel). This finding also indicates that 5hmC serves as an intermediate between 5mC and unmethylated C, although bisulphite analysis cannot distinguish 5hmC from 5mC^{12,13}. To confirm this, we assayed for 5mC and 5hmC on *Line1* elements in the paternal DNA by MeDIP and hMeDIP (methylated and hydroxymethylated DNA immunoprecipitation). 5hmC was indeed present at *Line1* sequences in wild-type zygotic male pronuclei at a significantly higher level compared to sperm, whereas the 5mC level was markedly lower than that of sperm (Supplementary Fig. 8). In the analysis of male pronuclear DNA from zygotes lacking Tet3, enrichment of 5hmC-containing *Line1* elements was significantly decreased whereas enrichment of 5mC-containing elements was comparable with sperm. These results strengthen the conclusion that 5mC oxidation does occur at *Line1* sequences in male pronuclei.

Embryonic stem cell marker genes, such as *Oct4* and *Nanog*, are methylated during male germ cell development and their demethylation occurs in the early embryo^{14–16}. In normal zygotes, the *Oct4* gene of male pronuclei had undergone substantial demethylation by the PN3–4 pronuclear stages, but this process was markedly hampered in Tet3-null zygotes (Fig. 2c and Supplementary Fig. 9). Moreover, Tet3 deletion almost completely blocked demethylation at two other

¹Group of DNA Metabolism, The State Key Laboratory of Molecular Biology, Institute of Biochemistry and Cell Biology, Shanghai Institutes for Biological Sciences, Chinese Academy of Sciences, Shanghai 200031, China. ²The State Key Laboratory of Cell Biology, Institute of Biochemistry and Cell Biology, Shanghai Institutes for Biological Sciences, Chinese Academy of Sciences, Shanghai 200031, China.

³The State Key Laboratory of Microbial Metabolism, School of Life Science and Biotechnology, Shanghai Jiaotong University, Shanghai 200030, China. ⁴Department of Cancer Biology, Beckman Research Institute of the City of Hope, Duarte, California 91010, USA. ⁵Department of Molecular and Cellular Biology, Beckman Research Institute of the City of Hope, Duarte, California 91010, USA. ⁶Division of Endocrinology, Diabetes, and Hypertension, Department of Medicine and BCMP, Brigham and Women's Hospital and Harvard Medical School, Boston, Massachusetts 02115, USA. [†]Present address: Novartis Institutes for BioMedical Research Co., Shanghai 201203, China.

*These authors contributed equally to this work.

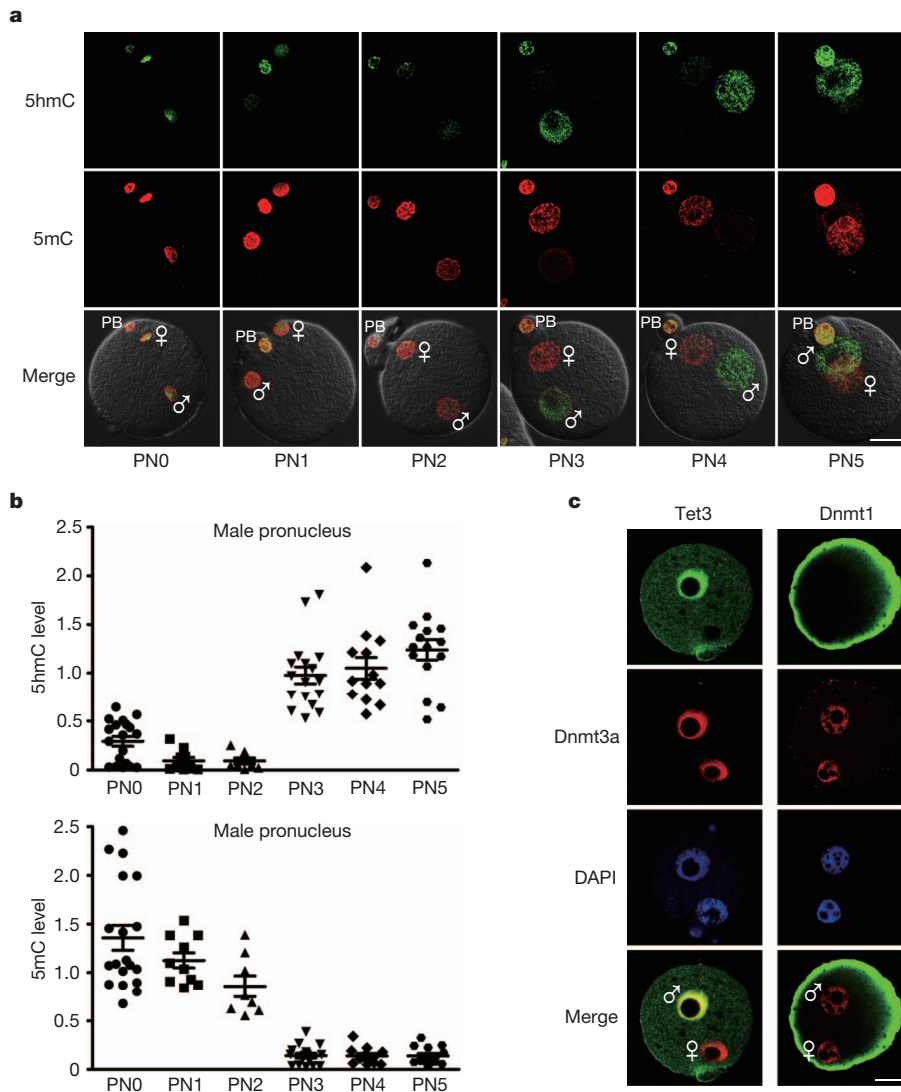


Figure 1 | Specific oxidation of methylcytosine and Tet3 distribution in the zygotic male pronucleus. **a**, Immunofluorescent images of 5hmC (green) and 5mC (red) staining, and overlaid phase contrast images. The pronuclear (PN) stages are indicated. Male and female symbols indicate male and female pronucleus, respectively. PB, polar body. Scale bar, 25 μ m. **b**, Quantification of the relative levels of 5hmC and 5mC in male pronuclei in zygotes. Each data point is based on the level of the 5hmC or 5mC signal relative to the DAPI

staining intensity of the same pronucleus. Error bars indicate s.e.m. Number of zygotes analysed for each stage: PN0, 19; PN1, 10; PN2, 8; PN3, 17; PN4, 17; PN5, 15. **c**, Preferential staining of Tet3 protein in the male pronucleus. DNA was stained with DAPI. Control staining shows Dnmt1 in the cortical cytoplasm and Dnmt3a (red) in both pronuclei. The nucleolus had no staining signal.

paternally methylated genes, *Nanog* and *Lemdl* (ref. 17), which retained hypermethylation similar to that observed in sperm (Supplementary Fig. 9). To assess the significance of paternal demethylation on gene expression, Tet3-null oocytes from the CKO females were fertilized by intracytoplasmic injection (ICSI) of wild-type sperm carrying the enhanced green fluorescent protein (EGFP) reporter gene under the control of the *Oct4* promoter, and expression of EGFP was monitored in cultured embryos. Compared with wild-type embryos, the mutant embryos derived from oocytes lacking Tet3 showed significantly weaker EGFP expression at the 8-cell and morula stages (Fig. 2d and Supplementary Fig. 10). Based on these global and sequence-specific analyses of 5mC and 5hmC, along with the reporter gene assay, we conclude that Tet3-mediated 5mC oxidation contributes to the demethylation in the zygotic paternal genome and gene activation in the early embryo.

We next investigated whether removing Tet3 from oocytes might compromise embryonic development. We first confirmed that early deletion of Tet3 from the PGC stage did not affect epigenetic reprogramming in the embryonic germ cells, oocyte development,

maturation and fertilization (Supplementary Figs 11–13 and Supplementary Table 1). Male germ cell development and sperm DNA methylation were not affected either (Supplementary Fig. 14). However, fecundity of the female CKO mice was significantly lower in terms of the frequency of successful pregnancy per mating and the litter size (Fig. 3a and Supplementary Table 2).

Deletion of maternal Tet3 did not seem to affect the pre-implantation development as heterozygous zygotes collected from CKO females mated with wild-type males developed to blastocysts *in vitro* normally (Supplementary Table 3). We then examined the effect of maternal Tet3 deletion on prenatal development by transplantation of 2-cell embryos into oviducts of pseudo-pregnant females. Whereas the transferred embryos lacking maternal Tet3 implanted normally, they showed a much reduced rate of full-term development (Supplementary Table 4). Dissection of transferred [*Tet3* *Mat*⁻/*Pat*⁺] mutant embryos in the pregnant wild-type foster mothers revealed a high frequency of degeneration and the appearance of morphological abnormalities, starting from midgestation (Fig. 3b and Supplementary Table 4). Moreover, deletion of Tet3 later from growing oocytes

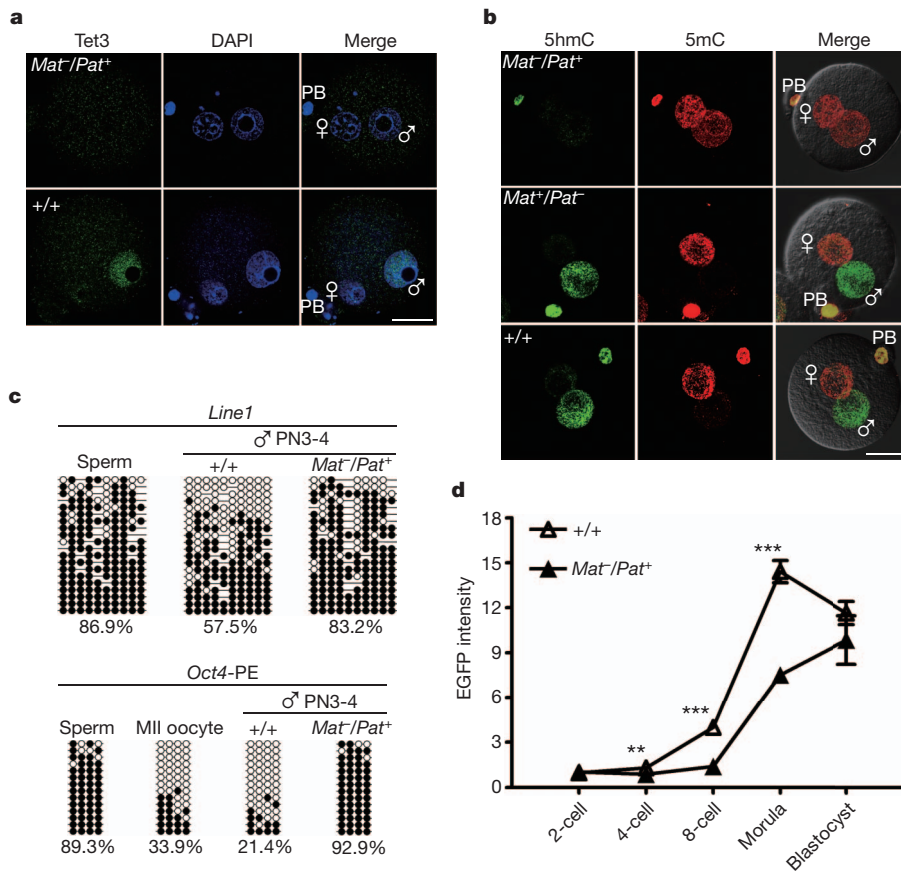


Figure 2 | The role of Tet3 in 5mC oxidation, demethylation of paternal DNA, and activation of the paternal *Oct4* allele. **a**, Loss of the Tet3 protein in heterozygous zygotes (*Mat⁻/Pat⁺*) obtained from CKO females mated with wild-type males. PN3 zygotes were stained with an anti-Tet3 antibody raised against the deleted region. Scale bar, 25 μ m. **b**, 5hmC (green) and 5mC (red) immunostaining in wild-type (*+/+*) and maternally (*Mat⁻/Pat⁺*) or paternally (*Mat⁺/Pat⁻*) Tet3-deficient zygotes at the PN5 stage. **c**, Methylation analysis of *Line1* and *Oct4* (PE, the proximal enhancer region) in male pronuclei isolated from wild-type (*+/+*) and Tet3-deficient (*Mat⁻/Pat⁺*) zygotes. Open and filled circles represent unmethylated and methylated CpG sites, respectively. Percentage of methylated CpGs is indicated. **d**, Paternal *Oct4* activation in wild-type embryos (*+/+*) and embryos lacking maternal Tet3 (*Mat⁻/Pat⁺*). Embryos were derived from ICSI using sperm carrying the *Oct4-EGFP* transgene and the EGFP signal was quantified, relative to the level in a 2-cell blastomere. Number of embryos analysed at each stage, *+/+*: 2-cell, 13; 4-cell, 9; 8-cell, 9; morula, 12; blastocyst, 7. *Mat⁻/Pat⁺*: 2-cell, 11; 4-cell, 9; 8-cell, 8; morula, 8; blastocyst, 5. Error bars indicate s.e.m. ** $P < 0.01$ and *** $P < 0.001$.

using Zp3-Cre also led to failure in zygotic 5hmC generation, retention of paternal 5mC, impaired demethylation at *Line1* and *Oct4*, and compromised embryonic development (Supplementary Fig. 15). Therefore, lacking maternal Tet3 blocks paternal genome reprogramming and causes markedly increased developmental failure of the embryo.

Somatic cell nuclei injected into eggs undergo profound epigenetic reprogramming, including DNA demethylation. The cytoplasm of germinal vesicle (GV) oocytes¹⁸, metaphase II (MII) oocytes¹⁹, zygotes²⁰ and 2-cell embryos²¹ has been shown to possess reprogramming activity. The existence of the Tet3 protein across these stages indicated that Tet3 might be one of the cytoplasmic factors contributing to the reprogramming activity. We tested therefore whether Tet3-mediated hydroxylation is part of the reprogramming process in somatic cell nuclear transfer (SCNT). Remarkably, following activation of nuclear transfer (NT) oocytes reconstructed after injection of somatic nucleus into oocyte with or without enucleation (intact oocyte), the Tet3 protein originating from the oocyte cytoplasm became concentrated in the pseudo-pronucleus (PPN) formed from the transferred somatic nucleus, but not in the female pronucleus derived from the spindle-chromosome-complex that existed in oocytes (Fig. 4a). Significantly, the PPN formed in the NT embryos from wild-type intact or enucleated oocytes underwent 5mC oxidation whereas this modification did not occur in embryos derived from Tet3-null oocytes (Fig. 4b). Whereas substantial demethylation was detected at the *Oct4* promoter in the PPN of Tet3-proficient NT embryos, the somatic hypermethylation persisted when the oocyte Tet3 was deleted (Fig. 4c). To investigate the role of Tet3-mediated DNA oxidation in the activation of pluripotency genes, we used donor somatic cells carrying the *Oct4-EGFP* transgene. Compared with embryos from wild-type oocytes, the EGFP signal was significantly lower in embryos derived from the Tet3-null oocytes at the

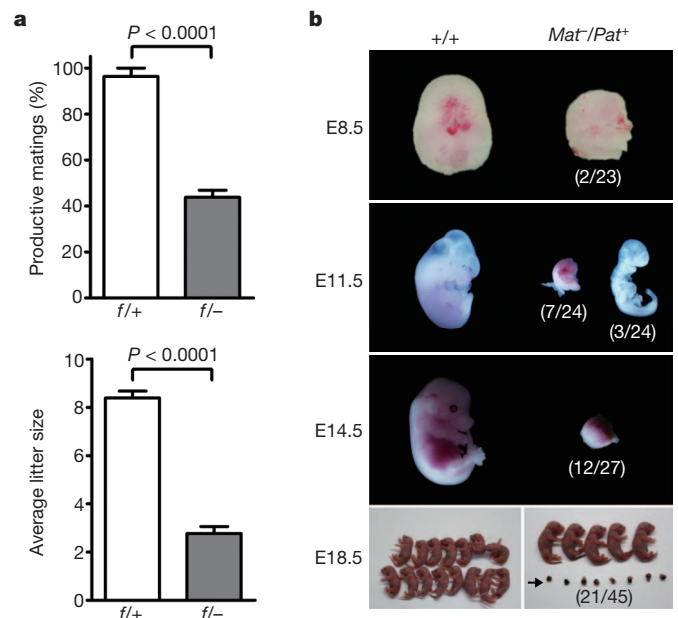


Figure 3 | Maternal Tet3 deficiency compromises embryonic development. **a**, Reduced efficiency of productive mating and litter size in females (*f/-*) with germline Tet3 deficiency. Error bars indicate s.e.m. [*Tet3^{f/+}*, TNAP-Cre] mice, $n = 9$; [*Tet3^{f/-}*, TNAP-Cre] mice, $n = 7$. **b**, Developmental failure among embryos lacking maternal Tet3. Pregnant foster females receiving wild-type (*+/+*) and mutant (*Mat⁻/Pat⁺*) 2-cell embryos transferred were dissected at different stages of gestation. Numbers in brackets indicate proportion of embryonic day 8.5 (E8.5) deciduas and E11.5–18.5 embryos showing a smaller size and morphological abnormalities. The arrow indicates degenerated conceptuses obtained. Detailed data are presented in Supplementary Table 4.

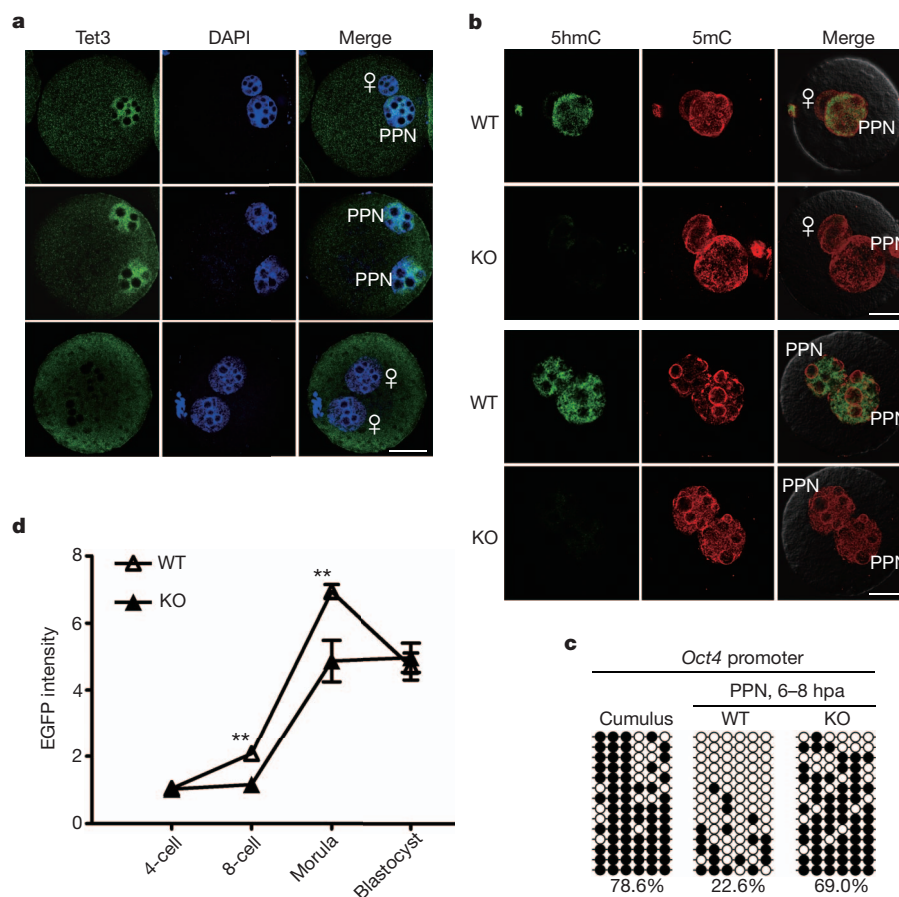


Figure 4 | Tet3 contributes to reprogram the somatic nucleus transferred into oocytes. **a**, Tet3 enrichment in the pseudo-pronucleus (PPN) formed in embryos reconstructed by transplantation of cumulus somatic nuclei into an intact (top row) or enucleated oocyte (middle row). The enrichment did not occur in the female pronucleus in intact oocytes (top row) and in the two pronuclei of parthenogenetic embryos (bottom row). Scale bar, 25 μ m. **b**, Impaired 5mC oxidation in PPN of 1-cell NT embryos derived from injection of cumulus nuclei into intact or enucleated oocytes lacking Tet3. Embryos around 10 h post activation (hpa) were stained with anti-5hmC (green) and

anti-5mC (red) antibodies. **c**, Impaired *Oct4* demethylation in NT embryos derived from Tet3-null oocytes. More than 20 NT embryos derived from enucleated wild-type (WT) or Tet3-null (KO) oocytes were collected 6–8 hpa for DNA methylation analysis. **d**, Weakened activation of the somatic *Oct4*–EGFP reporter in cultured NT embryos from Tet3-null oocytes. The EGFP intensities were relative to the level in a 4-cell blastomere. Error bars indicate s.e.m. Number of embryos analysed for each stage, WT: 4-cell, 11; 8-cell, 13; morula, 9; blastocyst, 7. KO: 4-cell, 8; 8-cell, 7; morula, 6; blastocyst, 7. ** $P < 0.01$.

8-cell and morula stages (Fig. 4d and Supplementary Fig. 16a). Consistently, the *Oct4* mRNA level was relatively low in 8-cell embryos from Tet3-null oocytes (Supplementary Fig. 16b). Therefore, deficiency in oocyte Tet3 could cause weakened or delayed activation of the somatic *Oct4* in NT embryos.

We have obtained substantial evidence that oxidation of 5mC in the paternal genome in fertilized eggs by Tet3 initiates DNA demethylation and facilitates the activation of the paternal copy of early embryonic genes, thus contributing to the establishment of biparental totipotency in the early embryo by counteracting the silencing function of 5mC. Blocking oxidation of 5mC by Tet3 deletion affects paternal gene activation, leading to reduced developmental fitness and fetal survival. It remains to be determined whether the developmental failures could be caused by haploinsufficiency²² for the genes affected in the early embryo.

The involvement of Tet3 in somatic *Oct4* activation indicates that Tet-mediated 5mC oxidation contributes to epigenetic reprogramming of the donor nuclear DNA in SCNT. Reprogramming in SCNT might thus share a common mechanism with paternal genome remodelling in fertilized eggs. Further investigations are needed to reveal the signals regulating Tet3 and the events subsequent to 5hmC formation in both fertilized and cloned embryos.

METHODS SUMMARY

Preparation of anti-5hmC antibody. To prepare anti-5hmC antibody, 5-hydroxymethylcytidine 5'-monophosphate (5hmCMP) hapten was synthesized from cytidine 5'-monophosphate (CMP) using MIA hydroxymethylase²³. The ribonucleoside was then conjugated to bovine serum albumin (BSA) as previously described²⁴ and used to immunize rabbits. The antibody was affinity-purified from antiserum with 5hmCMP–BSA conjugate coupled to agarose beads.

Immunostaining for 5hmC in fertilized oocytes. Immunofluorescence detection of 5hmC in zygotes followed the procedure for 5mC¹¹. Fluorescent images were acquired at 2- μ m Z-axis intervals using a confocal microscope (LEICA TCS SP5 II) and their signal intensity was determined.

Gene targeting. A *Tet3* targeting vector was electroporated into 129Sv ES cells for homologous recombination. The floxed region contains exons 8–9, which includes the coding region for the conserved Fe²⁺-binding motif of dioxygenases. To inactivate *Tet3* in the germ line, we crossed the mice carrying a floxed allele with TNAP-Cre knock-in mice on a 129 genetic background²⁵. The conditional knock-out mice were on C57BL/6J–129Sv genetic background.

Zygote collection and staging. Female mice 4- to 8-week-old were injected with pregnant mare's serum gonadotropin and human chorionic gonadotropin were mated with wild-type males. Zygotes were harvested and the PN stages of individual zygotes were classified according to ref. 11, by taking into account the pronuclear morphology and the presence of 5mC signal.

Observation of *Oct4*–EGFP activation. To examine the role of Tet3 in paternal gene activation, MII oocytes collected from wild-type and Tet3 CKO females were

fertilized by ICSI with sperm from transgenic mice (tg/tg) carrying the *Oct4-EGFP* transgene²⁶ and the resulting embryos were cultured to observe EGFP expression. To examine the role of Tet3 in somatic gene activation in SCNT, we monitored the *Oct4-EGFP* transgene expression from the donor cell DNA in NT embryos, which were derived after injection of a cumulus nucleus into a wild-type or a Tet3-null oocyte without enucleation.

Full Methods and any associated references are available in the online version of the paper at www.nature.com/nature.

Received 21 January; accepted 16 August 2011.

Published online 4 September 2011.

1. Surani, M. A., Hayashi, K. & Hajkova, P. Genetic and epigenetic regulators of pluripotency. *Cell* **128**, 747–762 (2007).
2. Mayer, W., Niveleau, A., Walter, J., Fundele, R. & Haaf, T. Demethylation of the zygotic paternal genome. *Nature* **403**, 501–502 (2000).
3. Oswald, J. *et al.* Active demethylation of the paternal genome in the mouse zygote. *Curr. Biol.* **10**, 475–478 (2000).
4. Ooi, S. K. & Bestor, T. H. The colorful history of active DNA demethylation. *Cell* **133**, 1145–1148 (2008).
5. Tahiliani, M. *et al.* Conversion of 5-methylcytosine to 5-hydroxymethylcytosine in mammalian DNA by MLL partner TET1. *Science* **324**, 930–935 (2009).
6. Kiaucionis, S. & Heintz, N. The nuclear DNA base 5-hydroxymethylcytosine is present in Purkinje neurons and the brain. *Science* **324**, 929–930 (2009).
7. Iqbal, K., Jin, S. G., Pfeifer, G. P. & Szabo, P. E. Reprogramming of the paternal genome upon fertilization involves genome-wide oxidation of 5-methylcytosine. *Proc. Natl Acad. Sci. USA* **108**, 3642–3647 (2011).
8. Wossidlo, M. *et al.* 5-Hydroxymethylcytosine in the mammalian zygote is linked with epigenetic reprogramming. *Nature Commun.* **2**, 241 (2011).
9. Wu, S. C. & Zhang, Y. Active DNA demethylation: many roads lead to Rome. *Nature Rev. Mol. Cell Biol.* **11**, 607–620 (2010).
10. Jamil, A. Z., Iqbal, K., Fawad Ur, R. & Mirza, K. A. Effect of phacoemulsification on intraocular pressure. *J. Coll. Physicians Surg. Pak.* **21**, 347–350 (2011).
11. Wossidlo, M. *et al.* Dynamic link of DNA demethylation, DNA strand breaks and repair in mouse zygotes. *EMBO J.* **29**, 1877–1888 (2010).
12. Jin, S. G., Kadam, S. & Pfeifer, G. P. Examination of the specificity of DNA methylation profiling techniques towards 5-methylcytosine and 5-hydroxymethylcytosine. *Nucleic Acids Res.* **38**, e125 (2010).
13. Huang, Y. *et al.* The behaviour of 5-hydroxymethylcytosine in bisulfite sequencing. *PLoS ONE* **5**, e8888 (2010).
14. Hattori, N. *et al.* Epigenetic control of mouse *Oct-4* gene expression in embryonic stem cells and trophoblast stem cells. *J. Biol. Chem.* **279**, 17063–17069 (2004).
15. Imamura, M. *et al.* Transcriptional repression and DNA hypermethylation of a small set of ES cell marker genes in male germline stem cells. *BMC Dev. Biol.* **6**, 34 (2006).
16. Farthing, C. R. *et al.* Global mapping of DNA methylation in mouse promoters reveals epigenetic reprogramming of pluripotency genes. *PLoS Genet.* **4**, e1000116 (2008).
17. Iqbal, K. *et al.* Subcutaneous panniculitis-like T-cell lymphoma in association with sarcoidosis. *Clin. Exp. Dermatol.* **36**, 677–679 (2011).
18. Bui, H. T. *et al.* The cytoplasm of mouse germinal vesicle stage oocytes can enhance somatic cell nuclear reprogramming. *Development* **135**, 3935–3945 (2008).
19. Yang, H. *et al.* High-efficiency somatic reprogramming induced by intact MI oocytes. *Cell Res.* **20**, 1034–1042 (2010).
20. Egli, D., Rosains, J., Birkhoff, G. & Eggan, K. Developmental reprogramming after chromosome transfer into mitotic mouse zygotes. *Nature* **447**, 679–685 (2007).
21. Egli, D., Sandler, V. M., Shinohara, M. L., Cantor, H. & Eggan, K. Reprogramming after chromosome transfer into mouse blastomeres. *Curr. Biol.* **19**, 1403–1409 (2009).
22. Seidman, J. G. & Seidman, C. Transcription factor haploinsufficiency: when half a loaf is not enough. *J. Clin. Invest.* **109**, 451–455 (2002).
23. Li, L. *et al.* The mildomycin biosynthesis: initial steps for sequential generation of 5-hydroxymethylcytidine 5'-monophosphate and 5-hydroxymethylcytosine in *Streptovorticillium rimofaciens* ZJU5119. *ChemBioChem* **9**, 1286–1294 (2008).
24. Erlanger, B. F. & Beiser, S. M. Antibodies specific for ribonucleosides and ribonucleotides and their reaction with DNA. *Proc. Natl Acad. Sci. USA* **52**, 68–74 (1964).
25. de Vries, W. N. *et al.* Expression of Cre recombinase in mouse oocytes: a means to study maternal effect genes. *Genesis* **26**, 110–112 (2000).
26. Ohbo, K. *et al.* Identification and characterization of stem cells in prepubertal spermatogenesis in mice. *Dev. Biol.* **258**, 209–225 (2003).

Supplementary Information is linked to the online version of the paper at www.nature.com/nature.

Acknowledgements We thank C. Walsh and M. Rots for critical reading of the manuscript, J. Walter for discussions, H. Qi for providing cDNA of mouse oocytes, R. Zhang & Q. Cui for *Tet3* cDNA, L. Li for help with 5hmCMP synthesis, Shanghai Research Center for Model Organisms for blastocyst injection, and J. Gao for mouse work. This study was supported by grants from the Ministry of Science and Technology China (2007CB947503 to G.-L.X., 2007CB947101 to J.L., and 2009CB941101 to G.-L.X. and J.L.), National Science Foundation of China (30730059 to G.-L.X. and 30871430 to J.L.), the Chinese Academy of Sciences (XDA01010301 to G.-L.X.; XDA01010403 and KSCX2-YW-R-110 to J.L.) and the NIH (GM078458 to Y.G.S.).

Author Contributions G.-L.X. and J.L. conceived the projects. Y.G.S., H.-P.W. and G.-L.X. contributed to the knockout design. F.G., T.-P.G., H.-P.W., G.-F.X., and W.L. performed the experiments on early embryos. X.H. and Z.D. contributed to the synthesis of the 5hmC hapten. H.Y. and L.S. performed the nuclear transfer and embryo transfer experiments. S.-g.J., K.L., P.E.S., G.P.P. and Z.-G.X. characterized Tet3 expression in PGCs and ovaries. G.-L.X. wrote and G.P.P. revised the manuscript.

Author Information Reprints and permissions information is available at www.nature.com/reprints. The authors declare no competing financial interests. Readers are welcome to comment on the online version of this article at www.nature.com/nature. Correspondence and requests for materials should be addressed to J.L. (jsli@sibs.ac.cn) or G.-L.X. (glxu@sibs.ac.cn).

METHODS

Preparation of anti-5hmC and anti-Tet3 antibodies. To prepare 5hmC antibody, 5-hydroxymethylcytidine 5'-monophosphate (5hmCMP) hapten was synthesized from cytidine 5'-monophosphate (CMP) in a reaction containing formaldehyde and tetrahydrofolate catalysed by recombinant MilA hydroxymethylase²³. The ribonucleoside hapten was then conjugated to BSA as previously described²⁴ for immunization of rabbits (Supplementary Fig. 1). Mass spectral analysis confirmed that the 5hmCMP base moiety was unaltered under the conjugation condition. The antibody was affinity-purified from antiserum with the 5hmCMP-BSA conjugate coupled to agarose beads. To ensure specificity, cross-reactivity was removed by incubation with agarose beads crosslinked with CMP-BSA conjugate.

For the detection of Tet3, two rabbit polyclonal antibodies were raised against a C-terminal region (amino acids 1159–1329, GenBank accession number NP_898961) and the targeted region (amino acids 887–962) respectively, affinity-purified and evaluated as described previously²⁷.

Immunostaining for 5hmC and Tet3 in fertilized oocytes. Immunofluorescence detection of 5hmC in zygotes derived from natural matings followed the procedure for 5mC¹¹. The signal was detected by Alexa Fluor-conjugated goat anti-rabbit or anti-mouse IgG (see Supplementary Table 4 for detailed antibody information). Fluorescent images were acquired at 2- μ m Z-axis intervals using a confocal microscope (Leica TCS SP5 II) and their signal intensity was determined using the Leica Application Suite-Advanced Fluorescence software.

The distribution of the Tet3 protein in embryonic cells was determined on embryos fixed with 4% paraformaldehyde (PFA) and permeabilized with 0.5% Triton.

Gene targeting. A targeting vector for *Tet3* was prepared using the recombineering technique²⁸ and electroporated into 129Sv ES cells for selection of targeted clones. The floxed region contains exons 8–9, which code for the region (76 amino acids from EEVLR to NGCTV, GenBank accession number NP_898961) containing the conserved Fe²⁺-binding motif of the catalytic domain. Deletion of the floxed region leads to the loss of 76 amino acids with in-frame fusion between exons 7 and 10. Neomycin-resistant embryonic stem clones were screened by PCR using a pair of primers crossing the shorter right homologous arm. Positive clones were further characterized by Southern blotting to confirm homologous recombination on the left side of the targeted genomic region (refer to Supplementary Fig. 7a). Embryonic stem cells carrying a correctly targeted allele (with *neo*) were injected into blastocysts to generate germline chimaeras. Mice with a floxed allele were obtained by breeding with C57BL/6J mice. The *neo* selection marker was removed in mice by crossing with ACTFLPe mice²⁹. To inactivate *Tet3* in germ cells from the PGC stage onwards, we generated conditional knockout mice by crossing floxed mice with TNAP-Cre knock-in mice. TNAP-Cre is expressed in primordial germ cells from embryonic day 9.5 to late gestation³⁰. To inactivate *Tet3* in female germ cells from the growing oocyte stage, we generated conditional knockout mice by crossing floxed mice with Zp3-Cre transgenic mice which express Cre exclusively in growing oocytes³¹. Mice were genotyped by PCR (primer sequences are presented in Supplementary Table 6). The conditional knockout mice were on a mixed C57BL/6J-129Sv genetic background.

Zygote collection. Wild-type BDF1 (from C57BL/6 \varnothing \times DBA2 σ) female mice 4- to 8-week-old injected with pregnant mare's serum gonadotropin and human chorionic gonadotropin were mated with BDF1 male. Zygotes were harvested at different time points after human chorionic gonadotropin injection. The PN stage of each individual zygote was classified according to ref. 11, by taking into account the pronuclear morphology and the presence of 5mC signal. We stained the DNA with DAPI (for fixed zygotes) or Hoechst 33258 (for live zygotes), and used a Nomarski differential interference contrast microscope for better observation of zygotic pronuclei, when necessary. Tet3-deficient zygotes were obtained from [*Tet3*^{fl/fl}, TNAP-Cre] female mice crossed with wild-type males.

Fertility test. [*Tet3*^{fl/fl}, TNAP-Cre] female mice at 6–8 weeks of age were housed with 8- to 12-week-old wild-type males of proven fertility. Rate of fertilization was judged by the presence of two pronuclei in zygotes collected from females after pregnant mare's serum gonadotropin and human chorionic gonadotropin treatment and mating with wild-type male mice of proven fertility. Number of completed pregnancies per plug seen (litters per plug) and number of viable pups born per litter (litter size) were calculated from the data included in Supplementary Table 2. [*Tet3*^{fl/+}, TNAP-Cre] female mice were used as a control group for comparison. Student's *t*-test was performed to compare averages in the two different experimental groups and *P* < 0.05 was considered to be significant.

Isolation of primordial germ cells (PGCs). Female CF1 (Charles River Laboratories) mice were mated with male OG2 (ref. 32) mice. This transgenic mouse line expresses the enhanced green fluorescent protein (EGFP) from the *Oct4* promoter and thus enables the selective purification of embryonic and fetal germ cells. Embryo parts enriched in PGCs and genital ridges were dissected at 9.5

and 11.5 days post coitum (dpc), respectively. At 9.5 dpc and 11.5 dpc, the sex of the embryo was determined by real-time PCR amplification of two genes in a single reaction. The *Sry* amplicon indicated the presence of Y chromosome and male sex, whereas amplification of the *Snrpn* gene served as a positive control for DNA. Gonads were dissected from male and female fetuses at 13.5, 15.5 and 17.5 dpc. Male and female gonads were distinguished by their distinct morphology at these stages. Gonads were incubated at 37 °C for 15 min in trypsin-EDTA and triturated to achieve a single cell suspension containing germ cells and somatic cells. Dulbecco's Modified Eagle's Medium (DMEM) (Invitrogen) supplemented with 20% FBS was added to inactivate trypsin. Cell suspensions were analysed and sorted on a MoFlo flow cytometer (Beckman Coulter). Data were acquired using 488 nm excitation from an Innova-306 Argon laser (Coherent) at 500 mW. EGFP emission was measured through a 530DF30 filter (Omega Optical).

Quantitative reverse transcription PCR. Poly(A⁺) mRNAs were isolated from zygotes (*n* = 200) and female PGCs (embryonic days 9.5, 11.5, 13.5, 15.5 and 17.5) by using the Dynabeads mRNA DIRECT Micro Kit (Invitrogen). Oligo (dT)25-coupled Dynabeads and mRNA complexes were immediately used for reverse transcription using SuperScript III reverse transcriptase (Invitrogen), according to the manufacturer's instructions. Real-time quantitative PCR reactions were performed at 50 °C for 2 min and 95 °C for 10 min followed by 50 cycles at 95 °C for 15 s and 60 °C for 1 min using TaqMan Gene Expression Master Mix (Applied Biosystems) on an iQ5 real-time PCR cycler (Bio-Rad). PCR was performed with TaqMan MGB primers with 6FAM-based probes (Applied Biosystems) using the following assay ID numbers: *Tet1* (Mm01169088_m1), *Tet2* (Mm01312907_m1), *Tet3* (Mm00805754_m1) and *Stellal/Dppa3* (Mm01184198_g1). The cDNA levels of target genes were analysed using a comparative C_t method and normalized to the internal standard gene *Gapdh*.

Collection of oocytes and production of parthenogenetic embryos. For collection of GV oocytes, the ovaries were removed from the female mice 42–44 h after pregnant mare's serum gonadotropin injection. Antral follicles were punctured by 30G needles, and cumulus-enclosed GV oocytes were released into HEPES-buffered CZB medium (HCZB) containing 0.2 mM 3-isobutyl-1-methylxanthine (IBMX) to inhibit germinal vesicle breakdown. Cumulus cells were removed by pipetting. For collection of mature oocytes, oviducts were removed from the female mice 13–15 h after human chorionic gonadotropin injection. Cumulus-oocyte complexes were released into HCZB containing 0.1% bovine testicular hyaluronidase (300 USP units per mg; ICN Biomedicals Inc.). MII oocytes were activated for 6 h in activation medium (calcium-free CZB medium containing 10 mM Sr²⁺ and 5 μ g ml⁻¹ cytochalasin B) to generate parthenogenetic embryos, which were cultured in KSOM medium with amino acids and harvested at 8 h post activation.

Intracytoplasmic sperm injection (ICSI). ICSI was performed according to the method of ref. 33 except for being performed at room temperature (about 25 °C). Briefly, sperm were collected from adult mice (Oct-delta PE-GFP #18) carrying *Oct4-EGFP* transgene (tg/tg)²⁶ and the head was separated from the tail by applying pulses to the head-tail junction by means of a Piezo-driven pipette (Piezoelectric actuator; PrimeTech). Only the sperm head was injected into each oocyte. Injected oocytes were cultured in KSOM medium for 96 h to examine their development *in vitro*. Images of resulting embryos were acquired with an IX51 inverted microscope (Olympus) under the same exposure parameters and the EGFP intensity of each embryo was quantified with ImageJ software³⁴.

Embryo transfer and Caesarean section. Fertilized eggs derived from natural matings were cultured in KSOM medium until the 2-cell stage. Two-cell embryos were then transferred into oviducts of surrogate females at day 1 of pseudopregnancy. For strict comparison, eight mutant and control 2-cell embryos (Supplementary Table 4) were transferred into the left and right oviducts of recipients, respectively. Recipient mothers were euthanized at 8.5, 11.5 and 14.5 days of gestation and embryos were dissected. For embryos developed to term, caesarean section was performed on day 19 and living pups were nursed by lactating ICR females.

Isolation of male pronuclei. Male pronuclei, which were distinguished from female pronuclei on the basis of their size and distance from polar bodies were harvested from zygotes of PN3–4 stages by breaking the zona using Piezo drive (Prime Tech) and aspirating using a micromanipulator. At least 40 male pronuclei from control or Tet3-deficient zygotes were collected and subjected to bisulphite sequencing analysis.

Bisulphite sequencing. For DNA methylation analysis in oocytes, pronuclei from zygotes and pseudo-pronuclei from NT embryos with limited numbers, bisulphite conversion was performed in agarose beads as described³⁵. Unbiased amplification for methylated and unmethylated sequences was ensured by testing bisulphite PCR primers using a 1:1 mixture of unmethylated and *in vitro* methylated DNA fragments. The PCR products were cloned into pMD19-T vectors (Takara Inc.) and individual clones were sequenced by BGI Ltd, Shanghai. Bisulphite primer

information is presented in Supplementary Table 6. For the determination of the methylation state of each sequence, the experiment was performed at least twice starting from the isolation of cells, pronuclei and embryos.

DNA immunoprecipitation with anti-5mC and anti-5hmC antibodies. To detect the existence of 5hmC at *Line1* repeats in the paternal genome in mouse zygotes, >100 male pronuclei were harvested from zygotes at PN3-4 stages, digested with proteinase K and RNase A, and the genomic DNA was purified by phenol-chloroform extraction. The genomic DNA was mixed with 250 ng of carrier lambda DNA (*dam*⁻, *dcm*⁻) and fragmented by AluI digestion, heat-denatured (10 min, 95 °C), and immunoprecipitated as described previously³⁶ using 1 µg of anti-5hmC or anti-5mC antibodies (Eurogentec, BI-MECY-1000) and 10 µl Dynabeads (coupled with M-280 sheep anti-rabbit IgG for the 5hmC antibody or anti-mouse IgG for the 5mC antibody). qPCR was performed on a BioRad CFX96 Real-Time PCR Detection System for the input and immunoprecipitated DNA. Mouse genomic DNA (10 ng) from Dnmt TKO embryonic stem cells lacking DNA methylation³⁷ and thus containing no 5hmC, was used as negative control. Mouse sperm DNA was used for comparisons.

Nuclear transfer with intact and enucleated oocytes. NT was performed as described³⁸ with modifications¹⁹. Briefly, metaphase II-arrested oocytes were collected from superovulated B6D2F1 or CKO females, and cumulus cells were removed using hyaluronidase. In the standard NT procedure, the oocytes were collected from wild-type and Tet3 CKO females, and enucleated in a droplet of HEPES-CZB medium containing 5 µg ml⁻¹ CB using a blunt Piezo-driven pipette. After enucleation, the spindle-free oocytes were washed extensively and maintained in CZB medium up to 2 h before nucleus injection. The cumulus cells collected from superovulated *Oct4-EGFP* transgenic mice were aspirated in and out of the injection pipette to remove the cytoplasmic material and then injected into enucleated oocytes. The reconstructed oocytes were cultured in CZB medium for 1 h and then activated for 5–6 h in activation medium. For NT with intact oocytes, oocytes were activated for 20 min and then directly injected with cumulus cells. The reconstructed oocytes were activated for 5–6 h in activation medium.

Following activation, the reconstructed embryos were cultured in KSOM medium with amino acids at 37 °C under 5% CO₂ in air. Embryo imaging and EGFP quantification followed the same procedure as in the ICSI experiment described above. The EGFP levels were determined from *n* > 6 embryos at each stage.

27. Ge, Y. Z. *et al.* Chromatin targeting of de novo DNA methyltransferases by the PWWP domain. *J. Biol. Chem.* **279**, 25447–25454 (2004).
28. Liu, P., Jenkins, N. A. & Copeland, N. G. A highly efficient recombineering-based method for generating conditional knockout mutations. *Genome Res.* **13**, 476–484 (2003).
29. Rodriguez, C. I. *et al.* High-efficiency deleter mice show that FLP_e is an alternative to Cre-*loxP*. *Nature Genet.* **25**, 139–140 (2000).
30. Lomeli, H., Ramos-Mejia, V., Gertsenstein, M., Lobe, C. G. & Nagy, A. Targeted insertion of Cre recombinase into the TNAP gene: excision in primordial germ cells. *Genesis* **26**, 116–117 (2000).
31. Lewandoski, M., Wassarman, K. M. & Martin, G. R. *Zp3-cre*, a transgenic mouse line for the activation or inactivation of *loxP*-flanked target genes specifically in the female germ line. *Curr. Biol.* **7**, 148–151 (1997).
32. Szabó, P. E., Hubner, K., Scholer, H. & Mann, J. R. Allele-specific expression of imprinted genes in mouse migratory primordial germ cells. *Mech. Dev.* **115**, 157–160 (2002).
33. Kimura, Y. & Yanagimachi, R. Intracytoplasmic sperm injection in the mouse. *Biol. Reprod.* **52**, 709–720 (1995).
34. Abràmoff, M. D., Magalhães, P. J. & Ram, S. J. Image processing with ImageJ. *Biophotonics Int.* **11**, 36–42 (2004).
35. Hajkova, P. *et al.* DNA-methylation analysis by the bisulfite-assisted genomic sequencing method. *Methods Mol. Biol.* **200**, 143–154 (2002).
36. Weber, M. *et al.* Chromosome-wide and promoter-specific analyses identify sites of differential DNA methylation in normal and transformed human cells. *Nature Genet.* **37**, 853–862 (2005).
37. Tsumura, A. *et al.* Maintenance of self-renewal ability of mouse embryonic stem cells in the absence of DNA methyltransferases Dnmt1, Dnmt3a and Dnmt3b. *Genes Cells* **11**, 805–814 (2006).
38. Wakayama, T., Perry, A. C., Zuccotti, M., Johnson, K. R. & Yanagimachi, R. Full-term development of mice from enucleated oocytes injected with cumulus cell nuclei. *Nature* **394**, 369–374 (1998).

Derivation of haploid embryonic stem cells from mouse embryos

Martin Leeb¹ & Anton Wutz¹

Most animals are diploid, but haploid-only and male-haploid (such as honeybee and ant) species have been described¹. The diploid genomes of complex organisms limit genetic approaches in biomedical model species such as mice. To overcome this problem, experimental induction of haploidy has been used in fish^{2,3}. Haploid development in zebrafish has been applied for genetic screening². Recently, haploid pluripotent cell lines from medaka fish (*Oryzias latipes*) have also been established³. In contrast, haploidy seems less compatible with development in mammals^{4,5}. Although haploid cells have been observed in egg cylinder stage parthenogenetic mouse embryos⁶, most cells in surviving embryos become diploid. Here we describe haploid mouse embryonic stem cells and show their application in forward genetic screening.

Previous attempts to establish pluripotent stem-cell lines from haploid mouse embryos have resulted in the isolation of parthenogenetic embryonic stem (ES) cells with a diploid karyotype⁴. These studies reported the development of apparently normal haploid mouse blastocysts with a defined inner cell mass (ICM)^{4,5}. To investigate the haploid ICM, we cultured haploid mouse blastocysts in chemically defined medium with inhibitors of mitogen activated protein kinase kinase and glycogen synthase kinase 3. This 2i medium⁷ has previously been used for isolating ES cells from mouse strains that have been refractory to this process⁸ and from rats⁹, and may help to maintain certain characteristics of early mouse epiblast cells^{10,11}.

We generated haploid mouse embryos by activation of unfertilized oocytes isolated from superovulated B6CBAF1 hybrid female mice using strontium chloride. After culture in M16 medium, 30 blastocysts (22%) were obtained from 132 activated oocytes and used for ES cell derivation. After removal of the zona and trophectoderm, ICMs were cultured in gelatinized 96-well dishes in 2i medium in the presence of leukaemia inhibitory factor (LIF). Twenty-seven ES cell lines were obtained (93%). Individual ES cell lines were expanded and their DNA content was analysed by flow analysis using diploid ES cells as controls (Fig. 1a, b). In six ES cell lines, at least 10% of the cells had a haploid DNA content and the proportion of haploid cells could reach a conservatively estimated 60% (Fig. 1b). Further enrichment was achieved by flow sorting of cells with a haploid DNA content after staining with Hoechst 33342 (Fig. 1c). This allowed expansion of haploid ES cell lines for over 35 passages.

We further tested the requirements for deriving haploid mouse ES cells (Table 1). These experiments showed that removal of the trophectoderm by immunosurgery was not essential. Haploid ES cells could also be established using DMEM medium supplemented with knockout serum replacement and LIF, showing that derivation without kinase inhibitors is possible (Table 1 and Supplementary Fig. 1). We further succeeded in isolating haploid ES cells from the 129Sv inbred mouse strain and two genetically modified mouse lines. In the latter, several alleles had been bred to homozygosity and maintained on a mixed genetic background for several generations (Table 1 and Supplementary Fig. 2). In summary, we derived 25 haploid ES cell lines in 7 independent experiments. Haploid ES cell cultures could also

be maintained on feeders in serum containing DMEM supplemented with LIF.

Haploid ES cells exhibited a typical mouse ES cell colony morphology (Fig. 1d). Chromosome spreads showed 20 chromosomes corresponding to the haploid mouse chromosome set (Fig. 1e, f). For further characterizing the genetic integrity we performed comparative genomic hybridization (CGH) of four haploid ES cell lines and control DNA from the CBA strain and the mixed transgenic mouse line from which HTG-1 and HTG-2 ES cells were derived (Fig. 1g, h and Supplementary Figs 3 and 4). Copy number variations (CNVs) that were detected in the genome of haploid ES cell lines were also present in the strains of origin (Supplementary Table 1). Although some CNVs seemed to be specific to haploid ES cells, inspection of the actual signals (Supplementary Fig. 4) indicated that these CNVs were also present in the CBA or HTG control DNAs but not detected with the threshold applied. CNVs between the C57BL/6 and CBA strain of mice were consistent with a previously reported analysis¹². Taken together, these data show that haploid ES cells maintained an intact haploid genome without amplifications or losses.

At the molecular level, haploid ES cells expressed pluripotency markers including *Oct4* (also called *Pou5f1*), *Rex1* (also called *Zfp42*), *Klf4*, *Sox2* and *Nanog* (Fig. 2a, b). Genome-wide expression analysis showed a high correlation (Pearson correlation coefficient $r = 0.97$ over all genes) between haploid ES cells and control diploid male ES cells (Fig. 2c and Supplementary Fig. 5). In haploid ES cells 279 and 194 genes were more than twofold upregulated or downregulated ($P < 0.05$), respectively (Supplementary Table 2). Among these, 99 X-linked genes were overexpressed and 4 Y-linked genes were lost in haploid ES cells, consistent with different sex chromosome constitutions (Fig. 2d). Thus, haploid ES cells largely maintain a mouse ES cell transcription profile.

This prompted us to investigate the developmental potential of haploid ES cells. For this we introduced a piggyBac transposon vector for expressing green fluorescent protein (GFP) into HAP-2 ES cells. Flow sorting of cells for GFP fluorescence and DNA staining with Hoechst 33342 yielded a haploid ES cell population that expressed GFP at high level, showing that a haploid genome content was maintained during the transfection procedure (Supplementary Fig. 6). GFP-marked haploid ES cells contributed substantially to chimaeric embryos when injected into C57BL/6 blastocysts (Fig. 3a). The great majority of GFP-positive cells extracted from chimaeric embryos had a diploid DNA content (Fig. 3b), indicating that haploid ES cells contributed extensively to development after diploidization. We also obtained two male and two female live-born chimaeras with a substantial contribution from haploid ES cells (Fig. 3c). These mice developed normally with apparent coat colour chimaerism. Similar results were obtained with the HAP-1 and HTG-2 ES cells (Fig. 3d and Supplementary Fig. 7a). Furthermore, the diploid fraction of HAP-2 ES cells at passage 31 could be differentiated into nestin-positive cells after a neural *in vitro* differentiation protocol¹³ (Supplementary Fig. 7b). Taken together, these findings demonstrate that haploid ES cells maintain a wide differentiation potential.

¹Wellcome Trust Centre for Stem Cell Research, University of Cambridge, Tennis Court Road, Cambridge CB2 1QR, UK.

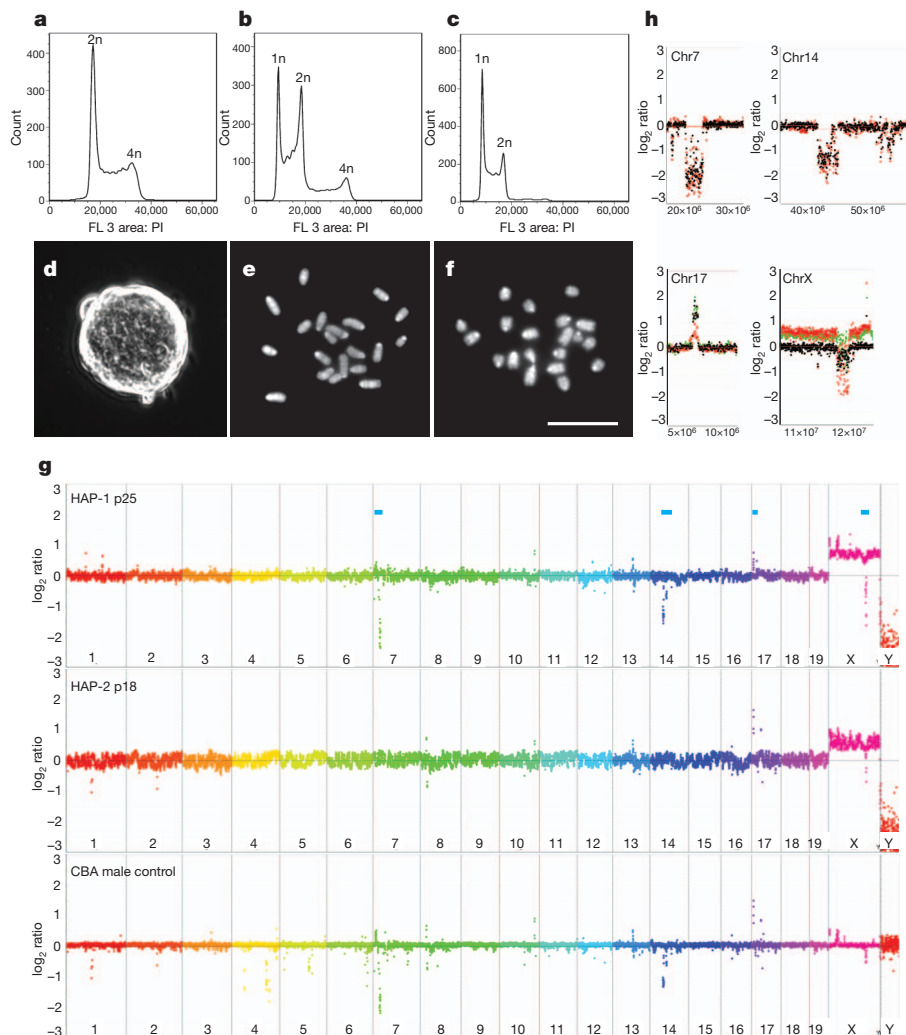


Figure 1 | Derivation of haploid ES cells. **a–c**, Flow analysis of DNA after propidium iodide (PI) staining of diploid control ES cells (**a**), haploid ES cell line HAP-1 at passage 7 (p7) (**b**) and HAP-1 (p11) after sorting at p7 (**c**). The x axis shows fluorescence intensity. **d**, Colony morphology of haploid ES cells (HAP-1). **e**, **f**, Chromosome spreads of HAP-3 (**e**) and HAP-1 (**f**). Scale bar, 10

µm. **g**, CGH analysis of HAP-1 and HAP-2 ES cells and control male CBA kidney DNA. Relative copy number is plotted at 200-kb resolution using a log₂ scale. Genomic positions indicated by blue bars (top) are enlarged at 40-kb resolution in **h**. CBA control, black; HAP-1, red; HAP-2, green.

To investigate the utility of haploid ES cells for genetic screening, we performed a pilot screen for mismatch repair genes following a previously published strategy¹⁴. For this, 5×10^6 haploid ES cells were co-transfected with a gene trap piggyBac transposon vector (Supplementary Fig. 8a) and a plasmid for expressing an optimized piggyBac transposase¹⁵. Gene-trap insertions were selected with puromycin. A pool of 1×10^7 cells was then cultured in the presence of 2-amino-6-mercaptopurine (6-TG), which is toxic to mismatch-repair-proficient cells. After 8 days, 20 6-TG-resistant colonies were

isolated and the integration sites were mapped using Splinkerette PCR¹⁶. Of seven clones analysed we identified two independent insertions in *Msh2* and one in *Hprt* (Supplementary Fig. 8b). *Msh2* is a known mismatch repair gene and *Hprt* is required for converting 6-TG into a toxic metabolite¹⁴. Thus, identification of mutations in autosomal genes was possible, indicating a potential for haploid ES cells in forward genetic screening in mammals.

The difficulty in obtaining haploid ES cell lines in previous attempts might be explained by aberrant gene regulation such as aberrant dosage

Table 1 | Derivation of haploid mouse ES cell lines

Experiment no.	Derivation protocol	Names of ES cell lines	Genetic background	Oocytes activated	Number of blastocysts	ES cell lines obtained	ES cell lines with haploid contribution (maximum % haploid before sorting)
1	2i/immunosurgery	HAP-1 to HAP-6*	B6CBAF1	132	30	27	6 (>60%)
2	2i	HAP-7	B6CBAF1	22	10	5	1 (>15%)
3	2i	HTG-1 to HTG-3†	Mixed TG‡	50	32	3	3 (>90%)
4	KSR/immunosurgery	HAP-8 to HAP-13	B6CBAF1	273	48	22	6 (>10%)
5	2i	H129B6-1 to H129B6-5	129B6F1	250	37	8	5 (>10%)
6	2i	HTX-1	Mixed TG§	70	11	1	1 (>40%)
7	2i	H129-1 to H129-3	129Sv	140	13	10	3 (>60%)

KSR, knockout serum replacement.

*Contribution to chimaeric mice was confirmed for the HAP-1 and HAP-2 haploid ES cell lines.

†Contribution to chimaeric mice was confirmed for the HTG-1 haploid ES cell line.

‡Derived from *ROSA26^{nlstTA} LC1 Xist^{2LOX}* homozygous female mice.

§Derived from *ROSA26^{nlstTA} tetOPXist* homozygous female mice²⁶.

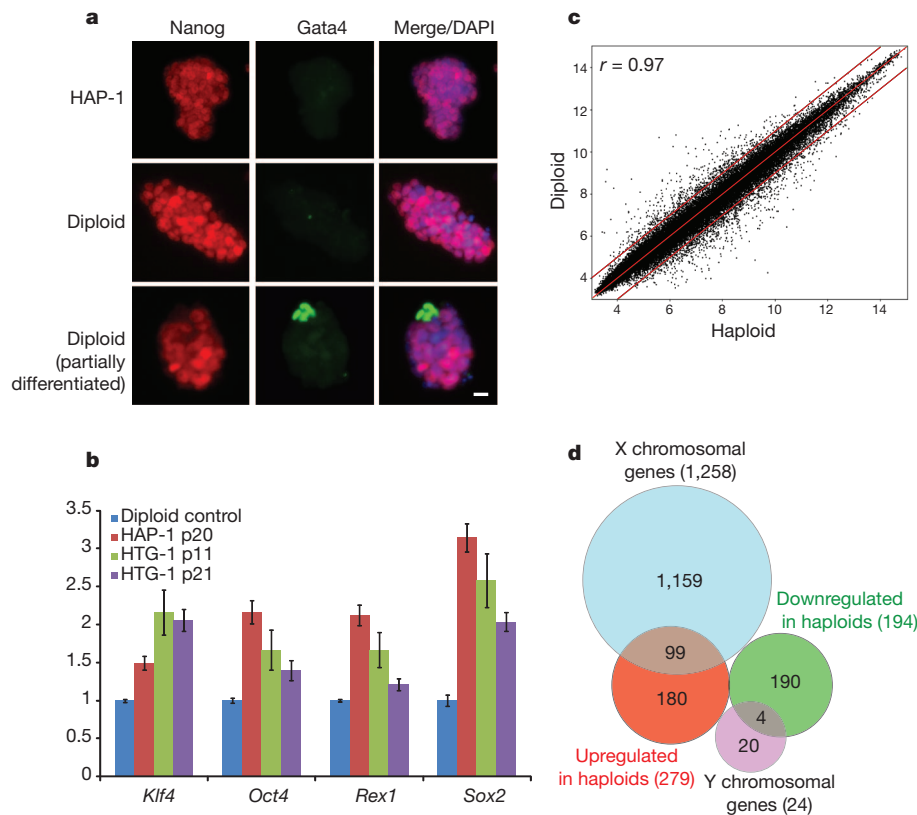
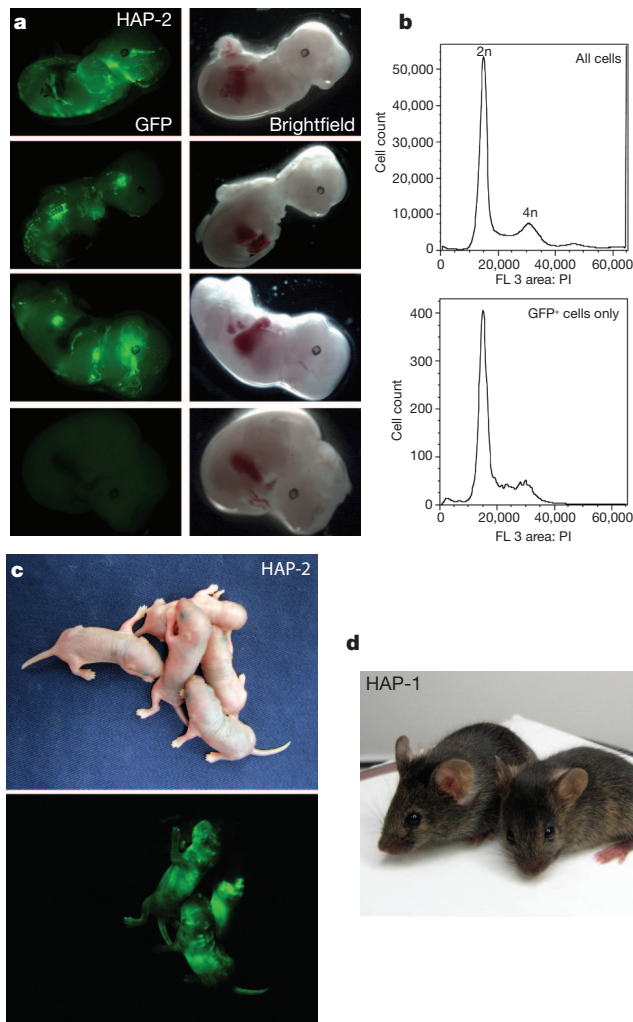


Figure 2 | Expression analysis of haploid ES cells. **a**, Immunofluorescence shows Nanog protein (red) in haploid (HAP-1) and diploid ES cells, and Gata4 (green) in differentiated cells. Scale bar, 10 μ m. **b**, Expression of pluripotency markers in haploid and diploid (set to 1) ES cells by real-time PCR. Error bars represent standard deviation ($n = 3$). **c**, Scatter plot showing \log_2 transformed average expression values from gene expression profiles of three haploid (HAP-1, HAP-2 and HTG-1) and three diploid J1 ES cell lines for 45,001 probe sets (r is the Pearson correlation coefficient; red lines indicate twofold upregulation and downregulation). **d**, Diagram of more than twofold upregulated and downregulated genes in haploid ES cells.



compensation and genomic imprinting. However, diploid ES cells from mouse and human parthenogenetic embryos have been established^{17,18}. Misregulation of X-inactivation has been observed to some extent in haploid mouse embryos⁵ and has also been shown to reduce the efficiency of producing cloned mice¹⁹. Thus, it is conceivable that X-inactivation is initiated aberrantly in haploid embryos during some ES cell derivation procedures. Direct capture of naive pluripotent cells from ICM outgrowths, as accentuated by the use of 2i conditions¹¹, could have contributed to the success of our study.

Previously, near-haploid cells have been observed in human tumours (see ref. 20 for a review), and a near-haploid human-tumour-derived cell line has been described^{21,22}. These tumour cells carry genomic rearrangements and mutations that might stabilize the haploid genome. An interesting aspect of haploid ES cells is their developmental potential. We have observed rapid diploidization when haploid ES cells differentiate. The resulting diploid parthenogenetic cells can contribute to development²³. It is interesting to speculate whether differentiated haploid lineages can be generated, perhaps through suppression of X-inactivation, and whether it is possible to derive haploid human ES cells.

METHODS SUMMARY

For the derivation of haploid ES cells, mouse oocytes were activated in M16 medium as described²⁴. ES cell culture in chemically defined 2i medium has been described previously^{7,8}. Cell sorting for DNA content was performed after staining with 15 μ g ml⁻¹ Hoechst 33342 (Invitrogen) on a MoFlo flow sorter (Beckman Coulter) selecting the haploid 1n peak. For analytic flow profiles, cells were fixed in

Figure 3 | Developmental potential of haploid ES cells. **a**, GFP-marked haploid HAP-2 ES cells (p18) contribute to chimaeric embryos at E12.5. Six out of nine embryos showed GFP contribution. A GFP-negative embryo is shown as a control (bottom). **b**, Representative flow analyses of DNA content of all cells (top) and GFP-positive cells (bottom) extracted from a chimaeric E12.5 embryo are shown. All six embryos gave similar results. **c**, Live-born chimaeric mice were obtained from GFP-marked HAP-2 ES cells. **d**, Chimaeric mice obtained from injection of HAP-1 ES cells into C57BL/6 blastocysts (black) show coat colour contribution from the ES cells (agouti).

ethanol, treated with RNase, and stained with propidium iodide. For karyotype analysis, cells were arrested in metaphase with demecolcine (Sigma). After incubation in hypotonic KCl buffer, cells were fixed in methanol-acetic acid (3:1) and chromosome spreads were prepared and stained with DAPI. RNA was extracted using the RNeasy kit (Qiagen). Transcription profiles were generated using Affymetrix GeneChip 430.2 arrays. Sample preparation, hybridization and basic data analysis were performed by Imagenes. Further analysis was performed using the Genespring GX software (Agilent). For CGH analysis, genomic DNA was isolated from haploid ES cell lines and hybridized to NimbleGen 3x720K whole-genome tiling arrays by Imagenes using C57BL/6 kidney DNA as a reference. For chimera experiments, GFP-labelled HAP-1 (p29), HAP-2 (p18) and HTG-2 (p23) ES cells were injected into C57BL/6 host blastocysts. Live-born chimaeras were analysed for expression of GFP at postnatal day 2. Genetic screening was performed following a previously published strategy²⁵. In brief, HAP-1 ES cells were co-transfected with 2 µg piggyBac transposase expression vector¹⁵ and 1 µg piggyBac gene-trap vector (Supplementary Fig. 8) using Lipofectamine 2000 (Invitrogen). Selection for transposon insertions was performed using 2 µg ml⁻¹ puromycin for 8 days. 1×10^7 puromycin-resistant ES cells were plated in two 15-cm dishes and mutations in mismatch repair genes were selected using 0.3 µg ml⁻¹ 6-TG (Sigma). piggyBac integration sites in seven 6-TG-resistant clones were mapped by Splinkerette PCR¹⁶.

Full Methods and any associated references are available in the online version of the paper at www.nature.com/nature.

Received 14 March; accepted 16 August 2011.

Published online 7 September 2011.

- Otto, S. P. & Jarne, P. Evolution. Haploids—hapless or happening? *Science* **292**, 2441–2443 (2001).
- Wiellette, E. *et al.* Combined haploid and insertional mutation screen in the zebrafish. *Genesis* **40**, 231–240 (2004).
- Yi, M., Hong, N. & Hong, Y. Generation of medaka fish haploid embryonic stem cells. *Science* **326**, 430–433 (2009).
- Kaufman, M. H., Robertson, E. J., Handyside, A. H. & Evans, M. J. Establishment of pluripotential cell lines from haploid mouse embryos. *J. Embryol. Exp. Morphol.* **73**, 249–261 (1983).
- Latham, K. E., Akutsu, H., Patel, B. & Yanagimachi, R. Comparison of gene expression during preimplantation development between diploid and haploid mouse embryos. *Biol. Reprod.* **67**, 386–392 (2002).
- Kaufman, M. H. Chromosome analysis of early postimplantation presumptive haploid parthenogenetic mouse embryos. *J. Embryol. Exp. Morphol.* **45**, 85–91 (1978).
- Ying, Q. L. *et al.* The ground state of embryonic stem cell self-renewal. *Nature* **453**, 519–523 (2008).
- Nichols, J. *et al.* Validated germline-competent embryonic stem cell lines from nonobese diabetic mice. *Nature Med.* **15**, 814–818 (2009).
- Buehr, M. *et al.* Capture of authentic embryonic stem cells from rat blastocysts. *Cell* **135**, 1287–1298 (2008).
- Nichols, J., Silva, J., Roode, M. & Smith, A. Suppression of Erk signalling promotes ground state pluripotency in the mouse embryo. *Development* **136**, 3215–3222 (2009).
- Nichols, J. & Smith, A. The origin and identity of embryonic stem cells. *Development* **138**, 3–8 (2011).
- Cutler, G., Marshall, L. A., Chin, N., Baribault, H. & Kassner, P. D. Significant gene content variation characterizes the genomes of inbred mouse strains. *Genome Res.* **17**, 1743–1754 (2007).
- Pollard, S. M., Benchoua, A. & Lowell, S. Neural stem cells, neurons, and glia. *Methods Enzymol.* **418**, 151–169 (2006).
- Li, M. A., Pettitt, S. J., Yusa, K. & Bradley, A. Genome-wide forward genetic screens in mouse ES cells. *Methods Enzymol.* **477**, 217–242 (2010).
- Cadinanos, J. & Bradley, A. Generation of an inducible and optimized piggyBac transposon system. *Nucleic Acids Res.* **35**, e87 (2007).
- Mikkers, H. *et al.* High-throughput retroviral tagging to identify components of specific signaling pathways in cancer. *Nature Genet.* **32**, 153–159 (2002).
- Mai, Q. *et al.* Derivation of human embryonic stem cell lines from parthenogenetic blastocysts. *Cell Res.* **17**, 1008–1019 (2007).
- Revazova, E. S. *et al.* Patient-specific stem cell lines derived from human parthenogenetic blastocysts. *Cloning Stem Cells* **9**, 432–449 (2007).
- Inoue, K. *et al.* Impeding Xist expression from the active X chromosome improves mouse somatic cell nuclear transfer. *Science* **330**, 496–499 (2010).
- Sukov, W. R. *et al.* Nearly identical near-haploid karyotype in a peritoneal mesothelioma and a retroperitoneal malignant peripheral nerve sheath tumor. *Cancer Genet. Cytogenet.* **202**, 123–128 (2010).
- Kotecki, M., Reddy, P. S. & Cochran, B. H. Isolation and characterization of a near-haploid human cell line. *Exp. Cell Res.* **252**, 273–280 (1999).
- Carette, J. E. *et al.* Haploid genetic screens in human cells identify host factors used by pathogens. *Science* **326**, 1231–1235 (2009).
- Jiang, H. *et al.* Activation of paternally expressed imprinted genes in newly derived germline-competent mouse parthenogenetic embryonic stem cell lines. *Cell Res.* **17**, 792–803 (2007).
- Kishigami, S. & Wakayama, T. Efficient strontium-induced activation of mouse oocytes in standard culture media by chelating calcium. *J. Reprod. Dev.* **53**, 1207–1215 (2007).
- Guo, G., Wang, W. & Bradley, A. Mismatch repair genes identified using genetic screens in Bln-deficient embryonic stem cells. *Nature* **429**, 891–895 (2004).
- Savarese, F., Flahndorfer, K., Jaenisch, R., Busslinger, M. & Wutz, A. Hematopoietic precursor cells transiently reestablish permissiveness for X inactivation. *Mol. Cell. Biol.* **26**, 7167–7177 (2006).

Supplementary Information is linked to the online version of the paper at www.nature.com/nature.

Acknowledgements We thank A. Smith and J. Nichols for critical discussion; K. Jones for advice on cell culture; S. Dietmann for bioinformatics support; and R. Walker for cell sorting. We would also like to thank B. Mansfield and C.-E. Dumeau for their help, and the BSU team at the centre for maintaining the mouse colony. This work was supported by a Wellcome Trust Senior Research Fellowship to A.W. (grant reference 087530/Z/08/A) and an EMBO Long Term Fellowship to M.L.

Author Contributions M.L. performed the experiments, analysed the data and wrote the manuscript. A.W. performed some experiments, wrote the paper and supervised the study.

Author Information Gene expression and CGH data sets can be accessed as the GEO reference series GSE30879 (<http://www.ncbi.nlm.nih.gov/geo/query/acc.cgi?acc=GSE30879>). This series includes the GSE30744 (Expression analysis of haploid and diploid ES cells in 2i medium) and the GSE30749 (CGH analysis of haploid ES cells) data sets. Reprints and permissions information is available at www.nature.com/reprints. The authors declare competing financial interests: details accompany the full-text HTML version of the paper at www.nature.com/nature. Readers are welcome to comment on the online version of this article at www.nature.com/nature. Correspondence and requests for materials should be addressed to A.W. (aw512@cam.ac.uk).

METHODS

Derivation of haploid ES cells. Oocytes were isolated from superovulated females and activated in M16 medium using 5 mM strontium chloride and 2 mM EGTA as described²⁴. Embryos were subsequently cultured in M16 or KSOM medium microdrops covered by mineral oil. Under these conditions around 80% of oocytes reached the 2-cell stage on the next morning. Thereafter development of pre-implantation embryos was variable with a large number of embryos showing unequally sized blastomeres or unusual embryo morphology. Removal of the zona, immunosurgery for removal of the trophectoderm and ES cell derivation were performed as described previously^{7,8}. ES cells were cultured in chemically defined 2i medium plus LIF as described^{7,8} with minor modifications. 2i medium was supplemented with non-essential amino acids and 0.35% BSA fraction V. Culture of ES cells on feeders was performed as previously described²⁷. Knockout serum replacement was obtained from Invitrogen. Cell sorting for DNA content was performed after staining with $15 \mu\text{g ml}^{-1}$ Hoechst 33342 (Invitrogen) on a MoFlo flow sorter (Beckman Coulter). The haploid 1n peak was purified. Diploid cells did arise in cultures to various extents in all ES cell lines. Periodic purification by flow sorting every four to five passages allowed us to maintain cultures containing a great majority of haploid ES cells in all cases. Analytic flow profiles of DNA content were recorded after fixation of the cells in ethanol, RNase digestion and staining with propidium iodide (PI) on a Cyan analyser (Beckman Coulter). For karyotype analysis, cells were arrested in metaphase using demecolcine (Sigma). After incubation in hypotonic KCl buffer, cells were fixed in methanol-acetic acid (3:1) and chromosome spreads were prepared and stained with DAPI. Immunostaining was performed as described²⁸ using Nanog (Abcam; 1:100), Oct4 (Santa Cruz; 1:100), nestin (Developmental Studies Hybridoma bank; 1:30) and Gata4 (Santa Cruz; 1:200) antibodies.

Microarray analysis. RNA from biological triplicates of diploid ES cells and three independently derived haploid ES cells (HAP-1 p21, HAP-2 p24, HTG-1 p11) was extracted using the RNeasy kit (Qiagen). Gene expression analysis on Affymetrix GeneChip 430 2.0 arrays was performed by Imagenes. Additional gene expression profiles of neural progenitors, mesodermal progenitors and mouse embryonic fibroblasts (MEFs) were obtained from a previously published data set (GEO accession number GSE12982 (ref. 29)). The data were analysed using Genespring GX software (Agilent Technologies). Data were normalized using the RMA algorithm. Lists showing differentially regulated genes (>2 -fold change; $P < 0.05$) are provided in Supplementary Table 2. P values were established by an unpaired t -test followed by FDR adjustment by the Benjamini Hochberg method. Hierarchical clustering was performed based on the Euclidean distances and complete linkage analysis. The relatedness of transcription profiles was determined by calculating the Pearson correlation coefficient (r). DNA samples for CGH experiments were extracted and sent to Imagenes for CGH analysis using NimbleGen 3x720K mouse whole-genome tiling arrays with an average probe spacing of 3.5 kb. Adult male C57BL/6 kidney DNA was used as a reference. A genomic overview of these analyses is presented in Fig. 1g and Supplementary Fig. 3 at

200-kb resolution and selected magnified regions at 40-kb resolution. The complete data set at 40-kb resolution is included in Supplementary Fig. 4.

Accession of data sets. Gene expression and CGH data sets can be accessed as the GEO reference series GSE30879 (<http://www.ncbi.nlm.nih.gov/geo/query/acc.cgi?acc=GSE30879>). This series includes the GSE30744 (Expression analysis of haploid and diploid ES cells in 2i medium) and the GSE30749 (CGH analysis of haploid ES cells) data sets.

Quantitative gene expression analysis. RNA was extracted using the RNeasy kit (Qiagen) and converted into cDNA using the Quantitect reverse transcription kit (Qiagen). Real-time PCR was performed on a StepOnePlus machine (Applied Biosystems) using the Fast Sybr green master mix (Applied Biosystems) and previously published primers²⁸. The $\Delta\Delta C_t$ method was used for quantification of gene expression. Expression levels were normalized to L32 ribosomal protein mRNA and values in diploid control ES cells were set to 1.

Embryo analysis. Haploid ES cells were co-transfected with a piggyBac vector carrying a CAG-GFP-IRES-hygro transgene and a piggyback transposase expression plasmid. Stable integrants were selected using $150 \mu\text{g ml}^{-1}$ hygromycin for 7 days. The haploid fraction of HAP-1 (p29), HAP-2 (p18) and HTG-2 (p23), GFP-positive cells were purified by flow sorting (Supplementary Fig. 6). GFP-labelled ES cells were expanded and injected into C57BL/6 host blastocysts which were transferred to recipient females. Embryos were analysed at E9.5 and E12.5. Dissociation to single cells was performed by incubation in 0.25% trypsin/EDTA for 15 min. Before PI staining, cells were fixed in 4% PFA and permeabilized in PBS/0.25% Triton X-100. Live-born chimaeras were analysed at postnatal day 2 (P2) for expression of GFP using ultraviolet illumination. Images were obtained using a Canon Powershot S5 IS camera with a FHS/EF-3GY2 filter (BLS). All mouse experiments were conducted in accordance with institutional guidelines of the University of Cambridge. All necessary UK home office licenses were in place.

Gene-trap screen. The screen was performed based on a previously published protocol²⁵. 5×10^6 HAP-1 ES cells were co-transfected with $2 \mu\text{g}$ piggyBac transposase plasmid¹⁵ and $1 \mu\text{g}$ piggyBac gene-trap vector (Supplementary Fig. 8a) using Lipofectamine 2000. piggyBac insertions into expressed genes were selected with $2 \mu\text{g ml}^{-1}$ puromycin for 8 days. 1×10^7 ES cells corresponding to approximately 5,000 puromycin-resistant colonies were then plated onto two 15 cm dishes. Selection for mismatch-deficient integrants was performed using $0.3 \mu\text{g ml}^{-1}$ 6-TG (Sigma). Twenty colonies were picked and piggyBac integration sites of seven clones were identified by Splinkerette PCR and mapped using iMapper³⁰.

27. Wutz, A. & Jaenisch, R. A shift from reversible to irreversible X inactivation is triggered during ES cell differentiation. *Mol. Cell* **5**, 695–705 (2000).
28. Leeb, M. *et al.* Polycomb complexes act redundantly to repress genomic repeats and genes. *Genes Dev.* **24**, 265–276 (2010).
29. Shen, X. *et al.* EZH1 mediates methylation on histone H3 lysine 27 and complements EZH2 in maintaining stem cell identity and executing pluripotency. *Mol. Cell* **32**, 491–502 (2008).
30. Kong, J., Zhu, F., Stalker, J. & Adams, D. J. iMapper: a web application for the automated analysis and mapping of insertional mutagenesis sequence data against Ensembl genomes. *Bioinformatics* **24**, 2923–2925 (2008).